Conception de nano-objets à base de MOFs pour des applications biomédicales

Heng Zhao

PSL UNIVERSITÉ PARIS

THÈSE DE DOCTORAT
DE L'UNIVERSITÉ PSL

Préparée à l'école normale supérieure et à l'école supérieure de physique et chimie industrielles de Paris

Conception de nano-objets à base de MOFs pour des applications biomédicales

Design of MOFs based nano-objects for biomedical applications

Soutenue par
Heng ZHAO
Le 16. 12. 2022

Ecole doctorale n° 397
Physique et chimie des matériaux

Spécialité
Chimie des matériaux

Composition du jury :

Hélène, SERIER-BRAULT Maître de Conférences, Université de Nantes	*Rapporteur*
Olivier, SANDRE Directeur de recherche, Université de Bordeaux	*Rapporteur*
Julien, NICOLAS Directeur de recherche, Université Paris Sud	*Président du jury*
Bich-Thuy, DOAN Chargée de recherche, Chimie ParisTech	*Examinateur*
Nathalie STEUNOU Professeur, Université de Versailles Saint-Quentin-en-Yvelines	*Co-directrice de thèse*
Christian SERRE Directeur de Recherche, École Normale Supérieure et École Supérieure de Physique et de Chimie Industrielles de Paris	*Directeur de thèse*
Eddy DUMAS Maître de Conférences, Université de Versailles Saint-Quentin-en-Yvelines	*Co-encadrant* *Membre Invité*
Florence GAZEAU Directeur de Recherche, Université Paris Cité	*Membre Invité*

ENS | PSL

ESPCI PARIS | PSL

THÈSE DE DOCTORAT

DE L'UNIVERSITÉ PSL

Acknowledgments

First of all, I would like to thank all the people who helped me during my PhD thesis at École Normale Supérieure (ENS) and École Supérieure de Physique et Chimie Industrielles de Paris (ESPCI) in my four years' PhD study. I would like to thank the Chinese Scholarship Council (CSC), which supported funding for my PhD thesis.

I would like to express my sincere appreciation to my thesis director **Dr. Christian Serre** for giving me the chance of interview and the acceptance to my application. Without your offer, I cannot start my PhD in the field of Metal-Organic Framworks (MOFs). Also, I would like to thank my co-director **Prof. Nathalie Steunou** and supervisor **Dr. Eddy Dumas** for their supervision. I appreciate all the discussions with you, which are vital for finishing my papers and thesis. Your broad knowledgeable, rigorous attitude and constructive views have impressed me a lot and will continue to guide me in the future academic career.

I am grateful to all the members of the thesis committee, **Dr. Hélène Serier-brault**, **Dr. Olivier Sandre**, **Dr. Julien Nicolas**, **Dr. Bich-Thuy Doan** for the acceptance to participate in the evaluation of this thesis and I appreciate all your time and efforts. I have gained a better understanding of the field through the discussions with you during the defense and your suggestions are definitely helpful for the future work.

I wish to show my deepest gratitude with all my heart to all collaborators, **Dr. Florent Carn**, **Prof. Florence Gazeau** and **Sonia Becharef** from Université Paris Cité, **Dr. Saad Sene**, **Dr. Gilles Patriarche**, **Dr. Christine Péchoux**, **Dr. Nathalie Guillou**, **Dr. Joseph Scola** and **Dr. Simona Mura** from Université Paris-Saclay, **Dr. Dris Ihiawakrim** and **Prof. Ovidiu Ersen** from Université de Strasbourg, **Dr. Sylvain Miraux** from Université de Bordeaux, **Dr. Nicolas Menguy** from Sorbonne Université. I would like also to thank **Dr. Bich-thuy Doan** and **Dr. Johanne Seguin** for the help with MRI and NIR fluorescence imaging. I learned a lot from all of you through the discussions with you, which I believe benefits very much for my entire PhD thesis.

I would also take this opportunity to give my special gratitude to all the biomedicine team colleagues in IMAP: **Angelika**, **Ioanna**, **Xin**, **Zhihao,** my intern **Camille**, **Yutong**, **Shaokang**, new visiting scholar **Meng**, former intern **Andrea**, **Lucile Fétiveau** from Celescreen Company and **Rosana** who is a postdoctoral researcher in a different field now. I appreciate these useful discussions with you and I will never forget the scene of solving instrumental problems together. Also, I enjoyed the monthly

biomeeting with our nanopore colleagues very much: **Ben**, **My-an**, **Manon** and especially **Dr. Mathilde Lepoitevin**, thank you for your help with series of trainings and administrative works.

I would like to thank IMAP colleagues at ENS: **Bingbing**, **Yuwei**, **Xinrui**, **Xingze**, **Xandi**, **Ahmad**, **Asma**, **Katrin**, **Ariana**, **Soraya**, **Edouard**. I will remember the enjoyable lunch time together forever. I would like to thank **Bernard Goetz** for the help of ICP MS, **Dr. Antoine Tissot** and **Dr. Iurii Dovgaliuk** for XRD, **Dr. Georges Mouchaham** for N_2 sorption. I would like to thank IMAP colleagues at ESPCI: **Wenqing**, **Audrey**, **Mathilde Renouard**, **Debanjan**, **Aysu** and **Mégane**. Thank **Dr. Farid Nouar** for the help of synthesis of MIL-100(Fe) MOF, **Dr. Vanessa Pimenta** for lab safety reminding. I would like to thank all our new nice colleges.

I would like to thank our former group colleagues for your accompanies: **Shan, Sujing**, **Qingfeng**, **Chenchen, Jiangliang, Raquel**, **Shyama**, **Ines**, **Florian**, **Oleksii**, **Fay**, **Kieu**, **Sarah**, **Johanne**, **Luke**, **John, Ella, Francesca**. Although you have left our group, the moments of having lunch together at ENS canteen and our daily lives in lab or in the bars are unforgettable.

I would like to thank **Boxin Huang**, **Changchong Chen**, **Xiaochen Huang** from **Prof. Yong Chen**'s group at ENS for the help with confocal imaging, **Marina Mariconti**, **Lucie Troisi**, **Farah El Fakih** and **Yunzhe Li** of **Prof. Damien Baigl**'s group at ENS for the reservation of plate reader, **Jean Bouvet** from **Prof. Nicolas Delsuc**'s group at ENS for the help with Elisa experiments. Also, it is a good experience to work in the cell lab members: **Marie-Aude Plamont**, **Dayana**, **Leonard**, **Audrey**, **Alvaro**, **Gabrielle**, etc. I would like to thank **Isabelle Aujard** for the use of lyophilizer and it is pleasant to share the same lab with you. I would like to thank **Eda**, **Ilan**, **Pauline**, **Ricard** and **Elza** of department of chemistry for your help. Meanwhile, I would like to thank my friends **Chenghao Xin** from ESPCI for the discussion about gold nanoparticles, **Yu Xiao**, **Huan Chen** and **Théotim Lucas** from Université Paris Cité for the help with cell experiments or photothermal studies. Meanwhile, I would like to thank **Dr. XiangZhen Xu** for the help of TEM test at ESPCI and **Bruno Bresson** for the training of SEM at IPGG.

Finally, I would like to show my deepest love to my family, particularly my parents, my sisters and my girlfriend. Your selfless love and support make me confident in completing this thesis.

Table of contents

Abbreviations

3-MA	3-Methyladenine
4,4′-DTBA	4,4′-Dithiobisbenzoic Acid
5-FAM	5-Carboxyfluorescein
5-FU	5-Fluorouracil
AS	Artesunate
ALI	Acute Lung Injury
AUR	Auraptene
BBDC	5-Boronobenzene-1,3-Dicarboxylic Acid
BSA	Bovine Serum Albumin
CAT	Catalase
CD	Cyclodextrin
CD44	Cluster Determinant 44
CDT	Chemodynamic Therapy
CIA	Collagen-Induced Arthritis
CLO	Clodronate
CO	Carbon Monoxide
COX	Cyclooxygenase
Cy	Cyanine
DMARDs	Disease-Modifying Antirheumatic Drugs
DEXP	Dexamethasone Sodium Phosphate
DOX	Doxorubicin Hydrochloride
DDS	Drug Delivery Systems
DHA	Dihydroartemisinin
EDS	Energy Dispersive Spectroscopy
EPR	Enhanced Permeability and Retention
ESCP	Ethoxysuccinato-Cisplatin
EV	Extracellular Vesicle
FA	Folic Acid
FDA	Food and Drug Administration
FL	Fluorescence
FLI	Fluorescence Imaging

GCs	Glucocorticoids
GSH	Glutathione
HA	Hyaluronic Acid
HAdase	Hyaluronidase
IBD	Inflammatory Bowel Disease
IBP	Ibuprofen
ICG	Indocyanine Green
IRFs	Interferon Regulatory Factors
IL-1β	Interleukin-1β
INOS	Inducible Nitric Oxide Synthase
KP	Ketoprofen
LA	Lactobionic Acid
LEF	Leflunomide
LPS	Lipopolysaccharide
LRET	Luminescent Energy Transfer
LSS	Liquid-Solid-Solution
MAPK	Mitogen-Activated Protein Kinase
MDR	Multidrug Resistance
MDT	Microwave Dynamic Therapy
MHT	Magnetic Hyperthymia Therapy
MIL	Materials of Institut Lavoisier
MOFs	Metal-Organic Frameworks
MR	Magnetic Resonance
MRI	Magnetic Resonance Imaging
mRNA	Messenger RNA
MSNs	Mesoporous Silica Nanoparticles
MTT	Microwave Thermal Therapy
MTX	Methotrexate
NCPs	Nanoscale Coordination Polymers
NCs	Nanoclusters
NF-κB	Nuclear Factor Kappa-B
NIR	Near-Infrared
NIRF	Near Infrared Fluorescent

nMOF	NanoMOF
NPs	Nanoparticles
NSAIDs	Non-Steroidal Anti-Inflammatory Drugs
NSF	Nephrogenic Systemic Fibrosis
OA	Osteoarthritis
PA	Photoacoustic
PAI	Photoacoustic Imaging
PB	Prussian Blue
PDA	Polydopamine
PDT	Photodynamic Therapy
PEG	Polyethylene Glycol
PET	Positron Emission Tomography
PL	Photoluminescence
PLGA	Poly(Lactic/Glycolic) Acid
PPy	Polypyrrole
PS	Photosensitizer
PTAs	Photothermal Agents
PTT	Photothermal Therapy
QDs	Quantum Dots
RA	Rheumatoid Arthritis
RAFT	Reversible Addition-Fragmentation Chain Transfer
RGD	Cyclic Arginine-Glycine-Aspartic Acid
RhB	Rhodamine B
ROS	Reactive Oxygen Species
SA	Sodium Aescinate
SDT	Sonodynamic Therapy
SLNs	Solid Lipid Nanoparticles
SMT	S-Methylisothiourea Sulfate
SNO	S-Nitrosothiol
SOD	Superoxide Dismutase
SiRNA	Small Interfering RNA
SPAAC	Strain-Promoted [3+2] Azide–Alkyne Cycloaddition
SPECT	Photon Emission Computer Tomography

SSZ	Sulfasalazine
TA	Tannic Acid
TCPP	Tetra(4-Carboxyphenyl)Porphine
TLRs	Toll-Like Receptors
TME	Tumor Microenvironment
TNBC	Triple-Negative Breast Cancer
TNF-α	Tumor Necrosis Factor-α
TPZ	Tirapazamine
UCNPs	Up-Converting Nanoparticles
UCL	Up-Conversion Luminescence
US	Ultrasound
USPIO	Ultra-Small Superparamagnetic Iron Oxide
VER	Verapamil Hydrochloride
ZGGO	Zinc Gallogermanate
ZIF-8	Zeolitic Imidazolate Framework-8

General Introduction

Inflammation represents an immune response of body triggered by multiple harmful stimuli such as infection, physical agents, radical oxygen species (ROS), metabolic stress (hypoxia). Excessive production of inflammatory mediators could be detrimental, contributing to the development of inflammatory diseases. Acute inflammation has been considered a defence of innate immune response induced by infection or injury. Apart from pathogens or injury, chronic inflammation can accompany various diseases such as cancer. Steroidal and nonsteroidal anti-inflammatory compounds are widely used in the treatment of inflammatory disorders to balance inflammatory and immune responses. However, their common side effects such as gastric irritation, ulceration, bleeding, renal failure, and hepatic failure cannot be ignored and the solution is to reduce medical dosage and improve therapeutic effect.

Nanobiotechnology has attracted considerable attention in drug delivery and various nanoparticles even exhibited unique thermal, magnetic, and optical properties. These nanocarriers could efficiently deliver imaging probes, therapeutic agents, or biological materials to reach target structures, which may provide opportunities in clinical treatment. Their key advantages include delivery of poorly water soluble molecular agents, protection of encapsulated agents, targeting specific organs/tissues or a cellular and subcellular specificity, controlled release of drugs, multimodal diagnostic and/or therapeutic functions. Nanoparticle-mediated drug delivery systems such as polymeric nanocarriers, lipid-based nanocarriers, and silica based nanocarriers have been used in inflammatory diseases such as rheumatoid arthritis and colitis therapies. Notably, noble metal nanoparticles such as gold nanoparticles, silver nanoparticles themselves possess anti-inflammatory properties, acting as antioxidants or inflammatory inhibitors.

Apart from aforementioned principal drug carriers, Metal-Organic Frameworks (MOFs) as a class of porous crystalline organometallic coordination polymer have witnessed their burst development in drug delivery, especially in the past 10 years, mainly due to their tunable composition, structure, pore size, and volume, easy functionalization, flexible network and/or accessible metal sites. Nontoxic MOFs consisting of endogenous cations (Ca^{2+}, $Fe^{2+/3+}$, and Zn^{2+}) and bioactive molecules as linkers are highly desired in biological applications. Among all the metals used in MOFs, iron is the least toxic and iron-based MOFs (Fe-MOFs) such as MIL-101 and MIL-100 have shown high drug loading and excellent biocompatibility. They are biodegradable and can be eliminated from body and more importantly, stimuli responsive drug release is observed in tumor microenvironment. Although cancer therapy is still the hotspot, more recently, MOFs have emerged as nanocarriers for anti-inflammatory drug delivery.

Theranostics combines therapeutic property and diagnostic imaging to treat disease with high therapeutic effects through a precise and personalized approach together with minimal side effects. As is mentioned, MOFs as porous materials are advantageous in drug delivery but their imaging properties are usually unsatisfactory. In parallel, as ideal imaging contrast agents of fluorescence imaging (FLI), magnetic resonance imaging (MRI) or computed tomography (CT), inorganic metal or metal oxide nanoparticles show low drug loading capacity. Thus, hierarchical multifunctional MOFs consisting of MOFs and inorganic nanoparticles are of great interest to improve physical and chemical properties and realize synergistic effects.

Guided by the concept "green synthesis", more and more MOFs can be synthesized in mild conditions such as nontoxic solvents and room temperature. This is of interest not only to meet the requirements of sustainable chemistry but also to develop novel hierarchical structure. For example, zeolitic imidazolate framework-8 (ZIF-8), which could be built from low-toxicity Zn^{2+} and 2-methylimidazole (2-MIM) in water or ethanol, has emerged as a potent platform in biomedical fields. Based on the facile synthesis method, various heterostructures consisting of ZIF-8 and guest nanoparticles have been fabricated. Similar with ZIF-8, our group has also developed a green room temperature synthesis protocol of MIL-100(Fe), and thus hierarchical NPs@MIL-100(Fe) MOFs are expected to construct by the same method.

In this thesis, we will first design and synthesize series of theranostic NPs@MIL-100(Fe) *via* an *in situ* room temperature synthesis strategy. Based on Maghnemite@MIL-100(Fe), we will study their drug loading capacity and release property of chemodrugs or anti-inflammatory drugs, biodegradation and anti-inflammatory or anti-cancer properties. Moreover, as a MRI imaging contrast agent, their magnetic properties will be tested. Also, we will focus on another hierarchical MOF atomically precise gold nanoclusters@MIL-100(Fe). Similarly, anti-inflammatory drug delivery will be studied. Gold nanoclusters could be anti-inflammatory agent and imaging contrast agent, synergistic anti-inflammation will be thus of interest. Apart from MIL-100(Fe), different MOFs such as ZIF-8 and UiO-66 will be chosen as candidates to encapsulate Au NCs for more potential bioapplications.

Summary

This thesis aims at inflammatory disease or cancer therapy through the construction of hierarchical theranostic inorganic particles or complexes associated with metal-organic frameworks (MOFs). These porous solids have attracted recently considerable attention in drug delivery and they are being further developed for theranostics for the purpose of personalized medicine in recent years. In terms of the construction of theranostic MOFs, one of the main strategies is to encapsulate inorganic nanoparticles into MOFs directly. However, the majority of works rely on complicated synthesis in harsh toxic conditions, which are major obstacles for practical applications particularly in biomedicine. To overcome this challenge, we have synthesized series of theranostic NPs@MOFs *via* an *in situ* room temperature synthesis strategy. Choosing MIL-100(Fe), a mesoporous poorly toxic iron carboxylate MOF, as a representative example, we have obtained for the first time maghemite@MIL-100(Fe) and gold nanoclusters@MIL-100(Fe) through this facile synthesis method. These composites nanoparticles exhibited a high drug loading capacity, stimuli-responsive drug release and excellent anti-inflammatory effects. Also, they showed great promises for imaging such as magnetic resonance imaging (MRI) and near infrared II window (NIR II) fluorescence imaging. Similarly, apart from MIL-100(Fe), Au NCs coated with cysteine with potentially improved optical features could also be encapsulated into zinc based MOF (ZIF-8) and zirconium based MOFs (UiO-66); their properties have not been fully investigated due to time limitations.

In detail, this thesis is divided into five chapters, as summarized below:

1. Introduction of nanoparticles for anti-inflammation and functional MOFs as theranostics
2. Hierarchical superparamagnetic MOFs nanovectors as theranostic anti-inflammatory nanomedicine
3. Atomically precise gold nanoclusters - MIL-100(Fe) for dexamethasone delivery and inflammatory disease synergistic therapy
4. Novel hybrid Au NCs@MOFs
5. General discussion and perspectives

Chapter 1 is divided in two parts, namely “nanoparticles for anti-inflammation” and “functional MOFs as Theranostics”. In the first part, the current research status of nanoparticles for anti-inflammation is summarized not only as drug delivery systems of anti-inflammatory drugs but also as anti-inflammatory agents themselves. As typical drug carriers, polymer based nanoparticles and lipid based nanoparticles have been widely used for anti-inflammatory drug delivery and even promising for clinical transfer. Meanwhile, mesoporous silica nanoparticles as porous materials were also shown to deliver on a controlled manner anti-inflammatory drugs. Other inorganic nanoparticles such as gold,

silver, zinc or cerium oxide nanoparticles possess intrinsic anti-inflammatory properties by downregulating pro-inflammatory cytokines express, inhibiting the activation of inflammatory pathway or decreasing the reactive oxygen species (ROS) production by enzyme-mimetic activities. Apart from aforementioned nanocarriers, biomimetic nanoparticles by camouflaging nanoparticles with cell membrane were able to reduce the immune system capture and elimination, facilitating targeting delivery, which is a novel direction. Especially, MOFs have showed great promises as drug delivery systems due to their huge porosity and large chemical and structural diversity in the past 15 years and those well-known biocompatible MOFs were exemplified accordingly. More recently, they have also emerged as drug delivery systems of anti-inflammatory drugs to treat inflammatory disease, although still at their infancy. Theranostics is a concept of combing therapy and diagnosis, and in the second part, "functional MOFs as theranostics" is summarized as a book chapter published in 2020 (Metal-Organic Frameworks for biomedical applications, Elsevier, 2020, 397-423). Considering the blooming development in the field in the past two to three years, we have updated it with newly published literatures. In brief, we mainly discussed the development of nanoscale MOFs for cancer and other diseases theranostics in the past decade, and series of theranostic MOFs such as magnetic nanoMOFs, nanoMOFs embedding noble metal nanoparticles, nanoMOFs coated with polymers, fluorescent nanoMOFs, phototherapeutic or nuclear medical imaging nanoMOFs along other stimuli-responsive nanoMOFs. Notably, hierarchical MOFs pave a new avenue to design advanced multimodal imaging and synergistic therapy systems.

In **Chapter 2**, a hierarchically porous nano-object (denoted as USPIO@MIL) combining a benchmark nanoMOF (MIL-100(Fe) nanoparticles) and ultra-small particles of superparamagnetic iron oxide (USPIO or maghemite) was synthesized through an *in situ* room temperature synthesis strategy. Briefly, to obtain USPIO@MIL heterostructures, preformed USPIO NPs were mixed with precursors of MIL-100(Fe) directly in water under stirring at room temperature. The protocol is facile, cost-effective, environmentally friendly and also scalable. The synergistic coupling of the physico-chemical and functional properties of USPIO and MIL-100(Fe) nanoparticles confer to these nano-objects valuable features such as high colloidal stability, biodegradability, low toxicity, high drug loading capacity as well as stimuli-responsive drug release and superparamagnetic properties. Notably, in addition to common fluorescence labeling techniques, as far we know, it was the first time to visualize the whole cellular internalization and degradation process of hierarchical USPIO@MIL NPs by Bio-TEM. After more than one week's monitoring, their biodegradability was substantially confirmed. This bimodal USPIO@MIL nanocarrier possessed a large drug loading capacity of anti-tumoral or anti-inflammatory drugs (doxorubicin or methotrexate), and surprisingly, the loading of doxorubicin

was found to be four times higher in comparison with previous reported MIL-100(Fe), maybe due to structural defects. Drug loaded USPIO@MIL exhibited stimuli responsive release, leading to high anti-inflammatory and anti-tumoral activities. In addition, USPIO@MIL nano-objects presented excellent relaxometric properties and their applicability as efficient contrast agent for magnetic resonance imaging was demonstrated. This chapter highlights the high potential of maghemite@MOF composite integrating the functions of imaging and therapy as theranostic anti-inflammatory formulation. Currently, this work has been submitted as a publication.

In **Chapter 3**, following the same strategy, Au NCs@MIL NPs were synthesized by encapsulating atomically precise glutathione protected gold nanoclusters ($Au_{25}SG_{18}$ NCs) into MIL-100(Fe). Dexamethasone phosphate (DexP) is a glucocorticoid anti-inflammatory drug, whose dimensions match the ones of the mesopores of MIL-100(Fe) while one expects the coordination of the phosphate groups of DexP onto the Lewis acid sites from MIL-100(Fe). As expected, the resulting DexP loaded hierarchical Au NCs@MIL NPs (Au NCs@MIL/Dex) showed a high drug loading capacity and stimuli responsive release of DexP, similar to MTX loaded USPIO@MIL in **Chapter 2**. Moreover, co-polymer hyaluronic acid-polydopamine (HA-PDA) could be used to coat the nanoMOF and slow down DexP release from Au NCs@MIL/Dex NPs in neutral physiological environment. Apart from DexP, gold nanoclusters could also act as anti-inflammatory therapeutic agent while exhibiting a potential in medical imaging. In terms of *in vitro* anti-inflammation, the drug loaded nanocarrier specifically inhibited inflammatory cells growth, scavenged intracellular reactive oxygen species (ROS) and downregulated pro-inflammatory cytokines secretion. As for an in depth study, they could block related inflammatory pathways such as the nuclear factor kappa B (NF-κB) pathway and the interferon regulatory factor (IRF) pathway efficiently. Altogether, the co-delivery of chemodrug and metallic nanoclusters by MOFs may provide a new approach for inflammatory disease therapy and diagnosis. This work is under preparation for publication.

Chapter 4 is dedicated to developing novel hybrid Au NCs@MOFs with enhanced optical properties. The NIR-II window fluorescence imaging property of $Au_{25}SG_{18}$ NCs was quenched in the presence of MIL-100(Fe). In this **Chapter 4**, cysteine (Cys) protected Au_{25} NCs ($Au_{25}Cys_{18}$ NCs) and different MOFs have been used in order to limit/remove this fluorescence quenching. Using the approach described in **Chapter 3**, a variety of Au NCs@MOFs nanoobjects were synthesized and characterized: $Au_{25}Cys_{18}$ NCs as well as different MOFs (MIL-100(Fe), ZIF-8(Zn), UiO-66(Zr)) were used. However, due to lack of time this was not possible to complete the set of advanced characterizations. Their possible application in bio-imaging, drug delivery, antimicrobial treatment or even in catalysis are finally discussed as perspectives.

In the last chapter, a general conclusion is proposed and meanwhile, perspectives such as *in vivo* anti-inflammation, anti-bacteria by combined chemodynamic and photodynamic therapy, NIR II window fluorescence imaging and catalysis are discussed. Subsequently, serval main co-authored works were also attached in the annexes.

Chapter 1 Introduction

This chapter contains two parts, namely "nanoparticles for anti-inflammation" and "functional MOFs as Theranostics". The latter one is adapted to the following book chapter:

Chapter 18 - Functional MOFs as Theranostics

Metal-Organic Frameworks for biomedical applications, (Ed: M. Mozafari), Elsevier, **2020**, 397-423.

Heng Zhao et al.

Table of Contents

1.1 Nanoparticles for anti-inflammation

Since two decades ago, nanoparticles have been widely used for drug delivery. **Figure 1.1.1** has been obtained by extracting data from Web of Science after crossing the terms “nanoparticles” and “drug delivery”. Obviously, this is still a very hot research topic with a publication of >10000 articles per year now and the growing tendency remains, revealing the strong interest of the scientific community for the discovery of nanoparticles for drug delivery. In terms of possible biomedical applications, it is dependent on not only the drug model but also the nanocarrier. Due to the unique thermal, fluorescent, and magnetic properties under external or internal stimulus, nanocarriers or nanoparticles (if not drug delivery) themselves could also be nanodrugs and imaging contrast agents, which are promising for diagnosis and therapy of cancer and other diseases.

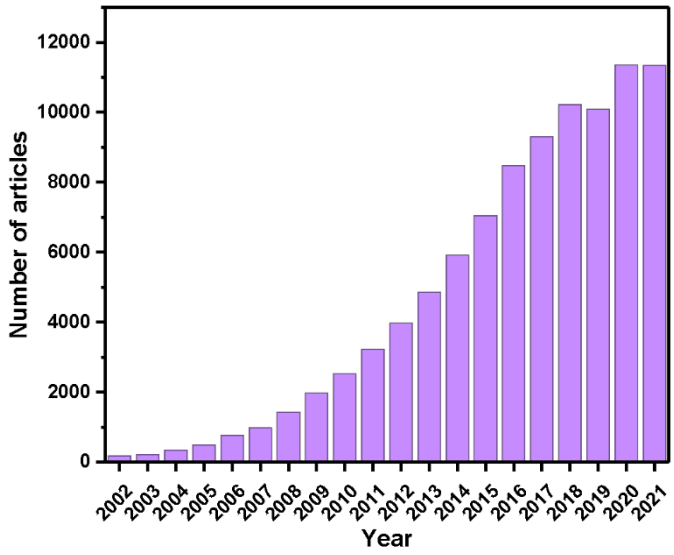

Figure 1.1.1 Number of publications of nanoparticles for drug delivery in the period 2002-2021. Data from Web of Science after crossing the terms “nanoparticles” and “drug delivery”.

As well established, cancer therapy has been a hotspot for decades and numerous nanocarriers or nanoformulations have been reported (**Figure 1.1.2**) and the trend keeps increasing. Compared with nanoparticles for cancer therapy, the use of nanoparticles for anti-inflammation is still at its infancy (**Figure 1.1.3**) with however a dramatical increase trend. Inflammation underlies a wide variety of physiological and pathological processes in all vertebrates, which is an immune response triggered by exogenous or endogenous noxious stimulus such as infection, tissue injury and malfunction of tissue.[1] The mechanism of inflammation is exceedingly complex, especially those non-infectious inflammation processes. Regardless of the puzzling cause and mechanism, inflammation presumably evolved in restoring homeostasis.[1] If the abnormal conditions are transient, an acute inflammatory

response may return the immune system to the basal homeostatic set points, whereas if they are sustained, chronic inflammation occurs.[1]

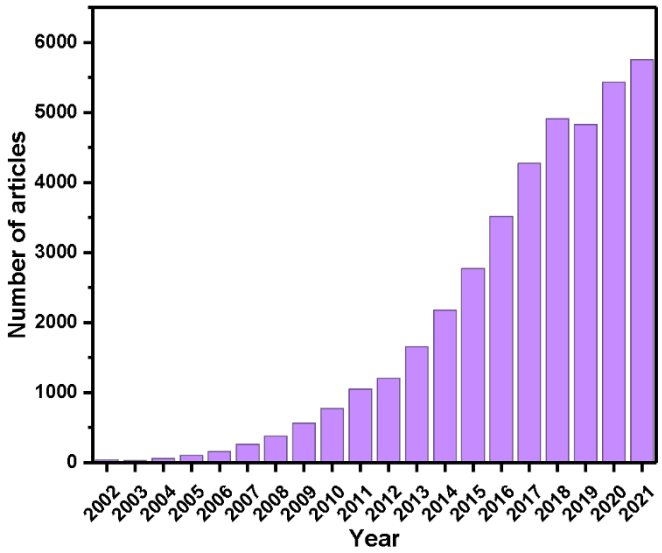

Figure 1.1.2 Number of publications of nanoparticles for cancer therapy in the period 2002-2021. Data from Web of Science after crossing the terms "nanoparticles" and "cancer therapy".

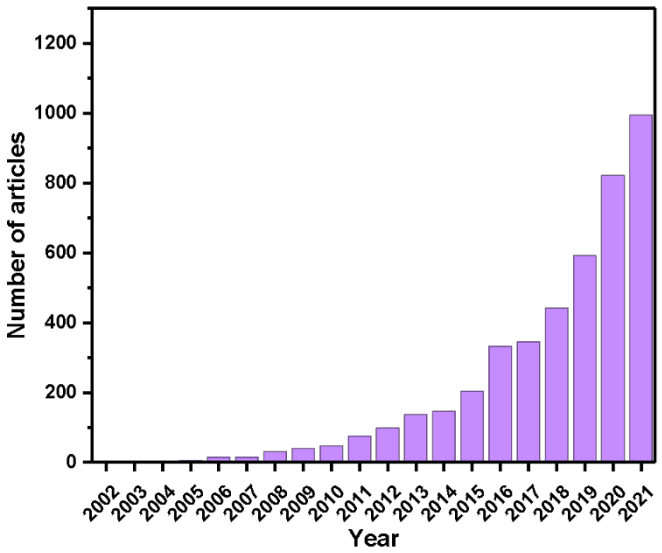

Figure 1.1.3 Number of publications of nanoparticles for anti-inflammatory in the period 2002-2021. Data from Web of Science after crossing the terms "nanoparticles" and "anti-inflammatory".

Chronic inflammatory diseases also increase the risk of developing many types of cancer.[2-4] Inflammatory responses play decisive roles at different stages of tumor development, including initiation, promotion, malignant conversion, invasion, and metastasis. In **Figure 1.1.4**, tumors that produce little cytokines result in constrained tumor growth. In contrast, an abundance of pro-inflammatory cytokines can lead to a level of inflammation that potentiates angiogenesis, thus favoring

neoplastic growth. In response to an altered balance of cytokines, high levels of monocytes and neutrophil infiltration can be associated with cytotoxicity, angiostasis and tumor regression. Therefore, anti-inflammatory therapy combined chemotherapy approach is one of the most popular therapeutic strategies to treat cancer. Notably, diverse cancer chemotherapy drugs are also commonly used to treat symptoms of inflammation.[5]

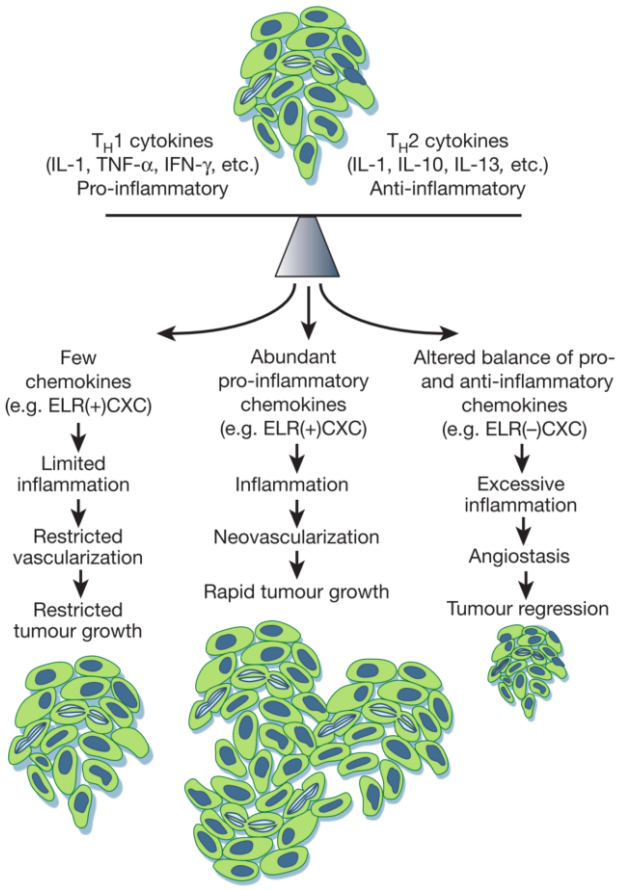

Figure 1.1.4 Cytokine and chemokine balances regulate neoplastic outcome. The balance of cytokines in any given tumor is critical for regulating the type and extent of inflammatory infiltrate that forms.

As for inflammatory disease, one can use rheumatoid arthritis (RA) as a representative example. It is considered as a chronic disease that cannot be cured and its aetiology is unknown, and therefore, no causal treatment is available.[6] RA is mainly characterized by inflammatory synovial hyperplasia and erosion of cartilage and bone and the mechanism of RA pathogenesis is related with macrophages, cytokines and inflammatory signaling pathways. As a type of innate immune cells, macrophages are with high plasticity and they can be polarized into two types, M1 macrophages and M2 macrophages, by various stimulating factors. M1 macrophages are known to secrete a variety of pro-inflammatory cytokines such as interleukin-1β (IL-1β), IL-6, tumor necrosis factor-α (TNF-α), etc. Also, M1 macrophages upregulate the expression of various proteins such as inducible nitric oxide synthase

(iNOS). M2 macrophages mainly exert anti-inflammatory effects by secreting pro-inflammatory cytokines such as IL-10. As an early sign of RA, macrophages influx in the synovial tissue and activated M1 macrophages secret a large number of pro-inflammatory cytokines and chemokines, triggering RA. Thus, it is important to regulate the dynamic balance of M1/M2 macrophages for RA inflammation regression and tissue repair.

The occurrence of RA is a complicated process, which is controlled by multiple signal pathways, so that blocking a certain signal pathway may be inefficient for RA therapy. The related signaling pathways include nuclear factor kappa-B (NF-κB) signaling pathway, Mitogen-activated protein kinase (MAPK) signaling pathway, Toll-like receptors (TLRs) signaling pathway, etc. NF-κB signaling pathway is one of the most important transcription factors. The activation of NF-κB signaling pathway can induce the production of TNF-α and IL-1β, and in turn, the upregulation of pro-inflammatory cytokines positively regulates the activation of NF-κB, resulting in amplified inflammatory response.[7] The use of NF-κB inhibitors is expected to block the effect. MAPK is a serine-threonine kinase that mediates intracellular signaling to transduce extracellular stimulus signals into the nucleus, regulating a variety of cellular activities such as cell proliferation, differentiation, survival, death, and transformation.[8] TLRs are expressed in innate immune cells such as dendritic cells (DCs) and macrophages as well as non-immune cells such as fibroblast cells and epithelial cells. The TLR family comprises 10 members (TLR1–TLR10) in human and 12 (TLR1–TLR9, TLR11–TLR13) in mouse.[9] TLRs play crucial roles in the innate immune system, primarily known for recognizing pathogen-associated molecular patterns. TLRs often recruit specific adaptor molecules such as myeloid differentiation protein 88 (MyD88) and TIR domain containing adapter inducing IFN-β (TRIF) to transmit biological signals, leading to activation of the transcription factors NF-κB and interferon regulatory factors (IRFs).[9]

As one of TLRs, TLR4 locates on the cell surface and it was first identified as the receptor for lipopolysaccharide (LPS), a component of outer membrane of Gram-negative bacteria. TLR4 mediated signaling pathways are the key players regulating the inflammatory response, and TLR4-mediated NF-κB hyper inflammatory signaling pathway is illustrated in **Figure 1.1.5**.[10] Briefly, LPS recognition by TLR4 leads to recruitment of TRIF/TRAM and TIRAP/MyD88 receptor complex. The signaling contains MyD88-dependent and MyD88-independent pathways and ultimately free NF-κB is released for nuclear translocation and pro-inflammatory cytokines production. Based on the intersection of multiple inflammatory signal pathways, designing one drug delivery system to inhibit these targets is a promising treatment for RA or other inflammatory disorders.

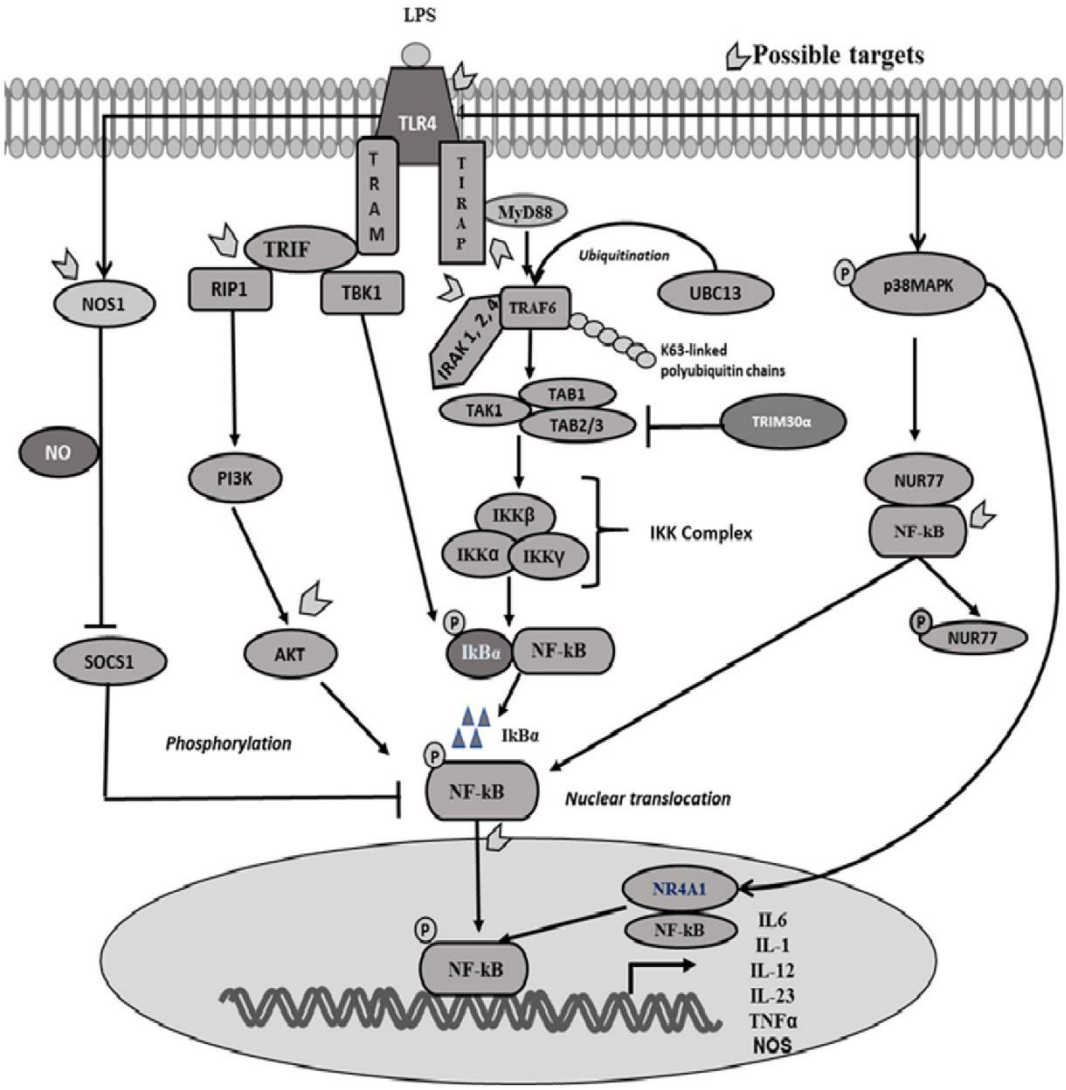

Figure 1.1.5 Overview of TLR4-mediated NF-κB hyper inflammatory signaling pathway.

The current anti-inflammatory treatments could alleviate symptoms, such as joint pain and swelling, and prevent disease progression and generally, three major classes of drugs are used in the clinic: glucocorticoids (GCs), non-steroidal anti-inflammatory drugs (NSAIDs) and disease-modifying antirheumatic drugs (DMARDs).[11] Corticosteroids are a class of steroid hormones involved in a wide range of physiological processes, including stress response, immune response and regulation of inflammation.[12-13] According to the action time, glucocorticoids can be divided into three types: short-acting (hydrocortisone and cortisone), intermediate-acting (prednisone, prednisolone, and methylprednisolone), and long-acting glucocorticoids (dexamethasone and betamethasone). Corticosteroids are commonly prescribed in combination with other anti-inflammatory drugs, such as NSAIDs and DMARDs. NSAIDs act through the inhibition of cyclooxygenase (COX) enzymes at sites of inflammation, achieving symptomatic relief in arthritis patients.[14] The prescribed NSAIDs are ibuprofen, flurbiprofen, diclofenac, celecoxib, indomethacin, meloxicam, piroxicam and naproxen.

DMARDs are first-line disease-modifying agents with potent efficacy in diminishing joint and cartilage damage, halting disease progression, and improving the mobility and overall function of inflamed joints.[15] Representative drugs include methotrexate (MTX), sulfasalazine (SSZ), leflunomide (LEF), iguratimod (IGU). Other inflammatory diseases such as inflammatory bowel disease (IBD), acute lung injury (ALI) and hepatitis will be also mentioned in this introduction. The general strategy to treat inflammatory diseases by nanoparticles is to construct nanocarriers of anti-inflammatory drugs or therapeutic nanoparticles with enzyme-mimic antioxidative properties to deplete excess reactive oxygen species (ROS).

This chapter will introduce different conventional nanoparticles or nanocarriers such as polymers based nanoparticles, lipid-based nanoparticles, inorganic nanoparticles and biomimetic nanoparticles for anti-inflammatory drug delivery. Interestingly, metal-organic frameworks (MOFs) have emerged as anti-inflammatory drug vectors in recent years, possessing great promises and this part will also discuss biocompatible MOFs and the current progress in anti-inflammation specifically.

1.1.1 Polymer-based nanoparticles

Polymer-based nanoparticles have been widely developed for drug delivery, mainly anti-inflammatory drugs here. Few typical polymers such as polysaccharides, polydopamine (PDA) and poly(lactic/glycolic) acid (PLGA) have been selectively listed and discussed as below.

1.1.1.1 Polysaccharides

Polysaccharides have been widely used for drug delivery applications due to their natural highly biodegradability, and interestingly they possess intrinsic anti-inflammatory properties. Herein three widely used polymers hyaluronic acid, chitosan and cyclodextrins are discussed below.

Hyaluronic acid (HA) is a linear polyanionic polysaccharide composed of a repeating disaccharide unit β-1,4-D-glucuronic acid-β-1,3-N-acetyl-D-glucosamine that is naturally present in hyaline cartilage, synovial fluid, and vitreous humor of the eye. HA can bind to overexpressed receptors in cancer cells such as cluster determinant 44 (CD44) for targeted cancer therapy, and HA is biocompatible and can be degraded by hyaluronidase (HAdase) to release drugs or molecules.[16] For these reasons, HA nanomedicines have been extensively studied in the drug delivery field to increase the colloidal stability and biocompatibility of the material, improve the delivery of drugs through passive and active targeting and even function as a gatekeeper to regulate the drug release.[16] Under inflammatory stimuli such as lipopolysaccharide (LPS), the CD44 expression of human synovial / peripheral monocytes /

macrophages increases. Since HA can specifically bind to CD44 of activated macrophages, and MTX was thus conjugated onto the HA backbone *via* the pH sensitive ester linkage, which is labile in the acidic environments such as the inflamed synovial fluid and the intracellular compartments, including endosomes. The cleavable HA-MTX conjugate was used for targeted therapy of rheumatoid arthritis, which could be effectively taken up by the activated macrophage and selectively accumulated into the inflammatory joint site of the collagen-induced arthritis (CIA) mice and it improved clinical outcomes compared to free MTX and suppressed pro-inflammatory cytokines.[17] Although the synthesis of HA-MTX conjugates is simple, it seems that they are not typical nanovectors and the premature MTX release in neutral physiological conditions is another concern. Interestingly, apart from the targeting ability of HA, HA backbone is cleavable in response to ROS. The conjugation of HA conferred up-conversion nanoparticles (UCNPs) not only water solubility but also biocompatibility and ROS recognizing properties. Thus, UCNPs were covalently conjugated with chromophore rhodamine B (RhB) labeled hyaluronic acid (*i.e.*, HAR-UCNP) for efficiently *in vitro* imaging reactive oxygen species and *in vivo* diagnosing rheumatoid arthritis (**Figure 1.1.6**).[18] In this process, RhB was an energy acceptor and its broad absorbance matched well with the green emission of UCNPs, so that the HA backbone cleavage triggered by ROS could inhibit the luminescent energy transfer (LRET) and allow rational metric up-conversion luminescence (UCL) emission as the detection signal. As a diagnosis system, HAR-UCNP showed potentials on ROS imaging, but it is not a drug delivery system and maybe the possible photothermal effects of UCNPs could be further studied.

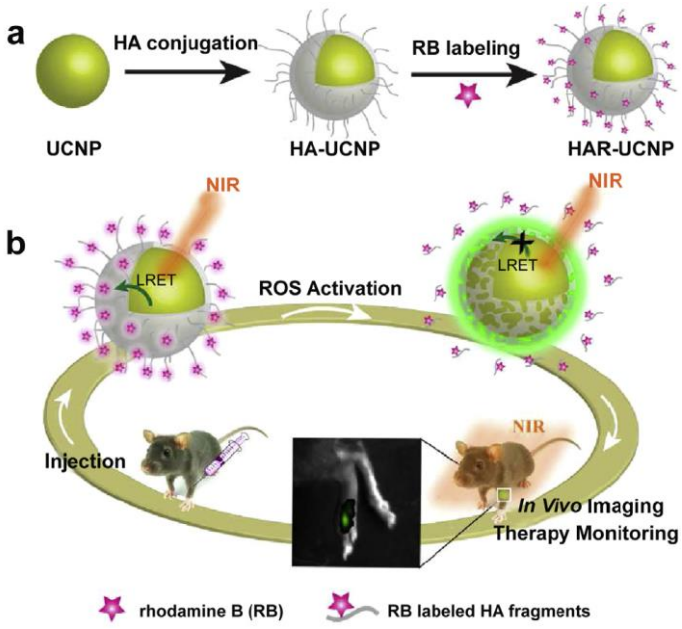

Figure 1.1.6 Schematic illustration of HAR-UCNP nanoprobes for ROS imaging and rheumatoid arthritis diagnosing. (a) The conjugation of HA confers UCNPs not only water solubility but also biocompatibility and ROS recognizing properties. The functional groups on HA backbone are available for conjugation of up-

conversion luminescence acceptor chromophores. (b) The LRET process of HAR-UCNPs towards ROS for rheumatoid arthritis diagnosing and therapy monitoring.

Chitosan is also a polycationic polysaccharide consisting of randomly distributed β-(1,4)-linked D-glucosamine (deacetylated) and N-acetyl-D-glucosamine (acetylated) units, which naturally exists in crustacean exoskeleton. Chitosan is also biocompatible and biodegradable (by lysozyme), which has been extensively used for the fabrication of numerous polymeric NPs for drug delivery applications.[19-21] In terms of anti-inflammation of ocular diseases, anti-inflammatory drugs such as prednisolone and dexamethasone have been encapsulated into chitosan nanoparticles.[22-23] Chitosan nanoparticles have also been investigated for the treatment of inflammatory bowel disease (IBD) with the loading of an amino acid without a carboxyl group taurine (2-aminoethanesulfonic acid) by intracolonic instillation, alleviating inflammation and oxidative stress.[24] In the treatment of inflammatory lung disease, nasal drug delivery method represents a promising strategy and chitosan nanoparticles loaded with hesperidin were developed for nasal delivery of the anti-inflammatory nanocomposite to inflammatory lungs.[25] Clodronate (CLO) as a first-generation bisphosphonate drug is a structural analogue of pyrophosphate, and metabolized to a cytotoxic analogue of ATP, resulting in the induction of cell apoptosis. In terms of potential arthritis treatment, an intra-articular delivery system has been constructed by loading chitosan-clodronate nanoparticles in poloxamer gel.[26] The drug loading of CLO was high (31.0% ± 5.4 w/w), but if chitosan-clodronate nanoparticles were not loaded in poloxamer gel, the release of CLO in 0.9% NaCl at 37 ^{o}C was more than 50% in 8 h, indicating that chitosan itself is not a good sustained release carrier. Notably, different molecular weight of chitosans showed different effects on their anti-inflammatory activities, and larger chitosans (300, 156 and 72 kDa) are anti-inflammatory whereas smaller chitosans (7.1 and 3.3 kDa) are pro-inflammatory in the RAW 264.7 macrophage model.[27]

Another major polysaccharide is cyclodextrin (CD), a series of natural amphiphilic cyclic oligosaccharides composed of 6, 7, or 8 D(+)-glucose units linked by α-1,4-linkages, and named α-, β-, or γ-CD, respectively.[28] In terms of the structure, cyclodextrin looks like a circular truncated microporous hydrophobic cone and recently numerous nanocarriers based on cyclodextrins have been developed.[29-30] Among the class of glucocorticoids, dexamethasone is the most frequently used anti-inflammatory and immunosuppressive drug used for treating rheumatoid arthritis (RA) but its poor pharmacokinetics and severe associated side effects limited its application. Dhananjay Jadhav *et al.* developed a cyclodextrin based nanoparticulate drug delivery system with an average particle size of 105 ± 15 nm to deliver dexamethasone sodium phosphate (DexP) for the treatment of rheumatoid

arthritis.[31] The encapsulation efficiency of optimized DEX-NPs was 65.40 ± 4.63% but it suffered from a burst release in the first 1 h, and 92% release at the end of 24 h.

Reactive oxygen species are side-products of mitochondrial oxidative metabolism and excessive ROS production results in various inflammatory diseases such as rheumatoid arthritis and inflammatory bowel disease. Superoxide dismutase (SOD) and catalase (CAT) are two antioxidant enzymes capable of respectively scavenging superoxide and hydrogen peroxide. However, oral delivery of enzyme is still a challenge for therapeutic applications due to its instability and easy degradation in the gastrointestinal tract. Cyclodextrin can self-assemble into nanoparticles in aqueous solution and achieve superior encapsulation of SOD and CAT by simply mixing with protein solution for effective treatment of dextran sulfate sodium-induced colitis by oral administration.[32]

Although these natural polysaccharides polymers show great promises in drug delivery and anti-inflammation, the limitations such as batch-to-batch variability and broad molecular weight distributions make them less reproducible and versatile. Moreover, concerning anti-inflammatory drugs delivery, some of them are promising in terms of drug loading, but the burst release shall be circumvented.

1.1.1.2 Polydopamine

Polydopamine (PDA) derived from self-polymerization of dopamine shows many unique chemical properties, which has attracted much attention in nanomedicine.[33] Owing to strong NIR absorption and photothermal conversion capacity (similar with melanin), good biodegradability, biocompatibility and negligible long-term toxicity, PDA-based materials present a great potential as excellent photothermal therapy (PTT) agent.[34] As a mussel-inspired material, PDA coating is one of the simplest and most versatile approaches used for functionalizing most substrates, including most metal oxides and noble metals as well as low energy surfaces such as polystyrene, poly(lactic-co-glycolic) acid (PLGA), graphene and carbon nanotubes.[35-36]

Photothermal therapy has its own limitations such as uneven distribution of hyperthermia and penetration depth of near-infrared (NIR) radiation, resulting in incomplete eradication of lesion. Fortunately, PDA nanoparticles or PDA-coated nanoparticles could also be carriers of anti-cancer drugs such as Dox and glucocorticoid anti-inflammatory drug such as Dex.[37-39]

Importantly, the phenol groups of PDA make this polymer an excellent free radical scavenging agent to eliminate ROS both *in vitro* and *in vivo*.[40] Interestingly, even degradable products of PDA or PDA extracts could limit the release of pro-inflammatory cytokines by downregulating TLR-4/MYD88

expression and NF-κB signaling pathway, which may also be related with ROS scavenging.[41] Zhao *et al.* developed bare PDA nanoparticles as an anti-inflammatory nano-drug for the treatment of acute inflammation-induced injury including acute peritonitis and acute lung injury (ALI). PDA NPs scavenged either H_2O_2- or LPS-induced cellular ROS and effectively suppressed the *in vivo* inflammation process.[42] Using a similar antioxidative therapy strategy, PDA NPs were also explored for the treatment of oxidative-stress-induced periodontal disease (**Figure 1.1.7**).[43] Although these promising results have been achieved, the bio-related mechanisms are not totally clear. Carmignani *et al.* have investigated the effects of PDA NPs size on their antioxidant and photothermal properties both *in vitro* and *ex vivo*. It was shown that nanoparticles with a larger diameter displayed higher NIR absorbance and superior resistance to degradation, and those small size (< 200 nm) PDA NPs induced both improved antioxidant properties and enhanced cellular uptake.[44] Although PDA is well known as free radicals scavengers, the pro-oxidant effect of donating electrons to O_2 to generate ROS under the irradiation of near-infrared light is also reported.[45-46] PDA is redox-active and can both accept electrons from reducing agents and donate electrons to various oxidants. The electron-donating ability of PDA depends on its redox state and could be affected by the combination of metal ions or near-infrared irradiation. The functions of PDA may vary in different conditions.

Figure 1.1.7 Schematic illustration of the typical synthesis of PDA NPs and their usages as efficient ROS scavengers in periodontal disease.

1.1.1.3 Poly(lactic/glycolic) acid

Among the range of biodegradable polymers, PLGA has been approved by the food and drug administration (FDA) for use in humans, and is being widely considered as a carrier for drugs or macromolecules. Non-steroidal anti-inflammatory drugs (NSAIDs) such as diclofenac sodium, diclofenac and naproxen, steroidal anti-inflammatory drugs such as prednisolone and dexamethasone, inhibitors such as rapamycin and carvedilol have been loaded into PLGA NPs to form pharmaceutical

formulation.[47-52] In terms of arthritis therapy, etoricoxib is a cyclooxygenase-2 (COX-2) selective NSAID with a lower risk of gastrointestinal toxicity, which was loaded into PLGA-PEG-PLGA nanoparticles to attenuate osteoarthritis progression by intra-articular injection.[53] As a biomacromolecule, small interfering RNA (siRNA) has also been loaded into PLGA nanoparticles and the siRNA-loaded nanoparticles mediated a dose-dependent tumor necrosis factor alpha (TNF-α) silencing in lipopolysaccharide-activated RAW 264.7 cells *in vitro* and there was no difference between the specific and the nonspecific siRNA treatment groups *in vivo* when the siRNA dose was low.[54] Moreover, PLGA NPs are also used to load NSAID pranoprofen or natural compound Licochalcone-A for ocular inflammation therapy.[55-57] The drawbacks of bare PLGA NPs lie mainly in their challenging scale up, a lack of specific target localization and burst release rate, while their *in vivo* behavior has not been fully characterized.[58]

1.1.2 Lipid-based nanoparticles

There are different types of lipid-based nanocarriers such as liposomes, solid lipid nanoparticles, and nanostructured lipid nanoparticles.

1.1.2.1 Liposomes

Liposomes are membrane-like vesicles consisting of one or more concentric bilayers, produced from natural nontoxic phospholipids and cholesterol, alternating aqueous and lipophilic compartments. Because of their size, amphiphilic properties, and biocompatibility, liposomes are highly suitable for drug delivery.[59] They can accommodate both hydrophilic and lipophilic drugs, respectively, into the aqueous compartment or the lipid bilayer. The pioneering work of countless liposome researchers have led to numerous clinical trials in such diverse areas as the delivery of anti-cancer, anti-fungal and antibiotic drugs, the delivery of gene medicines, and the delivery of anesthetics and anti-inflammatory drugs.[60] There are already plenty of liposomal formulations such as liposomal doxorubicin (Doxil) for anticancer and AmBisome for antifungal approved by US FDA and EMA (European Medicines Agency).[61]

1.1.2.2 Solid lipid nanoparticles

Solid lipid nanoparticles (SLNs) are highly studied as promising alternative carriers for drugs and diagnostics. Glucocorticoids are effective in treating IBD flares, but their considerable side effects limited their use. The incorporation of butyrate and dexamethasone into SLN has a significant positive anti-inflammatory effect in the human inflammatory bowel disease whole-blood model.[62-63] To

improve the solubility of NSAIDs in water and reduce the frequency of administration, SLNs are used for the controlled delivery of poorly water soluble NSAIDs such as ibuprofen (IBP), ketoprofen (KP), indomethacin, and nimesulide.[64-65] SLNs have showed high drug loading for naturally derived anti-inflammatory drugs such as curcumin (37 ± 2.5%) from rhizome of turmeric, sodium aescinate (SA, 76.5%) from the dried fruits of aesculus wilsonii Rehd and auraptene (AUR) (84.11 ± 3.30%), a bioactive antioxidant coumarin.[66-69] Atorvastatin is a highly lipophilic anti-hyperlipidemic drug which shows a poor oral bioavailability due to first-pass metabolism, and to achieve a better transdermal delivery, it is important to overcome skin barriers, and atorvastatin SLNs appeared as a promising approach for dermal delivery of an anti-inflammatory agent.[70] In terms of ocular drug delivery, to be effective, most drugs must penetrate across the eye's tissue barriers to reach therapeutic targets within the globe. Lipid nanoparticles represent promising alternatives to conventional and very popular ocular carrier systems.[71] Although SLNs showed a lot of advantages such as drug protection against harsh environment, ease of scalability, biocompatibility, and biodegradability, they still suffer from several drawbacks such as unpredictable gelation propensity and possibility of drug crystallization during the storage conditions and also the limitations are related to specific route of administration.[72-73]

1.1.2.3 Nanostructured Lipid carriers

Nanostructured lipid carriers are nano-sized colloidal drug delivery systems composed of biocompatible lipid core and surfactants. Phosphatidylserine-containing curcumin-loaded nanostructured lipid carriers exhibited enhanced anti-inflammatory activity.[74] Lipid nanoparticles have also been investigated for combining two therapeutic anti-inflammatory approaches dexamethasone palmitate nanoparticles (CDXP-NP) associated with TNF-α siRNA in a single drug delivery system.[75] Similarly, lipid nanoparticles also play a crucial role in delivering messenger RNA (mRNA) with anti-inflammatory properties by partially substituting cholesterol with Dex.[76] Lipid nanoparticles could be alternative drug delivery systems for sustained delivery of CO with the improved solubility of carbon monoxide-releasing molecules (CORMs).[77]

1.1.3 Biomimetic nanoparticles

Nanoparticle capture and elimination by the immune system are great obstacles for drug delivery. Camouflaging nanoparticles with cell membrane represents a promising strategy to communicate and negotiate with the immune system. As a novel class of nanotherapeutics, biomimetic nanoparticles are hybrid nanostructures in which the uppermost layer is similar to a cell membrane (*e.g.*, erythrocytes, immune cells, and platelets) and targeting inflammation based on cell membrane biomimetic

nanotechnology provides an opportunity for targeted drug delivery.[78] Zhang *et al.* have developed neutrophil-NPs as an anti-inflammatory strategy for rheumatoid arthritis management (**Figure 1.1.8**). Unlike existing unspecific targeting anti-cytokine agents, neutrophil-NPs provide a function-driven, broad-spectrum and disease-relevant blockade that dampens the inflammation cascade in the disease process.[79] In addition, the direct use of membrane from the effector cells of the disease allows neutrophil-NPs to neutralize highly relevant inflammatory factors without the need to identify them. Even if the target is known, the top-down fabrication of neutrophil-NPs can avoid the necessity to engineer binding motifs that are often difficult to synthesize and conjugate.

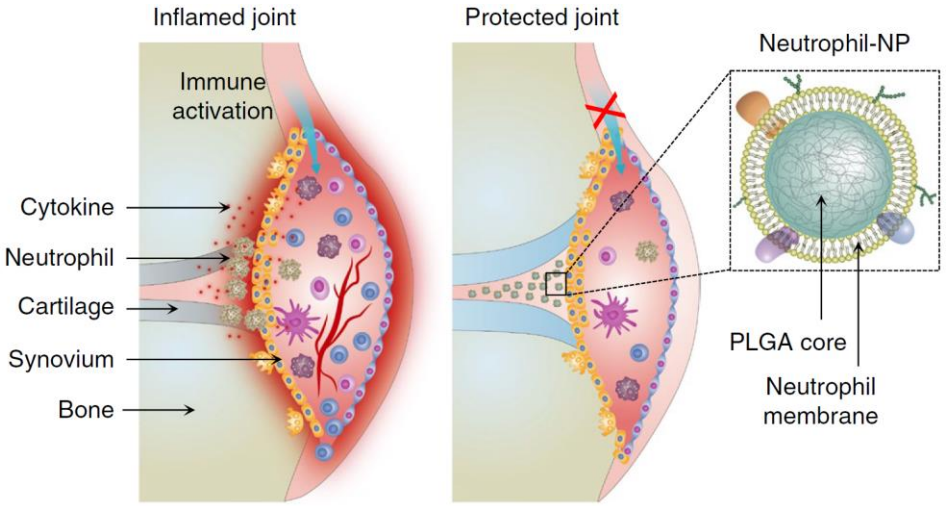

Figure 1.1.8 Schematic representation of neutrophil-NPs designed for suppressing synovial inflammation and ameliorating joint destruction in inflammatory arthritis. Neutrophil-NPs are constructed by wrapping polymeric cores in natural human neutrophil membranes, which mimic source cells to bind with immunoregulatory molecules without potentiating the immune cascades for disease progression.

Similarly, inspired by the intrinsic inflammation-targeting capacity of macrophages, a macrophage-derived microvesicle (MMV) coated nanoparticle (MNP) was developed to encapsulate a model drug tacrolimus for targeting RA.[80] Also, a targeted oral delivery system of yeast glucan particles (YGPs) carrying a clinically used anti-inflammatory drug methotrexate (MTX) to the inflamed sites in IBD mice for therapy is reported.[81]

1.1.4 Inorganic nanoparticles

Inorganic nanoparticles are nowadays widely considered for a wide range of biomedical applications and a lot of studies have been reported to develop porous drug carriers nanoparticles such as mesoporous silica nanoparticles for anti-inflammatory drug delivery or new metal and metal oxide nanoparticles like gold, silver, zinc and cerium oxide as anti-inflammatory agents.[82-83]

1.1.4.1 Mesoporous silica nanoparticles

As a versatile class of porous materials, mesoporous silica nanoparticles (MSNs) are promising drug carriers with the following features such as homogeneous size, high pore volume and surface area and potential surface functionalization, which allows to better control over drug loading and release of pharmaceuticals.[84-85] Although silica is considered as on the whole to be poorly toxic, their biodegradation is relatively slow and this is still under debate while physicochemical parameters such as size, shape, surface property, and structure might affect the biocompatibility.[86] Slow biodegradation might also cause the potential accumulation risk after intravenous injection of MSNs, and thereby might give rise to biosafety issues. To improve the biodegradability of silica-based mesoporous nanoparticles, a series of redox-, pH-, and enzyme- triggered biodegradable mesoporous organosilica nanoparticles (MONs) has been successfully developed recently.[87]

MSNs were firstly reported as a drug delivery system for loading ibuprofen, an anti-inflammatory drug, into the mesopores of MCM-41 type MSNs in 2001.[88] In addition, the loading and release of other nonsteroidal anti-inflammatory drug (NSAID) naproxen, nimesulide and indomethacin have also been studied.[89-91] Positive-charge functionalized MSNs have been studied for oral drug delivery of an anti-inflammatory drug sulfasalazine (used for bowel disease) and Orange II (a fluorescent tracing molecule).[92] These drugs can be remained trapped in the nanovehicle when passing through the stomach's acidic environment and be released in intestine where the environmental pH is close to neutral. In the treatment of osteoarthritis and rheumatoid arthritis, hollow MSNs were an ideal carrier for natural drug celastrol with poor solubility and were of high biocompatibility for intra-articular injection, presenting a pH-sensitive anti-inflammatory property.[93] Lin's group have constructed a nanosystem for catalytic treatment of rheumatoid arthritis by loading the parent ligand manganese porphyrins and their related Schiff base complexes in the cavity of an Mn-engineered hollow MSN after polyethylene glycol (PEG) modification (**Figure 1.1.9**).[94] After the degradation in pathological site, the *in situ* synthesized manganese porphyrin features both SOD and catalase-like activities, which can deplete intracellular ROS in M1 macrophages to facilitate their polarization shift toward anti-inflammatory M2 phenotype. Simultaneously, the Si-containing oligomers released from the manganese silicate nanocarrier will promote the biomineralization of hydroxyapatite by bone mesenchymal stem cells, synergizing the catalytic antiarthritic treatment. However, a lot of questions still need to be addressed before clinical application, including synthesis method optimization, the control of host-guest interaction to monitor the drug encapsulation and release, and extensive preclinical studies on acute and chronic toxicity.[86]

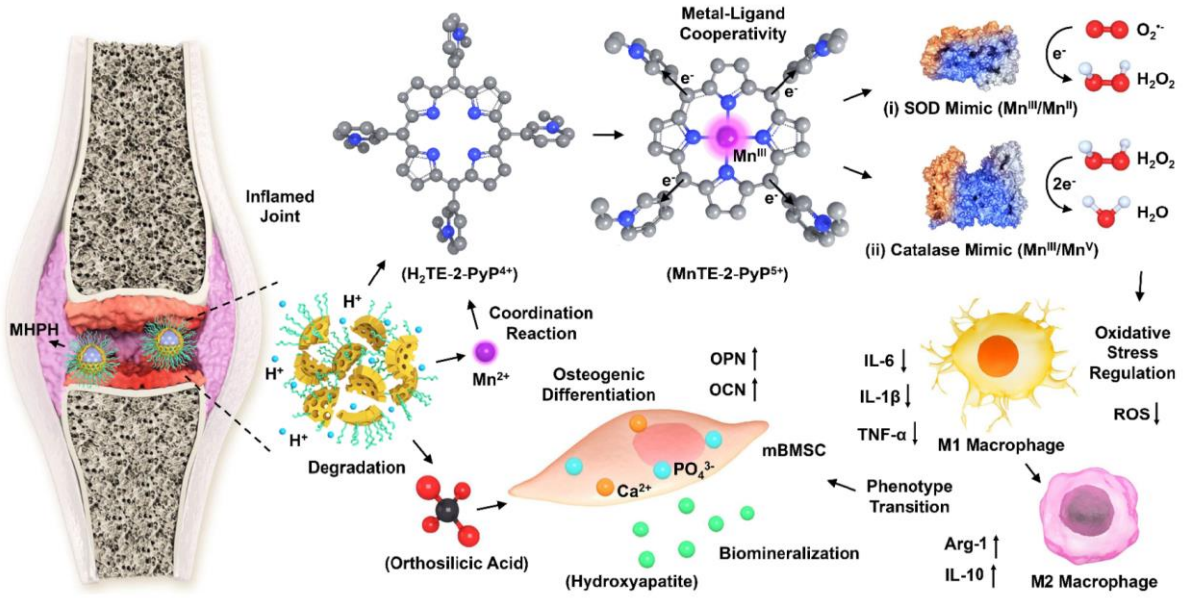

Figure 1.1.9 Schematic illustration for the therapeutic concept of a nanosystem of PEGylated 5,10,15,20-tetrakis(N-ethylpyridinium-2-yl)-porphyrin loaded Mn-engineered hollow MSN (Mn-HMSN-PEG-H_2TE-2-PyP^{4+}, denoted as MHPH) for catalytic anti-inflammatory treatments such as rheumatoid arthritis therapy.

1.1.4.2 Gold nanoparticles

Gold is an ancient drug with a long medical history. Intramuscular (IM) gold is the oldest disease modifying antirheumatic drugs (DMARDs), and it remains an ideal candidate for a step-up combination therapy strategy with MTX, since its mechanism of action is different from that of MTX.[95] The therapeutic effects could be attributed to two possible mechanisms: 1) gold binds to thiol-containing proteins and disturb receptor-ligand recognition; 2) gold ions can be sequentially oxidized in Au^{3+} by ROS, then reduced to Au^{+} by reacting with lysosomal enzymes, resulting in both a decrease of oxidative stress and an inhibition of lysosomal protease activity.[96]

Apart from ionic gold, gold nanoparticles (Au NPs) have interesting applications in medicine because of their particular physicochemical properties such as their high density and plasmonic properties, which are interesting for X-ray imaging or photothermal therapy. Au NPs are promising drug delivery systems of CO-releasing molecules (CORMs), antioxidant or anti-inflammatory siRNA for anti-inflammatory.[97-98] Au NPs also have intrinsic anti-inflammatory properties for improving inflammatory microenvironment *via* reducing regenerative cytokine production and decreasing ROS accumulation.[99-101] Macrophages make crucial contribution in the development of arthritis and acute lung injury (ALI), and upon stimulation, resting macrophages (M0) are polarized into the pro-inflammatory phenotype (classically activated, M1) and gold nanoparticles could repolarize macrophages from the M1 to anti-inflammatory M2 type.[102-103]

The anti-inflammatory activity of Au NPs is size-dependent, and Yang's group have studied series of peptide-gold nanoparticle hybrid in vitro and in a mouse model of acute lung injury and the peptide-Au NP hybrids with a Au NP core of 20 nm exhibited the most potent inhibitory activity on TLR4 activation and its downstream cytokine production in THP-1 cell-derived macrophages.[104] Surface chemistry of NPs can be used to generate pro- and anti-inflammatory responses in cells and animals. Khan's group studied the acute and subchronic pro-inflammatory cytokines mRNA expression effects of naked Au NPs (10 and 50 nm) in the liver and kidneys of rats and both of them significantly increased cytokines gene expression on day 1 which subsided on day 5.[105] Based on a 2 nm gold core, hydrophobic zwitterionic functionality boosted inflammatory outcomes, whereas hydrophilic zwitterionic nanoparticles generated minimal immunological responses and neutral particles generated a significant anti-inflammatory response both *in vitro* and *in vivo*.[106] These results provide important clues for controlling nanoparticle surface functionalities to regulate immune responses.

Although Au NPs exhibit excellent therapeutic efficacy in numerous studies, there still exists significant biosafety concerns. In terms of biodegradability, Alice *et al.* have monitored the biotransformation of citrate protected gold nanoparticles of different sizes (4, 15 and 22 nm) on primary fibroblasts up to 6 months and they revealed the unexpected degradation of Au NPs induced by ROS, and evidenced the recrystallization of 2.5-nm sulfur containing Au NPs and self-assembly of their degradation products into ultimate nanoleaves structure for possible elimination.[107] The general conclusion is that Au NPs are eventually degradable, but this process is size dependent (the smaller the faster). The use of Au NPs with different surface coatings, different morphologies or the use of different cell models may lead to different results, so that more works is still needed to better understand gold metabolism *in vivo*. Au nanoclusters (NCs) have been widely studied as antiphlogistic drug-free nanomedicines because of their biosafety, insignificant bioaccumulation in the body, and antioxidant effects.[108-110] Gold nanoclusters (1-2 nm) capped with N-acetylcysteine (Au NCs-NAC) displayed preferential renal enrichment (< 2 h) and longer retention (> 24 h) in acute kidney injury owing to the smaller size than kidney threshold (5.5 nm) and as a nanozyme-based antioxidant, Au NCs-NAC showed superiority in the restoration of renal function in AKI mice than free NAC by protecting the kidneys from oxidative injury and inflammation without systemic toxicity (**Figure 1.1.10**).[111]

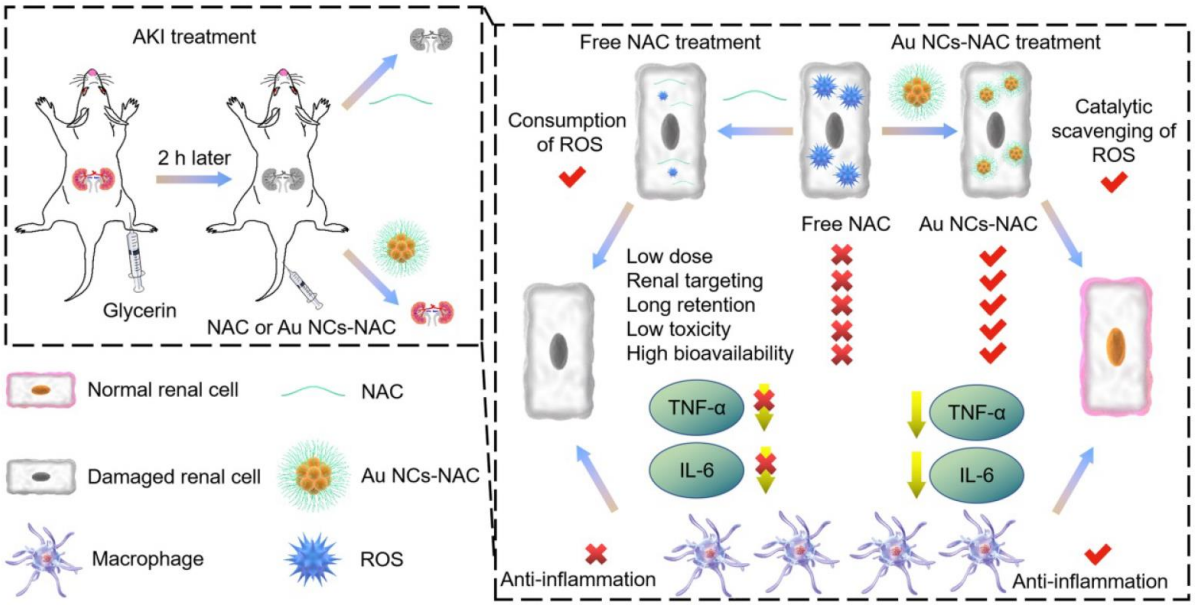

Figure 1.1.10 Schematic illustration of broad spectrum antioxidant and anti-inflammatory activities of ultrasmall Au NCs-NAC for AKI alleviation as compared with NAC.

Gao's group have synthesized a peptide coated gold cluster $Au_{25}Sv_9$ to evaluate its effects on inflammatory osteoclastogenesis *in vitro* and inflammation-induced bone destruction *in vivo* and gold clusters prevent inflammation-induced bone erosion through inhibiting the activation of NF-κB pathway.[112] Another gold cluster $Au_{29}SG_{27}$ NCs can effectively suppress both inflammation and bone damage in collagen-induced arthritis (CIA) in rats and also the dose-dependent efficacy of $Au_{29}SG_{27}$ NCs on the 30-day toxicity has been comprehensively evaluated.[113-114] Results showed that continuous intraperitoneal injection of 15 mg/kg (Au content) for 30 days resulted in slight hematological abnormalities and increases on organ coefficients (*i.e.*, organ weight to body weight) of kidney and adrenal gland, while 10 mg Au/kg did not cause any obvious toxicity and side effects and 5 mg Au/kg is the optimal dose of $Au_{29}SG_{27}$ NCs for RA therapy in rats, which provides a theoretical basis for further preclinical research.

1.1.4.3 Silver nanoparticles

Similar with gold nanoparticles, silver nanoparticles also possess anti-inflammatory property and they exert their anti-inflammatory effect through the TNF-*α* pathway in peritoneal adhesions without significant toxic effects.[115] Spherical silver nanoparticles and monodisperse hexagonal gold nanoparticles were synthesized by eco-friendly synthesis, and the nanoparticles reduced expression of inflammatory mediators and cyclooxygenase-2 (COX-2) was attenuated in lipopolysaccharide (LPS)-induced RAW 264.7 cell.[116] More specifically, Ag and Au nanoparticles could suppress activation of NF-kB signaling pathway *via* p38 MAPK.[116-117] Sun *et al.* synthesized an atomically precision $Au_{24}Ag_1$

"clusterzyme" that hosts an ultrahigh catalytic activity as well as antioxidative activity via atom manipulation (**Figure 1.1.11**). The designed artificial enzyme activates the Ag−S active site *via* lattice expansion in the oligomer atom layer, showing an antioxidant property 72 times higher than that of natural antioxidant Trolox.[118]

Figure 1.1.11 Schematic illustration of atomic engineering of Au_{25} clusters and $Au_{24}Ag_1$ clusterzyme's catalase-like (CAT-like) and glutathione peroxidase-like (GPx-like) activity.

1.1.4.4 Zinc oxide nanoparticles

Zinc oxide (ZnO) nanoparticles have also been as anti-inflammatory materials.[119-122] The anti-inflammatory activity and mechanisms of ZnO nanoparticles were systematically discussed in few reviews, including inhibition of pro-inflammatory mediator gene expression; downregulating the protein level of IL-6, IL-1β, IL-10, TNF-α and inhibiting NF-κB pathway by post-translational modification.[123-124] The usage of zinc ions is known for enhancing the anti-inflammatory effect of NSAIDs, and ZnO nanoparticles demonstrated beneficial effects over zinc oxide standard form on the anti-inflammatory and gastric activity of ketoprofen in rats.[125] ZnO NPs are also dietary supplements as they have immunomodulatory effect. Kidney nephropathy induced by cisplatin can be treated by antiapoptotic and anti-inflammatory effects of ZnO NPs along with their antioxidant activity.[126] Apart from various beneficial effects of ZnO NPs, the potential risks related to zinc oxide nanoparticles such as toxic effects cannot be ignored too.[127]

1.1.4.5 Cerium oxide (CeO_2) nanoparticles

Cerium (Ce) is a rare earth element that belongs to the lanthanide series of the periodic table. The basis for both the enzyme-mimetic and ROS/RNS scavenging capacity of CeO_2 NPs is dependent on the inherent physicochemical properties of nanoscale materials, the specific ability of CeO_2 NPs to absorb and release oxygen and the redox cycling between Ce^{4+} and Ce^{3+}.[128] CeO_2 nanoparticles with high Ce^{3+}/Ce^{4+} ratio exhibit high SOD-mimetic activity, whereas CeO_2 NPs with low Ce^{3+}/Ce^{4+} ratio on their surface function as efficient antioxidant CAT-mimetics, and whether or not a CeO_2 NPs behaves predominantly as a SOD-mimetic or as a CAT-mimetic is critically dependent on the purity of the

starting reagents.[128] The possible reactions of SOD-mimetic or CAT-mimetic involve the radical quenching and regeneration of oxidation states.

$Ce^{3+} + O_2^{\bullet-} + 2H^+ (aq) \rightarrow Ce^{4+} + H_2O_2$ (1)

$Ce^{4+} + O_2^{\bullet-} \rightarrow Ce^{3+} + O_2$ (2)

$H_2O_2 + 2Ce^{4+} + 2OH^- \rightarrow 2Ce^{3+} + 2H_2O + O_2$ (3)

Generally, CeO_2 NPs possess anti-inflammatory properties due to their role of free radicals scavenger and thus are able to decrease the ROS production but the size, morphology and Ce^{3+}/Ce^{4+} state of CeO_2 NPs should also be taken in consideration and their extrinsic properties such as agglomeration may result in a negative impact on anti-inflammatory effects.[129-131] Kim *et al.* synthesized ultrasmall citric acid-coated CeO_2 NPs with strong antioxidant properties that can alleviate inflammation induced edema and pain hypersensitivity by reducing secretion of proinflammatory cytokines and suppressing macrophage recruitment to the inflammation site and their biocompatibility and rapid excretion from the body were also verified in the study.[132] Dihydrolipoic acid-stabilized gold nanoclusters with cerium modification were employed for treatment of the RA rat model *in vitro* and *in vivo*, exhibiting extraordinary ROS scavenging and anti-inflammation effects by regulating macrophage polarization, and they were found to show superior enzyme-like activities compared with sole gold nanoclusters and be more effective than methotrexate.[133]

Considering the promising anti-inflammatory property of CeO_2 NPs, their toxicity should not be underestimated. In a complete *in vitro* toxicological assessment of the biological effects of CeO_2 NPs, CeO_2 NPs showed a reduced toxicity in acute exposure (24 h) to A549, Calu3 and 3T3 cells, but in subchronic exposures cytotoxic and inflammatory responses were observed in the human airway epithelial model after 60 days of exposure to CeO_2 NPs.[134] In another study, repeated oral exposure of CeO_2 NPs did not induce severe toxicities either up to the dose level of 1000 mg/kg.[135] All these results suggest a low toxicity of CeO_2 NPs, while further toxicity studies are required to better assess the potential risk to humans.

1.1.5 Nanoparticles of Metal-Organic Frameworks (nanoMOFs) for anti-inflammation

Metal–organic frameworks (MOFs) are a class of porous crystalline coordination polymers, consisting of metal nodes and organic linkers to form one-, two-, or three-dimensional structures. MOFs possess large surface areas and a versatile porosity making them widely used in various applications, such as gas adsorption and separation, catalysis, sensing, and biomedicine.[136] This part will first introduce few

biocompatible MOFs and then discuss the current progress of nanoMOFs for anti-inflammation. Interestingly, some enzyme-mimicking nanoMOFs act as intrinsic anti-inflammatory agent to downregulate oxidative stress, pro-inflammatory cytokines, etc. NanoMOFs are also promising for conventional anti-inflammatory drug delivery, biological agents delivery and more recently, hybrid nanoMOFs even potentiate anti-inflammatory applications.

1.1.5.1 Biocompatible MOFs

In the domain of drug delivery, one important challenge is the efficient delivery of drugs in the body using non-toxic carriers. Compared with most existing carrier materials, MOFs with the ability to tune their structures and porosities for better drug loadings are well suited as drug delivery systems and even for imaging applications. The framework of a biocompatible MOF consists of bioactive linkers and nontoxic cations (mainly Ca^{2+}, $Fe^{2+/3+}$ and Zn^{2+}) and these bioMOFs can deliver cargos *via* framework degradation.

1.1.5.1.1 Fe based MOFs

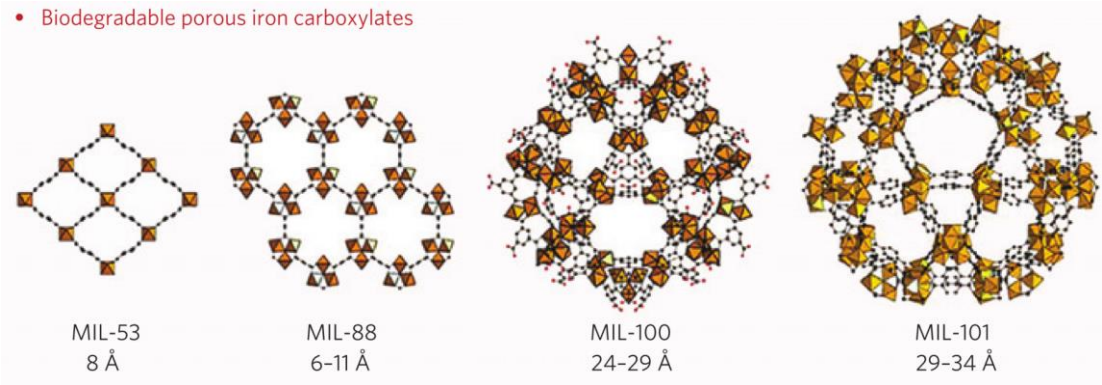

Figure 1.1.12 Crystalline structure of topical biodegradable Fe carboxylate based MOFs.

Poorly-toxic iron(III) carboxylate MOFs such as MIL-53(Fe), MIL-88(Fe), MIL-100(Fe) and MIL-101(Fe) (MIL stands for Materials of Institute Lavoisier) are either rigid or flexible microporous (< 2 nm) or mesoporous carriers (2-5 nm) (**Figure 1.1.12**). These nanoMOFs have been shown to behave as suitable nanocarriers for efficient controlled delivery of challenging drugs against cancer and AIDS.[137-138] In addition to drug loading, they exhibit some magnetic resonance imaging (MRI) properties due to paramagnetic iron atoms in their matrix particularly once they degraded into iron oxide nanoparticles once injected into blood. Especially, MIL-100(Fe) has been widely studied as drug carrier due to its high specific surface area (S_{BET}~2000 m^2/g, Vp~1,2 cm^3/g), high porosity (smaller cages ~25 Å and larger cages ~29 Å), and stability in a biological environment.[139-140] It can also be synthesized under green ambient pressure conditions as small nanoparticles (< 100 nm)[141] and its

surface can be easily functionalized by a wide range of biopolymers to confer them a better stability[142-146]. Large quantities of hydrophilic, hydrophobic, and amphiphilic drugs could be loaded, and the most important factors influencing drug encapsulation are the time of incorporation and the solubility of the drug tested.

Moreover, MIL-100(Fe) NPs are biodegradable and cytotoxicity studies have shown high biocompatibility, keeping iron homeostasis and the liver function intact. In terms of colloidal stability, MIL-100(Fe) nanoparticles tend to reversibly aggregate in body fluids depending on the pH, with usually a better colloidal stability in acidic conditions while there is a progressive aggregation in neutral ones. This benefits for intravenous lung targeting drug delivery but may lead to unspecific reticuloendothelial system (RES) capture.[147] MIL-100(Fe) NPs are also fragile in PBS (1.19 mM, pH 7.4) at 37°C and release large amounts (34 ± 3 wt%) of their constituting ligand (*i.e.*, trimesate) and lost their crystallinity within only 6 h. However the NPs maintained their initial sizes as the NPs turned into amorphous iron oxophosphates.[148-149] Note that the degradation mechanism of other Fe based MOFs is similar with MIL-100(Fe) and the process is dependent on with the phosphate concentration, the particle size or even synthesis method (crystallinity). Concerning these limitations, surface coatings may improve the colloidal stability and in some cases slowdown the kinetics of degradation. For instance, though the addition of BSA to the PBS medium (5.4% w/v), a significant reduction of ligand release was observed (15.1 ± 2.7 wt% vs 29.9 ± 2.1 wt% in PBS, after 24 h).[150]

1.1.5.1.2 Zinc based MOFs

Zn is an endogenous element, relevant to important biological functions and zinc based MOFs as nontoxic and biodegradable platforms are promising for biomedical applications.[151] ZIF-8 is the most popular Zn MOF due to its relative good stability under physiological conditions (PBS, pH 7.4). Its facile preparation based on the ambient temperature reaction between Zn^{2+} and 2-methylimidazole (2-MeIm) in polar solvents enables to accommodate directly, during its synthesis, various entities such as drugs, NPs and bio-macromolecules to establish multifunctional MOF based composites.[152] Additionally, the acid dependent degradability makes it highly attractive for the construction of pH-responsive drug delivery systems (DDSs). The mechanism of the ZIF-8 degradation was also attributed to the affinity of phosphate groups for Zn^{2+} cations and acidic conditions resulted in the protonation of the coordinate bonds of Zn-based NMOFs. The kinetic of decomposition of different particle size of ZIF-8 particles in PBS (10 mM, pH 7.4) showed that 79% and 88% of 2-MeIM was released for 2 μm and 250 nm ZIF-8, respectively, within the first hour treatment (faster than MIL-100(Fe)), and meanwhile insoluble zinc phosphate particles were formed.[153] As a drug carrier, ZIF-8 could be easily

decomposed in the acidic endo/lysosomal compartments and thus an abundant of Zn^{2+} release and ROS generation would enhance the cancer therapy or increase the toxicity.[154]

1.1.5.1.3 Phenol based MOFs

Polyphenols as a secondary metabolite of plants have been approved by FDA in food and medicine and most plant polyphenols such as tannic acid (TA), epigallocatechin gallate (EGCG), gallic acid (GA) and ellagic acid (EA), contain a common chemical group of pyrogallol, which could chelate with various metal ions (Fe^{3+}, Cu^{2+} and Mn^{2+}) to form phenol based MOFs in a simple, rapid and robust manner.[155-156] Metal-polyphenol coordination polymer (MPCPs) or phenol based MOFs have shown few advantages, which is described in **Figure 1.1.13**, and have been proposed for imaging and drug delivery.

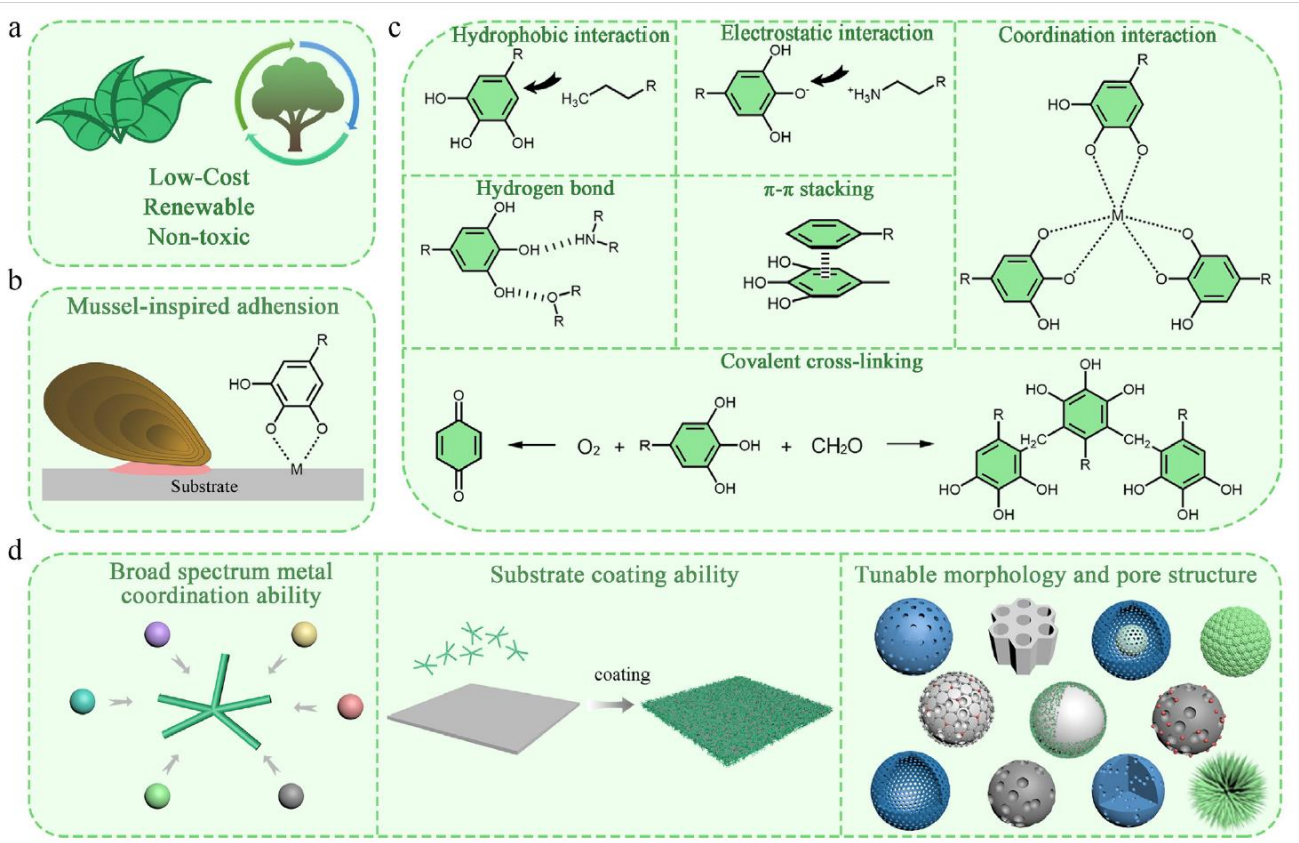

Figure 1.1.13 The advantages of plant polyphenols and the usage of MPCPs as a precursor. (a) Low-cost, renewable, non-toxic compounds, (b) mussel-inspired adhesion and (c) multiple interactions of plant polyphenols. (d) Broad-spectrum metal coordination ability, substrate coating ability and tunable morphology and pore structure of MPCPs and their derived mesoporous materials.

1.1.5.1.4 Cyclodextrin (CD) based MOFs

Cyclodextrin has been introduced as a drug carrier before, and here it also could be the backbone of MOFs. γ-CD as well as its derivatives and alkali metal cations (Li^+, Na^+, K^+, Rb^+, Cs^+) are involved in

the construction of CD-MOF.[157] Besides crystallinity and porous nature, cyclodextrin based MOFs are highly biocompatible and environmentally safe as it is derived from natural resources and they have attracted wide attention in biological sciences including drug delivery and cancer therapy. Although these CD-MOFs are soluble in water, these have been proposed for the non-covalent inclusion complexes for drug molecules like quercetin (QT), 5-fluorouracil (5-FU) and doxorubicin (DOX), enhancing their solubility, stability, bioavailability and safety and also they can be decorated with different functionalities to make them stimuli responsive for controlled drug release.[158-159] Interestingly, anti-inflammatory drug sodium diclofenac (DFNa) and curcumin could also be loaded in γ-CDs and the latter one was based on hydrogen bond type interaction between the OH group of cyclodextrin of CD-MOFs and the phenolic hydroxyl group of the curcumin.[160-161] The main drawbacks of CD-MOF based materials are their low water stability, strongly limiting them to the common practices.

1.1.5.1.5 Amino acid based MOFs

Amino acids have a terminal amino group and a terminal carboxyl group and potential sulfhydryl, hydroxyl, amino and carboxyl groups in their side chain, which affords abundant coordination sites for metal ions to synthesize amino acid based MOFs.[162] Aromatic amino acids phenylalanine (Phe) and tyrosine (Tyr) derivatives were synthesized first and chosen as the ligands to construct MOFs.[163] Wang *et al*. has reported a microporous zirconium amino acid MOF, MIP-202(Zr) (MIP stands for Materials of Institute of Porous Materials), constructed from natural *α*-amino acid L-aspartic acid by a green, scalable and facile preparation, showing a good chemical stability in solutions of wide pH range and boiling water and potential for biological and pharmaceutical applications.[164] Can et al. has synthesized biocompatible amino acid-based MOFs in ethanol under reflux by incorporating L-glutamic acid as organic ligand and the acetate salts of Co (II), Ni (II), and Cu (II) as metal nodes into MOF structure, exhibiting remarkable antibacterial activities against Escherichia coli and Staphylococcus aureus.[165] Various enantiopure amino acids such as L-tyrosine, L-histidine, L-tryptophan and L-glutamic acid are coordinated with Zn^{2+} or Co^{2+} ions to fabricate homochiral metal-organic frameworks for HPLC separation. However, amino acid based MOFs are scarcely studied for biomedical applications mainly due to their poor stability in water and/or their limited porosity to accommodate drugs.

1.1.5.1.6 Porphyrin based MOFs

Porphyrins belong to a class of heterocyclic macrocycles and these organic compounds are constructed from four conjugated pyrrole rings arranged in a circle with the connection of methylene bridges. Porphyrins have a total of 26 π-electrons, of which 18 π-electrons are in a planar, continuous

macrocycle.[166] Porphyrins have potent biological properties, including biocompatibility, effective clearance, long residence time in tumors and few side effects. Although it is possible to construct biofriendly porphyrin-based MOFs with biocompatible metal ions (*e.g.*, Fe, Zn, Ca, Mg), their development in biomedical applications is still at the early stage since their physicochemical properties and toxicology have not been fully investigated.[167] This stems probably from their complex preparation route involving toxic solvents although very promising anticancer *in vivo* results have been reported recently by W. Lin *et al.*[168-172]

1.1.5.2 nanoMOFs as intrinsic anti-inflammatory agent

Anti-inflammation is frequently associated with anti-oxidant property because excessive ROS will lead to irreversible cell damage and induce the activation of resident immune cells and inflict secondary tissue or organ injury. MOFs are of interests to act as enzymes mimics to remove the overproduction of these species.

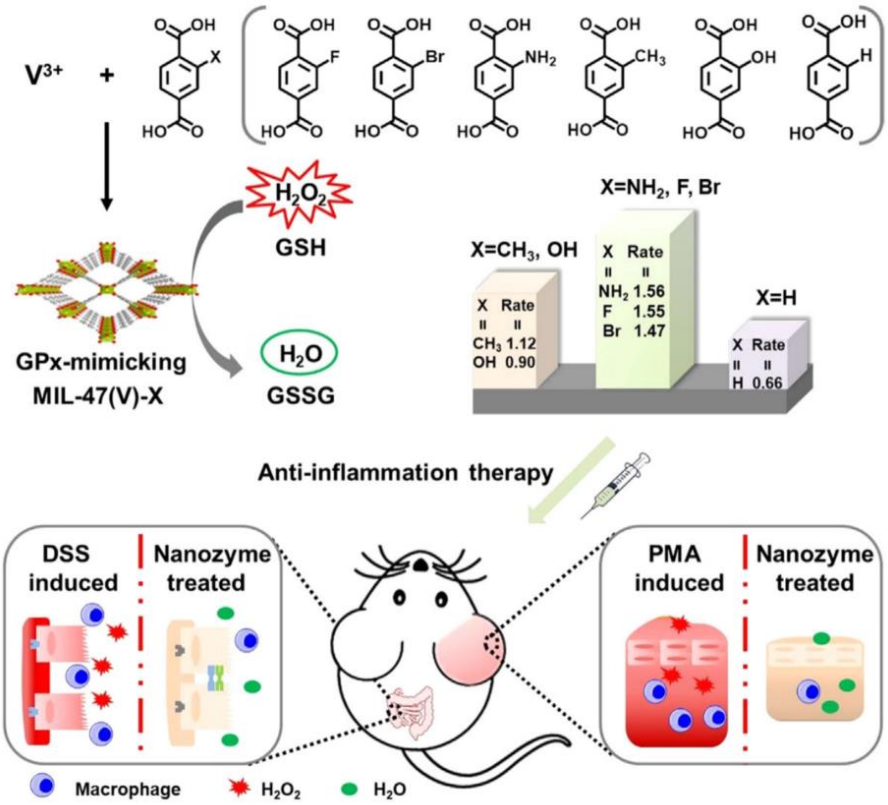

Figure 1.1.14 Illustration of the synthesis of rationally designed GPx-mimicking MIL47(V)-X MOF nanozymes for anti-inflammation therapy. Substituted terephthalate linkers (X=F, Br, NH_2, CH_3, OH, and H) were used to coordinate with vanadium metal ions to form isostructural MIL-47(V)-X MOFs with modulated GPx-mimicking activities. Among them, MIL-47(V)-NH_2 had the highest GPx-mimicking activity and was selected for further investigation in anti-inflammation therapy. Its excellent antioxidation ability can effectively attenuate inflammation in both ear-inflammation and colitis models.

Glutathione peroxidase (GPx) plays an important role in maintaining intracellular redox balance. It however suffers from some limitations common to most natural enzymes, namely low stability and poor availability. Specifically, Wu *et al.* has modulated the GPx-mimicking activities of the microporous vanadium terephthalate MIL-47(V)-X MOFs by varying the substitution of H in the 1,4-benzenedicarboxylicacid (BDC) ligand with F, Br, NH_2, CH_3, and OH. Among these isostructural MOFs of MIL-47(V)-X, MIL-47(V)-NH_2 as a ROS scavenger exhibits the highest GPx-mimicking activity *in vitro* and demonstrates a broad-spectrum anti-inflammatory effect toward both ear inflammation and colitis (**Figure 1.1.14**).[173]

To mimic an enzyme more efficiently, one possibility is to obtain nanoenzymes with the simulation of size and the three-dimensional architecture of natural enzymes. Bio-inspired Cu-TCPP MOF nanodots (denoted as CTMDs) were fabricated to mimic natural SOD for alleviating endotoxemia with the ability of renal enrichment and clearance (**Figure 1.1.15**). Together with the GPx-like activity, CTMDs could protect cell components *in vitro* as well as reduce the systemic inflammation and mortality in LPS-induced acute kidney injury during endotoxemia *in vivo*.[174]

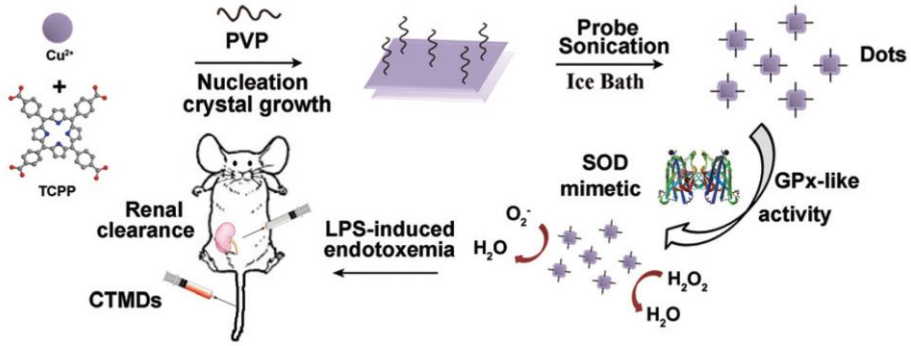

Figure 1.1.15 Scheme illustration of the synthesis of CTMDs and the treatment of acute kidney injury.

Sepsis is a life-threatening systemic inflammatory response to infection and circulating cell-free DNA (cfDNA) released by damaged cells could cause inflammation and has been associated with the progression of sepsis. As an alternative of anti-oxidant activity, elimination of inflammation related DNA is also an alternative approach to treat inflammatory diseases. The strategy is to use cationic nanoparticles (NPs) to bind and eliminate the anionic proinflammatory nucleic acids. Liu *et al.* created cationic MOFs "nanotraps" for scavenging inflammatory circulating DNA by grafting cationic polyethylenimine (PEI) polymers onto a zeolitic imidazolate framework-8 (PEI-g-ZIF) *via* a simple one-pot process (**Figure 1.1.16A**).[175] Authors compared PEI-g-ZIF NPs fabricated using PEI of 600, 1800, and 25k Da and with pure PEI (lacking ZIF), and *in vivo* study showed that the PEI 1800-g-ZIF

NPs effectively mitigated cecal ligation and puncture (CLP)-induced multiple organ damage and increased the survival rate of mice with severe sepsis, outperforming free PEI 1800.

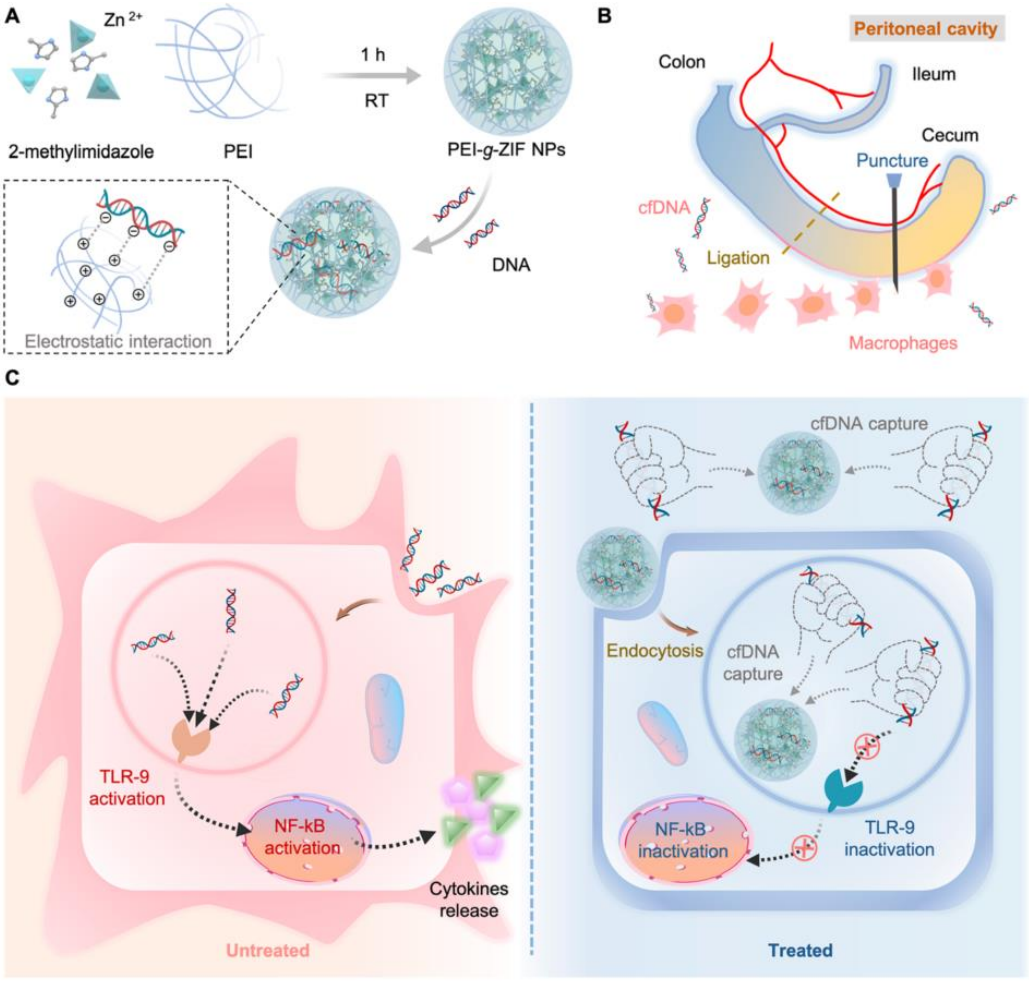

Figure 1.1.16 (A) Preparation of PEI-g-ZIF NPs. (B) CLP-induced sepsis model. (C) Schematic of inflammation in untreated sepsis (left) and sepsis treatment by cfDNA scavenging by PEI-g-ZIF NPs (right).

Magnesium (Mg) is an abundant mineral that contributes to the structural development of bone in the human body. Mg/HCOOH metal organic framework with a continuously release of Mg^{2+} for a long time was reported as a therapeutic compound for osteoarthritis.[176]

1.1.5.3 nanoMOFs for conventional anti-inflammatory drug delivery

MOFs are porous materials and it is common to explore their drug delivery capacity. As discussed before, methotrexate (MTX) has been used as a clinical drug for the treatment of rheumatoid arthritis (RA). To avoid the severe side-effects of MTX, Guo *et al.* employed phenolic-based MOFs as nanocarriers to deliver MTX for targeted rheumatoid arthritis therapy and better anti-inflammatory activity and biosafety of the nanosystem was confirmed in comparison of free MTX counterpart (**Figure 1.1.17**).[177] Herein, although there is a lack of characterization, MTX was first conjugated with

tannic acid (TA) and then coordinated with ferric ion (Fe^{3+}), followed by surface modification of hyaluronic acid (HA). Its facile and green preparation and exceptionally high drug loading capacity are the main advantages of this nanocarrier. Although tannic acid (TA) is a type of natural polyphenols and MOFs constructed by bioactive ligands are quite advantageous, authors did not demonstrate the formation of a crystalline and porous MOF structure.

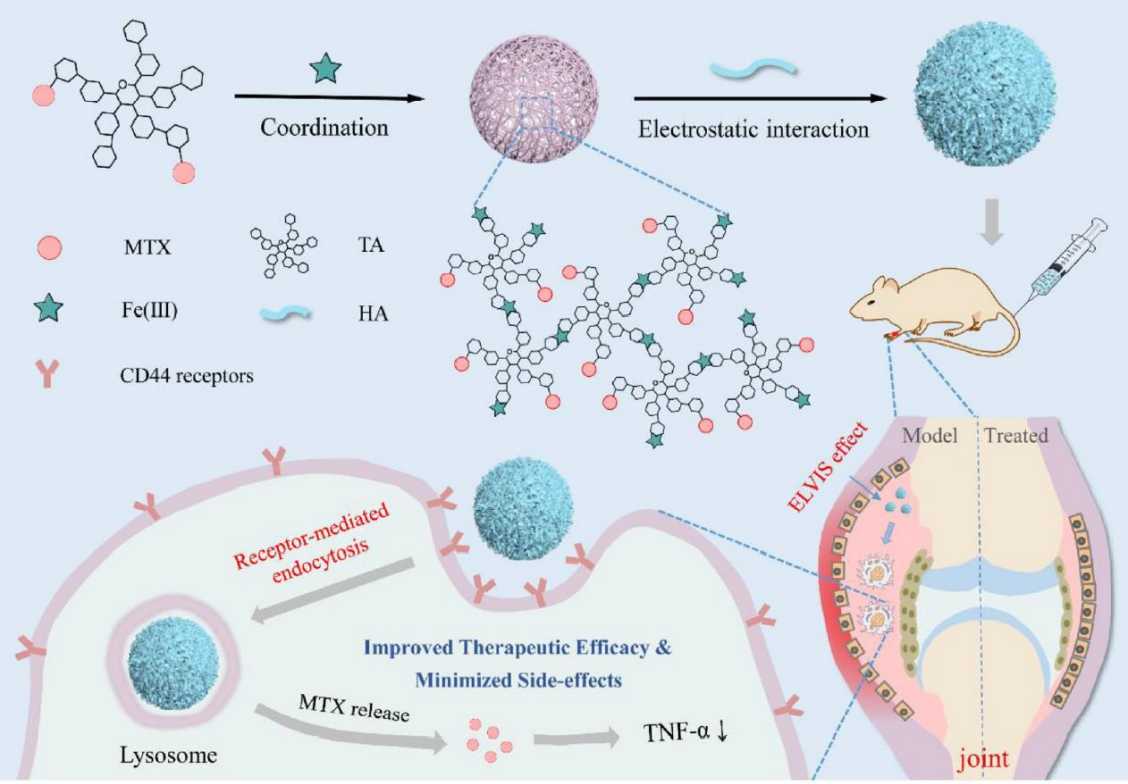

Figure 1.1.17 Schematic illustration the construction of MTX-TA/Fe^{3+}@HA for targeted RA treatment. MTX was covalently conjugated with TA, and then coordinated with Fe^{3+} to form the drug loading MOF with surface HA modification. Upon intravenous administration, the resulting MTX-TA/Fe^{3+}@HA could passively accumulate in the inflamed joints *via* ELVIS effect, and selectively deliver MTX into the activated macrophages through CD44 receptor-mediated endocytosis for RA therapy.

Encouraged by the anti-oxidative properties of CeO_2 NPs, Ce-MOF was also chosen as ROS scavenger and as the carrier for anti-inflammatory drugs.[178] Interestingly, the valence change of cerium ions upon ROS excitation alters the coordination between cerium and p-phthalic acid (PTA), thus inducing pore size transformation of Ce-MOF from mesopore to macropore (**Figure 1.1.18**). This MOF exhibited excellent drug loading of 5-Amino salicylic acid (5-ASA), a classical nonsteroidal anti-inflammation drug and laquinimod, an immunomodulator. Moreover, after the modification of poly(sodium4-styrenesulfonate) (PSS), the obtained Ce-MOF@PSS with negatively charged surface preferentially adheres to inflammatory intestine. Although Ce-MOF@PSS vehicle showed promising synergistic therapeutic effects on IBD *via* daily rectal enemas, the micrometer scale of Ce-MOF here and stability maybe a hurdle for translational nanomedicine. Currently, there is no systematic toxicological

assessment of Ce-MOFs, which should be similar with CeO_2 NPs, but more related studies are still required. Nevertheless, Ce-MOF is still a good candidate for inflammatory diseases therapy.

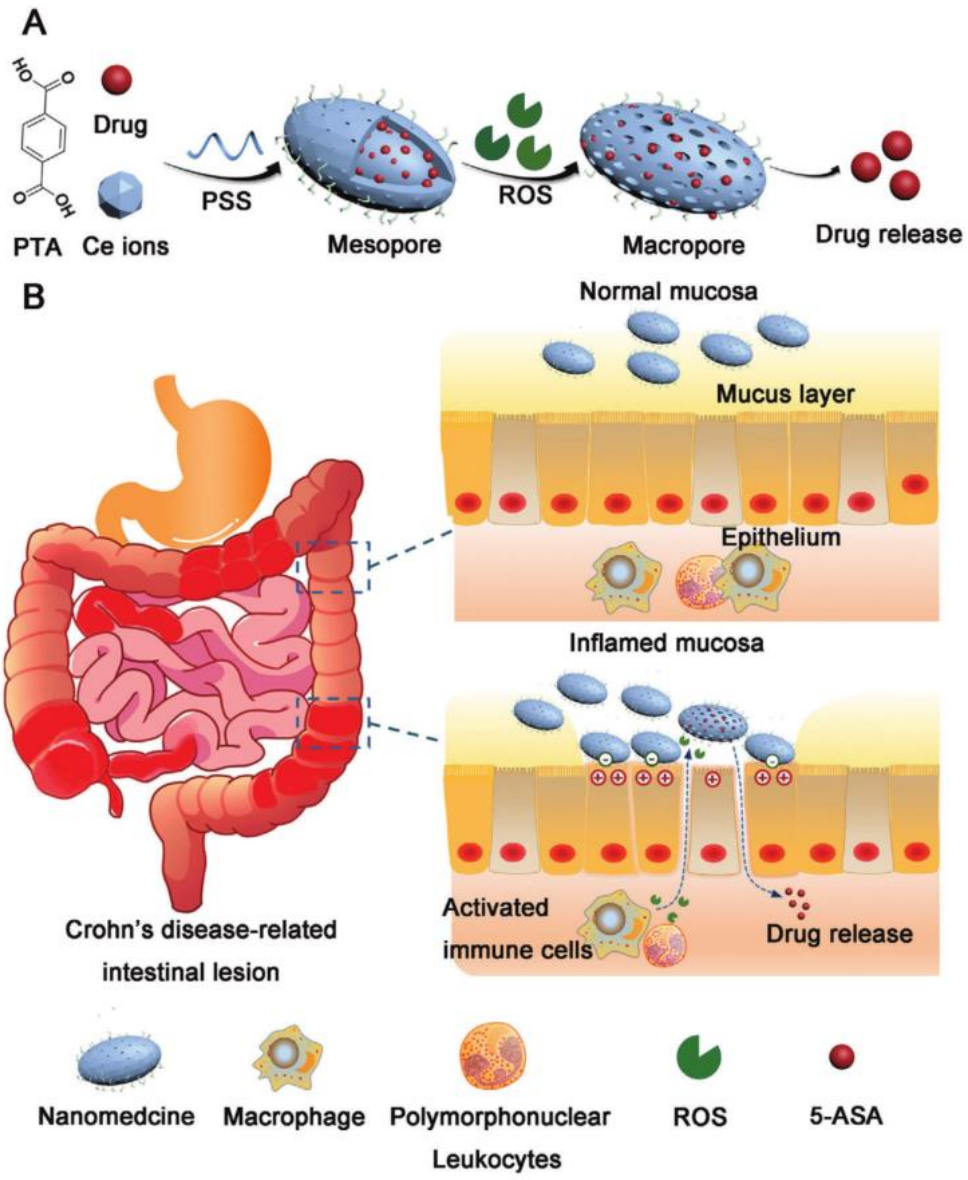

Figure 1.1.18 Synthesis of 5-ASA@Ce-MOF@PSS and drug release at inflammatory intestine. A) Fabrication and drug encapsulation of 5-ASA@CeMOF@PSS. B) Proposed mechanism for inflammation-targeting drug delivery by Ce-MOF@PSS.

1.1.5.4 nanoMOFs for biological agents delivery

1.1.5.4.1 SiRNA

Gene delivery is a recent treatment of inflammatory diseases, and an ideal drug delivery system should possess high loading capacity and protective effects against biological degradation. In **Figure 1.1.19,** TA-Fe^{3+} MOFs were prepared *via* coordination between tannic acid (TA) and Fe^{3+} and upon loading TNF-*α* siRNA, they were used for RA therapy [179] The MOF, although once again poorly characterized

with no analysis of the structure and porosity, show excellent biocompatibility, and enable rapid endo/lysosome escape of siRNA *via* the proton-sponge effect for effectively down-regulating cytokines. Importantly, such nanomedicine displays intrinsic radicals scavenging capability to eliminate a broad spectrum of ROS and nitrogen species (RONS), which in turn repolarizes the M1 macrophages into anti-inflammatory M2 phenotypes for enhanced RA therapy in combination with siRNA.

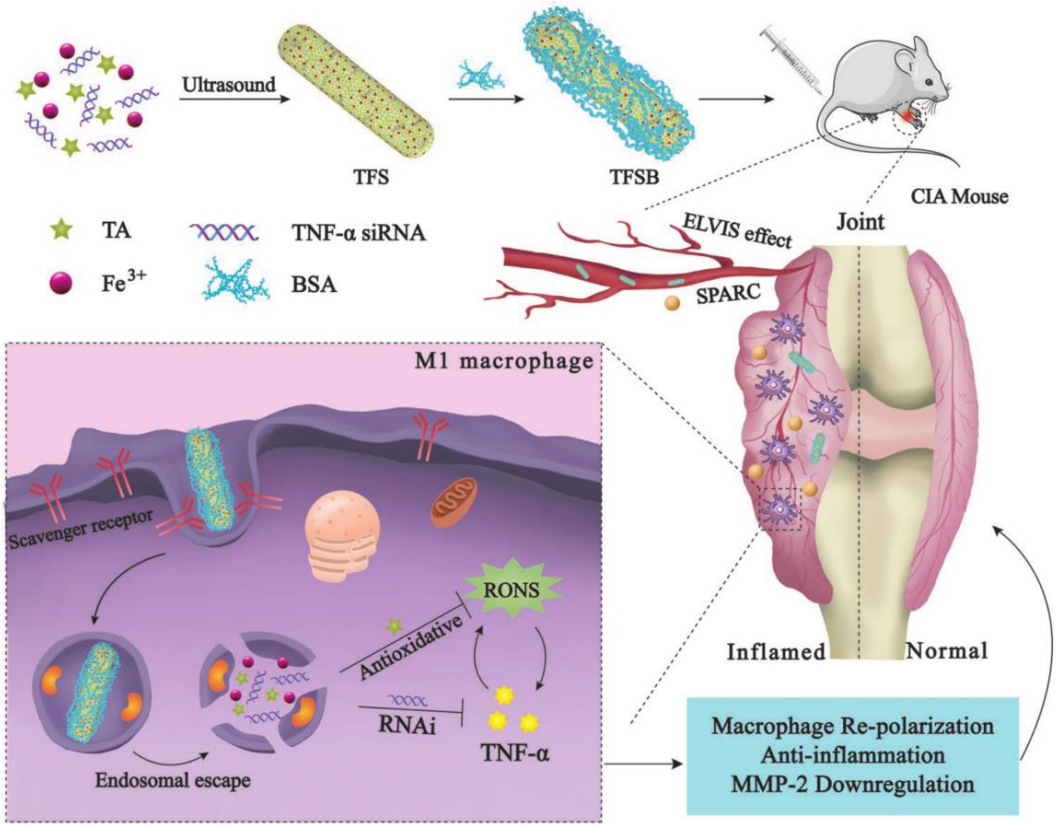

Figure 1.1.19 Schematic illustration of the construction of TFSB, and its *in vivo* application for RA therapy.

1.1.5.4.2 Catalase

As is mentioned before, activated macrophages (M1-type) in the synovium is believed to play a vital role in the progression of osteoarthritis (OA) and excessive ROS and mitochondrial dysfunction are their main features. One strategy of anti-inflammation is to simultaneously regulate intracellular gases and remedy mitochondrial function by inhibiting iNOS and H_2O_2. In **Figure 1.1.20**, catalase and S-Methylisothiourea sulfate (SMT) were encapsulated in ZIF-8 nanoparticles to catalyze the production of oxygen (O_2) from H_2O_2 and to inhibit iNOS, hence reducing NO production, respectively.[180-181] Results demonstrated that modified NPs were capable of inhibiting hypoxia-inducible factor 1α, further rescuing mitochondrial function.

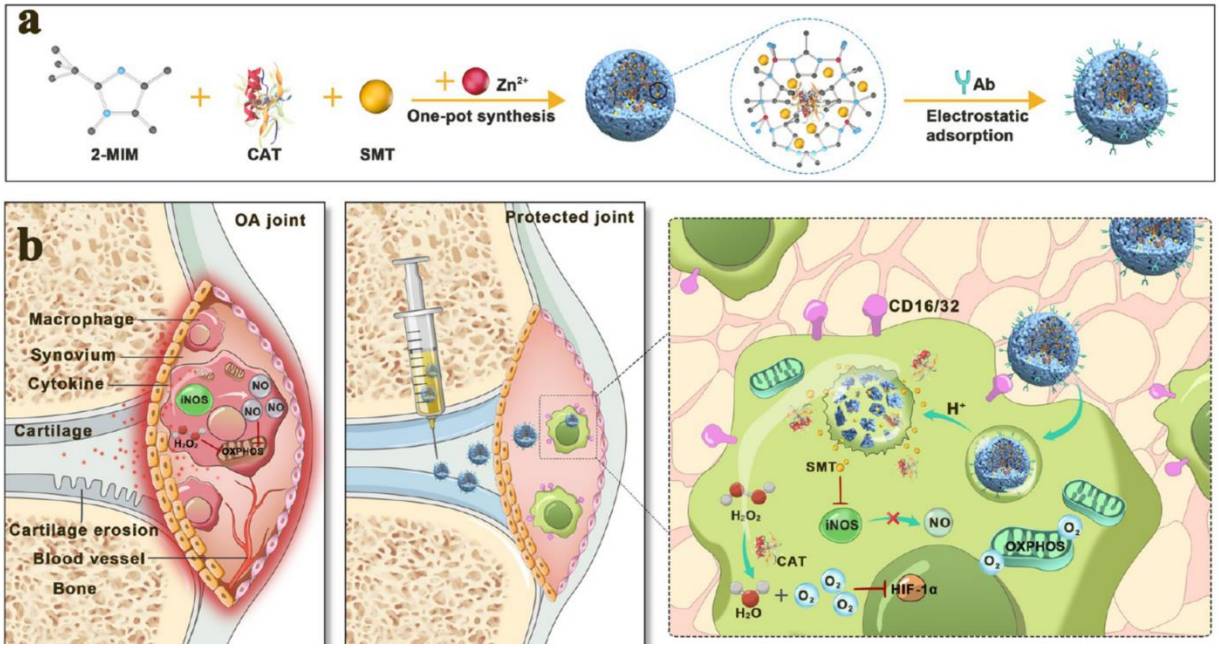

Figure 1.1.20 (a) Schematic illustration of the synthesis processes for CAT&SMT@ZIF-8-Ab NPs. (b) Modified ZIF-8 NPs target synovial macrophages to regulate intracellular gases and reprogram the metabolic pathway, thus attenuating OA.

1.1.5.5 Hybrid nanoMOFs for anti-inflammation

Compared with natural enzyme, nanozymes have expressed particular advantages such as low cost, high stability, multifunctionality, and ease of large-scale production, and hybrid nanoMOFs make anti-inflammation even more efficient based on nanoenzyme cascade reactions. A nanozyme-containing biomimetic cascade system (Pt-iNOS@ZIF) was designed by the co-precipitation approach of simultaneously loading enzyme molecules (iNOS) and Pt NPs into the ZIF-8 supporting matrix against hepatic ischemia-reperfusion injury (IRI).[182] Herein, the synthesized Pt nanozyme showed SOD/CAT-like properties and then iNOS enzyme could further catalyze L-Arginine (L-Arg) and O_2 to produce L-Citrulline (L-Cit) and NO. It can reduce oxidative stress and inhibit proinflammatory cytokines, resulting in effective prevention the liver from IRI (**Figure 1.1.21**). Also, Liu *et al.* integrated cascade nanozyme into a formulation of Pt@PCN222-Mn to eliminate excessive ROS in two forms of IBD (*i.e.*, ulcerative colitis and Crohn's disease).[183] Mn(III) active site in Mn SOD, was synthesized to mimic SOD.

Apart from the integration of nanoenzymes, the structure or function of hybrid nanoMOFs is very diverse. A hierarchical micro/nanofibrous scaffolds incorporated with curcumin loaded ZIF-8 NPs have been designed for enhanced diabetic wound healing *via* anti-oxidant and anti-inflammatory activities.[184]

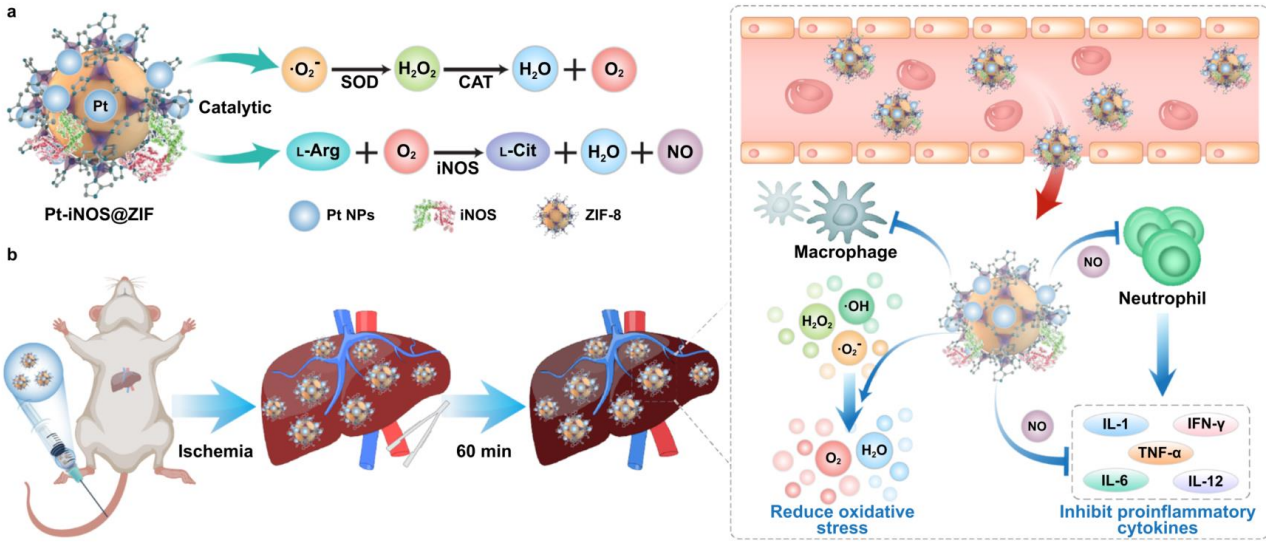

Figure 1.1.21 Schematic illustration of hepatic IRI prevention performance by Pt-iNOS@ZIF nanoreactor.

In conclusion, inflammatory response is associated with different diseases, and more and more nanocarriers have been developed for anti-inflammation. The general strategy is to deliver anti-inflammatory drugs and anti-oxidants or modulate inflammatory microenvironment. Recently, MOFs as potential drug delivery system emerged for anti-inflammation and theranostic MOFs could be a promising benign system that can be used to deliver anti-inflammatory drug, alleviate oxidative stress and monitor the progression of inflammatory diseases.

References

1. Medzhitov, R., Origin and Physiological Roles of Inflammation. *Nature* **2008,** *454* (7203), 428-435.
2. Greten, F. R.; Grivennikov, S. I., Inflammation and Cancer: Triggers, Mechanisms, and Consequences. *Immunity* **2019,** *51* (1), 27-41.
3. Coussens, L. M.; Werb, Z., Inflammation and Cancer. *Nature* **2002,** *420* (6917), 860-867.
4. Grivennikov, S. I.; Greten, F. R.; Karin, M., Immunity, Inflammation, and Cancer. *Cell* **2010,** *140* (6), 883-899.
5. Jayashree, S.; Nirekshana, K.; Guha, G.; Bhakta-Guha, D., Cancer Chemotherapeutics in Rheumatoid Arthritis: A Convoluted Connection. *Biomed Pharmacother* **2018,** *102*, 894-911.
6. Smolen, J. S.; Aletaha, D., Rheumatoid Arthritis Therapy Reappraisal: Strategies, Opportunities and Challenges. *Nat Rev Rheumatol* **2015,** *11* (5), 276-289.
7. Tak, P. P.; Firestein, G. S., NF-Kappab: A Key Role in Inflammatory Diseases. *J Clin Invest* **2001,** *107* (1), 7-11.
8. Kim, E. K.; Choi, E. J., Pathological Roles of MAPK Signaling Pathways in Human Diseases. *Biochim Biophys Acta* **2010,** *1802* (4), 396-405.
9. Kawasaki, T.; Kawai, T., Toll-Like Receptor Signaling Pathways. *Front Immunol* **2014,** *5*, 461.
10. Roy, A.; Srivastava, M.; Saqib, U.; Liu, D.; Faisal, S. M.; Sugathan, S.; Bishnoi, S.; Baig, M. S., Potential Therapeutic Targets for Inflammation in Toll-Like Receptor 4 (TLR4)-Mediated Signaling

Pathways. *Int Immunopharmacol* **2016,** *40*, 79-89.
11. Chen, L.; Wang, Y.; Sun, L.; Yan, J.; Mao, H. Q., Nanomedicine Strategies for Anti-Inflammatory Treatment of Noninfectious Arthritis. *Adv Healthc Mater* **2021,** *10* (11), 2001732.
12. Yu, Z.; Reynaud, F.; Lorscheider, M.; Tsapis, N.; Fattal, E., Nanomedicines for the Delivery of Glucocorticoids and Nucleic Acids as Potential Alternatives in the Treatment of Rheumatoid Arthritis. *Wiley Interdiscip Rev Nanomed Nanobiotechnol* **2020,** *12* (5), 1630.
13. Vandewalle, J.; Luypaert, A.; De Bosscher, K.; Libert, C., Therapeutic Mechanisms of Glucocorticoids. *Trends Endocrinol Metab* **2018,** *29* (1), 42-54.
14. Brune, K.; Patrignani, P., New Insights into the Use of Currently Available Non-Steroidal Anti-Inflammatory Drugs. *J Pain Res* **2015,** *8*, 105-118.
15. Smolen, J. S.; Landewe, R. B. M.; Bijlsma, J. W. J.; Burmester, G. R.; Dougados, M.; Kerschbaumer, A.; Mcinnes, I. B.; Sepriano, A.; Van Vollenhoven, R. F.; De Wit, M.; Aletaha, D.; Aringer, M.; Askling, J.; Balsa, A.; Boers, M.; Den Broeder, A. A.; Buch, M. H.; Buttgereit, F.; Caporali, R.; Cardiel, M. H.; De Cock, D.; Codreanu, C.; Cutolo, M.; Edwards, C. J.; Van Eijk-Hustings, Y.; Emery, P.; Finckh, A.; Gossec, L.; Gottenberg, J. E.; Hetland, M. L.; Huizinga, T. W. J.; Koloumas, M.; Li, Z.; Mariette, X.; Muller-Ladner, U.; Mysler, E. F.; Da Silva, J. A. P.; Poor, G.; Pope, J. E.; Rubbert-Roth, A.; Ruyssen-Witrand, A.; Saag, K. G.; Strangfeld, A.; Takeuchi, T.; Voshaar, M.; Westhovens, R.; Van Der Heijde, D., EULAR Recommendations for the Management of Rheumatoid Arthritis with Synthetic and Biological Disease-Modifying Antirheumatic Drugs: 2019 Update. *Ann Rheum Dis* **2020,** *79* (6), 685-699.
16. Kim, K.; Choi, H.; Choi, E. S.; Park, M. H.; Ryu, J. H., Hyaluronic Acid-Coated Nanomedicine for Targeted Cancer Therapy. *Pharmaceutics* **2019,** *11* (7), 301.
17. Shin, J. M.; Kim, S. H.; Thambi, T.; You, D. G.; Jeon, J.; Lee, J. O.; Chung, B. Y.; Jo, D. G.; Park, J. H., A Hyaluronic Acid-Methotrexate Conjugate for Targeted Therapy of Rheumatoid Arthritis. *Chem Commun (Camb)* **2014,** *50* (57), 7632-7635.
18. Chen, Z.; Liu, Z.; Li, Z.; Ju, E.; Gao, N.; Zhou, L.; Ren, J.; Qu, X., Upconversion Nanoprobes for Efficiently In Vitro Imaging Reactive Oxygen Species and In Vivo Diagnosing Rheumatoid Arthritis. *Biomaterials* **2015,** *39*, 15-22.
19. Matalqah, S. M.; Aiedeh, K.; Mhaidat, N. M.; Alzoubi, K. H.; Bustanji, Y.; Hamad, I., Chitosan Nanoparticles as a Novel Drug Delivery System: A Review Article. *Curr Drug Targets* **2020,** *21* (15), 1613-1624.
20. Tian, B.; Liu, Y.; Liu, J., Chitosan-Based Nanoscale and Non-Nanoscale Delivery Systems for Anticancer Drugs: A Review. *European Polymer Journal* **2021,** *154*, 110533.
21. Iacob, A. T.; Lupascu, F. G.; Apotrosoaei, M.; Vasincu, I. M.; Tauser, R. G.; Lupascu, D.; Giusca, S. E.; Caruntu, I. D.; Profire, L., Recent Biomedical Approaches for Chitosan Based Materials as Drug Delivery Nanocarriers. *Pharmaceutics* **2021,** *13* (4).
22. Yu, A.; Shi, H.; Liu, H.; Bao, Z.; Dai, M.; Lin, D.; Lin, D.; Xu, X.; Li, X.; Wang, Y., Mucoadhesive Dexamethasone-Glycol Chitosan Nanoparticles for Ophthalmic Drug Delivery. *Int J Pharm* **2020,** *575*, 118943.
23. Hanafy, A. F.; Abdalla, A. M.; Guda, T. K.; Gabr, K. E.; Royall, P. G.; Alqurshi, A., Ocular Anti-Inflammatory Activity of Prednisolone Acetate Loaded Chitosan-Deoxycholate Self-Assembled Nanoparticles. *Int J Nanomedicine* **2019,** *14*, 3679-3689.
24. Ahmed, O.; Abdel-Halim, M.; Farid, A.; Elamir, A., Taurine Loaded Chitosan-Pectin Nanoparticle Shows Curative Effect against Acetic Acid-Induced Colitis in Rats. *Chem Biol Interact* **2022,** *351*, 109715.
25. Jin, H.; Zhao, Z.; Lan, Q.; Zhou, H.; Mai, Z.; Wang, Y.; Ding, X.; Zhang, W.; Pi, J.; Evans, C. E.; Liu, X., Nasal Delivery of Hesperidin/Chitosan Nanoparticles Suppresses Cytokine Storm Syndrome in a Mouse Model of Acute Lung Injury. *Front Pharmacol* **2020,** *11*, 592238.
26. Russo, E.; Gaglianone, N.; Baldassari, S.; Parodi, B.; Croce, I.; Bassi, A. M.; Vernazza, S.; Caviglioli, G., Chitosan-Clodronate Nanoparticles Loaded in Poloxamer Gel for Intra-Articular

Administration. *Colloids Surf B Biointerfaces* **2016,** *143*, 88-96.
27. Chang, S. H.; Lin, Y. Y.; Wu, G. J.; Huang, C. H.; Tsai, G. J., Effect of Chitosan Molecular Weight on Anti-Inflammatory Activity in the RAW 264.7 Macrophage Model. *Int J Biol Macromol* **2019,** *131*, 167-175.
28. Li, J.; Loh, X. J., Cyclodextrin-Based Supramolecular Architectures: Syntheses, Structures, and Applications for Drug and Gene Delivery. *Adv Drug Deliv Rev* **2008,** *60* (9), 1000-1017.
29. Tian, B.; Liu, Y.; Liu, J., Smart Stimuli-Responsive Drug Delivery Systems Based on Cyclodextrin: A Review. *Carbohydr Polym* **2021,** *251*, 116871.
30. Gadade, D. D.; Pekamwar, S. S., Cyclodextrin Based Nanoparticles for Drug Delivery and Theranostics. *Adv Pharm Bull* **2020,** *10* (2), 166-183.
31. Jadhav, D.; Vavia, P., Dexamethasone Sodium Phosphate Loaded Modified Cyclodextrin Based Nanoparticles: An Efficient Treatment for Rheumatoid Arthritis. *J Pharm Sci* **2021,** *110* (3), 1206-1218.
32. Zeng, Z.; He, X.; Li, C.; Lin, S.; Chen, H.; Liu, L.; Feng, X., Oral Delivery of Antioxidant Enzymes for Effective Treatment of Inflammatory Disease. *Biomaterials* **2021,** *271*, 120753.
33. Batul, R.; Tamanna, T.; Khaliq, A.; Yu, A., Recent Progress in the Biomedical Applications of Polydopamine Nanostructures. *Biomater Sci* **2017,** *5* (7), 1204-1229.
34. Yang, P.; Zhu, F.; Zhang, Z.; Cheng, Y.; Wang, Z.; Li, Y., Stimuli-Responsive Polydopamine-Based Smart Materials. *Chem Soc Rev* **2021,** *50* (14), 8319-8343.
35. Cheng, W.; Zeng, X.; Chen, H.; Li, Z.; Zeng, W.; Mei, L.; Zhao, Y., Versatile Polydopamine Platforms: Synthesis and Promising Applications for Surface Modification and Advanced Nanomedicine. *ACS Nano* **2019,** *13* (8), 8537-8565.
36. Ryu, J. H.; Messersmith, P. B.; Lee, H., Polydopamine Surface Chemistry: A Decade of Discovery. *ACS Appl Mater Interfaces* **2018,** *10* (9), 7523-7540.
37. Wang, Z.; Duan, Y.; Duan, Y., Application of Polydopamine in Tumor Targeted Drug Delivery System and Its Drug Release Behavior. *J Control Release* **2018,** *290*, 56-74.
38. Jin, A.; Wang, Y.; Lin, K.; Jiang, L., Nanoparticles Modified by Polydopamine: Working as "Drug" Carriers. *Bioact Mater* **2020,** *5* (3), 522-541.
39. Ambekar, R. S.; Kandasubramanian, B., A Polydopamine-Based Platform for Anti-Cancer Drug Delivery. *Biomater Sci* **2019,** *7* (5), 1776-1793.
40. Hu, J.; Yang, L.; Yang, P.; Jiang, S.; Liu, X.; Li, Y., Polydopamine Free Radical Scavengers. *Biomater Sci* **2020,** *8* (18), 4940-4950.
41. Jin, L.; Yuan, F.; Chen, C.; Wu, J.; Gong, R.; Yuan, G.; Zeng, H.; Pei, J.; Chen, T., Degradation Products of Polydopamine Restrained Inflammatory Response of LPS-Stimulated Macrophages through Mediation TLR-4-MYD88 Dependent Signaling Pathways by Antioxidant. *Inflammation* **2019,** *42* (2), 658-671.
42. Zhao, H.; Zeng, Z.; Liu, L.; Chen, J.; Zhou, H.; Huang, L.; Huang, J.; Xu, H.; Xu, Y.; Chen, Z.; Wu, Y.; Guo, W.; Wang, J. H.; Wang, J.; Liu, Z., Polydopamine Nanoparticles for the Treatment of Acute Inflammation-Induced Injury. *Nanoscale* **2018,** *10* (15), 6981-6991.
43. Bao, X.; Zhao, J.; Sun, J.; Hu, M.; Yang, X., Polydopamine Nanoparticles as Efficient Scavengers for Reactive Oxygen Species in Periodontal Disease. *ACS Nano* **2018,** *12* (9), 8882-8892.
44. Carmignani, A.; Battaglini, M.; Sinibaldi, E.; Marino, A.; Vighetto, V.; Cauda, V.; Ciofani, G., In Vitro and ex Vivo Investigation of The Effects of Polydopamine Nanoparticle Size on Their Antioxidant and Photothermal Properties: Implications for Biomedical Applications. *ACS Applied Nano Materials* **2022,** *5* (1), 1702-1713.
45. Liu, H.; Qu, X.; Tan, H.; Song, J.; Lei, M.; Kim, E.; Payne, G. F.; Liu, C., Role of Polydopamine's Redox-Activity on Its Pro-Oxidant, Radical-Scavenging, and Antimicrobial Activities. *Acta Biomater* **2019,** *88*, 181-196.
46. Fu, Y.; Yang, L.; Zhang, J.; Hu, J.; Duan, G.; Liu, X.; Li, Y.; Gu, Z., Polydopamine Antibacterial Materials. *Mater Horiz* **2021,** *8* (6), 1618-1633.
47. Khanal, S.; Adhikari, U.; Rijal, N. P.; Bhattarai, S. R.; Sankar, J.; Bhattarai, N., pH-Responsive

PLGA Nanoparticle for Controlled Payload Delivery of Diclofenac Sodium. *J Funct Biomater* **2016,** *7* (3), 21.
48. Cooper, D. L.; Harirforoosh, S., Design and Optimization of PLGA-Based Diclofenac Loaded Nanoparticles. *Plos One* **2014,** *9* (1), 87326.
49. Acharya, S.; Praveena, J.; Guru, B. R., In Vitro Studies of Prednisolone Loaded PLGA Nanoparticles-Surface Functionalized With Folic Acid on Glioma and Macrophage Cell Lines. *Pharm Sci* **2020,** *27* (3), 407-417.
50. Cheraga, N.; Sun, N.-C.; Huang, X.-X.; Ye, Z.; Xiao, Q.-R.; Huang, N.-P., Optimized Rapamycin-Loaded Pegylated PLGA Nanoparticles: Preparation, Characterization and Pharmacokinetics Study. *J Drug Deliv Sci Technol* **2021,** *61*, 102144.
51. De S. L. Oliveira, A. L. C.; Dos Santos-Silva, A. M.; Da Silva-Júnior, A. A.; Garcia, V. B.; De Araújo, A. A.; De Geus-Oei, L.-F.; Chan, A. B.; Cruz, L. J.; De Araújo Júnior, R. F., Cholesterol-Functionalized Carvedilol-Loaded PLGA Nanoparticles: Anti-Inflammatory, Antioxidant, and Antitumor Effects. *J Nanopart Res* **2020,** *22* (5), 115.
52. Kim, D. H.; Martin, D. C., Sustained Release of Dexamethasone from Hydrophilic Matrices Using PLGA Nanoparticles for Neural Drug Delivery. *Biomaterials* **2006,** *27* (15), 3031-3037.
53. Liu, P.; Gu, L.; Ren, L.; Chen, J.; Li, T.; Wang, X.; Yang, J.; Chen, C.; Sun, L., Intra-Articular Injection of Etoricoxib-Loaded PLGA-PEG-PLGA Triblock Copolymeric Nanoparticles Attenuates Osteoarthritis Progression. *Am J Transl Res* **2019,** *11* (11), 6775-6789.
54. Te Boekhorst, B. C.; Jensen, L. B.; Colombo, S.; Varkouhi, A. K.; Schiffelers, R. M.; Lammers, T.; Storm, G.; Nielsen, H. M.; Strijkers, G. J.; Foged, C.; Nicolay, K., MRI-Assessed Therapeutic Effects of Locally Administered PLGA Nanoparticles Loaded with Anti-Inflammatory Sirna in a Murine Arthritis Model. *J Control Release* **2012,** *161* (3), 772-780.
55. Canadas, C.; Alvarado, H.; Calpena, A. C.; Silva, A. M.; Souto, E. B.; Garcia, M. L.; Abrego, G., In Vitro, ex Vivo and In Vivo Characterization of PLGA Nanoparticles Loading Pranoprofen for Ocular Administration. *Int J Pharm* **2016,** *511* (2), 719-727.
56. Galindo, R.; Sanchez-Lopez, E.; Gomara, M. J.; Espina, M.; Ettcheto, M.; Cano, A.; Haro, I.; Camins, A.; Garcia, M. L., Development of Peptide Targeted PLGA-Pegylated Nanoparticles Loading Licochalcone-A for Ocular Inflammation. *Pharmaceutics* **2022,** *14* (2), 285.
57. Abrego, G.; Alvarado, H.; Souto, E. B.; Guevara, B.; Bellowa, L. H.; Parra, A.; Calpena, A.; Garcia, M. L., Biopharmaceutical Profile of Pranoprofen-Loaded PLGA Nanoparticles Containing Hydrogels for Ocular Administration. *Eur J Pharm Biopharm* **2015,** *95* (Pt B), 261-270.
58. Sharma, S.; Parmar, A.; Kori, S.; Sandhir, R., PLGA-Based Nanoparticles: A New Paradigm in Biomedical Applications. *Trac Trends Anal Chem* **2016,** *80*, 30-40.
59. Araujo, J.; Gonzalez, E.; Egea, M. A.; Garcia, M. L.; Souto, E. B., Nanomedicines for Ocular Nsaids: Safety on Drug Delivery. *Nanomedicine* **2009,** *5* (4), 394-401.
60. Allen, T. M.; Cullis, P. R., Liposomal Drug Delivery Systems: From Concept to Clinical Applications. *Adv Drug Deliv Rev* **2013,** *65* (1), 36-48.
61. Crommelin, D. J. A.; Van Hoogevest, P.; Storm, G., The Role of Liposomes in Clinical Nanomedicine Development. What Now? Now What? *J Control Release* **2020,** *318*, 256-263.
62. Serpe, L.; Canaparo, R.; Daperno, M.; Sostegni, R.; Martinasso, G.; Muntoni, E.; Ippolito, L.; Vivenza, N.; Pera, A.; Eandi, M.; Gasco, M. R.; Zara, G. P., Solid Lipid Nanoparticles as Anti-Inflammatory Drug Delivery System in a Human Inflammatory Bowel Disease Whole-Blood Model. *Eur J Pharm Sci* **2010,** *39* (5), 428-436.
63. Dianzani, C.; Foglietta, F.; Ferrara, B.; Rosa, A. C.; Muntoni, E.; Gasco, P.; Della Pepa, C.; Canaparo, R.; Serpe, L., Solid Lipid Nanoparticles Delivering Anti-Inflammatory Drugs to Treat Inflammatory Bowel Disease: Effects in an In Vivo Model. *World J Gastroenterol* **2017,** *23* (23), 4200-4210.
64. Kumar, R.; Singh, A.; Garg, N.; Siril, P. F., Solid Lipid Nanoparticles for the Controlled Delivery of Poorly Water Soluble Non-Steroidal Anti-Inflammatory Drugs. *Ultrason Sonochem* **2018,**

40 (Pt A), 686-696.
65. Shah, R. M.; Eldridge, D. S.; Palombo, E. A.; Harding, I. H., Microwave-Assisted Formulation of Solid Lipid Nanoparticles Loaded with Non-Steroidal Anti-Inflammatory Drugs. *Int J Pharm* **2016,** *515* (1-2), 543-554.
66. Wang, J.; Zhu, R.; Sun, D.; Sun, X.; Geng, Z.; Liu, H.; Wang, S. L., Intracellular Uptake of Curcumin-Loaded Solid Lipid Nanoparticles Exhibit Anti-Inflammatory Activities Superior to Those of Curcumin through the NF-Kappab Signaling Pathway. *J Biomed Nanotechnol* **2015,** *11* (3), 403-415.
67. Wang, J.; Wang, H.; Xu, H.; Li, J.; Zhang, X.; Zhang, X., Solid Lipid Nanoparticles as an Effective Sodium Aescinate Delivery System: Formulation and Anti-Inflammatory Activity. *RSC Adv* **2022,** *12* (11), 6583-6591.
68. Wang, J.; Wang, H.; Zhu, R.; Liu, Q.; Fei, J.; Wang, S., Anti-Inflammatory Activity of Curcumin-Loaded Solid Lipid Nanoparticles in IL-1beta Transgenic Mice Subjected to the Lipopolysaccharide-Induced Sepsis. *Biomaterials* **2015,** *53*, 475-483.
69. Daneshmand, S.; Jaafari, M. R.; Movaffagh, J.; Malaekeh-Nikouei, B.; Iranshahi, M.; Seyedian Moghaddam, A.; Tayarani Najaran, Z.; Golmohammadzadeh, S., Preparation, Characterization, and Optimization of Auraptene-Loaded Solid Lipid Nanoparticles as a Natural Anti-Inflammatory Agent: In Vivo and In Vitro Evaluations. *Colloids Surf B Biointerfaces* **2018,** *164*, 332-339.
70. Shahraeini, S. S.; Akbari, J.; Saeedi, M.; Morteza-Semnani, K.; Abootorabi, S.; Dehghanpoor, M.; Rostamkalaei, S. S.; Nokhodchi, A., Atorvastatin Solid Lipid Nanoparticles as a Promising Approach for Dermal Delivery and an Anti-Inflammatory Agent. *AAPS Pharmscitech* **2020,** *21* (7), 263.
71. Souto, E. B.; Doktorovova, S.; Gonzalez-Mira, E.; Egea, M. A.; Garcia, M. L., Feasibility of Lipid Nanoparticles for Ocular Delivery of Anti-Inflammatory Drugs. *Curr Eye Res* **2010,** *35* (7), 537-552.
72. Lingayat, V. J.; Zarekar, N. S.; Shendge, R. S., Solid Lipid Nanoparticles: A Review. *Nanosci Nanotechnol Res* **2017,** *4* (2), 67-72.
73. Ghasemiyeh, P.; Mohammadi-Samani, S., Solid Lipid Nanoparticles and Nanostructured Lipid Carriers as Novel Drug Delivery Systems: Applications, Advantages and Disadvantages. *Res Pharm Sci* **2018,** *13* (4), 288-303.
74. Wang, J.; Kang, Y. X.; Pan, W.; Lei, W.; Feng, B.; Wang, X. J., Enhancement of Anti-Inflammatory Activity of Curcumin Using Phosphatidylserine-Containing Nanoparticles in Cultured Macrophages. *Int J Mol Sci* **2016,** *17* (6), 969.
75. Gurcan, S.; Tsapis, N.; Reynaud, F.; Denis, S.; Vergnaud, J.; Ozer, O.; Fattal, E., Combining Dexamethasone and TNF-Alpha Sirna Within the Same Nanoparticles to Enhance Anti-Inflammatory Effect. *Int J Pharm* **2021,** *598*, 120381.
76. Zhang, H.; Han, X.; Alameh, M. G.; Shepherd, S. J.; Padilla, M. S.; Xue, L.; Butowska, K.; Weissman, D.; Mitchell, M. J., Rational Design of Anti-Inflammatory Lipid Nanoparticles for Mrna Delivery. *J Biomed Mater Res A* **2022,** *110* (5), 1101-1108.
77. Qureshi, O. S.; Zeb, A.; Akram, M.; Kim, M. S.; Kang, J. H.; Kim, H. S.; Majid, A.; Han, I.; Chang, S. Y.; Bae, O. N.; Kim, J. K., Enhanced Acute Anti-Inflammatory Effects of CORM-2-Loaded Nanoparticles *Via* Sustained Carbon Monoxide Delivery. *Eur J Pharm Biopharm* **2016,** *108*, 187-195.
78. Wang, H.; Liu, Y.; He, R.; Xu, D.; Zang, J.; Weeranoppanant, N.; Dong, H.; Li, Y., Cell Membrane Biomimetic Nanoparticles for Inflammation and Cancer Targeting in Drug Delivery. *Biomater Sci* **2020,** *8* (2), 552-568.
79. Zhang, Q.; Dehaini, D.; Zhang, Y.; Zhou, J.; Chen, X.; Zhang, L.; Fang, R. H.; Gao, W.; Zhang, L., Neutrophil Membrane-Coated Nanoparticles Inhibit Synovial Inflammation and Alleviate Joint Damage in Inflammatory Arthritis. *Nat Nanotechnol* **2018,** *13* (12), 1182-1190.
80. Li, R.; He, Y.; Zhu, Y.; Jiang, L.; Zhang, S.; Qin, J.; Wu, Q.; Dai, W.; Shen, S.; Pang, Z.; Wang, J., Route to Rheumatoid Arthritis by Macrophage-Derived Microvesicle-Coated Nanoparticles. *Nano*

Lett **2019,** *19* (1), 124-134.
81. Sun, Y.; Duan, B.; Chen, H.; Xu, X., A Novel Strategy for Treating Inflammatory Bowel Disease by Targeting Delivery of Methotrexate through Glucan Particles. *Adv Healthc Mater* **2020,** *9* (6), 1901805.
82. Agarwal, H.; Nakara, A.; Shanmugam, V. K., Anti-Inflammatory Mechanism of Various Metal and Metal Oxide Nanoparticles Synthesized Using Plant Extracts: A Review. *Biomed Pharmacother* **2019,** *109*, 2561-2572.
83. Zheng, M.; Jia, H.; Wang, H.; Liu, L.; He, Z.; Zhang, Z.; Yang, W.; Gao, L.; Gao, X.; Gao, F., Application of Nanomaterials in the Treatment of Rheumatoid Arthritis. *RSC Advances* **2021,** *11* (13), 7129-7137.
84. Vallet-Regi, M.; Balas, F.; Arcos, D., Mesoporous Materials for Drug Delivery. *Angew Chem Int Ed* **2007,** *46* (40), 7548-7558.
85. Kwon, S.; Singh, R. K.; Perez, R. A.; Abou Neel, E. A.; Kim, H. W.; Chrzanowski, W., Silica-Based Mesoporous Nanoparticles for Controlled Drug Delivery. *J Tissue Eng* **2013,** *4*, 2041731413503357.
86. Tang, F.; Li, L.; Chen, D., Mesoporous Silica Nanoparticles: Synthesis, Biocompatibility and Drug Delivery. *Adv Mater* **2012,** *24* (12), 1504-1534.
87. Guan, L.; Chen, J.; Tian, Z.; Zhu, M.; Bian, Y.; Zhu, Y., Mesoporous Organosilica Nanoparticles: Degradation Strategies and Application in Tumor Therapy. *View* **2021,** *2* (5), 20200117.
88. Vallet-Regi, M.; Ramila, A.; Del Real, R. P.; Perez-Pariente, J., A New Property of MCM-41: Drug Delivery System. *Chem Mater* **2001,** *13* (2), 308-311.
89. Zid, L.; Zelenak, V.; Almasi, M.; Zelenakova, A.; Szucsova, J.; Bednarcik, J.; Sulekova, M.; Hudak, A.; Vahovska, L., Mesoporous Silica as a Drug Delivery System for Naproxen: Influence of Surface Functionalization. *Molecules* **2020,** *25* (20), 4722.
90. Liu, R.; Wang, X.; Fan, N.; Song, H.; Ma, P.; Li, C.; Li, J.; Sun, J., Superiority of Chiral-Handed Mesoporous Silica Nanoparticles in Delivering Nimesulide. *Mater Sci Eng B* **2021,** *269*, 115161.
91. Almeida Junior, S.; Pereira, P. M.; Totoli, V. S.; Neves, E. S.; Monochio, M.; Alvarenga, A. W. O.; Hori, J. I.; Braz, W. R.; Rocha, L. A.; Nassar, E. J.; Aldrovani, M.; Furtado, R. A., Incorporation of Indomethacin into a Mesoporous Silica Nanoparticle Enhances the Anti-Inflammatory Effect Indomethacin into aMesoporous Silica. *Eur J Pharm Sci* **2021,** *157*, 105601.
92. Lee, C.-H.; Lo, L.-W.; Mou, C.-Y.; Yang, C.-S., Synthesis and Characterization of Positive-Charge Functionalized Mesoporous Silica Nanoparticles for Oral Drug Delivery of an Anti-Inflammatory Drug. *Adv Funct Mater* **2008,** *18* (20), 3283-3292.
93. Jin, T.; Wu, D.; Liu, X. M.; Xu, J. T.; Ma, B. J.; Ji, Y.; Jin, Y. Y.; Wu, S. Y.; Wu, T.; Ma, K., Intra-Articular Delivery of Celastrol by Hollow Mesoporous Silica Nanoparticles for pH-Sensitive Anti-Inflammatory Therapy against Knee Osteoarthritis. *J Nanobiotechnology* **2020,** *18* (1), 94.
94. Yang, B.; Yao, H.; Yang, J.; Chen, C.; Guo, Y.; Fu, H.; Shi, J., In Situ Synthesis of Natural Antioxidase Mimics for Catalytic Anti-Inflammatory Treatments: Rheumatoid Arthritis as an Example. *J Am Chem Soc* **2022,** *144* (1), 314-330.
95. Lehman, A. J.; Esdaile, J. M.; Klinkhoff, A. V.; Grant, E.; Fitzgerald, A.; Canvin, J.; Group, M. S., A 48-Week, Randomized, Double-Blind, Double-Observer, Placebo-Controlled Multicenter Trial of Combination Methotrexate and Intramuscular Gold Therapy in Rheumatoid Arthritis: Results of the METGO Study. *Arthritis Rheum* **2005,** *52* (5), 1360-1370.
96. Takahashi, K.; Griem, P.; Goebel, C.; Gonzalez, J.; Gleichmann, E., The Antirheumatic Drug Gold, a Coin with two Faces: Au(I) and Au(III). Desired and Undesired Effects on the Immune System. *Met Based Drugs* **1994,** *1* (5-6), 483-496.
97. Fernandes, A. R.; Mendonca-Martins, I.; Santos, M. F. A.; Raposo, L. R.; Mendes, R.; Marques, J.; Romao, C. C.; Romao, M. J.; Santos-Silva, T.; Baptista, P. V., Improving the Anti-Inflammatory Response *Via* Gold Nanoparticle Vectorization of CO-Releasing Molecules. *ACS Biomater Sci Eng* **2020,** *6* (2), 1090-1101.

98. Li, J.; Chen, L.; Xu, X.; Fan, Y.; Xue, X.; Shen, M.; Shi, X., Targeted Combination of Antioxidative and Anti-Inflammatory Therapy of Rheumatoid Arthritis Using Multifunctional Dendrimer-Entrapped Gold Nanoparticles as a Platform. *Small* **2020,** *16* (49), 2005661.
99. Sumbayev, V. V.; Yasinska, I. M.; Garcia, C. P.; Gilliland, D.; Lall, G. S.; Gibbs, B. F.; Bonsall, D. R.; Varani, L.; Rossi, F.; Calzolai, L., Gold Nanoparticles Downregulate Interleukin-1beta-Induced Pro-Inflammatory Responses. *Small* **2013,** *9* (3), 472-477.
100. Ni, C.; Zhou, J.; Kong, N.; Bian, T.; Zhang, Y.; Huang, X.; Xiao, Y.; Yang, W.; Yan, F., Gold Nanoparticles Modulate the Crosstalk between Macrophages and Periodontal Ligament Cells for Periodontitis Treatment. *Biomaterials* **2019,** *206*, 115-132.
101. Dos Santos Haupenthal, D. P.; Mendes, C.; De Bem Silveira, G.; Zaccaron, R. P.; Correa, M.; Nesi, R. T.; Pinho, R. A.; Da Silva Paula, M. M.; Silveira, P. C. L., Effects of Treatment with Gold Nanoparticles in a Model of Acute Pulmonary Inflammation Induced by Lipopolysaccharide. *J Biomed Mater Res A* **2020,** *108* (1), 103-115.
102. Wang, L.; Zhang, H.; Sun, L.; Gao, W.; Xiong, Y.; Ma, A.; Liu, X.; Shen, L.; Li, Q.; Yang, H., Manipulation of Macrophage Polarization by Peptide-Coated Gold Nanoparticles and Its Protective Effects on Acute Lung Injury. *J Nanobiotechnology* **2020,** *18* (1), 38.
103. Park, J. Y.; Kwon, S.; Kim, S. H.; Kang, Y. J.; Khang, D., Triamcinolone-Gold Nanoparticles Repolarize Synoviocytes and Macrophages in an Inflamed Synovium. *ACS Appl Mater Interfaces* **2020,** *12* (35), 38936-38949.
104. Gao, W.; Wang, Y.; Xiong, Y.; Sun, L.; Wang, L.; Wang, K.; Lu, H. Y.; Bao, A.; Turvey, S. E.; Li, Q.; Yang, H., Size-Dependent Anti-Inflammatory Activity of a Peptide-Gold Nanoparticle Hybrid In Vitro and in a Mouse Model of Acute Lung Injury. *Acta Biomater* **2019,** *85*, 203-217.
105. Khan, H. A.; Abdelhalim, M. A.; Alhomida, A. S.; Al-Ayed, M. S., Effects of Naked Gold Nanoparticles on Proinflammatory Cytokines mRNA Expression in Rat Liver and Kidney. *Biomed Res Int* **2013,** *2013*, 590730.
106. Moyano, D. F.; Liu, Y.; Ayaz, F.; Hou, S.; Puangploy, P.; Duncan, B.; Osborne, B. A.; Rotello, V. M., Immunomodulatory Effects of Coated Gold Nanoparticles in LPS-Stimulated In Vitro and in Vivo Murine Model Systems. *Chem* **2016,** *1* (2), 320-327.
107. Balfourier, A.; Luciani, N.; Wang, G.; Lelong, G.; Ersen, O.; Khelfa, A.; Alloyeau, D.; Gazeau, F.; Carn, F., Unexpected Intracellular Biodegradation and Recrystallization of Gold Nanoparticles. *Proc Natl Acad Sci U S A* **2019,** *117(1)*, 103-113.
108. Wang, H. H.; Lin, C. J.; Tseng, Y. M.; Lee, H. I.; Lee, Y. N.; Yeh, H. I.; Yang, P. S.; Peng, H. Y.; Wu, Y. J., Dihydrolipoic Acid-Coated Gold Nanocluster Bioactivity against Senescence and Inflammation through the Mitochondria-Mediated JNK/AP-1 Pathway. *Nanomedicine* **2021,** *36*, 102427.
109. Sun, J.; Zhuang, P.; Wen, S.; Ge, M.; Zhou, Z.; Li, D.; Liu, C.; Mei, X., Folic Acid-Modified Lysozyme Protected Gold Nanoclusters as an Effective Anti-Inflammatory Drug for Rapid Relief of Gout Flares in Hyperuricemic Rats. *Mater Des* **2022,** *217*, 110642.
110. Sobska, J.; Waszkielewicz, M.; Podlesny-Drabiniok, A.; Olesiak-Banska, J.; Krezel, W.; Matczyszyn, K., Gold Nanoclusters Display Low Immunogenic Effect in Microglia Cells. *Nanomaterials (Basel)* **2021,** *11* (5), 1066.
111. Zhang, D. Y.; Tu, T.; Younis, M. R.; Zhu, K. S.; Liu, H.; Lei, S.; Qu, J.; Lin, J.; Huang, P., Clinically Translatable Gold Nanozymes with Broad Spectrum Antioxidant And Anti-Inflammatory Activity for Alleviating Acute Kidney Injury. *Theranostics* **2021,** *11* (20), 9904-9917.
112. Yuan, Q.; Gao, F.; Yao, Y.; Cai, P.; Zhang, X.; Yuan, J.; Hou, K.; Gao, L.; Ren, X.; Gao, X., Gold Clusters Prevent Inflammation-Induced Bone Erosion Through Inhibiting the Activation of NF-Kappab Pathway. *Theranostics* **2019,** *9* (7), 1825-1836.
113. Yuan, Q.; Zhao, Y.; Cai, P.; He, Z.; Gao, F.; Zhang, J.; Gao, X., Dose-Dependent Efficacy of Gold Clusters on Rheumatoid Arthritis Therapy. *ACS Omega* **2019,** *4* (9), 14092-14099.
114. Gao, F.; Yuan, Q.; Cai, P.; Gao, L.; Zhao, L.; Liu, M.; Yao, Y.; Chai, Z.; Gao, X., Au Clusters

Treat Rheumatoid Arthritis with Uniquely Reversing Cartilage/Bone Destruction. *Adv Sci (Weinh)* **2019,** *6* (7), 1801671.
115. Wong, K. K.; Cheung, S. O.; Huang, L.; Niu, J.; Tao, C.; Ho, C. M.; Che, C. M.; Tam, P. K., Further Evidence of the Anti-Inflammatory Effects of Silver Nanoparticles. *Chemmedchem* **2009,** *4* (7), 1129-1135.
116. Singh, P.; Ahn, S.; Kang, J. P.; Veronika, S.; Huo, Y.; Singh, H.; Chokkaligam, M.; El-Agamy Farh, M.; Aceituno, V. C.; Kim, Y. J.; Yang, D. C., In Vitro Anti-Inflammatory Activity of Spherical Silver Nanoparticles and Monodisperse Hexagonal Gold Nanoparticles by Fruit Extract of Prunus Serrulata: A Green Synthetic Approach. *Artif Cells Nanomed Biotechnol* **2018,** *46* (8), 2022-2032.
117. Parnsamut, C.; Brimson, S., Effects of Silver Nanoparticles and Gold Nanoparticles on IL-2, IL-6, And TNF-Alpha Production *Via* MAPK Pathway in Leukemic Cell Lines. *Genet Mol Res* **2015,** *14* (2), 3650-3668.
118. Sun, S.; Liu, H.; Xin, Q.; Chen, K.; Ma, H.; Liu, S.; Mu, X.; Hao, W.; Liu, S.; Gao, Y.; Wang, Y.; Pei, J.; Zhao, R.; Zhang, S.; Zhang, X.; Wang, H.; Li, Y.; Zhang, X. D., Atomic Engineering of Clusterzyme for Relieving Acute Neuroinflammation through Lattice Expansion. *Nano Lett* **2021,** *21* (6), 2562-2571.
119. Kim, M. H.; Seo, J. H.; Kim, H. M.; Jeong, H. J., Zinc Oxide Nanoparticles, a Novel Candidate for the Treatment of Allergic Inflammatory Diseases. *Eur J Pharmacol* **2014,** *738*, 31-39.
120. Nagajyothi, P. C.; Cha, S. J.; Yang, I. J.; Sreekanth, T. V.; Kim, K. J.; Shin, H. M., Antioxidant and Anti-Inflammatory Activities of Zinc Oxide Nanoparticles Synthesized Using Polygala Tenuifolia Root Extract. *J Photochem Photobiol B* **2015,** *146*, 10-17.
121. Agarwal, H.; Shanmugam, V. K., Synthesis and Optimization of Zinc Oxide Nanoparticles Using Kalanchoe Pinnata towards the Evaluation of Its Anti-Inflammatory Activity. *J Drug Deliv Sci Technol* **2019,** *54*, 101291.
122. Gad, S. S.; Fayez, A. M.; Abdelaziz, M.; Abou El-Ezz, D., Amelioration of Autoimmunity and Inflammation by Zinc Oxide Nanoparticles in Experimental Rheumatoid Arthritis. *Naunyn Schmiedebergs Arch Pharmacol* **2021,** *394* (9), 1975-1981.
123. Agarwal, H.; Shanmugam, V., A Review on Anti-Inflammatory Activity of Green Synthesized Zinc Oxide Nanoparticle: Mechanism-Based Approach. *Bioorg Chem* **2020,** *94*, 103423.
124. Kim, M.-H., Biological Effects of Zinc Oxide Nanoparticles on Inflammation. *Tang [Humanitas Medicine]* **2016,** *6* (4), 23.1-23.6.
125. Olbert, M.; Gdula-Argasinska, J.; Nowak, G.; Librowski, T., Beneficial Effect of Nanoparticles over Standard Form of Zinc Oxide in Enhancing the Anti-Inflammatory Activity of Ketoprofen in Rats. *Pharmacol Rep* **2017,** *69* (4), 679-682.
126. Barakat, L. A. A.; Barakat, N.; Zakaria, M. M.; Khirallah, S. M., Protective Role of Zinc Oxide Nanoparticles in Kidney Injury Induced by Cisplatin in Rats. *Life Sci* **2020,** *262*, 118503.
127. Keerthana, S.; Kumar, A., Potential Risks and Benefits of Zinc Oxide Nanoparticles: A Systematic Review. *Crit Rev Toxicol* **2020,** *50* (1), 47-71.
128. Nelson, B. C.; Johnson, M. E.; Walker, M. L.; Riley, K. R.; Sims, C. M., Antioxidant Cerium Oxide Nanoparticles in Biology and Medicine. *Antioxidants (Basel)* **2016,** *5* (2), 15.
129. Hirst, S. M.; Karakoti, A. S.; Tyler, R. D.; Sriranganathan, N.; Seal, S.; Reilly, C. M., Anti-Inflammatory Properties of Cerium Oxide Nanoparticles. *Small* **2009,** *5* (24), 2848-2856.
130. Wu, Y.; Ta, H. T., Different Approaches to Synthesising Cerium Oxide Nanoparticles and Their Corresponding Physical Characteristics, and ROS Scavenging and Anti-Inflammatory Capabilities. *J Mater Chem B* **2021,** *9* (36), 7291-7301.
131. Casals, E.; Gusta, M. F.; Piella, J.; Casals, G.; Jimenez, W.; Puntes, V., Intrinsic and Extrinsic Properties Affecting Innate Immune Responses to Nanoparticles: The Case of Cerium Oxide. *Front Immunol* **2017,** *8*, 970.
132. Kim, J.; Hong, G.; Mazaleuskaya, L.; Hsu, J. C.; Rosario-Berrios, D. N.; Grosser, T.; Cho-Park, P. F.; Cormode, D. P., Ultrasmall Antioxidant Cerium Oxide Nanoparticles for Regulation of Acute

Inflammation. *ACS Appl Mater Interfaces* **2021,** *13* (51), 60852-60864.
133. Lin, S.; Zhou, Z.; Xu, C.; Zeng, F.; Shi, Z.; Sun, J.; Mei, X.; Liu, C.; Li, D., Cytokine Regulation and Fast Inflammation Resolution in Early Rheumatoid Arthritis by Cerium-Modified Gold Nanoclusters. *ACS Appl Mater Interfaces* **2022,** *14* (16), 18053-18063.
134. Garcia-Salvador, A.; Katsumiti, A.; Rojas, E.; Aristimuno, C.; Betanzos, M.; Martinez-Moro, M.; Moya, S. E.; Goni-De-Cerio, F., A Complete *In Vitro* Toxicological Assessment of the Biological Effects of Cerium Oxide Nanoparticles: From Acute Toxicity to Multi-Dose Subchronic Cytotoxicity Study. *Nanomaterials (Basel)* **2021,** *11* (6), 1577.
135. Lee, J.; Jeong, J. S.; Kim, S. Y.; Lee, S. J.; Shin, Y. J.; Im, W. J.; Kim, S. H.; Park, K.; Jeong, E. J.; Nam, S. Y.; Yu, W. J., Safety Assessment of Cerium Oxide Nanoparticles: Combined Repeated-Dose Toxicity with Reproductive/Developmental Toxicity Screening and Biodistribution in Rats. *Nanotoxicology* **2020,** *14* (5), 696-710.
136. Simon-Yarza, T.; Mielcarek, A.; Couvreur, P.; Serre, C., Nanoparticles of Metal-Organic Frameworks: on the Road to in Vivo Efficacy in Biomedicine. *Adv Mater* **2018,** *30* (37), E1707365.
137. Horcajada, P.; Chalati, T.; Serre, C.; Gillet, B.; Sebrie, C.; Baati, T.; Eubank, J. F.; Heurtaux, D.; Clayette, P.; Kreuz, C.; Chang, J. S.; Hwang, Y. K.; Marsaud, V.; Bories, P. N.; Cynober, L.; Gil, S.; Ferey, G.; Couvreur, P.; Gref, R., Porous Metal-Organic-Framework Nanoscale Carriers as a Potential Platform for Drug Delivery and Imaging. *Nat Mater* **2010,** *9* (2), 172-178.
138. Liu, X.; Liang, T.; Zhang, R.; Ding, Q.; Wu, S.; Li, C.; Lin, Y.; Ye, Y.; Zhong, Z.; Zhou, M., Iron-Based Metal-Organic Frameworks in Drug Delivery and Biomedicine. *ACS Appl Mater Interfaces* **2021,** *13* (8), 9643-9655.
139. Quijia, C. R.; Lima, C.; Silva, C.; Alves, R. C.; Frem, R.; Chorilli, M., Application of MIL-100(Fe) in Drug Delivery and Biomedicine. *J Drug Deliv Sci Technol* **2020**, 102217.
140. Mileo, P. G. M.; Gomes, D. N.; Gonçalves, D. V.; Lucena, S. M. P., Mesoporous Metal–Organic Framework MIL-100(Fe) as Drug Carrier. *Adsorption* **2021,** *27* (7), 1123-1135.
141. Panchal, M.; Nouar, F.; Serre, C.; Benzaqui, M.; Sene, S.; Steunou, N.; Gimenez, M. Low Temperature Process for the Synthesis of MOF Carboxylate Nanoparticles. US20210277042, **2021**.
142. Gimenez-Marques, M.; Bellido, E.; Berthelot, T.; Simon-Yarza, T.; Hidalgo, T.; Simon-Vazquez, R.; Gonzalez-Fernandez, A.; Avila, J.; Asensio, M. C.; Gref, R.; Couvreur, P.; Serre, C.; Horcajada, P., Graftfast Surface Engineering to Improve MOF Nanoparticles Furtiveness. *Small* **2018,** *14* (40), 1801900.
143. Zimpel, A.; Preiß, T.; Röder, R.; Engelke, H.; Ingrisch, M.; Peller, M.; Rädler, J. O.; Wagner, E.; Bein, T.; Lächelt, U.; Wuttke, S., Imparting Functionality to MOF Nanoparticles by External Surface Selective Covalent Attachment of Polymers. *Chem Mater* **2016,** *28* (10), 3318-3326.
144. Liu, F.; Lin, L.; Zhang, Y.; Wang, Y.; Sheng, S.; Xu, C.; Tian, H.; Chen, X., A Tumor-Microenvironment-Activated Nanozyme-Mediated Theranostic Nanoreactor for Imaging-Guided Combined Tumor Therapy. *Adv Mater* **2019**, 1902885.
145. Cai, W.; Gao, H.; Chu, C.; Wang, X.; Wang, J.; Zhang, P.; Lin, G.; Li, W.; Liu, G.; Chen, X., Engineering Phototheranostic Nanoscale Metal-Organic Frameworks for Multimodal Imaging-Guided Cancer Therapy. *ACS Appl Mater Interfaces* **2017,** *9* (3), 2040-2051.
146. Agostoni, V.; Horcajada, P.; Noiray, M.; Malanga, M.; Aykac, A.; Jicsinszky, L.; Vargas-Berenguel, A.; Semiramoth, N.; Daoud-Mahammed, S.; Nicolas, V.; Martineau, C.; Taulelle, F.; Vigneron, J.; Etcheberry, A.; Serre, C.; Gref, R., A "Green" Strategy to Construct Non-Covalent, Stable and Bioactive Coatings on Porous MOF Nanoparticles. *Sci Rep* **2015,** *5*, 7925.
147. Simon-Yarza, T.; Gimenez-Marques, M.; Mrimi, R.; Mielcarek, A.; Gref, R.; Horcajada, P.; Serre, C.; Couvreur, P., A Smart Metal-Organic Framework Nanomaterial for Lung Targeting. *Angew Chem Int Ed* **2017,** *56* (49), 15565-15569.
148. Christodoulou, I.; Bourguignon, T.; Li, X.; Patriarche, G.; Serre, C.; Marlière, C.; Gref, R., Degradation Mechanism of Porous Metal-Organic Frameworks by In Situ Atomic Force Microscopy. *Nanomaterials* **2021,** *11* (3), 722.

149. Li, X.; Lachmanski, L.; Safi, S.; Sene, S.; Serre, C.; Greneche, J. M.; Zhang, J.; Gref, R., New Insights Into The Degradation Mechanism Of Metal-Organic Frameworks Drug Carriers. *Sci Rep* **2017,** *7* (1), 13142.
150. Bellido, E.; Guillevic, M.; Hidalgo, T.; Santander-Ortega, M. J.; Serre, C.; Horcajada, P., Understanding the Colloidal Stability of the Mesoporous MIL-100(Fe) Nanoparticles in Physiological Media. *Langmuir* **2014,** *30* (20), 5911-5920.
151. Bahrani, S.; Hashemi, S. A.; Mousavi, S. M.; Azhdari, R., Zinc-Based Metal-Organic Frameworks as Nontoxic and Biodegradable Platforms for Biomedical Applications: Review Study. *Drug Metab Rev* **2019,** *51* (3), 356-377.
152. Maleki, A.; Shahbazi, M. A.; Alinezhad, V.; Santos, H. A., The Progress and Prospect of Zeolitic Imidazolate Frameworks in Cancer Therapy, Antibacterial Activity, and Biomineralization. *Adv Healthc Mater* **2020**, 2000248.
153. Velásquez-Hernández, M. D. J.; Ricco, R.; Carraro, F.; Limpoco, F. T.; Linares-Moreau, M.; Leitner, E.; Wiltsche, H.; Rattenberger, J.; Schröttner, H.; Frühwirt, P.; Stadler, E. M.; Gescheidt, G.; Amenitsch, H.; Doonan, C. J.; Falcaro, P., Degradation of ZIF-8 in Phosphate Buffered Saline Media. *Crystengcomm* **2019,** *21* (31), 4538-4544.
154. Dong, K.; Wang, Z.; Zhang, Y.; Ren, J.; Qu, X., Metal-Organic Framework-Based Nanoplatform for Intracellular Environment-Responsive Endo/Lysosomal Escape and Enhanced Cancer Therapy. *ACS Appl Mater Interfaces* **2018,** *10* (38), 31998-32005.
155. Liu, P.; Shi, X.; Zhong, S.; Peng, Y.; Qi, Y.; Ding, J.; Zhou, W., Metal-Phenolic Networks for Cancer Theranostics. *Biomater Sci* **2021,** *9* (8), 2825-2849.
156. Guo, Y.; Sun, Q.; Wu, F. G.; Dai, Y.; Chen, X., Polyphenol-Containing Nanoparticles: Synthesis, Properties, and Therapeutic Delivery. *Adv Mater* **2021,** *33* (22), 2007356.
157. Roy, I.; Stoddart, J. F., Cyclodextrin Metal-Organic Frameworks and Their Applications. *Acc Chem Res* **2021,** *54* (6), 1440-1453.
158. Dummert, S. V.; Saini, H.; Hussain, M. Z.; Yadava, K.; Jayaramulu, K.; Casini, A.; Fischer, R. A., Cyclodextrin Metal-Organic Frameworks and Derivatives: Recent Developments and Applications. *Chem Soc Rev* **2022,** *51* (12), 5175-5213.
159. Han, Y.; Liu, W.; Huang, J.; Qiu, S.; Zhong, H.; Liu, D.; Liu, J., Cyclodextrin-Based Metal-Organic Frameworks (CD-Mofs) in Pharmaceutics and Biomedicine. *Pharmaceutics* **2018,** *10* (4), 271.
160. Abucafy, M. P.; Caetano, B. L.; Chiari-Andreo, B. G.; Fonseca-Santos, B.; Do Santos, A. M.; Chorilli, M.; Chiavacci, L. A., Supramolecular Cyclodextrin-Based Metal-Organic Frameworks as Efficient Carrier for Anti-Inflammatory Drugs. *Eur J Pharm Biopharm* **2018,** *127*, 112-119.
161. Moussa, Z.; Hmadeh, M.; Abiad, M. G.; Dib, O. H.; Patra, D., Encapsulation of Curcumin in Cyclodextrin-Metal Organic Frameworks: Dissociation of Loaded CD-MOFs Enhances Stability of Curcumin. *Food Chem* **2016,** *212*, 485-494.
162. Lv, D.; Nong, W.; Guan, Y., Edible Ligand-Metal-Organic Frameworks: Synthesis, Structures, Properties and Applications. *Coord Chem Rev* **2022,** *450*, 214234.
163. Xie, Y.; Yu, Z.; Huang, X.; Wang, Z.; Niu, L.; Teng, M.; Li, J., Rational Design of MOFs Constructed from Modified Aromatic Amino Acids. *Chemistry* **2007,** *13* (33), 9399-9405.
164. Wang, S.; Wahiduzzaman, M.; Davis, L.; Tissot, A.; Shepard, W.; Marrot, J.; Martineau-Corcos, C.; Hamdane, D.; Maurin, G.; Devautour-Vinot, S.; Serre, C., A Robust Zirconium Amino Acid Metal-Organic Framework for Proton Conduction. *Nat Commun* **2018,** *9* (1), 4937.
165. Can, M.; Demirci, S.; Sunol, A. K.; Sahiner, N., An Amino Acid, L-Glutamic Acid-Based Metal-Organic Frameworks and Their Antibacterial, Blood Compatibility, Biocompatibility, and Sensor Properties. *Microporous Mesoporous Mater* **2020,** *309*, 110533.
166. Rabiee, N.; Yaraki, M. T.; Garakani, S. M.; Garakani, S. M.; Ahmadi, S.; Lajevardi, A.; Bagherzadeh, M.; Rabiee, M.; Tayebi, L.; Tahriri, M.; Hamblin, M. R., Recent Advances in Porphyrin-Based Nanocomposites for Effective Targeted Imaging and Therapy. *Biomaterials* **2020,** *232*, 119707.
167. Chen, J.; Zhu, Y.; Kaskel, S., Porphyrin-Based Metal-Organic Frameworks for Biomedical

Applications. *Angew Chem Int Ed* **2021,** *60* (10), 5010-5035.
168. Hu, H.; Zhu, J.; Cao, L.; Wang, Z.; Gao, Y.; Yang, L.; Lin, W.; Wang, C., Light-Driven Proton Transport across Liposomal Membranes Enabled by Janus Metal-Organic Layers. *Chem* **2022,** *8* (2), 450-464.
169. Lu, K.; He, C.; Guo, N.; Chan, C.; Ni, K.; Lan, G.; Tang, H.; Pelizzari, C.; Fu, Y.-X.; Spiotto, M. T.; Weichselbaum, R. R.; Lin, W., Low-Dose X-Ray Radiotherapy–Radiodynamic Therapy *Via* Nanoscale Metal–Organic Frameworks Enhances Checkpoint Blockade Immunotherapy. *Nat Biomed Eng* **2018,** *2* (8), 600-610.
170. Ni, K.; Aung, T.; Li, S.; Fatuzzo, N.; Liang, X.; Lin, W., Nanoscale Metal-Organic Framework Mediates Radical Therapy to Enhance Cancer Immunotherapy. *Chem* **2019,** *5* (7), 1892-1913.
171. Luo, T.; Ni, K.; Culbert, A.; Lan, G.; Li, Z.; Jiang, X.; Kaufmann, M.; Lin, W., Nanoscale Metal-Organic Frameworks Stabilize Bacteriochlorins for Type I and Type II Photodynamic Therapy. *J Am Chem Soc* **2020,** *142* (16), 7334-7339.
172. Ni, K.; Lan, G.; Chan, C.; Duan, X.; Guo, N.; Veroneau, S. S.; Weichselbaum, R. R.; Lin, W., Ultrathin Metal-Organic-Layer Mediated Radiotherapy-Radiodynamic Therapy. *Matter* **2019,** *1* (5), 1331-1353.
173. Wu, J.; Yu, Y.; Cheng, Y.; Cheng, C.; Zhang, Y.; Jiang, B.; Zhao, X.; Miao, L.; Wei, H., Ligand-Dependent Activity Engineering of Glutathione Peroxidase-Mimicking MIL-47(V) Metal-Organic Framework Nanozyme for Therapy. *Angew Chem Int Ed* **2020,** *133 (3)*, 1247-1254.
174. Zhang, L.; Zhang, Y.; Wang, Z.; Cao, F.; Sang, Y.; Dong, K.; Pu, F.; Ren, J.; Qu, X., Constructing Metal–Organic Framework Nanodots as Bio-Inspired Artificial Superoxide Dismutase for Alleviating Endotoxemia. *Mater Horiz* **2019,** *6* (8), 1682-1687.
175. Liu, F.; Sheng, S.; Shao, D.; Xiao, Y.; Zhong, Y.; Zhou, J.; Quek, C. H.; Wang, Y.; Hu, Z.; Liu, H.; Li, Y.; Tian, H.; Leong, K. W.; Chen, X., A Cationic Metal-Organic Framework to Scavenge Cell-Free DNA for Severe Sepsis Management. *Nano Lett* **2021,** *21* (6), 2461-2469.
176. Li, Z.; Peng, Y.; Pang, X.; Tang, B., Potential Therapeutic Effects of Mg/HCOOH Metal Organic Framework on Relieving Osteoarthritis. *Chemmedchem* **2020,** *15* (1), 13-16.
177. Guo, L.; Chen, Y.; Wang, T.; Yuan, Y.; Yang, Y.; Luo, X.; Hu, S.; Ding, J.; Zhou, W., Rational Design of Metal-Organic Frameworks to Deliver Methotrexate for Targeted Rheumatoid Arthritis Therapy. *J Control Release* **2021,** *330*, 119-131.
178. Yin, Y.; Yang, J.; Pan, Y.; Gao, Y.; Huang, L.; Luan, X.; Lin, Z.; Zhu, W.; Li, Y.; Song, Y., Mesopore to Macropore Transformation of Metal-Organic Framework for Drug Delivery in Inflammatory Bowel Disease. *Adv Healthc Mater* **2021,** *10* (3), 2000973.
179. Guo, L.; Zhong, S.; Liu, P.; Guo, M.; Ding, J.; Zhou, W., Radicals Scavenging MOFs Enabling Targeting Delivery of Sirna for Rheumatoid Arthritis Therapy. *Small* **2022**, 2202604.
180. Szabo, C.; Southan, G. J.; Thiemermann, C., Beneficial Effects and Improved Survival in Rodent Models of Septic Shock with S-Methylisothiourea Sulfate, a Potent and Selective Inhibitor of Inducible Nitric Oxide Synthase. *Proc Natl Acad Sci U S A* **1994,** *91* (26), 12472-12476.
181. Zhou, F.; Mei, J.; Yang, S.; Han, X.; Li, H.; Yu, Z.; Qiao, H.; Tang, T., Modified ZIF-8 Nanoparticles Attenuate Osteoarthritis by Reprogramming the Metabolic Pathway of Synovial Macrophages. *ACS Appl Mater Interfaces* **2020,** *12* (2), 2009-2022.
182. Mu, J.; Li, C.; Shi, Y.; Liu, G.; Zou, J.; Zhang, D. Y.; Jiang, C.; Wang, X.; He, L.; Huang, P.; Yin, Y.; Chen, X., Protective Effect of Platinum Nano-Antioxidant and Nitric Oxide against Hepatic Ischemia-Reperfusion Injury. *Nat Commun* **2022,** *13* (1), 2513.
183. Liu, Y.; Cheng, Y.; Zhang, H.; Zhou, M.; Yu, Y.; Lin, S.; Jiang, B.; Zhao, X.; Miao, L.; Wei, C. W.; Liu, Q.; Lin, Y. W.; Du, Y.; Butch, C. J.; Wei, H., Integrated Cascade Nanozyme Catalyzes In Vivo ROS Scavenging for Anti-Inflammatory Therapy. *Sci Adv* **2020,** *6* (29), Eabb2695.
184. Wang, Y.; Ying, T.; Li, J.; Xu, Y.; Wang, R.; Ke, Q.; Shen, S. G. F.; Xu, H.; Lin, K., Hierarchical Micro/Nanofibrous Scaffolds Incorporated with Curcumin and Zinc Ion Eutectic Metal Organic Frameworks for Enhanced Diabetic Wound Healing *Via* Anti-Oxidant and Anti-Inflammatory

Activities. *Chem Eng J* **2020,** *402*, 126273.

1.2 Functional MOFs as theranostics

Inflammation response is involved in various diseases and MOFs as emerging anti-inflammatory agents or drug delivery systems are certainly of interest. As versatile drug vectors, nanoMOFs can encapsulate different drug molecules and so far have been mainly investigated in cancer treatment. To evaluate the therapeutic effects of nanoMOFs, it is also necessary to monitor the process by medical imaging in time, namely integration of diagnosis and treatment.

Since the publication of the book chapter “functional MOFs as theranostics”, in which most works are published before May 2019, a fast development of theranostic nanoMOFs in the past 3 years has occurred. Thus this was necessary to include some new important reported works in this field, so in this part, recent functional theranostic nanoMOFs are summarized based on the book chapter.

1.2 Functional MOFs as Theranostics

Heng Zhao[a], Christian Serre[a], Eddy Dumas[b], Nathalie Steunou[b]

[a]Institut des Matériaux Poreux de Paris, FRE 2000 CNRS, Ecole Normale Supérieure, Ecole Supérieure de Physique et de Chimie Industrielles de Paris, PSL Research University, Paris, France

[b]Lavoisier Institute of Versailles, UMR CNRS 8180, UVSQ Paris-Saclay University, Versailles, France

Common MOFs

MOF	Metal cluster/core	Ligand	Node
MIL-100(Fe)	FeO_6	Trimesic acid (BTC)	6-connected
MIL-101(Fe)	$Fe_3(\mu_3\text{-}O)_6(\mu_3\text{-}OH)_3$	Terephthalic acid (BDC)	6-connected
MIL-101(Fe)-NH_2	$Fe_3(\mu_3\text{-}O)_6(\mu_3\text{-}OH)_3$	2-aminobenzene-1,4-dicarboxylate (BDC-NH_2)	6-connected
MIL-127	$Fe_3(\mu 3\text{-}O)_6(\mu_3\text{-}OH)_3$	3,3′5,5′-azobenzenetetracarboxylate (Tazb)	6-connected
Fe-MIL-53-NH_2	$FeO_4(OH)_2$	Terephthalic acid (BDC)	6-connected
ZIF-8(Zn)	Zn^{2+}	2-methylimidazolate (MeIM)	4-connected
Uio-66(Zr)	$[Zr_6O_4(OH)_4]$	Terephthalic acid (BDC)	6-connected

1.2.1 Introduction

Theranostics combines therapeutic property and diagnostic imaging to treat disease with high therapeutic effects through a precise and personalized approach together with minimal side effects.[1] In recent years, it has become a hot topic with an increasing interest from chemists or scientists to explore novel theranostic nanoprobes.[2-3]

In terms of diagnosis, imaging techniques include Fluorescence imaging (FLI), Magnetic resonance imaging (MRI), Photoacoustic imaging (PAI). Ultrasound (US), single photon emission computer tomography (SPECT) imaging, computed tomography (CT) imaging, positron emission tomography

(PET) imaging, etc. *In vivo* FLI uses a sensitive camera to detect fluorescence emission from fluorophores in whole-body living small animals and to overcome the photon attenuation in living tissue, fluorophores such as indocarbocyanine dyes and quantum dots (QDs) with long emission at the near-infrared (NIR).[4] MRI is a non-invasive method of mapping the internal structure and certain aspects of function within the body, which is widely used in the diagnosis of pathology. The MRI contrast agents used to improve diagnostic accuracy in clinic are divided into T1 positive contrast agent such as gadolinium(III) chelates and T2 negative contrast agent such as superparamagnetic iron-oxide nanoparticle (SPION).[5-6] PAI is an emerging hybrid imaging technique that combines the high contrast of optical imaging with the high spatial resolution of ultrasound imaging. The PA effect is a phenomenon where substrates produce broadband acoustic waves at megahertz frequencies due to thermoelastic expansion after absorption of short laser pulses and then these acoustic waves will be detected by an ultrasound transducer and reconstructed into an image. PAI contrast agents contain small molecule NIR dye such as indocyanine green (ICG) and metallic nanostructures with a reasonable extinction coefficients and also nanomaterials for photoacoustic imaging in NIR II window is a new direction.[7-8] Other classical clinical imaging techniques such as US, PET, SPECT and CT would not be introduced here.

Concerning therapy, referring to cancer therapy in most cases, the methods are quite various, including chemotherapy, radiotherapy, photothermal therapy (PTT), chemodynamic therapy (CDT), photodynamic therapy (PDT), sonodynamic therapy (SDT), magnetic hyperthymia therapy (MHT), microwave thermal therapy (MTT), immunotherapy, gene therapy,, etc. Chemotherapy and radiotherapy together with surgery are the most common cancer therapy techniques in clinical, which would not be introduced repeatedly. Thermal treatments such as PTT, MHT and MTT are based on driving a part or the whole body above its normal temperature (37 ^{o}C) for a defined period of time. Briefly, PTT utilizes diverse photothermal agents (PTAs) with large light-to-heat conversion efficiencies such as plasmonic metallic nanoparticles, quantum dots, carbon nanotubes, and organic nanoparticles) to harvest NIR light and rapidly converts the light energy into heat to destroy tumors.[9] Tumor microenvironment (TME) is featured by acidity and the overproduction of hydrogen peroxide, and thus CDT was defined as in situ treatments using the Fenton reaction or Fenton-like reaction to generate •OH in tumor sites.[10] Briefly, under the mildly acidic conditions of the TME, iron-based nanomaterials could be dissolved into ferrous ions, thus initiating the Fenton reaction to generate •OH to trigger apoptosis and inhibit the tumor. PDT has emerged as a disease site specific treatment modality, which involves the administration of a tumor-localizing photosensitizer (PS) such as porphyrin or porphyrin-based macrocyclic structures followed by local illumination of the tumor with

light of a specific wavelength to activate the PS and the excited PS then transfers its energy to molecular oxygen, thus generating cytotoxic reactive oxygen species (ROS).[11] Eventually, ROS could further oxidize key cellular macromolecules leading to tumor cell ablation. Similarly, SDT therapy will rely on biological model, the sonosensitizer and the ultrasound parameters.[12] Other therapy techniques are also of interest and here we end up with the introduction of starvation therapy. Starvation therapy has emerged for suppressing tumor growth and survival through blocking blood flow or depriving their essential nutrients/oxygen supply and combination therapy of cancer starvation agents with other cancer treating approaches has demonstrated to be an efficient way.[13] In real application, multi-modal imaging and synergistic therapy are widely used for an efficient cancer therapy and multifunctional materials are thus desired.

Biocompatible metal-organic frameworks (MOFs), highly porous crystalline porous solids, have been widely known as drug delivery systems considering their large pore sizes/volumes and ideal drug adsorption capacities. Apart from drug delivery, nanoMOFs also have been considered as imaging agent to diagnose different diseases such as cancer or as therapeutic agent used in preclinical research.[14-18] Most of the nanoMOFs reaching a preclinical *in vivo* evaluation are based on Fe carboxylates or Zn azolates.[19-22] Until 2010, nanoMOFs have been mainly considered for imaging or therapy, and their use for theranostics gradually attracted researchers' attention particularly since 2015 where it encountered a rapid development.[23-27] Particularly, the construction of hybrid systems associating nanoMOFs with functional organic or inorganic nanoparticles paved the way for the development of multifunctional or multimodal nanoMOF theranostic probe.[14, 20, 28-29]

In this chapter, we mainly discuss the developments of cancer and other diseases theranostics based on nanoMOFs within the past decade, which includes topical MOFs such as MIL-100(Fe), MIL-101(Fe), ZIF-8(Zn) and UiO-66(Zr), etc. This contains the following sub-topics: stimuli-responsive nanoMOF, magnetic nanoMOFs, fluorescent nanoMOFs, nuclear medical imaging nanoMOFs, phototherapeutic nanoMOFs, etc. Note that a single type of nanoMOF system combines several features and applications at the same time and could match more than one classification.

1.2.2 Stimuli-responsive nanoMOF for theranostics

Among various nanoMOFs, the stimuli-responsive ones have garnered immense attention in biomedicine and they were designed to specifically change their property upon exposure to interior stimuli (*e.g.*, pH and GSH) in target tissues or external stimuli (*e.g.*, temperature, light, and magnetic field).[30-31] Encapsulation of stimuli-responsive molecules into MOFs paves the way for constructing novel stimuli-responsive systems able to trigger drug release at tumor site. Actually, most theranostic

nanoMOFs are stimuli-responsive, but specifically, only typical MOFs nanocarriers sensitive to tumor microenvironment are summarized as below.

1.2.2.1 pH responsive nanoMOF

ZIF-8 is well-known for physiological pH responsive drug delivery.[32] Meanwhile, Tumor cell autophagy increases the expression of inhibitory molecules to block antitumor cytotoxic responses, and thus autophagy inhibitors treatment could enhance the efficacy of anti-tumor therapy. Fang's group encapsulated autophagy inhibitor 3-methyladenine (3-MA) into ZIF-8 to build a pH-sensitive and tumor-targeting controlled drug delivery system denoted 3-MA@ZIF-8 NPs for antitumor application.[33] ZIF-8 framework was shown to be effective not only in drug control release but also in controlling autophagy by encapsulating autophagy inhibitors. Based on ZIF-8 MOF, pH-responsive theranostic nanoMOFs have been developed for imaging, tumor suppression and multidrug resistance (MDR), etc.[34-35]

1.2.2.2 GSH responsive nanoMOF

The high GSH concentration at tumor sites can be beneficial to trigger drug release from MOFs toward cancer cells. The introduction of disulfide bonds is a common strategy to construct GSH-responsive DDSs, and when it is exposed to high GSH in tumor microenvironment, the covalent bond will break and release the drug by redox reaction.[36] Zhu's group developed a novel and pH/GSH-responsive nanocarrier based on a ZIF-8 core and an organosilica shell containing disulfide bridges in its frameworks with antitumor drug DOX loading for controlled release and cancer treatment.[37] The disulfide bond could also be introduced in the ligand for the construction of stimuli-responsive MOF. Qi's group developed an intrinsic GSH-responsive MOFs carrier, denoted as MOF-Zr(DTBA), using 4,4′-dithiobisbenzoic acid (4,4′-DTBA) able to release drugs *in vivo*.[38] Curcumin (CCM) was further incorporated into MOF-Zr(DTBA) to construct CCM@MOF-Zr(DTBA). Its superior anticancer efficacy was verified through *in vitro* and *in vivo* experiments.

1.2.2.3 H_2O_2 responsive nanoMOF

For a better drug delivery, it is critical to pass biological barriers *in vivo*, biomimetic membrane camouflage of MOF strategy has been developed for the inhibition of tumor growth considering its advantageous homotypic targeting ability, prolonged circulation and phagocytosis prevention.[39] Li's group constructed a biomimetic cascade nanoreactor (designated as Mem@GOx@ZIF-8@BDOX) for tumor-targeted starvation therapy-amplified chemotherapy by assembling tumor cell membrane cloak and glucose oxidase (GOx) onto zeolitic imidazolate framework (ZIF-8) with the loading prodrug of

hydrogen peroxide (H_2O_2)-sensitive BDOX.[40] The biomimetic cascade nanoreactor could be for fluorescent imaging, and meanwhile, remarkably improve the therapeutic efficacy through the synergistic therapy.

1.2.2.4 Prospects of stimuli-responsive nanoMOF

Considering that MOFs have emerged as promising delivery vehicles, the construction of stimuli-responsive nanoMOFs is critical for the development of cancer theranostics, and Liu's group designed a general approach for the preparation of stimuli-responsive multifunctional MOFs.[41] Different types of MOFs including ZIF-8, MIL-101 and UiO-66 were synthesized firstly and then functionalized with polydopamine (PDA) after DOX loading, followed by the conjugation with targeting molecules for targeted drug delivery. Importantly, the stimuli-responsive multifunctional MOFs showed great potential in combined chemo-photothermal therapy.

For the purpose of precise therapy and reducing side effects, more smart targeting molecules-modified stimuli-responsive nanotheranostic probe with the ability of affording immune evasion shall be developed, and it is very meaningful to explore series of facile and general synthesis methods of stimuli-responsive nanoMOF hybrid composites based on tumor microenvironment.

1.2.3 Magnetic-based MOFs NPs for MRI guided therapy

Magnetic nanoMOFs are a class of nanomaterials combining the magnetic properties of the metal or metal-oxides nanoparticle with the drug loading ability of the nanoMOF. These systems are able to carry and deliver specific drugs in biological systems whose release is triggered on a controlled manner under the application of a magnetic field.[42-43] Magnetic resonance imaging (MRI) is a powerful imaging technique due to its ability to provide high spatial resolution and tissue penetration. In the presence case, the magnetic nanoparticles affect the relaxivity of the protons from water. High spin paramagnetic gadolinium (Gd) or iron (Fe) oxides superparamagnetic nanoparticles are typically integrated or coupled with nanoMOFs as MRI contrast agents.

1.2.3.1 Bare magnetic-based MOF NPs

1.2.3.1.1 Gd-based MOF NPs

As positive contrast agents, despite their potential high *in vivo* toxicity, Gd-based nanoMOFs produce a large shortening of the longitudinal relaxation time (T1) and high longitudinal relaxivity (r1). Boyes's *et al.* have prepared polymer-modified Gd nanoMOFs *via* a reversible addition-fragmentation chain

transfer (RAFT) polymerization for targeted imaging and treatment of cancer.[44] However, bimodal imaging (magnetic resonance and fluorescence microscopy) and cell growth inhibition were only considered at the *in vitro* level.

Yin's group also developed a Gd-carboxylate nanoMOFs theranostic platform for MRI-guided pH-responsive chemotherapy *in vivo* based on a 5-boronobenzene-1,3-dicarboxylic acid (BBDC) as a versatile ligand, leading to an enhanced permeability and retention (EPR) effect and glucose-mediated glucose-transported protein (GLUT1) tumor targeting; this led to: (i) an improved biocompatibility, (ii) efficient active targeting of tumors, and (iii) a pH responsive switch for leakage-free DOX delivery as three birds with one stone.[45]

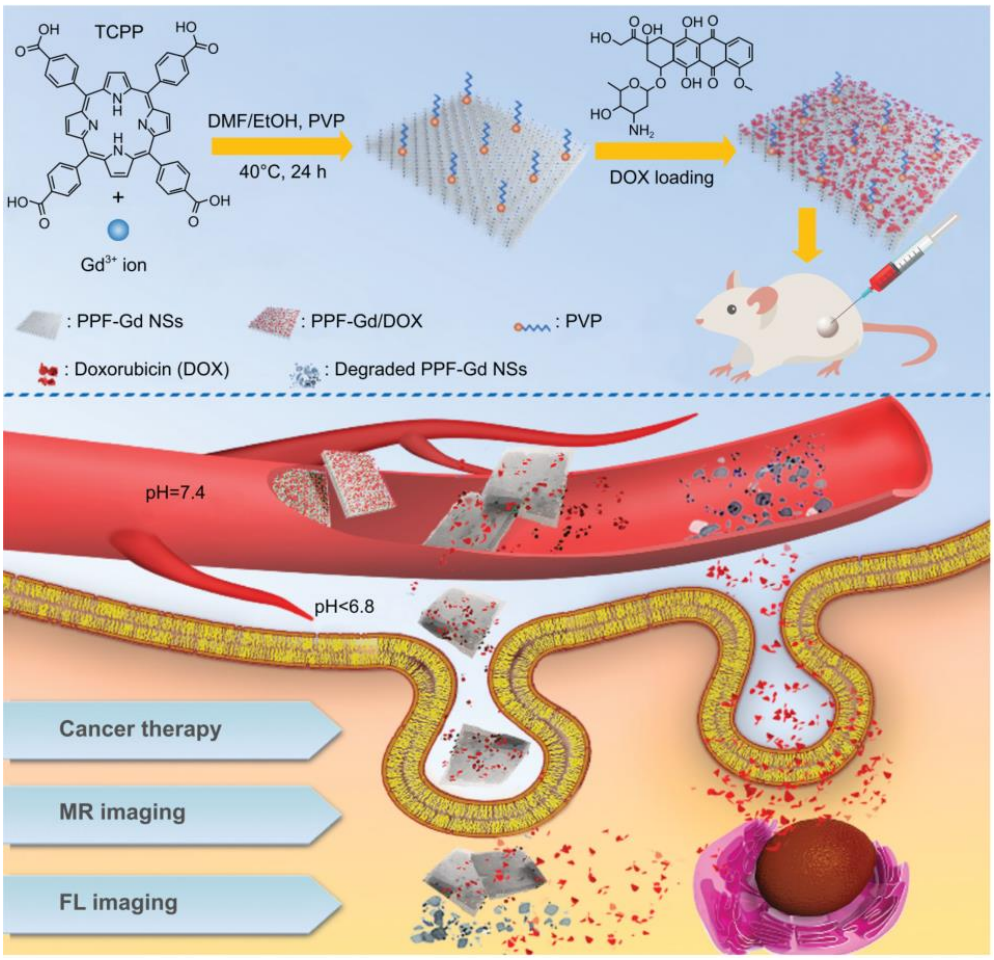

Figure 1.2.1 Schematic illustration of the fabrication of PPF-Gd NS-based drug delivery systems and their efficient cancer therapy and multimodal bioimaging.

Via utilizing photodynamic porphyrin carboxylate based MOFs ligand, Li's group developed a folic acid (FA) conjugated Gd-porphyrin MOF for fluorescence imaging (FLI) and MRI dual-modality imaging and photodynamic therapy (PDT) using zebrafish to develop tumor model of hepatocellular carcinoma.[46] The relaxivities of the resulting Gd-based nanoMOFs were significantly higher than

typical Gd chelates and the EPR effect took advantage of their higher molecular weights. Such a multi-modal imaging approach is attractive to guide cancer therapy clinically. 2D functional Gd-porphyrin MOF nanosheets (NSs) with high surface-to-volume ratio and surface charge were fabricated *via* a surfactant-assistant solvothermal method, and display superior performance in terms of drug (DOX) loading capacity (> 1500%) and persistent drug release, tumor tissue penetration (**Figure 1.2.1**).[47] Moreover, these biodegradable 2D nanomaterials were promising for enhanced fluorescence (FL) and T_1-weighted MR imaging and cancer chemotherapy.[47] However, the potential toxicity of Gd^{3+} ions such as nephrogenic systemic fibrosis (NSF) in patients, and undesired deposition in different tissues and large scale production have seriously to be addressed before translating into clinical application.[48]

1.2.3.1.2 Fe-carboxylate MOFs NPs

Considering the potential leaching of highly toxic Gd^{3+} ions from the *in vivo* degradation of Gd-carboxylate based nanoMOFs, highly porous nontoxic iron(III)-carboxylate nanoMOF have attracted so far a great deal of attention as drug nanocarriers.

To make nanoMOFs efficient theranostic systems, it is necessary to synthesize nanoparticles of several hundred nanometers with a narrow polydispersity. Among the large number of existing Fe-carboxylate MOFs, MIL-n materials combine several features of interest: a good chemical stability, a large porosity suitable for high drug payloads, a low toxicity and intrinsic imaging properties. Horcajada *et al.* has shown that MIL nanoMOFs with engineered cores and surfaces, are a class of nanocarriers for the controlled delivery of series of challenging antitumoral and retroviral drugs, which also possess interesting *in vivo* imaging properties.[49]

Lin's group also reported a strategy of delivering an imaging contrast agent organic fluorophore together with an anticancer drug ethoxysuccinato-cisplatin (ESCP) prodrug by postsynthetic grafting of the outer surface of the MIL-101(Fe) nanoMOF.[50]

To overcome the poor biodistribution of drugs with frequent dose-related side effects, Zhang's group reported a biocompatible nanoMOF based tumor targeting drug delivery systems (DDS) developed through a one-pot organic solvent-free "green" post-synthetic surface modification procedure. Authors started from the preformed MIL-101(Fe)-N_3 nanoMOF, then functionalized by a bicyclononyne functionalized β-cyclodextrin (β-CD) derivative (through strain-promoted [3+2] azide-alkyne cycloaddition (SPAAC)) further combined with an adamantane functionalized PEG polymer and targeting peptide cyclic arginine-glycine-aspartic acid (RGD) through host-guest interactions.[51] Due to the covalently linked pH-responsive benzoic imine bond and the redox responsive disulfide bond, this multifunctional DDS showed an acidic environment-enhanced tumor cell uptake and tumor

intracellular GSH-triggered drug release, which inhibited tumor growth effectively with minimal side effects.

1.2.3.1.3 Mn-based MOFs NPs

Manganese (II) (Mn^{2+}), although with a higher toxicity and lower daily dose compared to iron ions, has been demonstrated with its five unpaired 3d electrons to be an effective T1 contrast agent in MRI. Recently, Mn-based MOF have therefore been considered for theranostics.

Lin's group reported the self-assembly of a Mn-bisphosphonate nanoscale coordination polymers (NCPs) with a lipid and PEG coating; this theranostic NCP platform was capable of delivering a chemotherapeutic drug zoledronate (loading capacity of 63 ± 5 wt%) to cancer cells and behaved as an MRI contrast agent simultaneously.[52] Another strategy is to construct theranostic bimetallic MOFs, and Pan *et al.* synthesized a low toxicity bimetallic zeolitic imidazolate framework (Mn-ZIF-8) with a drug (5-FU) loading capacity of 25%, which showed favorable pH responsiveness and MRI for glioma diagnostic and therapeutic applications simultaneously.[53]

Considering the toxic adverse effects and resistance to drugs of chemotherapy, Yin's group developed theranostic Mn-porphyrin Zr(IV) carboxylate nanoMOFs; the bridging Mn-porphyrin ligand was used for a MRI-guided nitric oxide and photothermal synergistic therapy.[54] Interestingly, free-radical NO treatment was introduced to overcome the disadvantages of singlet oxygen ($^1O_2$)-based PDT due to the local hypoxia of tumor and through the formation of heat-sensitive NO donor S-Nitrosothiol (SNO). NO release and PTT were obtained simultaneously under near-infrared (NIR) light irradiation. Similarly, a multifunctional all-in-one theranostic platform by using mixed-ligand TCPP and Mn-TCPP was developed for FL, MRI, and PTI trimodal imaging, redox-responsive drug release, and enhanced photodynamic and photothermal therapy.[55]

1.2.3.2 Hybrid MOFs nanocomposites

The association of MOFs and functional nanoparticles has led to the creation of new multifunctional composites hybrid systems. However, until recently, these hybrid materials have been mainly considered for other applications such as hydrogen storage or heterogeneous catalysis.[56-59] In nanomedicine, series of hybrid nanostructures were recently constructed from nanoMOFs to form multifunctional drug-delivery systems.

1.2.3.2.1 Nano-objects based on MOFs and PB NPs

Chen's group developed core-shell Prussian Blue (PB) nanocube@Fe-BTC MOF for pH-responsive artemisinin delivery, MRI and fluorescence optical imaging (FOI)-guided chemo-/photo- thermal combinational cancer therapy.[60] Interestingly, dual nanoMOFs integrated the T1/T2 MRI, photothermal ability and photoluminescence properties of PB. Furthermore, this strategy was applied for the construction of PB@ZIF-8 nanoparticle system, and the endogenous degradation of ZIF-8 in acid tumor microenvironment was combined with exogenous NIR stimuli to realize efficient drug delivery [61]. A similar strategy was applied by using preformed PB nanocubes $Mn_3[Co(CN)_6]_2$.

1.2.3.2.2 Nano-objects based on MOFs and iron oxide NPs

Ultra-small super-paramagnetic magnetite (Fe_3O_4) nanoparticles have generated a widespread interest due to their potential applications in magnetic separation, magnetic hyperthermia, magnetic targeting, and MRI. Sahu's group incorporated Fe_3O_4 nanoparticles into a degradable zinc carboxylate metal organic framework (IRMOF-3) and the cancer chemotherapy drug paclitaxel was conjugated to the magnetic NMOFs through hydrophobic interactions for targeted anticancer drug delivery and MR imaging.[62] The targeting nanoparticles killed the cancer cells effectively, but only an *in vitro* model was considered so far. To some extent, these folic acid-conjugated magnetic NMOFs also showed a stronger T_2-weighted MRI contrast. Similar core–shell Fe_3O_4@MOF nanocomposites were also obtained with UiO-66 and Bio-MOF for simultaneous drug delivery and tumor visualization *via* MRI.[63-64]

Chen's group developed Fe_3O_4@C@Fe-BTC MOF nanoparticles through a layer-by-layer formation of Fe-BTC MOF at the surface of particles combining Fe_3O_4 and carbon dots. While Fe_3O_4@C imparts multimodal imaging properties (photoluminescence and MR) and magnetic targeting ability, Fe-BTC MOF was used for the co-delivery of the anti-cancer Dihydroartemisinin (DHA), the toxicity of which is increased in the presence of Fe(II).[65] Through the pH-responsive degradation of Fe-BTC MOF, Fe(III) was released in the tumor followed by its reduction into ferrous ions. The interaction of Fe(II) with DHA led to the production of ROS.

As an ultra-small superparamagnetic iron oxide (USPIO) NP, maghemite (γ-Fe_2O_3) is of a great interest. Steunou *et al.* designed through a post-synthetic strategy a maghemite-nanoMIL-100(Fe) bimodal nanovector as a platform for image-guided therapy[66]; when the maghemite content was of 10 wt%, this led to relaxivity values reaching those of the commercial USPIO systems, while keeping the drug delivery properties of the bare nanoMOF paving the way for their use in theranostics.

1.2.3.2.3 Nano-objects based on MOFs and MnO_2 NPs

In addition to these aforementioned Mn-based MOFs, MnO_2 also could be integrated into MOFs via a facile *in-situ* growth method by the decomposition of $KMnO_4$ for the construction of hybrid MnO_2-MOFs nanocomposites.[67-68]

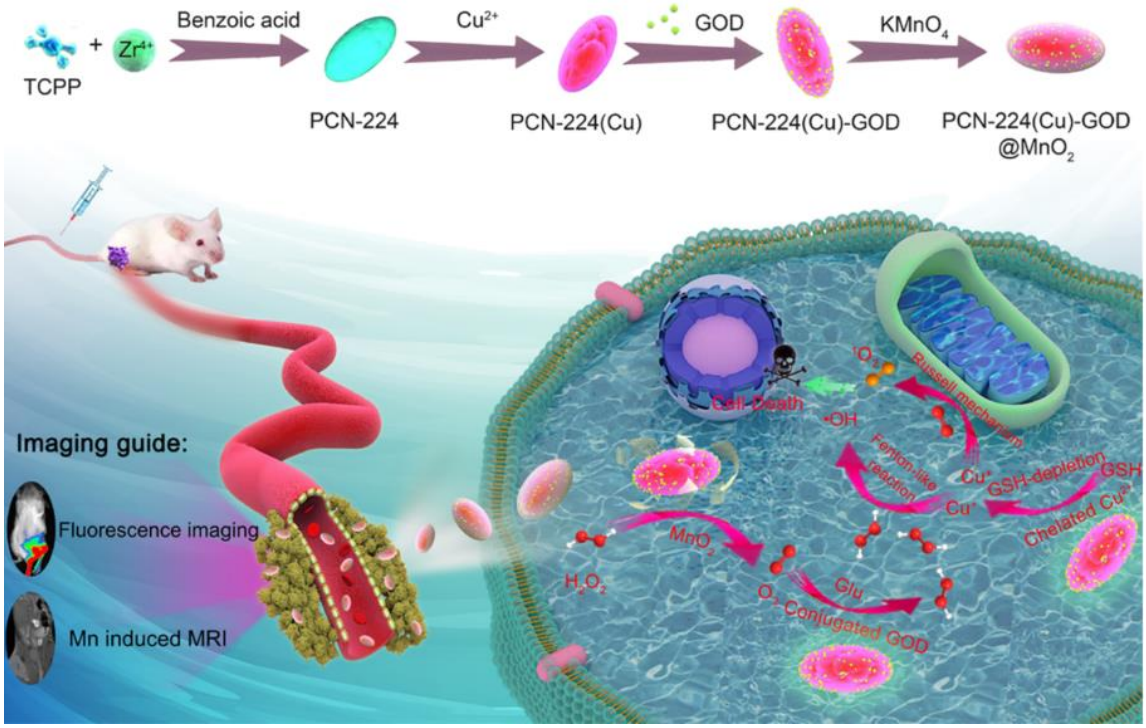

Figure 1.2.2 The main synthesis procedures and synergistic antitumor mechanism of PCN-224(Cu)-GOD@MnO_2 NPs.

In **Figure 1.2.2**, PCN-222(Zr) was first synthesized and Cu^{2+} was then coordinated with the TCPP ligand of PCN-224 due to the chelating effect, followed by the conjugation of glucose oxidase (GOD) outside PCN-224(Cu) *via* the reaction of the amino groups ($-NH_2$) of glucose oxidase with the functional carboxylic groups ($-COOH$) of the TCPP ligand, which was further coated by MnO_2 layer (named PCN-224(Cu)-GOD@MnO_2).[69] The surface coating of MnO_2 would protect GOD from damage in the blood circulation or normal cells and when the fusiform-like PCN-224(Cu)-GOD@MnO_2 was endocytosed into tumor cells, the MnO_2 layer could be decomposed by the excess H_2O_2 in the tumor microenvironment (TME), and the generated O_2 could alleviate tumor hypoxia and enhance the oxidation of Glucose by GOD. Meanwhile, the chelated Cu^{2+} could be reduced to Cu^{+} by GSH, thus producing $\bullet OH$ *via* the Fenton-like reaction or $^1O_2$ by the Russell mechanism (a spontaneous recombination reaction of peroxyl radicals). PCN-224(Cu)-GOD@MnO_2 was also a good agent for *in vivo* fluorescence imaging and T1 weighted MRI as it contains the TCPP ligand and Mn, and provides precise guidance for co-enhanced starvation and chemodynamic synergetic cancer

therapy.[69] Herein, the synthesis procedure is however quite complicated and as a result, reproducibility issues should be considered.

1.2.4 MOFs NPs for fluorescence imaging guided therapy

1.2.4.1 Fluorescent MOFs

TCPP and the 'extended' structure bis (2, 20-bipyridy) (5, 50-di-p-benzoicacid-[2, 20] bipyridinyl) ruthenium (II) dichloride (H_2L) exhibit fluorescence and singlet oxygen generation properties. [55, 70] Fluorescent MOFs could be then constructed using this molecule as the organic ligand and zirconium (Zr^{4+}) ions as the metal nodes.[70] The resulting biocompatible multifunctional H_2L-MOFs realized 94% DOX uptake and efficient *in vitro* photodynamic therapy and chemotherapy was confirmed. Although the fluorescence imaging diagnosis capability was validated *via in vivo* normal mice and tumor-bearing mice imaging, *in vivo* therapy was not studied in this work.

1.2.4.2 Fluorescent dyes encapsulation

Most near-infrared region (NIR) organic dyes such as Indocyanine green (ICG) are ideal imaging and photodynamic/photothermal therapy agents. However, their poor aqueous solubility, low cancer specificity, and low sensitivity in cancer theranostics have limited so far their clinic translation. Moreover, they showed a dose-dependent toxic effect. To overcome these issues, Liu's group developed hyaluronic acid (HA) and ICG-engineered MIL-100(Fe) nanoparticles (MOF@HA@ICG NPs) for imaging-guided, anticancer photothermal therapy (PTT).[71]

Apart from common direct encapsulation fluorescent dyes into MOFs, one can also use MOFs to pre-target lesion site, and subsequently label cells or tissues with the fluorescent molecules through bioorthogonal reaction without interfering with native biochemical processes. In **Figure 1.2.3**, metabolic labeling molecule 3-azido-d-alanine (d-AzAla) were first encapsulated into MIL-100 (Fe) NPs, and then the synthesized nanoobjects were delivered to the infection site *via* tail vein injection. Following a second injection of clickable fluorescent dyes (DBCO-Cy5) or antibacterial agents (AIE NPs-DBCO) with dibenzocyclooctyne (DBCO) group, d-AzAla was conjugated with DBCO-Cy5 or AIE NPs-DBCO through strain-promoted alkyne-azide cycloadditions (SPAAC) reaction in the infection site.[72] Herein, iron(III) in MIL-100 (Fe) can catalyze the decomposition of H_2O_2 and the coordination bond between trimesic acid and iron(III) breaks in the reaction. Then, d-AzAla could be selectively released from degraded MIL-100(Fe) in H_2O_2 oversecreted tissues, which was further

integrated into the cell walls of bacteria to label azido group to staphylococcus aureus (MRSA). Ultimately, a specific *in vivo* imaging of bacteria and image-guided antibacterial therapy was realized.

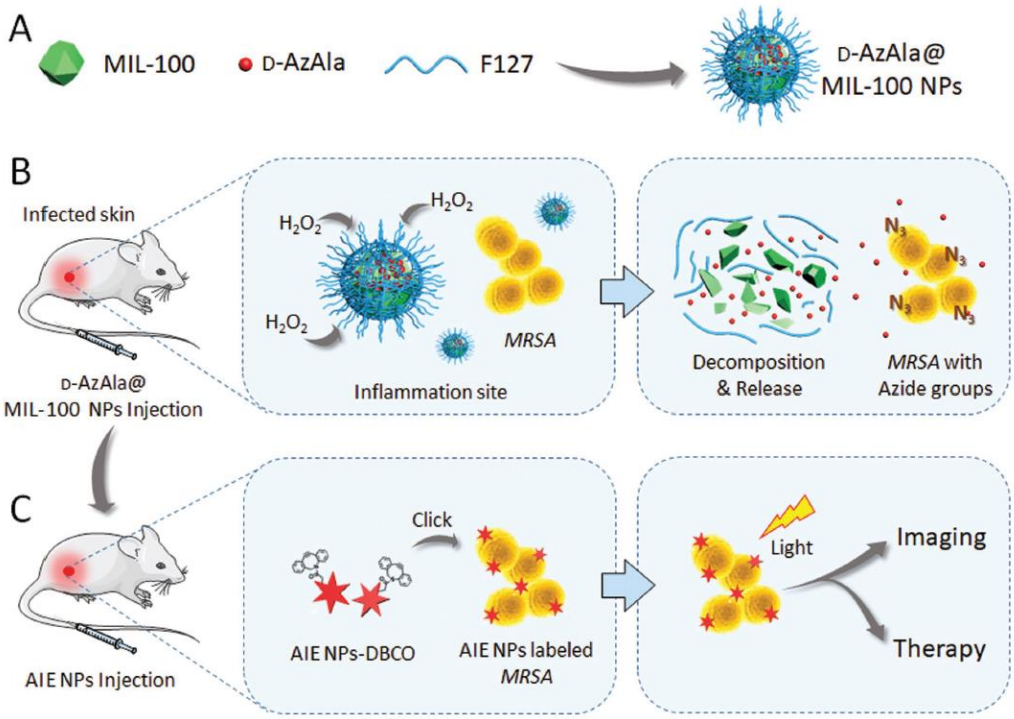

Figure 1.2.3 The proposed strategy of bacteria diagnosis and therapy by the H_2O_2-responsive MOFs assisted *in vivo* metabolic labeling of bacteria (methicillin-resistant Staphylococcus aureus (MRSA)). A) The synthesis of azido labeled D-AzAla@MIL-100(Fe) NPs (d-AzAla = 3-azido-D-alanine). B) The accumulation and decomposition of D-AzAla@MIL-100(Fe) NPs in the presence of H_2O_2 at the site of the infected tissue, followed by of internalization of invading bacteria. C) Ultrasmall AIE (aggregation-induced emission) NPs with dibenzocyclooctyne (DBCO) group bind with bacteria through click reaction for tracking and effective photodynamic therapy (PDT) of bacteria.[72]

Apart from MIL-100(Fe), NIR dyes were also combined to ZIF-8, MIL-53 or Fe(III) tetracarboxylate "socMOF" (or MIL-127), and the dye-MOF NPs inhibited tumor growth through photothermal or photodynamic therapy while exhibited outstanding NIR or fluorescence imaging capacity both *in vitro* and *in vivo*.[73-75] Damirin's group synthesized a smart multifunctional NMOF for MR/optical imaging and targeted drug delivery.[76] First, Fe-MIL-53-NH_2 was used for encapsulating the drug 5-fluorouracil (5-FU) and served as a MR contrast agent. Subsequently, the fluorescence imaging agent 5-carboxyfluorescein (5-FAM) and the targeting reagent folic acid (FA) were conjugated to the 5-FU-loaded Fe-MIL-53-NH_2. The obtained drug delivery system (DDS) showed both a good biocompatibility, tumor enhanced cellular uptake, strong cancer cell growth inhibitory effect, excellent fluorescence imaging, and finally an outstanding MRI capability.

1.2.4.3 Carbon dots

As a class of promising carbon materials, carbon dots (CDs) emerge as superior and universal fluorophores because of their excellent optical properties, small size and biocompatibility and they have shown great promises in various biomedical applications such as bioimaging, biosensing and drug delivery.[77] However, aggregation-induced fluorescence quenching of carbon dots is the main obstacle for their potential applications. MOFs could efficiently reduce the aggregation of carbon dots, thus enhancing their optical properties and meanwhile, benefiting from the ultrahigh porosity and tunable pore size of MOFs, CD@MOF composites are designed as fluorescent sensors.[78] Wang's group reported a two-step room temperature synthesis of green fluorescent C-dots incorporated into ZIF-8 as a simultaneous pH-responsive drug delivery and fluorescence imaging system.[79] These hybrid nanocomposites showed remarkable properties depending on the incorporated C-dots with versatile shapes and functions.

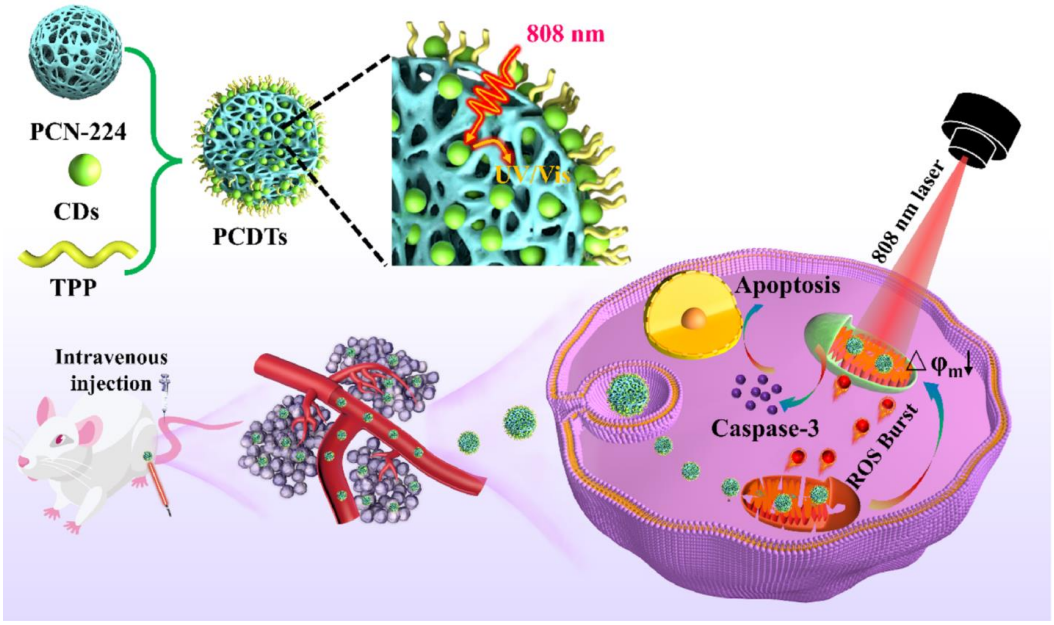

Figure 1.2.4 Schematic illustration of the structure of PCDTs and their application to 808 nm NIR light-activated and mitochondria-targeted PDT.

Porphyrin-based MOFs have been studied for PDT (§**1.2.5.1)**. and most porphyrins could only be sensitized by ultraviolet (UV)/visible light, limiting their *in vivo* application. Therefore, development of NIR light-activated porphyrinic MOFs for amplified PDT is still highly desirable. Weng *et al.* designed a "peeled pitaya-like" heterostructure PCN-224@CDs (donated as PCDTs), on which the external NP surface was further modified with triphenylphosphines (TPPs) for targeting mitochondria (**Figure 1.2.4**).[80] Under NIR laser irradiation, the abundant carbon dots could transfer the energy to the porphyrin MOF due to the tight coupling and short distance, so that $^1O_2$ generation efficacy was

enhanced. Apart from being photosensitizers, carbon dots possessed good up-conversion photoluminescence (PL) property and therefore *in vivo* fluorescence was also performed for biodistribution analysis. In this work, a mitochondria-targeted amplified PDT of cancer cells was achieved both *in vitro* and *in vivo*. However, there are only limited works on this topic, and more CD@MOF composites are desired for cancer or other diseases therapy.

1.2.5 MOF NPs for nuclear medical imaging guided therapy

1.2.5.1 Positron emission tomography (PET)

Compared to other imaging techniques, positron emission tomography (PET) imaging has superior detection sensitivity, deeper signal penetration, and better quantitative capacity, thus gaining more widespread use in both preclinical and clinical scenarios. Hong's group developed a biocompatible isotope zirconium-89 (^{89}Zr, $t_{1/2}$ = 78.4 h)-labeled UiO-66 nanoMOF platform for PET imaging and tumor targeting DOX delivery to treat tumor-bearing mice.[81] These functionalized ^{89}Zr-UiO-66 nanoMOFs with strong radiochemical and material stability are of interest as an image-guidable, tumor-selective cargo delivery nanoplatform. Boron neutron capture therapy (BNCT) is one of the most promising glioma therapies and Zr-TCPP MOFs were synthesized *via* a solvothermal reaction and then boric acid loaded as guest molecules.[82] TCPP had fluorescence properties and ^{89}Zr had positron emission properties. Based on an orthotopic glioma mice model, ^{89}Zr-MNCs nanoparticles were studied for PET imaging, which enabled accurate *in vivo* tracking their spatiotemporal distribution , especially in tumor for BNCT.

The size of nanoparticles might also affect their targeting and other features, but it is seldom studied due to lack of a biocompatible method to precisely control the particle size of MOFs and also a facile radiolabeling technique to trace nanoparticles *in vivo*. Liu's group used a modulator poly(allylamine hydrochloride) (PAH) to precisely tune the size of drug-loaded amorphous ZIF MOF particles at room temperature and analyze *in vivo* the impact between the particle size of MOFs and cancer theranostics through PET imaging.[83] Considering of the similar coordination properties of Zn^{2+} and Cu^{2+}, Cu-64 radiolabeled DOX@AZIF-8 (^{64}CuDOX@AZIF-8) was obtained by utilizing $^{64}CuCl_2$-mixed $ZnCl_2$ as the precursor. These 60 nm radiolabeled nanoMOFs exhibited a longer blood circulation with over than 50% higher tumor accumulation compared with larger particles of 130 nm. Although ZIF MOF is specifically promising for drug carrier, the toxicity of ZIF-8 nanoparticles cannot be ignored, which may severely limit its further clinical application.

Tumor hypoxia, a phenotype of inadequate O_2 supply in fast-growing tumors, could lead to drug resistance and poor therapeutic efficacy. Especially for radiotherapy, hypoxic cells are less sensitive to radiation damage than normoxic cells and thus O_2-evolving strategy is proposed for tumor therapy. Chen's group fabricated a PEGylated Zr/porphyrinic MOF-Au nanohybrid *via* an *in situ* growth method by reducing $HAuCl_4$ to NPs for O_2-evolving synergistic chemoradiotherapy (**Figure 1.2.5**).[84] The biodistribution of the nanomedicine was investigated by PET imaging through Cu-64 radiolabeling method. Herein, AuNPs as radiosensitizers were decorated on the surface of MOF to stabilize the nanocomposite, whereas the MOF scaffold acts as a container for loading chemotherapeutic drug doxorubicin, achieving an enhanced synergistic chemoradiotherapy. Notably, AuNPs or MOF alone contributed little to the production of O_2, but the nanohybrid showed a good performance in O_2 generation under the same condition.

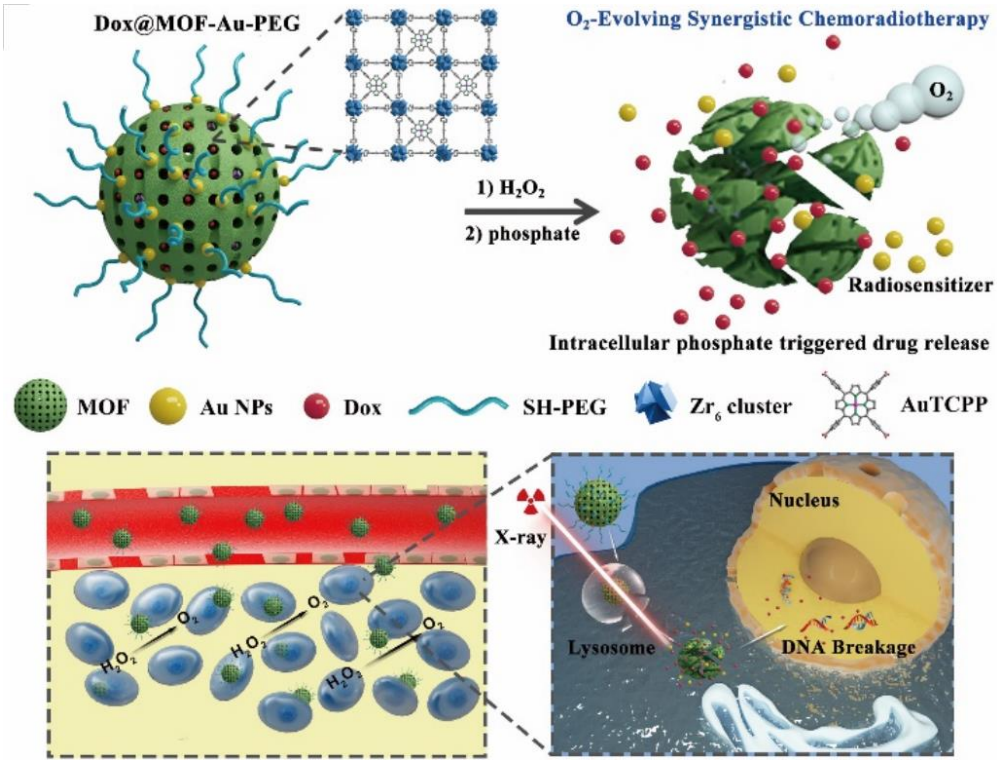

Figure 1.2.5 The main components of Dox@MOF-Au-PEG and the mechanism of O_2 self-supplying synergistic chemoradiotherapy.

1.2.5.2 Single photon emission computed tomography (SPECT)

From a clinical point of view, SPECT allowed images based on the distributions of imageable radionuclides such as ^{99m}Tc, ^{123}I , or ^{111}In in the body to be acquired and displayed as tomographic slices.[85] Liu's group fabricated PEG functionalized 2D-NMOFs composed of Zn^{2+} and tetra (4-carboxyphenyl) porphyrin (TCPP) labeled with the diagnostic radioisotope ^{99m}Tc for single photon emission computer tomography (SPECT) imaging and chemo-photodynamic cancer therapy.[86]

Through SPECT, efficient tumor homing of those ^{99m}Tc-labeled 2D-NMOFs was observed upon intravenous injection.

Utilizing nanoMOFs as a single nanoplatform to label various radionuclides for tumor imaging and radioisotope therapy (RIT) has been rarely studied. Liu's group first synthesized PEG modified ZrMOFs (PCN-224) with a size of ~140 nm and then metal radionuclides (^{99m}Tc and ^{177}Lu) were labeled onto MOFs *via* chelating with the porphyrin structure. Another metal radionuclide ^{125}I could also be labeled on MOFs *via* chemical substitution of hydrogen in the benzene ring. Importantly, these radionuclide-labeled PCN-PEG nanoparticles all exhibited high radiolabeling yield and were stable in different solutions. According to fluorescence and SPECT/CT imaging, these nanoparticles achieved high tumor accumulation after intravenous injection and ^{177}Lu-PCN-PEG exhibited significant tumor inhibition and prolonged survival time by RIT.[87]

1.2.5.3 Computed Tomography (CT)

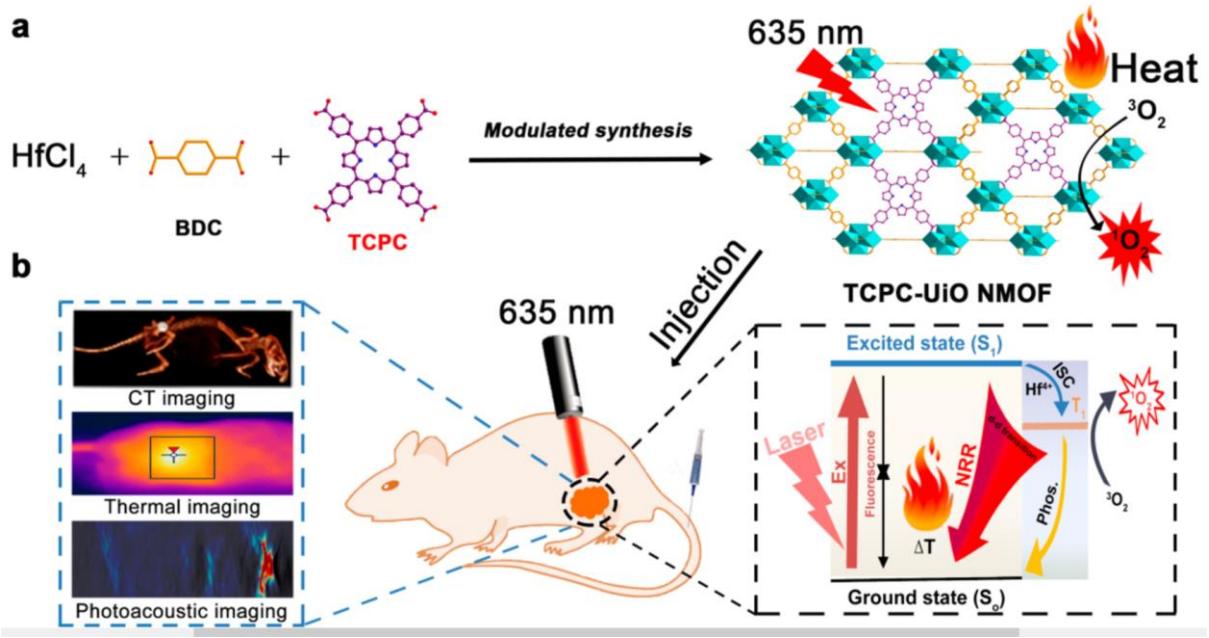

Figure 1.2.6 The synthesis and mechanism for cancer therapy of TCPC-UiO by light activation. (a) Synthesis of TCPC-UiO NMOF and schematic description of heat and singlet oxygen generation under laser irradiation. (b) Photophysical mechanism for cancer therapy under light activation of a combination therapy guided by CT/thermal/photoacoustic imaging.

Meanwhile, considering strong X-ray attenuating ability of the Hf element, Xie's group developed a multifunctional Hf-porphyrin NMOF platform [Hf/TCPP] with a high tirapazamine (TPZ) loading for Computed Tomography (CT) imaging that combined PDT and hypoxia-activated chemotherapy.[88] Hf/TCPP nanoparticles could efficiently produce ROS for PDT upon irradiation, while the depletion

of the oxygen did further enhance the hypoxic environment of tumors to induce the activation of TPZ associated with better *in vivo* efficacy. *Via* a mixed-component strategy, photoactive chlorin was incorporated into the Hf-UiO-66 archetype structure, named TCPC-UiO, in a view of multimodal CT/thermal/photoacoustic imaging, photodynamic and photothermal therapy (**Figure 1.2.6**).[89] TCPC-UiO showed an impressive anticancer activity against tumor-bearing mice *in vivo*, with a tumor inhibition rate above 90%.

Although not endogenous and poorly soluble in body fluids, ZrO_2 exhibits favorable biocompatibility with an extra property of enhanced computed tomography (CT) imaging efficiency. Meng's group developed biocompatible ZIF-8 nanoparticles by coating ZrO_2 onto the surface for chemo-microwave thermal tumor synergistic therapy.[90] Ionic liquid (IL) exhibited great prospects in microwave absorption and as a microwave sensitizer, IL was thus loaded into the pore of ZIF-8 for enhanced microwave thermal therapy and ZrO_2 could also act as an excellent CT contrast agent. Meaningfully, the toxicity problem of ZIF-8 nanoparticles successfully was solved by surface coating of ZrO_2, which could downregulate the degradation process of ZIF-8 and this strategy is believed to be helpful for further research.

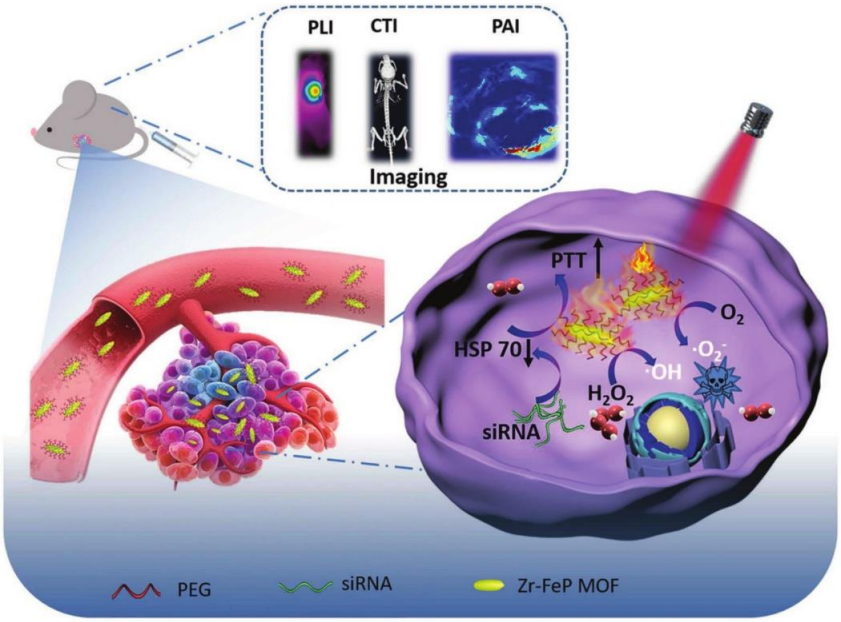

Figure 1.2.7 Multimode imaging diagnosis and combination of low-temperature PTT and PDT for cancer treatment based on siRNA/Zr-FeP MOF nanoshuttles.

As mentioned before, tumor hypoxia is a typical feature of solid tumors, which limits the applications in radiotherapy because of radiation resistance. Carbonic anhydrase IX (CA IX) as a cancer-related cell surface enzyme could catalyze the reversible conversion of carbon dioxide to bicarbonate ion and proton, endowing tumor cells with survival advantages in hypoxia.[91] Based on the upregulated

expression of carbonic anhydrase IX (CA IX) by hypoxia in tumor, Meng's group developed quercetin-modified Zr MOFs for simultaneously enhancing radiotherapy therapeutic effects and CT imaging.[92] Quercetin acts as a radiosensitizer here. The 1,4-benzenedicarboxylic acid produced from Zr-MOF biodegradation can strongly bind to the Zn^{2+} of CA IX, which can inhibit the catalytic activity of CA IX and result in downregulating tumor hypoxia. The as-prepared Zr-MOF-QU as CA IX inhibitor exhibited improved radiation mediated apoptosis.

Following again an "all-in-one" strategy, Dong's group developed zirconium-ferriporphyrin MOF (Zr-FeP MOF) nanoshuttles for multimodal imaging diagnosis, PDT and low-temperature PTT synergistic treatments (**Figure 1.2.7**).[93]

1.2.6 MOFs NPs for imaging guided phototherapy

Phototherapy, including photothermal therapy (PTT) and photodynamic therapy (PDT) is a highly effective, noninvasive, selective method for cancer treatment.[94]

1.2.6.1 Porphyrin-based MOFs

Porphyrin ligands are interesting for photodynamic therapy but their use is limited by their poor solubility, self-quenching and aggregation issues. Porphyrin-based MOFs have recently been reported as suitable candidates to overcome these problems. Ju's group designed multifunctional porphyrin-based MOFs NPs by assembling porphyrin, folate targeting-motif and dye-labelled peptide into MOF cages.[95] After folate receptor-mediated uptake, the nanoprobe could efficiently generate $^1O_2$ in mitochondria to induce cell apoptosis.

Zr(IV)-based porphyrinic MOF nanoparticles PCN-224 also attracted attention for tumor targeted photodynamic therapy and hypoxia-amplified bioreductive therapy[96-97]. Through cancer cell membrane coating, another novel cancer cell membrane@Pt(II) porphyrinic MOF (mPPt) was also developed as a biomimetic theranostic O_2-meter for cancer targeted photodynamic therapy and phosphorescence imaging[98]. In type II mechanism of photodynamic therapy (PDT), the ground triplet-state molecular oxygen ($^3O_2$) is transformed to the reactive singlet oxygen ($^1O_2$). However, the process is extremely dependent on oxygen (O_2), and the lack of O_2 will directly suppress the PDT efficacy. In the type I mechanism, O_2^{-}• molecule could be further converted to partially recyclable O_2 under the effects of intracellular superoxide dismutase (SOD) and part of them could be transformed to high toxic hydroxyl radical (OH•). To overcome a hypoxia microenvironment, Dong's group developed bacteriochlorin-based Hf MOFs termed DBBC-UiO as a NIR laser-induced O_2^{-}• generator for

photoacoustic imaging (PAI)-guided PDT through synergistic type I (O_2-independent) and type II mechanism for hypoxia tumor ablation (**Figure 1.2.8**).[99] Tumor-specific PAI and highly efficient hypoxic solid tumor ablation were shown in the experiment.

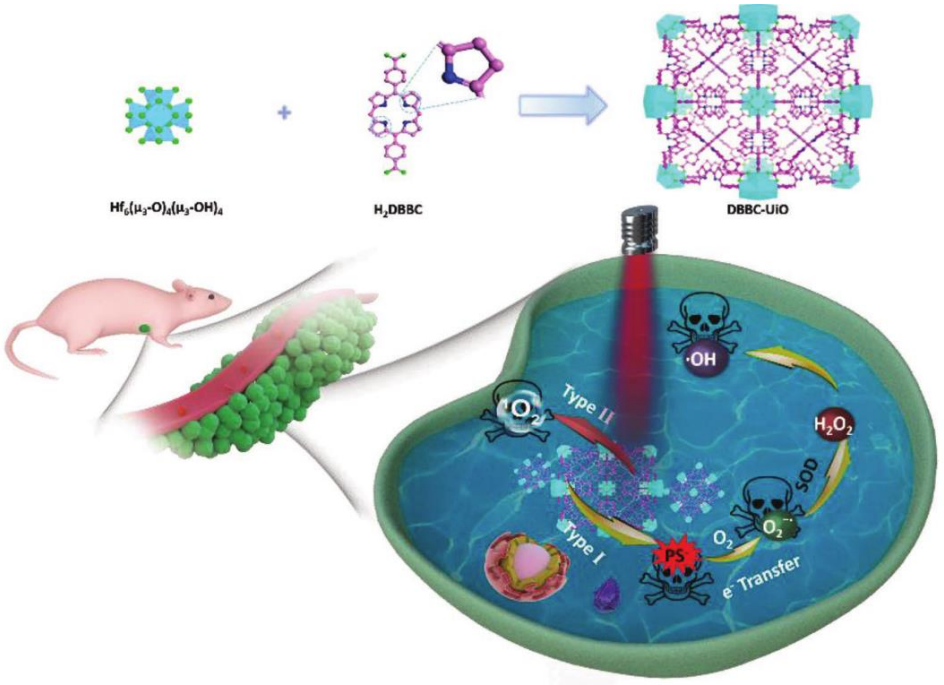

Figure 1.2.8 The synthetic procedure and photoinduced PDT mechanism of DBBC-UiO.

Although photodynamic therapy (PDT) is the most considered strategy of ROS generation, it suffers from critical limitations including tissue-penetration depth, high oxygen dependence, and phototoxicity. Sono-, radio-, microwave-, chemo-, thermos- and electro- dynamic therapies show good potential to overcome the drawbacks of PDT.[100] Meng's group prepared flexible Mn-doped UiO-66 nanocubes (NCs) with a small particle size (~60 nm) through a one-pot hydrothermal route. This led to a nanosystem combining microwave dynamic (MDT) and microwave thermal (MTT) therapies well suited to suppress the tumor cell growth *in vivo* and *in vitro* under mild microwave irradiation[101], highlighting the synergic effect between MTT and MDT.

1.2.6.2 Nano-objects based on MOFs and noble metal nanoparticles

Noble metal nanoparticles (NPs), especially anisotropic gold NPs (AuNPs), are broadly recognized as candidates for cancer theranostics because of their good biocompatibility, high light-to-heat conversion efficiency, and unique near-infrared (NIR) light absorption feature. Note that the elimination pathways of such nanoparticles is highly questionable particularly when the nanoparticles are non-degradable. In general, nanoparticles with a size of < 5 nm will undergo *in vivo* renal elimination *via* the kidneys and finally through urine. In the case of nanoparticles > 5 nm, the

biodegradable ones can be disassembled firstly and then return to the metabolic circulation while most non degradable nanoparticles (> 5 nm) will be retained in long term in liver non-parenchymal cells such as Kupffer cells, which act as barriers of hepatobiliary elimination.[102] In recent year, Au NPs-MOFs or plasmonic MOFs along with the encapsulation of drugs or functional molecules for cancer diagnosis or therapy has attracted a considerable attention.[103-105]

1.2.6.2.1 Au NRs@MOFs

Tang's group combined anisotropic gold nanorods (AuNRs) and ZIF-8 into core–shell nanostructures AuNRs@ZIF-8 as a multifunctional nanoplatform for near-infrared-induced synergistic chemo-photothermal therapy (**Figure 1.2.9**).[106] Gold nanorods with high NIR-light-triggered photothermal properties are good candidates for photothermal therapy, and its drug-loading capacity was improved through the ZIF-8 shell. However, this work was mainly focused on synergistic photothermal / chemotherapy and only photothermal imaging was performed, which was insufficient in terms of biodistribution.

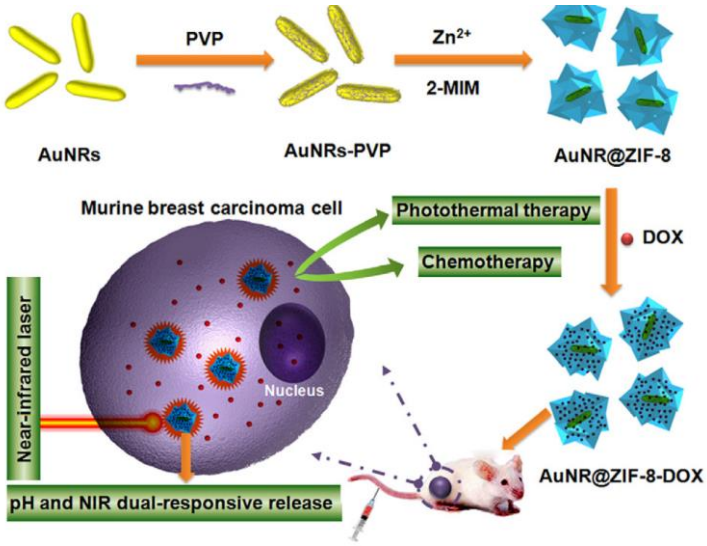

Figure 1.2.9 The fabrication of AuNR@ZIF-8 core–shell nanostructures as a novel multifunctional nanoplatform for synergistic chemo-photothermal cancer therapy both *in vitro* and *in vivo*.

To confer to the AuNRs@ZIF-8 heterostructure a multimodal imaging property, three types of NPs (Ag_2S, Ag_2Se, up-conversion nanoparticles (UCNP)) and the anticancer drug Dox were first introduced into ZIF-8 and then Au NRs were attached *via* electrostatic interaction (NPs@ZIF-8@Au NR-DOX).[107] Under NIR irradiation using an 808 nm laser, the tumor could be completely eliminated *in vivo* through computed tomography, photoacoustic, and NIR fluorescence imaging-guided photothermal / chemotherapy. Although these aforementioned heterostructure nanoparticles have shown a great potential as theranostic platform in tumor treatment, electrostatic attraction were not

strong enough to guarantee their structural stability. Han's group prepared a unique lactobionic acid (LA) modified AuNR/ZIF-8 Janus nanoplatform *via* a selective growth of ZIF-8 on the polyacrylic acid (PAA) side of preformed Janus Au NR/PAA nanoparticles. These original nano-objects were used for CT imaging guided liver cancer therapy by the combined effect of chemotherapy and PTT.[108]

Apart from ZIF-8 MOFs, Au NRs could also be integrated into Zr-TCPP and MIL-100(Fe). Zhang's group used functionalized gold nanorods to construct through a solvothermal method porphyrinic nanoMOFs-coated gold nanorods (AuNR@MOFs) for combined photodynamic / photothermal / chemotherapy of tumor. Camptothecin (CPT) was chosen as a model drug and through the triple synergistic therapy, the tumor cells were damaged efficiently both *in vitro* and *in vivo*.[109] Chien *et al.* introduced MIL-100(Fe) on the external surface of Au NRs through a NIR induced assisted synthesis and the resulting Au NRs@MIL-100 NPs were then modified by monocyte chemoattractant protein-1 (MCP-1) to increase cellular uptake and biocompatibility.[110] This theranostic platform showed an excellent antitumor efficacy and bioluminescence imaging under the laser treatment. Similarly, Guo's group designed a Au NRs@MIL-100 NP by *in situ* depositing MIL-100 on core-shell gold nanorods-mesoporous silica nanoparticles (GNRs-MSNs), followed by the surface modification of hyaluronic acid (HA), and this single platform integrated targeted synergistic photothermal / chemotherapy and tri-modal (MR/CT/PA) imaging.[111] Concerning MIL-100, the latter two studies lack of substantial characterizations such as porosity and crystalline structure to support the successful formation of MOF part in the structure and the thickness of MOFs layer seems not to be tunable.

Nevertheless, cetrimonium bromide (CTAB) is an indispensable surfactant used in the synthesis of Au NRs and its toxicity cannot be ignored and meanwhile more work needs to be done considering the total elimination of Au NRs. In the existence of Au NRs, the growth process of MOFs layer may vary even using the same reactants, so that it should be better characterized before biomedical application. Currently, the majority of reported Au NRs@MOFs is based on ZIF-8, and more Au NRs@MOFs structures are required for theranostics.

1.2.6.2.2 Au nanospheres@MOFs

The Au nanospheres (Au NSs) with a size of tens of nanometers could not only act as photothermal agents to kill cancer cells and promote drug release, but also enhanced Raman signal. Meanwhile, considering nanoscale metal organic frameworks (NMOFs) with high porosities and high internal surface areas as drug delivery system, Hu's group designed Raman tag-bridged core-shell Au@$Cu_3(BTC)_2$ nanoparticles for Raman imaging and synergistic chemo-photothermal therapy.[112] $Cu_3(BTC)_2$ MOFs with high porosities and high internal surface areas acted as drug delivery system

and Au NSs served as photothermal agents to produce hyperthermia and surface enhanced Raman scattering (SERS) substrates to enhance the Raman signal of 4-mercaptobenzoic acid in the structure. Theranostic applications for cell tracking and *in vivo* synergistic chemo-photothermal therapy of tumor were conducted, but the tumors were partially retained. Moreover, the toxicity of Cu ion and the elimination of Au nanosphere with large particle size may be a potential problem.

Yang's group has constructed pH and GSH responsive Au@ZIF-8 by growing ZIF-8 on the surface of PVP coated Au NSs (~ 25 nm) for tumor theranostics. Interestingly, in the presence of high GSH and lower pH, the self-assembly of Au NSs occurred because of the formation of interparticle H bonds and electrostatic interactions, and the aggregation of Au NSs resulted in strong coupling plasmonic resonance, enabling tumor microenvironment triggered PA imaging and PTT.[113] Herein, the aggregation of Au NSs were observed both in solution and in living cells *in vitro*, but it is unknown about their *in vivo* fate and long term toxicity. Moreover, the porosity of ZIF-8 was not exploited for drug delivery and also without any surface coating, which may lead to unspecific capture by Reticuloendothelial system (RES).

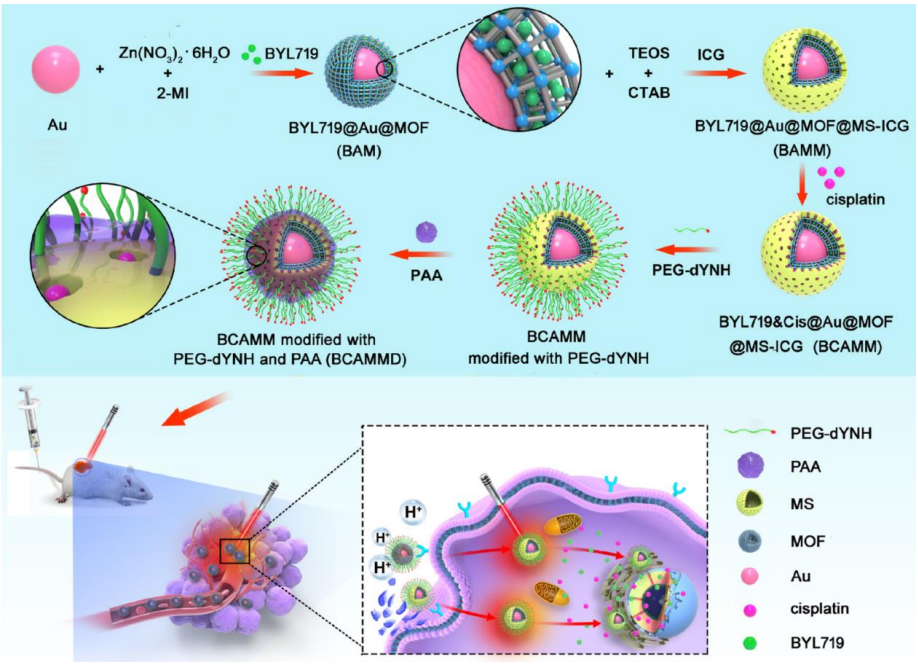

Figure 1.2.10 (a) Schematic illustration of synthetic procedure for BYL719-cisplatin loaded double shell nanoparticle (BYL719&Cisplatin@Au@MOF@MS-ICG, BCAMM) modified with dYNH targeting peptide (BCAMMD) and antitumor mechanisms of BCAMMD in tumor cell.

In another study, a multifunctional theranostic nanoplatform composed of an Au NS core (~20 nm) and a double-shell of ZIF-8 and mesoporous silica was designed for combating spinal metastasis of lung cancer.[114] Alpelisib (BYL719) as an inhibitor of α-selective phosphoinositide 3-kinase (PI3K)

that can inhibit the PI3K-Akt-mTOR signaling pathway of tumor cells was loaded into ZIF-8 and then indocyanine green (ICG) as a photothermal agent and cisplatin as a chemotherapeutic drug were conjugated onto the outmost mesoporous silica layer, followed by the conjugation of a targeting peptide dYNH and polymer PAA for specifically targeting metastatic tumor cells (**Figure 1.2.10**). However, this all-in-one strategy is quite complicated, making it less interesting for real applications.

1.2.6.2.3 Au nanoclusters@MOFs

Gold quantum dots are very small nanoparticles (a few nm) which exhibit distinctive optical and magnetic behaviors compared with larger gold nanoparticles. Au nanoclusters (AuNCs) have been extensively applied as fluorescent probes for various biomedical applications due to their unique chemical and physical properties[115-117], especially for cell imaging or detection [118-120] and even for *in vivo* theranostics[121]. There is also an interest in biomedicine for hybrid Au nanoclusters, such as Au_{25} nanoclusters.[122-124]

Yang's group has developed an inorganic–organic Fe_3O_4/ZIF-8-Au_{25} nanocomposite for magnetically targeted photodynamic/photothermal therapy. Briefly, upon 808 nm NIR light irradiation, the attached Au_{25} clusters can generate hyperthermia to produce a unique photothermal therapy modality, while an efficient singlet oxygen can also be produced for PDT. Furthermore, the encapsulated Fe_3O_4 nanocrystals could also serve as a PTT agent.[125] The introduction of small Au nanoclusters, when designing hybrid theranostic nanoMOFs, is quite advantageous not only due to their ability to produce ROS for photodynamic therapy, but also as a result of their easier renal clearance in comparison to larger inorganic nanoparticles.

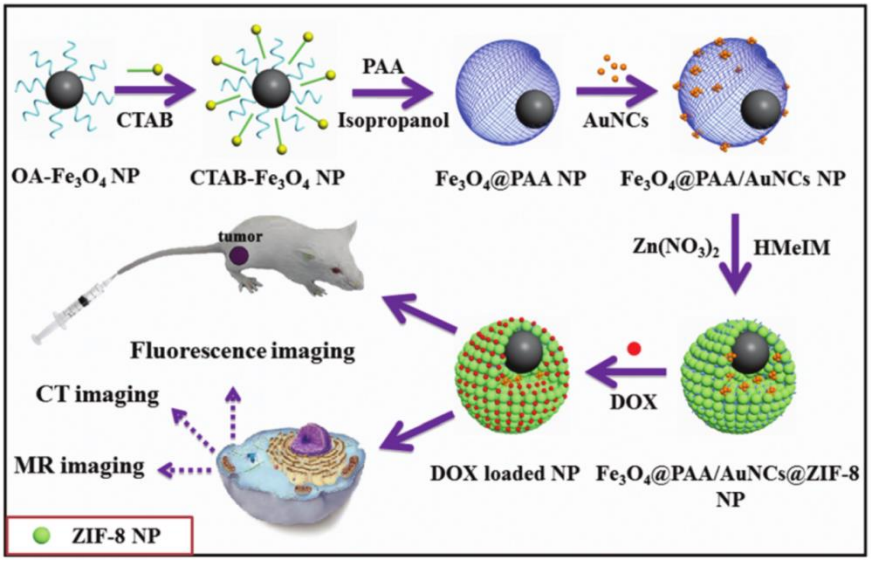

Figure 1.2.11 The preparation of Fe_3O_4@PAA/AuNCs/ZIF-8 composite NPs for simultaneous tri-modal cancer imaging and chemotherapy.

Wang's group designed a multifunctional Fe_3O_4@PAA/AuNCs/ZIF-8 NPs nanoplatform with a 130 nm size that combines MR, CT and fluorescence tri-modal imaging, ultrahigh anticancer drug loading and dual pH responsive drug release properties (**Figure 1.2.11**)[126]. In this work, Fe_3O_4@PAA core–shell NPs and GSH capped AuNCs were prepared respectively and then ZIF-8 was then formed at the surface of Fe_3O_4@PAA/AuNCs. Such multifunctional NPs are of interest for their multi-modal cancer diagnostics and visualized-synergistic therapy.

In another approach, the attachment of BSA modified AuNCs at the surface of MIL-101(Fe) was performed to build multifunctional theranostic nanoMOFs. MIL-101(Fe)@BSA-AuNCs presented MRI and fluorescence properties and was used as microwave sensitive reagent for microwave thermal therapy, MRI and fluorescence imaging (FI).[127]

1.2.6.2.4 Au nanostar@MOFs

To cure the triple-negative breast cancer (TNBC), one of the most dangerous subtypes among breast cancers, Zeng's group prepared core-shell gold nanostar@MIL-101-NH_2(Fe) whose surface is covalently modified by a short peptide ZD2 (sequence: Cys-Thr-Val-Arg-Thr-Ser-Ala-Asp-Cys) able to target the TNBC. This nano-object was used for T1-weighted MRI and photothermal therapy specifically targeting toward TNBC (**Figure 1.2.12**)[128]. MIL-101-NH_2(Fe) is a biocompatible and biodegradable MOF-bearing amino groups that could be further functionalized by ZD2 to achieve an active- targeted ability. MIL-101-NH_2(Fe) through its very large pores is able to upload record amounts of drugs which is of interest for further synergistic cancer therapy.

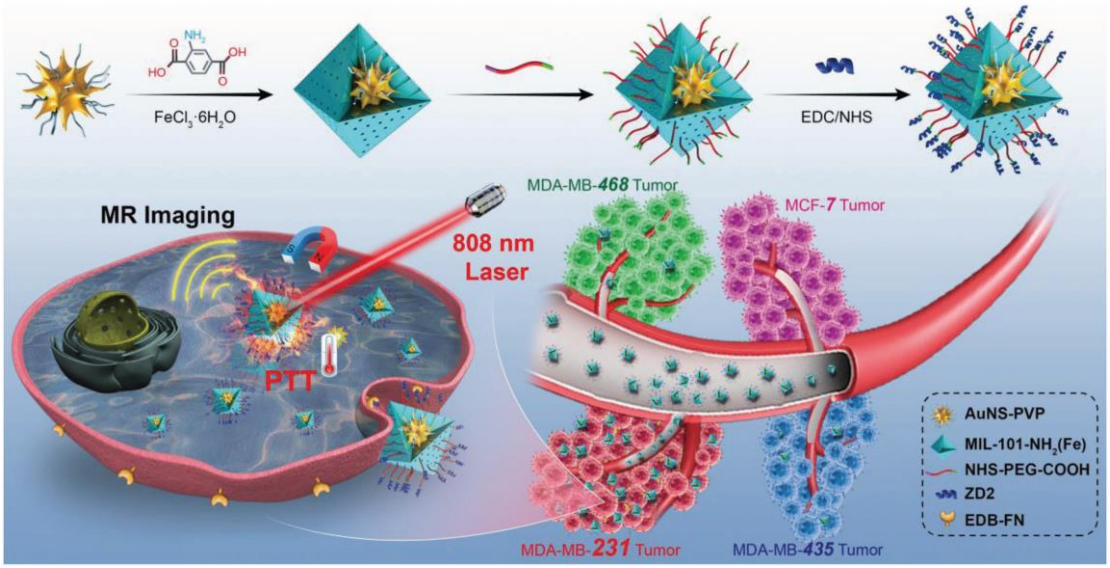

Figure 1.2.12 The synthesis of AuNS@MOF-ZD2 nanoprobes, and application for T1-weighted MRI and photothermal therapy specifically toward MDA-MB-231 tumor (TNBC).[128]

Chen's group has prepared a liposome-coated core-shell AuNS@Zr-TCPP MOFs nanocomposite encapsulated with gambogic acid (AZGL) for synergistic photothermal-photodynamic-chemotherapy of breast cancer.[129] Au NSs, TCPP and gambogic acid mediated mild PTT, PDT and chemotherapy, respectively. The accumulation feasibility of AZGL at the tumor site was verified through *in vivo* fluorescence imaging, and the fluorescence intensity of the tumor region continuously increased and reached the maximum value at 24 h post-injection. As mentioned in other works, long term *in vivo* toxicity or bio-degradation experiments are still missing.

Au NSs are also the second near-infrared (NIR-II) photothermal agent, which is advantageous for an effective tissue penetration and larger maximum permissible exposure. Lin's group has developed light-sensitive yolk-shell nanoparticles (YSNs) by integrating Au NSs as yolks and biodegradable ZIF-8 MOFs as shells for chemo-photothermal synergistic therapy (1064 nm laser irradiation).[130] The strong NIR II region absorbance made YSNs good candidates of NIR thermal imaging and photoacoustic (PA) imaging.

1.2.6.2.5 Nano-objects based on MOFs and up-conversion NPs (UNCPs)

Up-conversion nanoparticles (UCNPs), capable of converting near-infrared radiation to visible light, were chosen as optical probe in biological assays and medical imaging. MOFs-UCNPs nanocomposites exhibited better performances in bioimaging, drug delivery and therapy through the synergistic and complementary effects of MOFs and UCNPs components.[131-132] Bao *et al.* synthesized a core-shell nanoagent UCNPs@MIL-100(Fe) through a one-pot assembly of UCNPs, precursors of MOFs, etc.[133] Core-satellite UiO-68@UCNP superstructure with the encapsulation of dual-photosensitizer chlorin e6 (Ce6) and rose bengal (RB) was also developed for efficient photodynamic therapy under the guidance of fluorescence imaging and MRI, which minimized overheating effect.[134]

Another core-satellite structure MOF@UCNP composed of Zr(IV)-based porphyrinic MOF (PCN-224) and UCNPs was synthesized *via* DNA-mediated assembly method by Cha's group for photodynamic therapy (PDT).[135] Herein, singlet oxygen ($^1O_2$) was generated by Zr porphyrinic MOF NPs upon photo-irradiation in NIR. By assembling UCNPs with MOFs, it was possible to take advantage of the increased penetration of NIR light. UCNP NPs were used to excite the porphyrinic ligand due to their ability to absorb in the NIR and emit visible light. A high singlet oxygen production was observed under 980 nm irradiation by using the core-satellite UCNP-PCN-224 and this amount was significantly higher than what can be produced from simply mixing UNCPs and MOF NPs.

However, researches on MOFs-UCNPs are still at their infancy and more efforts should be made to overcome the key challenges.[131-132] In terms of synthesis, a versatile fabricating strategy for

conveniently integrating MOFs with UCNPs is urgently required and the underlying formation mechanism of MOFs-UCNPs is unclear. Concerning light-triggering therapy, the excitation wavelength of conventional UCNPs is concentrated in the NIR I window, and tissue penetration is a concern. Thus, developing NIR II-excited MOFs-UCNPs remains a key challenge. Last, biosafety concern of NPs use is always a barrier and the exploration of biodegradable MOFs-UCNPs may be beneficial for clinical application.

1.2.6.3 Nano-objects based on MOF and polymer

Polymers are commonly combined to MOF nanovectors not only to process and stabilize MOFs NPs but also to enhance their blood circulation and enable specific cell targeting. In addition, polymers were also used to impart physical properties such as PTT ability. Recently, polymer-MOF NPs have shown enhanced efficacy in cancer treatment and diagnosis, exhibiting enormous potentials for further clinical translations.[136] In the following, we will discuss recent examples in which polymers were used as photothermal agents or photosensitizers.

1.2.6.3.1 Core-Shell MOFs-polymer nanocomposites

As a type of photothermal agent, polypyrrole (PPy) has shown great potential for the photothermal treatment of cancer *in vitro* and *in vivo.* Fan's group fabricated multifunctional core-shell PPy@MIL-100(Fe) nanoparticles with PPy NPs acting as cores and the MIL-100(Fe) as the outer shell. Doxorubicin (DOX) was encapsulated in the MOF for a simultaneous photothermal therapy and chemotherapy of cancer cells. Herein, the introduction of PVP was used to facilitate the nucleation and growth of MIL-100(Fe) on the surface of PPy.[137] This resulted finally into an outstanding *in vivo* synergistic anticancer ability. Following a similar strategy, Wang's group further conducted Photoacoustic (PA) and MR dual-mode imaging and synergistic chemo-photothermal killing effects *in vitro* based on PPy@MIL-100 nanoparticles.[138] PPy core conferred the nanocomposites with strong NIR absorbance and high photothermal conversion efficiency (~40%), thus suitable for PAI and PTT. MIL-100(Fe) was utilized as nanocarrier of DOX for chemotherapy and also T_2 MRI contrast agent. However, these two studies were limited to *in vitro* theranostics.

PPy was also formed in situ in the presence of preformed MIL-53(Fe) particles which provide Fe^{3+} ions able to oxidize Py to PPy. PPy-MIL-53(Fe) nanocomposites with strong NIR absorbance can be applied for PPT to destroy cancerous cells while anticancer drug DOX could be loaded in the composite particles. These multifunctional nanocomposites can be of interest for tumor theranostics through a combined photothermal-chemotherapy.[139-140]

Polydopamine was also combined to MOFs due to its facile synthesis, biocompatibility and high photothermal conversion efficiency. Considering PDA as a template, core/shell PDA@ZIF-8 carrier was synthesized for simultaneously delivering a photosensitizer, methylene blue (MB) and a catalase (CAT) , thus realizing synergistic photodynamic and photothermal therapy.[141] Noteworthy. in **Figure 1.2.13**, Zhao's group reported a biomimetic multifunctional nanoplatform PCoA@M engineered with a core/shell PDA NPs@Co-MOF heterostructure, anethole trithione (ADT), and a macrophage membrane.[142] In the tumor microenvironment, Co^{2+} release from Co-MOF degradation would downregulate heat shock protein 90 (HSP90) expression, thereby improving the photothermal therapy effect of PDA. As a H_2S-releasing precursor, ADT could be decomposed to high concentration H_2S for efficient gas therapy. Moreover, ADT could change the balance between nicotinamide adenine dinucleotide/flavin adenine dinucleotide (NADH/FAD) during tumor glycolysis, namely starvation therapy. Macrophage membrane coating was for targeting tumor cells and prolonging blood circulation time. Finally, PTT-gas synergistic starvation therapy of orthotopic tumor and pulmonary metastasis was achieved under the guidance of fluorescence imaging. Although authors have performed series of animal experiments for imaging and therapy, the main concern still lies in the high toxicity of Co^{2+}.

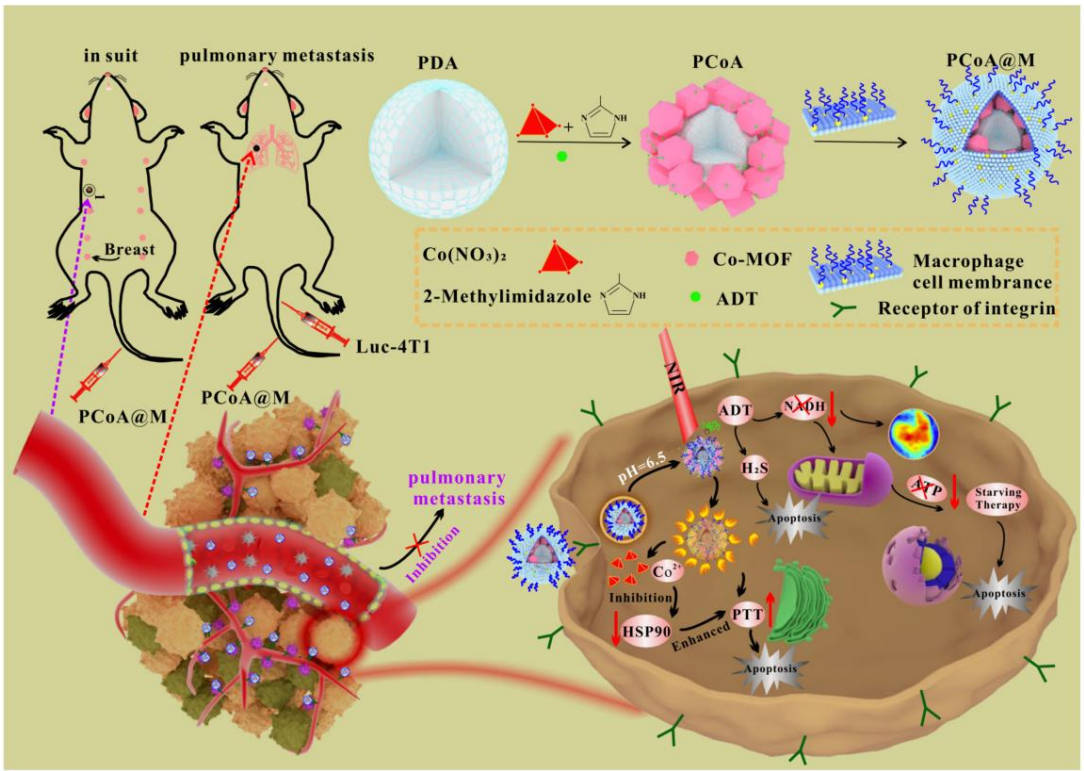

Figure 1.2.13 Synthesis and combined antitumor mechanism of PCoA@M.

As a class of 2D polymeric materials mainly composed of carbon and nitrogen atoms, graphitic carbon nitride (g-C_3N_4) nanosheets are obtained from polymerization of melamine, which has been regarded

as a suitable sustainable photocatalyst.[143] Meanwhile, they have received dramatical interest in the biomedical fields due to their optical and electronic properties.[144-145] Lee's group first designed an nanoscale core-shell platform based on DOX-loaded g-C_3N_4@ZIF-8 nanoparticles for photo-chemo therapy under dual-color imaging (the red fluorescence of DOX and the blue fluorescence of g-C_3N_4 nanosheets) .[146] Herein, g-C_3N_4 nanosheets were used as efficient visible-light photosensitizer for PDT. The combination of the chemotherapeutic effects of DOX and the PDT effect of g-C_3N_4 nanosheets led to a high synergistic therapeutic efficacy.

1.2.6.3.2 Surface coating of polymer on MOFs

To construct MOFs-polymer structures, another strategy consists of directly coating polymers on the external surface of MOFs. Guo *et al.* first mixed the precursors of ZIF-8 with DOX by a one-pot method to obtain ZIF-8/DOX and then ZIF-8/DOX nanoparticles was coated with polydopamine (PDA) and functionalized with PEG and Mn^{2+}. Herein, ZIF-8 was selected considering its intrinsic pH-dependent stability, and PDA was used for photoacoustic imaging and photothermal therapy while Mn^{2+} cations imparted T1 MRI properties. The *in vivo* study confirmed their efficient therapeutic efficiency, a paradigm of imaging guided chemo-photothermal therapy.

Based on MIL-100(Fe), Zhang *et al.* prepared hybrid particles by coating curcumin-loaded MIL-100(Fe) NPs with PDA-modified HA and studied them for photoacoustic imaging-guided chemo-/ photothermal cancer therapy (**Figure 1.2.16**).[147] A high photothermal conversion ability was achieved in these hybrid particles through the introduction of both curcumin and PDA-HA. The coating of HA-PDA resulted in a tumor-targeting ability as well as improved the stability of the nanoMOF in the blood, resulting in a significant antitumor effect after intravenous injection into tumor-bearing mice.

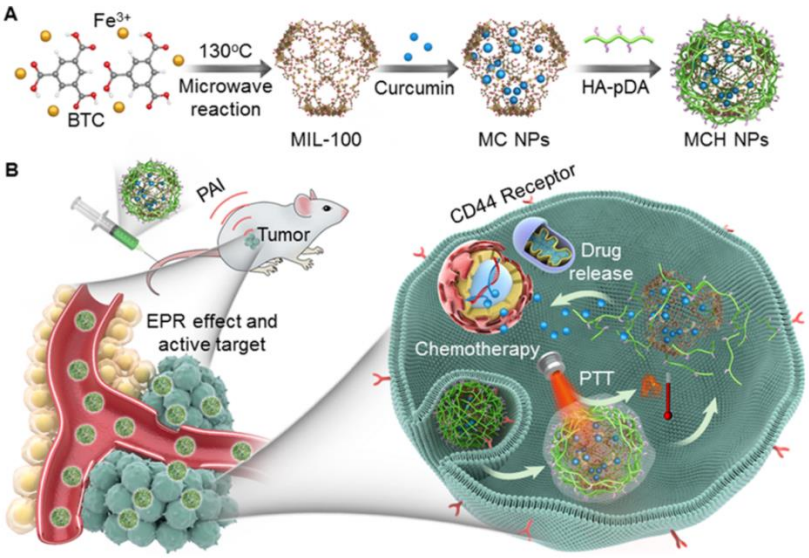

Figure 1.2.16 (A) The preparation of MCH NPs through the formation of MIL-100(Fe), curcumin loading and HA-PDA surface coating; (B) Under the guidance of PAI *in vivo*, efficient chemo-/photothermal combinational tumor therapy of MCH NPs was conducted *via* combinational enhanced penetration and retention (EPR) and tumor-targeting effects.[147]

Polyaniline (PAN) exhibits strong absorption coefficients, excellent photostability, but a poor water solubility. Wang *et al.* synthesized nanoscale polymer-MOF UiO-66@polyaniline with an appropriate particle size, good water-dispersibility, strong NIR absorbance, high photostability, and photothermal conversion efficiency suitable for PTT based cancer treatment *in vitro* and *in vivo* under guidance of photothermal imaging.[148] Due to its negatively charged surface, UiO-66 could adsorb aniline through electrostatic interaction that was further polymerized using ammonium persulfate as an oxidizing agent.

MOFs@polymer composites based on Zr dicarboxylate nanoMOFs, such as UiO-66@CyP (CyP means cyanine polymer), were used for NIR fluorescence imaging-guided PTT based cancer treatment by utilizing multi-component passerini reaction to realize the polymerization of NIR dye cyanine (Cy) on the surface of UiO-66 nanocrystals[149]. UiO-66 nanocrystals were used as templates for the polymerization, and the resulting UiO-66@CyP exhibited high PTT performance in cancer treatment. Note that the utilization of Zr for biomedical applications is highly questionable due to the exogeneous nature of Zr as well as the very low solubility in body fluids of the biodegradation products (Zr oxides/phosphates).

1.2.6.3.3 Janus MOFs-polymer nanocomposites

Multifunctional Janus nanoparticles (JNPs) with asymmetric compositions and independent functions have drawn extensive attention in biological fields. Wang's group prepared ZIF-8/polydopamine JNPs with hollow structure (H-ZIF-8/PDA JNPs) through a mild synthesis strategy.[150] After functionalization on PDA sides with a β-cyclodextrin (CDs) derivative, the resulting composite was loaded with hydrophobic and hydrophilic drug molecules. Moreover, due to the existence of PDA, H-ZIF-8/PDA JNPs owned strong near-infrared (NIR) absorption and the platform displayed pH/NIR dual-responsive drug release behaviors, resulting in a promising inhibition of tumor growth. It should be noted that, apart from thermal imaging, no other thermal related imaging was studied and facile synthesis should always be privileged.

1.2.7 Challenges

So far many new hybrid nanoMOFs systems have been constructed and have demonstrated, in most cases *in vitro*, a potential benefit that combines the DDS properties of the nanoMOFs and the imaging or stimuli-responsive behavior of the functional nanoparticles (organic or inorganic). However, when dealing with biomedical applications, this is necessary to consider the potential toxic effects of the system in play. In the case of such nanoMOFs hybrid systems, one should ideally demonstrate the biocompatibility, biodegradability and lack of accumulation into the body of the nanoparticles such as done previously with the bare porous iron(III) carboxylate materials.[26] Before constructing theranostic probe, *in vitro* and *in vivo* toxicity experiments should be considered for each nanocarrier. Besides, these nanosystems shall ideally be produced following green, environmentally friendly and energy-efficient routes using water or not toxic organic solvents such as alcohols.[151-152] Another very important parameter is to control the physical and chemical properties of the nanoparticles such as the particle size that should be smaller than 200 nm with an excellent control of the size distribution. This is likely that most of hybrid nanoMOFs candidates considered so far for bioapplications fail to meet these demanding criteria.

In addition, the colloidal stability of the hybrid nanoMOFs in different biological media shall strongly affect the biodistribution and pharmacokinetics *in vivo*.[153] If a considerable effort has been devoted to surface modification[106, 154-156], such as conjugating targeting molecule, coating with PEG or polymer, the stability of these systems could be improved, leading to a longer blood circulation half-life, better drug delivery abilities and therapeutic efficiencies.

1.2.8 Conclusion and Perspectives

This chapter gives a detailed description on the recent developments of hybrid nanoMOFs concerning theranostics. MOFs themselves are promising candidates for drug delivery and a large series of hybrid nanoMOFs based composites have been produced that bear magnetic, fluorescent or thermal properties suitable for imaging-guided therapy. In a view of future MOFs clinical use, one shall now focus on the development of optimal nontoxic multifunctional stimuli-responsive nanoMOFs formulations with a suitable stability in body fluids.

References

1. Kelkar, S. S.; Reineke, T. M., Theranostics: Combining Imaging and Therapy. *Bioconjug Chem* **2011,** *22* (10), 1879-1903.
2. Janib, S. M.; Moses, A. S.; Mackay, J. A., Imaging and Drug Delivery using Theranostic Nanoparticles. *Adv Drug Deliv Rev* **2010,** *62* (11), 1052-1053.
3. Ryu, J. H.; Lee, S.; Son, S.; Kim, S. H.; Leary, J. F.; Choi, K.; Kwon, I. C., Theranostic Nanoparticles for Future Personalized Medicine. *J Control Release* **2014,** *190*, 477-484.
4. Rao, J.; Dragulescu-Andrasi, A.; Yao, H., Fluorescence Imaging *In Vivo*: Recent Advances. *Curr Opin Biotechnol* **2007,** *18* (1), 17-25.
5. Wahsner, J.; Gale, E. M.; Rodriguez-Rodriguez, A.; Caravan, P., Chemistry of MRI Contrast Agents: Current Challenges and New Frontiers. *Chem Rev* **2019,** *119* (2), 957-1057.
6. Caravan, P.; Ellison, J., J.; Mcmurry, T. J.; Lauffer, R. B., Gadolinium(III) Chelates as MRI Contrast Agents: Structure, Dynamics, and Applications. *Chem Rev* **1999,** *99*, 60.
7. Huang, K.; Zhang, Y.; Lin, J.; Huang, P., Nanomaterials for Photoacoustic Imaging in the Second Near-Infrared Window. *Biomater Sci* **2019,** *7* (2), 472-479.
8. Weber, J.; Beard, P. C.; Bohndiek, S. E., Contrast Agents for Molecular Photoacoustic Imaging. *Nat Methods* **2016,** *13* (8), 639-650.
9. Jaque, D.; Martinez Maestro, L.; Del Rosal, B.; Haro-Gonzalez, P.; Benayas, A.; Plaza, J. L.; Martin Rodriguez, E.; Garcia Sole, J., Nanoparticles for Photothermal Therapies. *Nanoscale* **2014,** *6* (16), 9494-530.
10. Tang, Z.; Liu, Y.; He, M.; Bu, W., Chemodynamic Therapy: Tumour Microenvironment-Mediated Fenton and Fenton-Like Reactions. *Angew Chem Int Ed* **2019,** *58* (4), 946-956.
11. Lucky, S. S.; Soo, K. C.; Zhang, Y., Nanoparticles in Photodynamic Therapy. *Chem Rev* **2015,** *115* (4), 1990-2042.
12. Rosenthal, I.; Sostaric, J. Z.; Riesz, P., Sonodynamic Therapy-a Review of the Synergistic Effects of Drugs and Ultrasound. *Ultrason Sonochem* **2004,** *11* (6), 349-363.
13. Yu, S.; Chen, Z.; Zeng, X.; Chen, X.; Gu, Z., Advances in Nanomedicine for Cancer Starvation Therapy. *Theranostics* **2019,** *9* (26), 8026-8047.
14. Wu, M. X.; Yang, Y. W., Metal-Organic Framework (MOF)-Based Drug/Cargo Delivery and Cancer Therapy. *Adv Mater* **2017,** *29* (23), 1606134.
15. Lu, K.; Aung, T.; Guo, N.; Weichselbaum, R.; Lin, W., Nanoscale Metal-Organic Frameworks for Therapeutic, Imaging, and Sensing Applications. *Adv Mater* **2018,** *30* (37), 1707634.
16. Wang, H.-S., Metal–Organic Frameworks for Biosensing and Bioimaging Applications. *Coord Chem Rev* **2017,** *349*, 139-155.
17. Horcajada, P.; Serre, C.; Vallet-Regí, M.; Sebban, M.; Taulelle, F.; Férey, G., Metal–Organic Frameworks as Efficient Materials for Drug Delivery. *Angew Chem Int Ed* **2006,** *118* (36), 6120-6124.
18. Cunha, D.; Ben Yahia, M.; Hall, S.; Miller, S. R.; Chevreau, H.; Elkaïm, E.; Maurin, G.; Horcajada, P.; Serre, C., Rationale of Drug Encapsulation and Release from Biocompatible Porous Metal–Organic Frameworks. *Chem Mater* **2013,** *25* (14), 2767-2776.
19. Simon-Yarza, T.; Mielcarek, A.; Couvreur, P.; Serre, C., Nanoparticles of Metal-Organic Frameworks: on the Road to *In Vivo* Efficacy in Biomedicine. *Adv Mater* **2018,** *30* (37), 1707365.
20. He, C.; Liu, D.; Lin, W., Nanomedicine Applications of Hybrid Nanomaterials Built from Metal-Ligand Coordination Bonds: Nanoscale Metal-Organic Frameworks and Nanoscale Coordination Polymers. *Chem Rev* **2015,** *115* (19), 11079-11108.
21. Horcajada, P.; Gref, R.; Baati, T.; Allan, P. K.; Maurin, G.; Couvreur, P.; Ferey, G.; Morris, R. E.; Serre, C., Metal-Organic Frameworks in Biomedicine. *Chem Rev* **2012,** *112* (2), 1232-1268.
22. Mckinlay, A. C.; Morris, R. E.; Horcajada, P.; Ferey, G.; Gref, R.; Couvreur, P.; Serre, C., Biomofs: Metal-Organic Frameworks for Biological and Medical Applications. *Angew Chem Int Ed* **2010,** *49* (36), 6260-6266.

23. Della Rocca, J.; Lin, W., Nanoscale Metal-Organic Frameworks: Magnetic Resonance Imaging Contrast Agents and Beyond. *Eur J Inorg Chem* **2010,** *2010* (24), 3725-3734.
24. Huxford, R. C.; Della Rocca, J.; Lin, W., Metal-Organic Frameworks as Potential Drug Carriers. *Curr Opin Chem Biol* **2010,** *14* (2), 262-268.
25. Della Rocca, J.; Liu, D.; Lin, W., Nanoscale Metal-Organic Frameworks for Biomedical Imaging And Drug Delivery. *Acc Chem Res* **2011,** *44* (10), 957-968.
26. Cai, W.; Chu, C. C.; Liu, G.; Wang, Y. X., Metal-Organic Framework-Based Nanomedicine Platforms for Drug Delivery and Molecular Imaging. *Small* **2015,** *11* (37), 4806-4822.
27. Giménez-Marqués, M.; Hidalgo, T.; Serre, C.; Horcajada, P., Nanostructured Metal–Organic Frameworks and Their Bio-Related Applications. *Coord Chem Rev* **2016,** *307*, 342-360.
28. Beg, S.; Rahman, M.; Jain, A.; Saini, S.; Midoux, P.; Pichon, C.; Ahmad, F. J.; Akhter, S., Nanoporous Metal Organic Frameworks As Hybrid Polymer-Metal Composites for Drug Delivery and Biomedical Applications. *Drug Discov Today* **2017,** *22* (4), 625-637.
29. Zhu, W.; Zhao, J.; Chen, Q.; Liu, Z., Nanoscale Metal-Organic Frameworks and Coordination Polymers as Theranostic Platforms for Cancer Treatment. *Coord Chem Rev* **2019,** *398*, 113009.
30. Karimzadeh, S.; Javanbakht, S.; Baradaran, B.; Shahbazi, M.-A.; Hashemzaei, M.; Mokhtarzadeh, A.; Santos, H. A., Synthesis and Therapeutic Potential of Stimuli-Responsive Metal-Organic Frameworks. *Chem Eng J* **2021,** *408*, 127233.
31. Oroojalian, F.; Karimzadeh, S.; Javanbakht, S.; Hejazi, M.; Baradaran, B.; Webster, T. J.; Mokhtarzadeh, A.; Varma, R. S.; Kesharwani, P.; Sahebkar, A., Current Trends in Stimuli-Responsive Nanotheranostics Based on Metal–Organic Frameworks for Cancer Therapy. *Mater Today* **2022,** *57*, 192-224.
32. Liu, W.; Pan, Y.; Xiao, W.; Xu, H.; Liu, D.; Ren, F.; Peng, X.; Liu, J., Recent Developments on Zinc(II) Metal-Organic Framework Nanocarriers for Physiological pH-Responsive Drug Delivery. *Medchemcomm* **2019,** *10* (12), 2038-2051.
33. Chen, X.; Tong, R.; Shi, Z.; Yang, B.; Liu, H.; Ding, S.; Wang, X.; Lei, Q.; Wu, J.; Fang, W., MOF Nanoparticles with Encapsulated Autophagy Inhibitor in Controlled Drug Delivery System for Antitumor. *ACS Appl Mater Interfaces* **2018,** *10* (3), 2328-2337.
34. Lv, Y.; Ding, D.; Zhuang, Y.; Feng, Y.; Shi, J.; Zhang, H.; Zhou, T. L.; Chen, H.; Xie, R. J., Chromium-Doped Zinc Gallogermanate@Zeolitic Imidazolate Framework-8: A Multifunctional Nanoplatform for Rechargeable *In Vivo* Persistent Luminescence Imaging and pH-Responsive Drug Release. *ACS Appl Mater Interfaces* **2018,** *11* (2), 1907-1916.
35. Zhang, H.; Jiang, W.; Liu, R.; Zhang, J.; Zhang, D.; Li, Z.; Luan, Y., Rational Design of Metal Organic Framework Nanocarrier-Based Codelivery System of Doxorubicin Hydrochloride/Verapamil Hydrochloride for Overcoming Multidrug Resistance with Efficient Targeted Cancer Therapy. *ACS Appl Mater Interfaces* **2017,** *9* (23), 19687-19697.
36. Wang, Y.; Yan, J.; Wen, N.; Xiong, H.; Cai, S.; He, Q.; Hu, Y.; Peng, D.; Liu, Z.; Liu, Y., Metal-Organic Frameworks for Stimuli-Responsive Drug Delivery. *Biomaterials* **2020,** *230*, 119619.
37. Ren, S. Z.; Zhu, D.; Zhu, X. H.; Wang, B.; Yang, Y. S.; Sun, W. X.; Wang, X. M.; Lv, P. C.; Wang, Z. C.; Zhu, H. L., Nanoscale Metal-Organic-Frameworks Coated by Biodegradable Organosilica for pH and Redox Dual Responsive Drug Release and High-Performance Anticancer Therapy. *ACS Appl Mater Interfaces* **2019,** *11*(23), 20678-20688.
38. Lei, B.; Wang, M.; Jiang, Z.; Qi, W.; Su, R.; He, Z., Constructing Redox-Responsive Metal-Organic Framework Nanocarriers for Anticancer Drug Delivery. *ACS Appl Mater Interfaces* **2018,** *10* (19), 16698-16706.
39. Cheng, G.; Li, W.; Ha, L.; Han, X.; Hao, S.; Wan, Y.; Wang, Z.; Dong, F.; Zou, X.; Mao, Y.; Zheng, S. Y., Self-Assembly of Extracellular Vesicle-Like Metal-Organic Framework Nanoparticles for Protection and Intracellular Delivery of Biofunctional Proteins. *J Am Chem Soc* **2018,** *140* (23), 7282-7291.
40. Cheng, H.; Jiang, X. Y.; Zheng, R. R.; Zuo, S. J.; Zhao, L. P.; Fan, G. L.; Xie, B. R.; Yu, X. Y.;

Li, S. Y.; Zhang, X. Z., A Biomimetic Cascade Nanoreactor for Tumor Targeted Starvation Therapy-Amplified Chemotherapy. *Biomaterials* **2019,** *195*, 75-85.
41. Feng, J.; Xu, Z.; Dong, P.; Yu, W.; Liu, F.; Jiang, Q.; Wang, F.; Liu, X., Stimuli-Responsive Multifunctional Metal–Organic Framework Nanoparticles for Enhanced Chemo-Photothermal Therapy. *J Mater Chem B* **2019,** *7* (6), 994-1004.
42. Ricco, R.; Malfatti, L.; Takahashi, M.; Hill, A. J.; Falcaro, P., Applications of Magnetic Metal–Organic Framework Composites. *J Mater Chem A* **2013,** *1* (42), 13033.
43. Falcaro, P.; Ricco, R.; Yazdi, A.; Imaz, I.; Furukawa, S.; Maspoch, D.; Ameloot, R.; Evans, J. D.; Doonan, C. J., Application of Metal and Metal Oxide Nanoparticles@MOFs. *Coord Chem Rev* **2016,** *307*, 237-254.
44. Rowe, M. D.; Thamm, D. H.; Kraft, S. L.; Boyes, S. G., Polymer-Modified Gadolinium Metal-Organic Framework Nanoparticles Used as Multifunctional Nanomedicines for the Targeted Imaging and Treatment of Cancer. *Biomacromolecules* **2009,** *10* (4), 983-993.
45. Zhang, H.; Shang, Y.; Li, Y. H.; Sun, S. K.; Yin, X. B., Smart Metal-Organic Frameworks-Based Nanoplatforms for Imaging-Guided Precise Chemotherapy. *ACS Appl Mater Interfaces* **2019,** *11*, 1886−1895.
46. Chen, Y.; Liu, W.; Shang, Y.; Cao, P.; Cui, J.; Li, Z.; Yin, X.; Li, Y., Folic Acid-Nanoscale Gadolinium-Porphyrin Metal-Organic Frameworks: Fluorescence and Magnetic Resonance Dual-Modality Imaging and Photodynamic Therapy In Hepatocellular Carcinoma. *Int J Nanomedicine* **2019,** *14*, 57-74.
47. Xia, J.; Xue, Y.; Lei, B.; Xu, L.; Sun, M.; Li, N.; Zhao, H.; Wang, M.; Luo, M.; Zhang, C.; Huang, B.; Du, Y.; Yan, C. H., Multimodal Channel Cancer Chemotherapy by 2D Functional Gadolinium Metal-Organic Framework. *Natl Sci Rev* **2021,** *8* (7), Nwaa221.
48. Li, H.; Zeng, Y.; Zhang, H.; Gu, Z.; Gong, Q.; Luo, K., Functional Gadolinium-Based Nanoscale Systems for Cancer Theranostics. *J Control Release* **2021,** *329*, 482-512.
49. Horcajada, P.; Chalati, T.; Serre, C.; Gillet, B.; Sebrie, C.; Baati, T.; Eubank, J. F.; Heurtaux, D.; Clayette, P.; Kreuz, C.; Chang, J. S.; Hwang, Y. K.; Marsaud, V.; Bories, P. N.; Cynober, L.; Gil, S.; Ferey, G.; Couvreur, P.; Gref, R., Porous Metal-Organic-Framework Nanoscale Carriers as a Potential Platform for Drug Delivery and Imaging. *Nat Mater* **2010,** *9* (2), 172-178.
50. Taylor-Pashow, K. M.; Della Rocca, J.; Xie, Z.; Tran, S.; Lin, W., Postsynthetic Modifications of Iron-Carboxylate Nanoscale Metal-Organic Frameworks for Imaging and Drug Delivery. *J Am Chem Soc* **2009,** *131* (40), 14261-14263.
51. Wang, X. G.; Dong, Z. Y.; Cheng, H.; Wan, S. S.; Chen, W. H.; Zou, M. Z.; Huo, J. W.; Deng, H. X.; Zhang, X. Z., A Multifunctional Metal-Organic Framework Based Tumor Targeting Drug Delivery System for Cancer Therapy. *Nanoscale* **2015,** *7* (38), 16061-16070.
52. Liu, D.; He, C.; Poon, C.; Lin, W., Theranostic Nanoscale Coordination Polymers for Magnetic Resonance Imaging and Bisphosphonate Delivery. *J Mater Chem B* **2014,** *2* (46), 8249-8255.
53. Pan, Y. B.; Wang, S.; He, X.; Tang, W.; Wang, J.; Shao, A.; Zhang, J., A Combination of Glioma *In Vivo* Imaging and *In Vivo* Drug Delivery by Metal-Organic Framework Based Composite Nanoparticles. *J Mater Chem B* **2019,** *7* (48), 7683-7689.
54. Zhang, H.; Tian, X. T.; Shang, Y.; Li, Y. H.; Yin, X. B., Theranostic Mn-Porphyrin Metal-Organic Frameworks for Magnetic Resonance Imaging-Guided Nitric Oxide and Photothermal Synergistic Therapy. *ACS Appl Mater Interfaces* **2018,** *10* (34), 28390-28398.
55. Zhang, H.; Yin, X. B., Mixed-Ligand Metal-Organic Frameworks for All-in-One Theranostics With Controlled Drug Delivery and Enhanced Photodynamic Therapy. *ACS Appl Mater Interfaces* **2022,** *14* (23), 26528-26535.
56. Meilikhov, M.; Yusenko, K.; Esken, D.; Turner, S.; Van Tendeloo, G.; Fischer, R. A., Metals@MOFs - Loading MOFs with Metal Nanoparticles for Hybrid Functions. *Eur J Inorg Chem* **2010,** *2010* (24), 3701-3714.
57. Juan-Alcañiz, J.; Gascon, J.; Kapteijn, F., Metal–Organic Frameworks as Scaffolds for the

Encapsulation of Active Species: State of the Art and Future Perspectives. *J Mater Chem* **2012,** *22* (20), 10102.
58. Moon, H. R.; Lim, D. W.; Suh, M. P., Fabrication of Metal Nanoparticles in Metal-Organic Frameworks. *Chem Soc Rev* **2013,** *42* (4), 1807-1824.
59. Rösler, C.; Fischer, R. A., Metal–Organic Frameworks as Hosts for Nanoparticles. *Crystengcomm* **2015,** *17* (2), 199-217.
60. Wang, D.; Zhou, J.; Chen, R.; Shi, R.; Zhao, G.; Xia, G.; Li, R.; Liu, Z.; Tian, J.; Wang, H.; Guo, Z.; Wang, H.; Chen, Q., Controllable Synthesis of Dual-MOFs Nanostructures for pH-Responsive Artemisinin Delivery, Magnetic Resonance and Optical Dual-Model Imaging-Guided Chemo/Photothermal Combinational Cancer Therapy. *Biomaterials* **2016,** *100*, 27-40.
61. Wang, D.; Zhou, J.; Shi, R.; Wu, H.; Chen, R.; Duan, B.; Xia, G.; Xu, P.; Wang, H.; Zhou, S.; Wang, C.; Wang, H.; Guo, Z.; Chen, Q., Biodegradable Core-Shell Dual-Metal-Organic-Frameworks Nanotheranostic Agent for Multiple Imaging Guided Combination Cancer Therapy. *Theranostics* **2017,** *7* (18), 4605-4617.
62. Ray Chowdhuri, A.; Bhattacharya, D.; Sahu, S. K., Magnetic Nanoscale Metal Organic Frameworks for Potential Targeted Anticancer Drug Delivery, Imaging and as an MRI Contrast Agent. *Dalton Trans* **2016,** *45* (7), 2963-2973.
63. Zhao, H. X.; Zou, Q.; Sun, S. K.; Yu, C.; Zhang, X.; Li, R. J.; Fu, Y. Y., Theranostic Metal-Organic Framework Core-Shell Composites for Magnetic Resonance Imaging and Drug Delivery. *Chem Sci* **2016,** *7* (8), 5294-5301.
64. Nejadshafiee, V.; Naeimi, H.; Goliaei, B.; Bigdeli, B.; Sadighi, A.; Dehghani, S.; Lotfabadi, A.; Hosseini, M.; Nezamtaheri, M. S.; Amanlou, M.; Sharifzadeh, M.; Khoobi, M., Magnetic Bio-Metal-Organic Framework Nanocomposites Decorated with Folic Acid Conjugated Chitosan as a Promising Biocompatible Targeted Theranostic System for Cancer Treatment. *Mater Sci Eng C Mater Biol Appl* **2019,** *99*, 805-815.
65. Wang, D.; Zhou, J.; Chen, R.; Shi, R.; Xia, G.; Zhou, S.; Liu, Z.; Zhang, N.; Wang, H.; Guo, Z.; Chen, Q., Magnetically Guided Delivery of DHA And Fe Ions for Enhanced Cancer Therapy Based on pH-Responsive Degradation of DHA-Loaded Fe_3O_4@C@MIL-100(Fe) Nanoparticles. *Biomaterials* **2016,** *107*, 88-101.
66. Sene, S.; Marcos-Almaraz, M. T.; Menguy, N.; Scola, J.; Volatron, J.; Rouland, R.; Grenèche, J.-M.; Miraux, S.; Menet, C.; Guillou, N.; Gazeau, F.; Serre, C.; Horcajada, P.; Steunou, N., Maghemite-Nanomil-100(Fe) Bimodal Nanovector as a Platform for Image-Guided Therapy. *Chem* **2017,** *3* (2), 303-322.
67. Liu, Y.; Gong, C. S.; Lin, L.; Zhou, Z.; Liu, Y.; Yang, Z.; Shen, Z.; Yu, G.; Wang, Z.; Wang, S.; Ma, Y.; Fan, W.; He, L.; Niu, G.; Dai, Y.; Chen, X., Core-Shell Metal-Organic Frameworks with Fluorescence Switch to Trigger an Enhanced Photodynamic Therapy. *Theranostics* **2019,** *9* (10), 2791-2799.
68. Tian, X. T.; Cao, P. P.; Zhang, H.; Li, Y. H.; Yin, X. B., GSH-Activated MRI-Guided Enhanced Photodynamic- and Chemo-Combination Therapy with a MnO_2-Coated Porphyrin Metal Organic Framework. *Chem Commun* **2019,** *55* (44), 6241-6244.
69. Wang, Z.; Liu, B.; Sun, Q.; Dong, S.; Kuang, Y.; Dong, Y.; He, F.; Gai, S.; Yang, P., Fusiform-Like Copper(II)-Based Metal-Organic Framework through Relief Hypoxia and GSH-Depletion Co-Enhanced Starvation and Chemodynamic Synergetic Cancer Therapy. *ACS Appl Mater Interfaces* **2020,** *12* (15), 17254-17267.
70. Wang, Y. M.; Xu, Y.; Zhang, X.; Cui, Y.; Liang, Q.; Liu, C.; Wang, X.; Wu, S.; Yang, R., Single Nano-Sized Metal-Organic Framework for Bio-Nanoarchitectonics with *In Vivo* Fluorescence Imaging and Chemo-Photodynamic Therapy. *Nanomaterials* **2022,** *12* (2), 287.
71. Cai, W.; Gao, H.; Chu, C.; Wang, X.; Wang, J.; Zhang, P.; Lin, G.; Li, W.; Liu, G.; Chen, X., Engineering Phototheranostic Nanoscale Metal-Organic Frameworks for Multimodal Imaging-Guided Cancer Therapy. *ACS Appl Mater Interfaces* **2017,** *9* (3), 2040-2051.

72. Mao, D.; Hu, F.; Kenry; Ji, S.; Wu, W.; Ding, D.; Kong, D.; Liu, B., Metal-Organic-Framework-Assisted *In Vivo* Bacterial Metabolic Labeling and Precise Antibacterial Therapy. *Adv Mater* **2018,** *30* (18), 1706831.
73. Li, Y.; Xu, N.; Zhou, J.; Zhu, W.; Li, L.; Dong, M.; Yu, H.; Wang, L.; Liu, W.; Xie, Z., Facile Synthesis of a Metal-Organic Framework Nanocarrier for NIR Imaging-Guided Photothermal Therapy. *Biomater Sci* **2018,** *6* (11), 2918-2924.
74. Yang, P.; Men, Y.; Tian, Y.; Cao, Y.; Zhang, L.; Yao, X.; Yang, W., Metal-Organic Framework Nanoparticles with Near-Infrared Dye for Multimodal Imaging and Guided Phototherapy. *ACS Appl Mater Interfaces* **2019,** *11* (12), 11209-11219.
75. Cai, X.; Liu, B.; Pang, M.; Lin, J., Interfacially Synthesized Fe-Soc-MOF Nanoparticles Combined with ICG for Photothermal/Photodynamic Therapy. *Dalton Trans* **2018,** *47* (45), 16329-16336.
76. Gao, X.; Zhai, M.; Guan, W.; Liu, J.; Liu, Z.; Damirin, A., Controllable Synthesis of a Smart Multifunctional Nanoscale Metal-Organic Framework for Magnetic Resonance/Optical Imaging and Targeted Drug Delivery. *ACS Appl Mater Interfaces* **2017,** *9* (4), 3455-3462.
77. Zheng, X. T.; Ananthanarayanan, A.; Luo, K. Q.; Chen, P., Glowing Graphene Quantum Dots and Carbon Dots: Properties, Syntheses, and Biological Applications. *Small* **2015,** *11* (14), 1620-1636.
78. Li, B.; Suo, T.; Xie, S.; Xia, A.; Ma, Y.-j.; Huang, H.; Zhang, X.; Hu, Q., Rational design, synthesis, and applications of carbon dots@metal–organic frameworks (CD@MOF) based sensors. *TrAC Trends in Analytical Chemistry* **2021,** *135*, 116163
79. He, L.; Wang, T.; An, J.; Li, X.; Zhang, L.; Li, L.; Li, G.; Wu, X.; Su, Z.; Wang, C., Carbon Nanodots@Zeolitic Imidazolate Framework-8 Nanoparticles for Simultaneous pH-Responsive Drug Delivery and Fluorescence Imaging. *Crystengcomm* **2014,** *16* (16), 3259.
80. Xiang, Q.; Li, W.; Tan, Y.; Shi, J.; Dong, M.; Cheng, J.; Huang, J.; Zhang, W.; Gong, Y.; Yang, Q.; Yang, L.; Dong, H.; Zhang, X., Engineering of Upconversion Carbon Dots/Metal-Organic Frameworks "Peeled Pitaya-Like" Heterostructure for Mitochondria-Targeted Photodynamic Therapy. *Chem Eng J* **2022,** *444*, 136706.
81. Chen, D.; Yang, D.; Dougherty, C. A.; Lu, W.; Wu, H.; He, X.; Cai, T.; Van Dort, M. E.; Ross, B. D.; Hong, H., *In Vivo* Targeting and Positron Emission Tomography Imaging of Tumor with Intrinsically Radioactive Metal-Organic Frameworks Nanomaterials. *ACS Nano* **2017,** *11* (4), 4315-4327.
82. Wang, Z.; Chen, Z.; Zhang, Z.; Li, J.; Chen, K.; Liang, H.; Lv, L.; Chang, Y.; Liu, S.; Yang, W.; Yang, Z.; Yuan, H.; Meng, X.; Liu, T.; Wang, F.; Li, J.; Xing, G., Multifunctional High Boron Content MOFs Nano-Co-Crystals for Precise Boron Neutron Capture Therapy for Brain Glioma In Situ. *Nano Today* **2022,** *45*, 101558.
83. Duan, D.; Liu, H.; Xu, M.; Chen, M.; Han, Y.; Shi, Y.; Liu, Z., Size-Controlled Synthesis of Drug-Loaded Zeolitic Imidazolate Framework in Aqueous Solution and Size Effect on Their Cancer Theranostics *In Vivo*. *ACS Appl Mater Interfaces* **2018,** *10* (49), 42165-42174.
84. He, Z.; Huang, X.; Wang, C.; Li, X.; Liu, Y.; Zhou, Z.; Wang, S.; Zhang, F.; Wang, Z.; Jacobson, O.; Zhu, J. J.; Yu, G.; Dai, Y.; Chen, X., A Catalase-Like Metal-Organic Framework Nanohybrid for O_2 -Evolving Synergistic Chemoradiotherapy. *Angew Chem Int Ed* **2019,** *131* (26), 8844-8848.
85. Brandon, D.; Alazraki, A.; Halkar, R. K.; Alazraki, N. P., The Role Of Single-Photon Emission Computed Tomography and SPECT/Computed Tomography in Oncologic Imaging. *Semin Oncol* **2011,** *38* (1), 87-108.
86. Zhu, W.; Yang, Y.; Jin, Q.; Chao, Y.; Tian, L.; Liu, J.; Dong, Z.; Liu, Z., Two-Dimensional Metal-Organic-Framework as a Unique Theranostic Nano-Platform for Nuclear Imaging and Chemo-Photodynamic Cancer Therapy. *Nano Res* **2018,** *12* (6), 1307-1312.
87. Tao, Y.; Sun, Y.; Shi, K.; Pei, P.; Ge, F.; Yang, K.; Liu, T., Versatile Labeling of Multiple Radionuclides onto a Nanoscale Metal-Organic Framework for Tumor Imaging and Radioisotope Therapy. *Biomater Sci* **2021,** *9* (8), 2947-2954.

88. Liu, M.; Wang, L.; Zheng, X.; Liu, S.; Xie, Z., Hypoxia-Triggered Nanoscale Metal-Organic Frameworks for Enhanced Anticancer Activity. *ACS Appl Mater Interfaces* **2018,** *10* (29), 24638-24647.
89. Zheng, X.; Wang, L.; Liu, M.; Lei, P.; Liu, F.; Xie, Z., Nanoscale Mixed-Component Metal–Organic Frameworks with Photosensitizer Spatial-Arrangement-Dependent Photochemistry for Multimodal-Imaging-Guided Photothermal Therapy. *Chem Mater* **2018,** *30* (19), 6867-6876.
90. Su, L.; Wu, Q.; Tan, L.; Huang, Z.; Fu, C.; Ren, X.; Xia, N.; Chen, Z.; Ma, X.; Lan, X.; Zhang, Q.; Meng, X., High Biocompatible ZIF-8 Coated by ZrO2 for Chemo-Microwave Thermal Tumor Synergistic Therapy. *ACS Appl Mater Interfaces* **2019,** *11* (11), 10520-10531.
91. Pastorek, J.; Pastorekova, S., Hypoxia-Induced Carbonic Anhydrase IX as a Target for Cancer Therapy: From Biology to Clinical Use. *Semin Cancer Biol* **2015,** *31*, 52-64.
92. Ma, T.; Liu, Y.; Wu, Q.; Luo, L.; Cui, Y.; Wang, X.; Chen, X.; Tan, L.; Meng, X., Quercetin-Modified Metal-Organic Frameworks for Dual Sensitization of Radiotherapy in Tumor Tissues by Inhibiting the Carbonic Anhydrase IX. *ACS Nano* **2019,** *13* (4), 4209-4219.
93. Zhang, K.; Meng, X.; Cao, Y.; Yang, Z.; Dong, H.; Zhang, Y.; Lu, H.; Shi, Z.; Zhang, X., Metal-Organic Framework Nanoshuttle for Synergistic Photodynamic and Low-Temperature Photothermal Therapy. *Adv Funct Mater* **2018,** *28* (42), 1804634.
94. Guan, Q.; Li, Y. A.; Li, W. Y.; Dong, Y. B., Photodynamic Therapy Based on Nanoscale Metal-Organic Frameworks: from Material Design to Cancer Nanotherapeutics. *Chem Asian J* **2018,** *13* (21), 3122-3149.
95. Zhang, L.; Lei, J.; Ma, F.; Ling, P.; Liu, J.; Ju, H., A Porphyrin Photosensitized Metal-Organic Framework for Cancer Cell Apoptosis and Caspase Responsive Theranostics. *Cheml Commun* **2015,** *51* (54), 10831-10834.
96. Park, J.; Jiang, Q.; Feng, D.; Mao, L.; Zhou, H. C., Size-Controlled Synthesis of Porphyrinic Metal-Organic Framework and Functionalization for Targeted Photodynamic Therapy. *J Am Chem Soc* **2016,** *138* (10), 3518-3525.
97. Li, S. Y.; Cheng, H.; Qiu, W. X.; Zhang, L.; Wan, S. S.; Zeng, J. Y.; Zhang, X. Z., Cancer Cell Membrane-Coated Biomimetic Platform for Tumor Targeted Photodynamic Therapy and Hypoxia-Amplified Bioreductive Therapy. *Biomaterials* **2017,** *142*, 149-161.
98. Li, S. Y.; Xie, B. R.; Cheng, H.; Li, C. X.; Zhang, M. K.; Qiu, W. X.; Liu, W. L.; Wang, X. S.; Zhang, X. Z., A Biomimetic Theranostic O_2-Meter for Cancer Targeted Photodynamic Therapy and Phosphorescence Imaging. *Biomaterials* **2018,** *151*, 1-12.
99. Zhang, K.; Yu, Z.; Meng, X.; Zhao, W.; Shi, Z.; Yang, Z.; Dong, H.; Zhang, X., A Bacteriochlorin-Based Metal–Organic Framework Nanosheet Superoxide Radical Generator for Photoacoustic Imaging-Guided Highly Efficient Photodynamic Therapy. *Adv Sci* **2019**, 1900530.
100. Wang, S.; Tian, R.; Zhang, X.; Cheng, G.; Yu, P.; Chang, J.; Chen, X., Beyond Photo: Xdynamic Therapies in Fighting Cancer. *Adv Mater* **2021,** *33* (25), 2007488.
101. Fu, C.; Zhou, H.; Tan, L.; Huang, Z.; Wu, Q.; Ren, X.; Ren, J.; Meng, X., Microwave-Activated Mn-Doped Zirconium Metal-Organic Framework Nanocubes for Highly Effective Combination of Microwave Dynamic and Thermal Therapies Against Cancer. *ACS Nano* **2018,** *12* (3), 2201-2210.
102. Poon, W.; Zhang, Y. N.; Ouyang, B.; Kingston, B. R.; Wu, J. L. Y.; Wilhelm, S.; Chan, W. C. W., Elimination Pathways of Nanoparticles. *ACS Nano* **2019,** *13* (5), 5785-5798.
103. Dhakshinamoorthy, A.; Navalon, S.; Asiri, A. M.; Garcia, H., Gold-Nanoparticle-Decorated Metal-Organic Frameworks for Anticancer Therapy. *Chemmedchem* **2020,** *15* (23), 2236-2256.
104. Zheng, G.; Pastoriza-Santos, I.; Pérez-Juste, J.; Liz-Marzán, L. M., Plasmonic Metal-Organic Frameworks. *Smartmat* **2021,** *2* (4), 446-465.
105. Koh, C. S. L.; Sim, H. Y. F.; Leong, S. X.; Boong, S. K.; Chong, C.; Ling, X. Y., Plasmonic Nanoparticle-Metal–Organic Framework (NP–MOF) Nanohybrid Platforms for Emerging Plasmonic Applications. *ACS Mater Lett* **2021,** *3* (5), 557-573.
106. Gimenez-Marques, M.; Bellido, E.; Berthelot, T.; Simon-Yarza, T.; Hidalgo, T.; Simon-

Vazquez, R.; Gonzalez-Fernandez, A.; Avila, J.; Asensio, M. C.; Gref, R.; Couvreur, P.; Serre, C.; Horcajada, P., Graftfast Surface Engineering to Improve MOF Nanoparticles Furtiveness. *Small* **2018,** *14* (40), 1801900.
107. Zhang, H.; Hao, C.; Qu, A.; Sun, M.; Xu, L.; Xu, C.; Kuang, H., Heterostructures of MOFs and Nanorods for Multimodal Imaging. *Adv Funct Mater* **2018,** *28* (48), 1805320.
108. Zhang, H.; Zhang, Q.; Liu, C.; Han, B., Preparation of One Dimensional Nanorod/Metal Organic Framework Janus Nanoplatform *Via* Side-Specific Growth for Synergistic Cancer Therapy. *Biomaters Sci* **2019,** *7* (4), 1696-1704.
109. Zeng, J.-Y.; Zhang, M.-K.; Peng, M.-Y.; Gong, D.; Zhang, X.-Z., Porphyrinic Metal-Organic Frameworks Coated Gold Nanorods as a Versatile Nanoplatform for Combined Photodynamic/Photothermal/Chemotherapy of Tumor. *Adv Funct Mater* **2018,** *28* (8), 1705451.
110. Chien, W. C.; Cheng, P. H.; Cheng, X. J.; Chuang, C. C.; Huang, Y. T.; T, S. A.; Liu, C. H.; Lu, Y. J.; Wu, K. C., MCP-1-Functionalized, Core-Shell Gold Nanorod@Iron-Based Metal-Organic Framework (MCP-1/GNR@MIL-100(Fe)) for Photothermal Therapy. *ACS Appl Mater Interfaces* **2021,** *13* (44), 52092-52105.
111. Guo, H.; Yi, S.; Feng, K.; Xia, Y.; Qu, X.; Wan, F.; Chen, L.; Zhang, C., In Situ Formation of Metal Organic Framework onto Gold Nanorods/Mesoporous Silica with Functional Integration for Targeted Theranostics. *Chem Eng J* **2021,** *403*, 126432.
112. He, J.; Dong, J.; Hu, Y.; Li, G.; Hu, Y., Design of Raman Tag-Bridged Core-Shell Au@$Cu_3(BTC)_2$ Nanoparticles for Raman Imaging and Synergistic Chemo-Photothermal Therapy. *Nanoscale* **2019,** *11* (13), 6089-6100.
113. Wang, Z.; Yu, W.; Yu, N.; Li, X.; Feng, Y.; Geng, P.; Wen, M.; Li, M.; Zhang, H.; Chen, Z., Construction Of Cus@Fe-MOF Nanoplatforms for MRI-Guided Synergistic Photothermal-Chemo Therapy of Tumors. *Chem Eng J* **2020,** *400*, 125877.
114. Ma, Y.; Chen, L.; Li, X.; Hu, A.; Wang, H.; Zhou, H.; Tian, B.; Dong, J., Rationally Integrating Peptide-Induced Targeting and Multimodal Therapies in a Dual-Shell Theranostic Platform for Orthotopic Metastatic Spinal Tumors. *Biomaterials* **2021,** *275*, 120917.
115. Li, D.; Chen, Z.; Mei, X., Fluorescence Enhancement for Noble Metal Nanoclusters. *Adv Colloid Interface Sci* **2017,** *250*, 25-39.
116. Jiang, X.; Du, B.; Huang, Y.; Zheng, J., Ultrasmall Noble Metal Nanoparticles: Breakthroughs and Biomedical Implications. *Nano Today* **2018,** *21*, 106-125.
117. Kaur, N.; Aditya, R. N.; Singh, A.; Kuo, T. R., Biomedical Applications for Gold Nanoclusters: Recent Developments and Future Perspectives. *Nanoscale Res Lett* **2018,** *13* (1), 302.
118. Bai, X.; Xu, S.; Wang, L., Full-Range Ph Stable Au-Clusters in Nanogel for Confinement-Enhanced Emission and Improved Sulfide Sensing in Living Cells. *Anal Chem* **2018,** *90* (5), 3270-3275.
119. Li, Y.; Li, P.; Zhu, R.; Luo, C.; Li, H.; Hu, S.; Nie, Z.; Huang, Y.; Yao, S., Multifunctional Gold Nanoclusters-Based Nanosurface Energy Transfer Probe for Real-Time Monitoring of Cell Apoptosis and Self-Evaluating of Pro-Apoptotic Theranostics. *Anal Chem* **2016,** *88* (22), 11184-11192.
120. Wang, X.; Xia, J.; Wang, C.; Liu, L.; Zhu, S.; Feng, W.; Li, L., Preparation of Novel Fluorescent Nanocomposites Based on Au Nanoclusters and Their Application in Targeted Detection of Cancer Cells. *ACS Appl Mater Interfaces* **2017,** *9* (51), 44856-44863.
121. Zhang, C.; Li, C.; Liu, Y.; Zhang, J.; Bao, C.; Liang, S.; Wang, Q.; Yang, Y.; Fu, H.; Wang, K.; Cui, D., Gold Nanoclusters-Based Nanoprobes for Simultaneous Fluorescence Imaging and Targeted Photodynamic Therapy with Superior Penetration and Retention Behavior in Tumors. *Adv Functl Mater* **2015,** *25* (8), 1314-1325.
122. Katla, S. K.; Zhang, J.; Castro, E.; Bernal, R. A.; Li, X., Atomically Precise $Au_{25}(SG)_{18}$ Nanoclusters: Rapid Single-Step Synthesis and Application in Photothermal Therapy. *ACS Appl Mater Interfaces* **2018,** *10* (1), 75-82.
123. Miyata, S.; Miyaji, H.; Kawasaki, H.; Yamamoto, M.; Nishida, E.; Takita, H.; Akasaka, T.;

Ushijima, N.; Iwanaga, T.; Sugaya, T., Antimicrobial Photodynamic Activity and Cytocompatibility of $Au_{25}(Capt)_{18}$ Clusters Photoexcited by Blue LED Light Irradiation. *Int J Nanomedicine* **2017,** *12*, 2703-2716.
124. Zhang, X. D.; Chen, J.; Luo, Z.; Wu, D.; Shen, X.; Song, S. S.; Sun, Y. M.; Liu, P. X.; Zhao, J.; Huo, S.; Fan, S.; Fan, F.; Liang, X. J.; Xie, J., Enhanced Tumor Accumulation of Sub-2 nm Gold Nanoclusters for Cancer Radiation Therapy. *Adv Healthc Mater* **2014,** *3* (1), 133-141.
125. Yang, D.; Yang, G.; Gai, S.; He, F.; An, G.; Dai, Y.; Lv, R.; Yang, P., Au_{25} Cluster Functionalized Metal-Organic Nanostructures for Magnetically Targeted Photodynamic/Photothermal Therapy Triggered by Single Wavelength 808 nm Near-Infrared Light. *Nanoscale* **2015,** *7* (46), 19568-19578.
126. Bian, R.; Wang, T.; Zhang, L.; Li, L.; Wang, C., A Combination of Tri-Modal Cancer Imaging and *In Vivo* Drug Delivery by Metal-Organic Framework Based Composite Nanoparticles. *Biomater Sci* **2015,** *3* (9), 1270-1278.
127. Ma, X.; Ren, X.; Guo, X.; Fu, C.; Wu, Q.; Tan, L.; Li, H.; Zhang, W.; Chen, X.; Zhong, H.; Meng, X., Multifunctional Iron-Based Metal−Organic Framework as Biodegradable Nanozyme for Microwave Enhancing Dynamic Therapy. *Biomaterials* **2019**, 119223.
128. Zhang, L.; Liu, C.; Gao, Y.; Li, Z.; Xing, J.; Ren, W.; Zhang, L.; Li, A.; Lu, G.; Wu, A.; Zeng, L., ZD2-Engineered Gold Nanostar@Metal-Organic Framework Nanoprobes for T1 -Weighted Magnetic Resonance Imaging and Photothermal Therapy Specifically toward Triple-Negative Breast Cancer. *Adv Healthc Mater* **2018,** *7* (24), 1801144.
129. Li, R. T.; Zhu, Y. D.; Li, W. Y.; Hou, Y. K.; Zou, Y. M.; Zhao, Y. H.; Zou, Q.; Zhang, W. H.; Chen, J. X., Synergistic Photothermal-Photodynamic-Chemotherapy toward Breast Cancer Based on a Liposome-Coated Core-Shell AuNS@NMOFs Nanocomposite Encapsulated with Gambogic Acid. *J Nanobiotechnology* **2022,** *20* (1), 212.
130. Deng, X.; Liang, S.; Cai, X.; Huang, S.; Cheng, Z.; Shi, Y.; Pang, M.; Ma, P.; Lin, J., Yolk-Shell Structured Au Nanostar@Metal-Organic Framework for Synergistic Chemo-Photothermal Therapy in the Second Near-Infrared Window. *Nano Lett* **2019,** *19* (10), 6772-6780.
131. Liu, Q.; Wu, B.; Li, M.; Huang, Y.; Li, L., Heterostructures Made of Upconversion Nanoparticles and Metal-Organic Frameworks for Biomedical Applications. *Adv Sci* **2022,** *9* (3), 2103911.
132. Zhang, L.; Liu, M.; Fang, Z.; Ju, Q., Synthesis and Biomedical Application of Nanocomposites Integrating Metal-Organic Frameworks with Upconversion Nanoparticles. *Coord Chem Rev* **2022,** *468*, 214641.
133. Bao, W.; Liu, M.; Meng, J.; Liu, S.; Wang, S.; Jia, R.; Wang, Y.; Ma, G.; Wei, W.; Tian, Z., MOFs-Based Nanoagent Enables Dual Mitochondrial Damage in Synergistic Antitumor Therapy *Via* Oxidative Stress and Calcium Overload. *Nat Commun* **2021,** *12* (1), 6399.
134. Li, Z.; Qiao, X.; He, G.; Sun, X.; Feng, D.; Hu, L.; Xu, H.; Xu, H.-B.; Ma, S.; Tian, J., Core-Satellite Metal-Organic Framework@Upconversion Nanoparticle Superstructures *Via* Electrostatic Self-Assembly for Efficient Photodynamic Theranostics. *Nano Res* **2020,** *13* (12), 3377-3386.
135. He, L.; Brasino, M.; Mao, C.; Cho, S.; Park, W.; Goodwin, A. P.; Cha, J. N., DNA-Assembled Core-Satellite Upconverting-Metal-Organic Framework Nanoparticle Superstructures for Efficient Photodynamic Therapy. *Small* **2017,** *13* (24), 1700504.
136. Fu, D.-Y.; Liu, X.; Zheng, X.; Zhou, M.; Wang, W.; Su, G.; Liu, T.; Wang, L.; Xie, Z., Polymer-Metal-Organic Framework Hybrids for Bioimaging and Cancer Therapy. *Coord Chem Rev* **2022,** *456*, 214393.
137. Zhu, Y. D.; Chen, S. P.; Zhao, H.; Yang, Y.; Chen, X. Q.; Sun, J.; Fan, H. S.; Zhang, X. D., Ppy@MIL-100 Nanoparticles as a pH- and Near-IR-Irradiation-Responsive Drug Carrier for Simultaneous Photothermal Therapy and Chemotherapy of Cancer Cells. *ACS Appl Mater Interfaces* **2016,** *8* (50), 34209-34217.
138. Chen, X.; Zhang, M.; Li, S.; Li, L.; Zhang, L.; Wang, T.; Yu, M.; Mou, Z.; Wang, C., Facile Synthesis of Polypyrrole@Metal–Organic Framework Core–Shell Nanocomposites for Dual-Mode

Imaging and Synergistic Chemo-Photothermal Therapy of Cancer Cells. *J Mater Chem B* **2017,** *5* (9), 1772-1778.
139. Huang, J.; Li, N.; Zhang, C.; Meng, Z., Metal-Organic Framework as a Microreactor for In Situ Fabrication of Multifunctional Nanocomposites for Photothermal-Chemotherapy of Tumors *In Vivo*. *ACS Appl Mater Interfaces* **2018,** *10* (45), 38729-38738.
140. Cai, X.; Deng, X.; Xie, Z.; Shi, Y.; Pang, M.; Lin, J., Controllable Synthesis of Highly Monodispersed Nanoscale Fe-Soc-MOF and the Construction of Fe-Soc-MOF@Polypyrrole Core-Shell Nanohybrids for Cancer Therapy. *Chem Eng J* **2019,** *358*, 369-378.
141. Feng, J.; Yu, W.; Xu, Z.; Wang, F., An Intelligent ZIF-8-Gated Polydopamine Nanoplatform for *In Vivo* Cooperatively Enhanced Combination Phototherapy. *Chem Sci* **2020,** *11* (6), 1649-1656.
142. Cheng, K.; Liu, B.; Zhang, X.-S.; Zhang, R.-Y.; Zhang, F.; Ashraf, G.; Fan, G.-Q.; Tian, M.-Y.; Sun, X.; Yuan, J.; Zhao, Y.-D., Biomimetic Material Degradation for Synergistic Enhanced Therapy by Regulating Endogenous Energy Metabolism Imaging under Hypothermia. *Nat Commun* **2022,** *13* (1), 4567.
143. Cao, S.; Low, J.; Yu, J.; Jaroniec, M., Polymeric Photocatalysts Based on Graphitic Carbon Nitride. *Adv Mater* **2015,** *27* (13), 2150-2176.
144. Liao, G.; He, F.; Li, Q.; Zhong, L.; Zhao, R.; Che, H.; Gao, H.; Fang, B., Emerging Graphitic Carbon Nitride-Based Materials for Biomedical Applications. *Prog Mater Sci* **2020,** *112*, 100666.
145. Dong, Y.; Wang, Q.; Wu, H.; Chen, Y.; Lu, C. H.; Chi, Y.; Yang, H. H., Graphitic Carbon Nitride Materials: Sensing, Imaging and Therapy. *Small* **2016,** *12* (39), 5376-5393.
146. Chen, R.; Zhang, J.; Wang, Y.; Chen, X.; Zapien, J. A.; Lee, C. S., Graphitic Carbon Nitride Nanosheet@Metal-Organic Framework Core-Shell Nanoparticles for Photo-Chemo Combination Therapy. *Nanoscale* **2015,** *7* (41), 17299-17305.
147. Zhang, Y.; Wang, L.; Liu, L.; Lin, L.; Liu, F.; Xie, Z.; Tian, H.; Chen, X., Engineering Metal-Organic Frameworks for Photoacoustic Imaging-Guided Chemo-/Photothermal Combinational Tumor Therapy. *ACS Appl Mater Interfaces* **2018,** *10* (48), 41035-41045.
148. Wang, W.; Wang, L.; Li, Y.; Liu, S.; Xie, Z.; Jing, X., Nanoscale Polymer Metal-Organic Framework Hybrids for Effective Photothermal Therapy of Colon Cancers. *Adv Mater* **2016,** *28* (42), 9320-9325.
149. Yan, L.; Chen, X.; Wang, Z.; Zhang, X.; Zhu, X.; Zhou, M.; Chen, W.; Huang, L.; Roy, V. A. L.; Yu, P. K. N.; Zhu, G.; Zhang, W., Size Controllable And Surface Tunable Zeolitic Imidazolate Framework-8-Poly(Acrylic Acid Sodium Salt) Nanocomposites for pH Responsive Drug Release and Enhanced *In Vivo* Cancer Treatment. *ACS Appl Mater Interfaces* **2017,** *9* (38), 32990-33000.
150. Li, S.; Zhang, L.; Liang, X.; Wang, T.; Chen, X.; Liu, C.; Li, L.; Wang, C., Tailored Synthesis of Hollow MOF/Polydopamine Janus Nanoparticles for Synergistic Multi-Drug Chemo-Photothermal Therapy. *Chem Eng J* **2019,** *378*, 122175.
151. García Márquez, A.; Demessence, A.; Platero-Prats, A. E.; Heurtaux, D.; Horcajada, P.; Serre, C.; Chang, J.-S.; Férey, G.; De La Peña-O'Shea, V. A.; Boissière, C.; Grosso, D.; Sanchez, C., Green Microwave Synthesis of MIL-100(Al, Cr, Fe) Nanoparticles for Thin-Film Elaboration. *Eur J Inorg Chem* **2012,** *2012* (32), 5165-5174.
152. Agostoni, V.; Horcajada, P.; Noiray, M.; Malanga, M.; Aykac, A.; Jicsinszky, L.; Vargas-Berenguel, A.; Semiramoth, N.; Daoud-Mahammed, S.; Nicolas, V.; Martineau, C.; Taulelle, F.; Vigneron, J.; Etcheberry, A.; Serre, C.; Gref, R., A "Green" Strategy to Construct Non-Covalent, Stable and Bioactive Coatings on Porous MOF Nanoparticles. *Sci Rep* **2015,** *5*, 7925.
153. Bellido, E.; Guillevic, M.; Hidalgo, T.; Santander-Ortega, M. J.; Serre, C.; Horcajada, P., Understanding the Colloidal Stability of the Mesoporous MIL-100(Fe) Nanoparticles in Physiological Media. *Langmuir* **2014,** *30* (20), 5911-5920.
154. Bellido, E.; Hidalgo, T.; Lozano, M. V.; Guillevic, M.; Simon-Vazquez, R.; Santander-Ortega, M. J.; Gonzalez-Fernandez, A.; Serre, C.; Alonso, M. J.; Horcajada, P., Heparin-Engineered Mesoporous Iron Metal-Organic Framework Nanoparticles: Toward Stealth Drug Nanocarriers. *Adv*

Healthc Mater **2015,** *4* (8), 1246-1257.
155. Márquez, A. G.; Hidalgo, T.; Lana, H.; Cunha, D.; Blanco-Prieto, M. J.; Álvarez-Lorenzo, C.; Boissière, C.; Sánchez, C.; Serre, C.; Horcajada, P., Biocompatible Polymer–Metal–Organic Framework Composite Patches for Cutaneous Administration of Cosmetic Molecules. *J Mater Chem B* **2016,** *4* (43), 7031-7040.
156. Zimpel, A.; Preiß, T.; Röder, R.; Engelke, H.; Ingrisch, M.; Peller, M.; Rädler, J. O.; Wagner, E.; Bein, T.; Lächelt, U.; Wuttke, S., Imparting Functionality to MOF Nanoparticles by External Surface Selective Covalent Attachment of Polymers. *Chem Mater* **2016,** *28* (10), 3318-3326.

1.3 Objectives

MOFs are porous materials, which is promising for drug delivery due to their high drug loading and stimuli-responsive release. However, one cannot simply conclude that MOFs are better nanocarriers than other drug carriers, because the loading capacity is not the sole criterion; one shall take into account many other parameters such as synthesis route, stability, reproducibility, toxicity and biological efficacy. Importantly, the versatility and tunability of MOFs enable their assembly with other materials such as inorganic particles and polymers, leading to nanocarriers for theranostics. During the last five years, theranostic MOFs have achieved to date huge progresses, especially most of them were exploited for cancer treatment in terms of biomedical applications. The general criterion of an ideal MOF nanocarrier includes 1) low toxicity, 2) small size, 3) biodegradation, 4) "green" synthesis, 5) sufficient materials characterizations, etc. However, most works are not able to address these issues currently.

In terms of clinical applications, the prerequisite is to use a nontoxic nanocarrier, and endogenous metals (*i.e.*, Fe, Ca and Zn) based MOFs are first class candidates. Especially, mesoporous Fe MOFs (*i.e.*, MIL-100(Fe)) are of interest due to their favorable properties. As for synthesis, a lot of literatures relied on multiple-step reaction routines, toxic solvents or strict rection conditions, which would hamper possible scaleup or clinical transfer. "Green" synthesis at room temperature is thus highly desired. Actually, the synthesis of ZIF-8 at room temperature has been widely studied for drug or biomacromolecule delivery, but as for MIL-100(Fe), room temperature synthesis strategy is more challengeable and rarely reported before. Until recent years, our group has successfully synthesized MIL-100(Fe) and other MOFs in aqueous solution at room temperature. Moreover, theranostic MOFs should also be biodegradable, facilitating the elimination from the body to avoid long term toxicity. Also, the small particle size of MOFs is advantageous for a long blood circulation time to reach the target, realizing an efficient drug delivery. Alternatively, the degraded products could be assimilated again by the body. In many papers of MOFs for bioapplications, lack of materials characterizations is a general drawback and authors always named their nanocomposites as MOFs directly without systematic physicochemical characterizations. Actually, even using the same reactants under the same temperature, the obtained products could be different. For example, some "so-called" MIL-100(Fe) MOFs were even nonporous or amorphous, just Fe/BTC coordination complexes. Concerning the design of theranostic MOFs, it is important to consider all of these factors.

As demonstrated in the literature, there is a close relationship between inflammation and cancer. However, in terms of inflammatory disease therapy, MOFs are still at their initial stage according to

the first part of this introduction. In this thesis, the aim is to achieve these goals, namely constructing new theranostic MOFs in a mild reaction condition for the treatment of inflammatory disease. For the treatment of inflammatory disease such as rheumatoid arthritis, we have considered clinical drugs such as methotrexate and dexamethasone as well as MIL-100(Fe) NPs due to its high drug loading and low toxicity were considered. While bare Fe-MOFs themselves are not a good contrast agent for MRI, thermal-related imaging, etc, ultrasmall superparamagnetic iron oxide and atomically precise gold clusters were introduced as contrast agents for image guided therapy to monitor the drug delivery process or biodistribution in real time. The role of inorganic nanoparticles is not limited to imaging, their catalase or superoxide dismutase-like activity would be helpful in the treatment. Furthermore, guided by “green synthesis”, an *in situ* room temperature synthesis is proposed to construct different biocompatible NPs@MOFs for theranostics in the thesis.

Chapter 2

This chapter is adapted to the following manuscript:

Hierarchical superparamagnetic MOFs nanovectors as novel theranostic anti-inflammatory nanomedicine

(In Submission)

Heng Zhao et al.

Table of Contents

2.1 Contributions to this research

In this project, the aim is to develop multifunctional magnetic MOFs for magnetic resonance imaging (MRI), inflammatory diseases therapy and cancer therapy. The project started at Université de Versailles St Quentin en Yvelines. Dr. Saad Sene performed the synthesis of hierarchical USPIO@MIL nano-object combining MIL-100(Fe) and ultra-small particles of superparamagnetic iron oxide. In the beginning of my PhD study, I repeated the synthesis and then I characterized the synthesized materials by using many different techniques, such as PXRD, N_2 sorption isotherms, TEM, DLS, TGA, UV-Vis and FT-IR. Dr. Nathalie Guillou performed PXRD patterns (Rietveld refinement) measurement. Prof. Nicolas Menguy performed HRTEM measurements. Dris Ihiawakrim and Prof. Ovidiu Ersen performed electron tomography analysis. Dr. Jean-Marc Grenèche performed ^{57}Fe Mössbauer spectrometry. Dr. Joseph Scola measured magnetization curve and magnetic moments. Then, I studied the colloidal stability and chemical stability of USPIO@MIL in physiological media by DLS and TEM, respectively. Dr Xiangzhen Xu at ESPCI trained me for TEM measurement. In terms of drug delivery, Dr. Angelika Maria Mielcarek performed the preliminary study of loading methotrexate (MTX) by MIL-100(Fe). Afterwards, I studied the drug loading and release of MTX and doxorubicin (Dox) by HPLC and UV-Vis systematically. Bernard Goetz performed ICP-MS measurements. Concerning cell experiments, I investigated the cell cytotoxicity, cellular internalization by confocal microscopy, pro-inflammatory cytokines expression by Elisa kit based on RAW 264.7 cells. Dr. Simona Mura (Université Paris-Saclay) gave useful suggestions for pro-inflammatory cytokines evaluation. Dr. Christine Péchoux performed Bio-TEM to visualize the internalization and degradation process of USPIO@MIL NPs and the test was proposed by Prof. Florence Gazeau and Dr. Florent Carn. Meanwhile, I studied the cell cytotoxicity, cellular internalization by confocal microscopy and anticancer therapy on Hela cells. Dr. Sylvain Miraux performed *in vivo* MRI. Subsequently, I collected and discussed the results with my supervisors, colleagues or collaborators. Finally, based on these aforementioned experimental data, I integrated all the Figures together and wrote the first manuscript draft, followed by several times of revision of my supervisors and collaborators.

Hierarchical superparamagnetic MOFs nanovectors as novel theranostic anti-inflammatory nanomedicine

Heng Zhao,[†] Saad Sene,[‡] Angelika M. Mielcarek,[†] Sylvain Miraux,[§] Nicolas Menguy,[∥] Dris Ihiawakrim,[⊥] Ovidiu Ersen,[⊥] Christine Péchoux,[#] Nathalie Guillou,[‡] Joseph Scola,[▽] Jean-Marc Grenèche,[○] Farid Nouar,[†] Simona Mura,[¶] Florent Carn,[□] Florence Gazeau,[□] Eddy Dumas,[‡] Christian Serre,[,†] and Nathalie Steunou*[,†,‡]*

[†]Institut des Matériaux Poreux de Paris, ENS, ESPCI Paris, CNRS, PSL university, Paris, France.

[‡]Institut Lavoisier de Versailles, UMR CNRS 8180, Université de Versailles St Quentin en Yvelines, Université Paris Saclay, Versailles, France.

[§]Centre de Résonance Magnétique des Systèmes Biologiques, UMR5536, CNRS/Univ. Bordeaux 33076 Bordeaux, France.

[∥]Sorbonne Université, UMR CNRS 7590, MNHN, IRD, Institut de Minéralogie, de Physique des Matériaux et de Cosmochimie, IMPMC, 75005 Paris, France.

[⊥]Institut de Physique et Chimie des Matériaux de Strasbourg (IPCMS) UMR 7504 CNRS – Université de Strasbourg, 23 rue du Loess 67034 Strasbourg Cedex 2, France.

[#]Université Paris-Saclay, INRAE, AgroParisTech, GABI, 78350, Jouy-en-Josas, France.

[▽]Groupe d'Etudes de la Matière Condensée, UMR CNRS 8635, Université de Versailles St Quentin en Yvelines, Université Paris Saclay 78035 Versailles, France.

[○]Institut des Molécules et des Matériaux du Mans, UMR CNRS 6283, Université du Maine, 72085 Le Mans, France.

[¶]Institut Galien Paris-Saclay, UMR 8612, CNRS, Université Paris-Saclay, Faculté de Pharmacie, 5 rue Jean-Baptiste Clément, F92296 Châtenay-Malabry cedex, France.

[□]Laboratoire Matière et Systèmes Complexes (MSC), UMR CNRS 7057, Université de Paris, 75013 Paris, France.

*Corresponding Authors, E-mail: christian.serre@ens.fr (Christian Serre); E-mail: nathalie.steunou@ens.psl.eu (Nathalie Steunou)

2.2 Abstract

Among a plethora of drug nanocarriers, biocompatible nanoscale Metal Organic Frameworks (nanoMOFs) with large surface area and amphiphilic internal microenvironment have emerged as promising drug delivery platforms, mainly for cancer therapy. However, their application in biomedicine still suffers from shortcomings such as a limited chemical and/or colloidal stability and/or toxicity. Here, we report the design of a hierarchically porous nano-object (denoted as USPIO@MIL) combining a benchmark nanoMOF, (*that is*, the MIL-100(Fe)), and ultra-small particles of superparamagnetic iron oxide, (*that is*, maghemite), that is synthesized through a one-pot, cost-effective and environmentally friendly protocol. The synergistic coupling of the physico-chemical and functional properties of both nanoparticles confer to these nano-objects valuable features such as high colloidal stability, biodegradability, low toxicity, high drug loading capacity as well as stimuli-responsive drug release and superparamagnetic properties. This bimodal MIL-100(Fe)/maghemite nanocarrier once loaded with anti-tumoral and anti-inflammatory drugs (doxorubicin or methotrexate), leads to high anti-inflammatory and anti-tumoral activities. In addition, USPIO@MIL nano-object presents excellent relaxometric properties and its applicability as an efficient contrast agent for magnetic resonance imaging is herein demonstrated. This highlights the high potential of maghemite@MOF composite integrating the functions of imaging and therapy as theranostic anti-inflammatory formulation.

2.3 Keywords

Metal Organic Frameworks, maghemite, drug nanocarriers, theranostics, inflammatory disease.

2.4 Introduction

Inflammation is a complex mechanism of the body's defense, arising from multiple causes such as infectious agents (viruses, bacteria), radical oxygen species or metabolic stress (hypoxia). A large spectrum of pathologies such as sepsis, asthma, type 2 diabetes, neurodegenerative, cardiovascular and intestinal diseases, rheumatoid polyarthritis and also cancer are accompanied by an uncontrolled inflammatory response. The conventional treatment of such inflammatory diseases generally relies on the use of steroidal or nonsteroidal anti-inflammatory drugs, as well as anti-leukotrienes or pro-inflammatory cytokine inhibitors.[1] However, these treatments often lack from an optimal

pharmacological activity as a result of non-specific biodistribution, low bioavailability and/or short half-life into the body, together with high dosages required associated to off-target side effects.[1] To overcome such drawbacks, nanomedicines based on nanoparticles (NPs) such as liposomes loaded with anti-inflammatory drugs were developed and have shown therapeutic improvements of inflammatory diseases in pre-clinicals studies.[1] They were also applied in cancer treatment due to the relation observed between the tumor inflammatory microenvironment and cancer carcinogenesis, dissemination and metastasis.[2] However, only a very limited number of anti-inflammatory nanomedicines have succeeded to reach clinical trials.[3] Among key issues to be addressed, one can point out their insufficient stability in biological fluids, low drug loading capacity, uncontrolled drug delivery as well as their limited biocompatibility and safety.[1, 3] More importantly, their complex architecture often requires a multi-step synthesis which is a strong hurdle for the cost-effective scaling-up of their production. There is thus an urgent need to develop a novel generation of anti-inflammatory nanomedicines.

In this context, Metal Organic Frameworks (MOFs) have recently emerged as alternative drug-delivery platforms. MOFs are micro or meso-porous crystalline hybrid materials consisting of metal ions, clusters or chains interconnected by organic linkers.[4-8] Their unprecedented chemical and structural diversity,[4-8] high surface area as well as their suitable amphiphilic internal microenvironment, make these solids promising drug nanocarriers. Not only are these latter able to encapsulate a high diversity of active ingredients (drugs, biological gases, proteins, photosensitizers, etc.) but their drug loading capacities can reach record values, up to 2 g of drug per gram of empty MOF, surpassing those of any other drug nanocarrier.[9] Moreover, through a careful choice of the MOF and depending on the administration route, one can achieve in most cases a controlled, progressive, eventually stimuli-responsive, drug release, avoiding a therapeutically inactive burst-release. Their large diversity also endows them multiple functionalities of interest for therapy, diagnosis and imaging, thereby allowing the construction of theranostics nanovector.[10-14] Several types of inorganic cations can offer imaging contrast for magnetic resonance imaging (MRI), computed tomography (CT) or single photon emission computed tomography (SPECT) while organic ligands can impart therapeutic or imaging function, such as acting as chemotherapeutic prodrugs, photosensitizers or fluorescent dyes.[10-16] The therapeutic efficiency of these nanoMOFs can be further enhanced by integrating another material such as metals,

metal oxide NPs, (bio)polymers, enzymes, or nucleic acids, either anchored at the surface of nanoMOFs or alternatively encapsulated within their internal porosity.[17-20] While polymer coating has been shown to enhance the pharmacokinetics of MOF NPs (colloidal stability and blood circulation time), metal and metal oxide NPs could confer magnetic, plasmonic or luminescent properties of interest for multimodal imaging and diverse therapies (photothermal and photodynamic).[10-19, 21-22] Although significant progress has been achieved in this field, such nanoMOFs still face critical issues that are detrimental for their biomedical application. Due to their complex microstructure and multi-component composition, most MOFs nanocarriers present a high toxicity and/or a poor chemical or colloidal stability while their biodegradability or intracellular fate was rarely evaluated.[23] Moreover, these nanovectors are often prepared through complicated, multi-steps and time-consuming synthesis procedures relying on the use of organic solvents hampering their clinical translation. So far MOF platforms were reported mainly for cancer therapy[9-16] while their potential has barely been explored for inflammatory chronic diseases such as rheumatoid arthritis (RA).[24-29]

In light of these developments, some of us have reported in the past few years nano-objects (denoted as MIL/USPIO-cit) that consisted of mesoporous Fe^{3+} trimesate MOF (*i.e.*, MIL-100(Fe)) NPs whose outer surface was post-synthetically coated by citrate modified maghemite γ-Fe_2O_3-cit NPs.[18] This bimodal nanovector was shown to be a promising candidate for cancer theranostics due to its ability of coupling drug-delivery and MRI properties. However, the γ-Fe_2O_3-cit rate did not exceed 10 wt% while the colloidal stability of such nanovectors was not optimal in physiological conditions.[18] In the present article, a novel hierarchical superparamagnetic and stimuli-responsive MIL-100(Fe) / γ-Fe_2O_3 nano-object (denoted as USPIO@MIL) (Scheme 1) was synthesized through a direct cost-effective room temperature (RT) green approach. It consists of small MIL-100(Fe) nanoparticles (50 nm) in which γ-Fe_2O_3 NPs are homogeneously distributed in their core and at their surface. USPIO@MIL was able to encapsulate two drugs (either doxorubicin (Dox) or methotrexate (MTX)) with a high drug loading. Dox, a widely used anticancer drug has also shown its capacity to induce apoptosis of inflammatory neutrophils[30-31] while MTX is not only a chemotherapy agent but also the first-line conventional drug for rheumatoid arthritis (RA). Our objective was thus to design a novel type of anti-inflammatory nanomedicine for the treatment of chronic inflammatory disease such as RA. Note that RA is frequently accompanied by other diseases such as cancer[32] that can affect all body organs with

however, to date, no effective available therapy targeting simultaneous cancer and RA.[30-31] Noteworthy our new biodegradable multi-drug delivery system was shown to be very efficient to carry and release complementary anti-cancer and anti-inflammatory drugs to synergistically target both malignant cells and tumor inflammatory components.[32] USPIO@MIL and drug loaded analogues present a low cytotoxicity and an excellent colloidal stability in physiological conditions while their biodegradability was demonstrated through their internalization in macrophages and intracellular fate over a period of one week monitored by TEM. Remarkably, the stimuli-responsive drug release properties of USPIO@MIL/Dox (and also USPIO@MIL/MTX to a less extent) confer these nanovectors a high anti-tumoral and anti-inflammatory capability. Finally, due to its high γ-Fe_2O_3 rate of 20 wt%, USPIO@MIL nano-object exhibits a superparamagnetic behaviour suitable for its use as *in vivo* contrast agent for MRI, thereby paving the way for its applicability in image-guided therapy to diagnose and treat inflammatory diseases.

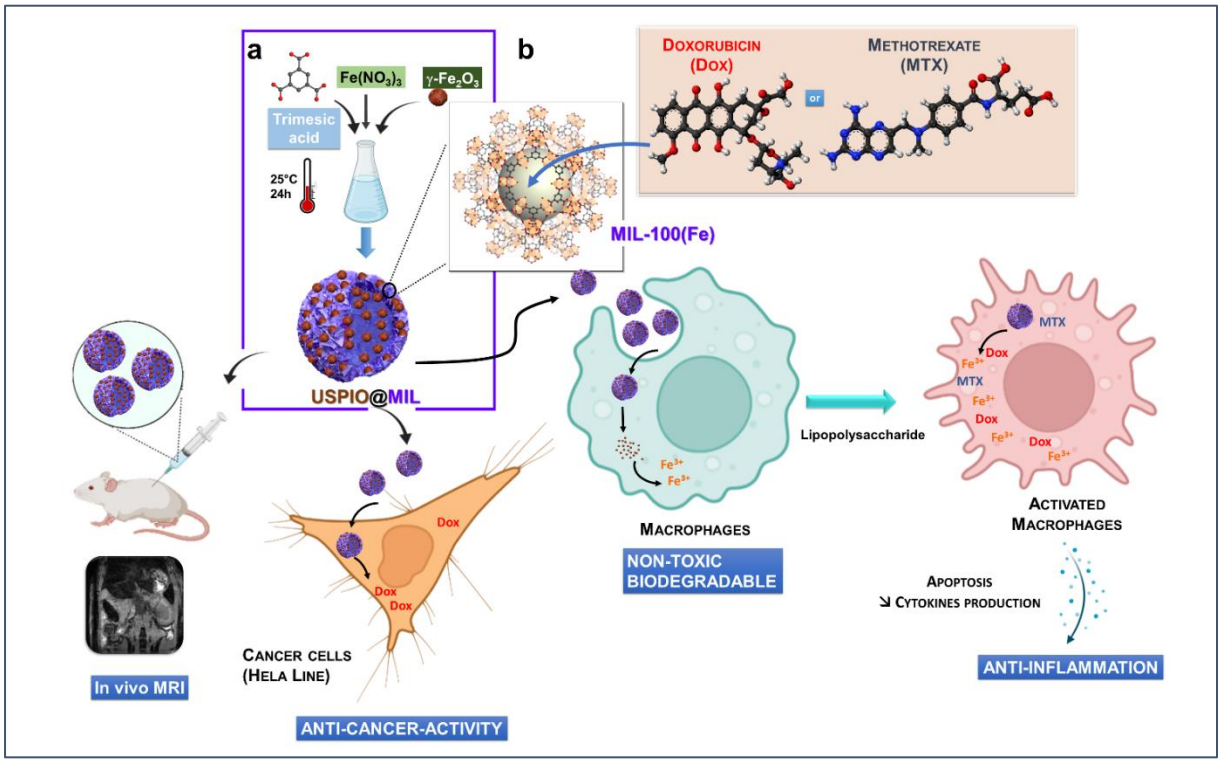

Scheme 1. Schematic illustration of a) synthesis of USPIO@MIL-100(Fe) nano-objects and b) their use as a theranostic platform for the treatment of cancer and inflammatory diseases.

2.5 Results and discussion

Synthesis of maghemite embedded MIL-100(Fe) nano-objects. The synthesis of USPIO@MIL nano-objects was derived from a protocol recently developed by some of us for the preparation of MIL-100(Fe) NPs (Figures S1 and S2).[33] This procedure consists of mixing the iron salt and the benzene tricarboxylic acid (1,3,5-BTC) ligand in water at RT, which is advantageous compared to conventional solvothermal synthesis (reflux or microwave), both from a technico-economic point of view and for the preparation of MOF-composites relying on fragile nano-objects (NPs, enzymes, etc.).[33-35] Firstly, the USPIO NPs were prepared by a coprecipitation method according to well-known procedures.[36-37] Their characterization by using PXRD, HRTEM, FT-IR and DLS have clearly shown the formation of maghemite (*i.e.*, γ-Fe_2O_3) NPs with a cubic deficient spinel structure (a = 0.836 (1) nm) and a particle diameter close to 7 nm (Figure S3). Then, the USPIO@MIL nano-objects were then

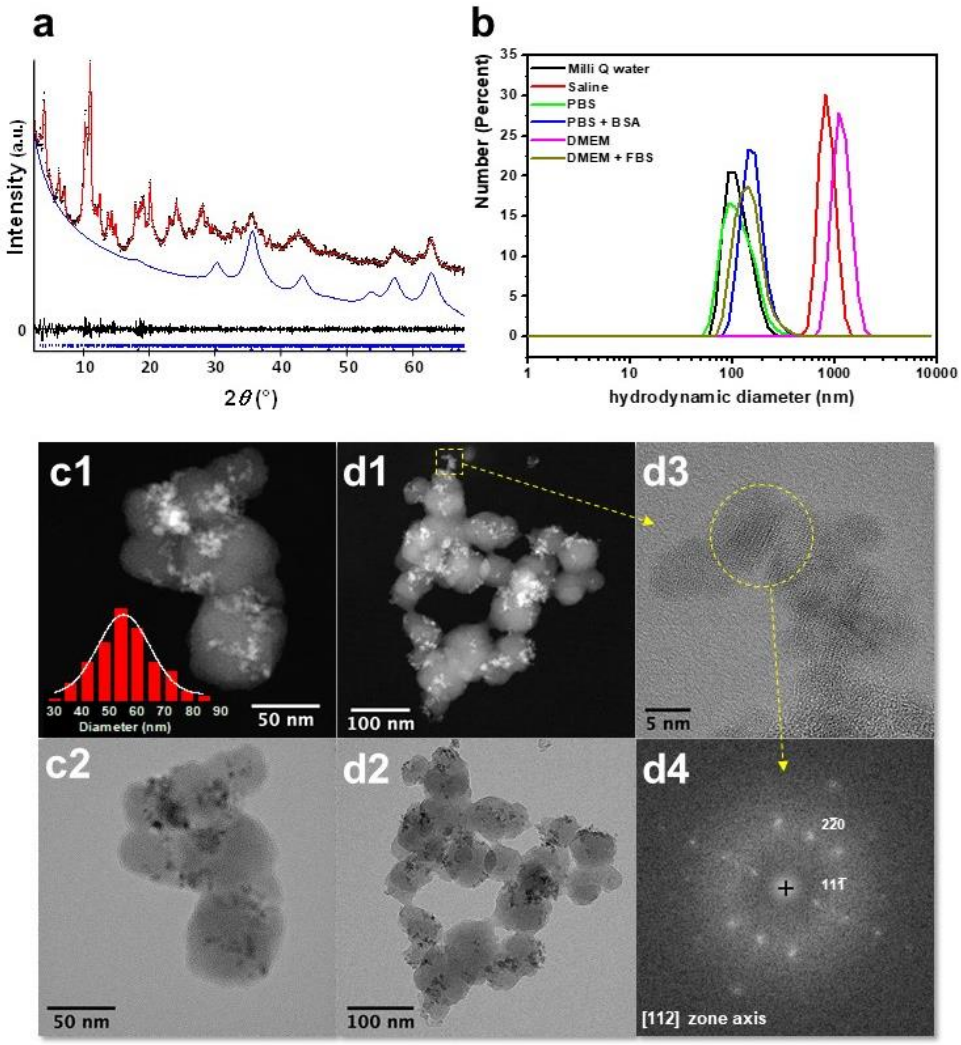

Figure 1. Characterizations of USPIO(20)@MIL. a) Refinement of USPIO(20)@MIL PXRD pattern (Rietveld refinement was performed for maghemite whereas a profile pattern matching was undertaken for the MIL-100(Fe) contribution) ($\lambda Cu \approx 1.5418$ Å); b) Hydrodynamic diameters of USPIO(20)@MIL at a concentration of 200 μg mL^{-1} in different media (Milli Q water, Saline, PBS, PBS + BSA, DMEM and DMEM + FBS) at RT. (c1-d1) STEM-HAADF and corresponding (c2-d2) TEM-BF images of USPIO(20)@MIL. (d3) HRTEM image of USPIO with (d4) FFT indexed with the cubic cell (a = 0.8346 nm). Inset of c1) particle size distribution (diameter = 56 ± 11 nm) of USPIO(20)@MIL NPs.

synthesized following an *in situ* approach, where the nanoMOF was formed at RT in the presence of γ-Fe_2O_3 NPs as a co-reactant in a reaction medium containing the iron salt and the organic ligand, keeping the same reaction conditions as those used for the bare MIL-100(Fe) (see Experimental section for details).[33] First, the USPIO@MIL nano-objects were prepared with a content of γ-Fe_2O_3 of 20 wt% (referred as USPIO(20)@MIL) as shown by the combination of Inductively Coupled Plasma Mass Spectroscopy (ICP-MS) and High Performance Liquid Chromatography (HPLC) (Table S1, Figure S4). The nano-objects have been fully characterized by combining Powder X-ray diffraction (PXRD), DLS, TEM, HAADF-STEM, N_2 porosimetry and FTIR (**Figures** 1, 2 and S5-S7). PXRD pattern of USPIO(20)@MIL superimposes well with those of both MIL-100(Fe) and γ-Fe_2O_3, according to the structureless refinement performed for maghemite and the profile matching for the MOF (Figure 1a). Accordingly, the TEM and HAADF-STEM (**Figures 1** and S7) images show that USPIO(20)@MIL consists of spheroidal particles of 56 ± 11 nm in diameter with a small size distribution which is close to the dimensions of the bare nanoMOF (40 ± 8 nm) (Figure S2). Note that the diameter and particle size distribution of MIL-100(Fe) NPs in USPIO(20)@MIL are significantly lower than that of MIL-100(Fe) NPs prepared by microwave assisted solvothermal protocol.[18, 38-39] The TEM and HAADF-STEM images show that the outer surface of USPIO@MIL NP is partially decorated by small aggregates of γ-Fe_2O_3 NPs while individual γ-Fe_2O_3 NPs cannot be observed (Figure 1). Electron tomography experiments were performed to further analyze the 3D architecture of USPIO(20)@MIL nanostructures and elucidate the location of the γ-Fe_2O_3 NPs. Degradation of the nanoMOF is observed upon exposure to the electron beam but it does not affect the observation of the embedded γ-Fe_2O_3 NPs. According to the 3D reconstruction of the USPIO(20)@MIL nano-objects, the γ-Fe_2O_3 NPs are concomitantly located at the outer surface of the MIL-100(Fe) NPs and also embedded in their core (**Figure 2**). This suggests that these entrapped γ-Fe_2O_3 NPs may act as anchors for the initial formation of MIL-100(Fe) seeds, followed by their further outward growth, gradually forming the hierarchical

porous USPIO(20)@MIL NPs, with the remaining USPIO being attached at the external surface of the composite. The spatial distribution and organization of γ-Fe_2O_3 NPs is different whether they are located at the surface or in the core of MIL-100(Fe). While γ-Fe_2O_3 NPs are strongly aggregated at the surface of nanoMOFs, they are randomly spatially distributed in the core of MIL-100(Fe). According to electron tomography, one can estimate a similar relative amount of the "surface" and "embedded" γ-Fe_2O_3 NPs within USPIO(20)@MIL although this quantification could only be performed on a limited number of nano-objects. The stoichiometry of iron oxides in USPIO(20)@MIL was finally

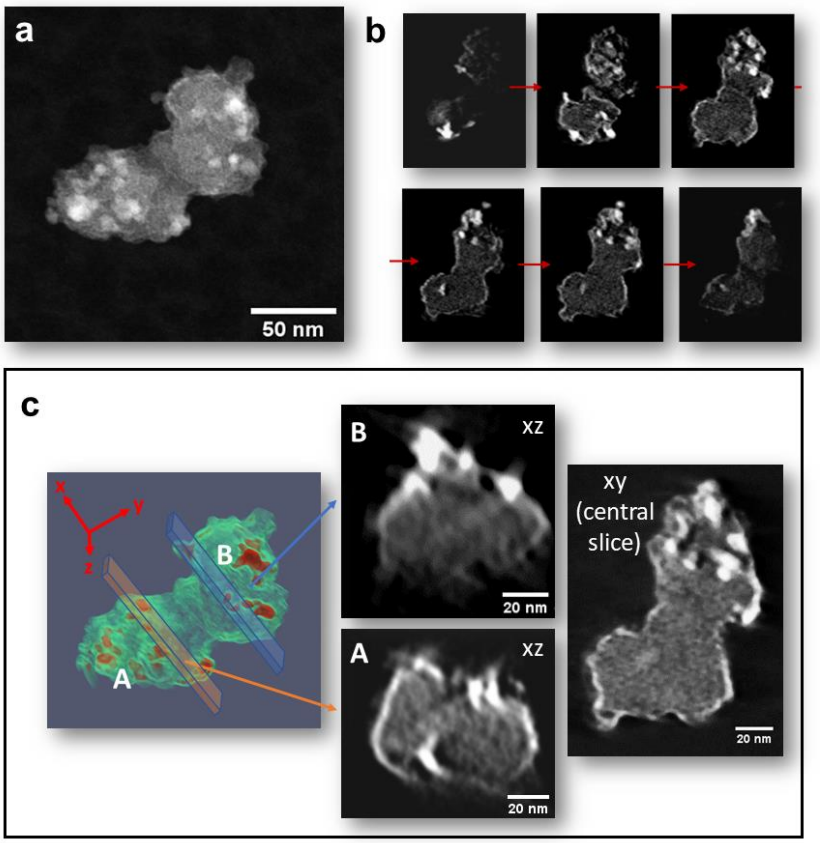

Figure 2. Electron tomography analysis of two typical aggregated USPIO(20)@MIL nano-objects. a, b) STEM-HAADF images, at 0° tilt, from the tilt series used to reconstruct the volume (a) and several slices extracted from the bottom to the top of the volume of the aggregate obtained by reconstruction (b); c) The 3D model of the two aggregated USPIO(20)@MIL nano-objects with γ-Fe_2O_3 NPs in red and MIL-100(Fe) NPs in green and three corresponding slices through the reconstruction parallel to either (xz) or (xy) planes.

assessed by ^{57}Fe Mössbauer spectrometry (300 and 77 K) in order to exclude a possible reduction of γ-Fe_2O_3 to Fe_3O_4 magnetite NPs during the formation of USPIO(20)@MIL. Note that both iron oxides cannot easily be distinguished by PXRD since they exhibit the inverse spinel crystalline structure with a close lattice parameter. The ^{57}Fe Mössbauer spectrum of USPIO(20)@MIL recorded at 77 K (see SI

for details and Figure S14) shows a broadened lines sextet that can be assigned to γ-Fe_2O_3 NPs while the central asymmetrical quadrupolar doublet results from both MIL-100(Fe) and small non-interacting γ-Fe_2O_3 NPs. The acquisition of ^{57}Fe Mössbauer spectra at both 300 K and 77 K allows thus to identify the presence of interacting and non-interacting γ-Fe_2O_3 NPs located presumably at the surface and in the core of MIL-100(Fe) particles as shown by TEM and electron tomography. The relative amount of both MIL-100(Fe) and γ-Fe_2O_3 estimated from the respective absorption areas (69% and 31%) is fully consistent with the quantification given by ICP-MS and HPLC (see above).

Similar USPIO(10)@MIL nanostructures with a lower γ-Fe_2O_3 content of 10 wt% could also be synthesized at RT by the *in situ* approach as shown by PXRD, N_2 porosimetry, TGA and TEM (Figure S8). This shows that the *in situ* route allows to tune the rate of USPIO while preserving the microstructure of nano-objects. For both USPIO(X)@MIL (X = 10 and 20), the TEM images show clearly that almost no USPIO was physically separated from MIL-100(Fe) NPs (Figures 1, S7 and S8), thus located either at the surface or embedded in the core of the nanoMOF. This is in contrast to the previously reported MIL/USPIO-cit nano-objects whose maximum thresholds could not exceed 10 wt% above which γ-Fe_2O_3 aggregates are simultaneously formed.[18] This clearly shows that the *in situ* approach can produce homogeneous USPIO@MIL nano-objects with a maghemite rate as high as 20 wt%.

Colloidal stability in serum conditions. To assess their intravenous administration and potential use as drug delivery systems, the colloidal stability of USPIO(20)@MIL was studied under different simulated physiological medium conditions. In contrast to a strong aggregation observed in the Dulbecco's Modified Eagle Medium (DMEM) cell culture medium, saline solution (0.9% NaCl) and phosphate buffer saline (PBS), an excellent colloidal stability of USPIO(20)@MIL NPs was observed in Milli Q water, in DMEM supplemented with fetal bovine serum (FBS) (10% v/v) and in PBS supplemented with bovine serum albumin (BSA) (5.4% v/v) since their hydrodynamic diameter (*i.e.*, ~140, 150 and 170 nm, respectively) remained constant for 24 h (Figures 1b and S9). Interestingly, as previously reported for MIL/USPIO-cit[18], the long term colloidal stability of USPIO(20)@MIL NPs was significantly enhanced by using DMEM and PBS buffer solutions containing serum and thus the most abundant plasma proteins in mammals, albumin (Figures S10 and S11). This may result from a possible adsorption of BSA at the surface of NPs as reported before.[18, 40] It is worth noting that

USPIO(20)@MIL NPs exhibit a superior colloidal stability in comparison to that of MIL/USPIO-cit NPs[18] as a result of their smaller mean diameter (170 nm for USPIO(20)@MIL and 380 nm for MIL/USPIO-cit) in PBS/BSA, which is beneficial for their intravenous administration. The long-term chemical stability of MIL-100(Fe) and USPIO(20)@MIL in PBS and PBS/BSA solutions was finally investigated by varying pH. According to the PXRD and TEM experiments (Figures S12 and S13), USPIO(20)@MIL NPs exhibit a good stability in PBS and PBS/BSA solutions at pH 5.1 for 24 h while a partial or complete degradation of MOF occurs for 24 h by increasing pH to 6.5 and 7.4, respectively. This is consistent with the previously reported degradation of these MIL-100(Fe) NPs in a highly concentrated aqueous phosphate solution at pH 7.4.[39]

Biodegradability and internal distribution in macrophages. In the next step, the cellular uptake of USPIO(20)@MIL by RAW 264.7 mouse macrophages was then investigated by combining confocal laser scanning microscopy (CLSM), TEM, and ICP-MS. For the CLSM experiments, the fluorescent dye Rhodamine B (RhB) was encapsulated in the mesopores of USPIO(20)@MIL (see SI for experimental details). Internalization of the RhB-labeled USPIO(20)@MIL nano-objects in the RAW 264.7 macrophages was clearly observed after an incubation time of 1 h (Figure S16). The fluorescence intensity of the cells increased until 4 h while remaining constant for a longer incubation time. 2D TEM slices images of RAW 264.7 cells incubated with USPIO(20)@MIL NPs were recorded to characterize the internalization of USPIO(20)@MIL in RAW 264.7 cells, elucidate their intracellular distribution and fate over a period of one week.

As shown in Figures 3a-c, after 30 min of incubation, USPIO(20)@MIL nano-object start to interact with the cell plasma membrane while a few nano-objects internalized into membrane-closed endosomes, without losing their bimodal nanostructure (small black dot and grey spheres in TEM images correspond respectively to γ-Fe_2O_3 and MIL-100(Fe) NPs). From 4 to 8 h (Figures 3d-i), a large amount of USPIO(20)@MIL NPs is accumulated in endosomes. After 12 h of incubation (Figures 3j-l), they start partially to degrade as revealed by the presence of individual γ-Fe_2O_3 NPs until their complete dissociation after an incubation time of 24 h (Figures 3m-o). This is in agreement with the degradation of the outer MIL-100(Fe) shell of Fe_3O_4@C@MIL-100(Fe) in Hela cells as previously reported.[41] The degradation of MIL-100(Fe) is, as expected, due to the high intracellular concentration of phosphates and iron reductants such as glutathione. In the following days (Figure

S17), γ-Fe_2O_3 NPs are more concentrated in lysosomes and the density of γ-Fe_2O_3 NPs in the cytoplasm as well as endo/lysosomal compartments is significantly reduced after 5 days, suggesting their progressive degradation as previously observed for iron oxide NPs. This process is certainly involved in Fe recycling into ferritin proteins.[42] Overall, this two-stage degradation profile of USPIO(20)@MIL

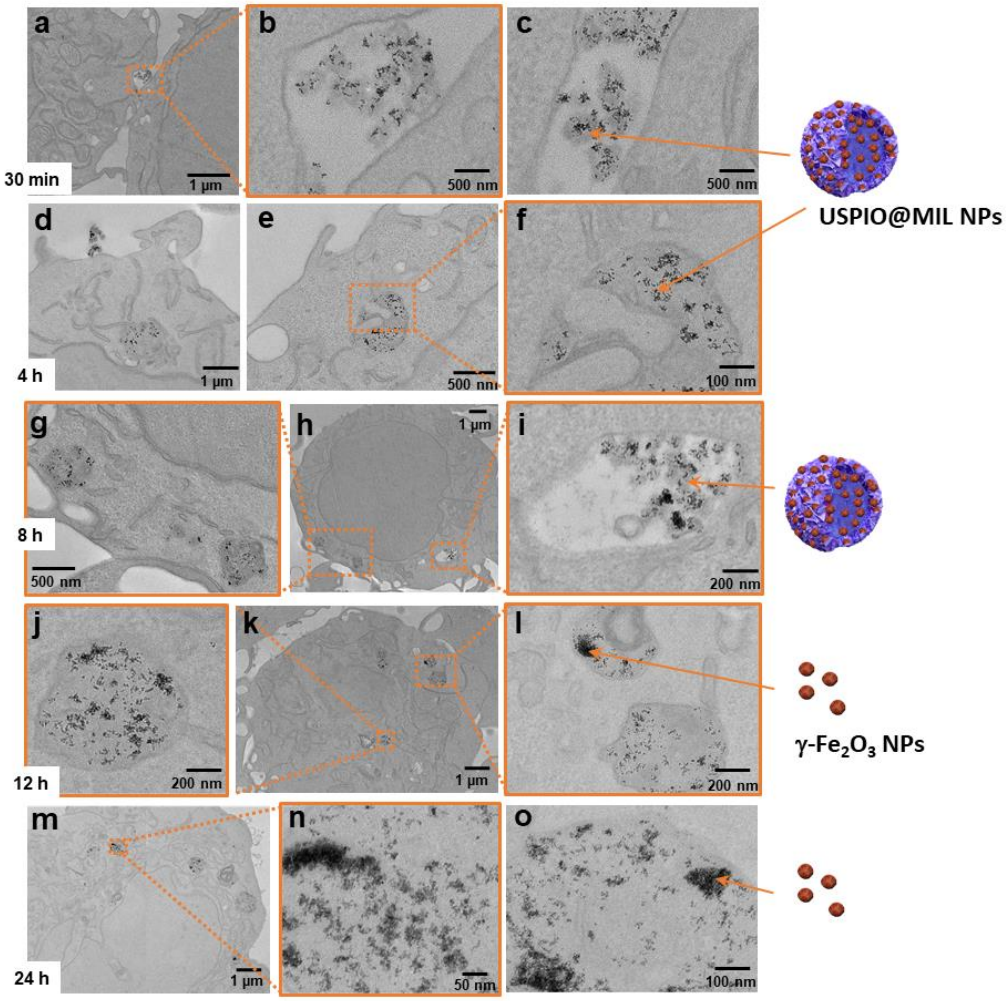

Figure 3. 2D TEM slices images of RAW 264.7 cells exposed to USPIO(20)@MIL (50 µg mL^{-1}) in 2% FBS/DMEM medium for different incubation times (30 min, 4 hours, 8 hours, 12 hours and 24 hours).

NPs clearly shows that these nano-objects are biodegradable after cell internalization. This is also associated with a high intracellular iron concentration, as shown by the quantification of the intracellular iron content by ICP-MS (Figure S18). In agreement with CLSM experiments, a progressive increase of the Fe^{3+} concentration is observed by increasing the incubation time until a plateau is reached after 6 h. Note that the evaluation of the biodegradability and intracellular fate of MOF based nanovectors as studied in the present article by TEM was rarely reported in literature.

pH- and glutathione (GSH) responsive release properties of nano-objects. For the development of USPIO(20)@MIL NPs as a theranostic nanocarrier, the drug-loading capacity and drug-release properties of MIL-100(Fe) need to be maintained after its assembly with USPIO. Interestingly, as shown by N_2 porosimetry, only a slight decrease in the BET area was observed with a value of 1460 ± 6 $m^2 \cdot g^{-1}$ for USPIO(20)@MIL, in comparison to that of pure MIL-100(Fe) NPs (1720 ± 6 $m^2 \cdot g^{-1}$), due to the presence of the dense non-porous USPIO (see Figures 4b and S1). It indicates that the porosity of MIL-100(Fe) is kept once combined with maghemite NPs. The encapsulation of an active payload and its kinetics of delivery in PBS was then studied using Dox and MTX, selected due to their combined chemotherapeutic and anti-inflammatory properties (Figure 4a).[1, 30-31, 43] Note that patients treated with Dox and MTX often suffer from severe non desirable off-target effects.[1, 24, 44] Therefore, selective delivery of those drugs may achieve upregulated efficacy and safety. MTX was encapsulated in the porosity of both MIL-100(Fe) and USPIO(20)@MIL with a loading ratio of 60 and 47 wt%, respectively (Figures S19 & S20, Table S2). This capacity is higher to that of MOFs previously reported.[45-48] Dox was encapsulated in MIL-100(Fe) and USPIO(20)@MIL with a loading of ~56 wt% and 50 wt% respectively (Figures S22 and S23, Table S3), which exceeded most previously reported studies using either ZIF-8 (~4.9%) or the microwave-prepared MIL-100 (~9.1%), MIL-101(Fe) (~13.4%) or Gd MOFs (~13.6%), and comparable to the mesoporous NU-1000(Zr) (~53.8%).[9, 18, 49-52] The N_2 adsorption/desorption isotherms and the pore size distribution are fully consistent with the encapsulation of both drugs in USPIO(20)@MIL (see Figures 4b and 4c). As shown by TEM, the drug loading did not affect the microstructure and morphology of both MIL-100(Fe) and USPIO(20)@MIL (see Figure S20).

To achieve efficient drug delivery from the circulation to the target inflammatory tissues, the pH-responsiveness of release kinetics of MTX and Dox across neutral to acidic conditions was investigated. Indeed, endosomes (pH ~ 5-6) and lysosomes (pH ~ 4-5) of normal tissues as well as the synovial tissue of patient with RA are low-pH environments in comparison to blood (pH ~ 7.4).[53-54] Moreover, the affected joints of RA feature hypoxic microenvironment and increased level of glutathione (GSH, L-γ-glutamyl-L-cysteinylglycine), resulting from synovial proliferation, lymphocyte infiltration, and neovascularization.[55-57] GSH is one of the important antioxidants present in the human body which protects cellular components from damage by free radicals.[55-58]

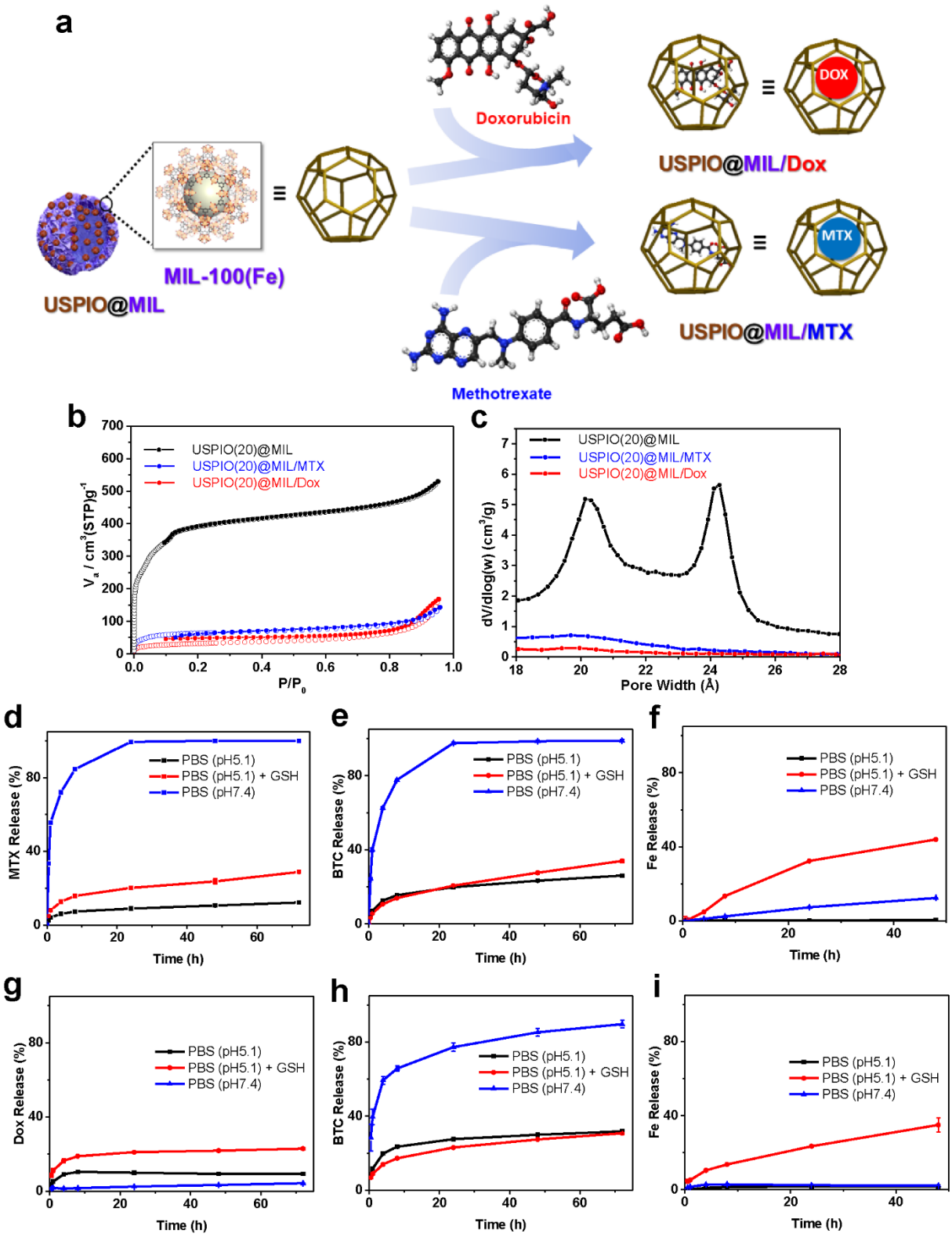

Figure 4. a) Scheme of the doxorubicin and methotrexate loading in USPIO@MIL, (b) N_2 sorption isotherms and (c) pore size distribution (PSD) derived from the Barrett-Joyner-Halenda (BJH) pore size model of USPIO(20)@MIL, USPIO(20)@MIL/Dox, USPIO(20)@MIL/MTX, (d-f) MTX, BTC and Fe ions release from USPIO@MIL/MTX in different PBS media, (g-i) Dox, BTC and Fe ions release from USPIO@MIL/Dox in different PBS media.

Advantageously, the presence of GSH at high concentration (10 mM) and low pH in inflammatory joints can here be exploited as a stimulus to trigger the MTX and Dox release from USPIO(20)@MIL delivery system. As shown in Figure 4d,g, the release rate of MTX and Dox from USPIO(20)@MIL greatly depends on pH. A fast release of MTX from USPIO(20)@MIL is observed in PBS at pH 7.4 with drug release of 30, 70 and 85% after 0.5, 4 and 8 h, respectively. The release of MTX is substantially slowed down at pH 5.1 in a medium containing PBS and GSH 10 mM (PBS/GSH) (Figure 4d) mostly as a consequence of the slower kinetics of MOF degradation under more acidic conditions.

The delivery profile of MTX follows two regimes: a fast release of about 17% of MTX in the first 8 h followed by a progressive one until reaching 30% of MTX released after 3 days. In contrast, a minimal delivery of Dox from USPIO(20)@MIL was observed at pH 7.4 over 3 days (Figure 4g) while in PBS/GSH medium at pH 5.1, it was slightly faster but kept progressive achieving a cumulative Dox delivery of about 20% after 3 days. The comparison between kinetics of Dox and MTX drug release and the degradation profiles of USPIO(20)@MIL (see Figures 4d-i) suggests that the delivery process of both drugs is driven by the combined effects of diffusion from the pores and/or drug-matrix interactions as well as a partial degradation of MIL-100(Fe) in PBS[39], that occurs more rapidly at pH 7.4 than 5.1. As shown by the quantification of 1,3,5-BTC and Fe released in the PBS media (Figure 4e, f, h, i), MIL-100(Fe) degrades relatively fast at pH 7.4 due to the strong complexing ability of phosphate at this pH towards Fe cations. However, the Dox delivery is limited as the result of specific strong interactions between Dox and Fe(III) metal site of MIL-100(Fe) as previously demonstrated[59-60] while MTX is likely to exhibit only dispersive weak interactions with the MOF framework. Noteworthy, the high Fe release in the PBS/GSH medium at pH 5.1 indicates the complete degradation of MIL-100(Fe) that results from a chemical reduction of Fe^{3+} centers by GSH as previously shown.[55-58, 61] Note that such high GSH levels are typically encountered in inflammatory diseases[62] which accelerates the degradation of the iron based USPIO(20)@MIL nano-object and thus triggers under acidic conditions the release of both Dox and MTX. The stimuli-responsive release properties of USPIO(20)@MIL/Dox can thus be exploited to selectively deliver Dox at the mildly acidic environment of inflamed joints. Note that the internalization of USPIO(20)@MIL in RAW 264.7 cells occurs within the first 8h (Figure 3) which means that the complete encapsulated Dox cargo can be administrated in cells while a significant amount of MTX is released before USPIO(20)@MIL can

accumulate into the cells. This means that the administration routes of these USPIO(20)@MIL/Dox and USPIO(20)@MIL/MTX formulations may be different. While both nanomedicines could be injected locally at the inflamed joint, USPIO(20)@MIL/Dox could also be alternatively intravenously injected.

***In vitro* assays**: cytotoxicity, anti-inflammatory and anti-cancer activity. In the next step, the *in vitro* cytotoxicity of USPIO(20)@MIL, USPIO(20)@MIL/MTX and USPIO(20)@MIL/Dox was assessed by a standard CCK-8 assay with different cell types (Hela tumor cells and RAW 264.7 cells) for an incubation time of 12 h and 24 h (see Experimental section for details). The viability of Hela cells exposed to USPIO(20)@MIL at a concentration of 20 and 50 µg mL^{-1}, was close to 92% and 91% after 12 h respectively and evolved slightly to 86% after 24 h (Figure S25). Similar results were obtained with the bare MIL-100(Fe) NPs as previously shown.[18] These results show that both MIL-100(Fe) and USPIO(20)@MIL present a low cytotoxicity to Hela cells. Moreover, their cytotoxicity to RAW 264.7 cells is negligible since the viability of macrophages incubated with both NPs at 50 µg mL^{-1} for 24 h is close to 80% (Figure S26). The *in vitro* cytotoxicity of USPIO(20)@MIL/MTX and USPIO(20)@MIL/Dox was then evaluated exposing them to normal macrophages. RAW 264.7 were thus incubated with either USPIO(20)@MIL/MTX or free MTX for 24 h. The concentration of MTX (23 µg mL^{-1}) was selected according to the MTX loading capacity of USPIO(20)@MIL. The cytotoxicity of USPIO(20)@MIL/MTX to normal macrophages is low since the viability of RAW 264.7 macrophages is close to 72% once exposed to USPIO(20)@MIL/MTX at a concentration of 50 µg mL^{-1} for 24 h (see Figure S27). In comparison, free MTX shows a high cytotoxic activity for normal macrophages decreasing cell viability to 34% at MTX concentration of 23 µg mL^{-1} which may due to its robust dihydrofolate reductase inhibition activity to induce cell death as previously reported.[24] Similar results are obtained with USPIO(20)@MIL/Dox in comparison to free Dox. While a very high cytotoxicity is shown for the RAW 264.7 macrophages exposed to free Dox (2.5 to 25 µg mL^{-1}), the RAW 264.7 viability is close to 100% when incubated with USPIO(20)@MIL/Dox at the concentration of 5 to 50 µg mL^{-1} (see Figure S27). Cell apoptosis assay by using calcein-AM/PI double staining was finally performed and confirms the low cytotoxicity of USPIO(20)@MIL/Dox and USPIO(20)@MIL/MTX to normal RAW 264.7 macrophages (Figure S28).

To evaluate the anti-inflammation ability of the nanovectors, the RAW 264.7 macrophages were pretreated with lipopolysaccharide (LPS) for activation. Note that activated macrophages are involved in inflammatory diseases, including RA, lupus, inflammatory osteoarthritis, and cancer.[1, 24, 44, 63-64] They play an important role in RA, due to their abundance in inflamed synovial membrane and joints. RAW 264.7 cells activated by LPS spontaneously reveal an increased intracellular ROS level (Figure S29). As reported previously, the magnitude of the inflammatory perturbation depends on the LPS concentration, that is known to increase the intracellular ROS level.[65] Once exposed to USPIO(20)@MIL and MIL-100(Fe) at 50 μg mL^{-1}, the viability of activated RAW 264.7 cells decreases to a value of ~36% and ~38% after 24 h of incubation (Figure S30). This shows that both USPIO(20)@MIL and MIL-100(Fe) nanovectors present a good anti-inflammatory efficacy associated to their fast internalization in macrophages and the high Fe^{3+} intracellular concentration (Figure S18). A similar phenomenon was previously reported for lipid-coated MIL-100(Fe) NPs whose internalization in different cell lines leads to their lysosomal degradation and iron delivery.[66] The high amount of lysosomal iron induces a pyroptosis cell death mechanism which is an inflammatory form of programmed cell death.[67] The identification of the cell death mechanism in play with the toxicity of activated RAW 264.7 cells in the presence of USPIO(20)@MIL and MIL-100(Fe), that is out of the scope of this study, and other cell death mechanisms induced by intracellular iron overexposure (ferroptosis) cannot be ruled out at this stage. However, it is worth noting that iron has been reported to trigger pyroptosis mediated by ROS that are produced in the presence of activated macrophages.[66, 68] Activated RAW 264.7 macrophages were further exposed to drug loaded nanovectors namely USPIO(20)@MIL/MTX and USPIO(20)@MIL/Dox. Notably, activated RAW 264.7 macrophages are much more sensitive to USPIO(20)@MIL/MTX than normal macrophages since the cell viability decreases to ~30% once incubated with the nano-objects at 50 μg mL^{-1} for 24 h (Figure S30). This shows that USPIO(20)@MIL/MTX can induce a selective damage towards inflammatory macrophages. When compared with the free MTX alone, the USPIO(20)@MIL/MTX exhibited a significant higher anti-inflammatory efficiency since the viability of activated RAW 264.7 was almost 100% when exposed to free MTX at 23 μg mL^{-1} for 24 h (Figure S30). The high efficiency of MTX formulated into USPIO(20)@MIL is certainly driven by the fast cellular internalization of USPIO(20)@MIL/MTX as previously shown. However, this anti-inflammatory activity is only slightly enhanced in comparison to USPIO(20)@MIL since the viability of activated RAW 264.7

exposed to USPIO(20)@MIL reached ~36% in the same conditions (50 µg mL^{-1} with 24 h of incubation time). Such results can be explained by a significant delivery of MTX cargo from USPIO(20)@MIL in PBS prior to the nano-objects internalization. Activated macrophages were also exposed to USPIO(20)@MIL/Dox at 5, 20, 50 µg mL^{-1} concentrations (Figure S31) in DMEM medium (see Experimental section for details). They were also incubated with free Dox at 2.5, 10, 25 µg mL^{-1} concentrations, which correspond to the amount of drug released from the nano-objects (at 5, 20, 50 µg mL^{-1}) respectively according to the release kinetics in PBS at 24 h (see above). When incubated with USPIO(20)@MIL/Dox at 5, 20, 50 µg mL^{-1}, cell viability decreased to ~89%, ~30%, and ~9%, respectively, in comparison with the non-treated cells. This cell viability is lower, for the two highest concentrations, than that obtained with USPIO(20)@MIL NPs for the same concentrations (*i.e.*, cell viability of ~88%, ~57%, and ~36% at 5, 20, 50 µg mL^{-1}) thereby showing the superior cytotoxic capability of USPIO(20)@MIL/Dox on activated macrophages (Figure S31). A strong decrease of the activated RAW 264.7 viability is also observed upon exposure to free Dox (*i.e.*, cell viability of ~30%, ~18% and ~18% at 2.5, 10, 25 µg mL^{-1}) but the free drug presents also a high cytotoxicity to normal macrophages even at very low concentration (2.5 µg mL^{-1}) (Figure S27). These results were confirmed by confocal microscopy. Activated RAW 264.7 macrophages were stained with calcein-AM/PI for discriminating living (green) cells and dead (red) cells. As shown in Figure 5a, a large amount of dead cells are observed for activated RAW 264.7 macrophages exposed to USPIO(20)@MIL/Dox. The high efficiency of Dox formulated into USPIO(20)@MIL NPs is certainly driven by the high local drug accumulation in the cell as a result of the fast internalization of USPIO(20)@MIL NPs in the macrophages as well as the slow and progressive delivery of Dox in PBS (Figure 4g).

To further confirm the anti-inflammatory capacity of the nanoformulations mentioned above, enzyme-linked immunosorbent assay (ELISA) assays were carried out to measure the concentrations of pro-inflammatory cytokines in cell culture media as crucial indexes of therapeutic efficacy. These cytokines including TNF-α, IL-1β, and IL-6 are crucial indicators for the pathological processes of RA.[63-64, 69] TNF-α is involved in the proliferation of synovial fibroblasts, activation of osteoblasts, and destruction of cartilage and bone. IL-1β induces cartilage metabolic disorder, bone absorption, and synovitis *via* promoting the release of other pro-inflammatory cytokines and proteinases while IL-6 is involved in activation of synovial fibroblasts and osteoblasts, leading to articular cartilage and bone

erosion.[63-64, 69] Activated macrophages are exposed to drug formulations of low concentrations in order to prevent the cell apoptosis mediated expression of pro-inflammatory cytokines. As shown in Figure

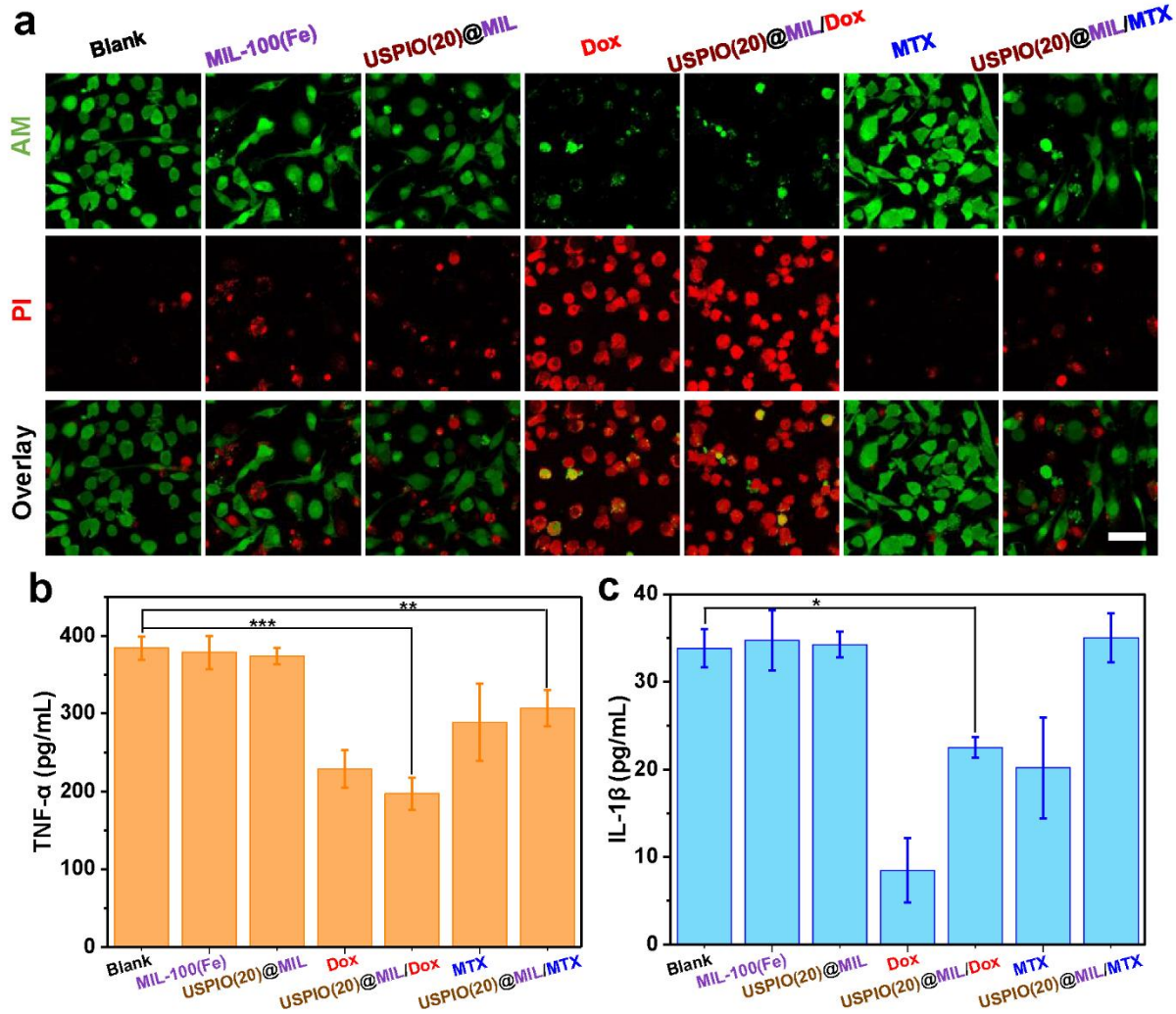

Figure 5. Anti-inflammatory properties of USPIO(20)@MIL/MTX and USPIO(20)@MIL/Dox. a) cell apoptosis assay by using calcein-AM/PI double staining of LPS (100 ng mL^{-1}, 48 h) activated RAW 264.7 macrophages incubated with different drug formulations ([MIL-100(Fe)] = 40 μg mL^{-1}, [USPIO(20)@MIL] = 50 μg mL^{-1}, [Dox] = 25 μg mL^{-1}, [USPIO(20)@MIL/Dox] = 50 μg mL^{-1}, [MTX] = 23 μg mL^{-1}, [USPIO(20)@MIL/MTX] = 50 μg mL^{-1}) for 24 h. For the representative images of (a), activated RAW 264.7 macrophages were stained with calcein-AM/PI for discriminating living (green) cells and dead (red) cells (scale bar = 50 μm). b-c) The concentrations of the inflammatory cytokines (b) TNF-α and (c) IL-1β in cell culture media after the treatment of different formulations ([MIL-100(Fe)] = 4 μg mL^{-1}, [USPIO(20)@MIL] = 5 μg mL^{-1}, [Dox] = 0.25 μg mL^{-1}, [USPIO(20)@MIL/Dox] = 5 μg mL^{-1}, [MTX] = 2.3 μg mL^{-1}, [USPIO(20)@MIL/MTX] = 5 μg mL^{-1}) for 24 h. Note that the concentration of Dox here was ten times lower than the loaded Dox of USPIO(20)@MIL/Dox to limit its toxicity. Results are shown as mean ± SD. *$P < 0.05$, **$P < 0.01$, ***$P < 0.001$.

5b,c and Figure S32, the concentrations of the three pro-inflammatory cytokines, TNF-α, IL-1β, and IL-6, are remarkably increased in the cell culture medium of MIL-100(Fe) and USPIO(20)@MIL. For the free MTX, free Dox, MTX and Dox formulated in USPIO(20)@MIL NPs, the concentration of pro-inflammatory cytokines was decreased in different degrees. In all cases a strong inhibition of IL-1β and TNF-α secretion was observed while the expression of IL-6 was moderately decreased. In contrast, USPIO(20)@MIL/MTX was mainly efficient to reduce the serum concentration of TNF-α. These results thus showed that USPIO(20)@MIL/Dox is prone to inhibit synovitis in the affected joints and also protect articular cartilage and bone against erosion and destruction due to its remarkable ability to reduce the production of pro-inflammatory cytokines.

Finally, the anti-cancer activity of USPIO(20)@MIL/Dox was evaluated by CCK-8 staining kit and confocal microscopy. The cell internalization process as monitored by confocal microscopy with time (Figure S33) was achieved in the first 8h of incubation. In the presence of USPIO(20)@MIL/Dox at 50 µg mL^{-1}, the viability of cancer Hela cells decreases to 8% (Figure S34). When compared to the viability of Hela cells exposed to free Dox (25% at 25 µg mL^{-1}), the USPIO(20)@MIL/Dox nano-object exhibited a higher anti-cancer efficiency as previously shown for surface decorated MIL/USPIO-cit nano-object (Figures S34 and S35).[18] This high efficacy is certainly induced by the fast internalization of nano-objects in the cancer cells and thus the subsequent intracellular drug accumulation. Furthermore, the encapsulation of Dox into nano-objects might overcome the resistance to Dox treatment that occurs in tumor cells as a result of the expression of P-glycoprotein (P-gp), which pumps out the drug from the cells.[70]

Relaxometric properties of nano-objects, *in vivo* MRI experiments. In the final step, we have evaluated the performance of USPIO(20)@MIL as T_2 MRI contrast agent due to the presence of γ-Fe_2O_3 NPs. As shown in Figure 6a, USPIO(20)@MIL could be easily separated using an external magnetic field, which suggests its excellent magnetic properties. For their potential use as MRI contrast agents, the r_2 relaxivity of USPIO(20)@MIL was assessed in PBS/BSA medium by measuring the T_2 (transverse) relaxation times of proton spins for different iron concentrations at 4.7 T (Figure 6b). As expected, pure maghemite nanoparticles exhibit the highest value of r_2 (171 mM^{-1} s^{-1}) in the same range of magnitude as commercial iron oxide contrast agents such as Endorem® or Sinerem®.[71-72] Noteworthy, by combining MIL-100(Fe) NPs with 20 wt% of USPIO, the r_2 value of ~93 mM^{-1} s^{-1}

is about 30 times higher than that of MIL-100(Fe) and comparable to the commercial Endorem® and Sinerem® (Table S4). Notably, the r_2 value of USPIO(10)@MIL (*i.e.*, 38 mM^{-1} s^{-1}) is lower, due to the smaller amount of γ-Fe_2O_3 relative to the total iron concentration. These results show that the relaxometric properties of these nano-objects can be finely tuned upon varying the maghemite content. With the exception of Fe_3O_4-ZIF-8,[73] Fe_3O_4@C@MIL-100(Fe)[41] and MIL-101(Fe)-NH_2/USPIO,[74] the r_2 value is higher to the previously reported magnetic based MOF NPs or comparable to the surface decorated MIL/USPIO-cit(10).[18] Note also that Fe_3O_4@C@MIL-100(Fe) NPs exhibit a poor crystallinity and low porosity (S_{BET} = 109 m^2 g^{-1}), suggesting that the MOF exhibits an amorphous character. Moreover, the low stability of ZIF-8 NPs in water and aqueous phosphate solutions is a critical issue for the biomedical application of Fe_3O_4-ZIF-8 due to detrimental Zn^{2+} ion burst release or toxicity effects. The high relaxivity of USPIO(20)@MIL is certainly related to the magnetic properties of USPIO(20)@MIL since the relaxivity rate (r_2) of a T_2-MRI contrast agent is proportional to the square of the saturation magnetization (M_{sat}). As shown by vibrating sample magnetometry (VSM) (see SI for experimental details and Figure S36), the USPIO(20)@MIL nano-objects present a superparamagnetic behaviour characteristic of maghemite NPs. The magnetization curve of USPIO(20)@MIL was fitted by the Langevin model, considering maghemite NPs with a diameter of ~6 nm. Noteworthy, as shown in Table S5, the values of saturation magnetization of USPIO(20)@MIL and USPIO(10)@MIL (*i.e.*, 68 and 71 Am^2 kg^{-1} respectively) are fully consistent with those previously reported for USPIO. Interestingly, these values are significantly higher than those of most porous magnetic MOFs-based composites previously reported (see Table S5). Encouraged by their good relaxometric properties, T_2-weighted MRI of USPIO(20)@MIL was further evaluated *in vivo*. 90 µL of USPIO(20)@MIL at 10 mg mL^{-1} in PBS/BSA (5.4% w/v) medium corresponding to a concentration of ~250 µmol Fe kg^{-1}, was injected in the mouse tail vein and MR images were recorded before and just after USPIO(20)@MIL injection. In Figure 6c, an homogenous decrease of signal was observed in the mouse liver and spleen right after the contrast agent injection on the T2*-weighted images. For example, in the liver, the contrast agent generated a 56% decrease of signal-to-noise ratio ($\Delta SNR = SNR_{before} - SNR_{after} = 19.4 - 8.5 = 10.9$) due to the high T_2* effect. These results demonstrate that USPIO(20)@MIL can be used as a highly performing T_2 MRI contrast agent.

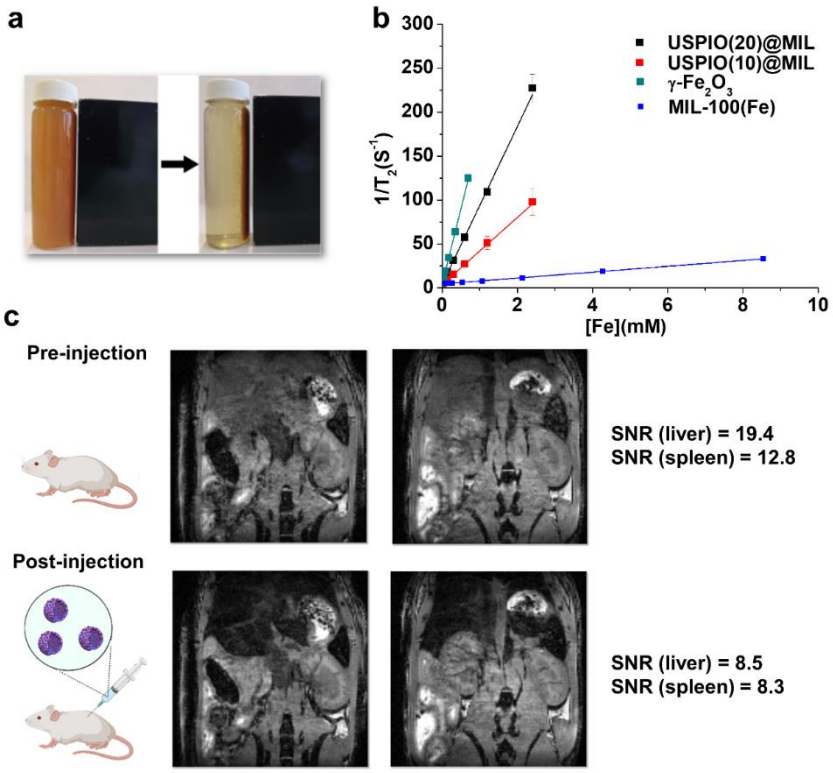

Figure 6. a) photograph showing the separation of USPIO(20)@MIL from aqueous solution under an external magnetic field; b) Transverse relaxation rates ($1/T_2$, s^{-1}) as a function of iron concentration for γ-Fe_2O_3, MIL-100(Fe) and USPIO(X)@MIL (X=10 & 20) prepared in PBS/BSA solution at pH 7.5; c) T2*-weighted gradient echo images of the mouse abdomen before and after injection of contrast agent USPIO(20)@MIL.

2.6 Conclusion

In conclusion, we report the design of a novel hybrid nano-object coupling MIL-100(Fe) and maghemite NPs that was prepared through a direct cost-effective and reliable green protocol at RT. According to TEM and electron tomography, the hierarchical nanostructure of these nano-objects consists of maghemite NPs located either at the surface or embedded in the core of MIL-100(Fe) NPs. We have shown that the synergistic combination of the physico-chemical of both NPs associated to the encapsulation of two complementary drugs (Dox and MTX) could be fully exploited to create a multifunctional theranostic platform for the therapy of inflammatory diseases. This nanovector exhibits an excellent colloidal stability under simulated intravenous conditions, low cytotoxicity and an extremely high Dox and MTX loading efficacy. Their pH- and GSH responsive Dox/MTX release properties are mainly driven by an interplay between drug/MOF interactions and the biodegradability of MOFs, as revealed by the complete characterization of their internalization, intracellular distribution and fate in macrophages by CLSM and TEM. Remarkably, USPIO(20)@MIL/Dox and

USPIO(20)@MIL/MTX nanovectors present an excellent anti-inflammatory efficacy ascribed to their high toxicity directed towards activated macrophages and their ability to reduce the secretion of inflammatory cytokines. Moreover, USPIO(20)@MIL/Dox exhibits a high anti-tumoral activity associated to the progressive delivery of its encapsulated Dox cargo to the cancer cells. Therefore, USPIO(20)@MIL/Dox can be considered as a dual-targeting therapeutic strategy, inhibiting tumor growth and reducing the inflammation. Finally the USPIO(20)@MIL nanovectors exhibits a superparamagnetic behavior inherent in the presence of maghemite NPs and thus can be used as T_2 MRI contrast agents for theranostics.

2.7 Experimental section

Chemicals. All chemicals were used as received without any further purification: Iron(III) chloride hexahydrate ($FeCl_3 \cdot 6H_2O$; 98%), iron(II) chloride tetrahydrate ($FeCl_2 \cdot 4H_2O$; 98%), iron(III) nitrate nonahydrate ($Fe(NO_3)_3 \cdot 9H_2O$; 98%) and L-Glutathione reduced (GSH, >98%) were purchased from Alfa Aesar. 1,3,5-benzenetricarboxylic acid (1,3,5-BTC; 95%), Lipopolysaccharides (LPS), 2′,7′-Dichlorofluorescin Diacetate (DCF-DA), glutaraldehyde solution 25% and sodium cacodylate trihydrate (≥ 98%) were purchased from Sigma Aldrich. Methotrexate (MTX, >98%) was purchased from TCI. Doxorubicin HCl was purchased from Carbosynth (UK). Cell counting kit-8 (CCK-8), Calcein-AM solution were purchased from Dojindo. Propidium Iodide (PI) was purchased from Invitrogen. Hoechst33342 were purchased from Abcam. Proinflammatory cytokines (IL-1β, IL-6 and TNF-α) Duoset Elisa Kits were purchased from R&D Systems. Physiological media were prepared with phosphate buffered saline (PBS, Sigma Aldrich) and bovine serum albumin (BSA, Sigma Aldrich). Ultrapure water was obtained with the Milli Q purification system (Merck Millipore, France).

Characterization techniques. Powder X-ray diffraction patterns (PXRD) were collected with a Siemens D5000 diffractometer (θ-2θ) using Cu Kα radiation (λ = 1.5418 Å). For USPIO@MIL NPs Refinements were carried out with the TOPAS program. Profile fittings and Rietveld refinement in the case of the maghemite for USPIO(10)@MIL sample were performed using fundamental parameters approach to model the instrument function and determine crystallite size. Thermogravimetric analyses (TGA) were performed on a Perkins Elmer SDA 6000 apparatus. Samples were heated up to 600 °C

with a heating rate of 5 °C min^{-1} under an oxygen atmosphere. Transmission IR spectra were recorded in the 400-4000 cm^{-1} range, with 4 cm^{-1} resolution on a Nicolet Nexus spectrometer. N_2 sorption isotherms were obtained at 77 K using a Belsorp Mini (Bel, Japan). Prior to the analysis, approximately 30 mg of samples were evacuated for 5 h at 120°C under primary vacuum. Brunauer-Emmett-Teller (BET) surface and pore volume were estimated at a relative pressure lower than 0.25. TEM observations were performed using a Zeiss EM902 Transmission Electron Microscope (Plateforme de microscopie et d'imagerie de l'INRA, Jouy en Josas, France). TEM images were also recorded on a JEOL 2100F microscope operating at 200 kV, equipped with a Schottky emission gun, a high resolution UHR pole piece and a Gatan US4000 CCD camera. High-angle annular dark field imaging in scanning transmission electron microscope mode (STEM-HAADF) experiments were performed on a JEOL JEM 2100F microscope installed at IMPMC (Paris, France), operating at 200 kV, equipped with a field emission gun, a JEOL detector with an ultrathin window allowing detection of light elements and a scanning TEM (STEM) device, which allows Z-contrast imaging in HAADF mode. Samples were prepared by deposition of one droplet of colloidal suspensions onto a carbon-coated copper grid and left to dry in air. Electron tomography analysis was carried out in the cryo-mode using a JEOL 2100 FEG S/TEM microscope operated at 200 kV equipped with a spherical aberration corrector. For the acquisition of high-angular annular dark field (HAADF) images in the scanning TEM (STEM) mode, we used a spot size of 0.13 nm, a current density of 140 pA, a camera focal length of 8 cm, corresponding to inner and outer diameters of the annular detector of about 73 and 194 mrad. The acquisition of tilt series was performed using the tomography plug-in of the Digital Micrograph software, which controls the specimen tilt step by step, the defocusing and the specimen drift. The HAADF and BF tilt series in the STEM were acquired simultaneously by using the ADF and BF detectors and tilting the specimen in the angular range of ± 60° using an increment of 2° in the equal mode, giving thus a total of 61 images in each series. The as-obtained images were spatially aligned by cross correlating consecutive images using IMOD software. For the volume calculation, we used the algebraic reconstruction technique (ART) implemented in the TomoJ plugin working in the ImageJ software. Finally, the visualization and the analysis of the volumes were carried out using the displaying capabilities and the isosurface rendering method in the Slicer software. The particle diameter of γ-Fe_2O_3, MIL-100(Fe) and USPIO(20)@MIL was measured by Dynamic Light Scattering (DLS) on a Zetasizer NanoZS (Malvern Instruments). NPs (~ 0.1 - 0.2 mg mL^{-1}) were dispersed at RT

in aqueous solutions by using an ultrasound tip (Digital Sonifer 450, Branson) during 1 minute at 10% amplitude. Their surface charge was also evaluated by recording ζ-potential with the Zetasizer NanoZS.

Synthesis of MIL-100(Fe) Nanoparticles. MIL-100(Fe) NPs were prepared according to the patent.[33] 0.72 g of $Fe(NO_3)_3 \cdot 9H_2O$ (1.78 mmol) was dissolved in 90 mL of distilled water. 0.25 g of trimesic acid (1.19 mmol) was then added to this solution and the suspension was allowed to stir for 48 h at room temperature. The mixture was then centrifuged at 14500 rpm for 10 min. An orange solid was thus obtained. The as-synthesized MIL-100(Fe) NPs were then washed by two centrifugation/redispersion cycles in water followed by two centrifugation/redispersion cycles in absolute ethanol. The MIL-100(Fe) NPs were stored in EtOH and could be redispersed in water before use.

Synthesis of Maghemite (γ-Fe_2O_3) Nanoparticles (USPIO). Maghemite NPs were synthesized according to reported protocols.[36-37] 20 mL of sodium hydroxide (15 mol L^{-1}) were mixed under vigorous stirring with an aqueous solution containing 20 mL of $FeCl_3 \cdot 6H_2O$ (1 mol L^{-1}) and 5 mL of $FeCl_2 \cdot 4H_2O$ (2 mol L^{-1}) in HCl (2 mol L^{-1}). A black precipitate was obtained by magnetic settling and washed with 20 mL of water. The precipitate was then stirred for 15 min in 30 mL of HNO_3 (2 mol L^{-1}). For a complete oxidation of magnetite to maghemite, the precipitate was then mixed with 10 mL of $Fe(NO_3)_3 \cdot 9H_2O$ (0.35 mol L^{-1}) at 80 °C for 30 min. The precipitate was finally peptised in 30 mL of HNO_3 (2 mol L^{-1}) for 10 minutes before being washed 3 times with 10 mL of acetone. The colloidal solution of γ-Fe_2O_3 was stored in 20 mL of water with a final pH between 2 and 3 and a weight concentration around 65 g L^{-1}.

Synthesis of USPIO@MIL Nanoparticles. The USPIO@MIL nano-objects were prepared by adding under stirring a colloidal solution containing 70 or 30 mg of maghemite NPs to an aqueous solution of $Fe(NO_3)_3 \cdot 9H_2O$ (70 mL, 0.72 g). The suspension was then sonicated for 2 minutes at 20% amplitude. 250 mg of trimesic acid (1.2 mmol) were then added and the mixture was stirred for 24 h at RT. The brown precipitate was isolated by magnetic settling and then centrifuged at 14500 rpm for 10 min. The solid was then washed by one centrifugation/redispersion cycle in water followed by three centrifugation/redispersion cycles in absolute ethanol. The USPIO@MIL NPs were stored in EtOH and could be redispersed in water before use. By using 70 or 30 mg of γ-Fe_2O_3 NP during the synthesis,

it was possible to obtain USPIO@MIL nano-objects with 20 or 10 wt% of γ-Fe_2O_3 content, respectively.

Colloidal stability of MIL-100(Fe) and USPIO@MIL nano-objects. MIL-100(Fe) and USPIO(20)@MIL in EtOH were centrifuged and re-dispersed at a concentration of 200 μg mL^{-1} in different media: Milli Q water, 0.9% NaCl aqueous solution (Saline), PBS (pH7.4, 10 mmol·L^{-1}), PBS solution with 5.4% w/v bovine serum albumin (BSA), Dulbecco's Modified Eagle Medium (DMEM) and 90% DMEM + 10% fetal bovine serum (FBS). After sonication (10% amplitude for 30 seconds), the samples' hydrodynamic diameters were recorded over 3 experimental replicates. The Zeta potentials of MIL-100(Fe) and USPIO(20)@MIL in Mill Q water were also recorded.

Furthermore, the long term colloidal stability of USPIO(20)@MIL was studied by measuring the evolution of their diameter with time at 37 °C, in three different media to mimic the blood environment, namely Milli Q water, a pure neutral PBS solution and a PBS solution (10 mmol·L^{-1}) with 5.4% w/v BSA. Values of diameter and PdI were recorded over a period of 24h (289 runs, 10 measurements per run and 30 seconds per measurement).

Cellular uptake study by confocal laser scanning microscopy and ICP-MS. The cellular uptake of the USPIO(20)@MIL was evaluated by CLSM and ICP-MS on RAW 264.7 macrophages. Cells were seeded into 6-well plate (2×10^5 cells/well) and maintained overnight. The medium was then replaced with 2 mL of complete medium containing USPIO(20)@MIL or USPIO(20)@MIL/RhB (50 μg mL^{-1}), followed by an incubation at 37°C for 1 h, 2 h, 4 h, 6 h and 8 h. As for CLSM, after the removal of the MOF containing media, RAW 264.7 cells were washed with PBS for three times. Then the as prepared samples were imaged by CLSM (ZEISS LSM780, Germany). The laser excitation wavelength is 543 nm. For quantification of the cellular uptake of the USPIO(20)@MIL in RAW 264.7 cells by ICP-MS, after incubation, cells were washed with PBS (pH 7.4) and then trypsinized, harvested by centrifugation, washed again with PBS. Subsequently, the pellet was treated by concentrated nitric acid overnight before dilution with 2% nitric acid for ICP MS (Fe) test.

TEM of cells. All chemicals were used as received without any further purification: glutaraldehyde solution 25% (Sigma-Aldrich), sodium cacodylate trihydrate (Sigma-Aldrich, ≥ 98%). RAW 264.7 cells were seeded into a 6-well plate at 2×10^5 cells per well in 2 mL of complete medium, and cultured

in a 5% CO_2 atmosphere at 37 °C overnight. The culture medium was then replaced with 2 mL of complete medium containing USPIO(20)@MIL at a concentration of 50 μg mL^{-1} for 30 min, 4 h, 8 h, 12 h and 24 h and after washing with PBS were maintained in 2% FBS supplemented DMEM medium for 1, 2, 5, and 8 days at 37 °C. After certain intervals, the medium was removed and cells were firstly washed twice with PBS and once with 0.2 M Na cacodylate buffer pH 7.2, and then fixed with 2% glutaraldehyde in 0.1 M Na cacodylate buffer pH 7.2, for 1 hour at room temperature. Samples were then contrasted with Oolong Tea Extract (OTE) 0.5% in cacodylate buffer, postfixed with 1% osmium tetroxide containing 1.5% potassium cyanoferrate, gradually dehydrated in ethanol (30% to 100%) and substituted gradually in mix of ethanol-epon and embedded in Epon. (Delta microscopie – France). Thin sections (80 nm) were collected onto 200 mesh copper grids. Grids were examined with Hitachi HT7700 electron microscope operated at 80kV (Elexience – France), and images were acquired with a charge-coupled device camera (AMT).

Encapsulation of methotrexate in USPIO(20)@MIL. Firstly, 30 mg of MTX was totally dissolved in 30 mL 10 mM HCl solution with foil wrap, after stirring at 200 rpm under 55ºC in the incubator for 1 hour. Then 30 mg of MIL-100(Fe) or USPIO(20)@MIL was dispersed in the prepared MTX solution (1 mg mL^{-1}). Other weight ratios (1:0.25, 1:0.5 and 1:2) of MOFs to MTX were also studied. The resulting suspension was stirred at 200 rpm under 37ºC overnight. The MTX loaded MIL-100(Fe) and USPIO(20)@MIL nano-objects (*i.e.*, MIL-100(Fe)/MTX or USPIO(20)@MIL/MTX NPs) were washed with 10 mM HCl three times. The loading capacity of MIL-100(Fe) or USPIO(20)@MIL was determined by UV-Vis spectrophotometer at 306 nm (maximum absorbance wavelength of MTX) and HPLC. The mobile phase of HPLC is 25:75 v/v methanol: ammonium acetate buffer (0.05 $mol \cdot L^{-1}$, pH 6.0). A flow rate of 1 $mL \cdot min^{-1}$ and a sample injection volume of 25 μL were used during all analyses. Then, the present of loading capacity (LC) or entrapment efficiency (EE) was calculated using the following equation:

LC = (Mass of total drug - Mass of free drug) / Mass of total MOF
EE = (Mass of total drug - Mass of free drug) / Mass of total drug

MTX release of USPIO(20)@MIL/MTX. Typically, after the loading of MTX (MOF : MTX = 1:1), USPIO(20)@MIL/MTX HCl solution (1 mg mL^{-1}) was divided into 1.5 mL aliquots and after an extra centrifuge/redisperse step, the cumulative release behavior of MTX from USPIO(20)@MIL/MTX (1

mg mL^{-1}) was investigated in PBS (pH 5.1 and pH 7.4) with or without GSH for different times (0.5 h, 1 h, 4 h, 8 h, 24 h, 48 h and 72 h). At different time intervals, the suspension of USPIO(20)@MIL/MTX was centrifuged (13400 rpm, 15 min) and 0.5 mL of the release medium was replaced by the same volume of fresh medium. The concentration of released MTX and ligand BTC (in PBS) was measured by HPLC. The release ferric ions was investigated by ICP-MS. Similarly, the release of MTX in DMEM and DMEM + 10% FBS from USPIO(20)@MIL/MTX also was monitored by HPLC.

Encapsulation of doxorubicin in USPIO(20)@MIL. 5 mg of USPIO(20)@MIL was dispersed in 1.5 mL of Dox solution (10 mg mL^{-1}, Milli-Q water). The resulting suspension was stirred at 200 rpm at 37°C for 24 h. The Dox loaded USPIO(20)@MIL nano-objects (*i.e.*, USPIO(20)@MIL/Dox) were washed with Mill-Q water three times. The loading capacity of USPIO(20)@MIL/Dox was determined by UV-Vis spectrophotometer at 480 nm (maximum absorbance wavelength of Dox).

Doxorubicin release of USPIO(20)@MIL/Dox. The cumulative release behaviour of Dox from USPIO(20)@MIL/Dox (1mg mL^{-1}, 1.5 mL) was investigated in PBS (pH 5.1 and pH 7.4) with or without GSH for different times (0.5 h, 1 h, 4 h, 8 h, 24 h, 48 h and 72 h). At different time intervals, the suspension of USPIO(20)@MIL/Dox was centrifuged (13400 rpm, 15 min) and 0.5 mL of the release medium was replaced by the same volume of fresh medium. The concentration of released Dox (in PBS) was measured by UV-Vis spectrophotometer. The release of ligand BTC and ferric ions were investigated by HPLC and ICP-MS, respectively. Similarly, the release of Dox from MIL-100(Fe) and USPIO(20)@MIL/Dox was also studied in phenol red free DMEM (for UV-Vis detection).

Cell Culture. RAW 264.7 macrophage cells and Hela cells were cultured in high glucose Dulbecco's Modified Eagle Medium (DMEM) containing 10% FBS and 1% penicillin and streptomycin at 37°C in a humidified 5% CO_2 atmosphere.

***In vitro* cytotoxicity assay of USPIO(20)@MIL and MIL-100(Fe).** Hela cells in logarithmic phase were rinsed twice in PBS and then treated with 1 mL Trypsin to form 10^5/mL cells suspension. 100 µL Hela cells suspension were seeded in 96-well plates (10^4/well) and incubated overnight. Then, MIL-100(Fe) or USPIO(20)@MIL in DMEM/FBS at different concentrations (10, 20, 50, 100 and 200 µg mL^{-1}) was added to each well, incubated for 12 or 24 hours at 37 °C and under 5% of CO_2. 10 µL

CCK-8/well were added to the cells and after incubation for further 2 hours, 96-well plate was transferred into a microplate reader (excitation at 450 nm) for UV-Vis absorbance analysis. The resulting UV-Vis absorbance values were normalized to the UV-Vis absorbance signals value of the control groups. All the experimental points were assessed triple, with error bars representing standard error of the mean. The cell cytotoxicity of MTX was further studied on RAW 264.7 cells, following the same protocol.

Cell survival rate (%) = $[(A_{\text{Experimental group}} - A_{\text{blank group}}) / (A_{\text{Control group}} - A_{\text{blank group}})] \times 100\%$

***In vitro* cytotoxicity assay of USPIO(20)@MIL/MTX and USPIO(20)@MIL/Dox.** RAW 264.7 cells were seeded into a 96-well plate at a density of 1×10^4 cells per well and allowed to adhere overnight. The *in vitro* cytotoxicity of RAW 264.7 cells after incubation for 24 h with MIL-100(Fe) (40 μg mL^{-1}), USPIO(20)@MIL (50 μg mL^{-1}), USPIO(20)@MIL/MTX with equivalent free MTX at 23 μg mL^{-1} and USPIO(20)@MIL/Dox with equivalent free Dox at 25 μg mL^{-1} was evaluated as previously described as before. Meanwhile, different concentrations of USPIO(20)@MIL/Dox (5, 10, 20, 50 and 100 μg mL^{-1}) and equivalent free Dox (2.5, 5, 10, 25 and 50 μg mL^{-1}) were also studied on RAW 264.7 cells. To visualize the toxicity effects to normal RAW 264.7 cells, the staining of Live & Dead cells was performed by calcein AM/PI co-staining and observed at 488 and 543 nm. Calcein AM is a hydrophobic compound, which passes easily through cell membranes into live cells and is used for cell viability assays and PI is membrane impermeant and generally excluded from viable cells, which is commonly used for identifying dead cells. First, RAW 264.7 cells were seeded into 35 mm confocal dishes at a density of 1×10^4 cells per dish and after the treatment of different formula ([MIL-100(Fe)] = 40 μg mL^{-1}, [USPIO(20)@MIL] = 50 μg mL^{-1}, [Dox] = 25 μg mL^{-1}, [USPIO(20)@MIL/Dox] = 50 μg mL^{-1}, [MTX] = 23 μg mL^{-1} and [USPIO(20)@MIL/MTX] = 50 μg mL^{-1}). The cells were stained by AM/PI (dilution ×1000) containing DMEM for 15 min and then washed with PBS for confocal imaging.

Anti-inflammatory capacity of USPIO(20)@MIL/MTX and USPIO(20)@MIL/Dox. To investigate the anti-inflammatory capacity of MTX or Dox loaded USPIO(20)@MIL, RAW 264.7 cells were first activated by lipopolysaccharide (LPS). To verify the successful construction of inflammatory model, intracellular ROS production was detected by dichlorofluorescein diacetate (DCF-DA) probe. DCF-DA could be oxidized to green fluorescent-dichlorofluorescein by intracellular

ROS. Thus, the fluorescence intensity could reflect the levels of reactive oxygen species (ROS) in the cells. RAW 264.7 cells were seeded at a density of 1×10^5 cells/mL into a confocal dish and incubated at 37 °C under 5% CO_2 overnight. Then, the cells were incubated with LPS at a concentration of 100 ng mL^{-1} for 48 h. The media was replaced with 2 mL serum-free medium containing DCF-DA (10 μM) and cultured for 30 min in dark. The nucleus was stained by Hoechst. After washing with PBS, a confocal laser microscope was used for ROS imaging at an excitation wavelength of 488 nm.

After this activation step, the DMEM medium was replaced by a fresh DMEM medium containing MIL-100 (Fe), USPIO(20)@MIL, and USPIO(20)@MIL/MTX at a concentration of 40, 50 and 50 μg mL^{-1}, respectively. For comparison, activated RAW 264.7 cells were exposed to free MTX at a concentration of 23 μg mL^{-1}. After 24 h incubation, 10 μL CCK-8 was added to each well and after incubation for further 2 hours, the 96-well plate was transferred into a microplate reader (excitation at 450 nm) for UV-Vis absorbance analysis. Then, the anti-inflammatory capacity of Dox loaded USPIO(20)@MIL was also investigated. After the same activation step, the DMEM medium was replaced by a fresh DMEM medium containing USPIO(20)@MIL and USPIO(20)@MIL/Dox at a concentration of 5, 20 or 50 μg mL^{-1}. For comparison, activated RAW 264.7 cells were exposed to free Dox at a concentration of 25 μg mL^{-1}. To visualize the inhibition effects of activated RAW 264.7 cells, RAW 264.7 cells were seeded into confocal dishes, followed by similar treatment for AM/PI staining.

Evaluation of the concentrations of pro-inflammatory cytokines by enzyme-linked immunosorbent assay (ELISA) assays. In comparison to previous experiments, the concentrations of formulations were 10 times lower in order to maintain a cell viability higher than 80%. RAW 264.7 cells were first seeded into 12-well plate at a density of 1×10^5 cells/mL and after the step of LPS activation, cells were further treated with different formulations ([MIL-100(Fe)] = 4 μg mL^{-1}, [USPIO(20)@MIL] = 5 μg mL^{-1}, [Dox] = 0.25 μg mL^{-1} (100 times lower), [USPIO(20)@MIL/Dox] = 5 μg mL^{-1}, [MTX] = 2.3 μg mL^{-1}, [USPIO(20)@MIL/MTX] = 5 μg mL^{-1}) for 24 h, and each group was prepared in triplicate. Then, the supernatant was collected and centrifuged to remove cells pellets and materials for next step detection. Briefly, mouse tumor necrosis factor alpha (TNF-α) DY410 DuoSet® ELISA, R&D Systems; mouse Interleukin 1 beta (IL-1β) DY401 DuoSet® ELISA, R&D Systems; mouse interleukin 6 (IL-6) DY406 DuoSet ELISA, R&D Systems were used to access TNF-α, IL-1β, and IL-6 concentrations from cell culture media samples by the standard ELISA technique,

namely sandwich ELISAs (Capture antibody + sample or standard + Detection antibody). Following the manufacturer's instructions, the samples were finally diluted by five times for ELISA assays based on absorbance values of the recombinant mouse standard.

Cytotoxicity of USPIO(20)@MIL/Dox. First, the cellular uptake of the USPIO(20)@MIL/Dox was evaluated by CLSM on Hela cells. Cells were seeded into confocal dishes (2×10^5 cells per dish) and maintained overnight. The medium was then replaced with 2 mL of complete medium containing USPIO(20)@MIL/Dox (50 μg mL^{-1}), followed by an incubation at 37 ºC for 1 h, 2 h, 4 h, 6 h and 8 h. Then cells were washed with PBS for three times to remove the residual media and stained by Hoechst (dilution ×5000) for 15 min. Then the as prepared samples were imaged by CLSM (ZEISS LSM780, Germany). The laser excitation wavelength of Hoechst and Dox was 405 nm and 488 nm, respectively.

Hela cells were seeded into a 96-well plate at a density of 1×10^4 cells per well and allowed to adhere overnight. Then, different formula were added to each well, including control groups such as MIL-100(Fe) (40 μg mL^{-1}), USPIO(20)@MIL (50 μg mL^{-1}) and equivalent free Dox (25 μg mL^{-1}) as well as experimental groups USPIO(20)@MIL/Dox at a centration of 50 μg mL^{-1}. After 24 h, 10 μL CCK-8 were added to each well and after incubation for further 2 hours, 96-well plate was transferred into a microplate reader (excitation at 450 nm) for UV-Vis absorbance analysis. Similarly, the therapeutic effects of the USPIO(20)@MIL/Dox was also evaluated through AM/PI staining by CLSM on Hela cells. Hela cells were seeded into 35 mm confocal dishes at a density of 1×10^4 cells per dish and after the treatment of different formula, the cells were stained by AM/PI (dilution ×1000) containing DMEM for 15 min and then washed with PBS for confocal imaging. The laser excitation wavelength of AM and PI was 488 nm and 543 nm, respectively.

Relaxivity Measurements. The T_2 relaxation time were measured in 4.7 T field strength. For each type of sample (USPIO(20)@MIL, USPIO(10)@MIL, MIL-100(Fe) and γ-Fe_2O_3), a stock solution was prepared in physiological conditions at pH 7.5 with PBS solution at 0.02 mol L^{-1} and 5.4% w/v BSA. Two-fold serial dilutions were then performed in the same medium and 7 aliquots of 800 μL were then prepared for T_2 measurements with iron concentrations ranging from ~ 8.56 to 0.01 mM. The Fe content was then determined using a NexloN 300X ICP-MS (PerkinElmer, Waltham, MA, U.S.A.). Samples were digested in 5 M HNO_3 solution for 24 h before their dilution in 2% HNO_3 for quantitative analysis. Standard calibration curve was performed using a series of Fe standard solution

(5 to 100 ppb). T_2 relaxation time experiments were performed on a 4.7 T Bruker Biospec system (Ettlingen, Germany) equipped with a birdcage resonator for radio-frequency excitation and signal reception. T_2 measurements were performed at 25°C with a CPMG (Carr–Purcell–Meiboon–Gill) imaging sequence (TR, 5000 or 10000 ms; inter echo-time, 5 ms; number of echo images, 256; FOV, 50 × 50 mm; matrix, 128 × 128; slice thickness, 2 mm). Relaxation data were analyzed with home-made software developed on Igor Pro (Wavemetrics, Lake Oswego, OR, USA). For each sample, the time evolutions of the magnetization were fitted according to mono-exponential functions. Relaxation rate R_2 (= $1/T_2$) was reported as a function of iron concentration to determine the relaxivity rate (r_2) of each sample.

***In vivo* MRI experiments.** All animal experimental protocols were approved by the Animal Care and Use Institutional Ethics Committee of Bordeaux, France (Approval No. 5012032-A). *In vivo* experiments were performed on a 7T Bruker Biospec System equipped with a gradient system capable of 660 mT/m maximum strength and 110-µs rise time. A volume resonator (86 mm inner diameter, active length = 70 mm) operating in quadrature mode was used for excitation, and a four-element phased array coil (total outer dimensions: 30 × 25 mm^2) was used for signal reception. Balb/C mice (23-25g) were purchased from a commercial breeder (Charles River, Paris, France). Mice were anesthetized with isoflurane (1.0-1.5% in air). The animals were positioned within the magnet with the liver placed at the center of the MR coil. A bolus of 90 µL of the sample was injected in the mouse tail vein while inside the magnet after the acquisition of pre-contrast T_2*-weighted and T_1-weighted acquisitions. The sample consists of USPIO(20)@MIL at 12 mg mL^{-1} in PBS-BSA media (PBS 0.01 mol/L + BSA 5.4% w/v). This corresponds to a concentration of ~250 µmol Fe/kg which is typically used for in vivo MRI by using USPIO contrast agents. A 3D gradient echo T_2*-weighted sequence was performed before (pre-contrast) and after (post-contrast) contrast agent injection with the following parameters: TE/TR = 2/12 ms; flip angle: 15°; Field-Of-View: 35 × 25 × 22 mm; Matrix: 128 × 128 × 64; spatial resolution: 273 × 195 × 343 µm. Number of excitations: 2; total acquisition time: 3 min 16 sec. A 3D T_1-weighted Ultra-Short Echo time (UTE) sequence was performed before and after contrast agent injection with the following parameters: TE/TR = 0.031/5 ms; flip angle: 30°; Field-Of-View: 35 × 35 × 35 mm; Matrix: 128 × 128 × 128; spatial resolution: 273 × 273 × 273 µm; number of spokes: 51360; total acquisition time: 4 min 16 sec.

Statistical Analysis. The results are represented as means ± SD. A minimum sample number of 3 was employed to ensure statistical power. Statistical analysis was performed by using two-tailed Student's t test for two groups. P values > 0.05 represented nonsignificance (N.S.). P values < 0.05 represented statistically significant, P values: *p < 0.05, **p < 0.01, ***p < 0.001 (unpaired, two-tailed t tests).

Associated content

Supporting Information

The supporting information is available free of charge. Additional characterization data of MIL-100(Fe), maghemite nanoparticles and USPIO@MIL nano-objects; the colloidal stability of MIL-100(Fe) and USPIO(20)@MIL nano-objects; the characterization of USPIO@MIL by ^{57}Fe Mössbauer spectroscopy; Synthesis of USPIO(20)@MIL/RhB; the analysis of cellular uptake of USPIO(20)@MIL nano-objects by RAW 264.7 macrophages; TEM of RAW 264.7 macrophages; Encapsulation and release of methotrexate from USPIO@MIL; the encapsulation and release of doxorubicin from USPIO@MIL; the analysis of the anti-inflammatory capacity of USPIO(20)@MIL/MTX and USPIO(20)@MIL/Dox; the analysis of the anti-cancer activity of USPIO(20)@MIL/Dox; the relaxometry and magnetic properties of USPIO(20)@MIL nano-objects.

Author information

Corresponding Author

*E-mail: christian.serre@ens.fr
*E-mail: nathalie.steunou@ens.psl.eu

Notes

The authors declare no competing financial interest.

Acknowledgment

H.Z. is grateful for the support from CSC grant (grant number 201808320434). The authors acknowledge Nicolas Tsapis (Institut Galien, Université paris-saclay) for fruitful discussions. This work has benefited from the facilities and expertise of MIMA2 MET – GABI, INRA, Agroparistech, 78352 Jouy-en-Josas, France. MIMA2: https://doi.org/10.15454/1.5572348210007727E12.

References

1. Brusini, R.; Varna, M.; Couvreur, P. Advanced Nanomedicines for the Treatment of Inflammatory Diseases. *Adv Drug Deliv Rev* **2020**, *157*, 161-178.
2. Molinaro, R.; Corbo, C.; Livingston, M.; Evangelopoulos, M.; Parodi, A.; Boada, C.; Agostini, M.; Tasciotti, E. Inflammation and Cancer: In Medio Stat Nano. *Curr Med Chem* **2018**, *25*, 4208-4223.
3. Hua, S.; de Matos, M. B. C.; Metselaar, J. M.; Storm, G. Current Trends and Challenges in the Clinical Translation of Nanoparticulate Nanomedicines: Pathways for Translational Development and Commercialization. *Front Pharmacol* **2018**, *9*, 790.
4. Horcajada, P.; Gref, R.; Baati, T.; Allan, P. K.; Maurin, G.; Couvreur, P.; Ferey, G.; Morris, R. E.; Serre, C. Metal-Organic Frameworks in Biomedicine. *Chem Rev* **2012**, *112*, 1232-1268.
5. Lu, K.; Aung, T.; Guo, N.; Weichselbaum, R.; Lin, W. Nanoscale Metal-Organic Frameworks for Therapeutic, Imaging, and Sensing Applications. *Adv Mater* **2018**, *30*, 1707634.
6. Wang, L.; Zheng, M.; Xie, Z. Nanoscale Metal-Organic Frameworks for Drug Delivery: A Conventional Platform with New Promise. *J Mater Chem B* **2018**, *6*, 707-717.
7. Wu, M. X.; Yang, Y. W. Metal-Organic Framework (MOF)-Based Drug/Cargo Delivery and Cancer Therapy. *Adv Mater* **2017**, *29*, 1606134.
8. Abánades Lázaro, I.; Forgan, R. S. Application of Zirconium MOFs in Drug Delivery and Biomedicine. *Coord Chem Rev* **2019**, *380*, 230-259.
9. Horcajada, P.; Chalati, T.; Serre, C.; Gillet, B.; Sebrie, C.; Baati, T.; Eubank, J. F.; Heurtaux, D.; Clayette, P.; Kreuz, C.; Chang, J. S.; Hwang, Y. K.; Marsaud, V.; Bories, P. N.; Cynober, L.; Gil, S.; Ferey, G.; Couvreur, P.; Gref, R. Porous Metal-Organic-Framework Nanoscale Carriers as a Potential Platform for Drug Delivery and Imaging. *Nat Mater* **2010**, *9*, 172-178.
10. Cai, W.; Chu, C. C.; Liu, G.; Wang, Y. X. Metal-Organic Framework-Based Nanomedicine Platforms for Drug Delivery and Molecular Imaging. *Small* **2015**, *11*, 4806-4822.
11. Demir Duman, F.; Forgan, R. S. Applications of Nanoscale Metal-Organic Frameworks as Imaging Agents in Biology and Medicine. *J Mater Chem B* **2021**, *9*, 3423-3449.
12. Osterrieth, J. W. M.; Fairen-Jimenez, D. Metal-Organic Framework Composites for Theragnostics and Drug Delivery Applications. *Biotechnol J* **2021**, *16*, 2000005.
13. Zhu, W.; Zhao, J.; Chen, Q.; Liu, Z. Nanoscale Metal-Organic Frameworks and Coordination Polymers as Theranostic Platforms for Cancer Treatment. *Coord Chem Rev* **2019**, *398*, 113009.
14. Zhao, H.; Serre, C.; Dumas, E.; Steunou, N. Chapter 18 - Functional MOFs As Theranostics. In *Metal-Organic Frameworks for Biomedical Applications*; Mozafari, M., Ed.; Elsevier, 2020; pp 397-423.
15. Peller, M.; Böll, K.; Zimpel, A.; Wuttke, S. Metal–Organic Framework Nanoparticles for Magnetic Resonance Imaging. *Inorg. Chem Front* **2018**, *5*, 1760-1779.
16. Zhang, H.; Shang, Y.; Li, Y. H.; Sun, S. K.; Yin, X. B. Smart Metal-Organic Frameworks-Based Nanoplatforms for Imaging-Guided Precise Chemotherapy. *ACS Appl Mater Interfaces* **2019**, *11*, 1886-1895.
17. Ettlinger, R.; Moreno, N.; Ziółkowska, N.; Ullrich, A.; Krug von Nidda, H. A.; Jirák, D.; Kerl, K.; Bunzen, H. *In Vitro* Studies of Fe_3O_4 -ZIF-8 Core-Shell Nanoparticles Designed as Potential Theragnostics. *Part Part Syst Charact* **2020**, *37*, 2000185.
18. Sene, S.; Marcos-Almaraz, M. T.; Menguy, N.; Scola, J.; Volatron, J.; Rouland, R.; Grenèche, J.-M.; Miraux, S.; Menet, C.; Guillou, N.; Gazeau, F.; Serre, C.; Horcajada, P.; Steunou, N. Maghemite-nanoMIL-100(Fe) Bimodal Nanovector as a Platform for Image-Guided Therapy. *Chem* **2017**, *3*, 303-322.

19. Liu, J.; Huang, J.; Zhang, L.; Lei, J. Multifunctional Metal-Organic Framework Heterostructures for Enhanced Cancer Therapy. *Chem Soc Rev* **2021**, *50*, 1188-1218.
20. Velásquez-Hernández, M. d. J.; Linares-Moreau, M.; Astria, E.; Carraro, F.; Alyami, M. Z.; Khashab, N. M.; Sumby, C. J.; Doonan, C. J.; Falcaro, P. Towards Applications of Bioentities@MOFs in Biomedicine. *Coord Chem Rev* **2021**, *429*, 213651.
21. Bellido, E.; Hidalgo, T.; Lozano, M. V.; Guillevic, M.; Simon-Vazquez, R.; Santander-Ortega, M. J.; Gonzalez-Fernandez, A.; Serre, C.; Alonso, M. J.; Horcajada, P. Heparin-Engineered Mesoporous Iron Metal-Organic Framework Nanoparticles: Toward Stealth Drug Nanocarriers. *Adv Healthcare Mater* **2015**, *4*, 1246-1257.
22. Agostoni, V.; Horcajada, P.; Noiray, M.; Malanga, M.; Aykac, A.; Jicsinszky, L.; Vargas-Berenguel, A.; Semiramoth, N.; Daoud-Mahammed, S.; Nicolas, V.; Martineau, C.; Taulelle, F.; Vigneron, J.; Etcheberry, A.; Serre, C.; Gref, R. A "Green" Strategy to Construct Non-Covalent, Stable and Bioactive Coatings on Porous MOF Nanoparticles. *Sci Rep* **2015**, *5 (1)*, 7925.
23. Orellana-Tavra, C.; Mercado, S. A.; Fairen-Jimenez, D. Endocytosis Mechanism of Nano Metal-Organic Frameworks for Drug Delivery. *Adv Healthcare Mater* **2016**, *5*, 2261-2270.
24. Guo, L.; Chen, Y.; Wang, T.; Yuan, Y.; Yang, Y.; Luo, X.; Hu, S.; Ding, J.; Zhou, W. Rational Design of Metal-Organic Frameworks to Deliver Methotrexate for Targeted Rheumatoid Arthritis Therapy. *J Control Release* **2021**, *330*, 119-131.
25. Li, Z.; Peng, Y.; Pang, X.; Tang, B. Potential Therapeutic Effects of Mg/HCOOH Metal Organic Framework on Relieving Osteoarthritis. *ChemMedChem* **2020**, *15*, 13-16.
26. Liu, Y.; Cheng, Y.; Zhang, H.; Zhou, M.; Yu, Y.; Lin, S.; Jiang, B.; Zhao, X.; Miao, L.; Wei, C. W.; Liu, Q.; Lin, Y. W.; Du, Y.; Butch, C. J.; Wei, H. Integrated Cascade Nanozyme Catalyzes *In Vivo* ROS Scavenging for Anti-Inflammatory Therapy. *Sci Adv* **2020**, *6*, eabb2695.
27. Wang, Y.; Ying, T.; Li, J.; Xu, Y.; Wang, R.; Ke, Q.; Shen, S. G. F.; Xu, H.; Lin, K. Hierarchical Micro/Nanofibrous Scaffolds Incorporated with Curcumin and Zinc Ion Eutectic Metal Organic Frameworks for Enhanced Diabetic Wound Healing *Via* Anti-Oxidant and Anti-Inflammatory Activities. *Chem Eng J* **2020**, *402*, 126273.
28. Yin, Y.; Yang, J.; Pan, Y.; Gao, Y.; Huang, L.; Luan, X.; Lin, Z.; Zhu, W.; Li, Y.; Song, Y. Mesopore to Macropore Transformation of Metal-Organic Framework for Drug Delivery in Inflammatory Bowel Disease. *Adv Healthcare Mater* **2021**, *10*, 2000973.
29. Zhou, F.; Mei, J.; Yang, S.; Han, X.; Li, H.; Yu, Z.; Qiao, H.; Tang, T. Modified ZIF-8 Nanoparticles Attenuate Osteoarthritis by Reprogramming the Metabolic Pathway of Synovial Macrophages. *ACS Appl Mater Interfaces* **2020**, *12*, 2009-2022.
30. Lai, X.; Wang, S.; Hu, M.; Sun, Y.; Chen, M.; Liu, M.; Li, G.; Deng, Y. Dual Targeting Single Arrow: Neutrophil-Targeted Sialic Acid-Modified Nanoplatform for Treating Comorbid Tumors and Rheumatoid Arthritis *Int J Pharm* **2021**, *607*, 121022.
31. Wang, S.; Lai, X.; Li, C.; Chen, M.; Hu, M.; Liu, X.; Song, Y.; Deng, Y., Sialic Acid-Conjugate Modified Doxorubicin Nanoplatform for Treating Neutrophil-Related Inflammation. *J Controlled Release* **2021**, *337*, 612-627.
32. D'Arrigo, G.; Navarro, G.; Di Meo, C.; Matricardi, P.; Torchilin, V. Gellan Gum Nanohydrogel Containing Anti-Inflammatory and Anti-Cancer Drugs: A Multi-Drug Delivery System for a Combination Therapy in Cancer Treatment. *Eur J Pharm Biopharm.* **2014**, *87*, 208-216.
33. Panchal, M.; Nouar, F.; Serre, C.; Benzaqui, M.; Sene, S.; Steunou, N.; Giménez Marqués, M. Low Temperature Process for the Synthesis of MOF Carboxylate Nanoparticles. US 20210277042, **2021**.

34. Dai, S.; Tissot, A.; Serre, C. Metal-Organic Frameworks: From Ambient Green Synthesis to Applications. *Bull Chem Soc Jpn* **2021**, *94*, 2623-2636.
35. Benzaqui, M.; Wahiduzzaman, M.; Zhao, H.; Hasan, M. R.; Steenhaut, T.; Saad, A.; Marrot, J.; Normand, P.; Grenèche, J.-M.; Heymans, N.; De Weireld, G.; Tissot, A.; Shepard, W.; Filinchuk, Y.; Hermans, S.; Carn, F.; Manlankowska, M.; Téllez, C.; Coronas, J.; Maurin, G.; Steunou, N.; Serre, C. A Robust Eco-Compatible Microporous Iron Coordination Polymer for CO_2 Capture. *J Mater Chem A* **2022**, *10*, 8535-8545.
36. Vayssieres, L.; Chaneac, C.; Tronc, E.; Jolivet, J. P. Size Tailoring of Magnetite Particles Formed by Aqueous Precipitation: An Example of Thermodynamic Stability of Nanometric Oxide Particles. *J Colloid Interface Sci* **1998**, *205*, 205-212.
37. Bee, A.; Massart, R.; Neveu, S. Synthesis of Very Fine Maghemite Particles. *J Magn Magn Mater* **1995**, *149*, 6-9.
38. García Márquez, A.; Demessence, A.; Platero-Prats, A. E.; Heurtaux, D.; Horcajada, P.; Serre, C.; Chang, J.-S.; Férey, G.; de la Peña-O'Shea, V. A.; Boissière, C.; Grosso, D.; Sanchez, C. Green Microwave Synthesis of MIL-100 (Al, Cr, Fe) Nanoparticles for Thin-Film Elaboration. *Eur. J Inorg Chem* **2012**, *2012*, 5165-5174.
39. Christodoulou, I.; Bourguignon, T.; Li, X.; Patriarche, G.; Serre, C.; Marlière, C.; Gref, R. Degradation Mechanism of Porous Metal-Organic Frameworks by *In Situ* Atomic Force Microscopy. *Nanomaterials* **2021**, *11*, 722.
40. Bellido, E.; Guillevic, M.; Hidalgo, T.; Santander-Ortega, M. J.; Serre, C.; Horcajada, P. Understanding the Colloidal Stability of the Mesoporous MIL-100(Fe) Nanoparticles in Physiological Media. *Langmuir* **2014**, *30*, 5911-5920.
41. Wang, D.; Zhou, J.; Chen, R.; Shi, R.; Xia, G.; Zhou, S.; Liu, Z.; Zhang, N.; Wang, H.; Guo, Z.; Chen, Q. Magnetically Guided Delivery of DHA and Fe Ions for Enhanced Cancer Therapy Based On pH-Responsive Degradation of DHA-Loaded Fe_3O_4@C@MIL-100(Fe) Nanoparticles. *Biomaterials* **2016**, *107*, 88-101.
42. Volatron, J.; Carn, F.; Kolosnjaj-Tabi, J.; Javed, Y.; Vuong, Q. L.; Gossuin, Y.; Menager, C.; Luciani, N.; Charron, G.; Hemadi, M.; Alloyeau, D.; Gazeau, F. Ferritin Protein Regulates the Degradation of Iron Oxide Nanoparticles. *Small* **2017**, *13*, 1602030.
43. Jayashree, S.; Nirekshana, K.; Guha, G.; Bhakta-Guha, D. Cancer Chemotherapeutics in Rheumatoid Arthritis: A Convoluted Connection. *Biomed Pharmacother* **2018**, *102*, 894-911.
44. Heo, R.; You, D. G.; Um, W.; Choi, K. Y.; Jeon, S.; Park, J. S.; Choi, Y.; Kwon, S.; Kim, K.; Kwon, I. C.; Jo, D. G.; Kang, Y. M.; Park, J. H. Dextran Sulfate Nanoparticles as a Theranostic Nanomedicine for Rheumatoid Arthritis. *Biomaterials* **2017**, *131*, 15-26.
45. Lin, W.; Cui, Y.; Yang, Y.; Hu, Q.; Qian, G. A Biocompatible Metal-Organic Framework As a pH and Temperature Dual-Responsive Drug Carrier. *Dalton Trans* **2018**, *47*, 15882-15887.
46. Rowe, M. D.; Thamm, D. H.; Kraft, S. L.; Boyes, S. G. Polymer-Modified Gadolinium Metal-Organic Framework Nanoparticles Used As Multifunctional Nanomedicines for the Targeted Imaging and Treatment of Cancer. *Biomacromolecules* **2009**, *10*, 983-993.
47. Lin, W.; Hu, Q.; Jiang, K.; Cui, Y.; Yang, Y.; Qian, G. A Porous Zn-Based Metal-Organic Framework for pH and Temperature Dual-Responsive Controlled Drug Release. *Microporous Mesoporous Mater* **2017**, *249*, 55-60.
48. Lin, W.; Hu, Q.; Jiang, K.; Yang, Y.; Yang, Y.; Cui, Y.; Qian, G. A Porphyrin-Based Metal-Organic Framework As a pH-Responsive Drug Carrier. *J Solid State Chem* **2016**, *237*, 307-312.

49. Kundu, T.; Mitra, S.; Patra, P.; Goswami, A.; Diaz Diaz, D.; Banerjee, R. Mechanical Downsizing of a Gadolinium(III)-Based Metal-Organic Framework for Anticancer Drug Delivery. *Chem Eur J* **2014**, *20*, 10514-10518.
50. Vasconcelos, I. B.; Silva, T. G. d.; Militão, G. C. G.; Soares, T. A.; Rodrigues, N. M.; Rodrigues, M. O.; Costa, N. B. d.; Freire, R. O.; Junior, S. A. Cytotoxicity and Slow Release of the Anti-Cancer Drug Doxorubicin from ZIF-8. *RSC Adv* **2012**, *2*, 9437-9442.
51. Wang, X. G.; Dong, Z. Y.; Cheng, H.; Wan, S. S.; Chen, W. H.; Zou, M. Z.; Huo, J. W.; Deng, H. X.; Zhang, X. Z. A Multifunctional Metal-Organic Framework Based Tumor Targeting Drug Delivery System for Cancer Therapy. *Nanoscale* **2015**, *7*, 16061-16070.
52. Zhao, X.; Liu, S.; Hu, C.; Liu, Y.; Pang, M.; Lin, J. Controllable Synthesis of Monodispersed NU-1000 Drug Carrier for Chemotherapy. *ACS Appl Bio Mater* **2019**, *2*, 4436-4441.
53. Wang, X.; Yang, B.; Xu, X.; Su, M.; Xi, M.; Yin, Z., Dextran Sulfate-Modified pH-Sensitive Layered Double Hydroxide Nanocomposites for Treatment of Rheumatoid Arthritis. *Drug Deliv. Transl Res* **2021**, *11*, 1096-1106.
54. Alam, M. M.; Han, H. S.; Sung, S.; Kang, J. H.; Sa, K. H.; Al Faruque, H.; Hong, J.; Nam, E. J.; Kim, I. S.; Park, J. H.; Kang, Y. M. Endogenous Inspired Biomineral-Installed Hyaluronan Nanoparticles as pH-responsive Carrier of Methotrexate for Rheumatoid Arthritis. *J Controlled Release* **2017**, *252*, 62-72.
55. Wang, Y.; Yan, J.; Wen, N.; Xiong, H.; Cai, S.; He, Q.; Hu, Y.; Peng, D.; Liu, Z.; Liu, Y. Metal-Organic Frameworks for Stimuli-Responsive Drug Delivery. *Biomaterials* **2020**, *230*, 119619.
56. Mateen, S.; Moin, S.; Zafar, A.; Khan, A. Q. Redox Signaling in Rheumatoid Arthritis and the Preventive Role of Polyphenols. *Clin Chim Acta* **2016**, *463*, 4-10.
57. Mura, S.; Nicolas, J.; Couvreur, P. Stimuli-Responsive Nanocarriers for Drug Delivery. *Nat Mater* **2013**, *12*, 991-1003.
58. Sun, Q.; Wang, Z.; Liu, B.; He, F.; Gai, S.; Yang, P.; Yang, D.; Li, C.; Lin, J. Recent Advances on Endogenous/Exogenous Stimuli-Triggered Nanoplatforms for Enhanced Chemodynamic Therapy. *Coord Chem Rev* **2022**, *451*, 214267.
59. Zhu, Y.; Xin, N.; Qiao, Z.; Chen, S.; Zeng, L.; Zhang, Y.; Wei, D.; Sun, J.; Fan, H. Bioactive MOFs Based Theranostic Agent for Highly Effective Combination of Multimodal Imaging and Chemo-Phototherapy. *Adv Healthcare Mater* **2020**, *9*, 2000205.
60. Anand, R.; Borghi, F.; Manoli, F.; Manet, I.; Agostoni, V.; Reschiglian, P.; Gref, R.; Monti, S. Host-Guest Interactions in Fe(III)-Trimesate MOF Nanoparticles Loaded with Doxorubicin. *J Phys Chem B* **2014**, *118*, 8532-8539.
61. Liu, J.; Wu, M.; Pan, Y.; Duan, Y.; Dong, Z.; Chao, Y.; Liu, Z.; Liu, B. Biodegradable Nanoscale Coordination Polymers for Targeted Tumor Combination Therapy with Oxidative Stress Amplification. *Adv Funct Mater* **2020**, *30*, 1908865.
62. Gambhir, J. K.; Lali, P.; Jain, A. K. Correlation Between Blood Antioxidant Levels and Lipid Peroxidation in Rheumatoid Arthritis. *Clin Biochem* **1997**, *30*, 351-355.
63. Yang, M.; Ding, J.; Feng, X.; Chang, F.; Wang, Y.; Gao, Z.; Zhuang, X.; Chen, X. Scavenger Receptor-Mediated Targeted Treatment of Collagen-Induced Arthritis by Dextran Sulfate-Methotrexate Prodrug. *Theranostics* **2017**, *7*, 97-105.
64. Yang, M.; Ding, J.; Zhang, Y.; Chang, F.; Wang, J.; Gao, Z.; Zhuang, X.; Chen, X. Activated Macrophage-Targeted Dextran-Methotrexate/Folate Conjugate Prevents Deterioration of Collagen-Induced Arthritis in Mice. *J Mater Chem B* **2016**, *4*, 2102-2113.

65. Chen, M.; Amerigos, J. C. K.; Su, Z.; Guissi, N. E. I.; Xiao, Y.; Zong, L.; Ping, Q. Folate Receptor-Targeting and Reactive Oxygen Species-Responsive Liposomal Formulation of Methotrexate for Treatment of Rheumatoid Arthritis. *Pharmaceutics* **2019**, *11*,582.
66. Ploetz, E.; Zimpel, A.; Cauda, V.; Bauer, D.; Lamb, D. C.; Haisch, C.; Zahler, S.; Vollmar, A. M.; Wuttke, S.; Engelke, H. Metal-Organic Framework Nanoparticles Induce Pyroptosis in Cells Controlled by the Extracellular pH. *Adv Mater* **2020**, *32*, 1907267.
67. Tang, D.; Kang, R.; Berghe, T. V.; Vandenabeele, P.; Kroemer, G. The Molecular Machinery of Regulated Cell Death. *Cell Res* **2019**, *29*, 347-364.
68. Nakamura, K.; Fujiwara, T.; Ishii, T.; Harigae, H.; Ogasawara, K. Cellular Labile Iron Activates NLRP3 Inflammasome. *Blood* **2014**, *124*, 2723-2723.
69. Orr, C.; Vieira-Sousa, E.; Boyle, D. L.; Buch, M. H.; Buckley, C. D.; Canete, J. D.; Catrina, A. I.; Choy, E. H. S.; Emery, P.; Fearon, U.; Filer, A.; Gerlag, D.; Humby, F.; Isaacs, J. D.; Just, S. A.; Lauwerys, B. R.; Le Goff, B.; Manzo, A.; McGarry, T.; McInnes, I. B.; *et al*. Synovial Tissue Research: A State-of-the-art Review. *Nat Rev Rheumatol* **2017,** *13*, 463-475.
70. Guo, B.; Villeneuve, D. J.; Hembruff, S. L.; Kirwan, A. F.; Blais, D. E.; Bonin, M.; Parissenti, A. M. Cross-Resistance Studies of Isogenic Drug-Resistant Breast Tumor Cell Lines Support Recent Clinical Evidence Suggesting That Sensitivity to Paclitaxel May Be Strongly Compromised by Prior Doxorubicin Exposure. *Breast Cancer Res Treat* **2004,** *85*, 31-51.
71. Vuong, Q. L.; Berret, J. F.; Fresnais, J.; Gossuin, Y.; Sandre, O. A Universal Scaling Law to Predict the Efficiency of Magnetic Nanoparticles As MRI T_2-Contrast Agents. *Adv. Healthcare Mater.* **2012,** *1*, 502-512.
72. Casula, M. F.; Floris, P.; Innocenti, C.; Lascialfari, A.; Marinone, M.; Corti, M.; Sperling, R. A.; Parak, W. J.; Sangregorio, C. Magnetic Resonance Imaging Contrast Agents Based on Iron Oxide Superparamagnetic Ferrofluids. *Chem Mater* **2010,** *22*, 1739-1748.
73. Lin, J.; Xin, P.; An, L.; Xu, Y.; Tao, C.; Tian, Q.; Zhou, Z.; Hu, B.; Yang, S. Fe_3O_4-ZIF-8 Assemblies As pH and Glutathione Responsive T_2-T_1 Switching Magnetic Resonance Imaging Contrast Agent for Sensitive Tumor Imaging *In Vivo*. *Chem Commun* **2019,** *55*, 478-481.
74. Xu, Z.; Chen, Y.; Chen, M.; Chen, W.; Cheng, Y., Assembly of USPIO/MOF Nanoparticles with High Proton Relaxation Rates for Ultrasensitive Magnetic Resonance Sensing. *J Mater Chem C* **2021,** *9*, 11915-11923.

TOC Figure

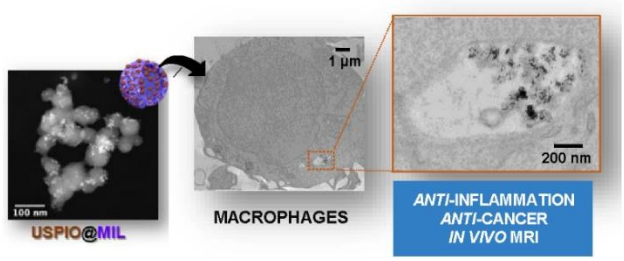

Supplementary Information

1-Characterization of MIL-100(Fe) Nanoparticles

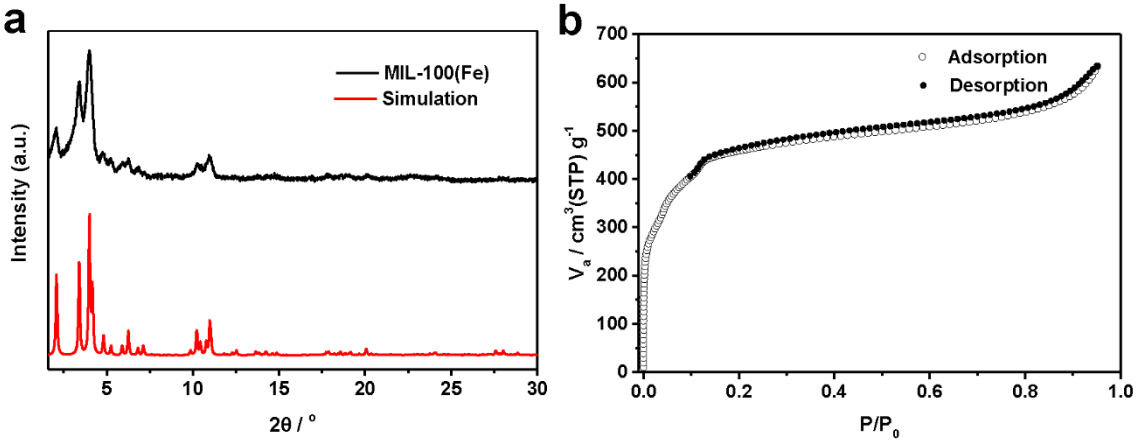

Figure S1. Characterizations of MIL-100(Fe): a) Powder X-Ray diffraction pattern measurements and (b) Nitrogen adsorption and desorption isotherms.

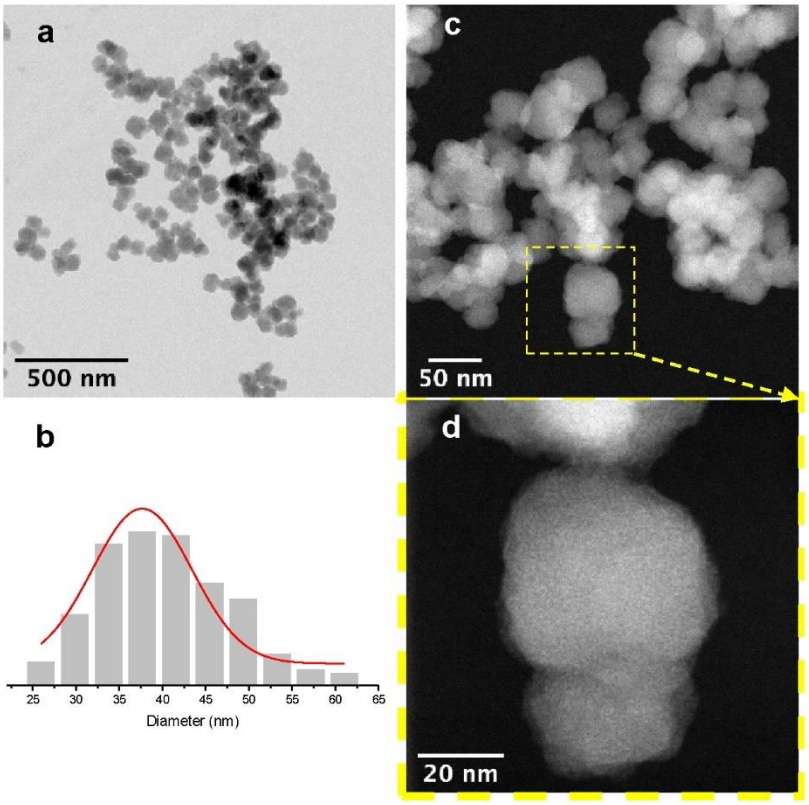

Figure S2. a) TEM bright field and (c-d) STEM-HAADF images of MIL-100(Fe) nanoparticles, (b) Size distribution of MIL-100(Fe) nanoparticles. (Diameter = 40 ± 8 nm)

The Bragg peaks of the powder X-ray diffraction (PXRD) patterns are consistent with the crystalline structure of MIL-100(Fe) NPs. N_2 adsorption/desorption isotherm is typical of MIL-100(Fe) with a

BET surface area of 1700 m^2 g^{-1}. TEM showed spheroidal MIL-100(Fe) NPs with a diameter of 40 nm.

2-Characterization of Maghemite (γ-Fe_2O_3) Nanoparticles (USPIO)

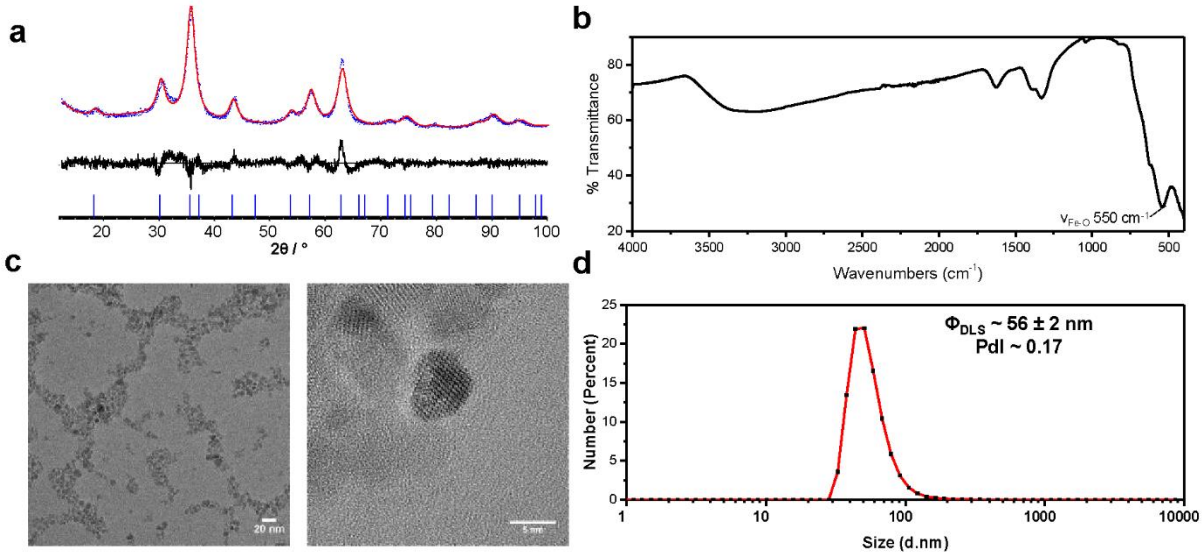

Figure S3. Characterizations of maghemites γ-Fe_2O_3: a) Rietveld-refinement on γ-Fe_2O_3 diffractogram; b) Infrared spectrum; c) HRTEM images; d) Size distribution by DLS.

X-Ray diffraction measurements showed that the nanoparticles present the typical spinel structure. The calculated lattice parameter, 0.8360 (3) nm, is close to that of maghemite (0.8346 nm, JCPDS file 39-1346). The mean size of the nanoparticles estimated from X-ray pattern (5.4 ± 0.1 nm) is also in agreement with the TEM observations (7 ± 3 nm). The IR band of γ-Fe_2O_3 at 550 cm^{-1} was assigned to stretching vibration of the Fe-O bond.

3-Characterization of USPIO(20)@MIL nano-objects

Determination of the USPIO content. After drying in vacuum overnight, ~5 mg USPIO(20)@MIL and MIL-100(Fe) were accurately weighed and then degraded with 1 mL concentrated HCl under 80°C for 12 h. After centrifugation (13400 rpm, 15min), Fe ion in the supernatant was separated from BTC (white precipitate) because BTC cannot be dissolved in concentrated HCl. The supernatant was diluted by 2% HNO_3 solution for ICP MS analysis (Fe ion) and the precipitate was then dissolved in 1 mL EtOH for HPLC test. The mobile phase of HPLC is 50:50 v/v methanol : phosphate buffer (0.02 M NaH_2PO_4 and Na_2HPO_4, pH 2.5, adjusted by H_3PO_4). A flow rate of 0.8 mL min^{-1} and a sample

injection volume of 50 μL were used during all analyses.

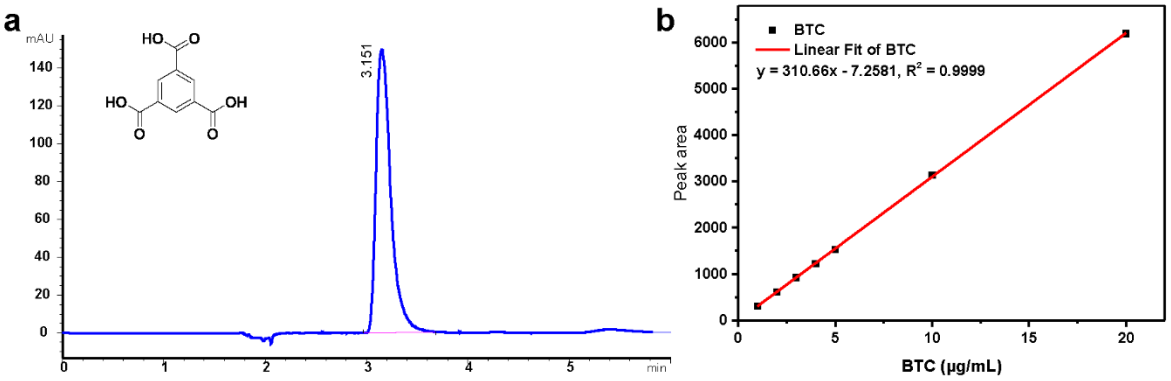

Figure S4. The high-performance liquid chromatography (HPLC) spectrum and calibration curve of BTC.

Table S1. The ratio of Fe ion (ICP-MS) to BTC (HPLC) of MIL-100(Fe) and USPIO(20)@MIL.

Sample	Weight (mg)	ICP-Fe (mg)	HPLC-BTC (mg)	Fe : BTC (mol/mol)	Fe_2O_3 wt%
USPIO(20)@MIL	5.2	1.42	1.85	2.896	20.5
MIL-100(Fe)	4.7	0.667	1.67	1.502	

In bare MIL-100(Fe), the ratio of Fe to BTC was close to 1.5, which was in consistent with the theoretical one. According to the calculation below, the weight ratio of γ-Fe_2O_3 in USPIO(20)@MIL was ~20%.

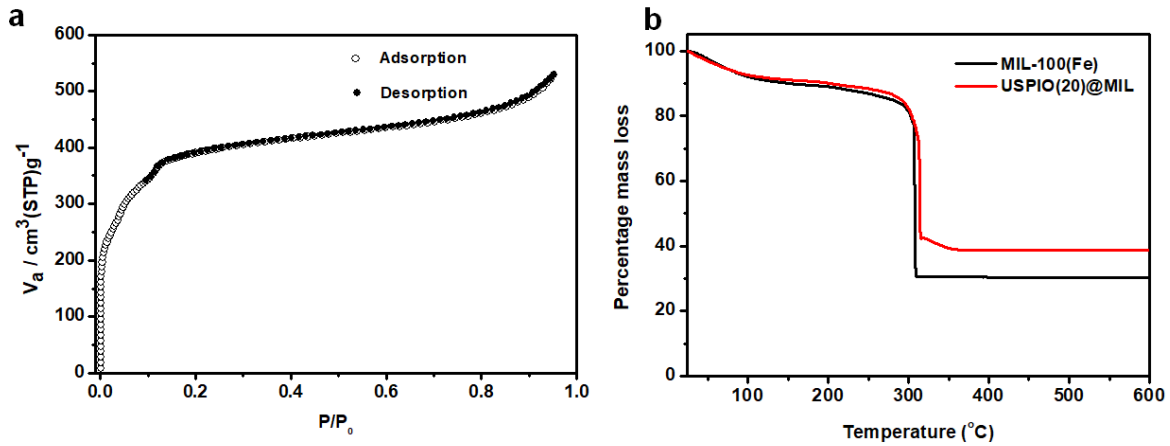

Figure S5. a) Nitrogen sorption isotherms at 77 K (P_0 = 1atm) and (b) TGA of USPIO(20)@MIL.

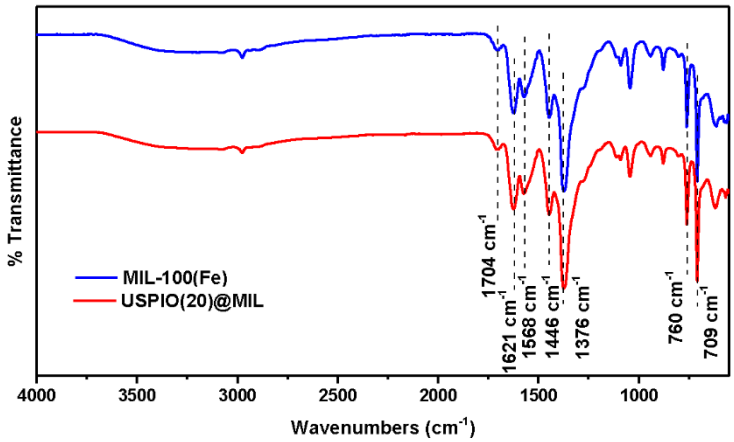

Figure S6. FT-IR spectra of MIL-100(Fe) and USPIO(20)@MIL.

The FT-IR spectra of both MIL-100(Fe) and and USPIO(20)@MIL exhibit characteristic vibration bands at 1621, 1568, 1446, 1376, 760 and 709 cm^{-1}. The bands at 1624 and 1376 cm^{-1} are assigned to v(C–O) bond of carboxylate groups coordinated to the iron centers of the MOF. The free ligand is also observed through the C=O stretching vibration band at 1704 cm^{-1}.

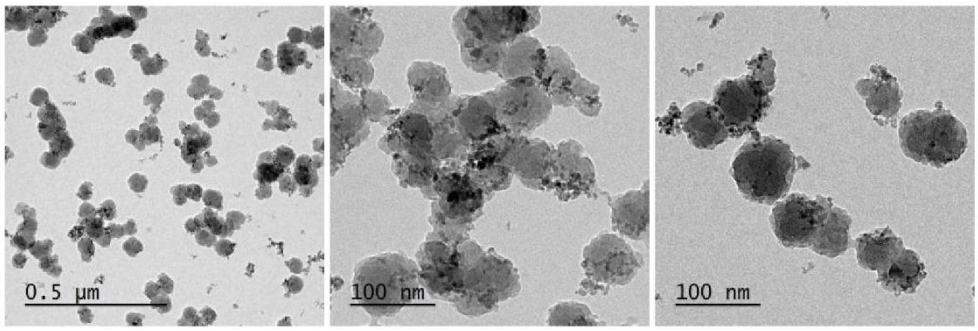

Figure S7. TEM images of and USPIO(20)@MIL nano-objects.

4-Characterization of USPIO(10)@MIL nano-objects

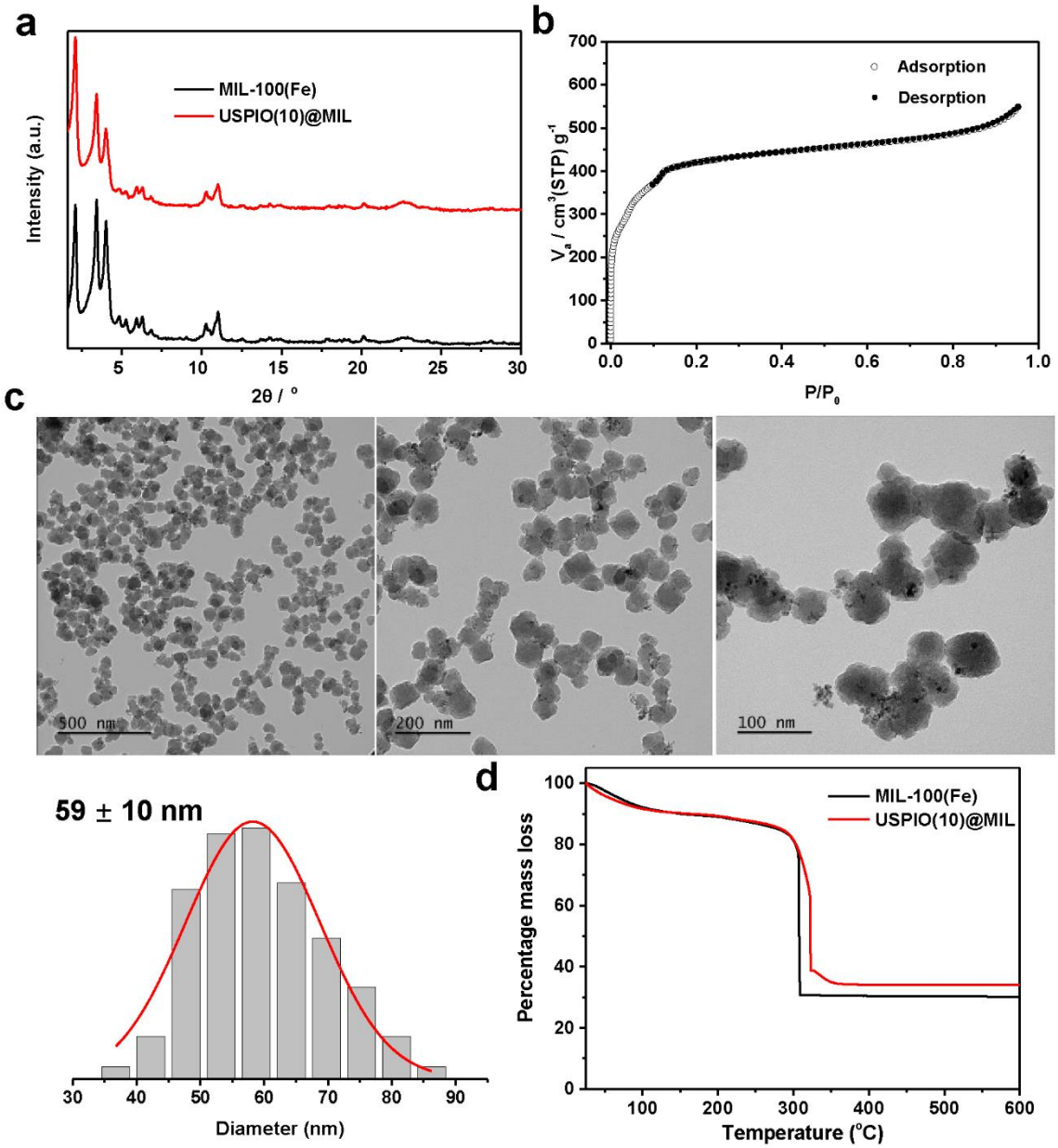

Figure S8. Characterizations of USPIO(10)@MIL: a) PXRD diagram; b) N_2 adsorption / desorption isotherms; c) TEM images; d) TGA.

5-Colloidal stability of MIL-100(Fe) and USPIO@MIL nano-objects

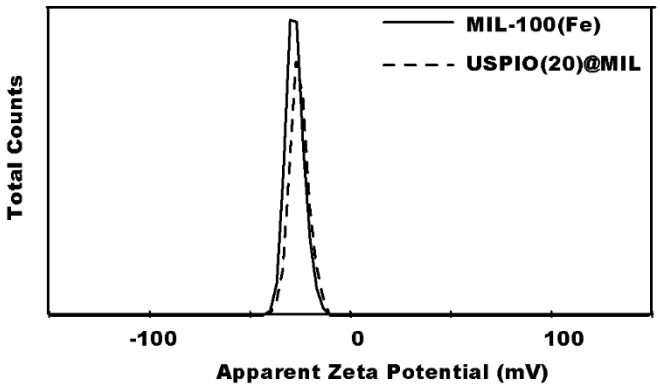

Figure S9. Zeta potentials of MIL-100(Fe) and USPIO(20)@MIL in Milli Q water.

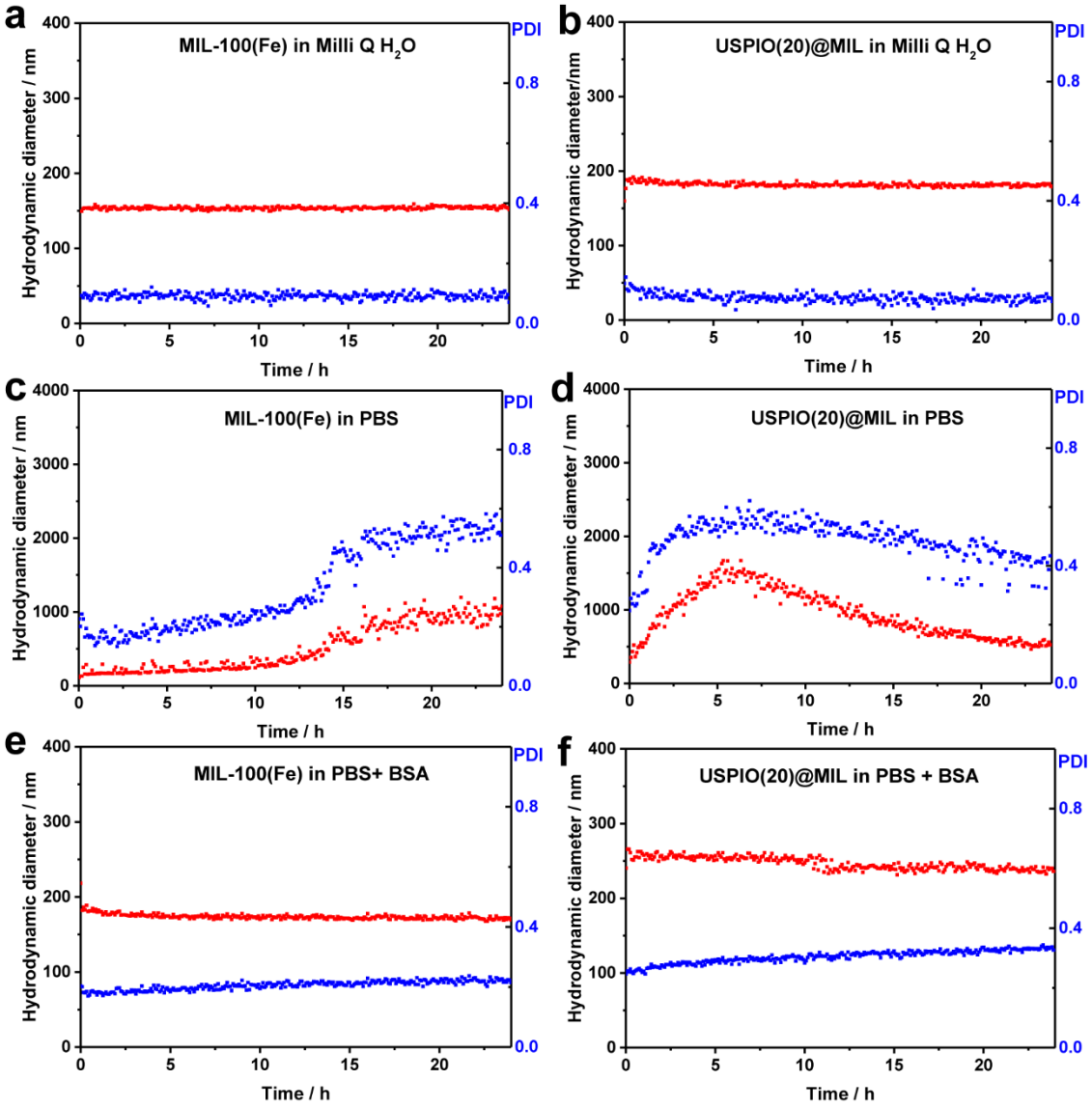

Figure S10. Evolution of the average particle diameter (by intensity) (red line) and polydispersity index (PdI) (blue line) of MIL-100(Fe) and USPIO(20)@MIL in (a-b) Milli Q water, (c-d) 10 mM PBS (pH

7.4), (e-f) 10 mM PBS (pH 7.4) + 5.4% w/v BSA over a time period of 24 h.

To confirm the impact of bovine serum albumin on the colloidal stability of USPIO(20)@MIL NPs, USPIO(20)@MIL NPs were redispersed into DMEM, 90% DMEM + 10% FBS and PBS solution (10 mmol L^{-1}) at the pH of 5.1 and 6.5 with or without 5.4% w/v BSA, respectively. The average particle diameter was also monitored at regular interval for a period of 24 h.

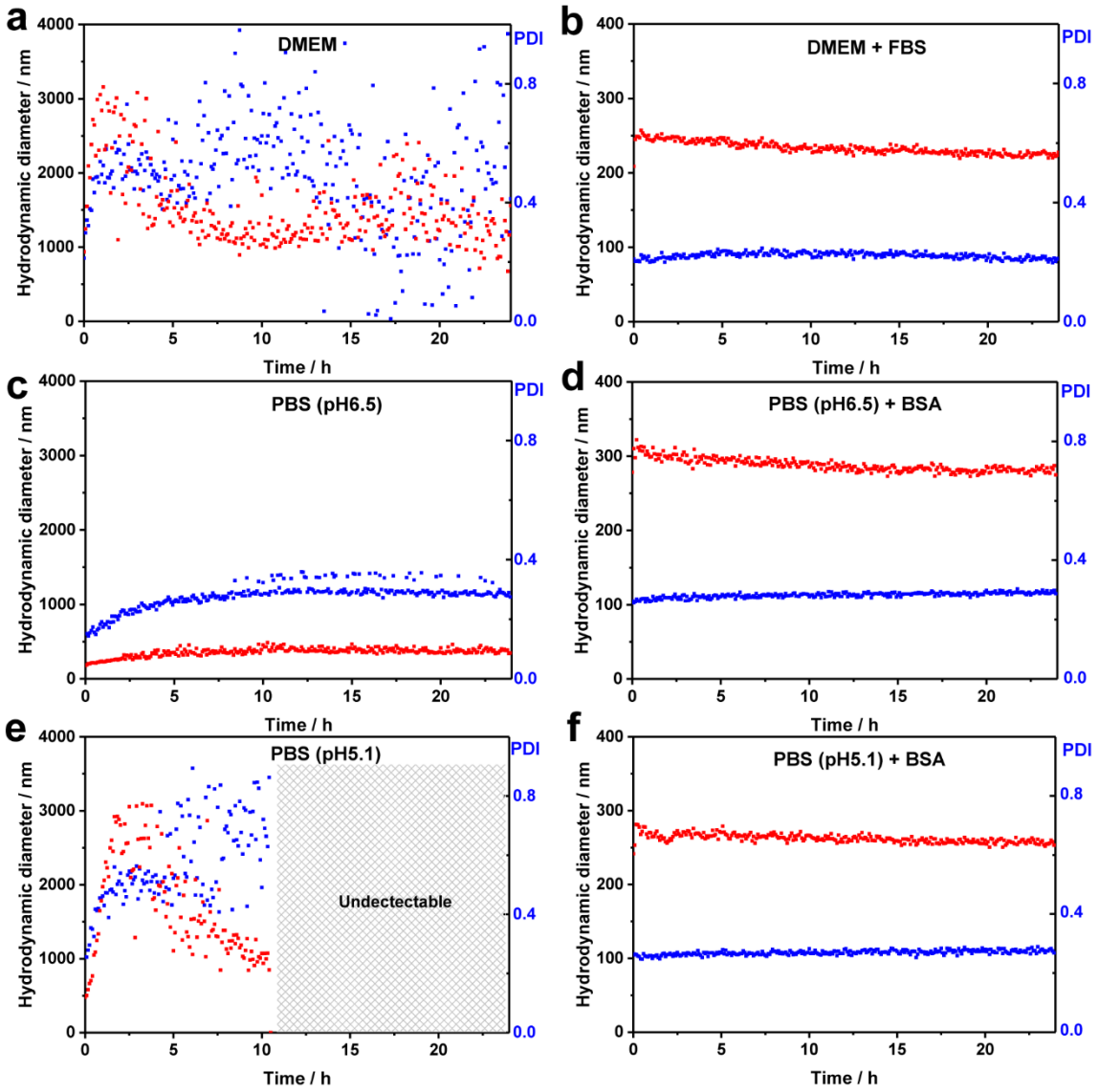

Figure S11. Evolution of the average particle diameter (by intensity) (red line) and polydispersity index (PdI) (blue line) of USPIO(20)@MIL in (a) DMEM, (b) 90% DMEM + 10% FBS, (c) 10 mM PBS (pH 6.5), (d) 10 mM PBS (pH 6.5) + 5.4% w/v BSA, (e) 10 mM PBS (pH 5.1) and (f) 10 mM PBS (pH 5.1) + 5.4% w/v BSA over a time period of 24 hours.

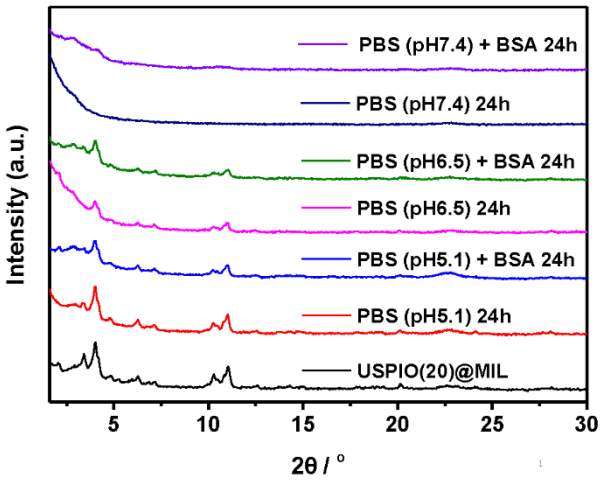

Figure S12. PXRD patterns of 1 mg mL^{-1} USPIO(20)@MIL NPs after mixing in 0.01M PBS (pH = 5.1, 6.5 and 7.4) with or without 5.4% w/v BSA at 37°C for 24 hours.

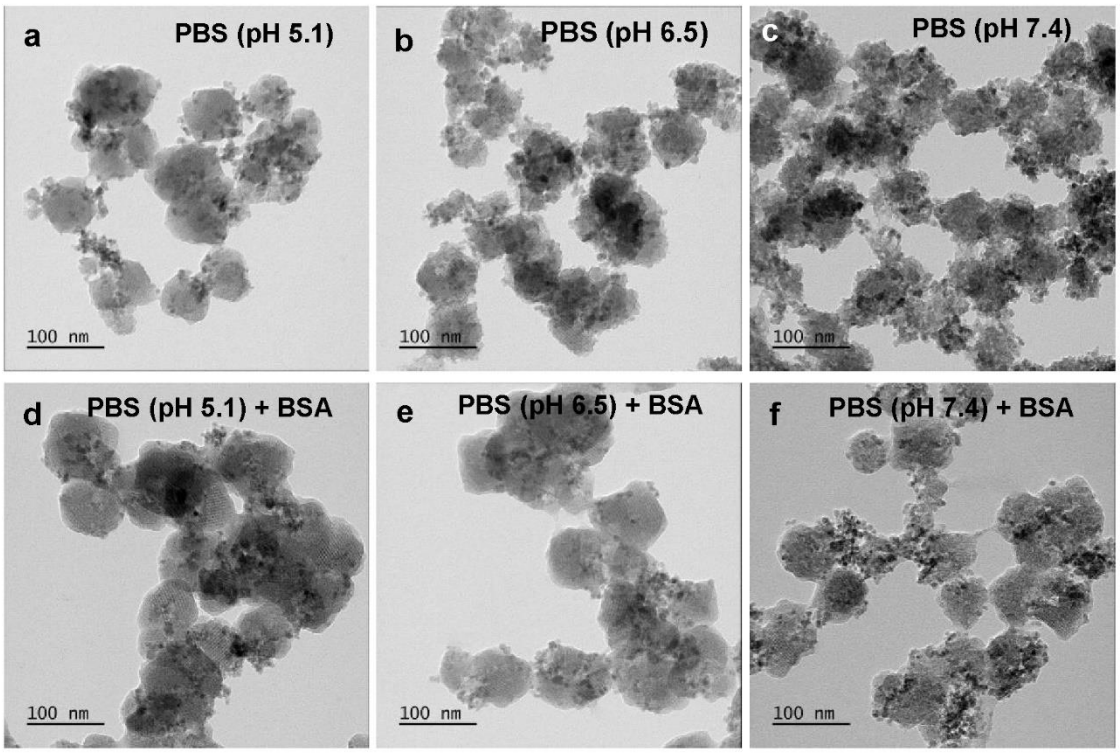

Figure S13. TEM observations of USPIO(20)@MIL NPs obtained after mixing in 0.01M PBS at the pH of (a, d) 5.1, (b, e) 6.5 and (c, f) 7.4 with or without 5.4% w/v BSA at 37°C for 24 hours. The sample was washed in H_2O before TEM grid preparation.

6-^{57}Fe Mössbauer spectroscopy.

The ^{57}Fe Mössbauer spectra were obtained using a ^{57}Co/Rh γ-ray source, mounted on a conventional constant acceleration vibrating electromagnetic transducer. They were performed on a powdered sample containing about 15 mg of Fe at 300 and 77 K in a zero magnetic field and at 77 K under a 0.04 T magnetic field oriented perpendicular to the γ-beam. The calibration is obtained using a α-Fe foil and the values of isomer shift were referred to that of α-Fe at 300 K. After registration of a spectrum with a large velocity scale (not shown here), the spectrum at 300 K (Figure S14 top) results in only a quadrupolar feature which consists of an asymmetrical quadrupolar doublet: its description can be obtained by considering a quadrupolar spectrum (blue) corresponding to that of MIL-100(Fe) and a second quadrupolar component (red) attributed to γ-Fe_2O_3 NPs. Indeed, taking into account the diameter of γ-Fe_2O_3 NPs (7 ± 3 nm), they should exhibit fast superparamagnetic relaxation phenomena giving rise to a quadrupolar structure. Their respective proportions of both MIL-100(Fe) and γ-Fe_2O_3 are 66 and 34%, in rather fair agreement with the quantification by HPLC / ICP-MS (69-31%). At

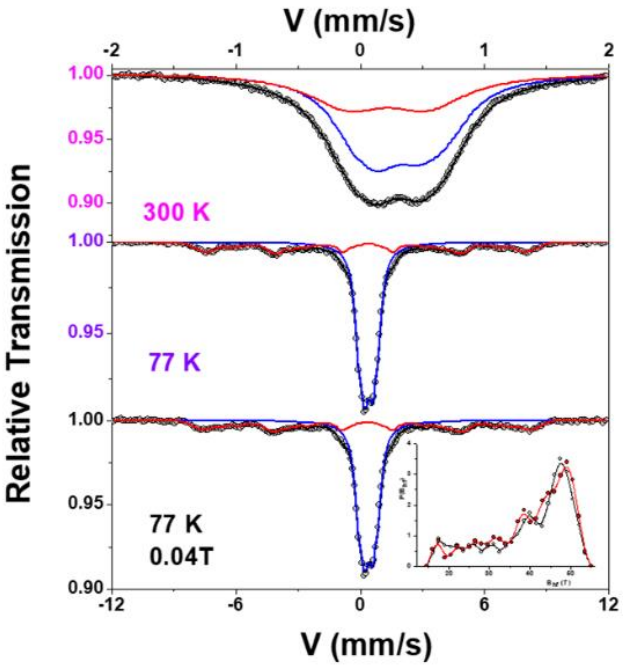

Figure S14. ^{57}Fe Mössbauer spectra of USPIO(20)@MIL recorded at 300 K(top) and 77 K (middle) in a zero magnetic field and at 77 K under a 0.04 T magnetic field.

77 K, as shown in Figure S14 (middle), a part of the quadrupolar structure splits into a magnetic sextet composed of broadened and asymmetrical lines. In addition to the central quadrupolar feature corresponding to the MIL-100(Fe) component, the magnetic sextet assigned to γ-Fe_2O_3

NPs was described by means of a hyperfine field distribution. The 69 and 31% proportions estimated at 77 K are fully consistent with the experimental values (the small disagreement at 300 K is due to the small difference in the Lamb-Mössbauer factors characteristics of the two phases). The presence of non-interacting γ-Fe_2O_3 NPs cannot be clearly excluded and it is not possible to distinguish the aggregated γ-Fe_2O_3 NPs at the surface of USPIO(20)@MIL and those located in the core of USPIO(20)@MIL (see Figure S14 bottom).

7-Cellular uptake of USPIO(20)@MIL by RAW 264.7 macrophages

Synthesis of USPIO(20)@MIL/RhB. To observe the cellular uptake of USPIO(20)@MIL, USPIO(20)@MIL was loaded with a fluorescent dye Rhodamine B (RhB). Typically, 1 mL RhB stock solution (1mg mL^{-1}) was first diluted in 4 mL Milli Q water, then added to 5 mg of USPIO(20)@MIL and kept stirring at 600 rpm for 24 h with the protection of tin foil. The resulting USPIO(20)@MIL/RhB nanoparticles were collected by centrifugation and washed repeated with Milli Q water to remove the free RhB. Then, the final product was redispersed in 5 mL Milli Q water with tin foil covering and kept in 4°C fridge until use.

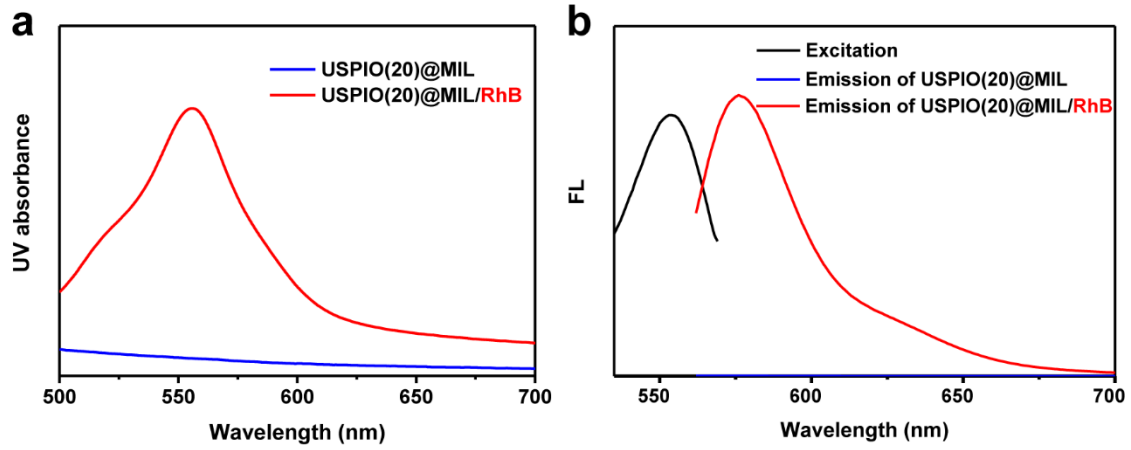

Figure S15. a) UV-vis spectra of USPIO(20)@MIL and USPIO(20)@MIL/RhB, (b) Fluorescence emission spectra of USPIO(20)@MIL and USPIO(20)@MIL/RhB (λ_{em}= 576 nm).

While the bare USPIO(20)@MIL NPs do not display any absorbance peak in the visible spectrum, USPIO(20)@MIL/RhB presents one peak at 550 nm. Moreover, USPIO(20)@MIL/RhB NPs present fluorescence properties (λ_{em} = 576 nm) by excitation with visible light while the USPIO(20)@MIL NPs do not exhibit any fluorescence properties.

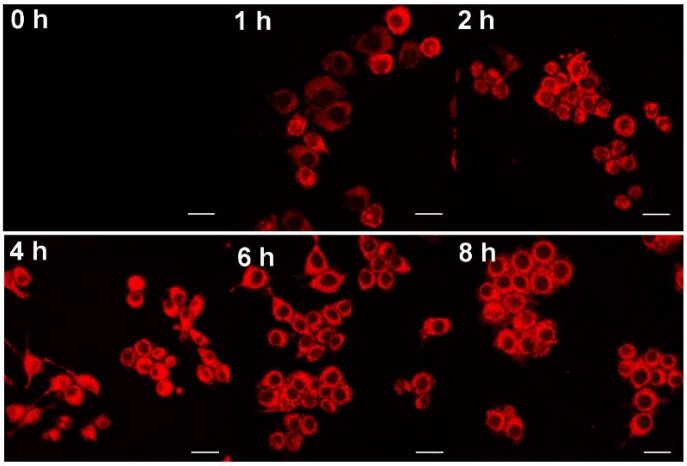

Figure S16. Internalization of Rhodamine-labeled USPIO(20)@MIL in RAW 264.7 macrophages as shown by CLSM (Scale bar = 20 μm).

TEM of cells.

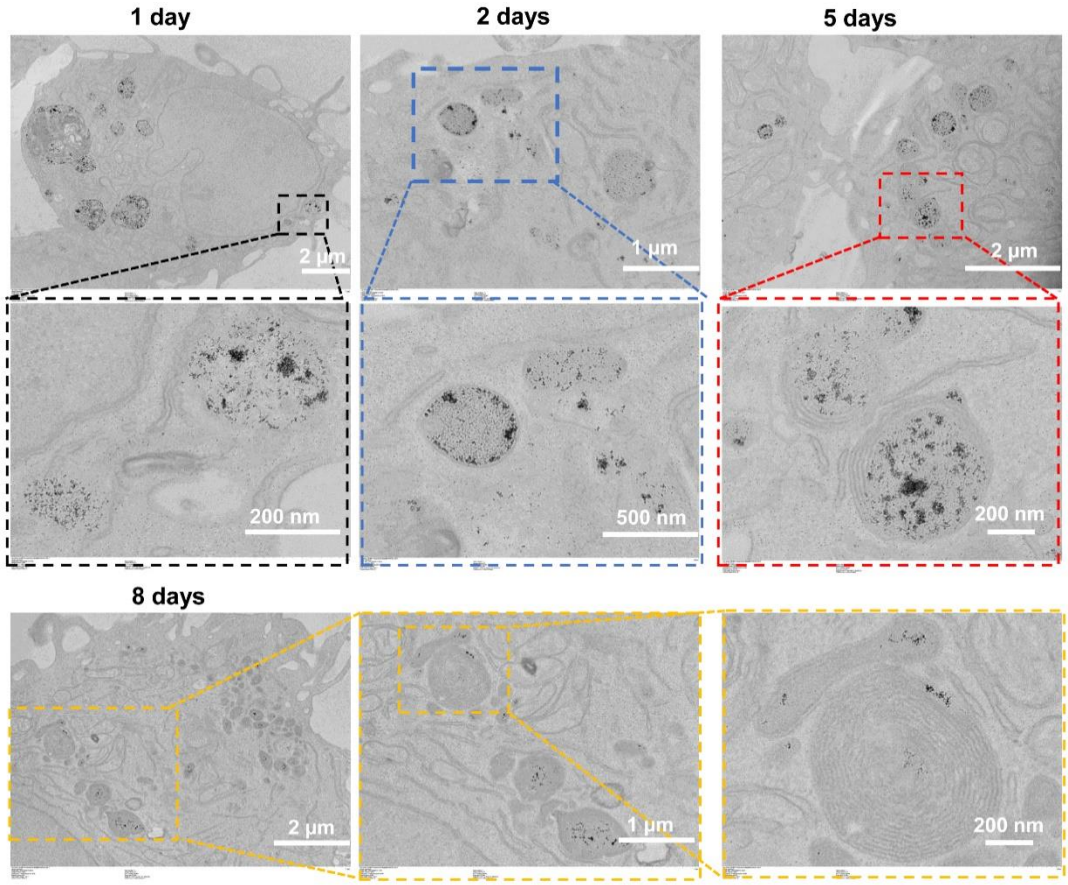

Figure S17. 2D TEM slices images of RAW 264.7 cells at different times (1 day, 2, 4 or 8 days) after incubation with USPIO(20)@MIL (50 μg mL^{-1}) for 24 h.

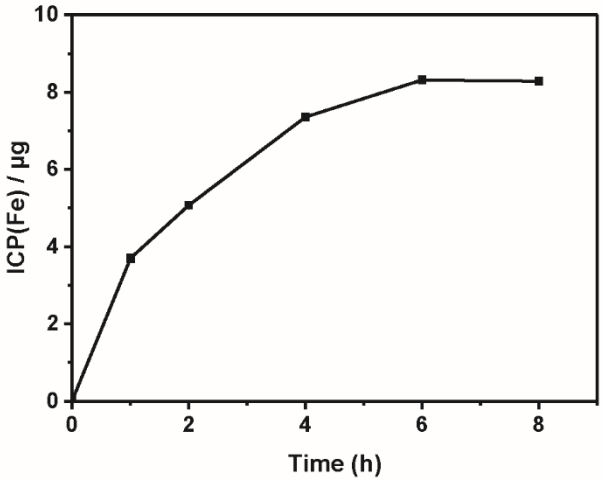

Figure S18. Quantification of the intracellular Fe^{3+} as a function of the incubation time of RAW 264.7 macrophages with USPIO(20)@MIL NPs.

8-Encapsulation and Release of Methotrexate

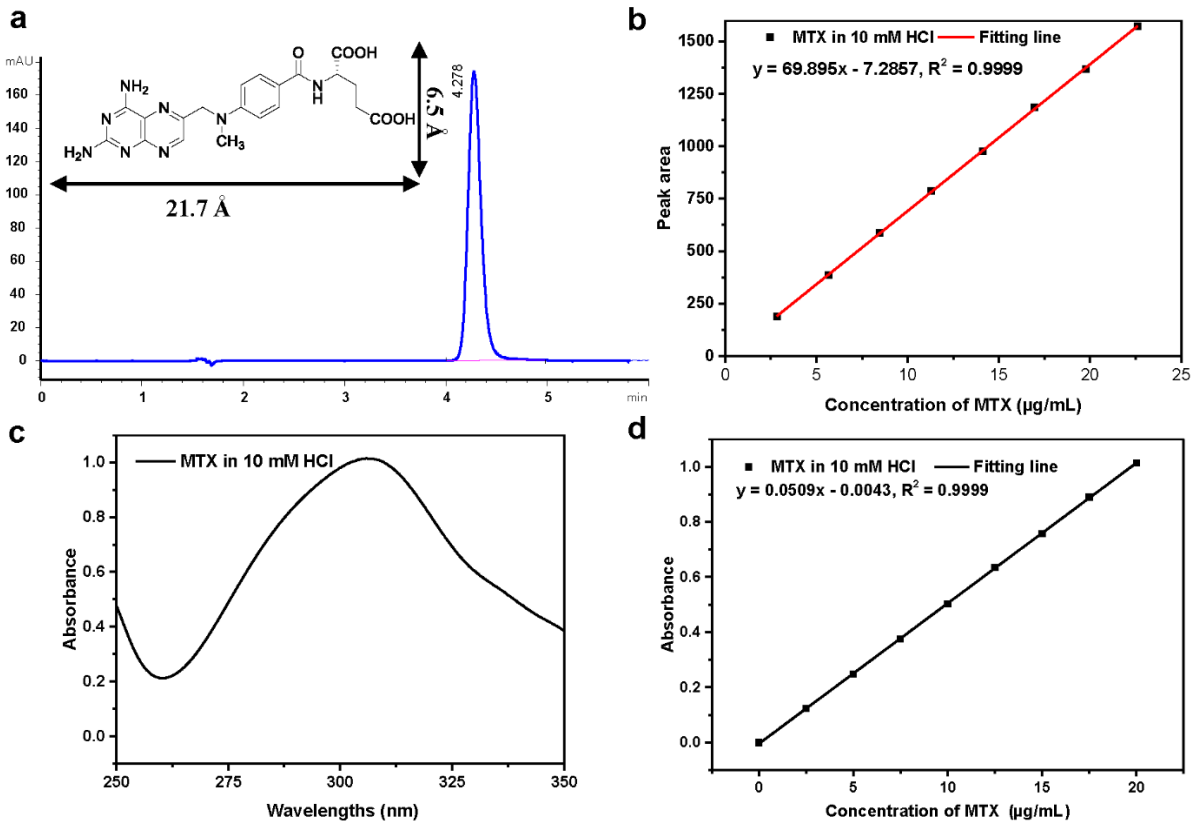

Figure S19. a) HPLC chromatogram of MTX (Inserted: Molecular structure of MTX); b) MTX calibration curves in 10 mM HCl by HPLC; c) UV-Vis spectrum of MTX; d) MTX calibration curves in 10 mM HCl by UV-Vis.

Table S2. MTX loading capacity (LC) or entrapment efficiency (EE) of MIL-100(Fe) and

USPIO(20)@MIL.

Weight Ratio (MOF : MTX)	**MIL-100(Fe)/MTX** LC (%)	EE (%)	**USPIO(20)@MIL/MTX** LC (%)	EE (%)
1:0.25	25 ± 0.01	99 ± 0.05	25 ± 0.04	99 ± 0.2
1:0.5	46 ± 0.03	92 ± 0.05	43 ± 0.05	86 ± 0.1
1:1	60 ± 1	60 ± 1	47 ± 3	47 ± 3
1:2	61 ± 5	30 ± 3	46 ± 10	23 ± 5

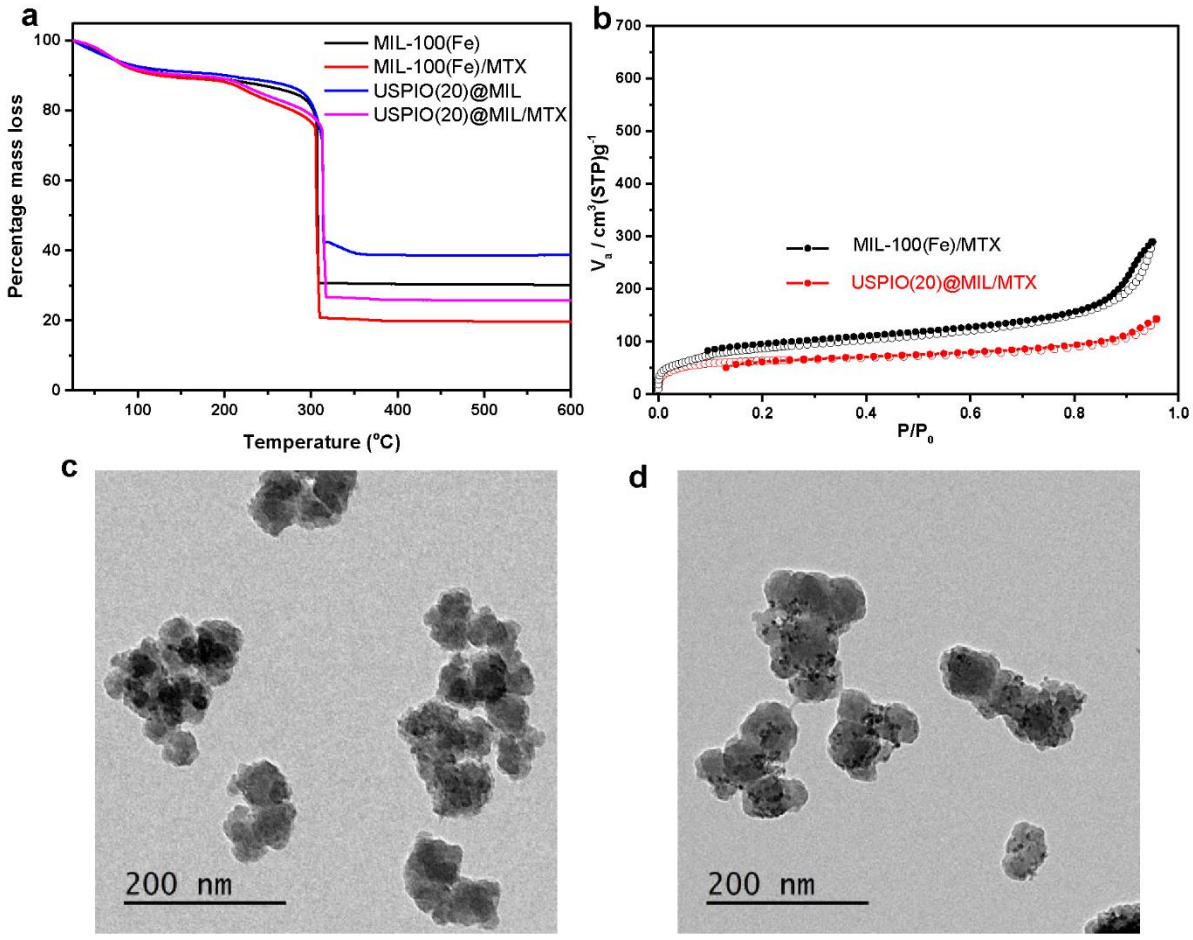

Figure S20. a) TGA and (b) N_2 adsorption / desorption isotherms of MIL-100(Fe)/MTX and USPIO(20)@MIL/MTX. TEM images of (c) MIL-100(Fe)/MTX and (d) USPIO(20)@MIL/MTX.

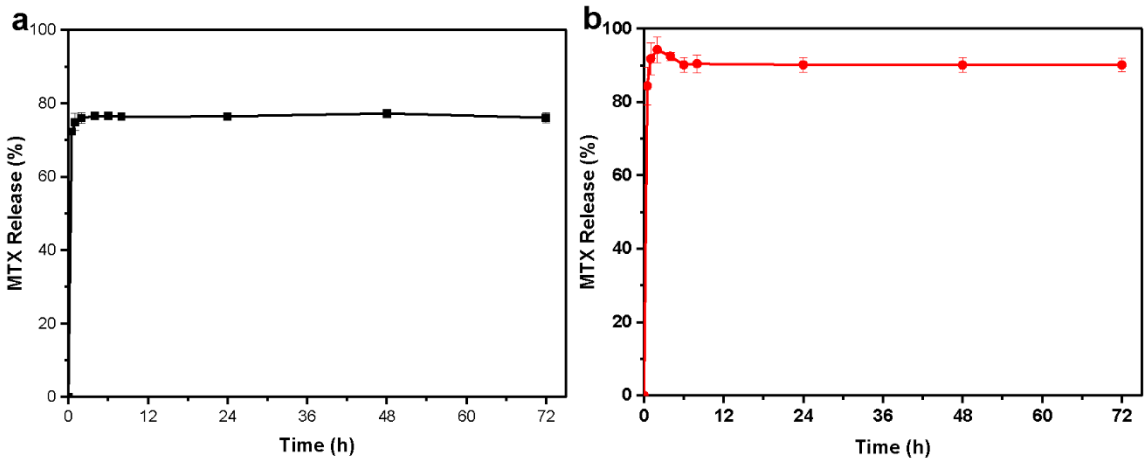

Figure S21. MTX release in (a) DMEM and (b) DMEM + 10% FBS from USPIO(20)@MIL/MTX by HPLC.

9-Encapsulation and release of doxorubicin.

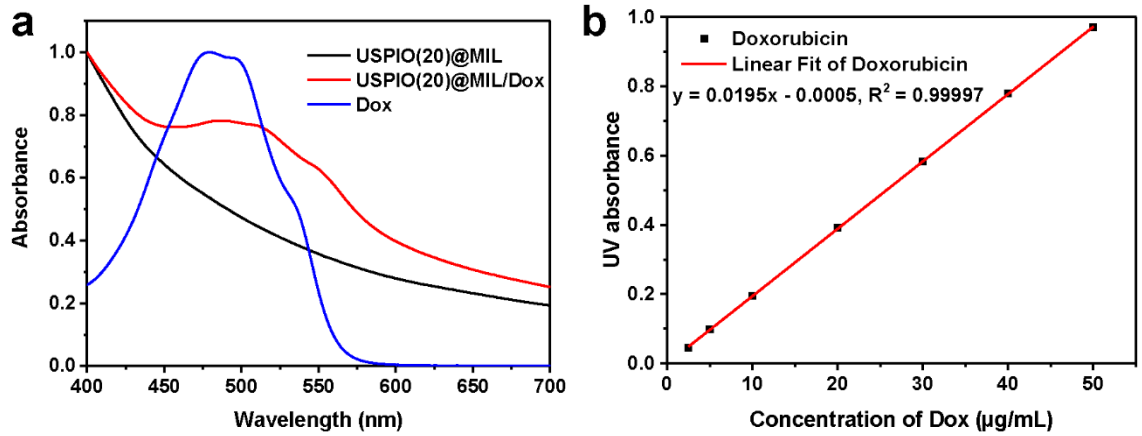

Figure S22. a) Normalized UV-Vis spectra of USPIO(20)@MIL, USPIO(20)@MIL/Dox and Dox. b) Calibration curve of Doxorubicin in water by UV-Vis spectroscopy.

Table S3. Dox loading capacity (LC) or entrapment efficiency (EE) of MIL-100(Fe) and USPIO(20)@MIL.

Weight Ratio	**MIL-100(Fe)/Dox**		**USPIO(20)@MIL/Dox**	
(MOF : Dox)	LC(%)	EE(%)	LC(%)	EE(%)
1 : 0.25	24.96 ± 0.01	99.8 ± 0.01	24.85 ± 0.01	99.39 ± 0.04
1 : 0.5	48.3 ± 0.4	96.6 ± 0.8	43.4 ± 0.5	86.8 ± 1
1 : 1	57.3 ± 0.6	57.3 ± 0.6	48.4 ± 1.6	48.4 ± 1.6
1 : 3	55.8 ± 0.5	18.6 ± 0.2	49.9 ± 4.3	16.6 ± 1.4

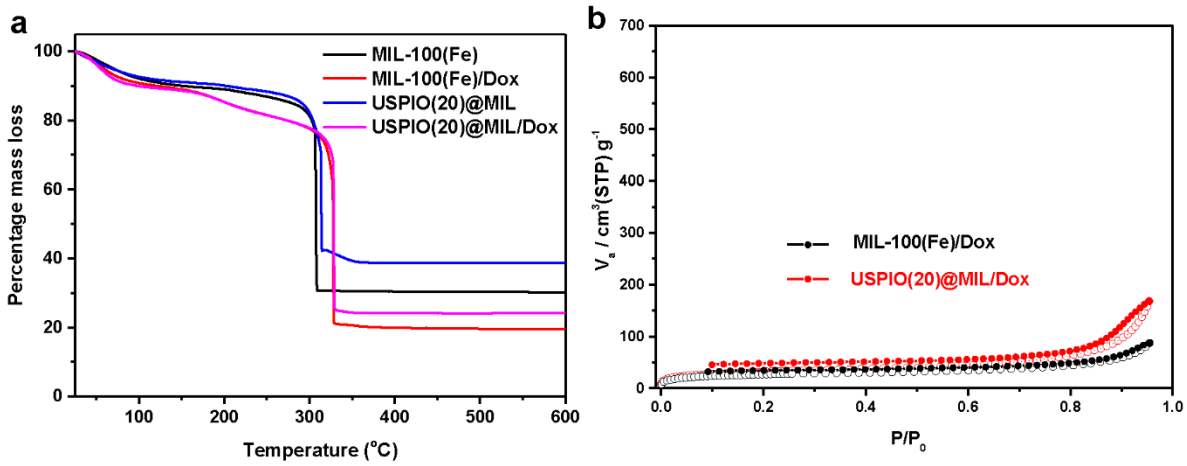

Figure S23. a) TGA and (b) N_2 adsorption/desorption isotherms of MIL-100(Fe)/Dox and USPIO(20)@MIL/Dox.

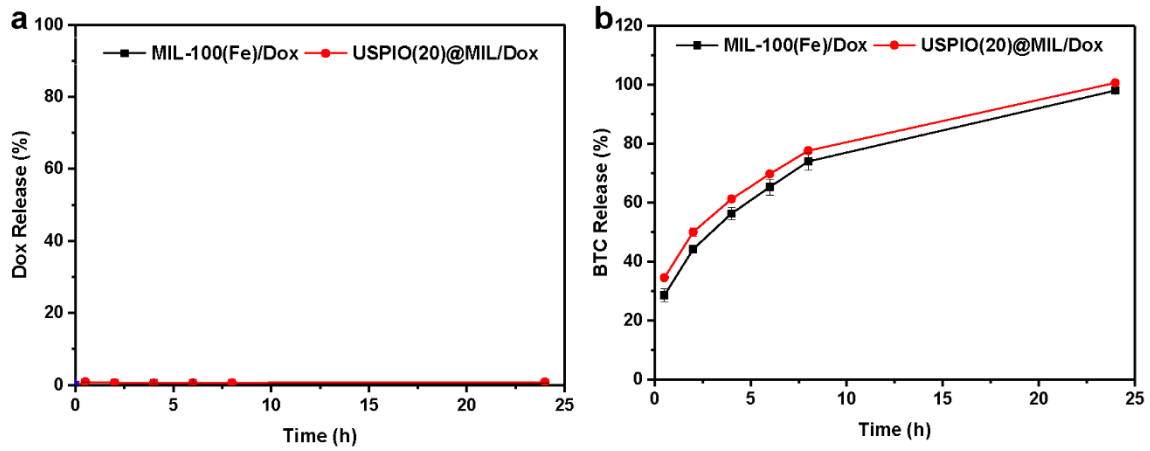

Figure S24. a) Dox and (b) BTC release of MIL-100(Fe)/Dox and USPIO(20)@MIL/Dox in phenol-free DMEM.

10-*In vitro* cytotoxicity assay of MIL-100(Fe), USPIO(20)@MIL, USPIO(20)@MIL/MTX and USPIO(20)@MIL/Dox

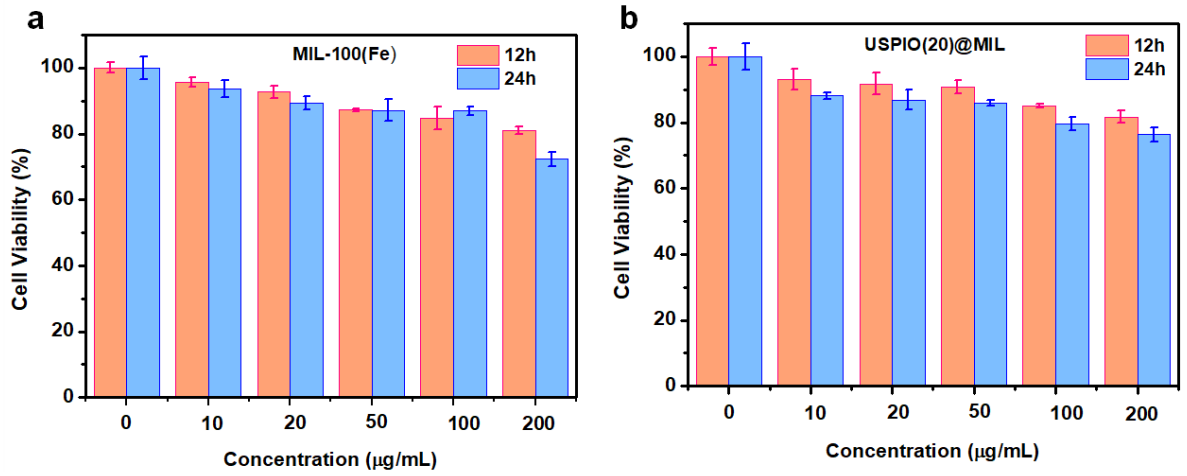

Figure S25. Normalized Hela cells viability obtained after incubation with (a) MIL-100(Fe) and (b) USPIO(20)@MIL at different concentrations for 12 and 24 h.

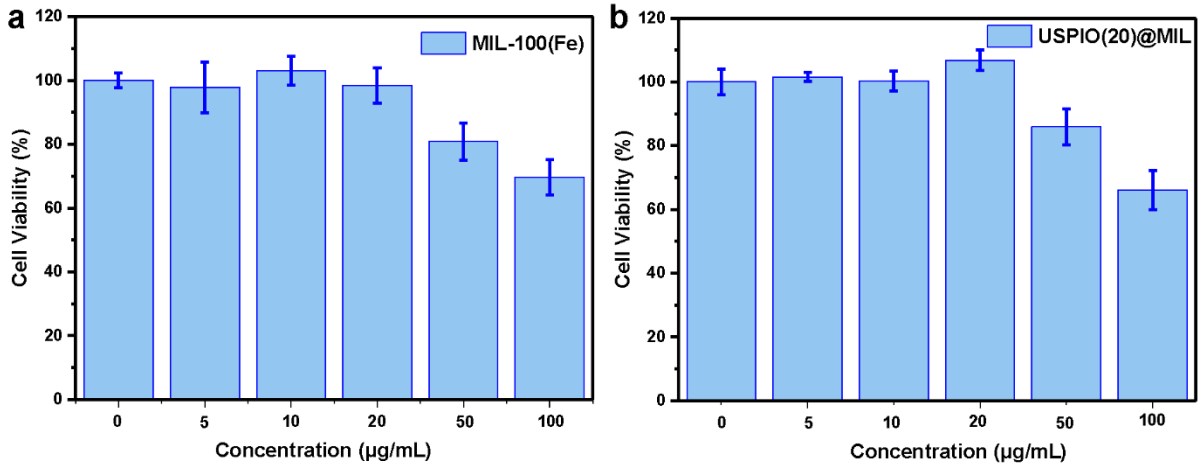

Figure S26. Normalized cell viability of RAW 264.7 macrophages after incubation with (a) MIL-100(Fe) and (b) USPIO(20)@MIL for 24 h.

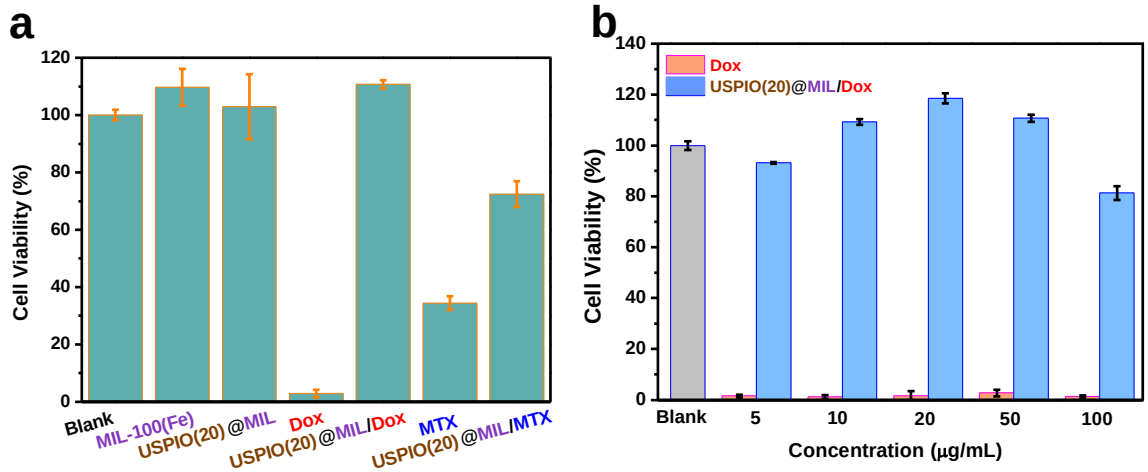

Figure S27. a) Cell viability of normal RAW 264.7 macrophages after incubation for 24 h with MIL-100(Fe), USPIO(20)@MIL, USPIO(20)@MIL/MTX at 50 μg mL^{-1} and with free MTX at 23 μg mL^{-1} and USPIO(20)@MIL/Dox at 50 μg mL^{-1} and with free Dox at 25 μg mL^{-1}. (b) Cell viability of RAW 264.7 macrophages exposed for 24 h to USPIO(20)@MIL/Dox and equivalent free Dox of different concentrations.

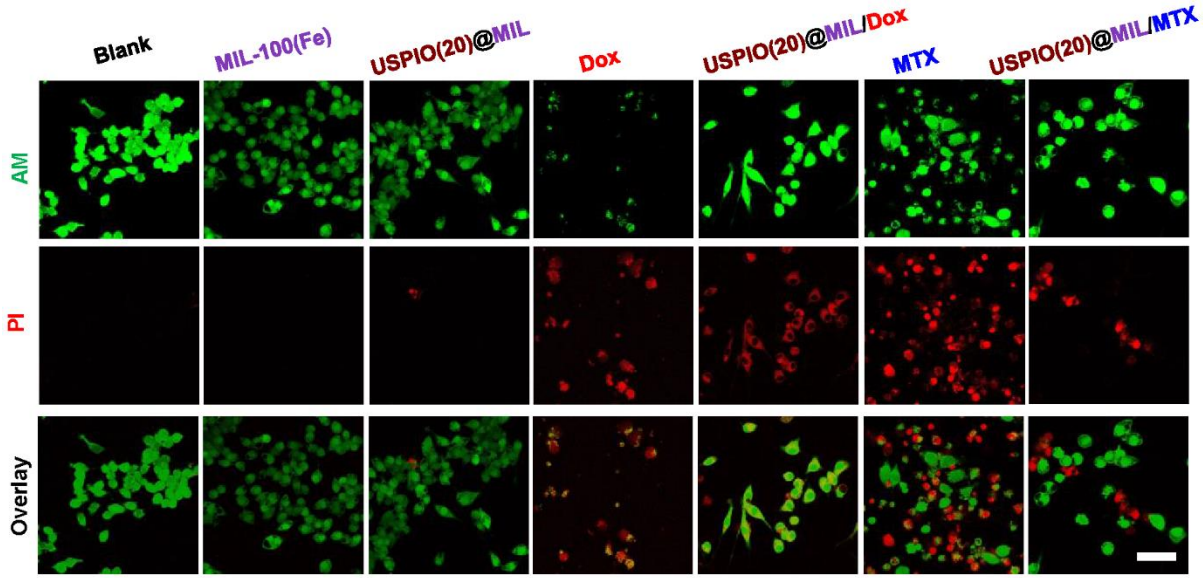

Figure S28. AM/PI staining of normal RAW 264.7 macrophages after co-culture with MIL-100(Fe), USPIO(20)@MIL, Dox, USPIO(20)@MIL/Dox, MTX and USPIO(20)@MIL/MTX for 24 h. Live & dead cells were stained by green and red, respectively. [MIL-100(Fe)] = 40 μg mL^{-1}, [USPIO(20)@MIL] = 50 μg mL^{-1}, [Dox] = 25 μg mL^{-1}, [USPIO(20)@MIL/Dox] = 50 μg mL^{-1}, [MTX] = 23 μg mL^{-1} and [USPIO(20)@MIL/MTX] = 50 μg mL^{-1}. Scale bar = 50 μm.

11-Anti-inflammatory capacity of USPIO(20)@MIL/MTX and USPIO(20)@MIL/Dox

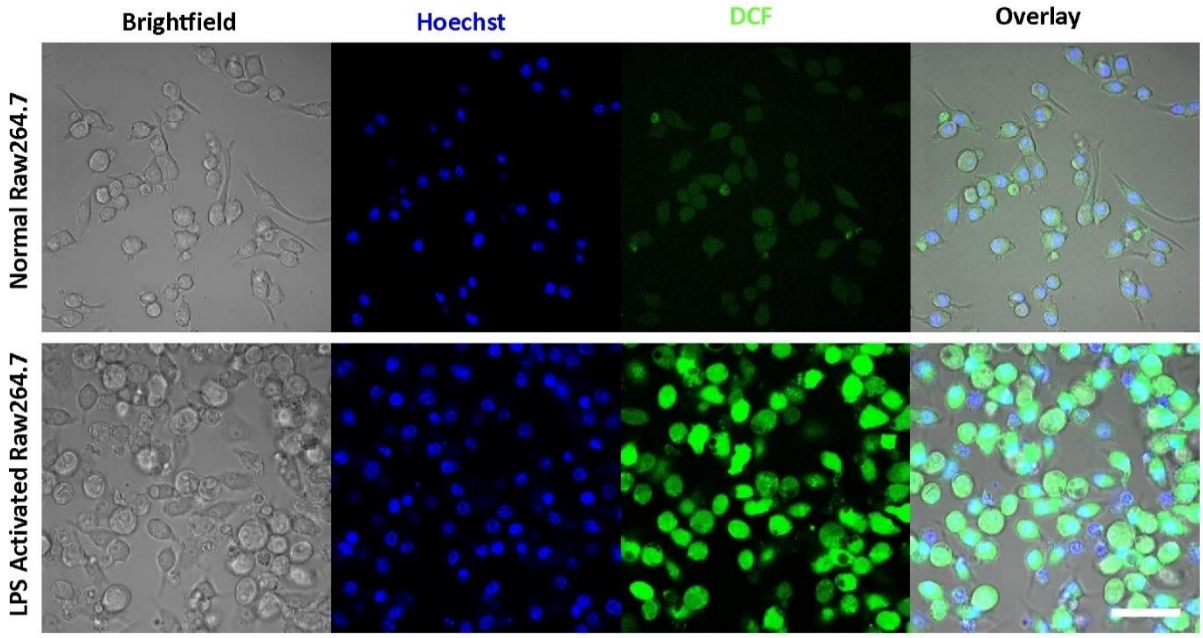

Figure S29. *In vitro* ROS (DCF-DA fluorescence) imaging on normal RAW 264.7 cells and LPS activated RAW 264.7 cells and Hoechst as a nucleus staining dye. Scale bar = 50 µm.

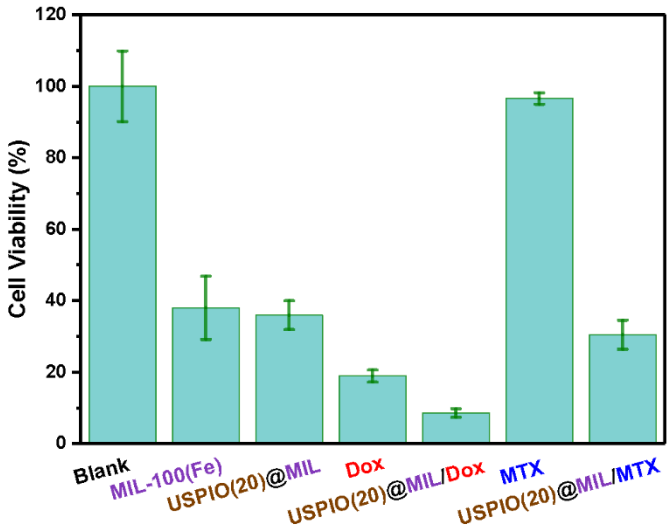

Figure S30. Anti-inflammatory properties of USPIO(20)@MIL/MTX and USPIO(20)@MIL/Dox. Cell viability assay by using CCK-8 staining of LPS (100 ng mL^{-1}, 48 h) activated RAW 264.7 macrophages incubated with different drug formulations ([MIL-100(Fe)] = 40 µg mL^{-1}, [USPIO(20)@MIL] = 50 µg mL^{-1}, [Dox] = 25 µg mL^{-1}, [USPIO(20)@MIL/Dox] = 50 µg mL^{-1}], [MTX] = 23 µg mL^{-1}, [USPIO(20)@MIL/MTX] = 50 µg mL^{-1}) for 24 h.

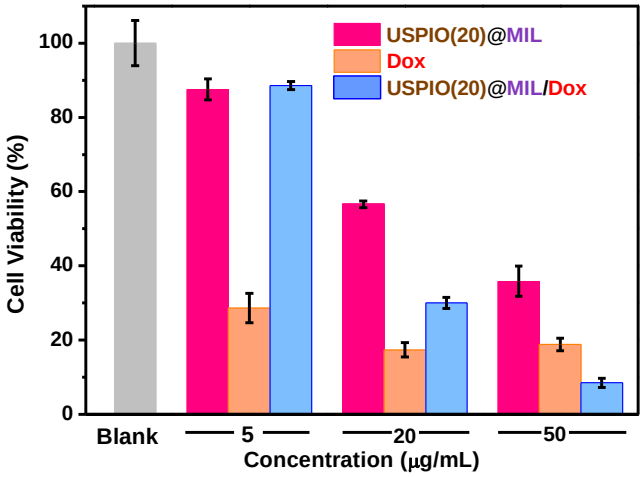

Figure S31. Cell viability of LPS activated RAW 264.7 macrophages incubated with different concentrations of USPIO(20)@MIL (5, 20 and 50 µg mL^{-1}), USPIO(20)@MIL/Dox and equivalent free Dox (2.5, 10 and 25 µg mL^{-1}) for 24h.

12-Evaluation of the concentrations of pro-inflammatory cytokines by enzyme-linked immunosorbent assay (ELISA) assays

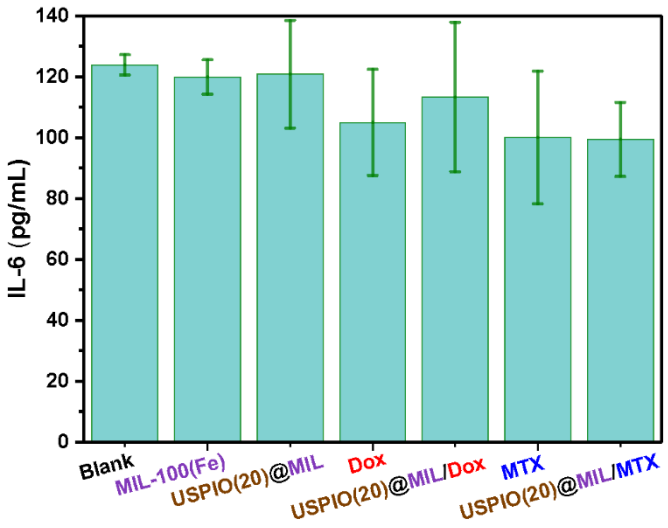

Figure S32. The concentrations of the inflammatory cytokines IL-6 in cell culture media after the treatment of different formulations ([MIL-100(Fe)] = 4 µg mL^{-1}, [USPIO(20)@MIL] = 5 µg mL^{-1}, [Dox] = 0.25 µg mL^{-1}, [USPIO(20)@MIL/Dox] = 5 µg mL^{-1}, [MTX] = 2.3 µg mL^{-1}, [USPIO(20)@MIL/MTX] = 5 µg mL^{-1}) for 24 h. Note that the concentration of Dox here was ten times lower than the loaded Dox of USPIO(20)@MIL/Dox to limit its toxicity. Results are shown as mean ± SD.

13-Cytotoxicity of USPIO(20)@MIL/Dox

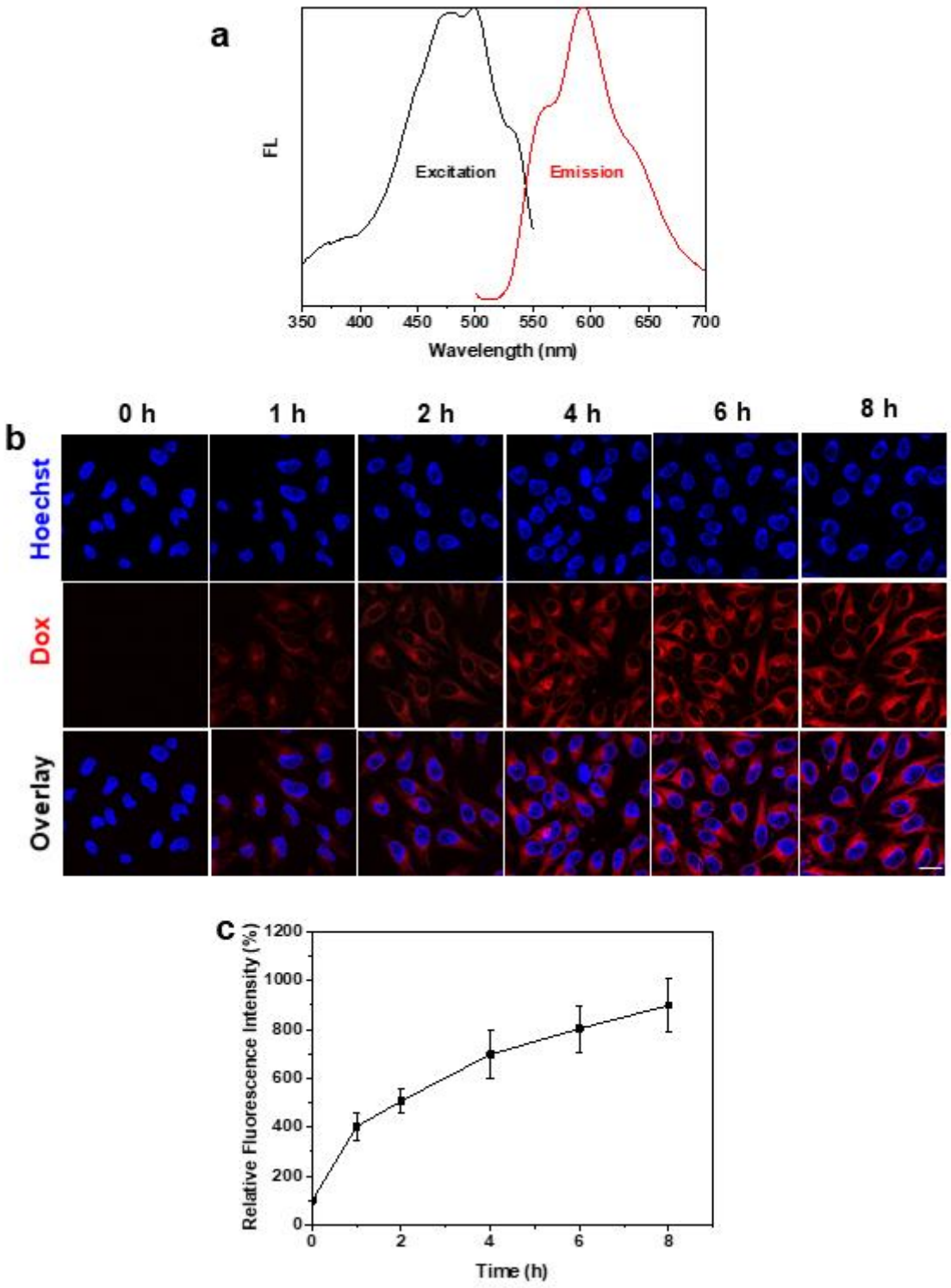

Figure S33. a) Excitation and fluorescence spectra of USPIO(20)@MIL/Dox in water. b) Internalization of USPIO(20)@MIL/Dox in Hela cells as shown by CLSM (Scale bar = 10 µm) and (c) quantification of the intracellular relative fluorescence intensity of Dox as a function of the incubation time of Hela cells with USPIO(20)@MIL NPs.

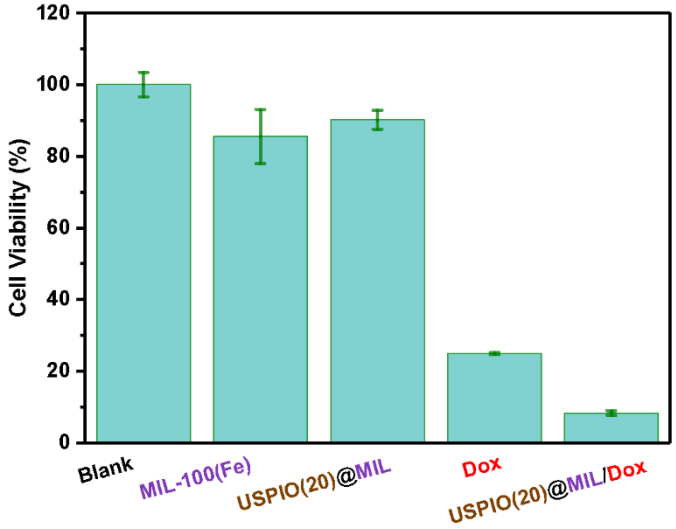

Figure S34. Cell viability of Hela cells incubated for 24 h with MIL-100(Fe), USPIO(20)@MIL, Dox and USPIO(20)@MIL/Dox at the concentrations of 40, 50, 25 and 50 μg mL^{-1}, respectively.

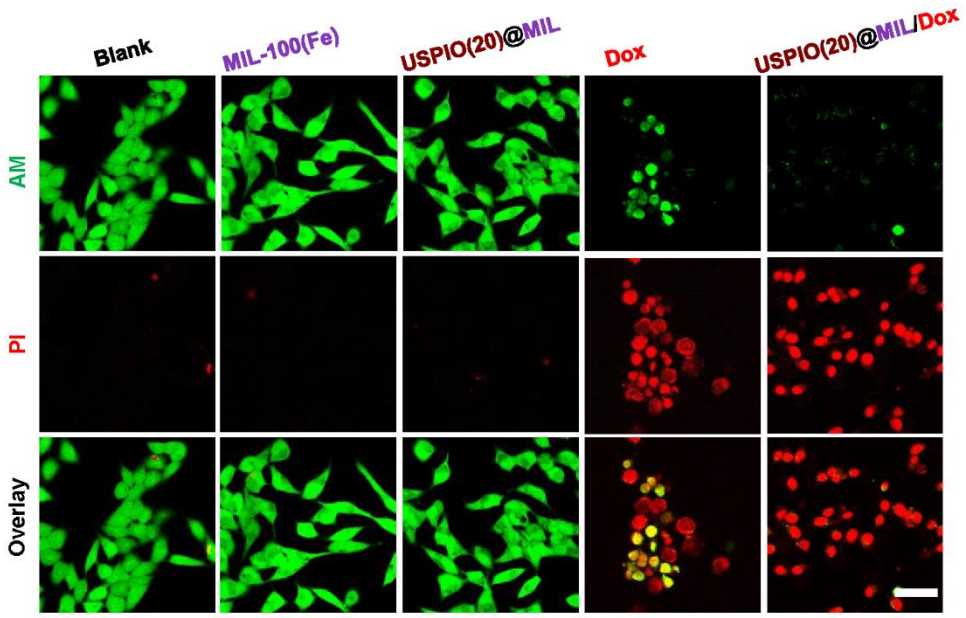

Figure S35. AM/PI staining of Hela cells after the incubation for 24 h with MIL-100(Fe), USPIO(20)@MIL, Dox and USPIO(20)@MIL/Dox at the concentrations of 40, 50, 25 and 50 μg mL^{-1}, respectively. Scale bar = 50 μm.

14-Relaxometry and magnetic properties of USPIO@MIL nano-objects.

Table S4. Relaxivity r_2 values of iron oxide NPs per mM Fe^{3+}

NPs/nano-objects	Relaxivity r_2[a] ($mM^{-1}.s^{-1}$)	Hydrodynamic diameter of nano-object (nm)	Surface modification	Reference
γFe_2O_3	171 ± 10	7 (3)	-	This paper
MIL-100(Fe)	3 ± 1	38 (7)	-	This paper
USPIO(20)@MIL	93 ± 2	49(10)	-	This paper
USPIO(10)@MIL	38 ± 2	49(10)	-	This paper
MIL/USPIO-cit (10)	93 ± 4	163 (77)	Citrate	[1]
MIL/USPIO-cit(1)	21 ± 2	155 (40)	Citrate	[1]
γ-Fe_2O_3	205	13	citrate	[2]
γ-Fe_2O_3	133	16	PAA_{2k}[b]	[2]
γ-Fe_2O_3	69.8/86.5	9	PAA_{2k}[b]	[2]
γ-Fe_2O_3	70	8	DMSA[c]	[2]
γ-Fe_2O_3	145	15	dextran	[2-3]
Endorem®	100	228-80	dextran	[4-5]
Sinerem®	90	50	-	[4]
Fe_3O_4 /ZIF-8-Au_{25}	35.49	-	-	[6]
Fe_3O_4-ZIF-8	372	-	-	[7]
PEG-NH_2@Fe_3O_4-ZIF-8	25.25	97 (8)	-	[8]
FePt-MOF	27.1	-	-	[9]
MIL-S	13.53	60	-	[10]
MIL-M	31.28	350	-	[10]
MIL-L	50.80	730	-	[10]
Fe_3O_4@C@MIL-100(Fe)	352.45	-	-	[11]
USPIO/MIL-101(Fe)-NH_2	170.96	450	-	[12]

[a]r_2 values per mM Fe^{3+}; [b]PAA_{2k}: poly(sodium acrylate); [c]DMSA: Dimercapto-succinic acid

Characterization of the magnetic properties. Nano-objects were dispersed in a PVA matrix and dried in a cylindrical Teflon mold. The magnetic moment of the samples was measured by a Quantum Design vibrating sample magnetometer (VSM) operating at a vibrating frequency of 40 Hz, with an integration time of 1 s. Calibration was performed on a high purity nickel sample with the same dimensions as the samples. Blank samples of a PVA matrix and of MIL-100(Fe) dispersed in PVA showed only a linear

dependence of magnetic moment with applied field and no superparamagnetic contribution; magnetic curves were analyzed after subtraction of the linear component. The magnetic moment of a single particle was obtained by Langevin fit of the experimental data with a fitting error less than 1%. The magnetization of a single particle was calculated using the effective diameter of the γ-Fe_2O_3 particles.

Finally, the overall accuracy can be safely estimated as 10%. Thermal variation of the zero-field cooled and field cooled (ZFC-FC) magnetization at H = 16 kA/m (*i.e.*, 200 Oe) reveals superparamagnetism at room temperature for USPIO(20)@MIL and USPIO(10)@MIL nano-objects. The ZFC-FC curve of USPIO(20)@MIL shown in Figure S15 is typical for well-dispersed γ-Fe_2O_3 superparamagnetic NPs.[13] The saturation magnetization at T = 300 K was obtained from the magnetic moment of each sample measured while the applied field was cycled. The magnetic field was driven above the saturation field which was 1.5 × 10^6 A m^{-1} (*i.e.*, 20 kOe) for USPIO@MIL samples. For all measured samples, the magnetization was fully reversible upon magnetic field cycling. The coercive fields H_{coer} were below the detection limit which was 1.6 kA m^{-1} (*i.e.*, 20 Oe). Both H_{coer} and T_{max} are consistent with an assembly of N quasi-independent particles and the Langevin model was applied at room temperature to get the saturation magnetization M_{sat} of the USPIO:

$$m(H) = M_{sat}\int_0^{\infty} N(D)\frac{\pi D^3}{6}\left(\coth(x) - \frac{1}{x}\right)\mathrm{d}D, \quad x = M_{sat}\frac{\pi D^3}{6}\frac{\mu_0 H}{k_B T},$$

where N(D) is the number of USPIO having the diameter D, T is the temperature, k_B the Boltzmann constant and μ_0 the magnetic induction of the vacuum.

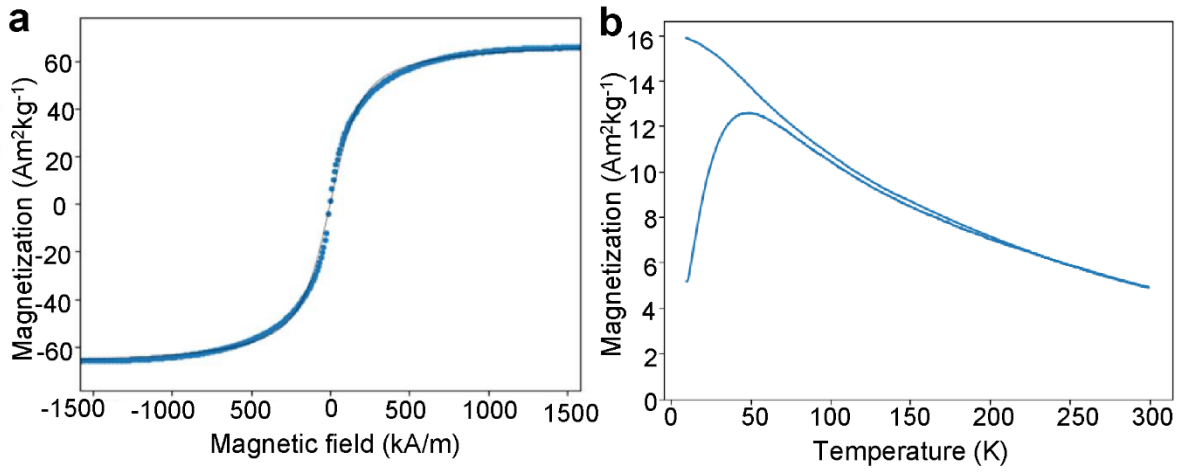

Figure S36. a) Magnetization curve of USPIO(20)@MIL at 300 K (solid black line) and Langevin fit (dotted blue line); b) Magnetic moments of USPIO(20)@MIL (blue line) under an applied magnetic field of 200 Oe after zero field cooling then field cooling.

Table S5. Saturation magnetization and magnetic moments of hybrid nano-objects measured by VSM.

Nanoparticles/nano-objects	M_{sat} 300 K (A m^2 kg^{-1})	Reference
USPIO(20) @MIL	68	This work
USPIO(10) @MIL	71	This work
MIL/USPIO(10)	39	[1]
MIL/USPIO-cit(10)	62	[1]
MIL-53(Al)-Fe-AA-13	0.2	[14]
ZIF-8-Fe-AA-CS3	6.3	[14]
ZIF-8-Fe-AA-I3	1.8	[14]
MagNP@PDA@ZIF-8	3.1	[15]
Fe_3O_4@PAA/AuNCs-ZIF-8	8.2	[16]
Fe_3O_4-Au_{25}-ZIF-8	9.1	[6]
Fe_3O_4-ZIF-8	18.9	[7]
Fe_3O_4@PDA@ZIF-90	9.2	[17]
Fe_3O_4@C@MIL-100(Fe)	44.39	[11]
Fe_3O_4@UiO-66	51.58	[18]
Fe_3O_4-COOH@MIL-101(Cr)	10.1	[19]
m-ZIF-90	7	[20]
Fe_3O_4/SiO_2@UiO-66(Zr)	21.7	[21]
Fe_3O_4@SiO_2–MIL-101(Cr)	21	[22]
Fe_3O_4@ZIF-8	14.38	[23]
PEG-NH_2@Fe_3O_4-ZIF-8	6.6	[8]
Fe_3O_4@MOF-808	40.35	[24]
Au-Fe_3O_4@MIL-100(Fe)	53.41	[25]
Fe_3O_4@ZIF-8	54.6	[26]
USPIO/MIL-101(Fe)-NH_2	30	[12]

References

1. Sene, S.; Marcos-Almaraz, M. T.; Menguy, N.; Scola, J.; Volatron, J.; Rouland, R.; Grenèche, J.-M.; Miraux, S.; Menet, C.; Guillou, N.; Gazeau, F.; Serre, C.; Horcajada, P.; Steunou, N. Maghemite-nanoMIL-100(Fe) Bimodal Nanovector As a Platform for Image-Guided Therapy. *Chem* **2017**, *3*, 303-322.
2. Vuong, Q. L.; Berret, J. F.; Fresnais, J.; Gossuin, Y.; Sandre, O. A Universal Scaling Law to Predict the Efficiency of Magnetic Nanoparticles as MRI T_2-Contrast Agents. *Adv Healthcare Mater* **2012**, *1*, 502-512.
3. Trotier, A. J.; Lefrancois, W.; Renterghem, K. V.; Franconi, J. M.; Thiaudiere, E.; Miraux, S. Positive Contrast High-Resolution 3D-Cine Imaging of the Cardiovascular System in Small Animals Using a UTE Sequence and Iron Nanoparticles at 4.7, 7 and 9.4 T. *J Cardiovasc Magn Reson* **2015**, *17*, 1-10.
4. Casula, M. F.; Floris, P.; Innocenti, C.; Lascialfari, A.; Marinone, M.; Corti, M.; Sperling, R. A.; Parak, W. J.; Sangregorio, C. Magnetic Resonance Imaging Contrast Agents Based on Iron Oxide Superparamagnetic Ferrofluids. *Chem Mater* **2010**, *22*, 1739-1748.
5. Kostopoulou, A.; Velu, S. K.; Thangavel, K.; Orsini, F.; Brintakis, K.; Psycharakis, S.; Ranella, A.; Bordonali, L.; Lappas, A.; Lascialfari, A. Colloidal Assemblies of Oriented Maghemite Nanocrystals and Their NMR Relaxometric Properties. *Dalton Trans* **2014**, *43*, 8395-8404.
6. Yang, D.; Yang, G.; Gai, S.; He, F.; An, G.; Dai, Y.; Lv, R.; Yang, P. Au_{25} Cluster Functionalized Metal-Organic Nanostructures for Magnetically Targeted Photodynamic/Photothermal Therapy Triggered by Single Wavelength 808 nm Near-Infrared Light. *Nanoscale* **2015**, *7*, 19568-19578.
7. Lin, J.; Xin, P.; An, L.; Xu, Y.; Tao, C.; Tian, Q.; Zhou, Z.; Hu, B.; Yang, S. Fe_3O_4-ZIF-8 Assemblies As pH and Glutathione Responsive T_2-T_1 Switching Magnetic Resonance Imaging Contrast Agent for Sensitive Tumor Imaging *In Vivo*. *Chem Commun* **2019**, *55*, 478-481.
8. Ettlinger, R.; Moreno, N.; Ziółkowska, N.; Ullrich, A.; Krug von Nidda, H. A.; Jirák, D.; Kerl, K.; Bunzen, H. *In Vitro* Studies of Fe_3O_4-ZIF-8 Core–Shell Nanoparticles Designed As Potential Theragnostics. *Part Part Syst Charact* **2020**, *37*, 2000185.
9. Meng, Y.; Zhang, D.; Chen, X.; Dai, Z.; Yao, X.; Cui, P.; Yu, D.; Zhang, G.; Zheng, X. FePt Nanoparticles Embedded in Metal–Organic Framework Nanoparticles for Tumor Imaging and Eradication. *ACS Appl Nano Mater* **2020**, *3*, 4494-4503.
10. Dehghani, S.; Alam, N. R.; Shahriarian, S.; Mortezazadeh, T.; Haghgoo, S.; Golmohamadpour, A.; Majidi, B.; Khoobi, M. The Effect of Size and Aspect Ratio of Fe-MIL-88B-NH_2 Metal-Organic Frameworks on Their Relaxivity and Contrast Enhancement Properties in MRI: *In Vitro* and *In Vivo* Studies. *J Nanopart Res* **2018**, *20*, 1-16.
11. Wang, D.; Zhou, J.; Chen, R.; Shi, R.; Xia, G.; Zhou, S.; Liu, Z.; Zhang, N.; Wang, H.; Guo, Z.; Chen, Q. Magnetically Guided Delivery of DHA and Fe Ions for Enhanced Cancer Therapy Based on pH-Responsive Degradation of DHA-Loaded Fe_3O_4@C@MIL-100(Fe) Nanoparticles. *Biomaterials* **2016**, *107*, 88-101.
12. Xu, Z.; Chen, Y.; Chen, M.; Chen, W.; Cheng, Y. Assembly of USPIO/MOF Nanoparticles with High Proton Relaxation Rates for Ultrasensitive Magnetic Resonance Sensing. *J Mater Chem C* **2021**, *9*, 11915-11923.
13. Prene, P.; Tronc, E.; Jolivet, J.; Livage, J.; Cherkaoui, R.; Nogues, M.; Dormann, J.; Fiorani, D. Magnetic Properties of Isolated γ-Fe_2O_3 Particles. *IEEE Trans Magn* **1993**, *29*, 2658-2660.
14. Wu, Y. N.; Zhou, M.; Li, S.; Li, Z.; Li, J.; Wu, B.; Li, G.; Li, F.; Guan, X. Magnetic Metal-Organic Frameworks: γ-Fe_2O_3@MOFs *Via* Confined *In Situ* Pyrolysis Method for Drug Delivery. *Small* **2014**, *10*, 2927-2936.
15. Zhou, J.; Wang, P.; Wang, C.; Goh, Y. T.; Fang, Z.; Messersmith, P. B.; Duan, H. Versatile Core-Shell Nanoparticle@Metal-Organic Framework Nanohybrids: Exploiting Mussel-Inspired

Polydopamine for Tailored Structural Integration. *ACS Nano* **2015**, *9*, 6951-6960.
16. Bian, R.; Wang, T.; Zhang, L.; Li, L.; Wang, C. A Combination of Tri-Modal Cancer Imaging and *In Vivo* Drug Delivery by Metal-Organic Framework Based Composite Nanoparticles. *Biomater Sci* **2015**, *3*, 1270-1278.
17. Chen, J.; Liu, J.; Hu, Y.; Tian, Z.; Zhu, Y. Metal-Organic Framework-Coated Magnetite Nanoparticles for Synergistic Magnetic Hyperthermia and Chemotherapy with pH-Triggered Drug Release. *Sci Technol Adv Mater* **2019**, *20*, 1043-1054.
18. Zhao, H. X.; Zou, Q.; Sun, S. K.; Yu, C.; Zhang, X.; Li, R. J.; Fu, Y. Y. Theranostic Metal-Organic Framework Core-Shell Composites for Magnetic Resonance Imaging and Drug Delivery. *Chem Sci* **2016**, *7*, 5294-5301.
19. Wei, J. P.; Qiao, B.; Song, W. J.; Chen, T.; li, F.; Li, B. Z.; Wang, J.; Han, Y.; Huang, Y. F.; Zhou, Z. J. Synthesis of Magnetic Framework Composites for the Discrimination of Escherichia Coli at the Strain Level. *Anal Chim Acta* **2015**, *868*, 36-44.
20. Fang, J.; Yang, Y.; Xiao, W.; Zheng, B.; Lv, Y. B.; Liu, X. L.; Ding, J. Extremely Low Frequency Alternating Magnetic Field-Triggered and MRI-Traced Drug Delivery by Optimized Magnetic Zeolitic Imidazolate Framework-90 Nanoparticles. *Nanoscale* **2016**, *8*, 3259-3263.
21. Zhang, W.; Yan, Z.; Gao, J.; Tong, P.; Liu, W.; Zhang, L. Metal-Organic Framework Uio-66 Modified Magnetite@Silica Core-Shell Magnetic Microspheres for Magnetic Solid-Phase Extraction of Domoic Acid from Shellfish Samples. *J Chromatogr A* **2015**, *1400*, 10-18.
22. Huo, S. H.; Yan, X. P. Facile Magnetization of Metal-Organic Framework MIL-101 for Magnetic Solid-Phase Extraction of Polycyclic Aromatic Hydrocarbons in Environmental Water Samples. *Analyst* **2012**, *137*, 3445-3451.
23. Zheng, J.; Cheng, C.; Fang, W.; Chen, C.; Yan, R.; Huai, H.; Wang, C. Surfactant-Free Synthesis of a Fe_3O_4@ZIF-8 Core–Shell Heterostructure for Adsorption of Methylene Blue. *CrystEngComm* **2014**, *16*, 3960-3964.
24. Jia, Y.; Wang, Y.; Yan, M.; Wang, Q.; Xu, H.; Wang, X.; Zhou, H.; Hao, Y.; Wang, M. Fabrication of Iron Oxide@MOF-808 as a Sorbent for Magnetic Solid Phase Extraction of Benzoylurea Insecticides in Tea Beverages and Juice Samples. *J Chromatogr A* **2020**, *1615*, 460766.
25. Ke, F.; Wang, L.; Zhu, J. Multifunctional Au-Fe_3O_4@MOF Core-Shell Nanocomposite Catalysts with Controllable Reactivity and Magnetic Recyclability. *Nanoscale* **2015**, *7*, 1201-1208.
26. Zhang, T.; Zhang, X.; Yan, X.; Kong, L.; Zhang, G.; Liu, H.; Qiu, J.; Yeung, K. L. Synthesis of Fe_3O_4@ZIF-8 Magnetic Core–Shell Microspheres and Their Potential Application in a Capillary Microreactor. *Chem Eng J* **2013**, *228*, 398-404.

Chapter 3

This chapter is adapted to the following manuscript:

Atomically precise Gold nanoclusters - MIL-100(Fe) for dexamethasone delivery and inflammatory disease synergistic therapy.

(In Submission)

Heng Zhao et al.

Table of Contents

3.1 Contributions to this research

In this work, for the purpose of developing theranostic MOFs for inflammatory diseases therapy, I first conducted the literature survey of atomically precise gold nanoclusters (Au NCs) and Au@MOFs. Inspired by our previous work on USPIO@MIL, I assembled glutathione capped Au_{25} NCs into MIL-100(Fe), namely Au_{25}SG@MIL through an *in situ* room temperature synthesis, which has not been reported in the literature. I characterized the synthesized materials by using many different techniques, such as PXRD, N_2 sorption isotherms, TEM, DLS, TGA, UV-Vis, FT-IR and ^{1}H NMR. Dr. Gilles Patriarche (Université Paris-Saclay) performed the HAADF-STEM measurements. Then, I studied the drug loading and release of Au_{25}SG@MIL by HPLC. Bernard Goetz performed ICP-MS measurements. In terms of cell experiments, I investigated the cell cytotoxicity, cellular internalization by confocal microscope, pro-inflammatory cytokines expression by Elisa kit based on RAW 264.7 cells. For the in depth understanding of the anti-inflammatory mechanism and, I studied the inflammatory pathways such as the nuclear factor kappa B (NF-κB) pathway and the interferon regulatory factor (IRF) pathway study with the help of Sonia Becharef and under the supervision of Prof. Florence Gazeau (Université Paris Diderot) Next, I have performed all the data analysis and discussed the results with my supervisors and colleagues. Finally, I plotted the figures and wrote the first manuscript draft and my supervisors and collaborators helped me to revise it.

Atomically precise Gold nanoclusters - MIL-100(Fe) for dexamethasone delivery and inflammatory disease synergistic therapy.

Heng Zhao,[a] Sonia Becharef,[b] Florent Carn,[b] Gilles Patriarche,[c] Simona Mura,[d] Eddy Dumas,[e] Florence Gazeau,[b] Christian Serre,[e] Nathalie Steunou.[a,e]

[a] H. Zhao, Dr. C. Serre, Prof. N. Steunou
Institut des Matériaux Poreux de Paris, ENS, ESPCI Paris, CNRS, PSL university, Paris, France.

[b] S. Becharef, Dr. F. Carn, Prof. F. Gazeau

Laboratoire Matière et Systèmes Complexes (MSC), UMR CNRS 7057, Université Paris Diderot, 75013 Paris, France.

[c] Dr G. Patriarche
Université Paris-Saclay, CNRS, Centre de Nanosciences et de Nanotechnologies, 91120 Palaiseau, France.

[d] Dr S. Mura
Institut Galien Paris-Saclay, UMR 8612, CNRS, Université Paris-Saclay, Faculté de Pharmacie, 5 rue Jean-Baptiste Clément, F-92296 Châtenay-Malabry cedex, France.

[e] Dr E. Dumas, Prof. N. Steunou
Institut Lavoisier de Versailles, UMR CNRS 8180, Université de Versailles St Quentin en Yvelines, Université Paris Saclay, Versailles, France.

3.2 Abstract

In terms of inflammatory disease treatment, various therapeutic strategies have been proposed. To improve the biological half-life and bioavailability of free clinic drugs, nanocarriers were developed for the enhancement of drug absorption and biodistribution in inflammatory sites; In particular, nanoparticles of biocompatible Metal Organic Frameworks (MOFs) are of interest. Also, gold nanoclusters can be used as anti-inflammatory therapeutic agent and potential imaging contrast agent. Herein, we successfully encapsulated atomically precise gold nanoclusters (Au NCs) into biodegradable mesoporous MIL-100(Fe) *via* an *in situ* room temperature synthesis for the delivery of glucocorticoid dexamethasone phosphate (DexP) and inflammatory disease synergisic therapy. The drug loaded nanocarrier specifically inhibits inflammatory cells growth, scavenges intracellular reactive oxygen species (ROS) and downregulates pro-inflammatory cytokines secretion. It also

inhibits related inflammatory pathways such as the nuclear factor kappa B (NF-κB) pathway and the interferon regulatory factor (IRF) pathway efficiently. The co-delivery of chemodrug and metallic nanoclusters by MOFs may provide a new approach for inflammatory disease.

3.3 Introduction

Inflammation that involves a wide variety of physiological and pathological processes, is an adaptive response triggered by noxious stimuli and conditions.[1] As an incurable chronic autoimmune inflammatory disease, rheumatoid arthritis (RA) is characterized by synovial joint inflammation, and irreversible destruction of cartilage and bone tissue, which can lead to disability, inability to participate in work and social activities, and increased mortality.[2-3] One of the main clinical pathological features is the inflammatory cell infiltration in the joint and these inflammatory macrophages cause synovial hyperplasia and are responsible of the release of some proinflammatory factors such as tumor necrosis factor-α (TNF-α), interleukin-1β (IL-1β), interleukin-6 (IL-6), resulting in bone erosion and cartilage tissue damage. At present, the primary goal of treatment for patients with RA is to inhibit the progression of structural damage by achieving either clinical remission or low levels of disease activity.[4]

To treat RA, the commonly used antirheumatic drugs in clinical are non-steroidal anti-inflammatory drugs (NSAID), corticosteroids, and disease-modifying anti-rheumatic drugs (DMARD). Due to the short biological half-life and poor bioavailability, high and frequent administration of drugs is required, which may cause serious side effects. Encapsulation of the drug in the nanocarriers allowing specific drug delivery can enhance drug absorption and biodistribution in inflammatory sites. RA is featured by low-pH and hypoxic microenvironment and glutathione (GSH) functions as an intracellular reductant in redox processes. In particular, nanoparticles of biocompatible Metal Organic Frameworks (MOFs) have widely been used as stimuli-responsive drug nano-carriers. Their large surface area, amphiphilic internal microenvironment as well as their possible functionalization make these materials suitable to host a large variety of drugs with a high loading capacity.[5]

The biological use of gold as a drug can be traced back to 2500 B.C., and Au(I) thiomalate was commonly used in arthritis more than 60 years ago.[6-7] Gold salt shows a slow onset action in anti-inflammation and the possible mechanism may involve the Au(I)/Au(III) redox system: i) Au(I) scavenges reactive oxygen species (ROS); ii) the formed Au(III) irreversibly denatures or interferes with lysosomal enzymes.[8] In recent years, with the development of nanomedicine, gold nanoparticles

(Au NPs) were exploited for a diverse array of biomedical applications.[9-10] Specifically, Au NPs were suggested as a novel option for treatment of RA or other inflammatory diseases and they were involved in different inflammatory signaling pathways such as nuclear factor kappa-B (NF-κB) signaling pathway and Toll-like receptors (TLRs) signaling pathway, leading to a decrease of reactive oxygen species (ROS) production and pro-inflammatory cytokines expression, etc.[11-13] Hong Yang *et al.* reported that Au NPs were beneficial to limit TLRs signaling pathway, which plays a central role in the pathophysiology of many inflammatory diseases.[14] Meanwhile, gold nanoclusters (Au NCs) possess multienzyme mimetic activity, and thus can effectively eliminate ROS[15] and N-acetylcysteine capped Au NCs showed broad-spectrum antioxidant activity and anti-inflammatory activity in acute kidney injury.[16] Atomically precise Au NCs, emerging link between discrete atoms and plasmonic nanoparticles, showed intriguing physical-chemical properties, such as luminescence, magnetism and catalysis. Their properties can be rationalized in terms of their quantum size effect and Au_{25} NCs are of interest due to their easy preparation, high stability, and easy functionalization.[17-19] In particular, peptide protected Au_{25} NCs have been reported to inhibit the expression of crucial pro-inflammation cytokines and the activation of NF-κB pathway, reducing the severity of inflammation-induced bone and cartilage destruction.[20]

Inflammatory disease is a complicated process and single model therapy or inhibition of certain inflammatory pathway is often inefficient. Thereby, combining different therapeutic modalities to treat inflammatory disease possess great promises and Au@MOFs based nano-objects consisting of MOFs and Au NPs could be good candidates for a synergistic therapy as a result of their high porosity and functionality. Recently, various Au@MOFs have been developed such as Au NRs@ZIF-8 for near-infrared-induced synergistic chemo-photothermal therapy, $Au@Cu_3(BTC)_2$ nanoparticles for Raman imaging and synergistic chemo-photothermal therapy, Fe_3O_4/ZIF-8-Au_{25} nanocomposite for magnetically targeted photodynamic / photothermal therapy and Au nanostar@MIL-101-NH_2(Fe) for T1-weighted MRI and photothermal therapy.[21-23] However, to the best of our knowledge, these Au@MOFs were only used for cancer theranostics and they have not been reported yet in inflammatory disease therapy. Moreover, both the MOF component and the noble metal part of nano-objects should be non-toxic and biodegradable. As a class of well-known mesoporous MOFs, MIL-100(Fe) showed great promises for drug delivery[24-25] and thus, our purpose is to design biodegradable Au NCs/MIL-100(Fe) nano-objects for anti-inflammatory application.

In this work, we developed a new theranostic anti-inflammatory nanocarrier based on atomically precise glutathione protected Au nanoclusters ($Au_{25}SG_{18}$ NCs) assembled with MIL-100(Fe) (Au NCs@MIL-100). This nano-object was synthesized *via* an *in situ* room temperature green protocol

(Scheme 1). Furthermore, it was able to encapsulate the clinical drug glucocorticoid dexamethasone phosphate (DexP) with a high loading capacity. Finally, the in vitro cytotoxicity assay based on lipopolysaccharide (LPS) stimulated inflammatory models has shown that this Au@MIL/DexP nanocarrier presents a high anti-inflammation capacity and the mechanism of inhibition of multiple inflammatory signal pathways such as NF-κB and Interferon regulatory factor (IRF) has been further demonstrated on THP1-dual cells, an anti-inflammatory screening cell model.

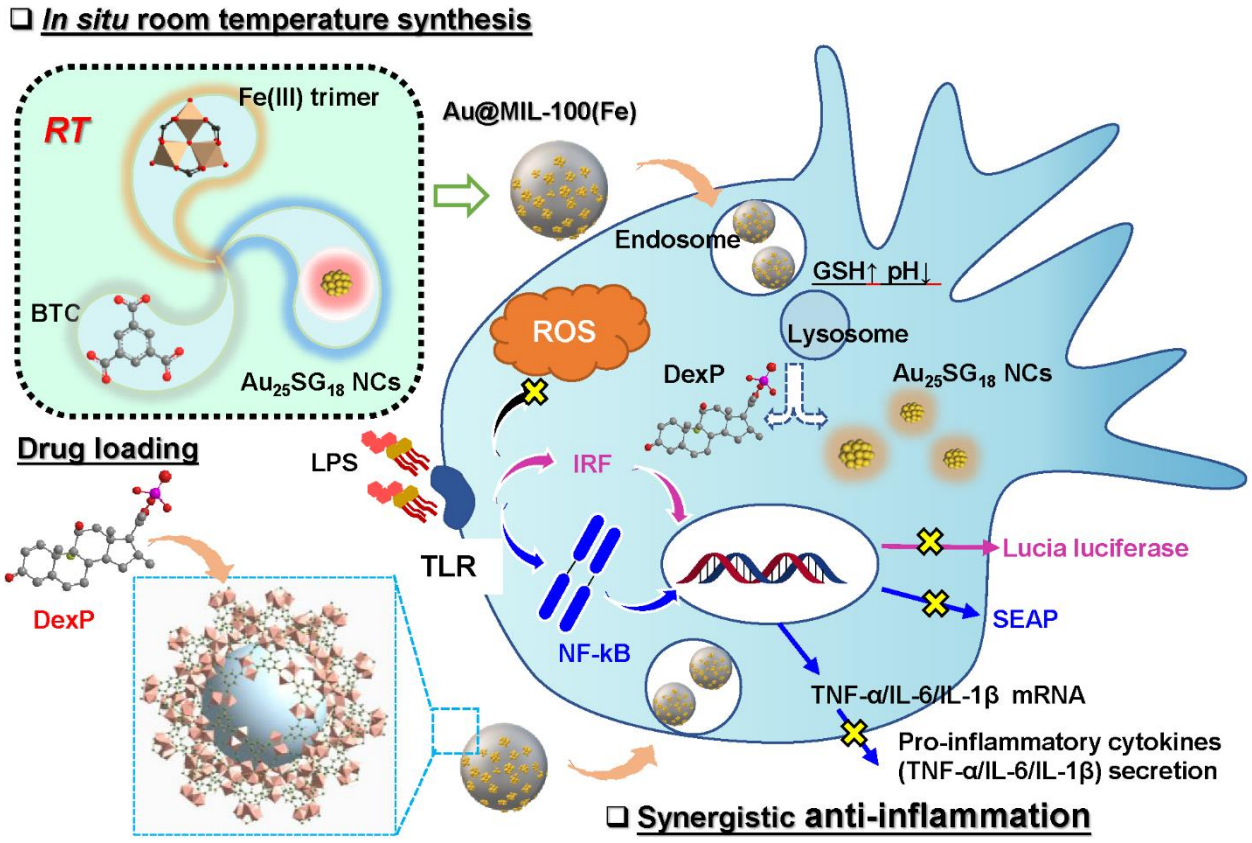

Scheme 1. Schematic illustration of synthesis of Au NCs@MIL-100(Fe) nano-objects and their use as a theranostic platform for synergistic anti-inflammation. LPS: lipopolysaccharide; TLR: Toll-like receptor; ROS: reactive oxygen species; DexP: Dexamethasone phosphate; GSH: Glutathione; IRF: Interferon regulatory factor pathway; NF-κB: Nuclear factor kappa B pathway; SEAP: Secreted embryonic alkaline phosphatase.

3.4 Results and discussion

Encouraged by a previous patent of some of us, the hybrid gold nanoclusters - MIL-100(Fe) (denoted as Au@MIL) nano-object was prepared through an *in situ* room temperature synthesis method by mixing the pre-synthesized $Au_{25}SG_{18}$ NCs with the precursors of MIL-100(Fe), namely $Fe(NO_3)_3$ and trimesic acid (BTC).[26] $Au_{25}SG_{18}$ NCs were synthesized by a glutathione (GSH) etching method as previously reported.[27-28] The diameter of these $Au_{25}SG_{18}$ NCs is 1.6 ± 0.3 nm as shown by transmission electron microscopy (TEM). Their characterization by ultraviolet-visible (UV-Vis) and fluorescence

(FL) emission spectra (Figure S1) is fully consistent with that previously reported.[27-28] Au(X)@MIL (X= l and h) nano-objects were prepared with different Au content (atomical ratio of Au to Fe, l = 1.6 at% and h = 7.8 at%) by tuning the initial amount of $Au_{25}SG_{18}$ NCs (10 mg and 50 mg) used in the synthesis. This Au content was evaluated by ICP-MS (see table S1). Au(X)@MIL NPs were further characterized by powder X-ray diffraction (PXRD), thermogravimetric analysis (TGA), nitrogen adsorption and desorption isotherms, TEM, high-angle annular dark-field scanning TEM (STEM-HAADF) and energy dispersive X-ray spectroscopy (EDS) mapping images (**Figure 1-2**).

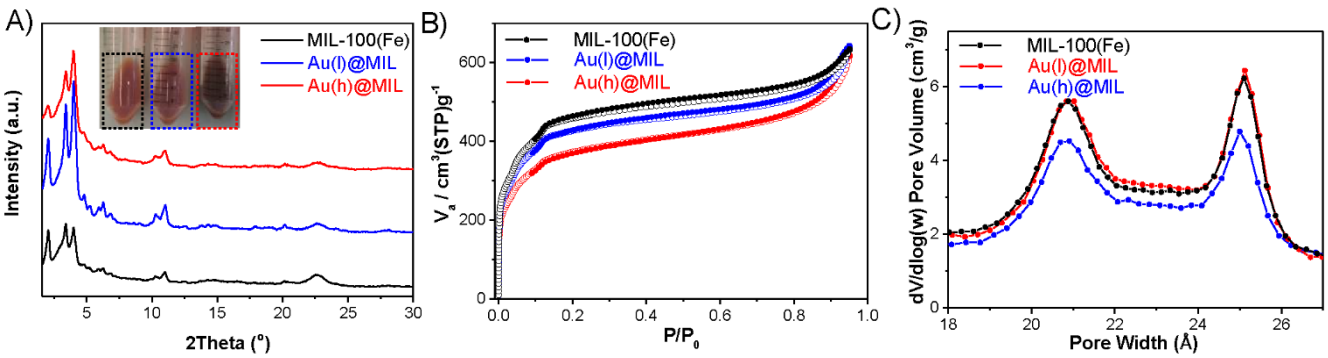

Figure 1. Characterizations of Au@MIL. A) PXRD patterns (λ_{Cu} =1.5406 Å), B) Nitrogen absorption and desorption isotherms and C) pore size distribution (BJH Adsorption: Halsay, Kruk-Jaroniec-Sayari) at 77 K (P_0 = 1atm) of MIL-100(Fe), Au(l)@MIL and Au(h)@MIL.

The PXRD patterns of Au(l)@MIL and Au(h)@MIL nanoobjects indicated that there was no significant crystallinity loss after embedding $Au_{25}SG_{18}$ NCs into MIL-100(Fe) (Figure 1A). Due to the ultrasmall size of $Au_{25}SG_{18}$ NCs, no PXRD peak of Au NCs was observed in the pattern. In Figure S6 and S7, the TGA profiles and FT-IR spectra of Au(X)@MIL are comparable to that of MIL-100(Fe) due to the large amount of the MOF in those nano-objects., According to N_2 porosimetry, Au(l)@MIL and Au(h)@MIL present a high porosity as shown by their BET area of 1650 m^2 g^{-1} and 1427 m^2 g^{-1} respectively. The BET area of Au(h)@MIL is lower than that of the bare MIL-100(Fe) NPs (1720 m^2 g^{-1}), due to the presence of a larger amount of $Au_{25}SG$ NCs (Figure 1C). As shown in Figure 1C, the pore size distribution of Au(l)@MIL and Au(h)@MIL is similar to that of the bare MIL-100(Fe) (two types of mesoporous cages of free apertures of ca. 25 Å and 29 Å)[29] (Figure 1D), indicating the successful formation of the MIL-100(Fe) in the presence of $Au_{25}SG_{18}$ NCs. Moreover, the two mesoporous cages of MIL-100(Fe) in the Au(X)@MIL nano-objects are still accessible to N_2 and thus are presumably not occupied by $Au_{25}SG_{18}$ NCs. Such nano-object are thus prone to encapsulate drugs with a high drug loading capacity. The morphology and composition of Au(l)@MIL and Au(h)@MIL were characterized by TEM, HRTEM, STEM-HAADF and EDS mapping (Figures 2, S2-4). The Au(l)@MIL and Au(h)@MIL, nano-objects consist of MIL-100(Fe) NPs with a diameter of about 39 and 46 nm respectively (Figure S2) decorated by $Au_{25}SG_{18}$ NCs with diameter up to 2 nm (Figures 2A

& S3). The HRTEM images clearly indicated that $Au_{25}SG_{18}$ NCs with a high crystallinity were homogeneously distributed in the hybrid nano-objects (Figures 2A & S3). $Au_{25}SG_{18}$ NCs could act as bio-imaging agent and therapeutic agent, and a higher ratio of $Au_{25}SG_{18}$ NCs into MOFs is advantageous for imaging and therapy. Herein, Au(h)@MIL NPs was thus selected for the following steps. The colloidal stability of Au(h)@MIL was firstly investigated by varying pH (Figure S9). Since pH 3 is close to the point of zero charge of Au(h)@MIL, their hydrodynamic diameter reached around 1500 nm, as previously reported for pure MIL-100(Fe)[30]. In mild acidic environment such as pH 5 and pH 6, the surface charge of Au(h)@MIL was lower than -20 mV and their hydrodynamic diameter was close to 150 nm, indicating their high colloidal stability. In contrast, due to the decrease of the surface charge Au(h)@MIL at pH 7 (-10 mV), these nano-objects present a higher hydrodynamic diameter (253 ± 14 nm), and thus a weak colloidal stability in neutral PBS buffer in long time monitoring. Furthermore, the colloidal stability of Au(h)@MIL was studied under different simulated physiological media conditions, including Milli Q water (MQ H_2O), neutral phosphate buffer saline (PBS), NaCl solution (0.9% NaCl), the cell culture medium Dulbecco's Modified Eagle Medium (DMEM), and DMEM supplemented with fetal bovine serum (FBS) (90/10% v/v) medium (DMEM + FBS). In contrast to a strong aggregation observed in DMEM and 0.9% NaCl, Au(h)@MIL showed a progressive increase of hydrodynamic diameters in PBS, especially after 4 hours and an excellent colloidal stability in MQ H_2O and DMEM + FBS since their hydrodynamic diameter of ~150 nm remained constant for 24 h as shown by dynamic lighting scattering (DLS) (Figure S8). This may result from the small size of single Au(h)@MIL nanoparticle and meanwhile the adsorption of FBS at the surface of nano-objects is certainly prone to enhance their colloidal stability due to the formation of a protein corona as previously observed for MIL-100(Fe) nanocarrier.[31]

To design a drug delivery system, a high drug loading capacity and sustained drug release property are required to ensure the therapeutic efficacy and limit the amount of nanocarrier.[32] As described before, the porosity of MIL-100(Fe) in Au@MIL is preserved once combined with $Au_{25}SG_{18}$ NCs. The drug loading and release of Au@MIL in physiological media was thus studied. Clinically, RA is often treated with glucocorticoids and dexamethasone (Dex) is a potent corticosteroid with gluconeogenic, immunosuppressive and anti-inflammatory properties. MOFs such as ZIF-8[33-34], Zn−Mg-MOF74[35] and CD-MOF[36-37] have been studied for Dex delivery for bone implants or ocular drug delivery, showing encouraging loading efficiency from ~6% to ~16% and sustained release in PBS for a few weeks. Notably, even with the same MOF, the encapsulation of DexP could be diverse: for example, the Dex@ZIF-8-SCM enabled surprisingly high Dex loading capacity of 80 wt%, about 15 times higher than aforementioned ZIF-8.[38] Although ZIF-8 MOFs showed promising loading capacity, their

stability in phosphate buffered saline (PBS) is always a concern.[39] Here we have selected dexamethasone bearing a phosphate groups in order to enhance the interactions with MIL-100(Fe) through the possible coordination of the phosphate groups with the coordinatively unsaturated Fe site. This possible host/guest interaction may enhance the drug loading and lead to a progressive drug release.

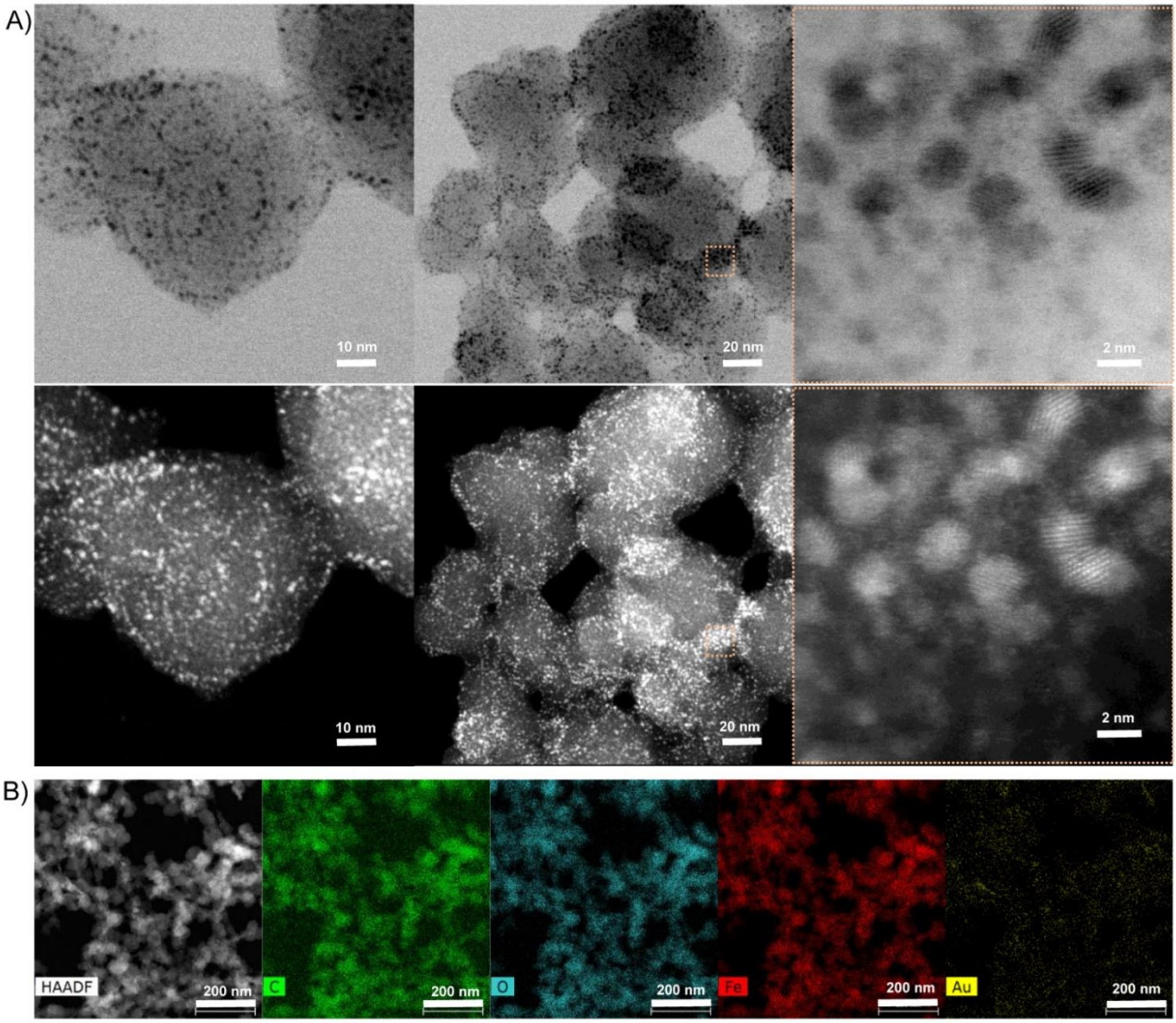

Figure 2. A) TEM, HRTEM and STEM-HAADF and (B) EDS mapping images of Au(h)@MIL.

Herein, DexP was encapsulated in MIL-100(Fe) and Au(h)@MIL *via* direct immersion of MOF in DexP aqueous solution. The drug loading capacity of MIL-100(Fe) and Au(h)@MIL was ~49 wt% and ~43 wt% respectively at the weight ratio of MOF : DexP = 1 : 0.5 according to HPLC measurement (Figure S10, Table S2). Importantly, in Figure S11 the PXRD patterns of MIL-100/DexP and Au(h)@MIL/DexP are consistent with that of MIL-100(Fe), indicating that the crystalline structure of MIL-100(Fe) is preserved upon the encapsulation of DexP. The encapsulation of DexP in the

mesopores of MIL-100(Fe) is also confirmed by N_2 porosimetry since the BET area of Au(h)@MIL/DexP decreased dramatically. According to the pore size distribution derived from the Barrett-Joyner-Halenda (BJH) pore-size model (Figures S12B and S12D), DexP mostly occupy the large mesopores of MIL-100(Fe) while a few DexP molecules also present in the small mesoporous cage of the MOF. The drug loaded MOFs were also investigated by TGA and a significant difference in Figure S13 could attribute to the loading of Dex-P, which may substitute certain BTC and coordinate with Fe sites during the drug loading process, thus changing the thermal stability. Considering of the similar drug loading capacity and the risk of damaging MOF crystalline structure, a lower weight ratio of MOF : DexP = 1 : 0.5 other than 1 : 1 was employed for the following study.

Glucocorticoid therapy is associated with multiple serious adverse effects in a dose-dependent manner, and therefore it is of importance to achieve efficient drug delivery. The endolysosomal system of macrophage cells is featured by low-pH and high-GSH and the responsiveness of DexP release kinetics was thus investigated here. As shown in **Figure 3A**, the release rate of DexP from Au(h)@MIL/DexP greatly depends on pH since a fast release occurs in neutral PBS while a sustained release is observed in acidic pH. At pH 7.4, 52%, 73% and 86% of DexP were released after 1, 4 and 8 h, respectively. The release of DexP is substantially slowed down in PBS (pH 5.1) and PBS (pH 5.1) containing 10 mM GSH (PBS + GSH) as a consequence of the slower kinetics of MOF degradation in more acidic conditions, achieving a cumulative DexP delivery of about 20% after 2 days.

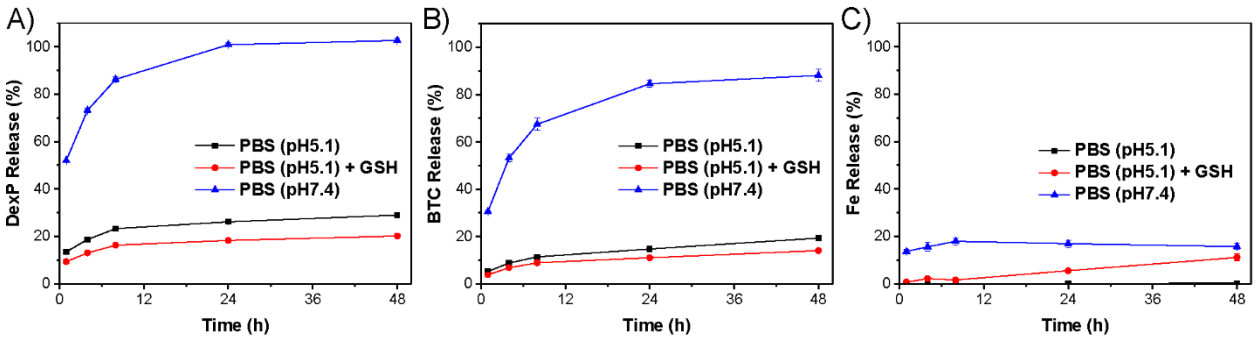

Figure 3. A) DexP and (B) BTC release of Au(h)@MIL/DexP-HP in PBS (pH 5.1), PBS (pH 5.1) with 10 mM GSH and PBS (pH 7.4) by HPLC. (C) Fe release of Au(h)@MIL/DexP in PBS (pH 5.1), PBS (pH 5.1) with 10 mM GSH and PBS (pH 7.4) by ICP-MS.

To full understanding the process of drug release process, the quantification of the ligand BTC of the MOF was also measured in the PBS media (Figure 3B). Obviously, the release of BTC showed the same trend as DexP and this further confirmed that the drug release is mainly driven by the degradation of MIL-100(Fe). In this process, the competitive substitution of BTC by phosphate from PBS in the coordination shell of Fe in MOF is prone to take place. As an example, Au(h)@MIL/DexP degraded

fast at pH 7.4 which might be due to the strong complexing ability of phosphate at this pH towards Fe cations. The Fe release profile is notably different from that of BTC release at pH 7.4. This may be explained by the precipitation of Fe-phosphate phase as previously shown.[40-41] The stimuli-responsive release properties of Au(h)@MIL/DexP can thus be exploited to selectively deliver DexP to inflamed joints by local injection or by oral administration in the case of RA therapy.

To mitigate the rapid drug release observed at pH 7.4, the surface of Au@MIL was coated by a polymer. In pathogenesis of RA, certain cell receptors such as CD44, folate receptor beta (FR-β) are overexpressed on inflamed cells, which is similar with some cancer cells. Hyaluronic acid (HA) as a naturally occurring polysaccharide, has been extensively investigated for targeting cancer therapy since it specifically binds to the HA receptor (CD44).[42] Inspired by the bionics of marine mussels, polydopamine (PDA) constructed by dopamine self-polymerization showed outstanding adhesive properties and has been widely used for the improvement of coating stability and immobilization of drug molecules.[43-45] To combine the targeting ability and adhesive property, bioactive hyaluronic acid - polydopamine (HA-PDA) co-polymer was thus used for the surface functionalization of Au(h)@MIL or Au(h)@MIL/DexP. As for the synthesis of HA-PDA, HA was firstly oxidized by sodium periodate and then reacted with dopamine and the successful synthesis of HA-PDA was confirmed by ^{1}H NMR and FT-IR (Figure S14). In the ^{1}H NMR spectra, the characteristic peak of aldehyde groups on HA-CHO was at about 5.1 ppm, and the characteristic peak of PDA of HA-PDA was at ~7.0 ppm. In the FT-IR spectra, a peak at ~1720 cm^{-1}, corresponding to the absorbance peak of aldehyde groups on HA-CHO disappeared after the reaction with PDA. After the surface modification of HA-PDA on Au(h)@MIL (*i.e.*, Au(h)@MIL-HP), the nano-object was characterized by PXRD again and the crystalline structure was still intact and meanwhile the color of the sample evolved from dark-brown to black (Figure S15).

As described before, the hydrodynamic diameter and surface charge of Au(h)@MIL were pH-dependent. Interestingly, after the surface coating of HA-PDA, the surface charge of Au(h)@MIL-HP became more negative at pH 7 and meanwhile the hydrodynamic diameter (by Number) was even decreased from 253 ± 14 nm to 146 ± 6 nm, suggesting a better physiological colloidal stability (Figure S16). The surface modification is certainly driven by the strong coordination bond between open Fe site on the surface of MIL-100(Fe) moiety and phenolic hydroxyl group of co-polymer HA-PDA. Given the possible protection effects of HA-PDA, the release of DexP from Au(h)@MIL/DexP-HP was also studied in the same conditions as before and the drug release was observed to be much slower in neutral PBS (Figure S17A). HA-PDA chains are prone to partially limit the accessibility of the mesopores of MIL-100(Fe) at their external surface and thus a slowdown drug release was achieved.

However, the BTC release profile of Au(h)@MIL/DexP-HP was almost the same as Au(h)@MIL/DexP (Figure S17B). BTC is much smaller than Dex-P and meanwhile easier to be substituted by free small phosphate ions from PBS. The Fe release profile of Au(h)@MIL/DexP-HP was also similar to that of Au(h)@MIL/DexP in acidic PBS with or without GSH and even lower in neutral PBS. Although the chemical stability of Au(h)@MIL was not substantially improved upon surface modification, a better colloidal stability and a more progressive drug release in neutral pH were achieved.

To evaluate the *anti*-inflammatory performance of the different MOF formulations developed in this study, we realized a comprehensive screening of the different compounds on *in vitro* models of the monocyte/macrophage system. RAW 264.7 murine macrophage cell line was co-incubated with different concentrations of $Au_{25}SG_{18}$ NCs, MIL-100(Fe), Au(h)@MIL, free DexP (equiv. loading capacity), Au(h)@MIL/DexP and Au(h)@MIL/DexP-HP for 24 h. Cell cytotoxicity was investigated by a standard CCK-8 assay. The viability of RAW 264.7 cells exposed to all the groups except DexP group was around 80% up to the concentration of 100 μg mL^{-1} (Figure S18). LPS is a component of outer membrane of Gram-negative bacteria, which could bind extracellular domain of TLR4 of macrophage cells to trigger MyD88-dependent pathway, thus leading to the activation of IRF and NF-κB and the increase of oxidative stress of macrophage cells.[46-47] Herein, LPS activated macrophage cells (M1) were then used as an *in vitro* inflammatory model. Subsequently, the cell viability of LPS activated RAW 264.7 cells treated with DexP was similar with the case of non-activated cells. However, the viability of inflammatory cells exposed to MIL-100(Fe) and Au(h)@MIL nano-object decreased to 13% and 17% at the concentration of 50 μg mL^{-1}, and Au(h)@MIL/DexP and Au(h)@MIL/DexP-HP nano-object exhibited a slightly higher cell viability of 30% (Figure S18). Interestingly these results highlight a selective toxicity of MIL-100(Fe) complexes for inflammatory cells in comparison to unactivated macrophages, which is not achieved by DexP free drug.

To confirm the successful coating of Au@MIL by HA-PDA and its *in vitro* targeting ability, the cell internalization process of Au@MIL was investigated by CLSM experiments. The fluorescent dye Rhodamine B (RhB) was encapsulated in the mesopores of Au@MIL (denoted as Au(h)@MIL/RhB) (see SI for experimental details) and meanwhile the obtained Au(h)@MIL/RhB was further coated with HA-PDA (denoted as Au(h)@MIL/RhB-HP). The cell internalization of Au(h)@MIL/RhB and Au(h)@MIL/RhB-HP by normal macrophage cells and LPS activated RAW 264.7 macrophage cells were monitored by confocal microscopy at 0 h, 1 h, 4 h and 8 h. In comparison with Au(h)@MIL/RhB, Au(h)@MIL/RhB-HP showed a faster and higher internalization in activated RAW 264.7 cells due to the binding of the targeting group HA of Au(h)@MIL/RhB-HP to overexpressed CD44 receptor. This

effect was not observed with normal RAW 264.7 cells, thereby showing that Au(h)@MIL-HP exerts a targeting ability of towards activated RAW 264.7 cells (**Figure 4** and S19). Therefore, the surface coating with HA-PDA, not only improved the colloidal stability, but also conferred an enhanced targeting ability for LPS-activated inflammatory cells, which can be beneficial to realize a precise drug delivery for *in vivo* application.

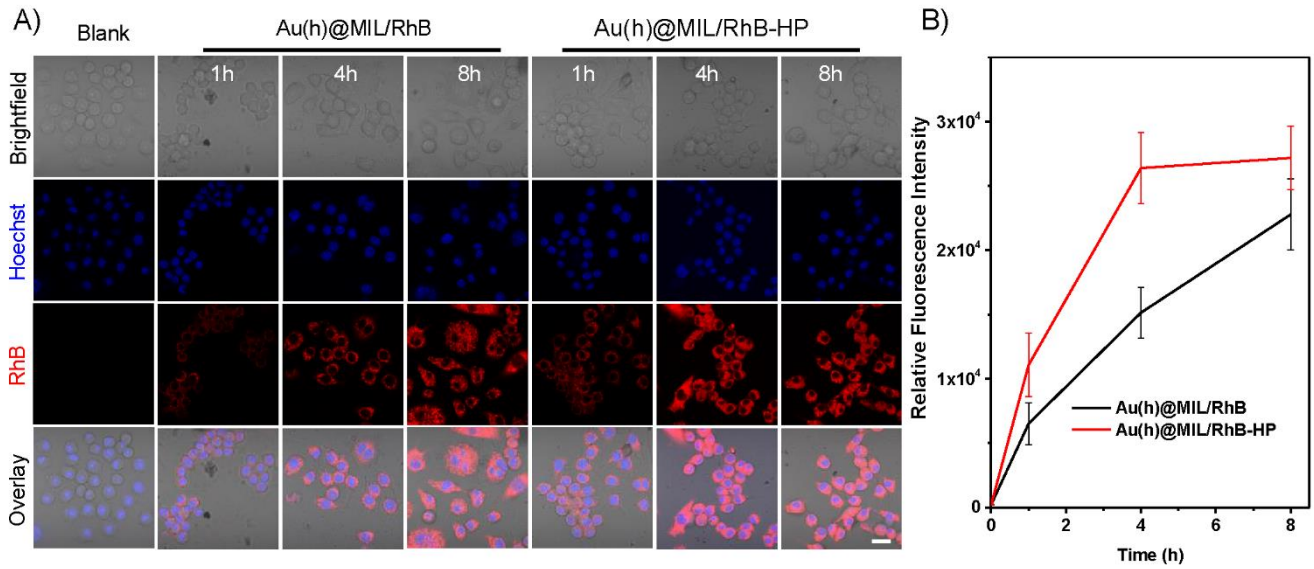

Figure 4. A-B) The cellular uptake of Au(h)@MIL/RhB and Au(h)@MIL/RhB-HP (50 μg mL^{-1}) by LPS (100 ng mL^{-1}, 48 h) activated RAW 264.7 macrophages. Scale bar = 20 μm.

In order to elucidate the mechanisms that are involved in the anti-inflammation activity of Au@MIL, we performed additional screening of anti-oxidative or anti-inflammatory properties. We first focused on Au(h)@MIL/DexP to investigate the role of Dex and $Au_{25}SG_{18}$ NCs. 2',7'-dichlorofluorescein diacetate (DCF-DA) was thus used to investigate intracellular ROS level by confocal microscopy. In **Figure 5A**, we observed a significant enhancement of fluorescence (directly proportional to ROS level) of the LPS activated macrophages compared to normal ones, and the fluorescence decreased dramatically upon treatment with Au(h)@MIL, DexP and Au(h)@MIL/DexP. In contrast, incubation with MIL-100(Fe) only slightly decrease the ROS level of activated macrophages. The results confirmed the ability of Au(h)@MIL, DexP and Au(h)@MIL/DexP to scavenge free radicals that are induced by LPS activation. Then, enzyme-linked immunosorbent assay (ELISA) assays were carried out to measure the concentrations of pro-inflammatory cytokines in cell culture media as crucial indexes of anti-inflammatory efficacy. As shown in Figure 5B-D, the concentrations of the three pro-inflammatory cytokines, TNF-α, IL-1β, and IL-6 were remarkably decreased in the cell culture medium of activated macrophages (M1) exposed to DexP and Au(h)@MIL/DexP. Notably, Au(h)@MIL showed better inhibition effects to aforementioned proinflammatory cytokines than MIL-

100(Fe) probably due to the anti-inflammatory effects of Au NCs. Au(h)@MIL/DexP appears as an excellent candidate to reduce the production of pro-inflammatory cytokines, in addition to its anti-oxidative effect. Herein, DexP and $Au_{25}SG_{18}$ NCs in the Au(h)@MIL/DexP nano-object served as anti-oxidants and pro-inflammatory cytokines regulation agents.

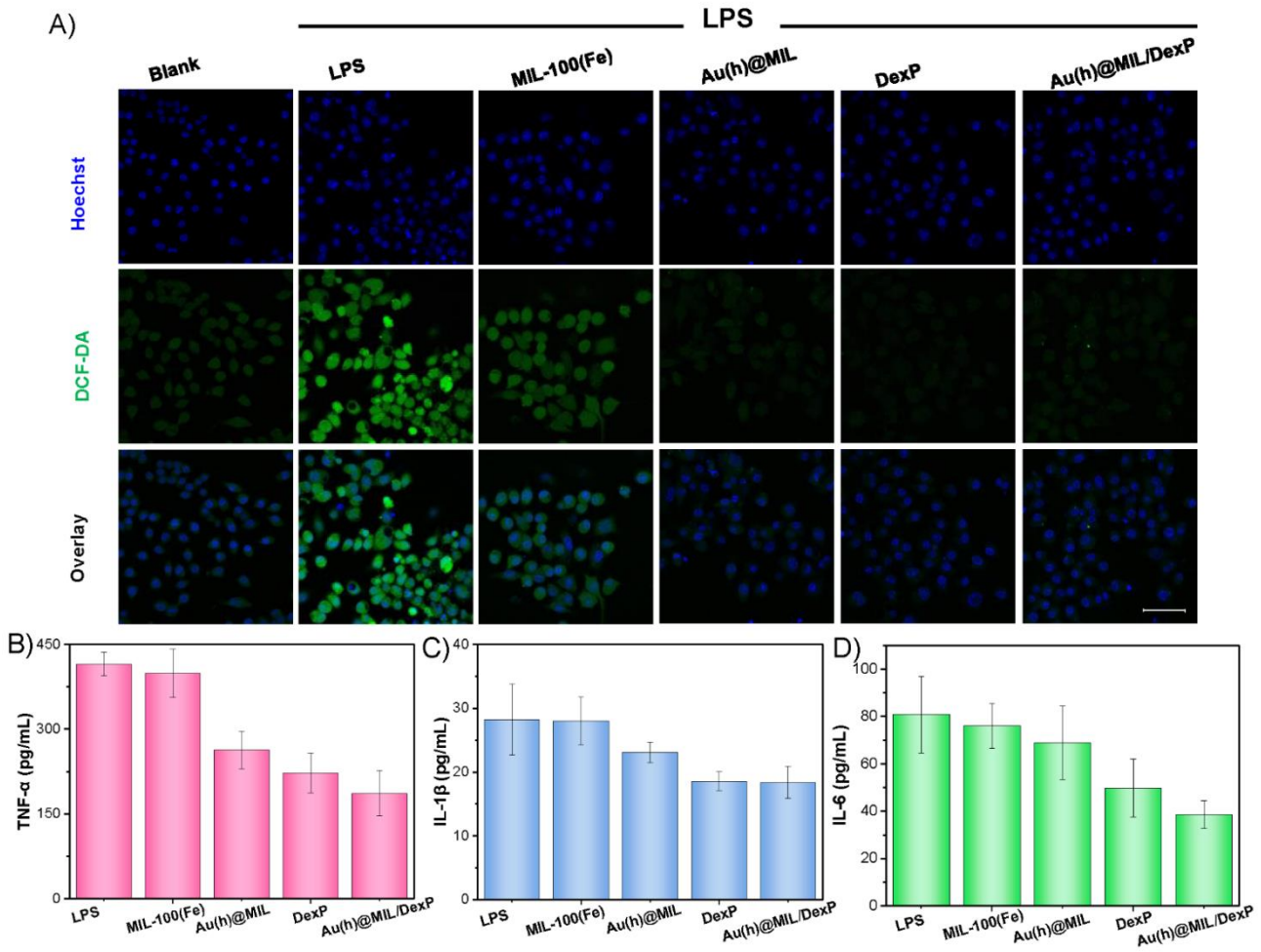

Figure 5. Anti-oxidant and anti-inflammatory properties of Au(h)@MIL/DexP. A) Intracellular ROS imaging by using DCF-DA staining of RAW 264.7 macrophages incubated with MIL-100(Fe), Au(h)@MIL, DexP and Au(h)@MIL/DexP in the presence of LPS (100 ng mL^{-1}) for 24 h. The concentrations of pro-inflammatory cytokines (B) TNF-α, (C) IL-1β and (D) IL-6 in cell culture media were measured by Elisa assay after the treatment of different formulations ([(MIL-100(Fe)] = 1 µg mL^{-1}, [Au(h)@MIL] = 1 µg mL^{-1}, [DexP] = 0.4 µg mL^{-1}, [Au(h)@MIL/DexP] = 1 µg mL^{-1}) to LPS activated RAW 264.7 macrophages (100 ng mL^{-1}, 48 h) for 24 h. Scale bar = 50 µm. Results are shown as mean ± SD.

For further elucidating the molecular pathways that are modified by our compounds, we used human monocytic THP1-dual cells, a modified cell line designed for TLR signaling screening specifically, allowing the simultaneous study of the NF-κB pathway activation, by monitoring the activity of secreted embryonic alkaline phosphatase (SEAP), and the IRF pathway activation, by assessing the activity of Lucia luciferase. THP1-dual monocytes were first differentiated into macrophage cells (M0)

by PMA treatment and then were exposed with the same formula as before at the concentration of 5 or 50 μg mL^{-1} with or without LPS (100 ng mL^{-1} or 1000 ng mL^{-1}) stimulation. Different from RAW 264.7 cells, negligible toxicity of all the groups with or without LPS at a concentration as high as 50 μg mL^{-1} was observed (Figure S20). In terms of IRF pathway, its expression depended on the concentration of LPS, and with the increase of LPS concentration from 0 ng mL^{-1} to 100ng mL^{-1}, then to 1000 ng mL^{-1}, the expression of IRF pathway increased (**Figure** 6A-C). Without the activation of LPS, all the groups stayed at a very low level of IRF expression, showing these compounds would not trigger inflammation. Obviously, free DexP and Au(h)@MIL/DexP were able to significantly reduce the LPS-induced IRF activity. Particularly, the reduction of IRF activity of Au(h)@MIL/DexP group was much higher than free DexP or Au(h)@MIL alone at the concentration of 50 μg mL^{-1} under LPS (100 ng mL^{-1}) activation, further demonstrating their synergistic anti-inflammatory effect (Figure 6B).

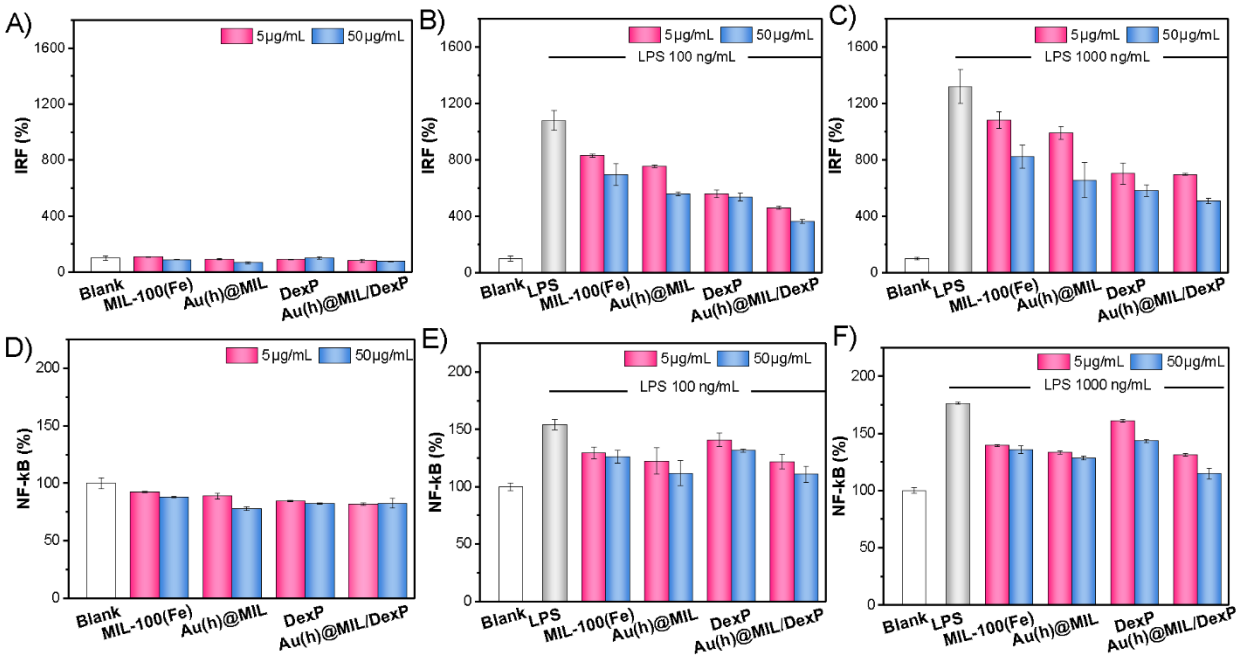

Figure 6. Anti-inflammatory screening of Au(h)@MIL/DexP. A-C) IRF and (D-F) NF-κB activation of THP1-dual macrophage cells after the treatment of different formula: MIL-100(Fe), Au(h)@MIL, DexP and Au(h)@MIL/DexP at the concentration of 5 or 50 μg mL^{-1} in coincubation with or without LPS (100 ng mL^{-1} or 1000 ng mL^{-1}) for 24 h. IRF and NF-κB were quantified by using QUANTI-Luc and QUANTI-Blue, respectively. Results are shown as mean ± SD.

Concerning NF-κB pathway, it was different from IRF pathway, since it was less sensitive to LPS activation. Surprisingly, DexP only showed negligible down-regulation effects. However, a clear decrease of NF-κB expression was observed in MIL-100(Fe), Au(h)@MIL, and Au(h)@MIL/DexP group at the concentration of 50 μg mL^{-1} under LPS (100 ng mL^{-1}) activation, suggesting both MOF part and Au NCs part of Au(h)@MIL/DexP made certain contribution to the inhibition of NF-κB activity. Consistent with cytokine production assays, Au(h)@MIL/DexP can effectively alleviated

TLR mediated IRF and NF-κB signaling pathways. Notably, the anti-inflammatory process was not strictly concentration-dependent, and only a slight difference between the concentration of 5 and 50 μg mL^{-1} of Au(h)@MIL/DexP was observed in terms of the two pathways). All in all, this synergistic therapeutic platform could selectively kill LPS activated RAW 264.7 macrophage cells and efficiently downregulate pro-inflammatory cytokines secretion of LPS activated RAW 264.7 macrophage cells at a concentration as low as 1 μg mL^{-1}. Additionally, Au(h)@MIL/DexP could inhibit both IRF and NF-κB signaling pathways in LPS-activated human macrophages.

3.5 Conclusion

In summary, through an *in situ* RT synthesis, atomically precise gold nanoclusters could be successfully integrated into MIL-100(Fe) and the encapsulation capacity of gold nanocluster was tunable for the construction of hybrid Au@MIL-100(Fe). The hybrid nano-object shows high dexamethasone loading capacity and sustained release in acidic pH, which is of interest for the treatment of inflammation disease. Moreover, this drug delivery system could selectively kill inflammatory cells and down-regulate pro-inflammatory cytokines generation. Moreover, a broad inhibitory activity of two parallel signaling cascades, NF-κB and IRF pathways was also observed. Apart from this promising synergistic therapeutic effects, Au NCs possess great potentials as contrast agents for X-ray computed tomography (CT) imaging due to their high atomic number. The versatility of MOFs is also advantageous in modulating inflammation in a very controlled way. Altogether, the strategy of co-delivery of conventional anti-inflammatory drugs and theranostic noble metal nanoclusters by MOFs may provide a new approach for new generation synergistic chemotherapy and "chrysotherapy" of inflammatory diseases.

Acknowledgements

Heng Zhao is grateful for the support from CSC grant (grant number201808320434). Heng Zhao would like to thank Shan Dai at ENS for the constructive discussion, Bernard Goetz at ENS for the measurement of ICP-MS, and Xiangzhen Xu at ESPCI for the help of TEM observation. Florence Gazeau and Sonia Becharef are thankful to Jean Philippe Herbeuval for providing the THP1-dual cells.

Conflict of interest

The authors declare no conflict of interest.

Keywords

Metal-organic frameworks • gold nanoclusters • room temperature synthesis • nanovectors • anti-inflammation

References

1. Medzhitov, R., Origin and Physiological Roles of Inflammation. *Nature* **2008,** *454* (7203), 428-35.
2. Lee, D. M.; Weinblatt, M. E., Rheumatoid Arthritis. *The Lancet* **2001,** *358* (9285), 903-911.
3. Firestein, G. S., Evolving Concepts of Rheumatoid Arthritis. *Nature* **2003,** *423* (6937), 356-361.
4. Smolen, J. S.; Breedveld, F. C.; Burmester, G. R.; Bykerk, V.; Dougados, M.; Emery, P.; Kvien, T. K.; Navarro-Compan, M. V.; Oliver, S.; Schoels, M.; Scholte-Voshaar, M.; Stamm, T.; Stoffer, M.; Takeuchi, T.; Aletaha, D.; Andreu, J. L.; Aringer, M.; Bergman, M.; Betteridge, N.; Bijlsma, H.; Burkhardt, H.; Cardiel, M.; Combe, B.; Durez, P.; Fonseca, J. E.; Gibofsky, A.; Gomez-Reino, J. J.; Graninger, W.; Hannonen, P.; Haraoui, B.; Kouloumas, M.; Landewe, R.; Martin-Mola, E.; Nash, P.; Ostergaard, M.; Ostor, A.; Richards, P.; Sokka-Isler, T.; Thorne, C.; Tzioufas, A. G.; van Vollenhoven, R.; de Wit, M.; van der Heijde, D., Treating Rheumatoid Arthritis to Target: 2014 Update of the Recommendations of an International Task Force. *Ann Rheum Dis* **2016,** *75* (1), 3-15.
5. Horcajada, P.; Gref, R.; Baati, T.; Allan, P. K.; Maurin, G.; Couvreur, P.; Ferey, G.; Morris, R. E.; Serre, C., Metal-Organic Frameworks in Biomedicine. *Chem Rev* **2012,** *112* (2), 1232-1268.
6. Research Sub-Committee Of The Empire Rheumatism, C., Gold Therapy in Rheumatoid Arthritis: Final Report of a Multicentre Controlled Trial. *Ann Rheum Dis* **1961,** *20* (4), 315-334.
7. Brown, D. H.; Smith, W. E., The Chemistry of the Gold Drugs Used in the Treatment of Rheumatoid Arthritis. *Chem Soc Rev* **1980,** *9* (2), 217-240.
8. Takahashi, K.; Griem, P.; Goebel, C.; Gonzalez, J.; Gleichmann, E., The Antirheumatic Drug Gold, a Coin with Two Faces: Au(I) and Au(III). Desired and Undesired Effects on the Immune System. *Met Based Drugs* **1994,** *1* (5-6), 483-496.
9. Versiani, A. F.; Andrade, L. M.; Martins, E. M. N.; Scalzo, S.; Geraldo, J. M.; Chaves, C. R.; Ferreira, D. C.; Ladeira, M.; Guatimosim, S.; Ladeira, L. O.; da Fonseca, F. G., Gold Nanoparticles and Their Applications in Biomedicine. *Future Virology* **2016,** *11* (4), 293-309.
10. Elahi, N.; Kamali, M.; Baghersad, M. H., Recent Biomedical Applications of Gold Nanoparticles: A Review. *Talanta* **2018,** *184*, 537-556.
11. Faa, G.; Gerosa, C.; Fanni, D.; Lachowicz, J. I.; Nurchi, V. M., Gold - Old Drug with New Potentials. *Curr Med Chem* **2018,** *25* (1), 75-84.
12. Zheng, M.; Jia, H.; Wang, H.; Liu, L.; He, Z.; Zhang, Z.; Yang, W.; Gao, L.; Gao, X.; Gao, F., Application of Nanomaterials in the Treatment of Rheumatoid Arthritis. *RSC Advances* **2021,** *11* (13), 7129-7137.
13. Hornos Carneiro, M. F.; Barbosa, F., Jr., Gold Nanoparticles: A Critical Review of Therapeutic Applications and Toxicological Aspects. *J Toxicol Environ Health B Crit Rev* **2016,** *19* (3-4), 129-148.
14. Yang, H.; Fung, S. Y.; Xu, S.; Sutherland, D. P.; Kollmann, T. R.; Liu, M.; Turvey, S. E., Amino Acid-Dependent Attenuation of Toll-like Receptor Signaling by Peptide-Gold Nanoparticle Hybrids. *ACS Nano* **2015,** *9* (7), 6774-6784.
15. Sun, S.; Liu, H.; Xin, Q.; Chen, K.; Ma, H.; Liu, S.; Mu, X.; Hao, W.; Liu, S.; Gao, Y.; Wang, Y.; Pei, J.; Zhao, R.; Zhang, S.; Zhang, X.; Wang, H.; Li, Y.; Zhang, X. D., Atomic Engineering of Clusterzyme for Relieving Acute Neuroinflammation through Lattice Expansion. *Nano Lett* **2021,** *21*

(6), 2562-2571.
16. Zhang, D. Y.; Tu, T.; Younis, M. R.; Zhu, K. S.; Liu, H.; Lei, S.; Qu, J.; Lin, J.; Huang, P., Clinically Translatable Gold Nanozymes with Broad Spectrum Antioxidant and Anti-Inflammatory Activity for Alleviating Acute Kidney Injury. *Theranostics* **2021,** *11* (20), 9904-9917.
17. Chakraborty, I.; Pradeep, T., Atomically Precise Clusters of Noble Metals: Emerging Link between Atoms and Nanoparticles. *Chem Rev* **2017,** *117* (12), 8208-8271.
18. Kang, X.; Zhu, M., Tailoring the Photoluminescence of Atomically Precise Nanoclusters. *Chem Soc Rev* **2019,** *48* (8), 2422-2457.
19. Kang, X.; Chong, H.; Zhu, M., $Au_{25}(SR)_{18}$: The Captain of the Great Nanocluster Ship. *Nanoscale* **2018,** *10* (23), 10758-10834.
20. Yuan, Q.; Gao, F.; Yao, Y.; Cai, P.; Zhang, X.; Yuan, J.; Hou, K.; Gao, L.; Ren, X.; Gao, X., Gold Clusters Prevent Inflammation-Induced Bone Erosion through Inhibiting the Activation of NF-kappaB Pathway. *Theranostics* **2019,** *9* (7), 1825-1836.
21. Yang, D.; Yang, G.; Gai, S.; He, F.; An, G.; Dai, Y.; Lv, R.; Yang, P., Au_{25} Cluster Functionalized Metal-Organic Nanostructures for Magnetically Targeted Photodynamic/Photothermal Therapy Triggered by Single Wavelength 808 nm Near-Infrared Light. *Nanoscale* **2015,** *7* (46), 19568-19578.
22. He, J.; Dong, J.; Hu, Y.; Li, G.; Hu, Y., Design of Raman Tag-Bridged Core-Shell $Au@Cu_3(BTC)_2$ Nanoparticles for Raman Imaging and Synergistic Chemo-Photothermal Therapy. *Nanoscale* **2019,** *11* (13), 6089-6100.
23. Zhang, L.; Liu, C.; Gao, Y.; Li, Z.; Xing, J.; Ren, W.; Zhang, L.; Li, A.; Lu, G.; Wu, A.; Zeng, L., ZD2-Engineered Gold Nanostar@Metal-Organic Framework Nanoprobes for T1 -Weighted Magnetic Resonance Imaging and Photothermal Therapy Specifically Toward Triple-Negative Breast Cancer. *Adv Healthc Mater* **2018,** *7* (24), 1801144.
24. Mileo, P. G. M.; Gomes, D. N.; Gonçalves, D. V.; Lucena, S. M. P., Mesoporous Metal–Organic Framework MIL-100(Fe) as Drug Carrier. *Adsorption* **2021,** *27* (7), 1123-1135.
25. Quijia, C. R.; Lima, C.; Silva, C.; Alves, R. C.; Frem, R.; Chorilli, M., Application of MIL-100(Fe) in Drug Delivery and Biomedicine. *J Drug Deliv Sci Technol* **2020**, 102217.
26. M. Panchal, F. Nouar, C. Serre, M. Benzaqui, S. Sene, N. Steunou, M. Giménez Marqués, US20210277042, **2021**.
27. Shichibu, Y.; Negishi, Y.; Tsunoyama, H.; Kanehara, M.; Teranishi, T.; Tsukuda, T., Extremely High Stability of Glutathionate-Protected Au_{25} Clusters Against Core Etching. *Small* **2007,** *3* (5), 835-839.
28. Negishi, Y.; Nobusada, K.; Tsukuda, T., Glutathione-Protected Gold Clusters Revisited: Bridging the Gap Between Gold(I)-Thiolate Complexes and Thiolate-Protected Gold Nanocrystals. *J Am Chem Soc* **2005,** *127* (14), 5261-5270.
29. Horcajada, P.; Surble, S.; Serre, C.; Hong, D. Y.; Seo, Y. K.; Chang, J. S.; Greneche, J. M.; Margiolaki, I.; Ferey, G., Synthesis and Catalytic Properties of MIL-100(Fe), an Iron(III) Carboxylate with Large Pores. *Chem Commun* **2007,** (27), 2820-2822.
30. Sene, S.; Marcos-Almaraz, M. T.; Menguy, N.; Scola, J.; Volatron, J.; Rouland, R.; Grenèche, J.-M.; Miraux, S.; Menet, C.; Guillou, N.; Gazeau, F.; Serre, C.; Horcajada, P.; Steunou, N., Maghemite-nanoMIL-100(Fe) Bimodal Nanovector as a Platform for Image-Guided Therapy. *Chem* **2017,** *3* (2), 303-322.
31. Bellido, E.; Guillevic, M.; Hidalgo, T.; Santander-Ortega, M. J.; Serre, C.; Horcajada, P., Understanding the Colloidal Stability of the Mesoporous MIL-100(Fe) Nanoparticles in Physiological Media. *Langmuir* **2014,** *30* (20), 5911-5920.
32. Shen, S.; Wu, Y.; Liu, Y.; Wu, D., High Drug-Loading Nanomedicines: Progress, Current Status, and Prospects. *Int J Nanomedicine* **2017,** *12*, 4085-4109.
33. Ran, J.; Zeng, H.; Cai, J.; Jiang, P.; Yan, P.; Zheng, L.; Bai, Y.; Shen, X.; Shi, B.; Tong, H., Rational Design of a Stable, Effective, and Sustained Dexamethasone Delivery Platform on a Titanium Implant: An Innovative Application of Metal Organic Frameworks in Bone Implants. *Chem Eng J*

2018, *333*, 20-33.
34. Sarkar, C.; Chowdhuri, A. R.; Garai, S.; Chakraborty, J.; Sahu, S. K., Three-Dimensional Cellulose-Hydroxyapatite Nanocomposite Enriched with Dexamethasone Loaded Metal–Organic Framework: A Local Drug Delivery System for Bone Tissue Engineering. *Cellulose* **2019,** *26* (12), 7253-7269.
35. Xiao, T.; Fan, L.; Liu, R.; Huang, X.; Wang, S.; Xiao, L.; Pang, Y.; Li, D.; Liu, J.; Min, Y., Fabrication of Dexamethasone-Loaded Dual-Metal-Organic Frameworks on Polyetheretherketone Implants with Bacteriostasis and Angiogenesis Properties for Promoting Bone Regeneration. *ACS Appl Mater Interfaces* **2021,** *13* (43), 50836-50850.
36. Bello, M. G.; Yang, Y.; Wang, C.; Wu, L.; Zhou, P.; Ding, H.; Ge, X.; Guo, T.; Wei, L.; Zhang, J., Facile Synthesis and Size Control of 2D Cyclodextrin-Based Metal–Organic Frameworks Nanosheet for Topical Drug Delivery. *Part Part Syst Charact* **2020,** *37* (11), 2000147.
37. Zhao, K.; Guo, T.; Wang, C.; Zhou, Y.; Xiong, T.; Wu, L.; Li, X.; Mittal, P.; Shi, S.; Gref, R.; Zhang, J., Glycoside Scutellarin Enhanced CD-MOF Anchoring for Laryngeal Delivery. *Acta Pharm Sin B* **2020,** *10* (9), 1709-1718.
38. Liang, N.; Ren, N.; Feng, Z.; Sun, Z.; Dong, M.; Wang, W.; Liu, F.; Sun, C.; Zhou, W.; Xing, Z.; Wang, J.; Liu, C.; Liu, H., Biomimetic Metal-Organic Frameworks as Targeted Vehicles to Enhance Osteogenesis. *Adv Healthc Mater* **2022**, *11*, 2102821.
39. Velásquez-Hernández, M. d. J.; Ricco, R.; Carraro, F.; Limpoco, F. T.; Linares-Moreau, M.; Leitner, E.; Wiltsche, H.; Rattenberger, J.; Schröttner, H.; Frühwirt, P.; Stadler, E. M.; Gescheidt, G.; Amenitsch, H.; Doonan, C. J.; Falcaro, P., Degradation of ZIF-8 in Phosphate Buffered Saline Media. *CrystEngComm* **2019,** *21* (31), 4538-4544.
40. Christodoulou, I.; Bourguignon, T.; Li, X.; Patriarche, G.; Serre, C.; Marlière, C.; Gref, R., Degradation Mechanism of Porous Metal-Organic Frameworks by *In Situ* Atomic Force Microscopy. *Nanomaterials* **2021,** *11* (3), 722.
41. Li, X.; Lachmanski, L.; Safi, S.; Sene, S.; Serre, C.; Greneche, J. M.; Zhang, J.; Gref, R., New Insights into the Degradation Mechanism of Metal-Organic Frameworks Drug Carriers. *Sci Rep* **2017,** *7* (1), 13142.
42. Kim, K.; Choi, H.; Choi, E. S.; Park, M. H.; Ryu, J. H., Hyaluronic Acid-Coated Nanomedicine for Targeted Cancer Therapy. *Pharmaceutics* **2019,** *11* (7), 301.
43. Lee, H.; Dellatore, S. M.; Miller, W. M.; Messersmith, P. B., Mussel-Inspired Surface Chemistry for Multifunctional Coatings. *Science* **2007,** *318* (5849), 426-430.
44. Yang, P.; Zhu, F.; Zhang, Z.; Cheng, Y.; Wang, Z.; Li, Y., Stimuli-Responsive Polydopamine-Based Smart Materials. *Chem Soc Rev* **2021,** *50* (14), 8319-8343.
45. Wang, Z.; Duan, Y.; Duan, Y., Application of Polydopamine in Tumor Targeted Drug Delivery System and Its Drug Release Behavior. *J Control Release* **2018,** *290*, 56-74.
46. Gill, R.; Tsung, A.; Billiar, T., Linking Oxidative Stress to Inflammation: Toll-Like Receptors. *Free Radic Biol Med* **2010,** *48* (9), 1121-1132.
47. Lucas, K.; Maes, M., Role of the Toll Like Receptor (TLR) Radical Cycle in Chronic Inflammation: Possible Treatments Targeting the TLR4 Pathway. *Mol Neurobiol* **2013,** *48* (1), 190-204.

TOC Figure

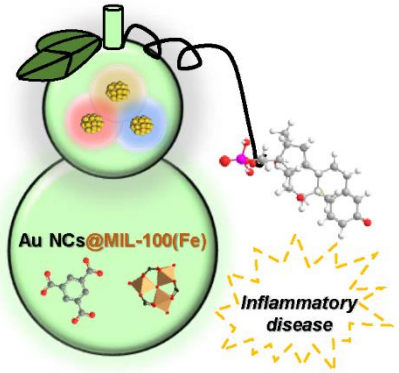

Gold nanoclusters - MIL-100(Fe) nanovectors combining MIL-100(Fe) nanoparticles and atomically precise gold nanoclusters were synthesized through an *in situ* room temperature protocol with high drug loading capacity of dexamethasone phosphate as well as stimuli-responsive drug release and inherent anti-inflammatory property of gold, leading to a synergistic anti-inflammation.

Supplementary Information

Experimental section

Chemicals.

All chemicals were used as received without any further purification: iron(III) nitrate nonahydrate ($Fe(NO_3)_3 \cdot 9H_2O$, 98%), Dexamethasone 21-phosphate disodium salt (DexP), L-Glutathione reduced (GSH, >98%) and Potassium Chloride were purchased from Alfa Aesar. 1,3,5-benzenetricarboxylic acid (1,3,5-BTC, 95%), Lipopolysaccharides (LPS), 2′,7′-Dichlorofluorescin Diacetate(DCF-DA), Hydrogen tetrachloroaurate(III) trihydrate ($HAuCl_4 \cdot 3H_2O$, ≥99.9% trace metals basis), Hyaluronic acid (HA), Sodium borohydride ($NaBH_4$, ≥98.0%), Dopamine hydrochloride (DA), Ammonium acetate and Potassium phosphate monobasic, Sodium chloride, phosphate buffered saline (PBS), Sodium phosphate monobasic dehydrate ($NaH_2PO_4 \cdot 2H_2O$) and Sodium phosphate, dibasic (Na_2HPO_4) were from Sigma-Aldrich. Cell counting kit-8 (CCK-8), were purchased from Dojindo. Propidium Iodide (PI), Pam3CSK4, QUANTI-Blue™, QUANTI-Luc™ and THP1-dual cells were purchased from Invitrogen. Hoechst33342 were purchased from Abcam. Proinflammatory cytokines (IL-1β, IL-6 and TNF-α) Duoset Elisa Kits and DuoSet ELISA Ancillary Reagent Kit 2 were purchased from R&D Systems. Acetonitrile, Methanol, Ethanol, Nitric acid (HNO_3, 70%) and Hydrochloric Acid (HCl, 37%) unless specified and Sodium hydroxide (NaOH) were obtained from Fisher Chemical. Ultrapure water was obtained with the MilliQ purification system (Merck Millipore, France).

Characterization techniques.

Powder X-ray diffraction patterns (PXRD) data were recorded on a high-throughput Bruker D8 Advance diffractometer working on transmission mode and equipped with a focusing Göbel mirror producing CuKα radiation (λ = 1.5418 Å) and a LynxEye detector. Thermogravimetric analyses (TGA) were performed on a Perkins Elmer SDA 6000 apparatus. Samples were heated up to 600°C with a heating rate of $5°C \cdot min^{-1}$ under an oxygen atmosphere. Transmission IR spectra were recorded in the 400-4000 cm^{-1} range, with 4 cm^{-1} resolution on a Nicolet Nexus spectrometer. N_2 sorption isotherms were obtained at 77 K using a Micromeritics Tristar instrument. Prior to the analysis, approximately 30 mg of samples were evacuated for 5 h at 120°C under primary vacuum. Brunauer-Emmett-Teller (BET) surface and pore volume were estimated at a relative pressure lower than 0.25. TEM images were recorded on a JEOL 2010 TEM microscope operated at 200 kV. High resolution TEM images (HRTEM) were acquired on a Titan Themis 200 microscope operating at 200 kV. This microscope is equipped with a Ceta 16M hybrid camera from ThermoFischer Scientific capable of working under

low electron irradiation conditions. The HRTEM images were obtained in low dose condition with an irradiation current between 100 and 250 electrons per square angstroms. High-angle annular dark field imaging in scanning transmission electron microscope mode (STEM-HAADF) images were acquired a camera length of 110 mm (inner/outer collection angles were respectively 69 mrad and 200 mrad). Samples were prepared by deposition of one droplet of colloidal suspensions onto a carbon-coated copper grid and left to dry in air. ICP-MS was performed with an Agilent 7850 elemental analyzer. High Performance Liquid Chromatography (HPLC) analysis was performed by a Waters Alliance e2695 Separations Module (Waters, Milford, MA) equipped with a UV-Vis detector Waters 2998. A SunFire-C18 reverse-phase column (5 µm, 4.6 mm × 150 mm, Waters) was employed. The particle diameter was measured by Dynamic Light Scattering (DLS) on a Zetasizer NanoZS (Malvern Instruments). NPs (~0.1 - 0.2 mg mL^{-1}) were dispersed at RT in aqueous solutions by using an ultrasound tip (Digital Sonifer 450, Branson) during 1 minute at 10% amplitude. Their surface charge was also evaluated by recording ζ-potential with the Zetasizer NanoZS.

Synthesis of MIL-100(Fe) Nanoparticles.

MIL-100(Fe) NPs were prepared according to the patent.[1] 0.72 g of $Fe(NO_3)_3 \cdot 9H_2O$ (1.78 mmol) was dissolved in 90 mL of distilled water. 0.25 g of trimesic acid (1.19 mmol) was then added to this solution and the suspension was allowed to stir for 48 h at room temperature. The mixture was then centrifuged at 14500 rpm for 10 min. An orange solid was thus obtained. The as-synthesized MIL-100(Fe) NPs were then washed by two centrifugation/redispersion cycles in water followed by two centrifugation/redispersion cycles in absolute ethanol. The MIL-100(Fe) NPs were stored in EtOH and could be redispersed in water before use.

Synthesis of $Au_{25}SG_{18}$ Nanoclusters ($Au_{25}SG_{18}$ NCs).

$Au_{25}SG_{18}$ nanoclusters (NCs) were synthesized according to reported protocols.[2-3] 2.0 mmol of GSH (614 mg) was added to the methanol solution of $HAuCl_4$ (50mM, 100 mL). The mixture was then cooled to ~0°C in a cool bath for 30 min. Then, the pre-cooled aqueous solution of $NaBH_4$ (0.2 M, 25 mL) was injected rapidly into this mixture under vigorous stirring. The mixture was allowed to react for another hour. The resulting precipitate was collected and washed repeatedly with methanol. Finally, the precipitate was dried in vacuum to obtain the Au:SG clusters as a dark-brown powder. Au:SG clusters were dissolved in an aqueous solution (14 mL) of GSH (130.7 mg), and the solution was stirred under an air at 328 K. After 3 h, the products were centrifuged to collect the supernatant, followed by dialysis with a molecular weight cut-off of 3000 Da in Milli Q water for 2 days and lyophilization.

Synthesis of Au@MIL Nanoparticles.

In the synthesis of Au@MIL NPs, a colloidal solution containing 10 or 50 mg of $Au_{25}SG_{18}$ NCs were added to 90 mL $Fe(NO_3)_3 \cdot 9H_2O$ (0.72 g, 1.78 mmol) aqueous solution under stirring. 0.25 g trimesic acid (1.2 mmol) was then added and the mixture was stirred for 24 h at room temperature. The brown dark precipitate was centrifuged at 14500 rpm for 10 min. The solid was then washed by two centrifugation/redispersion cycles in water followed by two centrifugation/redispersion cycles in absolute ethanol. The Au@MIL NPs were stored in EtOH and could be redispersed in water before use. These Au@MIL NPs can be prepared by tuning the initial amount of $Au_{25}SG_{18}$ NCs (*i.e.*, 10 and 50 mg of Au_{25} NCs), leading to samples respectively labeled as Au(l)@MIL and Au(h)@MIL.

Determination of the gold content.

1 mg Au(l)@MIL and Au(h)@MIL were accurately prepared and degraded with 1 mL fresh aqua regia for 12 h, respectively. The solution was diluted by 2% HNO_3 solution for ICP MS analysis (Fe and gold ions). In parallel, 1 mg Au(l)@MIL and Au(h)@MIL were treated with KOH, after centrifugation (13400 rpm, 15min), the recollected BTC in the supernatant (Fe ion became precipitate) was then diluted by PBS and further quantified by HPLC. The mobile phase of HPLC is 50:50 v/v methanol: phosphate buffer (0.02 M NaH_2PO_4 and Na_2HPO_4, pH 2.5, adjusted by H_3PO_4). A flow rate of 0.8 mL/min and a sample injection volume of 25 μL were used during all analyses and UV detection was at 242 nm.

Colloidal stability of Au(h)@MIL NPs.

Au(h)@MIL NPs in EtOH were centrifuged and re-dispersed in different media: Milli Q water, 0.9% NaCl aqueous solution (Saline), PBS (pH7.4, 10 $mmol \cdot L^{-1}$), Dulbecco's Modified Eagle Medium (DMEM) and 90% DMEM + 10% fetal bovine serum (FBS) at a concentration of 200 $\mu g\ mL^{-1}$. After sonication (10% amplitude for 30 seconds), the samples' hydrodynamic diameters were recorded over 3 experimental replicates. Furthermore, the long-time colloidal stability of Au(h)@MIL NPs in Mill Q water, PBS and DMEM + FBS was also studied by measuring the evolution of their hydrodynamic diameter with time. Values of diameter and PdI were recorded at a period of 24h (289 runs and 10 measurements per run and 30 seconds per measurement).

Encapsulation of dexamethasone phosphate (DexP) in Au(h)@MIL.

10 mg of Au(h)@MIL in Milli-Q water was mixed with 0.5 mL of DexP stock solution (10 $mg\ mL^{-1}$). The resulting suspension was stirred at 200 rpm under 25ºC for 24 h. The DexP loaded Au(h)@MIL nano-objects (*i.e.*, Au(h)@MIL/DexP) were washed with Mill-Q water three times. The loading

capacity of Au(h)@MIL/DexP was determined by HPLC. The mobile phase of HPLC is 50:50 v/v methanol: phosphate buffer (0.02 M NaH_2PO_4 and Na_2HPO_4, pH 2.5, adjusted by H_3PO_4). A flow rate of 0.8 mL min^{-1} and a sample injection volume of 25 μL were used during all analyses and UV detection was at 242 nm. Then, the present of loading capacity (LC) or entrapment efficiency (EE) was calculated using the following equation:

LC = (Mass of total drug - Mass of free drug) / Mass of total MOF
EE = (Mass of total drug - Mass of free drug) / Mass of total drug

Dexamethasone release of Au(h)@MIL/DexP.

The cumulative release behaviour of DexP from Au(h)@MIL/DexP and Au(h)@MIL/DexP-HP (1 mg mL^{-1}, 1.5 mL) was investigated in PBS (pH 7.4) and PBS (pH 5.1) with or without 10 mM GSH for different incubation time (1 h, 4 h, 8 h, 24 h and 48 h). At different time intervals, the suspension of Au(h)@MIL/Dex or Au(h)@MIL/Dex-HP was centrifuged (13400 rpm, 15 min) and 0.5 mL of the release medium was replaced by the same volume of fresh medium. The concentration of released DexP and ligand BTC was measured by HPLC.

Synthesis of Au(h)@MIL-HP or Au(h)@MIL/DexP-HP.

To synthesize hyaluronic acid-polydopamine (HA-PDA) copolymer, firstly, 1 g of hyaluronic acid (HA) was dissolved in 250 mL deionized water, then 0.52 g of sodium periodate was added. After stirring at room temperature for 24 h, aldehyde groups-bearing hyaluronic acid (HA-CHO) was obtained by dialysis and lyophilization. Then, 90 mg of HA-CHO and 462 mg of dopamine hydrochloride were dissolved in deionized water. The pH of the mixture was adjusted to 8.0 with diluted NaOH solution and the mixture was stirred under room temperature for 24 h. Similarly, after dialysis and lyophilization, the product was obtained. Au(h)@MIL-HP and Au(h)@MIL/DexP-HP nanoparticles were prepared by mixing Au(h)@MIL and Au(h)@MIL/DexP solution respectively with HA-PDA solution at the weight ratio of 1:1 under stirring.

Cells and culture conditions.

RAW 264.7 macrophage cells were cultured in high glucose Dulbecco's Modified Eagle Medium (DMEM) containing 10% FBS and 1% penicillin and streptomycin at 37°C in a humidified 5% CO_2 atmosphere. THP1-Dual cells were purchased from InvivoGen and were cultured in RPMI 1640 containing 10% FBS, 1% penicillin and streptomycin and 10 μg mL^{-1} Blasticidin, 100 μg mL^{-1} Zeocin™ and 100 μg mL^{-1} of Normocin™ at 37°C in a humidified 5% CO_2 atmosphere according to the manufacturer's manual.

***In vitro* cytotoxicity assay.**

RAW 264.7 cells in logarithmic phase were rinsed twice in PBS and then treated with a cell scraper to form 10^5/mL cells suspension. 100 µL RAW 264.7 cells suspension were seeded in 96-well plates (10^4/well) and incubated overnight. Then, different formula including DexP, MIL-100(Fe), Au(h)@MIL, Au(h)@MIL/DexP and Au(h)@MIL/DexP-HP in DMEM/FBS at different concentrations (1, 2, 5, 10, 20, 50 and 100 µg mL^{-1}) was added to each well, incubated for 24 hours at 37°C and under 5% of CO_2. 10 µL CCK-8/well was added to the cells and after incubation for further 2 hours, 96-well plate was transferred into a microplate reader (excitation at 450 nm) for UV-Vis absorbance analysis. The resulting UV-Vis absorbance value were normalized to the UV-Vis absorbance signals value of the control groups. All the experimental points were assessed triple, with error bars representing standard error of the mean. The cell cytotoxicity of DexP and Au(h)@MIL/DexP was further studied on RAW 264.7 cells, following the same protocol.

$$\text{Cell viability (\%)} = \frac{A_{\text{Experimental group}} - A_{\text{Blank group}}}{A_{\text{Control group}} - A_{\text{Blank group}}} \times 100\%$$

Cellular uptake study by confocal laser scanning microscopy.

The cellular uptake of Au(h)@MIL and Au(h)@MIL-HP was evaluated by CLSM on normal RAW 264.7 macrophages and LPS activated RAW 264.7 macrophages. Au(h)@MIL was first labelled by a fluorescent dye Rhodamine B (RhB). Typically, 1 mL RhB aqueous solution (1 mg mL^{-1}) was added to 5 mg of Au(h)@MIL under stirring at 600 rpm for 24 h. After centrifugation and washing with Milli Q water repeatedly, the resulting Au(h)@MIL/RhB was redispersed in 5 mL Milli Q water with tin foil covering and kept in 4 ºC fridge until use. As for the synthesis of Au(h)@MIL/RhB-HP, an extra step was to mix Au(h)@MIL/RhB with HA-PDA at the weight ratio of 1:1. RAW 264.7 cells were seeded into 35 mm confocal dishes (1×10^5 cells/mL) and maintained overnight and as for LPS activated RAW 264.7 macrophages, cells were first treated with 100 ng mL^{-1} LPS for 48 h and then the medium was replaced with fresh complete medium containing Au(h)@MIL/RhB (50 µg mL^{-1}) or Au(h)@MIL/RhB-HP (50 µg mL^{-1}), followed by an incubation at 37ºC for 1 h, 4 h and 8 h. As for CLSM imaging, after the removal of the MOF containing media, the nucleus was stained by Hoechst. Then, the as prepared samples were imaged by CLSM (ZEISS LSM780, Germany). The laser excitation wavelength is 543 nm.

Inhibition of inflammatory cells.

Similar with *in vitro* cytotoxicity assay, *in vitro* anti-inflammatory study was based on inflammatory cells. After adhesion overnight, RAW 264.7 cells were treated with LPS for 48 h before the treatment of Au(h)@MIL, DexP, Au(h)@MIL/DexP and Au(h)@MIL/DexP-HP in DMEM/FBS at different concentrations (1, 2, 5, 10, 20, 50 and 100 μg mL^{-1}). After one day's incubation, 10 μL CCK-8 was added to each well for measurement of UV-Vis absorbance. The survival rate of inflammatory cells were thus compared.

ROS scavenging properties.

To investigate the reactive oxygen species (ROS) scavenging capacity, RAW 264.7 cells were co-cultured with different formula (MIL-100(Fe), Au(h)@MIL, DexP and Au(h)@MIL/DexP) in the presence of lipopolysaccharide (LPS) at a concentration of 100 ng mL^{-1} for 24 h. After the removal of the aforementioned materials containing supernatant, fresh serum-free medium containing dichlorofluorescein diacetate (DCF-DA, 10 μM) for ROS imaging and Hoechst for nucleus staining was added for 30 min in dark. A confocal laser microscope was used to detect intracellular ROS level. The green fluorescence intensity represents the intracellular ROS level.

Pro-inflammatory cytokines downregulation.

To investigate the down regulation effect of pro-inflammatory cytokines of DexP loaded Au(h)@MIL, RAW 264.7 cells were seeded at a density of 1×10^5 cells/mL into a 6-well plate and incubated at 37°C under 5% CO_2 overnight and then the cells were incubated with LPS at a concentration of 100 ng mL^{-1} for 48h. After this activation step, the DMEM medium was replaced by a fresh DMEM medium containing MIL-100 (Fe), Au(h)@MIL, and Au(h)@MIL/DexP at a concentration of 1 μg mL^{-1}. For comparison, activated Raw 264.7 cells were exposed to free DexP at a concentration of 0.4 μg mL^{-1} for 24 hours. Then, the supernatant was collected and centrifuged to remove cells pellets and materials for next step detection. Briefly, mouse tumor necrosis factor alpha (TNF-α) DY410 DuoSet® ELISA, R&D Systems; mouse Interleukin 1 beta (IL-1β) DY401 DuoSet® ELISA, R&D Systems; mouse interleukin 6 (IL-6) DY406 DuoSet ELISA, R&D Systems were used to access TNF-α, IL-1β, and IL-6 concentrations from cell culture media samples by the standard ELISA technique, namely sandwich ELISAs (Capture antibody + sample or standard + Detection antibody). Following the manufacturer's instructions, the samples were finally diluted by five times for ELISA assays based on absorbance values of the recombinant mouse standard.

***NF-κB* and *IRF* pathways blockade.**

THP1-dual cell line allowed the simultaneous study of the NF-κB pathway, by monitoring the activity of SEAP, and the interferon regulatory factor (IRF) pathway, by assessing the activity of Lucia luciferase. Similar with cytotoxicity study, THP1-dual cells were seeded into a 24-well plate at a density of 5×10^5 cells/mL with PMA (50 ng mL^{-1}) to adhere for two days. Subsequently, adherent THP1-Dual cells were treated by different formula (DexP, MIL-100(Fe), Au(h)@MIL, and Au(h)@MIL/DexP) with or without LPS (100 ng mL^{-1} or 1000 ng mL^{-1}) for 24 hours. Firstly, the cell viability of THP1-Dual cells was analyzed using a CCK-8 assay kit. After 2 h of incubation, cell viability was determined by the intensity of 590 nm emission under the excitation of 550 nm. In a parallel experiment, the supernatant was collected after one step of centrifuged to remove floating cells pellets and materials. Following the manual's procedures, NF-κB and IRF induction and luciferase activity in the supernatant were quantified by QUANTI-Blue (InvivoGen) and QUANTI-Luc (InvivoGen), respectively. Changes from baseline were calculated as -fold changes, normalized against unstimulated control cells. 96-well plate was transferred into a microplate reader for UV-Vis absorbance (NF-κB) analysis and fluorescence analysis (IRF).

Statistical analysis.

All experimental results were exhibited as the mean ± standard deviation and the statistical significance among the groups was analyzed using one-way ANOVA. Differences with a p value < 0.05 were considered to be statistically significant. Statistical significance was assigned for $*p < 0.05$, $**p < 0.01$ and $***p < 0.001$.

Results and Discussion

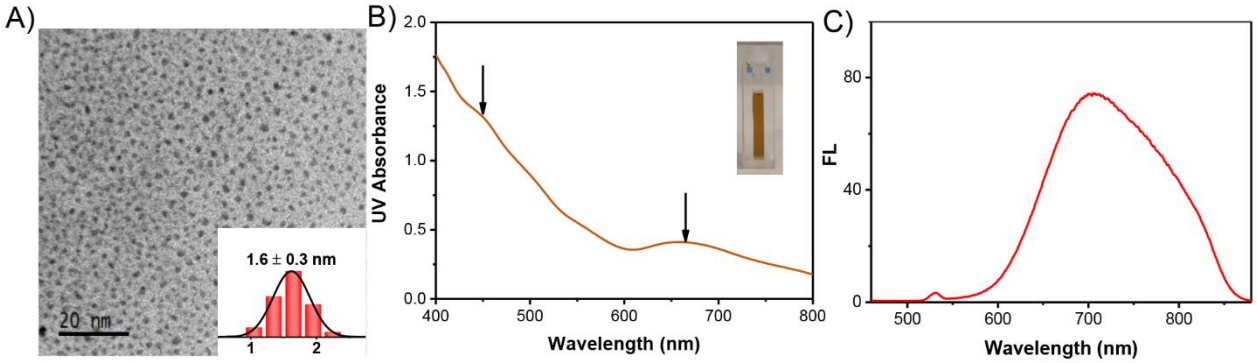

Figure S1. A) TEM (statistical analysis figure inserted), B) UV-Vis and C) FL spectra of $Au_{25}SG_{18}$ NCs. The particle size distribution of $Au_{25}SG_{18}$ NCs was 1.6 ± 0.3 nm. $Au_{25}SG_{18}$ NCs exhibited two distinct absorption peaks at 450 and 665 nm and they associated with the Au 6sp intraband and interband transitions of the bulk gold, respectively, which was consistent with previous literature. The excitation wavelength used was 450 nm and the corresponding emission peak was ~700 nm.

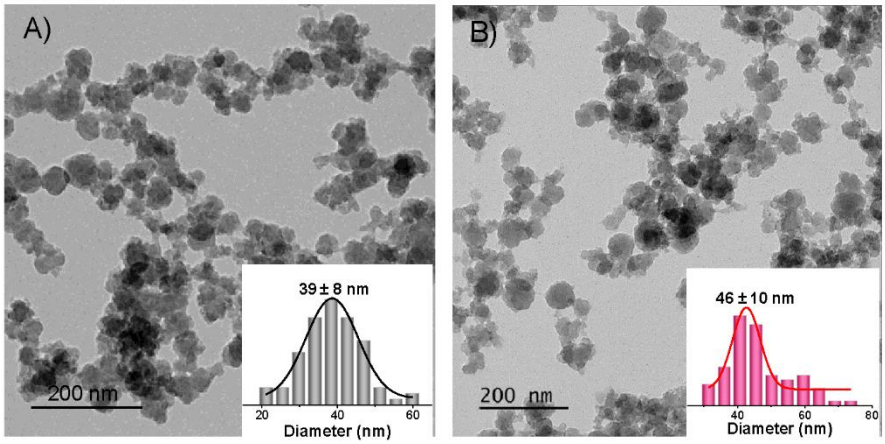

Figure S2. TEM observations of (A) Au(l)@MIL and (B) Au(h)@MIL. The particle size distribution of Au(l)@MIL and Au(h)@MIL is 39 ± 8 nm and 46 ± 10 nm, respectively.

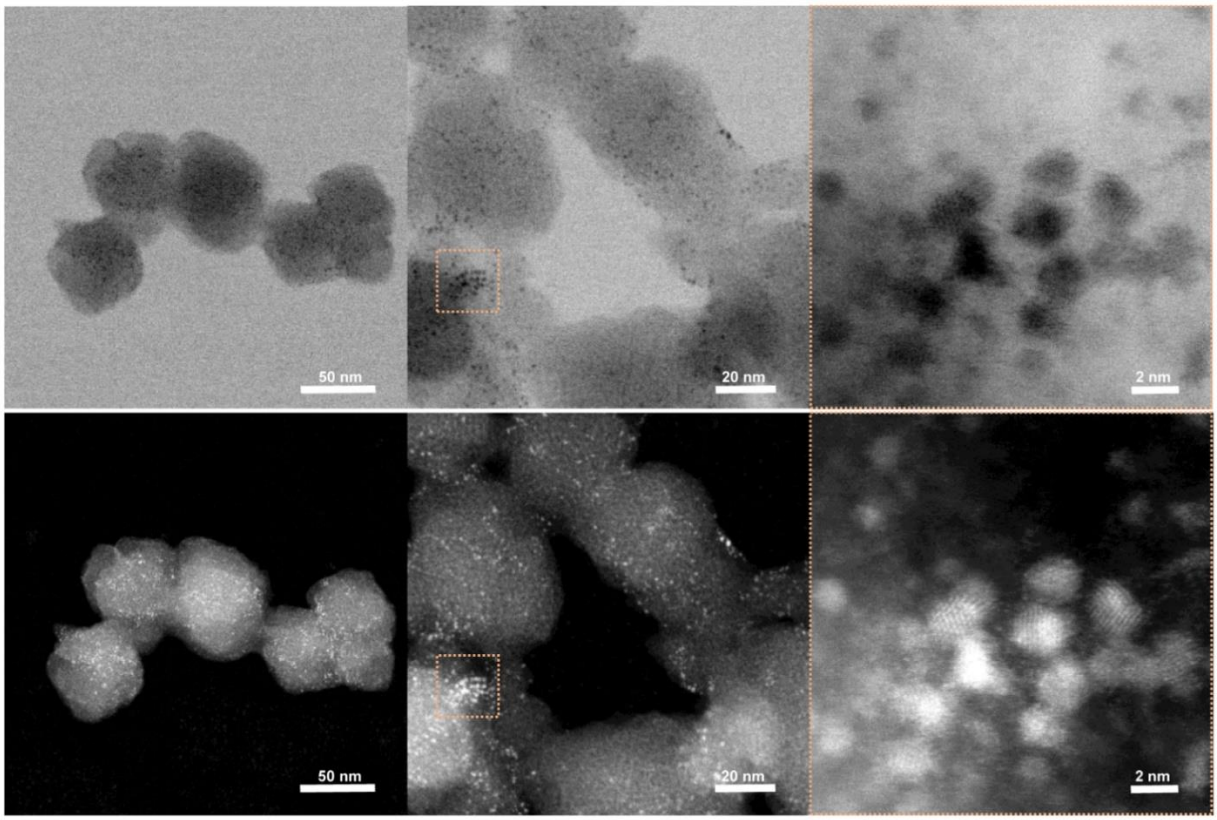

Figure S3. TEM, HRTEM and STEM-HAADF of Au(l)@MIL.

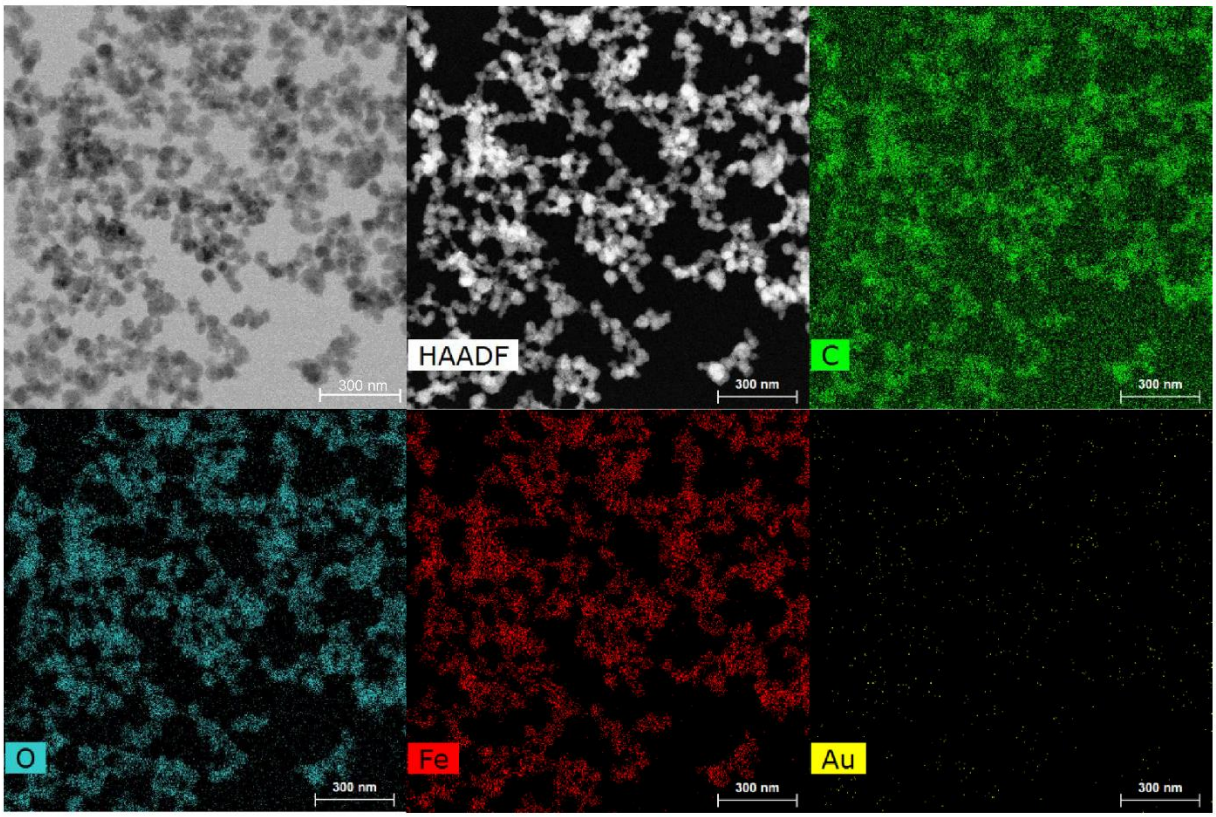

Figure S4. STEM-HAADF and EDS mapping images of Au(l)@MIL.

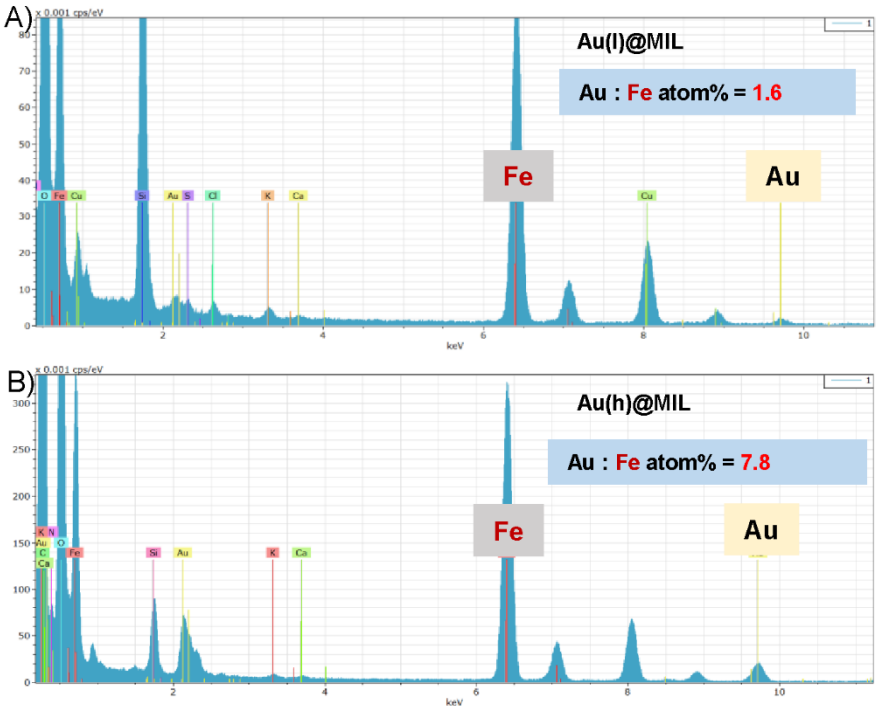

Figure S5. EDS of Au(l)@MIL and Au(h)@MIL by STEM. (Normalized atomic ratio between Au and Fe).

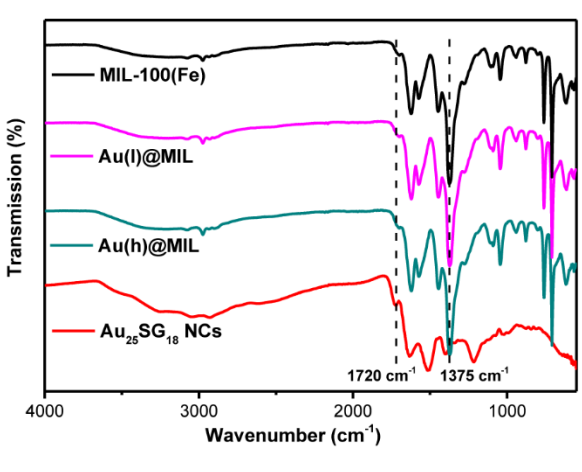

Figure S6. FT-IR spectra of MIL-100(Fe), Au(l)@MIL, Au(h)@MIL and $Au_{25}SG_{18}$ NCs. The sharp band at ~1375 cm^{-1} and the weak band at ~1720 cm^{-1} could be assigned to the stretching of the carboxylate groups and carboxyl groups of the organic linker BTC or GSH, respectively.

Table S1. The atomic ratio of Au ion (ICP-MS) to Fe (ICP-MS) to BTC (HPLC) of Au(l)@MIL and Au(h)@MIL.

Sample	Weight (mg)	ICP-Fe (μg)	ICP-Au (μg)	BTC (μg)	Fe : Au : BTC (molar ratio)
Au(l)@MIL	1	135.4	6.5	422.5	100 : 1.4 : 83
Au(h)@MIL	1	121.3	33	368.5	100 : 7.7 : 80.7

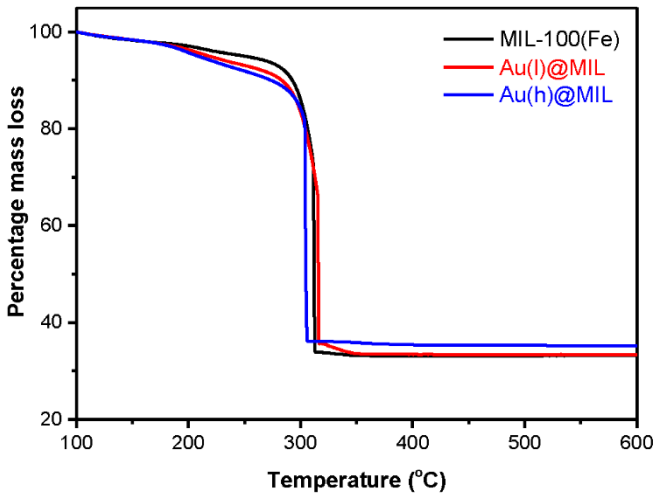

Figure S7. TGA of MIL-100(Fe), Au(l)@MIL and Au(h)@MIL.

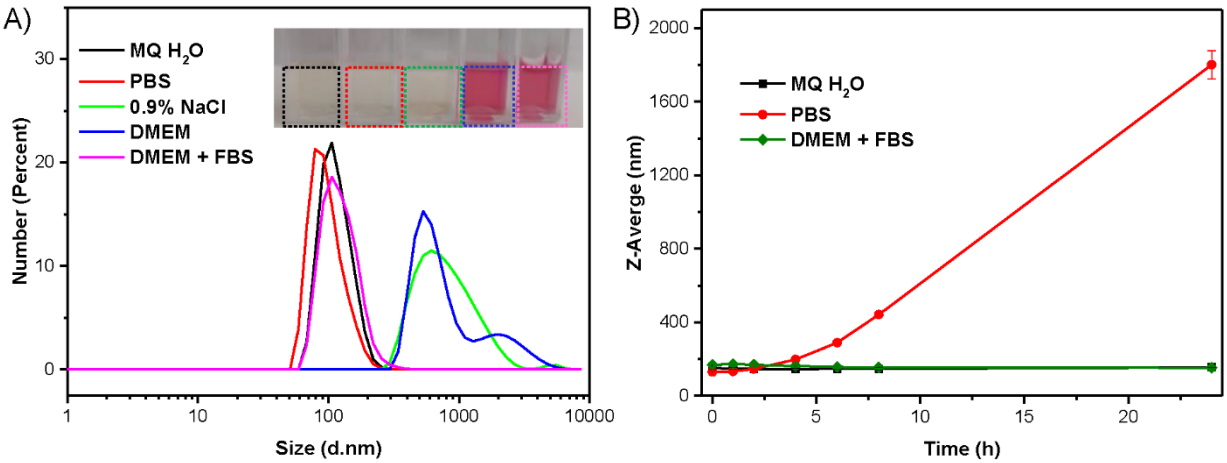

Figure S8. A) The hydrodynamic diameters of Au(h)@MIL at a concentration of 100 μg mL^{-1} in different media (Milli Q water, PBS, 0.9% NaCl, DMEM and DMEM + FBS) at room temperature. B) Long term colloidal stability of Au(h)@MIL was conducted through monitoring evolution of the average particle diameter (by Z-Average) in Milli Q water, PBS and DMEM + FBS over 24 hours.

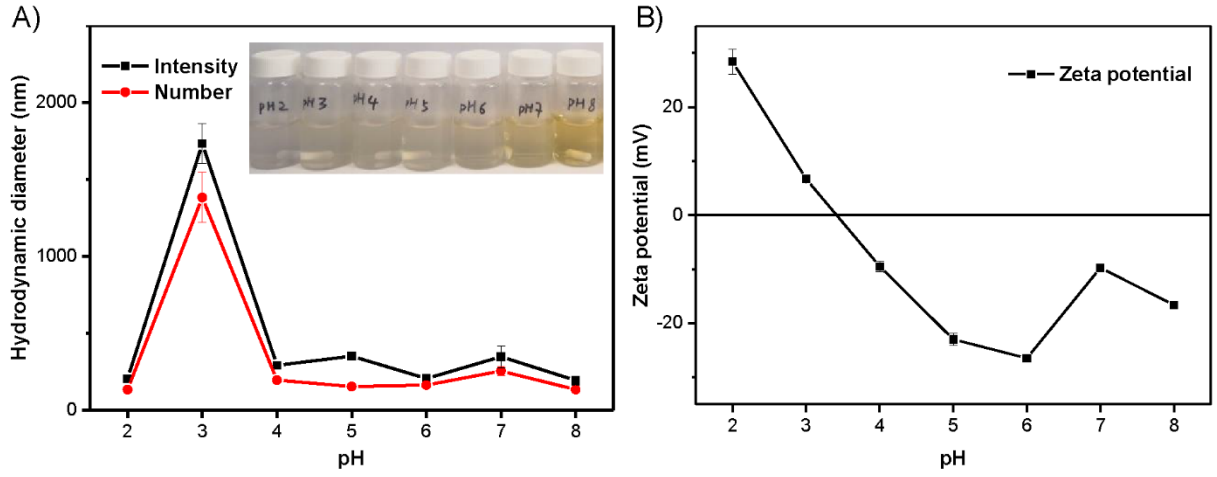

Figure S9. A) pH dependent hydrodynamic diameters and (B) Zeta potentials of Au(h)@MIL at a concentration of 100 μg mL^{-1}.

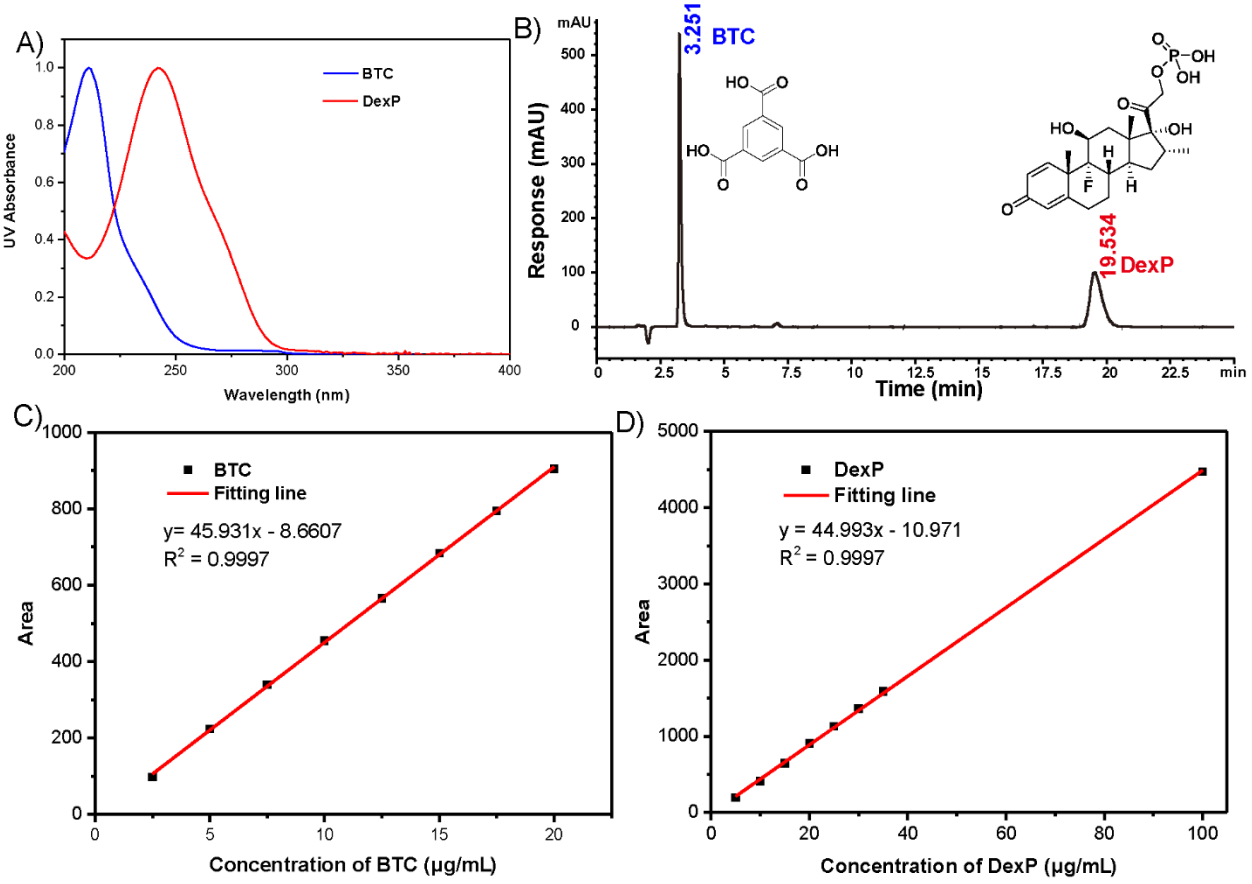

Figure S10. A) UV-vis spectra and B) HPLC chromatogram (Inserted: Molecular structure) of BTC and DexP; calibration curves of **(**C) BTC and (D) DexP in water by HPLC.

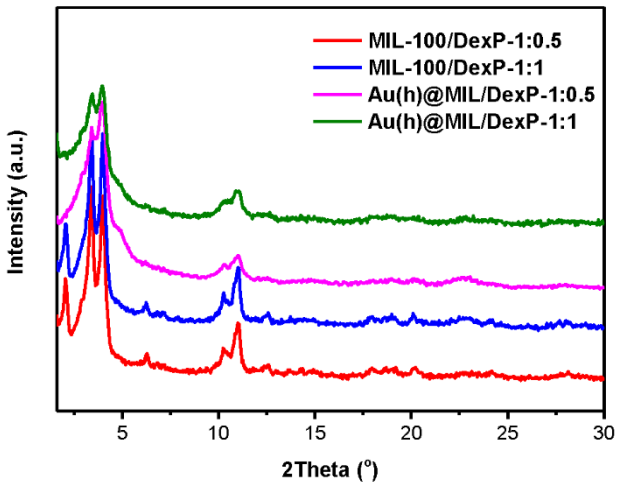

Figure S11. PXRD patterns (λ_{Cu} = 1.5406 Å) of MIL-100(Fe)/DexP and Au(h)@MIL/DexP.

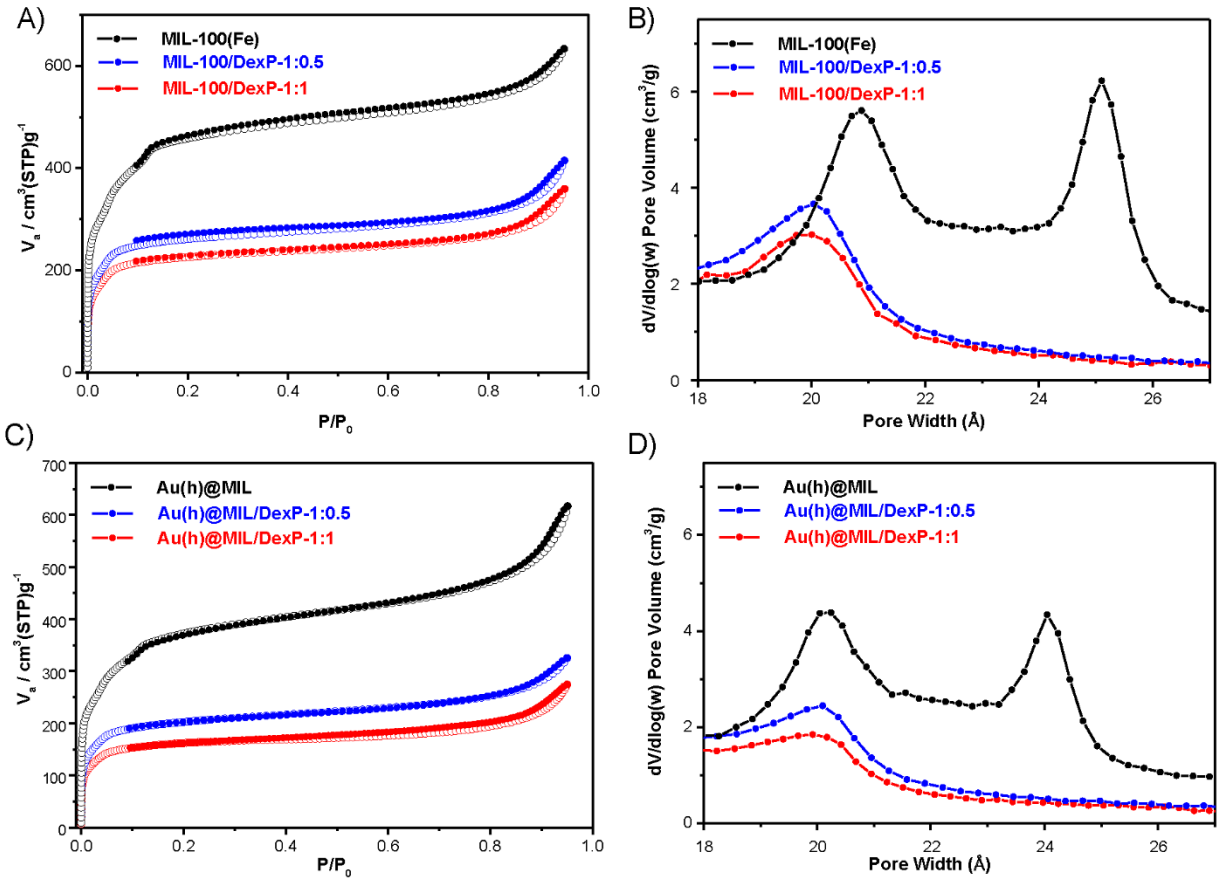

Figure S12. A, C) Nitrogen absorption and desorption isotherms and corresponding (B, D) pore size distribution (BJH Adsorption: Halsay, Kruk-Jaroniec-Sayari) at 77 K (P_0 = 1atm) of MIL-100(Fe)/DexP and Au(h)@MIL/DexP.

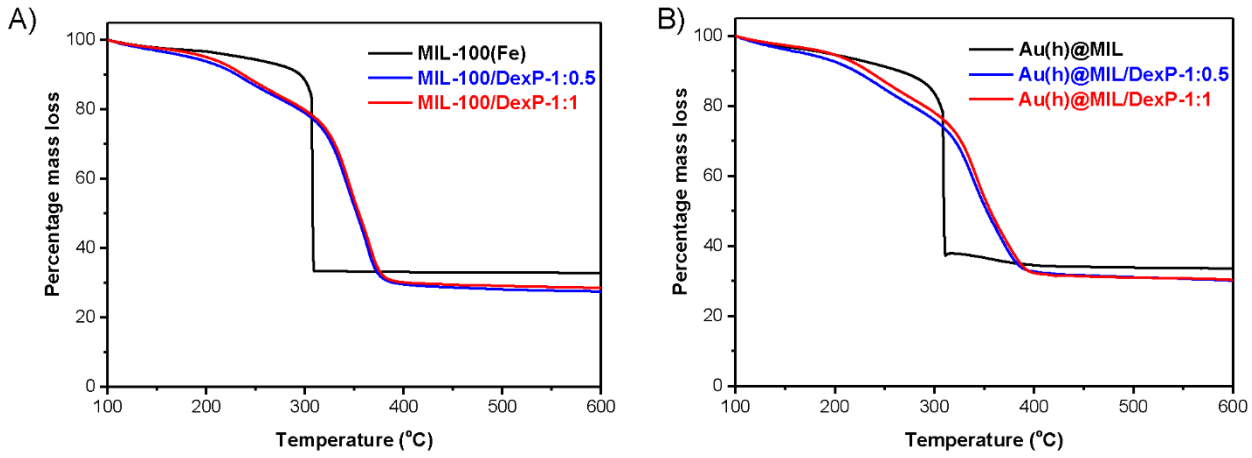

Figure S13. TGA of (A) MIL-100(Fe)/DexP and (B) Au(h)@MIL/DexP.

Table S2. Dex loading capacity (LC) or entrapment efficiency (EE) of MIL-100(Fe) and Au(h)@MIL.

Weight Ratio (MOF : DexP)	**MIL-100(Fe)/DexP**		**Au(h)@MIL/DexP**	
	LC (%)	EE (%)	LC (%)	EE (%)
1 : 0.5	49.1 ± 0.1	98.1 ± 0.3	43.3 ± 0.2	86.6 ± 0.4
1 : 1	60.4 ± 1.7	60.4 ± 1.7	46.6 ± 0.2	46.6 ± 0.2

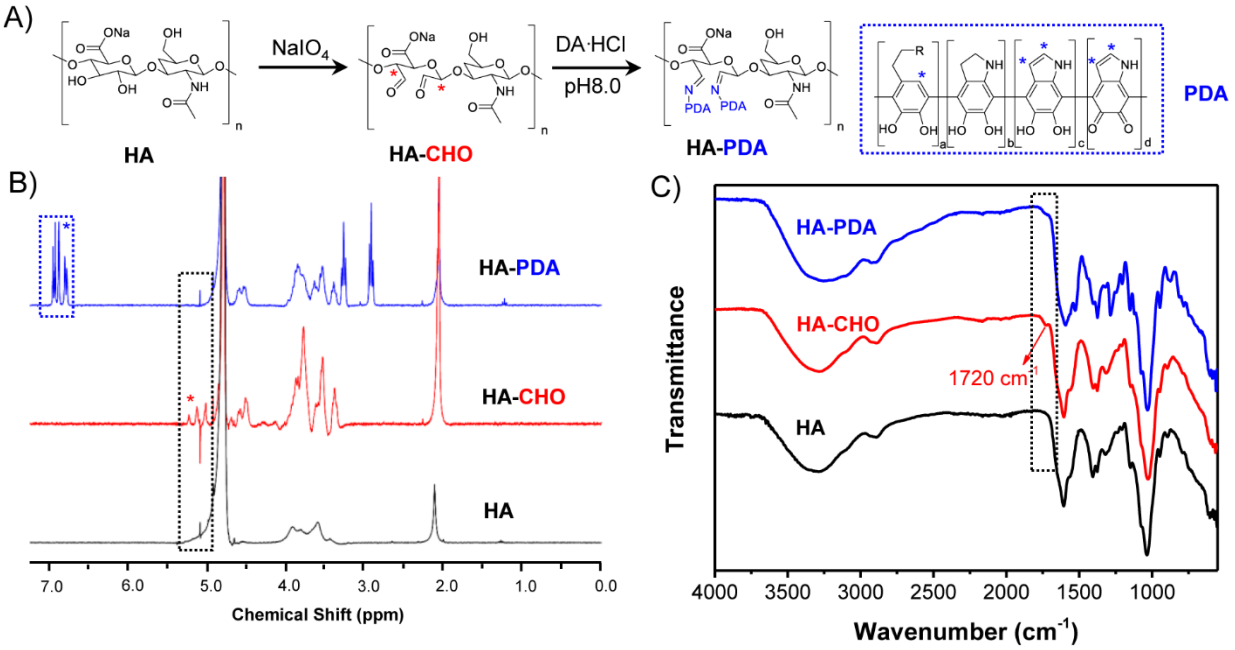

Figure S14. Characterizations of HA-PDA. A) Illustration figure of the reaction route of HA-PDA; B) ^{1}H NMR spectra and (C) FT-IR spectra of HA-PDA, HA-CHO and HA.

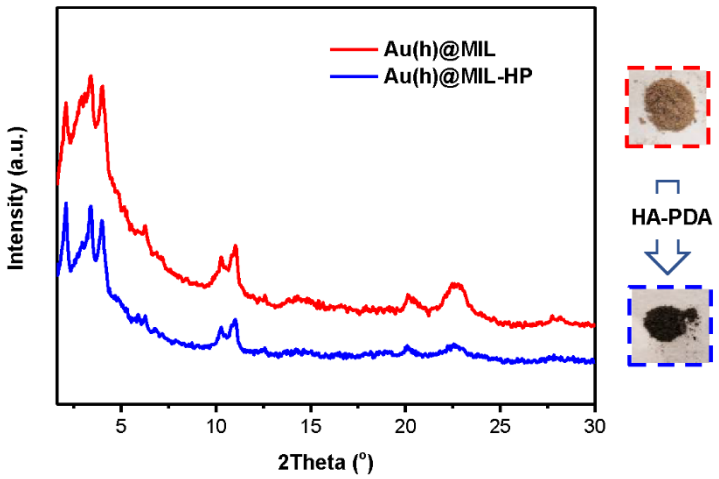

Figure S15. A) PXRD patterns (λ_{Cu} = 1.5406 Å) of Au(h)@MIL and Au(h)@MIL-HP (Photos before and after surface coating of HA-PDA were shown).

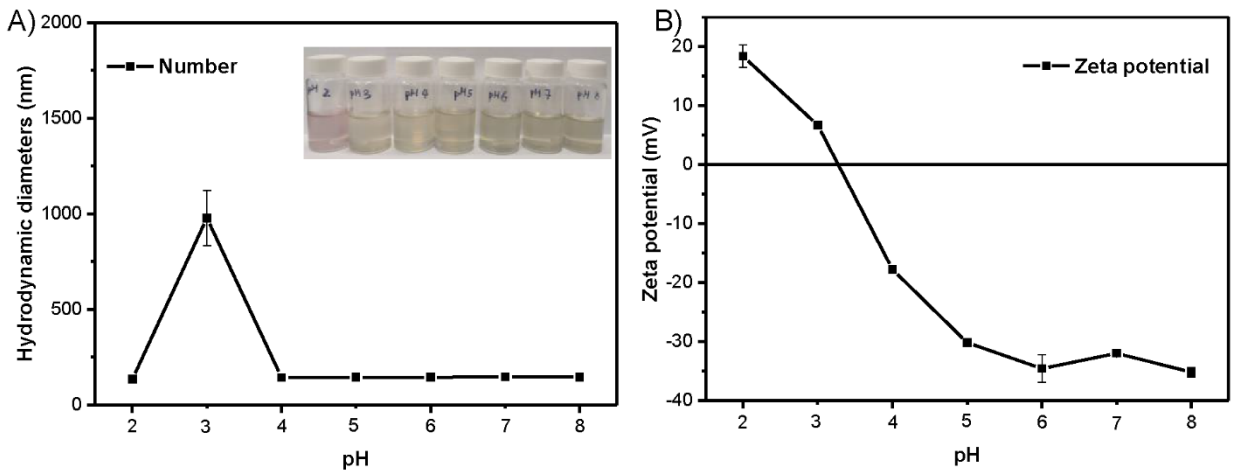

Figure S16. A) pH dependent hydrodynamic diameter (by number) and (B) Zeta potential changes of Au(h)@MIL-HP.

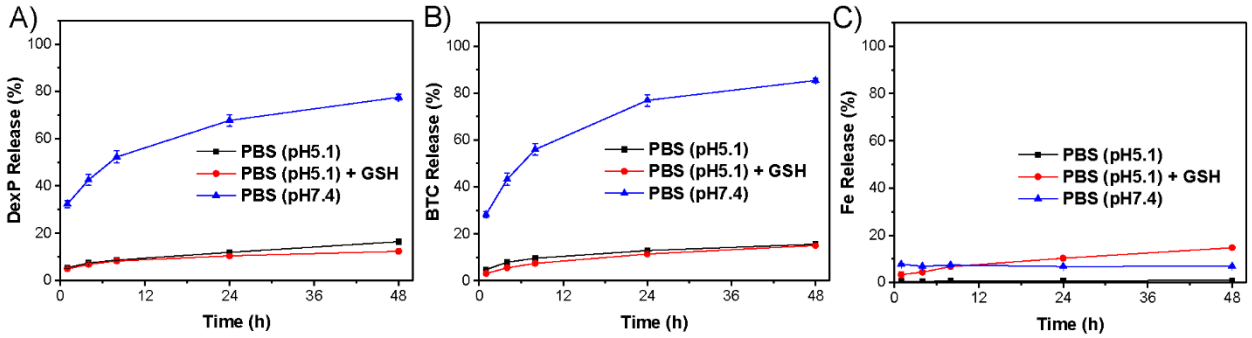

Figure S17. A) DexP and (B) BTC release of Au(h)@MIL/DexP-HP in PBS (pH5.1), PBS (pH5.1) with 10 mM GSH and PBS (pH7.4) by HPLC. (C) Fe release of Au(h)@MIL/DexP-HP in PBS (pH5.1), PBS (pH5.1) with 10 mM GSH and PBS (pH7.4) by ICP-MS.

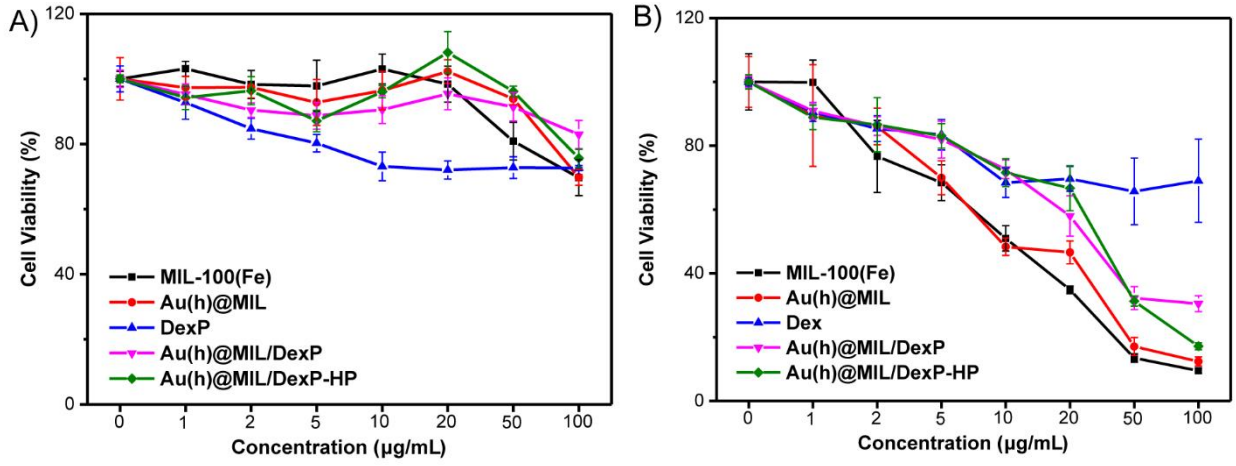

Figure S18. Cell viability of (A) normal RAW 264.7 macrophage cells and (B) LPS activated RAW 264.7 macrophage cells after incubation with different concentrations of MIL-100(Fe), Au(h)@MIL, DexP, Au(h)@MIL/DexP and Au(h)@MIL/DexP-HP for 24 hours.

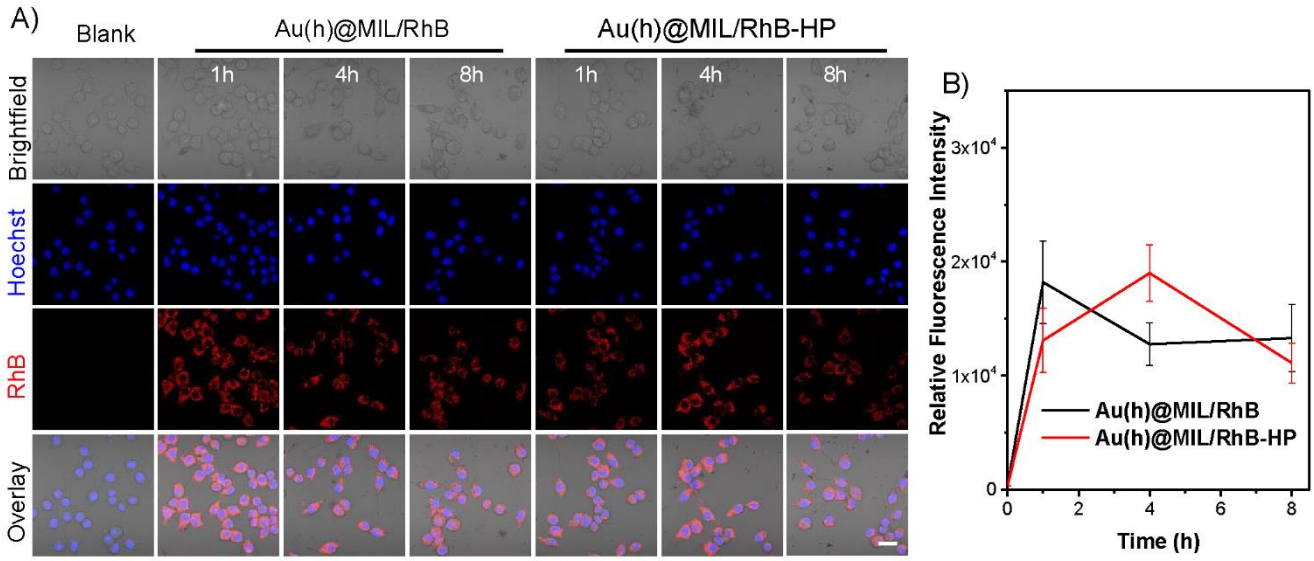

Figure S19. The cellar uptake of Au(h)@MIL/RhB and Au(h)@MIL/RhB-HP (50 μg mL^{-1}) by normal RAW 264.7 macrophage cells. Scale bar = 20 μm.

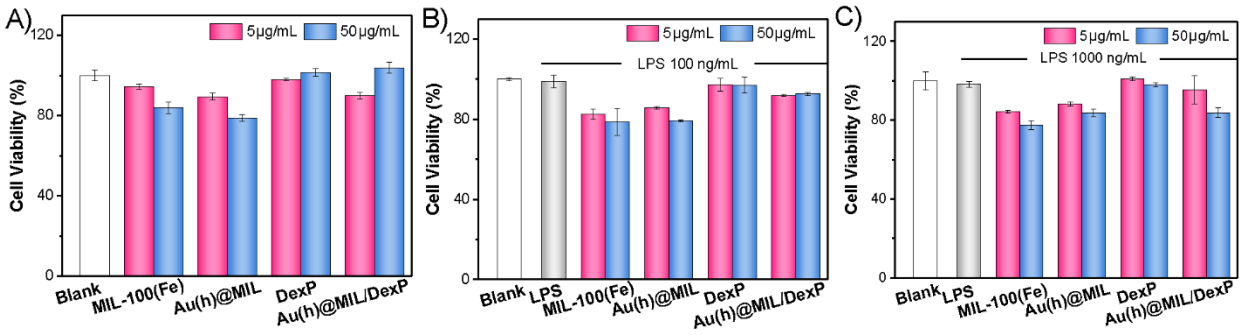

Figure S20. The cell viability of (A) normal THP1-dual macrophage cells, and THP1-dual macrophage cells treated with (B) 100 ng mL^{-1} and (C) 1000 ng mL^{-1} LPS along with different formula: MIL-100(Fe), Au(h)@MIL, DexP and Au(h)@MIL/DexP at the concentration of 5 or 50 μg mL^{-1} for 24 h. Cell viability assay was quantified by using CCK-8 kit. Results are shown as mean ± SD.

References

1. M. Panchal, F. Nouar, C. Serre, M. Benzaqui, S. Sene, N. Steunou, M. Giménez Marqués, US20210277042, **2021**.
2. Negishi, Y.; Nobusada, K.; Tsukuda, T., Glutathione-protected gold clusters revisited: bridging the gap between gold(I)-thiolate complexes and thiolate-protected gold nanocrystals. *J Am Chem Soc* **2005,** *127* (14), 5261-5270.
3. Shichibu, Y.; Negishi, Y.; Tsunoyama, H.; Kanehara, M.; Teranishi, T.; Tsukuda, T., Extremely high stability of glutathionate-protected Au25 clusters against core etching. *Small* **2007,** *3* (5), 835-839.

Chapter 4

This chapter "Novel hybrid Au NCs@MOFs" devotes to the construction of novel fluorescent Au NCs@MOFs *via in situ* room temperature synthesis.

Table of Contents

4.1 Introduction

This chapter is based on the work realized during the internship of Mrs Camille Baland, a third year license intern (from Ecole Normale Supérieure de Lyon) that I supervised directly.

Near-infrared II (NIR-II) imaging in 1100-1700 nm has shown great promise for medical diagnosis due to its deep penetration and high resolution in biological tissue.[1-4] Most NIR-II fluorophores and probes are still in their infancy and current NIR-II fluorescent probes contain rare earth-doped nanoparticles, quantum dots, single-walled carbon nanotubes, small molecule dyes, conjugated polymers and gold nanoclusters (Au NCs).[2] As mentioned in the previous chapters, Au NCs composed of a well-defined number of gold atoms exhibit excellent biocompatibility, easy surface functionalization and outstanding pharmacokinetics.

It is worth noting that minor changes in the composition of monolayer-protected atomically precise nanoclusters, such as the number of metal atoms and/or the change of the protecting ligand, might have a drastic effect on the physicochemical properties of the sample.[5-6] Recently, Au NCs have been reported for emitting strong fluorescence in NIR-II region.[7-8] Through NIR-II fluorescence imaging, Au_{25} nanoclusters consisting of 25 gold atoms and 18 peptide ligands allow high-resolution imaging of cancer metastasis and kidney elimination without any acute or long-term toxicity.[9] Li *et al.* discovered that glutathione-capped gold nanoclusters ($Au_{25}SG_{18}$) could efficiently bind to hydroxyapatite of bone matrix and NIR-II fluorescence imaging revealed the targeted delivery of $Au_{25}SG_{18}$ to bones, benefiting from the abundant carboxylic acids side chains in $Au_{25}SG_{18}$.[10]

In comparison with $Au_{25}SG_{18}$, L-cysteine (Cys) capped Au_{25} NCs ($Au_{25}Cys_{18}$) showed a stronger NIR-II fluorescence signal, but they were scarcely studied for *in vivo* imaging.[9] Interestingly, protein-capped ultrasmall Au NCs containing cysteine residues are also good NIR-II photoluminescence agents.[11-12] Despite of various promising properties, the quick renal clearance of Au_{25} NCs will hinder possible theranostic applications and meanwhile drug delivery is another challenge for them. Thus, the construction of heterostructure Au_{25} NCs@MOFs is of particular interest. Luo *et al.* have synthesized $Au_{25}SG_{18}$-ZIF-8 nanocomposites by positioning $Au_{25}SG_{18}$ NCs inside and outside ZIF-8.[13] Based on aggregation-induced emission (AIE) enhancement of gold nanoclusters in metal-organic frameworks, AuNCs@ZIF-8 NPs have also been used as biosensors.[14-15] Ma *et al.* have coupled fluorescent gold nanoclusters (BSA-Au NCs) with the surface of MIL-101(Fe)-NH_2 NPs for fluorescence imaging and magnetic resonance imaging (FI/MRI) guided microwave enhancing dynamic therapy.[16] Yang *et al.* have attached captopril capped Au_{25} NCs ($Au_{25}Capt_{18}$) on Fe_3O_4/ZIF-8 nanocomposite *via* surface decoration for magnetically targeted photodynamic / photothermal therapy upon 808 nm NIR light

irradiation.[17] Apart from bioapplications, Au_{25} NCs@MOFs are also of interest in catalysis. Yun *et al.* have developed sandwich cluster composite nanocatalyst ZIF-8@Au_{25}Cys@ZIF-67 for both 4-nitrophenol reduction and terminal alkyne carboxylation with CO_2 under ambient conditions.[18]

In **Chapter 3**, Au_{25}SG@MIL-100(Fe) NPs consisted of $Au_{25}SG_{18}$ and MIL-100(Fe) have been synthesized *via* a green *in situ* room temperature synthesis method, and similarly we report here the construction of a series of Au_{25}@MOFs nanocomposites. To the best of our knowledge, Au_{25}@MOFs have not been reported yet for NIR-II fluorescence imaging. Briefly, in this chapter we first studied NIR-II fluorescence imaging property of $Au_{25}SG_{18}$ NCs and Au_{25}SG@MIL-100(Fe) and a fluorescence quenching phenomenon was observed. To circumvent the fluorescence quenching issue, two possibilities could be explored concomitantly: select better fluorescence imaging agents and consider non colored MOFs. Thus, we further synthesized Au_{25}Cys@MIL-100(Fe), Au_{25}Cys@ZIF-8 and Au_{25}Cys@UiO-66. Although the synthesis and characterization of these nanocomposites have not been fully investigated due to time limit considerations, NIR-II fluorescence imaging guided therapy is very promising and will be explored in the near future..

4.2 Chemicals and instruments

Chemicals: All chemicals were used as received without any further purification: iron(III) nitrate nonahydrate ($Fe(NO_3)_3{\cdot}9H_2O$, 98%), L-glutathione reduced (GSH, >98%) and potassium chloride were purchased from Alfa Aesar. 1,3,5-benzenetricarboxylic acid (1,3,5-BTC, 95%), hydrogen tetrachloroaurate(III) trihydrate ($HAuCl_4{\cdot}3H_2O$, ≥99.9% trace metals basis), L-cysteine (Cys, 97%), sodium chloride, phosphate buffered saline (PBS), sodium phosphate monobasic dehydrate ($NaH_2PO_4{\cdot}2H_2O$) and sodium phosphate, dibasic (Na_2HPO_4) were purchased from Sigma-Aldrich. Acetonitrile, methanol, ethanol, nitric acid (HNO_3, 70%), acetic acid (98+%), hydrochloric acid (HCl, 37%) and sodium hydroxide (NaOH) unless specified were obtained from Fisher Chemical. Ultrapure water was obtained with the MilliQ purification system (Merck Millipore, France).

Instruments: Powder X-ray diffraction patterns (PXRD) data were recorded on a high-throughput Bruker D8 Advance diffractometer working on transmission mode and equipped with a focusing Göbel mirror producing CuKα radiation (λ = 1.5418 Å) and a LynxEye detector. Scanning electron microscope (SEM) images were recorded with FEI Magellan 400 scanning electron microscope. Thermogravimetric analyses (TGA) were performed on a Perkins Elmer SDA 6000 apparatus. Samples were heated up to 600 °C with a heating rate of 5 °C min^{-1} under an oxygen atmosphere. Transmission IR spectra were recorded in the 550-4000 cm^{-1} range, with 4 cm^{-1} resolution on a Nicolet iS5 FTIR ThermoFisher spectrometer. N_2 sorption isotherms were obtained at 77 K using a Micromeritics Tristar

instrument (pre-activating samples at 120 °C under vacuum, 5 hours). Prior to the analysis, approximately 30 mg of samples were evacuated for 5 h at 120 °C under primary vacuum. Brunauer-Emmett-Teller (BET) surface and pore volume were estimated at a relative pressure lower than 0.25. TEM images were recorded on a JEOL 2010 TEM microscope operated at 200 kV. Samples were prepared by deposition of one droplet of colloidal suspensions onto a carbon-coated copper grid and left to dry in air. ICP-MS was performed with an Agilent 7850 elemental analyzer.The particle diameter was measured by Dynamic Light Scattering (DLS) on a Zetasizer NanoZS (Malvern Instruments). NPs (~100-200 μg mL^{-1}) were dispersed at RT in aqueous solutions by using an ultrasound tip (Digital Sonifer 450, Branson) during 1 minute at 10% amplitude. Their surface charge was also evaluated by recording ζ-potential with the Zetasizer NanoZS.

4.3 Methods

Concerning Au_{25} NCs synthesis, all glassware was cleaned with fresh aqua regia first and washed with ultrapure water thoroughly.

$Au_{25}SG_{18}$ NCs and $Au_{25}SG$@MIL-100 synthesis

The synthesis details have been given in Chapter 3.

$Au_{25}Cys_{18}$ NCs synthesis

$Au_{25}Cys_{18}$ NCs were first synthesized following a typical protocol.[19] Aqueous solutions of $HAuCl_4 \cdot 3H_2O$ (20 mM, 0.25 mL) and cysteine (5 mM, 2 mL) were mixed in water (2.35 mL), leading to the formation of Cys-Au(I) complexes. An aqueous NaOH solution (1 M, 0.3 mL) was then introduced into the reaction mixture, followed by the addition of 0.1 mL of $NaBH_4$ solution (prepared by dissolving 43 mg of $NaBH_4$ powder in 10 mL of 0.2 M NaOH solution). After 3 hours , $Au_{25}Cys_{18}$ NCs were collected and then purified using a superfilter centrifuge tube (molecular cut-off of 3 kDa).

$Au_{25}Cys$@MIL-100 synthesis

To prepare $Au_{25}Cys$@MIL NPs, a colloidal solution containing 10 or 20 mg of Au_{25} NCs was added to 90 mL of an aqueous solution of $Fe(NO_3)_3 \cdot 9H_2O$ (0.72 g, 1.78 mmol) under stirring. 0.25 g of trimesic acid (1.2 mmol) was then added and the mixture was stirred for 24 hours at room temperature. The dark brown precipitate was centrifuged at 14500 rpm for 10 min. The solid was then washed by two centrifugation / redispersion cycles in water followed by two centrifugation / redispersion cycles

in absolute ethanol. $Au_{25}Cys(X)$@MIL NPs (X = 10 or 20 mg) were stored in EtOH and could be redispersed in water before use.

Synthesis of ZIF-8 nanoparticles

ZIF-8 nanoparticles were synthesized according to literature by mixing an aqueous solution of $Zn(NO_3)_2 \cdot 6H_2O$ with an aqueous solution of 2-methylimidazole (2-MIM) directly under stirring at room temperature with minor modifications.[20] In a typical synthesis, 5 mL of a 0.05 M aqueous solution of $Zn(NO_3)_2$ were poured into 5 mL of a 3.5 M aqueous solution of 2-MIM stirred at 600 rpm for 10 min, followed by three centrifugation / redispersion cycles in in water and then stored in ethanol.

Synthesis of Au_{25}Cys@ZIF-8 nanoparticles

Inspired by the synthesis of Au_{25}SG@ZIF-8[13], Au_{25}Cys@ZIF-8 NPs were synthesized *via* an *in situ* growth at room temperature. Pre-synthesized $Au_{25}Cys_{18}$ NCs in aqueous solution (14 mg, 1 mL) were added to a solution of $Zn(NO_3)_2 \cdot 6H_2O$ (0.05M, 10 mL) drop by drop. Then, the mixture was stirred for 5 min, followed by the addition of a solution of 2-MIM (3.5 M, 10 mL). A slightly brown slurry solution was obtained and after stirring for 10 min, the product was centrifuged and washed three times with water. Au_{25}Cys@ZIF-8 nanoparticles were stored in ethanol.

Synthesis of UiO-66(Zr) nanoparticles

First, Zr_6 oxoclusters were prepared following a previously reported protocol.[21] $ZrCl_4$ (10 g, 42 mmol) was added into a mixture of 15 mL of acetic acid and 25 mL of isopropanol under stirring at 600 rpm and the mixture was heated at 120 °C for 1 h. The product was collected through centrifugation at 14500 rpm and then washed with acetone. The obtained white powder of Zr_6 oxoclusters were dried under vacuum. Then, UiO-66 was synthesized by a protocol reported with minor modifications described recently recently.[22] 300 mg of Zr_6 oxoclusters were dispersed in 2 mL of acetic acid and 5 mL of H_2O. The resulting suspension was stirred at 600 rpm until it became completely colorless. A solution of terephthalic acid (BDC, 200 mg) in EtOH (40 mL) was then added. After one day of reaction at room temperature, the solid was collected by centrifugation at 14500 rpm for 30 min and then thoroughly washed with H_2O and EtOH repeatedly. The resultant solid was stored in EtOH.

Synthesis of Au_{25}Cys@UiO-66 nanoparticles

30 mg of Zr_6 oxoclusters were dispersed in 0.2 mL acetic acid and 0.5 mL H_2O under stirring at 600 rpm until the mixture became completely colorless. Subsequently, 7.5 mg of $Au_{25}Cys_{18}$ NCs in 0.5 mL H_2O was added drop by drop into the previous mixture at 600 rpm, followed by the addition of a

solution of 20 mg terephthalic acid (BDC) in 4 mL EtOH. After one day at room temperature, the solid obtained was collected by centrifugation at 14500 rpm for 30 min and then thoroughly washed with H_2O and EtOH repeatedly. The resultant solid was stored in EtOH.

NIR-II fluorescence imaging

Different concentration (20, 50, 100, 200 and 1000 μg mL^{-1}) of $Au_{25}SG_{18}$ NCs and $Au_{25}SG$@MIL (*i.e.*, Au(h)@MIL in Chapter 3) were prepared in both water and PBS. Then, these samples were transferred to a black 96-well plate (200 μL/well) for NIR-II fluorescence imaging (Ex = 808 nm, Em = 1200 nm).

Drug loading

30 mg of ZIF-8, Au_{25}Cys@ZIF-8, UiO-66 or Au_{25}Cys@UiO-66 were dispersed in 3 mL of an aqueous solution of methotrexate (MTX) (10 mg mL^{-1}, diluted MTX injection). The resulting suspension was stirred at 200 rpm at 37 ^{o}C overnight. The MTX loaded nano-objects were then collected by centrifugation at 14500 rpm for 10 min and washed with water three times. The final products were stored in water (10 mg/mL) at 4 ^{o}C until use. The loading capacity of these MOFs was determined by TGA and HPLC.

4.4 Results and discussion

4.4.1 NIR II fluorescence imaging

NIR-II fluorescence imaging of $Au_{25}SG_{18}$ NCs and $Au_{25}SG$@MIL (*i.e.*, Au(h)@MIL in **Chapter 3**) was first investigated (λ_{ex} = 808 nm, λ_{em} = 1200 nm). As shown in Figure **11**, $Au_{25}SG_{18}$ NCs display a nonlinear concentration dependent fluorescence in both water and PBS.

In contrast, the fluorescence of $Au_{25}SG_{18}$ NCs was quenched in $Au_{25}SG$@MIL in water in the range of 20 to 1000 µg mL^{-1}. However, its fluorescence was surprisingly partly recovered in PBS. Fe^{3+} ions are well-known fluorescence quencher and are assumed to preferentially bind with nitrogen atoms of amino groups and/or oxygen atoms of carboxyl groups of the glutathione molecule of noble metal NCs, leading to the observed fluorescence quenching.[23-24]

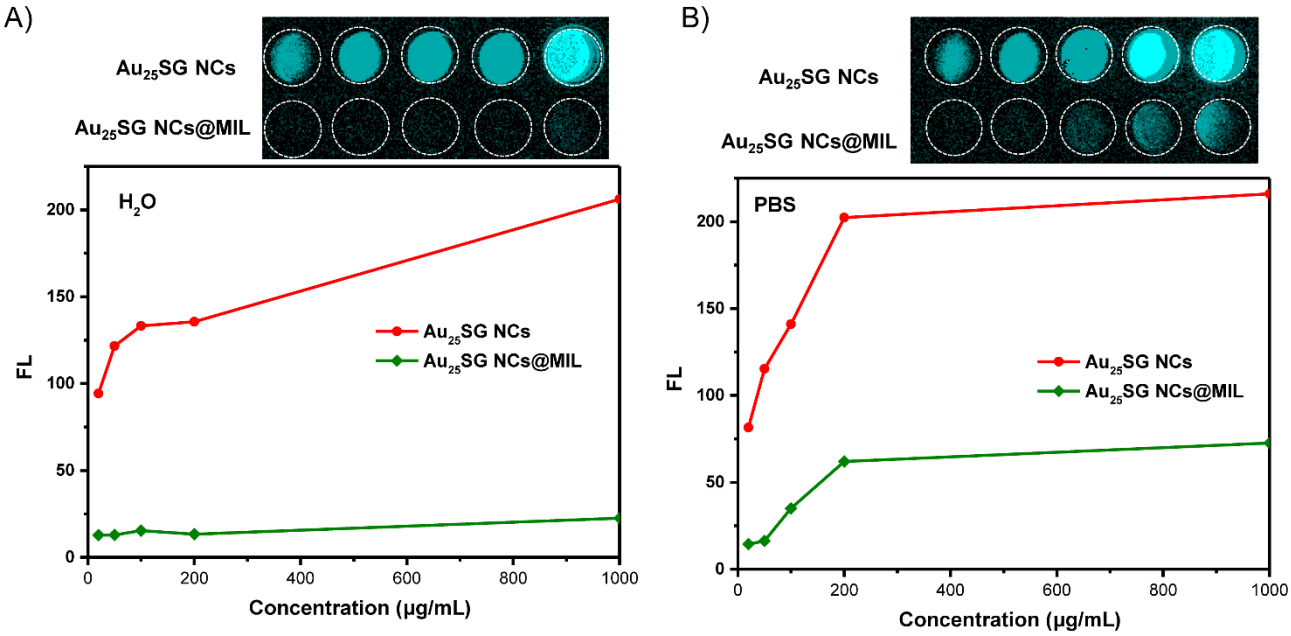

Figure 4.1 The fluorescence intensity (Inserted: NIR-II images) of $Au_{25}SG_{18}$ NCs and $Au_{25}SG$ NCs@MIL at different concentrations in (A) water and (B) PBS (λex = 808 nm).

The partial fluorescence recovery of $Au_{25}SG_{18}$ NCs was indeed caused by the relatively fast degradation of MIL-100(Fe) nanoparticles in neutral PBS because of the competition for Fe^{3+} in the presence of phosphate salts, so that $Au_{25}SG_{18}$ NCs were progressively released from the heterostructure. The fluorescence recovery of $Au_{25}SG_{18}$ NCs could therefore be used for real-time monitoring of drug delivery, especially for stimuli responsive drug release.[25]

The fluorescent $Au_{25}Cys_{18}$ NCs, known to exhibit a stronger NIR-II fluorescence signal in comparison with $Au_{25}SG_{18}$, were thus considered[9] and different $Au_{25}Cys_{18}$ NCs encapsulated MOFs designed. Then $Au_{25}Cys_{18}$ NCs@MOF composites were produced with nanosized MIL-100(Fe), as well as ZIF-

8(Zn) and UiO-66(Zr), that are alternative benchmark nanoMOFs for drug delivery, albeit their utilization in biomedicine can be controversial due to potential toxicity.

4.4.2 Au_{25}Cys@MIL-100

$Au_{25}Cys_{18}$ NCs were first synthesized by a NaOH-mediated $NaBH_4$ reduction method[19] and the scheme of the synthesis is given as in **Figure 4.2** The synthesized $Au_{25}Cys_{18}$ NCs were further characterized by UV-Vis absorbance spectroscopy and TEM. As shown in **Figure 4.3A**, similar with $Au_{25}SG_{18}$ NCs, $Au_{25}Cys_{18}$ NCs exhibited two distinct absorbance peaks at 440 and 670 nm, which is associated with the Au 6sp intraband and interband transitions of the bulk gold, respectively.[26] The diameter of $Au_{25}Cys_{18}$ NCs is 1.5 ± 0.4 nm (**Figure 4.3B**).

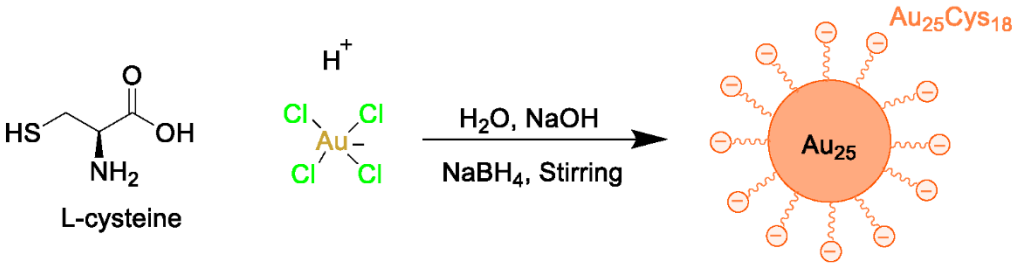

Figure 4.2 Scheme of the synthesis of $Au_{25}Cys_{18}$ NCs.

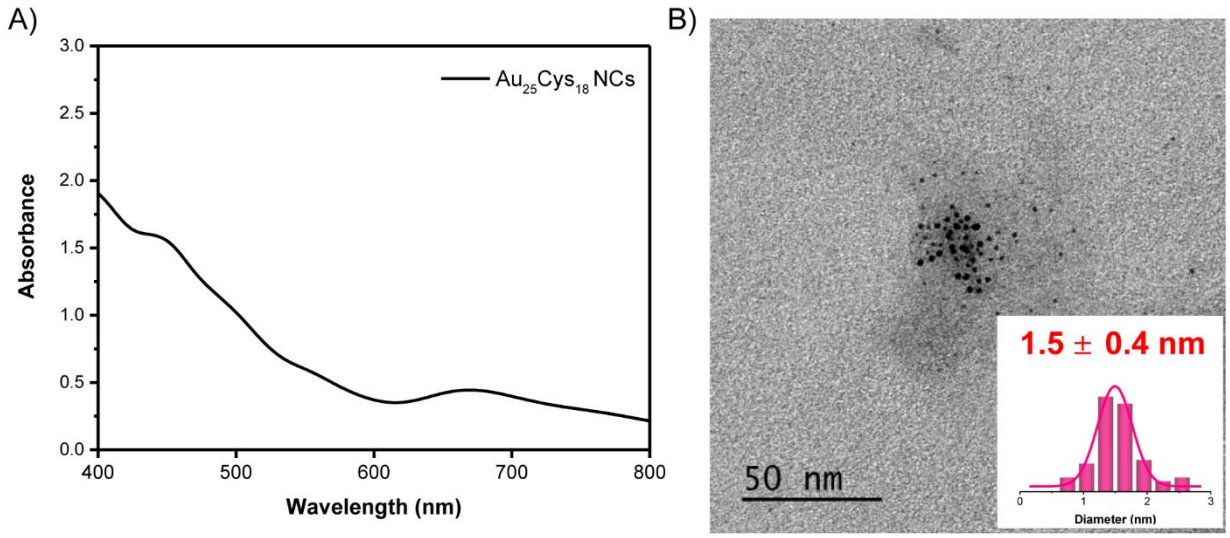

Figure 4.3 A) UV-Vis and (B) TEM and statistical analysis of $Au_{25}Cys_{18}$ NCs. The particle size of $Au_{25}Cys_{18}$ NCs is 1.5 ± 0.4 nm.

$Au_{25}Cys(X)$@MIL-100 (X = 10 or 20 mg) nanoparticles with different content of $Au_{25}Cys_{18}$ NCs, namely $Au_{25}Cys(10)$@MIL and $Au_{25}Cys(20)$@MIL, were successfully prepared and characterized by

PXRD, TEM and DLS. In **Figure 4.4**, PXRD patterns of $Au_{25}Cys(10)$@MIL and $Au_{25}Cys(20)$@MIL were consistent with the one of MIL-100(Fe) and $Au_{25}Cys_{18}$ NCs did not affect the formation of the nanoMOF significantly. TEM images (**Figure 4.5**) of $Au_{25}Cys(10)$@MIL and $Au_{25}Cys(20)$@MIL showed an average diameter of ~40 nm with a monodisperse size distribution, similar to what was observed with $Au_{25}SG$@MIL (~45 nm) in **Chapter 3**. Moreover, the hydrodynamic diameter (~120 nm) and surface charge (~-20 mV) (**Figure 4.6**) of $Au_{25}Cys(10)$@MIL and $Au_{25}Cys(20)$@MIL were also quite close. However, we cannot conclude on the exact location of $Au_{25}Cys_{18}$ NCs in the heterostructure, inside or outside the nanoMOF, and more characterizations such as HAADF-STEM shall be carried out to verify it. Furthermore, fluorescence imaging properties need to be measured.

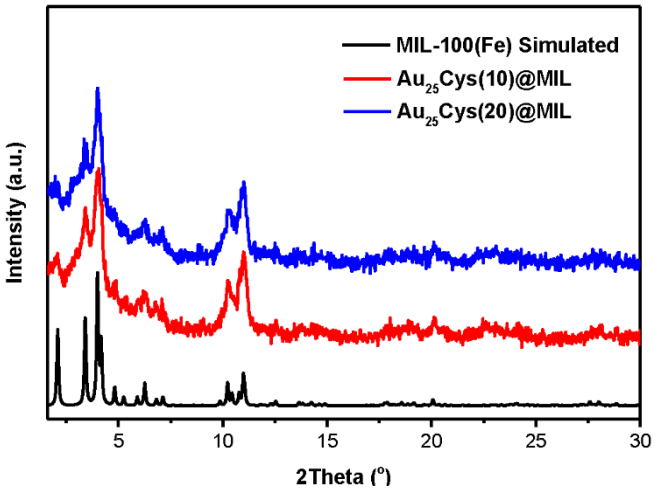

Figure 4.4 PXRD patterns (λ_{Cu} = 1.5406 Å) of $Au_{25}Cys(10)$@MIL and $Au_{25}Cys(20)$@MIL.

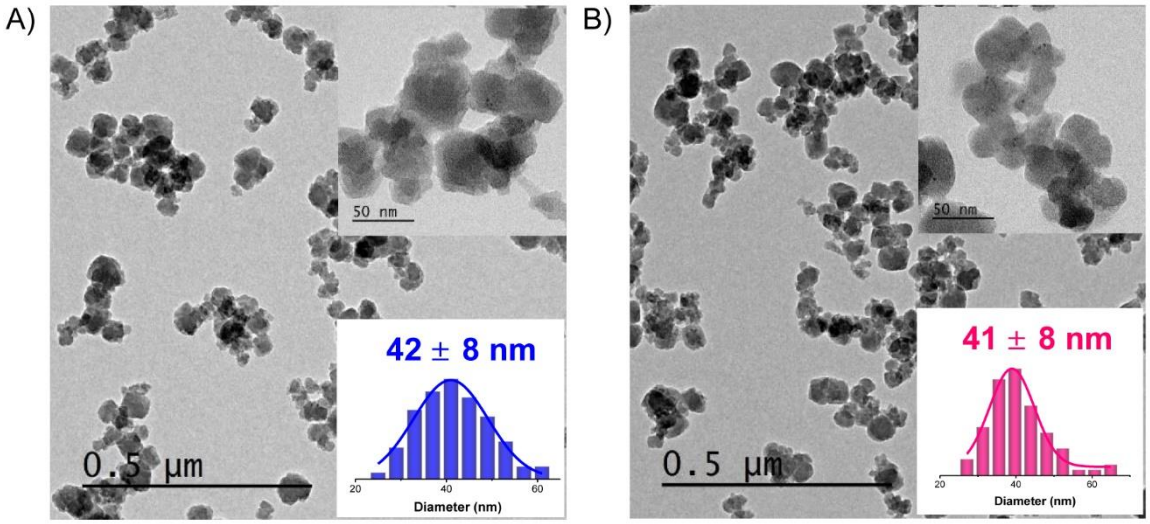

Figure 4.5 TEM images of (A) $Au_{25}Cys(10)$@MIL and (B) $Au_{25}Cys(20)$@MIL (inserted statistical analysis Figure). The particle size of $Au_{25}Cys(10)$@MIL and $Au_{25}Cys(20)$@MIL is 42 ± 8 nm and 41 ± 8 nm, respectively.

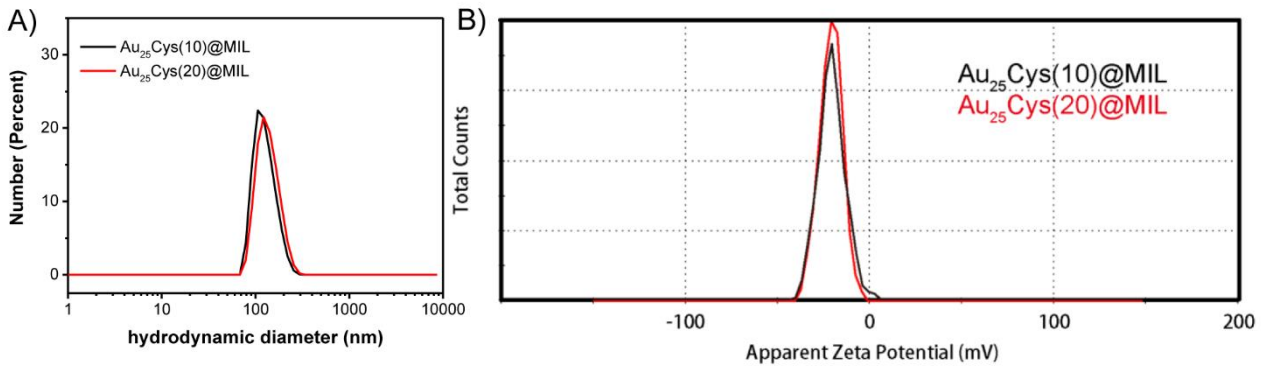

Figure 4.6 A) Hydrodynamic diameters (HDs) and B) Zeta potentials of Au_{25}Cys(10)@MIL and Au_{25}Cys(20)@MIL at a concentration of 100 μg mL^{-1}.

4.4.3 Au_{25}Cys@ZIF-8

As mentioned in previous chapters, ZIF-8 has been widely studied as a drug delivery system due to its facile synthesis and acidic responsive stability. Herein, the synthesis of Au_{25}Cys@ZIF-8 also followed an *in situ* room temperature approach in water. Furthermore, ZIF-8 and Au_{25}Cys@ZIF-8 were characterized by different techniques, including PXRD, FT-IR, SEM, N_2 adsorption and desorption isotherms and TGA.

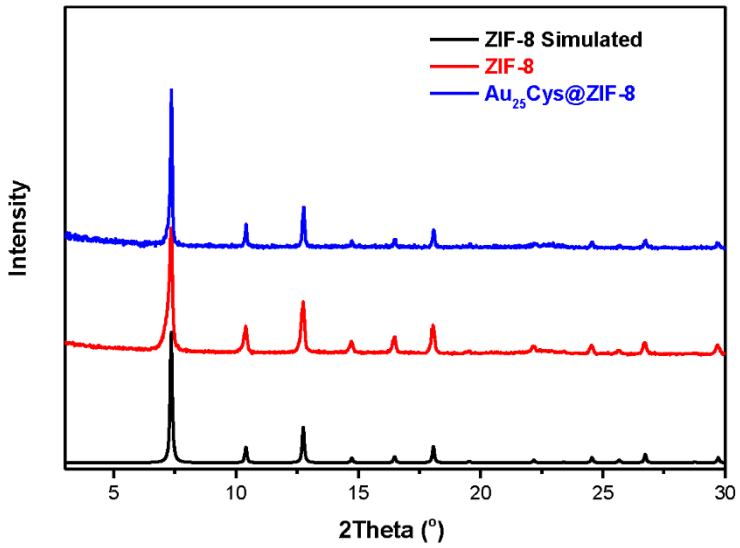

Figure 4.7 PXRD patterns (λ_{Cu} ~ 1.5406 Å) of ZIF-8 and Au_{25}Cys@ZIF-8.

The PXRD pattern of Au_{25}Cys@ZIF-8 showed that there was no significant crystallinity loss after assembling $Au_{25}Cys_{18}$ NCs with ZIF, indicating that the addition of $Au_{25}Cys_{18}$ NCs did not affect the ZIF skeleton (**Figure 4.7**). There is no observed peak of Au clusters in the PXRD pattern, indicating that the size of $Au_{25}Cys_{18}$ NC is too small to be observed. Both ZIF-8 and Au_{25}Cys@ZIF-8 were also studied by FT-IR spectroscopy. In **Figure 4.8**, the bands at 3134 cm^{-1}, 2961 cm^{-1}, 2931 cm^{-1}, and at

1584 cm^{-1} can be attributed to the stretching vibrations of the aromatic and aliphatic C–H and –NH– of imidazole in ZIF-8 or $Au_{25}Cys$@ZIF-8.[27]

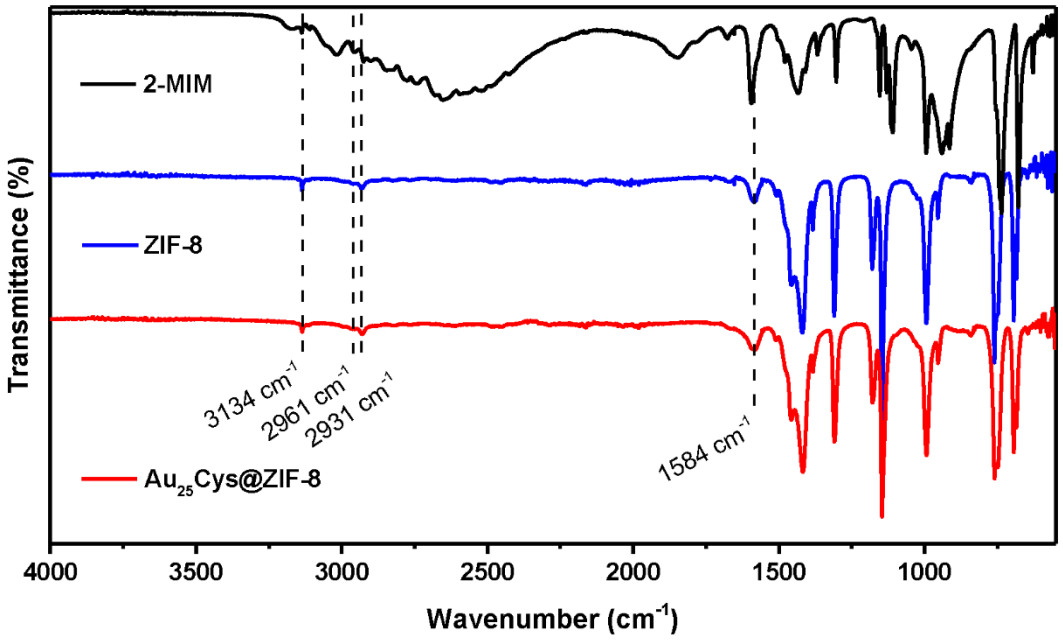

Figure 4.8 FT-IR spectra of ZIF-8 and $Au_{25}Cys$@ ZIF-8.

According to SEM analysis (see **Figure 4.9**) the average diameter of ZIF-8 and $Au_{25}Cys$@ZIF-8 is 160 ± 33 nm and 217 ± 40 nm, respectively. The nanoparticles were monodisperse in size and (shape) homogeneous in the SEM images. Energy dispersive spectroscopy (EDS) analysis gave an atomic ratio of Au to Zn close to 8% (**Table 4.1**). This ratio can be tuned by changing the initial amount of $Au_{25}Cys_{18}$ NCs in the synthesis in our preliminary study. As for future potential fluorescence imaging or catalysis application, a selection of $Au_{25}Cys$@ZIF-8 NPs with different encapsulation of $Au_{25}Cys_{18}$ NCs would be necessary. Meanwhile, the initial addition of $Au_{25}Cys_{18}$ NCs affects the final particle size and the cost should also be taken into consideration for practical applications.

The colloidal stability of ZIF-8 and $Au_{25}Cys$@ZIF-8 was also studied. DLS analysis of ZIF-8 and $Au_{25}Cys$@ZIF-8 showed a hydrodynamic diameter in ethanol of 212 ± 12 nm and 267 ± 18 nm, respectively (see **Figure 4.10A**). Their hydrodynamic diameters increased by only ~50 nm in comparison to the corresponding SEM diameters, suggesting the monodisperse character of ZIF-8 and $Au_{25}Cys$@ZIF-8 again. Meanwhile, it has to be noticed that the color of a suspension of $Au_{25}Cys$@ZIF-8 was much darker than a suspension of ZIF-8 (**Figure 4.10B**). In conclusion, $Au_{25}Cys_{18}$ NCs clearly affect the formation of ZIF-8 leading to an increase of the particle size, measured by SEM or by DLS, of the $Au_{25}Cys$@ZIF-8 NPs compared to ZIF-8 NPs. The hypothesis is that the formation of Au−Cys−Zn linkage slows down self-assembling of $Au_{25}Cys_{18}$ NCs and ZIF-8,

leading to large particle sizes. Further works need to be done in order to see if the size of the final $Au_{25}Cys$@ZIF-8 NPs can be effectively tuned by controlling the amount of $Au_{25}Cys_{18}$ NCs added or by varying the concentration of Zn^{2+} and 2-MIM during the synthesis.[28-30]

As for potential *in vivo* application, a hydrodynamic diameter below 200 nm and a good colloidal stability in physiological media are expected. Thus, to further improve the colloidal stability or the targeting ability of $Au_{25}Cys$@ZIF-8, these nanoobjects could be further functionalized/capped for instance using an additional surface coating with a biopolymer such as hyaluronic acid or polyethylene glycol (PEG).

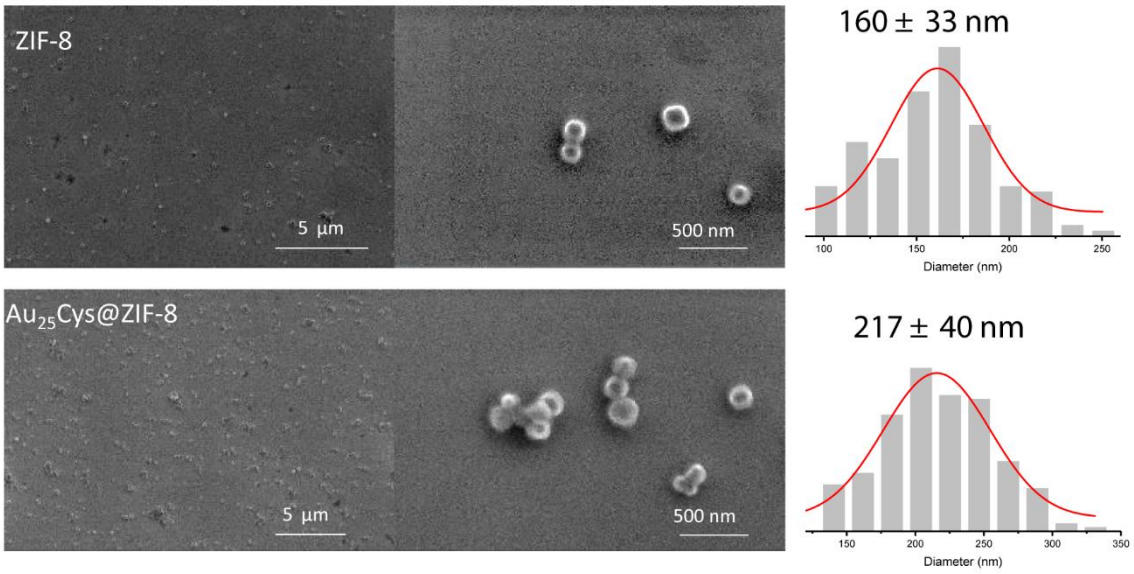

Figure 4.9 SEM images and statistical analysis of ZIF-8 and $Au_{25}Cys$@ZIF-8.

Table 4.1 EDS analysis of $Au_{25}Cys$@ZIF-8

Sample	Zn-K	Au-K
Point 1	91.9 ± 2.6	8.1 ± 1.2
Point 2	87.7 ± 2.5	12.3 ± 1.7
Point 3	93.1 ± 2.6	6.9 ± 1.2
Point 4	91.5 ± 2.6	8.5 ± 1.2
Point 5	92.0 ± 2.5	8.0 ± 1.2

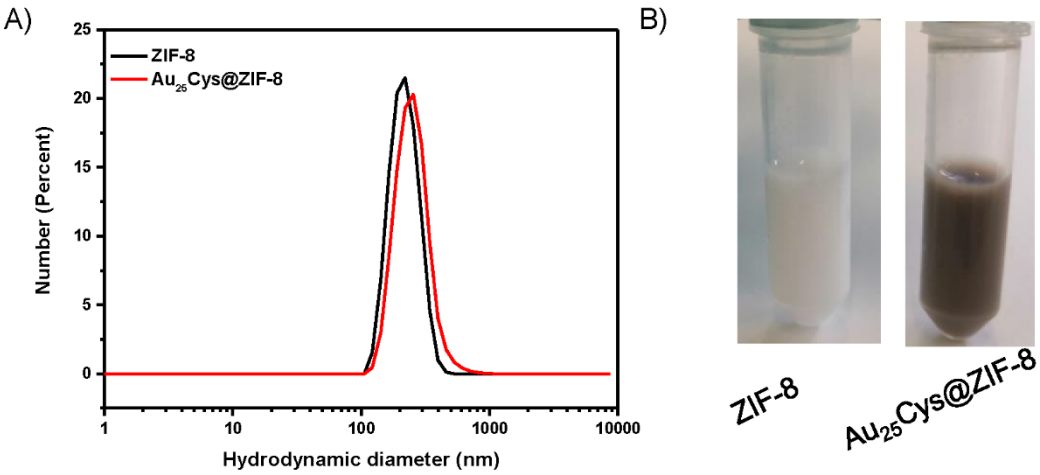

Figure 4.10 A) Hydrodynamic diameters (by number) and (B) pictures of ZIF-8 and Au_{25}Cys@ZIF-8 suspensions in EtOH.

N_2 porosimetry results of ZIF-8 and Au_{25}Cys@ZIF-8 are shown in **Figure 4.11**. A slight decrease of the BET area was observed when comparing Au_{25}Cys@ZIF-8（1490 m^2 g^{-1}）with ZIF-8（1670 m^2 g^{-1}）, suggesting the successful assembly of $Au_{25}Cys_{18}$ NCs and ZIF-8. TGA was carried out under O_2 flow to evaluate the thermal stability of ZIF-8 and Au_{25}Cys@ZIF-8. Based on TGA analysis, a better thermal stability was observed after integrating $Au_{25}Cys_{18}$ NCs into ZIF-8 (see **Figure 4.12**). All the results shown here tend to confirm the successful synthesis of Au_{25}Cys@ZIF-8 heterostructure.

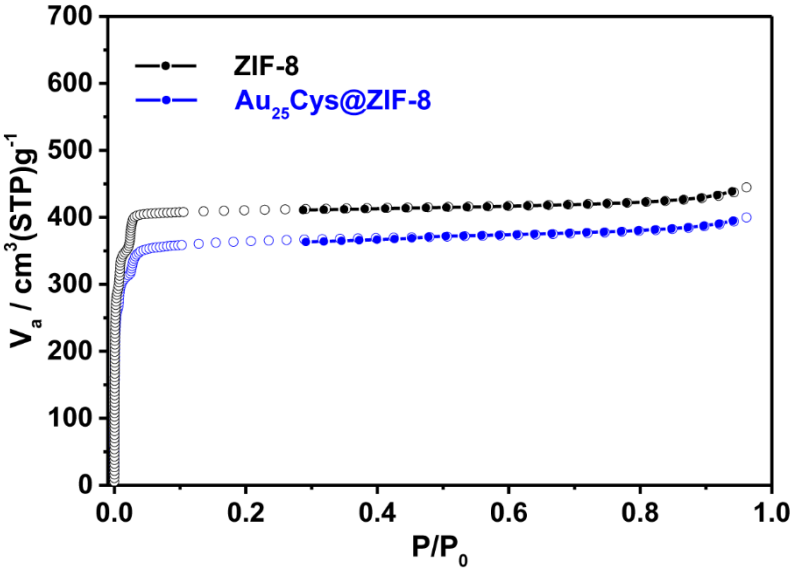

Figure 4.11 N_2 adsorption-desorption isotherms (77K, P_0 = 1 atm) of ZIF-8 and Au_{25}Cys@ ZIF-8.

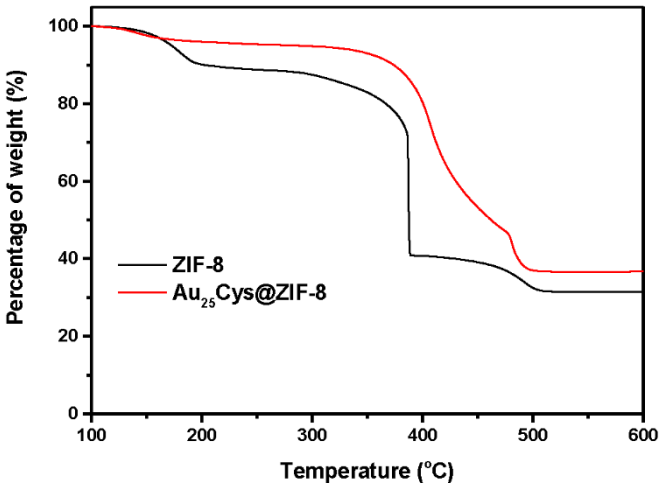

Figure 4.12 TGA of ZIF-8 and Au_{25}Cys@ZIF-8 under oxygen flow with a measuring speed at 5 °C min^{-1}.

4.4.5 Au_{25}Cys@UiO-66

For the synthesis of UiO-66 and Au_{25}Cys@UiO-66, acetic acid was introduced as a modulator in order to control the growth of UiO-66. The MOF nanocrystal size results from a subtle interplay between different equilibria such as linker deprotonation, linker complexation, modulator deprotonation and termination.[31-32] It was clearly shown that the presence of an acid modulator can increase or reduce the crystal size of Zr MOFs and a significant amount of acid limits the deprotonation of the linker upon decreasing the pH and can also compete with the organic linker for the coordination of the metal, thereby slowing down the metal-linker complexation and leading to large particle sizes.[21, 33-34] The crystalline structure of UiO-66 and Au_{25}Cys@UiO-66 was first investigated. They showed very similar PXRD patterns, matching well the simulated pattern of UiO-66 (see **Figure 4.13**). Also, the synthesis of Zr_6 oxoclusters, precursors of UiO-66, was confirmed by XRD analysis. Similar FT-IR spectra were also observed for UiO-66 and Au_{25}Cys@UiO-66 (see **Figure 4.14**), with the expected characteristic peaks from the structural unit $(Zr_6O_4)(OH)_4(CO_2)n$ formed by coordination of the metal Zr_6 clusters with terephthalic acid at 1573 cm^{-1} and 1397 cm^{-1}.

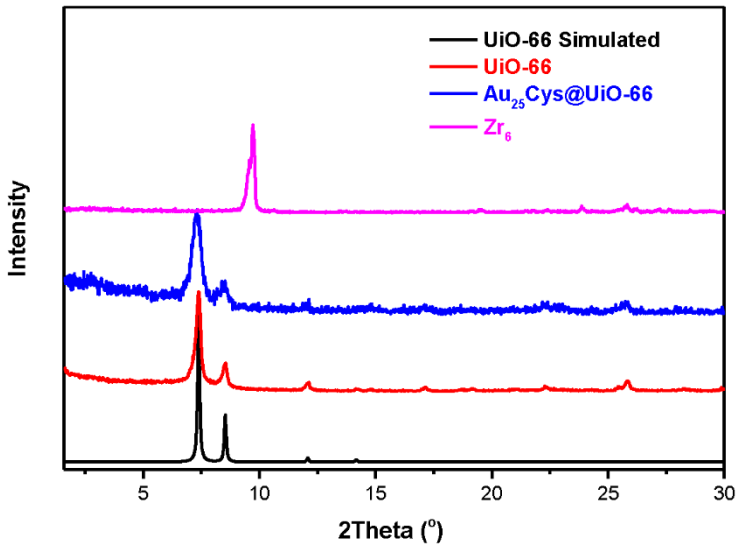

Figure 4.13 PXRD patterns (λ_{Cu} ~ 1.5406 Å) of UiO-66, Au_{25}Cys@UiO-66 and Zr_6 clusters.

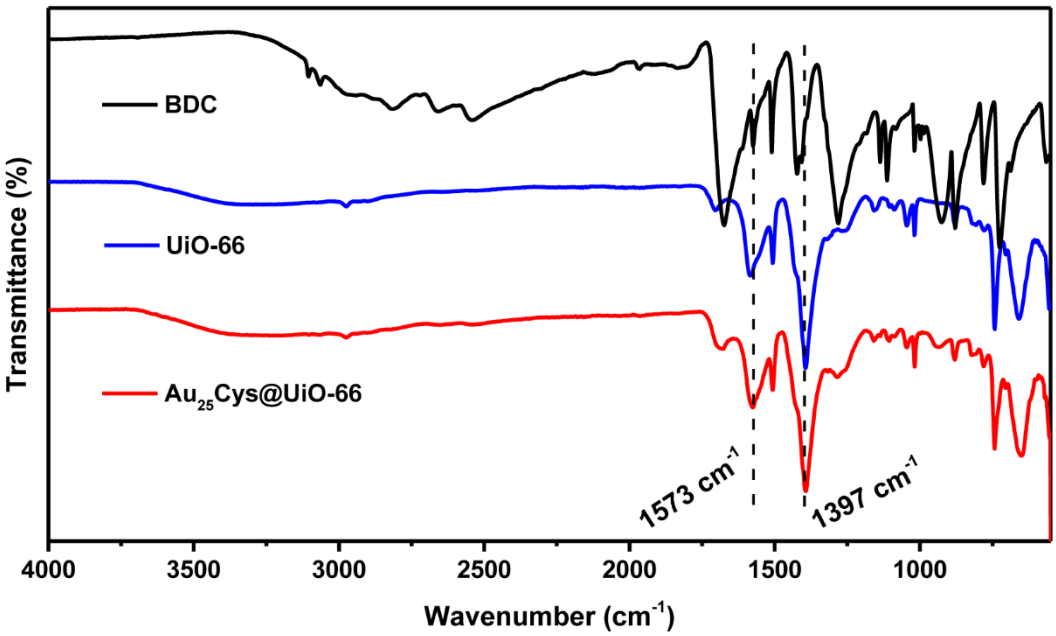

Figure 4.14 FT-IR spectra of BDC, UiO-66 and Au_{25}Cys@UiO-66.

According to previous results,[22] Cu NCs@UiO-66-NH_2 MOFs were already obtained with small sizes (~80 nm), and a smaller particle size of UiO-66 NPs would be highly beneficial for biomedical applications. SEM analysis gave an average diameter of about 30 nm for both UiO-66 and Au_{25}Cys@UiO-66 nanoparticles (see **Figure 4.15**). Aggregates were clearly observed in SEM images. The SEM samples were prepared in EtOH, and the hydrodynamic diameters were also measured in EtOH by DLS. UiO-66 and Au_{25}Cys@UiO-66 had a hydrodynamic diameter of 53 ± 16 nm and 83 ± 9 nm (see **Figure 4.16.A**), respectively, indicating a slight aggregation in EtOH. Nevertheless, the size of the Au_{25}Cys@UiO-66 NPs remained smaller compared to Au_{25}SG@MIL studied in **Chapter 3**.

Moreover, suspension of $Au_{25}Cys$@UiO-66 NPs became totally black due to the introduction of $Au_{25}Cys_{18}$ NCs (see **Figure 4.16.B**).

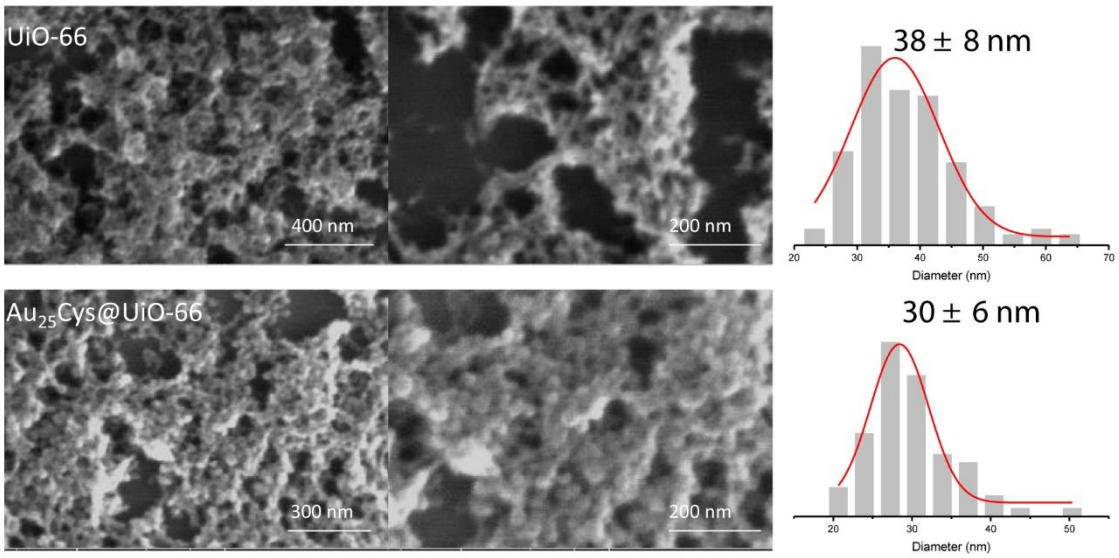

Figure 4.15 SEM images of UiO-66 and $Au_{25}Cys$@UiO-66. The particle size of UiO-66 and $Au_{25}Cys$@UiO-66 was 30 ± 8 nm and 30 ± 6 nm, respectively.

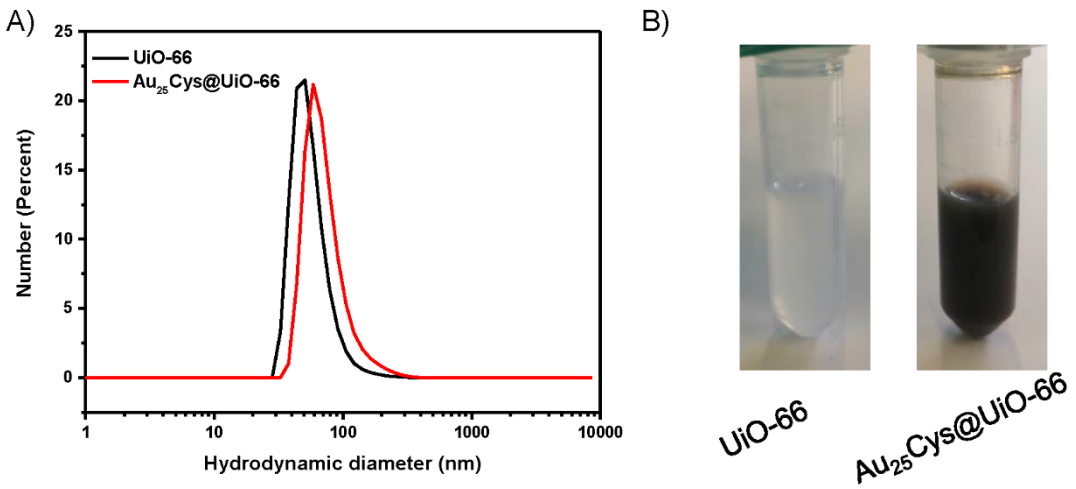

Figure 4.16 A) Hydrodynamic diameters (by number) and (B) pictures of UiO-66 and $Au_{25}Cys$@UiO-66 in EtOH.

The colloidal stability of UiO-66 and $Au_{25}Cys$@UiO-66 was found to be pH-dependent. The surface charges were around 0 mV at pH 5 and pH 7, thus leading to strong aggregation at these pH values (**Table 4.2**). At pH 2.7, the hydrodynamic diameters of UiO-66 and $Au_{25}Cys$@UiO-66 were 72 ± 12 nm and 84 ± 12 nm, respectively (see **Figure 4.17** and **Table 4.2**) with a surface charge of ~30 mV, leading to a good colloidal stability. Furthermore, the hydrodynamic diameters were studied in physiological media, and interestingly, while $Au_{25}Cys$@UiO-66 showed a diameter of ~98 nm in neutral PBS, a significant aggregation was observed in acidic PBS (see **Table 4.2**), contrary to what

was observed with MIL-100(Fe) or Au_{25}SG@MIL in **Chapter 3**. Although the small size of individual Au_{25}Cys@UiO-66 particle makes it interesting for *in vivo* applications, further surface modification might be necessary to slow down degradation, prevent aggregation and/or ensure a good targeting of these nanoMOFs.

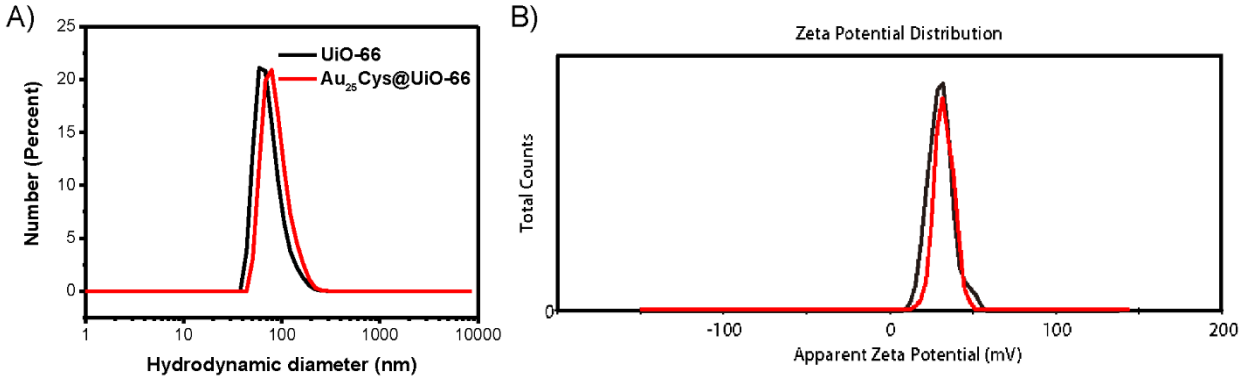

Figure 4.17 A) Hydrodynamic diameters (by number) and (B) Zeta potentials of UiO-66 and Au_{25}Cys@UiO-66 in water (pH = 2.7).

Table 4.2 Hydrodynamic diameters (HDs, by number) and (B) Zeta potentials of UiO-66 and Au_{25}Cys@UiO-66 in water and PBS at various pH.

	UiO-66		Au_{25}Cys@UiO-66	
	HDs (nm)	Zeta potential (mV)	HDs (nm)	Zeta potential (mV)
Water (pH 2.7)	72 ± 12	31.5 ± 2.2	84 ± 12	33.2 ± 0.6
Water (pH 5)	852 ± 49	5.2 ± 0.1	904 ± 252	6.5 ± 0.1
Water (pH 7)	853 ± 448	-6.3 ± 0.1	Not reliable	-0.2 ± 0.1
PBS (pH 5.1)	143 ± 35	-	962 ± 112	-
PBS (pH 7.4)	95 ± 14	-	98 ± 5	-

N_2 porosimetry analysis of UiO-66 and Au_{25}Cys@UiO-66 at 77K has been carried out, leading to a BET area of 1481 m^2 g^{-1} and 952 m^2 g^{-1}, respectively. The significant decrease of the BET area of Au_{25}Cys@UiO-66 (~35%) indicated the presence of a significant amount of $Au_{25}Cys_{18}$ NCs in Au_{25}Cys@UiO-66 (see **Figure 4.18**). According to TGA analysis (see **Figure 4.19**), the weight percentage of Au_{25}Cys@UiO-66 decreased more significantly before 400 ºC due to the existence of $Au_{25}Cys_{18}$. Meanwhile, from the isotherms, the interparticular N_2 uptake of Au_{25}Cys@UiO-66 occurred at a lower P/P_0 than that of UiO-66, suggesting a smaller size. After the integration of

$Au_{25}Cys_{18}$ NCs, $Au_{25}Cys$@UiO-66 are still microporous which is promising in a view of drug delivery applications. Importantly, NIR II fluorescence properties of $Au_{25}Cys$@UiO-66 need to be studied.

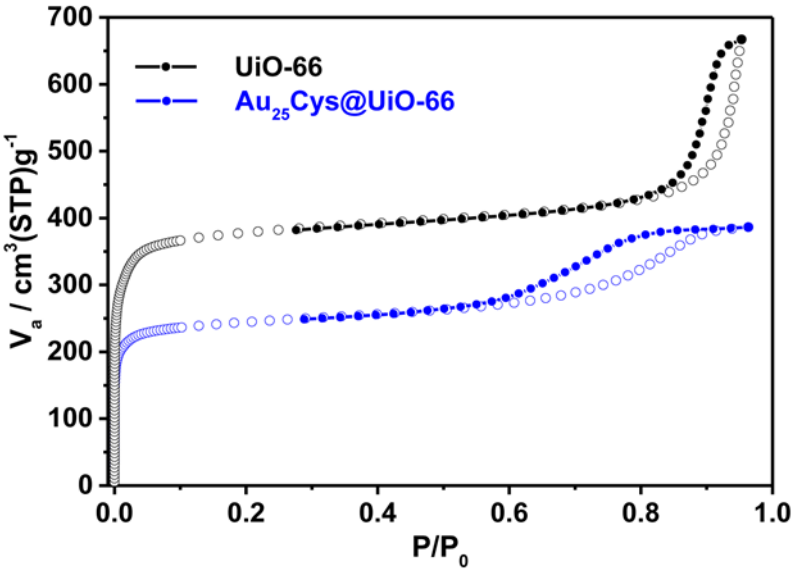

Figure 4.18 N_2 adsorption-desorption isotherms at 77K (P_0 =1 atm) of UiO-66 and $Au_{25}Cys$@UiO-66.

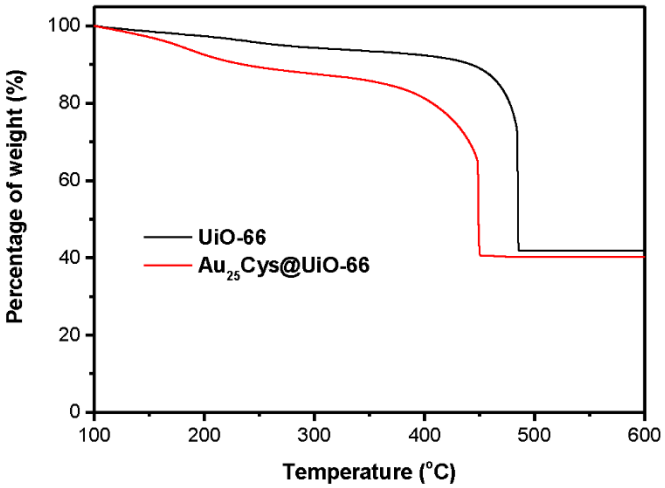

Figure 4.19 TGA of UiO-66 and $Au_{25}Cys$@UiO-66 under oxygen flow with a measuring speed at 5 °C min^{-1}.

4.4.6 Preliminary drug loading tests

Apart from MIL-100(Fe), ZIF-8 and UiO-66 nanoparticles are also promising candidates for drug delivery, as discussed in the introduction. As already mentioned in **Chapter 2**, MTX is a promising drug model for anti-tumor and anti-inflammation, but the burst release in neutral PBS is a drawback for intravenous injection. ZIF-8 showed a high drug loading capacity (~70%) with an acidic responsive release for MTX.[35-36] UiO-66 also showed a high adsorption capacity and a great affinity to MTX and ethylenediamine functionalized UiO-66-NH_2 (UiO-66-EDA) even exhibited an adsorption capacity of

MTX as high as 540.78 mg/g.[37-38] MTX was thus selected for the preliminary studies on the stability of MOFs and Au_{25}Cys@MOF during drug loading. After the encapsulation of MTX, no significant crystallinity loss was observed by PXRD for ZIF-8, UiO-66 and their corresponding heterostructures Au_{25}Cys@ZIF-8 and Au_{25}Cys@UiO-66 (see **Figure 4.20**). Due to time limitations, it was not possible to further analyze our MTX loaded Au_{25}Cys@MOF. The drug loading capacity needs to be studied by HPLC and TGA and the drug or metal ions release shall be monitored by HPLC and ICP-MS in the near future.

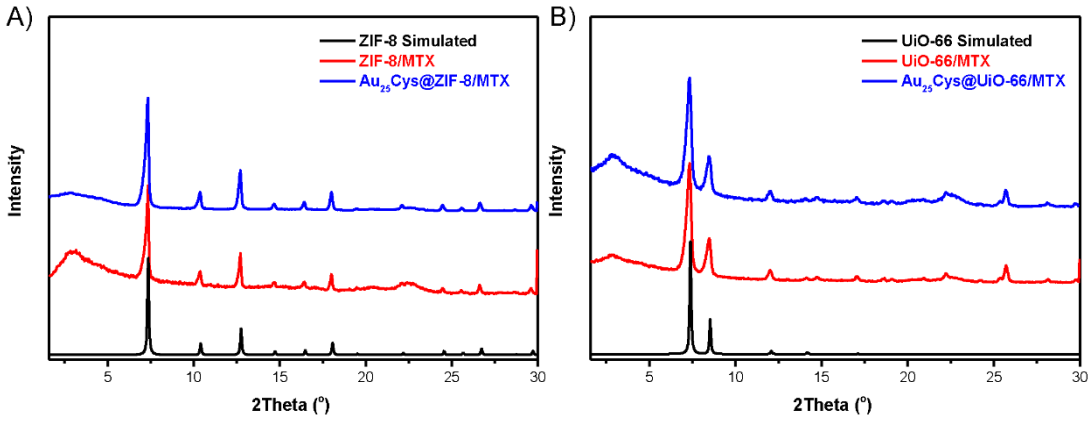

Figure 4.20 PXRD (λ_{Cu} = 1.5406 Å) of (A) ZIF-8, ZIF-8/MTX, Au_{25}Cys@ZIF-8/MTX and (B) UiO-66, UiO-66/MTX, Au_{25}Cys@UiO-66/MTX.

4.5 Conclusion

In this chapter, series of Au NCs/MOFs nanoobjects have been synthesized *via* an *in situ* room temperature approach for possible NIR-II fluorescence imaging and photodynamic therapy. Herein, based on the same MOF, namely MIL-100(Fe), different ligand cysteine protected Au_{25} NCs could be assembled into heterostructures (*i.e.*, Au_{25}Cys@MIL-100). Although significant fluorescence quenching effects of Au_{25}SG@MIL-100 have been observed, this is still promising for further NIR triggered photodynamic study. Alternatively, Au_{25}Cys NCs could also be assembled into different nanoMOFs (*i.e.*, Au_{25}Cys@ZIF-8 and Au_{25}Cys@UiO-66), which were characterized by PXRD, SEM, DLS, N_2 porosimetry analysis, etc. Notably, the obtained UiO-66 nanoparticles and Au_{25}Cys@UiO-66 nanoobjects even showed a particle size as small as ~30 nm by SEM. When compared with bare UiO-66, Au_{25}Cys@UiO-66 exhibited significant decrease of BET area. Currently, there is still a need to complete this work to better understand the NIR-II fluorescence imaging, ROS generation and drug delivery properties of these composites. Apart from anti-cancer, they could be of interest for other applications such as antibacterial, catalysis, sensing, etc.

References

1. Dai, H.; Wang, X.; Shao, J.; Wang, W.; Mou, X.; Dong, X., NIR-II Organic Nanotheranostics for Precision Oncotherapy. *Small* **2021,** *17* (44), 2102646.
2. Gong, L.; Shan, X.; Zhao, X. H.; Tang, L.; Zhang, X. B., Activatable NIR-II Fluorescent Probes Applied in Biomedicine: Progress and Perspectives. *ChemMedChem* **2021,** *16* (16), 2426-2440.
3. Li, B.; Zhao, M.; Lin, J.; Huang, P.; Chen, X., Management of Fluorescent Organic/Inorganic Nanohybrids for Biomedical Applications in the NIR-II Region. *Chem Soc Rev* **2022,** *51*, 7692-7714.
4. Lei, Z.; Zhang, F., Molecular Engineering of NIR-II Fluorophores for Improved Biomedical Detection. *Angew Chem Int Ed* **2021,** *60* (30), 16294-16308.
5. Kang, X.; Zhu, M., Tailoring the Photoluminescence of Atomically Precise Nanoclusters. *Chem Soc Rev* **2019,** *48* (8), 2422-2457.
6. Jin, R., Atomically Precise Metal Nanoclusters: Stable Sizes and Optical Properties. *Nanoscale* **2015,** *7* (5), 1549-1565.
7. Liu, J.; Liang, J.; Xue, J.; Liang, K., Metal-Organic Frameworks as a Versatile Materials Platform for Unlocking New Potentials in Biocatalysis. *Small* **2021,** *17* (32), 2100300.
8. Li, S.; Ma, Q.; Wang, C.; Yang, K.; Hong, Z.; Chen, Q.; Song, J.; Song, X.; Yang, H., Near-Infrared II Gold Nanocluster Assemblies with Improved Luminescence and Biofate for *In Vivo* Ratiometric Imaging of H_2S. *Anal Chem* **2022,** *94* (5), 2641-2647.
9. Liu, H.; Hong, G.; Luo, Z.; Chen, J.; Chang, J.; Gong, M.; He, H.; Yang, J.; Yuan, X.; Li, L.; Mu, X.; Wang, J.; Mi, W.; Luo, J.; Xie, J.; Zhang, X. D., Atomic-Precision Gold Clusters for NIR-II Imaging. *Adv Mater* **2019,** *31* (46), 1901015.
10. Li, D.; Liu, Q.; Qi, Q.; Shi, H.; Hsu, E. C.; Chen, W.; Yuan, W.; Wu, Y.; Lin, S.; Zeng, Y.; Xiao, Z.; Xu, L.; Zhang, Y.; Stoyanova, T.; Jia, W.; Cheng, Z., Gold Nanoclusters for NIR-II Fluorescence Imaging of Bones. *Small* **2020,** *16* (43), 2003851.
11. Wang, W.; Kong, Y.; Jiang, J.; Xie, Q.; Huang, Y.; Li, G.; Wu, D.; Zheng, H.; Gao, M.; Xu, S.; Pan, Y.; Li, W.; Ma, R.; Wu, M. X.; Li, X.; Zuilhof, H.; Cai, X.; Li, R., Engineering the Protein Corona Structure on Gold Nanoclusters Enables Red-Shifted Emissions in the Second Near-infrared Window for Gastrointestinal Imaging. *Angew Chem Int Ed* **2020,** *59* (50), 22431-22435.
12. Bertorelle, F.; Wegner, K. D.; Peric Bakulic, M.; Fakhouri, H.; Comby-Zerbino, C.; Sagar, A.; Bernado, P.; Resch-Genger, U.; Bonacic-Koutecky, V.; Le Guevel, X.; Antoine, R., Tailoring the NIR-II Photoluminescence of Single Thiolated Au25 Nanoclusters by Selective Binding to Proteins. *Chemistry* **2022,** *28* (39), 202200570.
13. Luo, Y.; Fan, S.; Yu, W.; Wu, Z.; Cullen, D. A.; Liang, C.; Shi, J.; Su, C., Fabrication of $Au_{25}(SG)_{18}$ -ZIF-8 Nanocomposites: A Facile Strategy to Position $Au_{25}(SG)_{18}$ Nanoclusters Inside and Outside ZIF-8. *Adv Mater* **2018,** *30* (6), 1704576.
14. Xia, M.; Sui, Y.; Guo, Y.; Zhang, Y., Aggregation-Induced Emission Enhancement of Gold Nanoclusters in Metal-Organic Frameworks for Highly Sensitive Fluorescent Detection of Bilirubin. *Analyst* **2021,** *146* (3), 904-910.
15. Cai, Y.; Zhu, H.; Zhou, W.; Qiu, Z.; Chen, C.; Qileng, A.; Li, K.; Liu, Y., Capsulation of AuNCs with AIE Effect into Metal-Organic Framework for the Marriage of a Fluorescence and Colorimetric Biosensor to Detect Organophosphorus Pesticides. *Anal Chem* **2021,** *93* (19), 7275-7282.
16. Ma, X.; Ren, X.; Guo, X.; Fu, C.; Wu, Q.; Tan, L.; Li, H.; Zhang, W.; Chen, X.; Zhong, H.; Meng, X., Multifunctional Iron-Based Metal-Organic Framework as Biodegradable Nanozyme for Microwave Enhancing Dynamic Therapy. *Biomaterials* **2019,** *214*, 119223.
17. Yang, D.; Yang, G.; Gai, S.; He, F.; An, G.; Dai, Y.; Lv, R.; Yang, P., Au_{25} Cluster Functionalized Metal-Organic Nanostructures for Magnetically Targeted Photodynamic/Photothermal Therapy Triggered by Single Wavelength 808 Nm Near-Infrared Light. *Nanoscale* **2015,** *7* (46), 19568-19578.
18. Yun, Y.; Sheng, H.; Bao, K.; Xu, L.; Zhang, Y.; Astruc, D.; Zhu, M., Design and Remarkable Efficiency of the Robust Sandwich Cluster Composite Nanocatalysts ZIF-8@Au_{25}@ZIF-67. *J Am*

Chem Soc **2020,** *142* (9), 4126-4130.
19. Yuan, X.; Zhang, B.; Luo, Z.; Yao, Q.; Leong, D. T.; Yan, N.; Xie, J., Balancing the Rate of Cluster Growth, Etching for Gram-Scale Synthesis of Thiolate-Protected Au(25) Nanoclusters with Atomic Precision. *Angew Chem Int Ed* **2014,** *53* (18), 4623-4627.
20. Pan, Y.; Liu, Y.; Zeng, G.; Zhao, L.; Lai, Z., Rapid Synthesis of Zeolitic Imidazolate Framework-8 (ZIF-8) Nanocrystals in an Aqueous System. *Chem Commun (Camb)* **2011,** *47* (7), 2071-2073.
21. Dai, S.; Simms, C.; Dovgaliuk, I.; Patriarche, G.; Tissot, A.; Parac-Vogt, T. N.; Serre, C., Monodispersed MOF-808 Nanocrystals Synthesized *Via* a Scalable Room-Temperature Approach for Efficient Heterogeneous Peptide Bond Hydrolysis. *Chem Mater* **2021,** *33* (17), 7057-7066.
22. Dai, S.; Kajiwara, T.; Ikeda, M.; Romero-Muniz, I.; Patriarche, G.; Platero-Prats, A. E.; Vimont, A.; Daturi, M.; Tissot, A.; Xu, Q.; Serre, C., Ultrasmall Cu Nanoclusters in Zirconium Metal-Organic Frameworks for the Photoreduction of CO_2. *Angew Chem Int Ed* **2022,** *134*, 202211848.
23. Chen, Z.; Lu, D.; Zhang, G.; Yang, J.; Dong, C.; Shuang, S., Glutathione Capped Silver Nanoclusters-Based Fluorescent Probe for Highly Sensitive Detection of Fe^{3+}. *Sens Actuators B Chem* **2014,** *202*, 631-637.
24. Zheng, S.; Yin, H.; Li, Y.; Bi, F.; Gan, F., One–Step Synthesis of L-Tryptophan-Stabilized Dual-Emission Fluorescent Gold Nanoclusters and Its Application for Fe^{3+} Sensing. *Sens Actuators B Chem* **2017,** *242*, 469-475.
25. Yin, X.; Yang, B.; Chen, B.; He, M.; Hu, B., Multifunctional Gold Nanocluster Decorated Metal-Organic Framework for Real-Time Monitoring of Targeted Drug Delivery and Quantitative Evaluation of Cellular Therapeutic Response. *Anal Chem* **2019,** *91* (16), 10596-10603.
26. Negishi, Y.; Nobusada, K.; Tsukuda, T., Glutathione-protected gold clusters revisited: bridging the gap between gold(I)-thiolate complexes and thiolate-protected gold nanocrystals. *J Am Chem Soc* **2005,** *127* (14), 5261-5270.
27. Zhang, L.; Gao, Y.; Sun, S.; Li, Z.; Wu, A.; Zeng, L., pH-Responsive Metal-Organic Framework Encapsulated Gold Nanoclusters with Modulated Release to Enhance Photodynamic Therapy/Chemotherapy in Breast Cancer. *J Mater Chem B* **2020,** *8* (8), 1739-1747.
28. Tanaka, S.; Kida, K.; Okita, M.; Ito, Y.; Miyake, Y., Size-controlled Synthesis of Zeolitic Imidazolate Framework-8 (ZIF-8) Crystals in an Aqueous System at Room Temperature. *Chem Lett* **2012,** *41* (10), 1337-1339.
29. Beh, J. J.; Lim, J. K.; Ng, E. P.; Ooi, B. S., Synthesis and size control of zeolitic imidazolate framework-8 (ZIF-8): From the Perspective of Reaction Kinetics and Thermodynamics of Nucleation. *Mater Chem Phys* **2018,** *216*, 393-401.
30. Zheng, G.; Chen, Z.; Sentosun, K.; Perez-Juste, I.; Bals, S.; Liz-Marzan, L. M.; Pastoriza-Santos, I.; Perez-Juste, J.; Hong, M., Shape Control in ZIF-8 Nanocrystals and Metal Nanoparticles@ZIF-8 Heterostructures. *Nanoscale* **2017,** *9* (43), 16645-16651.
31. Forgan, R. S., Modulated Self-Assembly of Metal-Organic Frameworks. *Chem Sci* **2020,** *11* (18), 4546-4562.
32. Marshall, C. R.; Staudhammer, S. A.; Brozek, C. K., Size Control over Metal-Organic Framework Porous Nanocrystals. *Chem Sci* **2019,** *10* (41), 9396-9408.
33. Gibbons, B.; Bartlett, E. C.; Cai, M.; Yang, X.; Johnson, E. M.; Morris, A. J., Defect Level and Particle Size Effects on the Hydrolysis of a Chemical Warfare Agent Simulant by UiO-66. *Inorg Chem* **2021,** *60* (21), 16378-16387.
34. Dai, S.; Nouar, F.; Zhang, S.; Tissot, A.; Serre, C., One-Step Room-Temperature Synthesis of Metal(IV) Carboxylate Metal-Organic Frameworks. *Angew Chem Int Ed* **2021,** *60* (8), 4282-4288.
35. Samiei Foroushani, M.; Zahmatkeshan, A.; Arkaban, H.; Karimi Shervedani, R.; Kefayat, A., A Drug Delivery System Based on Nanocomposites Constructed from Metal-Organic Frameworks and Mn_3O_4 Nanoparticles: Preparation and Physicochemical Characterization for BT-474 and MCF-7 Cancer Cells. *Colloids Surf B Biointerfaces* **2021,** *202*, 111712.

36. Wang, Y.; Jia, M.; Zheng, X.; Wang, C.; Zhou, Y.; Pan, H.; Liu, Y.; Lu, J.; Mei, Z.; Li, C., Microvesicle-Camouflaged Biomimetic Nanoparticles Encapsulating a Metal-Organic Framework for Targeted Rheumatoid Arthritis Therapy. *J Nanobiotechnology* **2022,** *20* (1), 253.
37. Molavi, H.; Moghimi, H.; Taheri, R. A., Zr-Based MOFs with High Drug Loading for Adsorption Removal of Anti-Cancer Drugs: A Potential Drug Storage. *Appl Organomet Chem* **2020,** *34* (4), 5549.
38. Aghajanzadeh, M.; Zamani, M.; Molavi, H.; Khieri Manjili, H.; Danafar, H.; Shojaei, A., Preparation of Metal–Organic Frameworks UiO-66 for Adsorptive Removal of Methotrexate from Aqueous Solution. *J Inorg Organomet Polym Mater* **2017,** *28* (1), 177-186.

General Conclusion and Perspectives

To meet the requirements of precise and personalized medicine, multifunctional nanocarriers that enable multimodality imaging, stimuli-responsive drug release, and image-guided targeted synergistic therapies are urged to develop. Metal-organic frameworks (MOFs), a sub-class of crystalline porous hybrid materials, have during the past decades demonstrated strong promises in biomedicine. Based on their large pore sizes and volumes, biodegradable character and low toxicity, iron(III) carboxylate MOFs are of a particular interest in drug delivery. Currently, if MOFs have been mainly investigated to treat cancer, they have not yet been intensively considered for inflammatory disease therapy. Recently several strategies have been proposed to combine MOFs with nano-objects bearing stimuli responsive features, to develop new generations of multimodal MOF based nanocarriers. As for practical applications, facile and universal "green synthesis" of nanocarriers is also highly desired. Herein, the main goals in this thesis are:

1) Developing biocompatible hierarchical MOFs, combining magnetic or optically active nano-objects, *via* an *in situ* room temperature strategy
2) Exploiting their drug delivery capacities
3) Evaluating the prepared theranostic MOFs for the treatment of cancer and inflammatory diseases.

Following an introduction (**Chapter 1**) to "nanoparticles for anti-inflammation" and "functional MOFs for theranostics", in **Chapter 2**, we have prepared new hierarchical nanocarriers USPIO@MIL NPs that consist of (i) maghemite nanoparticles (USPIO) as a magnetic resonance imaging (MRI) contrast agent suitable for diagnosis and (ii) iron carboxylate nanoMOFs (MIL-100(Fe)) due to their mesoporous and biodegradable properties. These smart theranostic MOFs nanovectors were synthesized through a one-pot, cost-effective and environmentally friendly protocol. The synergistic coupling of the physico-chemical and functional properties of both nanoparticles conferred to these nano-objects valuable features such as high colloidal stability, biodegradability, low toxicity, high drug loading capacity as well as stimuli-responsive drug release. Herein, the rate of USPIO in USPIO@MIL was tunable and the loading capacity of USPIO could be as high as 20 wt%. In contrast, the maximum value of USPIO in previous MIL/USPIO by surface decoration strategy was only 10 wt%. These USPIO nanoparticles were embedded inside the heterostructure or located on the surface through the *in situ* room temperature synthesis. The TEM size of USPIO(20)@MIL was ~50 nm, and it possessed a hydrodynamic diameter of < 200 nm in various of physiological media, thereby leading to a better colloidal stability. Based on RAW 264.7 macrophage cells, the biodegradability of USPIO(20)@MIL was investigated for more than one week by Bio-TEM, and USPIO@MIL could be efficiently

internalized into endosomes after 4 hours' co-incubation. The *in vitro* degradation process of these nano-objects involved two stages, a fast degradation of their MIL-100(Fe) moieties within 24 h and gradual degradation of maghemite nanoparticles in the following one week. USPIO@MIL showed a drug loading capacity of methotrexate (MTX) and doxorubicin (DOX) of ~50 wt%, and a similar GSH-responsive sustained drug release (~20% release in 24 h) was observed in acidic phosphate-buffered saline (PBS). Interestingly, MTX and DOX loaded USPIO@MIL exhibited a burst and negligible drug release in neutral PBS, respectively within initial 24 h. Moreover, they showed promising *in vivo* MRI properties and valuable *in vitro* anti-inflammation and anti-tumor effects. In terms of *in vitro* anti-inflammation, DOX loaded USPIO(20)@MIL showed specific inhibition effects on inflammatory RAW 264.7 macrophage cells and downregulates the expression of pro-inflammatory cytokines. Also, DOX loaded USPIO(20)@MIL could kill Hela cells efficiently, even better than equivalent free DOX. The r_2 value of USPIO(20)@MIL was ~93 mM^{-1} s^{-1}, ~30 times higher than that of MIL-100(Fe) and a significant decrease of MRI signal was observed in the mouse liver and spleen after injection of USPIO(20)@MIL.

In **Chapter 3**, similarly, we have synthesized theranostic Au@MIL MOFs by assembling atomically precise fluorescent and biodegradable gold nanoclusters ($Au_{25}SG_{18}$ NCs) with the MIL-100(Fe). The TEM size of Au@MIL MOFs was ~45 nm and their colloidal stability was also similar with that of USPIO(20)@MIL in **Chapter 2**. These nanocarriers showed high drug loading (~40 wt%) and stimuli-responsive drug release of the glucocorticoid dexamethasone phosphate (DexP). Hyaluronic acid-polydopamine (HA-PDA) coating has been studied for the functionalization of Au@MIL, which could slow down the release of DexP and target inflammatory macrophage cells. The co-delivery of chemodrugs and inorganic nanoclusters by nanoMOFs led to an efficient anti-inflammation by scavenging reactive oxygen species (ROS), downregulating pro-inflammatory cytokines secretion and inhibiting inflammatory cells growth, etc. The in-depth anti-inflammatory mechanism of DexP loaded Au@MIL was further investigated on THP1-dual cells, and the nuclear factor kappa B (NF-κB) pathway and the interferon regulatory factor (IRF) pathway were blocked in the process. Although $Au_{25}SG_{18}$ NCs were good NIR-II fluorescence agents, the fluorescence of $Au_{25}SG_{18}$ NCs@MIL-100(Fe) NPs were quenched. In **Chapter 4**, based on cysteine capped Au_{25} NCs ($Au_{25}Cys_{18}$ NCs) with good NIR-II imaging properties under laser irradiation, we further developed series of hierarchical diamagnetic Zn or Zr based nanoMOFs (*i.e.*, ZIF-8 and UiO-66) *via* an *in situ* room temperature synthesis and their perspectives are discussed as below.

Overall, the main 'synthesis and *in vitro*' goals of this thesis have been achieved, and whilst *in vivo* anti-inflammatory or anti-tumoral applications need to be carried out in the future to fully demonstrate

the therapeutic efficiency of these nanovectors. This work will hopefully facilitate the green synthesis of hierarchical theranostic nanoMOFs and the future development of NIR-II window fluorescence imaging, anti-inflammatory or even anti-bacterial applications.

Perspectives:

Theranostic MOFs have been increasingly attracting attention for cancer therapy. Through an *in situ* room temperature synthesis, series of hierarchical theranostic nanoMOFs are obtained and some of them have been investigated for *in vitro* anti-inflammation or anti-tumor in our work. However, there are still many points that need to be addressed in a near future.

1) In **Chapter 2**, we have developed MTX loaded USPIO@MIL NPs. A burst release of methotrexate (MTX) in neutral PBS and a sustained release in acidic PBS were observed, respectively. Based on lipopolysaccharide (LPS) activated RAW 264.7 cells, we have however achieved a high anti-inflammatory activity. In a view of *in vivo* anti-inflammation application, oral administration is thus proposed for the treatment of **gastritis** and **inflammatory bowel disease** considering their acid environment. In terms of **rheumatoid arthritis**, an intra-articular administration might be suitable for sustained release.

2) As for DOX loaded USPIO@MIL NPs, the release of Dox is very slow even triggered by 10 mM glutathione (GSH) at acidic pH due to the strong coordination bond between DOX and open Fe site of MIL-100(Fe). For better therapeutic efficiency, a combined chemotherapy and **photothermal therapy** is thus proposed. Photothermal agents such as organic dyes or plasmonic nanoparticles could be easily co-encapsulated into heterostructures to realize photothermal therapy that would trigger the drug release. Additionally, in terms of intravenous injection, further surface modification might improve the colloidal and/or chemical stability (and prevent from a strong burst release) while conferring the required targeting ability.

3) In **Chapter 3**, encouraged by the promising *in vitro* anti-inflammatory and anti-oxidative effects of $Au_{25}SG_{18}$@MIL-100(Fe), *in vivo* synergistic anti-inflammation could be further studied in the future. Notably, the **chemical stability** of MIL-100(Fe) in neutral PBS is however a concern. In our study, HA-PDA coating did not change the ligand trimesic acid (BTC) release rate compared with uncoated $Au_{25}SG_{18}$@MIL-100(Fe). Different coating strategies employing covalent phosphate binding biopolymers might circumvent this issue. Alternatively, following the strategy of delivering anti-inflammatory drugs together with superoxide dismutase (SOD) and catalase (CAT) enzyme-like metallic nanoparticles or nanoclusters, MIL-100(Fe) might also be replaced by other biocompatible

and more stable MOFs such as Fe/Tannic acid (TA) MOF and PCN222 MOF, with a particular attention on the *in vivo* toxicity.

4) In **Chapter 4**, as already known, $Au_{25}Cys_{18}$ NCs are promising **NIR-II imaging** agents, and $Au_{25}Cys_{18}$@ZIF-8 and $Au_{25}Cys_{18}$@UiO-66 are of interest for NIR-II imaging guided chemotherapy. Also, *In situ* room temperature synthesis of MOFs based nano-objects is a versatile and universal strategy and novel hierarchical MOFs might be beneficial for not only biomedical applications but also catalysis, etc.

Annex-1

CHAPTER 18

Functional MOFs as theranostics

Heng Zhao[a], Christian Serre[a], Eddy Dumas[b], Nathalie Steunou[b]

[a]Institut des Matériaux Poreux de Paris, FRE 2000 CNRS, Ecole Normale Supérieure, Ecole Supérieure de Physique et de Chimie Industrielles de Paris, PSL Research University, Paris, France [b]Lavoisier Institute of Versailles, UMR CNRS 8180, UVSQ Paris-Saclay University, Versailles, France

Abbreviations

3-MA	3-methyladenine
4,4′-DTBA	4,4′-dithiobisbenzoic acid
5-FAM	5-carboxyfluorescein
5-FU	5-fluorouracil
AS	artesunate
BBDC	5-boronobenzene-1,3-dicarboxylic acid
BSA	bovine serum albumin
CO	carbon monoxide
Cy	cyanine
DOX	doxorubicin hydrochloride
DDS	drug delivery systems
DHA	dihydroartemisinin
EPR	enhanced permeability and retention
ESCP	ethoxysuccinato-cisplatin
EV	extracellular vesicle
FA	folic acid
GSH	glutathione
HA	hyaluronic acid
ICG	indocyanine green
LA	lactobionic acid
LSS	liquid-solid-solution
MDR	multidrug resistance
MDT	microwave dynamic therapy
MIL	materials of institut lavoisier
MOF	metal-organic frameworks
MRI	magnetic resonance imaging
MTT	microwave thermal therapy
NCPs	nanoscale coordination polymers
NCs	nanocubes
NIR	near-infrared
NIRF	near-infrared fluorescent
nMOF	nanoMOF
NPs	nanoparticles

Metal-Organic Frameworks for Biomedical Applications. https://doi.org/10.1016/B978-0-12-816984-1.00020-2

NSF nephrogenic systemic fibrosis
PAI photoacoustic imaging
PB Prussian blue
PDA polydopamine
PDT photodynamic therapy
PEG polyethylene glycol
PET positron emission tomography
PPy polypyrrole
PTT photothermal therapy
QDs quantum dots
RAFT reversible addition-fragmentation chain transfer
RGD cyclic arginine-glycine-aspartic acid
ROS reactive oxygen species
SNO S-nitrosothiol
SPAAC strain-promoted [3 + 2] azide-alkyne cycloaddition
SPECT photon emission computer tomography
TCPP tetra(4-carboxyphenyl)porphine
TNBC triple-negative breast cancer
UCNPs upconverting nanoparticles
USPIO ultra-small superparamagnetic iron oxide
VER verapamil hydrochloride
ZGGO zinc gallogermanate
ZIF-8 zeolitic imidazolate framework-8
β-CD β-cyclodextrin

Common MOFs

MOF	Metal cluster/ core	Ligand	Node
MIL-100(Fe)	FeO_6	Trimesic acid (BTC)	6-connected
MIL-101(Fe)	$Fe_3(\mu_3\text{-}O)_6(\mu_3\text{-}OH)_3$	Terephthalic acid (BDC)	6-connected
MIL-101(Fe)-NH_2	$Fe_3(\mu_3\text{-}O)_6(\mu_3\text{-}OH)_3$	2-aminobenzene-1,4-dicarboxylate (BDC-NH_2)	6-connected
MIL-127	$Fe_3(\mu3\text{-}O)_6(\mu_3\text{-}OH)_3$	3,3′,5,5′-azobenzenetetracarboxylate (Tazb)	6-connected
Fe-MIL-53-NH_2	$FeO_4(OH)_2$	Terephthalic acid (BDC)	6-connected
ZIF-8(Zn)	Zn^{2+}	2-methylimidazolate (MeIM)	4-connected
Uio-66(Zr)	$[Zr_6O_4(OH)_4]$	Terephthalic acid (BDC)	6-connected

18.1 Introduction

Theranostics combines therapeutic property and diagnostic imaging to treat disease with high therapeutic effects through a precise and personalized approach together with minimal side effects. In recent years, it has become a hot topic with an increasing interest from chemists or scientists to explore novel theranostic nanoprobes [1, 2].

Biocompatible metal-organic frameworks (MOFs), highly porous crystalline porous solids, have been widely known as drug delivery systems considering their large pore sizes/volumes and ideal drug adsorption capacities. Apart from drug delivery, nanoMOFs also have been considered as imaging agent to diagnose different diseases such as cancer or as therapeutic agent used in preclinic research [3–7]. Most of the nanoMOFs reaching a preclinical in vivo evaluation are based on Fe carboxylates or Zn azolates [8–11]. Until 2010, nanoMOFs have been mainly considered for imaging or therapy, and their use for theranostics gradually attracted researchers' attention particularly since 2015 where it encountered a rapid development [12–16]. Particularly, the construction of hybrid systems associating nanoMOFs with functional organic or inorganic nanoparticles paved the way for the development of multifunctional or multimodal nanoMOF theranostic probe [3, 9, 17].

In this chapter, we mainly discuss the developments of cancer theranostics based on nanoMOFs within the past decade, which includes topical MOFs such as MIL-100(Fe), ZIF-8(Zn) and UiO-66(Zr), etc. This contains the following subchapters: magnetic nanoMOFs, noble metal nanoparticles-encapsulated nanoMOFs, polymer-assisted nanoMOFs, fluorescent nanoMOFs, phototherapeutic nanoMOFs, nuclear medical imaging nanoMOFs, and other stimuli-responsive nanoMOF. Note that a single type of nanoMOF system combines several features and applications at the same time and could match more than one classification.

18.2 MOFs NPs with multitherapy and MR/optical imaging properties

18.2.1 Magnetic-based MOFs NPs

Magnetic nanoMOFs is a class of nanomaterials combining the magnetic properties of the metal or metal-oxides nanoparticle with the drug-loading ability of the nanoMOF. These systems are able to carry and deliver specific drugs in biological systems whose release is triggered on a controlled manner under the application of a magnetic field [18, 19]. Magnetic resonance imaging (MRI) is a powerful imaging technique due to its ability to provide high spatial resolution and tissue penetration. In the present case, the magnetic nanoparticles affect the relaxivity of the protons from water. High spin paramagnetic gadolinium (Gd) or iron (Fe) oxides superparamagnetic nanoparticles are typically integrated or coupled with nanoMOFs as MRI contrast agents.

18.2.1.1 Gd-based MOF NPs

As positive contrast agents, Gd-based nanoMOFs produce a large shortening of the longitudinal relaxation time (T1) and high longitudinal relaxivity (r1). Boyes's et al. have prepared polymer-modified Gd nanoMOFs via a reversible addition-fragmentation chain transfer (RAFT) polymerization for targeted imaging and treatment of cancer [20]. However, bimodal imaging (magnetic resonance and fluorescence microscopy) and cell growth inhibition were only considered at the in vitro level.

Yin's group also developed a Gd-carboxylate nanoMOFs theranostic platform for MRI-guided pH-responsive chemotherapy in vivo based on a 5-boronobenzene-1,3-dicarboxylic acid (BBDC) as a versatile ligand, leading to an enhanced permeability and retention (EPR) effect and glucose-mediated glucose-transported protein (GLUT1) tumor targeting; this led to: (i) an improved biocompatibility, (ii) efficient active targeting of tumors, and (iii) a pH-responsive switch for leakage-free DOX delivery as three birds with one stone [21].

Via utilizing photodynamic porphyrin carboxylate as Gd MOFs ligand, Li's group developed a FA-conjugated Gd-porphyrin MOF for fluorescence imaging and MRI dual-modality imaging and photodynamic therapy using zebrafish to develop tumor model of Hepatocellular carcinoma [22]. The relaxivities of the resulting Gd-based nanoMOFs were significantly higher than typical Gd chelates and the EPR effect took advantage of their higher molecular weights. Such a multimodal imaging approach is attractive to guide cancer therapy clinically.

18.2.1.2 Fe-carboxylate MOFs NPs

Considering the potential leaching of highly toxic Gd^{3+} ions from the in vivo degradation of Gd-carboxylate-based nanoMOFs, which may lead to nephrogenic systemic fibrosis (NSF) in patients, highly porous nontoxic iron(III)-carboxylate nanoMOFs have attracted so far a great deal of attention as drug nanocarriers.

To make nanoMOFs efficient theranostic systems, it is necessary to synthesize nanoparticles of several hundred nanometers with a narrow polydispersity. Among the large number of existing Fe-carboxylate MOFs, MIL-n materials combine several features of interest: a good chemical stability, a large porosity suitable for high dug payloads, a low toxicity, and intrinsic imaging properties. Horcajada et al. have shown that MIL nanoMOFs with engineered cores and surfaces are a class of nanocarriers for the controlled delivery of series of challenging antitumoral and retroviral drugs, which also possess interesting in vivo imaging properties and opens the way for theranostics, or personalized patient treatments [23].

Lin's group also reported a strategy of delivering an imaging contrast agent organic fluorophore together with an anticancer drug ethoxysuccinato-cisplatin (ESCP) prodrug by postsynthetic grafting of the outer surface of the MIL-101(Fe) nanoMOF (MIL stands for Materials of Institut Lavoisier) [24].

To overcome the poor biodistribution of drugs with frequent dose-related side effects, Zhang's group reported a biocompatible nanoMOF-based tumor targeting Drug Delivery Systems (DDS) developed through a one-pot organic solvent-free "green" postsynthetic surface modification procedure. Authors started from the preformed MIL-101(Fe)-N_3 nanoMOF, then functionalized by a bicyclononyne functionalized β-cyclodextrin (β-CD) derivative (through strain-promoted [3 + 2] azide-alkyne cycloaddition (SPAAC)) further combined with an adamantane functionalized PEG polymer and targeting peptide cyclic arginine-glycine-aspartic

acid (RGD) through host-guest interactions [25]. Due to the covalently linked pH-responsive benzoic imine bond and the redox-responsive disulfide bond, this multifunctional DDS showed an acidic environment-enhanced tumor cell uptake and tumor intracellular GSH-triggered drug release, which inhibited tumor growth effectively with minimal side effects.

Based on MIL-100(Fe) nanoparticles and through SPAAC reaction, Liu et al. designed a novel two-steps strategy for specific in vivo imaging of bacteria based on the metabolic labeling technique for image-guided antibacterial therapy (Fig. 18.1) [26]. Herein, 3-azido-d-alanine (d-AzAla) was first labeled on MIL-100 (Fe) NPs and after intravenous injection and d-AzAla was selectively integrated into the cell walls of bacteria, which was then confirmed by fluorescence imaging from DBCO-Cy5.

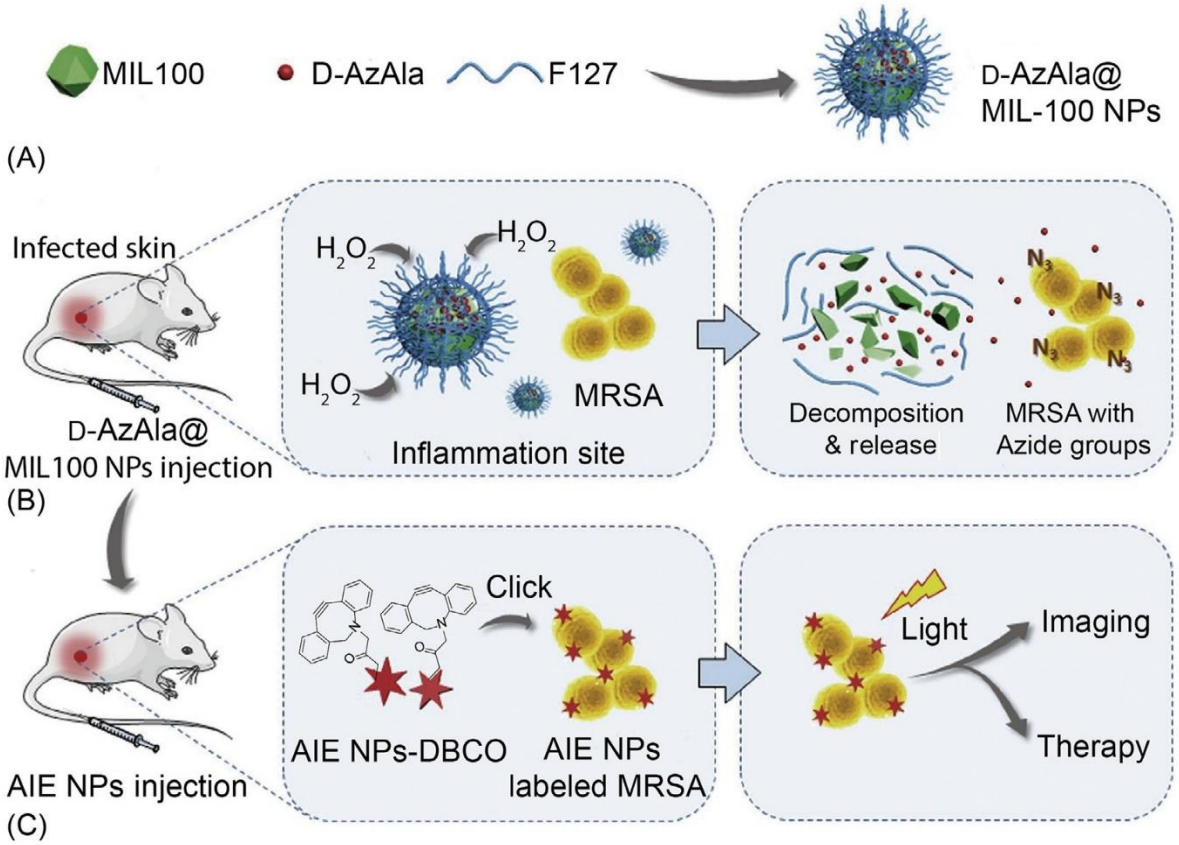

Fig. 18.1

The proposed strategy of bacteria diagnosis and therapy by the H_2O_2-responsive MOFs assisted in vivo metabolic labeling of bacteria (methicillin-resistant *Staphylococcus aureus* (MRSA)). (A) The synthesis of azido-labeled D-AzAla@MIL-100 (Fe) NPs (d-AzAla = 3-azido-D-alanine). (B) The accumulation and decomposition of D-AzAla@MIL-100 (Fe) NPs in the presence of H_2O_2 at the site of the infected tissue, followed by internalization of invading bacteria. (C) Ultra-small AIE (aggregation-induced emission) NPs with dibenzocyclooctyne (DBCO) group bind with bacteria through click reaction for tracking and effective photodynamic therapy (PDT) of bacteria [26].

In another study, Liu et al. synthesized under ambient conditions pH-responsive nanoparticles of coordination polymers (denoted Fe-CPNDs) via a simple and scalable method based on the reaction among Fe^{3+} ions, gallic acid, and poly(vinylpyrrolidone) [27]. As a class of renal clearable nanomedicine, these ultra-small nanoparticles of Fe-CPNDs (5.3 nm) were used for pH-sensitive MRI-guided photothermal therapy which completely suppressed tumor growth. In short, one can consider that based on the very low toxicity and the interesting photothermal/photodynamic properties of these nanoMOFs, solely Fe(III) carboxylate nanoMOFs could be considered as safe and efficient candidates for theranostics in nanomedicine. However, the potential challenges for clinical translation may still be limited by their current lack of commercialization.

18.2.1.3 Composite nano-objects based on Fe-carboxylate MOFs

The association of MOFs and functional nanoparticles has led to the creation of new multifunctional composites hybrid systems. However, until recently, these hybrid materials have been mainly considered for other applications such as hydrogen storage or heterogeneous catalysis [28–31]. In nanomedicine, series of hybrid nanostructures were recently constructed from nanoMOFs to form multifunctional drug delivery systems.

Chen's group developed core-shell Prussian Blue (PB) nanocube@Fe-BTC MOF for pH-responsive artemisinin delivery, MRI, and fluorescence optical imaging(FOI)-guided chemo/photothermal combinational cancer therapy [32]. Interestingly, dual nanoMOFs integrated the T1/T2 MRI, photothermal ability, and photoluminescence properties of PB. Furthermore, this strategy was applied for the construction of PB@ZIF-8 nanoparticle system, and the endogenous degradation of ZIF-8 in acid tumor microenvironment was combined with exogenous NIR stimuli to realize efficient drug delivery [33].

Ultra-small superparamagnetic magnetite (Fe_3O_4) nanoparticles have generated a widespread interest due to their potential applications in magnetic separation, magnetic hyperthermia, magnetic targeting, and MRI. Sahu's group incorporated Fe_3O_4 nanoparticles into a degradable zinc carboxylate metal-organic framework (IRMOF-3) and the cancer chemotherapy drug paclitaxel was conjugated to the magnetic NMOFs through hydrophobic interactions for targeted anticancer drug delivery and MR imaging [34]. The targeting nanoparticles killed the cancer cells effectively, but only an in vitro model was considered so far. To some extent, these folic acid-conjugated magnetic NMOFs also showed a stronger T_2-weighted MRI contrast.

Chen's group developed Fe_3O_4@C@Fe-BTC MOF nanoparticles through a layer-by-layer formation of Fe-BTC MOF at the surface of particles combining Fe_3O_4 and carbon dots. While Fe_3O_4@C imparts multimodal imaging properties (photoluminescence and MR) and magnetic targeting ability, Fe-BTC MOF was used for the co-delivery of the anticancer Dihydroartemisinin (DHA), the toxicity of which is increased in the presence of Fe(II) [35].

Through the pH-responsive degradation of Fe-BTC, MOF Fe(III) was released in the tumor followed by its reduction into ferrous ions. The interaction of Fe(II) with DHA led to the production of reactive oxygen species (ROS). A similar strategy was applied by using preformed PB nanocubes $Mn_3[Co(CN)_6]_2$. Similar core-shell Fe_3O_4@nanoMOF composites were also obtained with UiO-66 and Bio-MOF for simultaneous drug delivery and tumor visualization via MRI [36, 37].

As an ultra-small superparamagnetic iron oxide (USPIO) NP, maghemite (γ-Fe_2O_3) is of great interest. Steunou et al. designed through a postsynthetic strategy a maghemite-nanoMIL-100 (Fe) bimodal nanovector as a platform for image-guided therapy [38]; when the maghemite content was of 10 wt%, this led to relaxivity values reaching those of the commercial USPIO systems, while keeping the drug delivery properties of the bare nanoMOF paving the way for their use in theranostics.

18.2.1.4 Mn-based MOFs NPs

Manganese(II) (Mn^{2+}), although with a higher toxicity and lower daily dose compared to iron ions, has been demonstrated with its five unpaired 3d electrons to be an effective T1 contrast agent in MRI. Recently, Mn-based MOFs have, therefore, been considered for theranostics.

Lin's group reported the self-assembly of a Mn-bisphosphonate nanoscale coordination polymers (NCPs) with a lipid and PEG coating; this theranostic NCP platform was capable of delivering a chemotherapeutic drug to cancer cells and behaved as an MRI contrast agent simultaneously to cancer cells with high cargo loadings [39].

Considering the toxic adverse effects and resistance to drugs of chemotherapy, Yin's group developed theranostic Mn-porphyrin Zr(IV) carboxylate nanoMOFs; the bridging Mn-porphyrin ligand was used for a MRI-guided nitric oxide and photothermal synergistic therapy [40]. Interestingly, free-radical NO treatment was introduced to overcome the disadvantages of singlet oxygen ($^1O_2$)-based PDT due to the local hypoxia of tumor and through the formation of heat-sensitive NO donor S-Nitrosothiol (SNO). NO release and PTT were obtained simultaneously under near-infrared (NIR) light irradiation.

18.2.2 MOFs NPs for photodynamic and photothermal therapy

Phototherapeutic therapy, including photothermal therapy (PTT) and photodynamic therapy (PDT), is an highly effective, noninvasive, selective method for cancer treatment [41]. Meng's group prepared flexible Mn-doped UiO-66 nanocubes (NCs) with a small particle size ($\sim$60 nm) through a one-pot hydrothermal route. This led to a nanosystem combining microwave dynamic (MDT) and microwave thermal (MTT) therapies well suited to suppress

the tumor cell growth in vivo and in vitro under mild microwave irradiation [42], highlighting the synergic effect between MTT and MDT.

Porphyrin ligands are interesting for photodynamic therapy, but their use is limited by their poor solubility, self-quenching, and aggregation issues. Porphyrin carboxylate-based MOFs are a recent subclass of MOFs with a good biocompatibility, although they are still produced using toxic solvents, emitting bright red fluorescence for fluorescence imaging; they exhibit also photosensitizing properties suitable for photodynamic therapy. Ju's group designed multifunctional porphyrin-based MOFs NPs by assembling porphyrin, folate targeting-motif, and dye-labeled peptide into MOF cages [43]. After folate receptor-mediated uptake, the nanoprobe could efficiently generate $^1O_2$ in mitochondria to induce cell apoptosis.

Zr(IV)-based porphyrinic MOF nanoparticles PCN-224 also attracted attention for tumor-targeted photodynamic therapy and hypoxia-amplified bioreductive therapy [44, 45]. Through cancer cell membrane coating, another novel cancer cell membrane@Pt(II) porphyrinic MOF (mPPt) was also developed as a biomimetic theranostic O_2-meter for cancer-targeted photodynamic therapy and phosphorescence imaging [46]. In type II mechanism of photodynamic therapy (PDT), the ground triplet-state molecular oxygen ($^3O_2$) is transformed to the reactive singlet oxygen ($^1O_2$). However, the process is extremely dependent on oxygen (O_2), and the lack of O_2 will directly suppress the PDT efficacy. In the type I mechanism, O_2^{-}• molecule could be further converted to partially recyclable O_2 under the effects of intracellular superoxide dismutase (SOD) and part of them could be transformed to high toxic hydroxyl radical (OH•). To overcome a hypoxia microenvironment, Dong's group developed bacteriochlorin-based Hf MOFs termed DBBC-UiO as a NIR laser-induced O_2^{-}• generator for photoacoustic imaging (PAI)-guided PDT through synergistic type I (O_2-independent) and type II mechanism for hypoxia tumor ablation (Fig. 18.2) [47]. Tumor-specific PAI and highly efficient hypoxic solid tumor ablation were shown in the experiment.

18.2.3 Nano-objects based on MOFs and inorganic NPs for optical imaging, photodynamic/photothermal therapy

Noble metal nanoparticles (NPs), especially anisotropic gold NPs (AuNPs), are broadly recognized as candidates for cancer theranostics because of their good biocompatibility, high light-to-heat conversion efficiency, and unique near-infrared (NIR) light absorption feature. Note, however, that the elimination pathways of such nanoparticles are highly questionable particularly when the nanoparticles are nondegradable. In general, nanoparticles with a size of <5 nm will undergo in vivo renal elimination via the kidneys and finally through urine. In the case of nanoparticles >5 nm, the biodegradable ones can be disassembled first and then return to the metabolic circulation, while most nondegradable nanoparticles (>5 nm) will be retained in long term in liver nonparenchymal cells such as Kupffer cells, which act as barriers of hepatobiliary elimination [48].

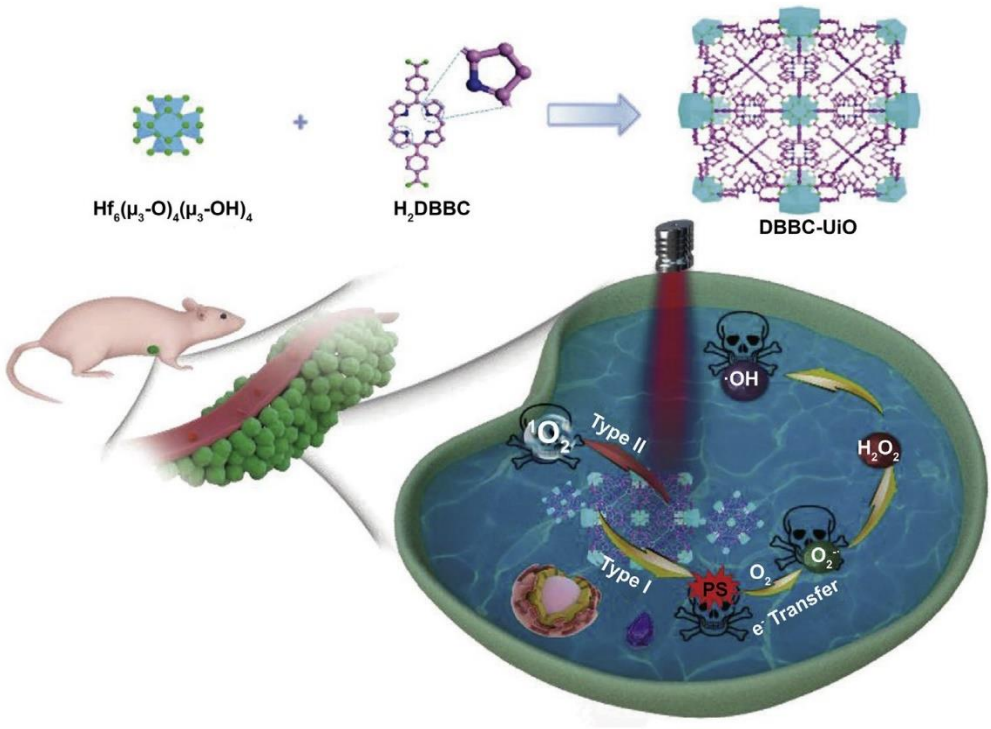

Fig. 18.2
The synthetic procedure and photo-induced PDT mechanism of DBBC-UiO.

18.2.3.1 Core-shell Au NRs@MOFs

Tang's group combined anisotropic gold nanorods (AuNR) and ZIF-8 into core-shell nanostructures AuNRs@ZIF-8 as a multifunctional nanoplatform for near-infrared-induced synergistic chemo-photothermal therapy (Fig. 18.3) [49]. Gold nanorods with high NIR-light-triggered photothermal properties are good candidates for photothermal therapy, and its drug-loading capacity was improved through the ZIF-8 shell. However, this work was mainly focused on photothermal therapy and more work needs to be done considering the questionable elimination of nondegradable Au NPs.

Through similar strategy, Li's group developed biocompatible Au@Ag nanorod@ZIF-8 core-shell nanoparticles for surface-enhanced Raman scattering (SERS) imaging and doxorubicin (DOX) delivery. For a better SERS signal, 4-aminothiophenol (4-ATP) was adsorbed on the surface of Au@Ag nanorod and the ZIF-8 shell played the role of the drug carrier and also improved the stability and biocompatibility of the SERS tag. A targeting drug therapy and imaging was shown in vitro [50].

Zhang's group used functionalized gold nanorods to construct through a solvothermal method porphyrinic nanoMOFs-coated gold nanorods (AuNR@MOFs) for combined photodynamic/photothermal/ chemotherapy of tumor. Camptothecin (CPT) was chosen as a

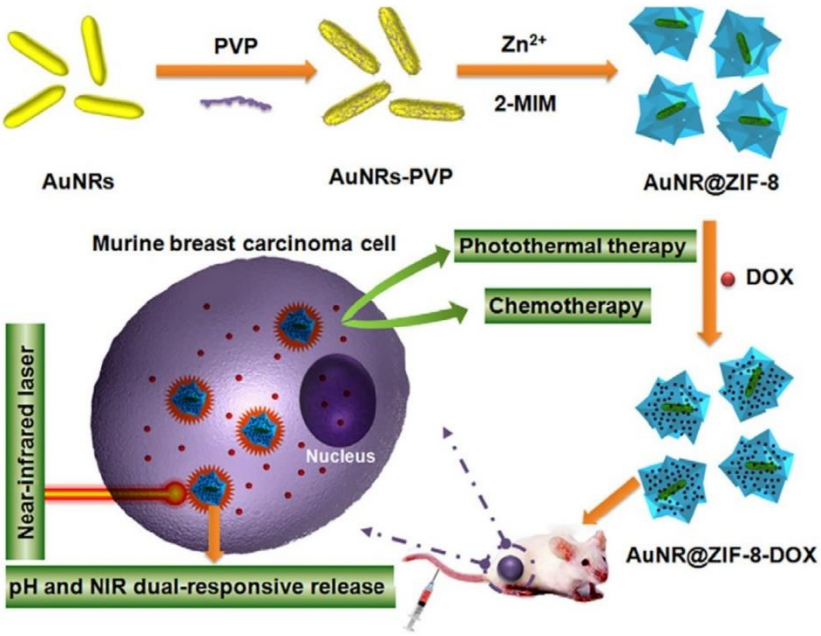

Fig. 18.3
The fabrication of AuNR@ZIF-8 core-shell nanostructures as a novel multifunctional nanoplatform for synergistic chemo-photothermal cancer therapy both in vitro and in vivo.

model drug, and through the triple synergistic therapy, the tumor cells were damaged efficiently both in vitro and in vivo [51].

Janus nanoparticles have shown also to have a great potential as theranostic platform in tumor treatment, but were mainly limited to oxides and metals. Interestingly, Han's group prepared a unique lactobionic acid (LA)-modified AuNR/ZIF-8 Janus nanoplatform via a selective growth of ZIF-8 on the polyacrylic acid (PAA) side of preformed Janus Au NR/ PAA nanoparticles. These original nano-objects were used for CT imaging-guided liver cancer therapy by the combined effect of chemotherapy and PTT [52].

18.2.3.2 Nano-objects based on MOFs and Au nanospheres/nanoclusters

The Au nanosphere with a size of tens of nanometers could not only act as photothermal agents to kill cancer cells and promote drug release, but also enhanced Raman signal. Meanwhile, considering nanoscale metal-organic frameworks (NMOFs) with high porosities and high internal surface areas as drug delivery system, Hu's group designed Raman tag-bridged core-shell Au@$Cu_3(BTC)_2$ nanoparticles for Raman imaging and synergistic chemo-photothermal therapy [53]. Theranostic applications for cell tracking and in vivo synergistic chemo-photothermal therapy of tumor were conducted, but the tumors were partially retained. Moreover, the toxicity of Cu ion and the elimination of Au nanosphere with large particle size may be a potential problem.

Gold quantum dots are very small nanoparticles (a few nm) which exhibit distinctive optical and magnetic behaviors compared with larger gold nanoparticles. Au nanoclusters (AuNCs) have been extensively applied as fluorescent probes for various biomedical applications due to their unique chemical and physical properties [54–56], especially for cell imaging or detection [57–59] and even for in vivo theranostics [60]. There is also an interest in biomedicine for hybrid Au nanoclusters, such as Au_{25} nanoclusters [61–63].

Yang's group has developed an inorganic-organic Fe_3O_4/ZIF-8-Au_{25} nanocomposite for magnetically targeted photodynamic/photothermal therapy. Briefly, upon 808 nm NIR light irradiation, the attached Au_{25} clusters can generate hyperthermia to produce a unique photothermal therapy modality, while an efficient singlet oxygen can also be produced for PDT. Furthermore, the encapsulated Fe_3O_4 nanocrystals could also serve as a PTT agent [64]. The introduction of small Au nanoclusters, when designing hybrid theranostic nanoMOFs, is quite advantageous not only due to their ability to produce ROS for photodynamic therapy, but also as a result of their easier renal clearance in comparison to larger inorganic nanoparticles.

Wang's group designed a multifunctional Fe_3O_4@PAA/AuNCs/ZIF-8 NPs nanoplatform with a 130 nm size that combines MR, CT, and fluorescence tri-modal imaging, ultrahigh anticancer drug-loading, and dual pH-responsive drug release properties (Fig. 18.4) [65]. In this work, Fe_3O_4@PAA core-shell NPs and GSH-capped AuNCs were prepared, respectively,

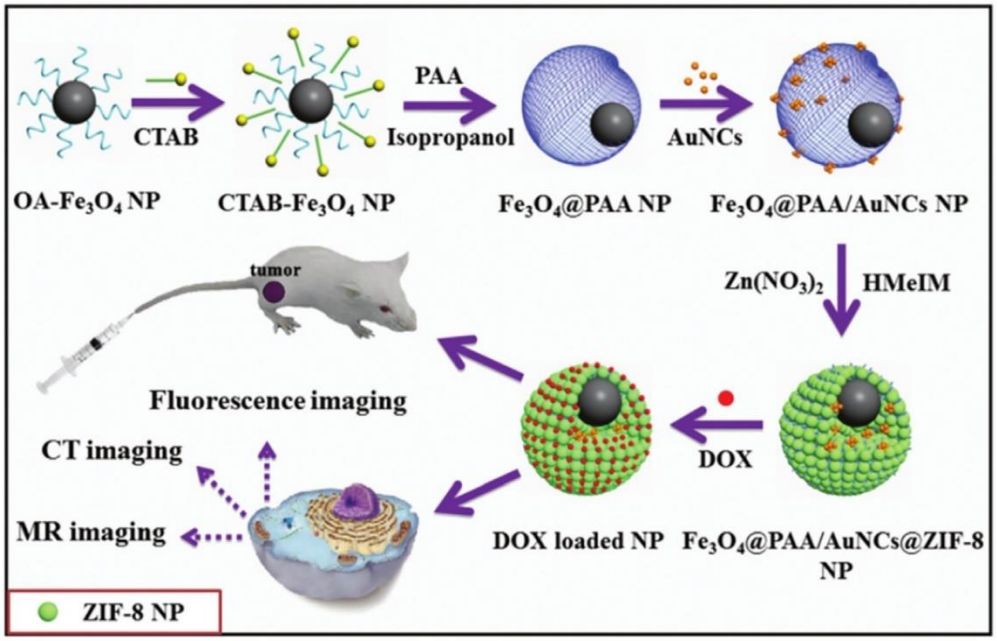

Fig. 18.4
The preparation of Fe_3O_4@PAA/AuNCs/ZIF-8 composite NPs for simultaneous tri-modal cancer imaging and chemotherapy.

and then ZIF-8 was formed at the surface of Fe_3O_4@PAA/AuNCs. Such multifunctional NPs are of interest for their multimodal cancer diagnostics and visualized-synergistic therapy.

In another approach, the attachment of BSA-modified AuNCs at the surface of MIL-101(Fe) was performed to build multifunctional theranostic nanoMOFs. MIL-101(Fe)@BSA-AuNCs presented MRI and fluorescence properties and was used as microwave-sensitive reagent for microwave thermal therapy, MRI, and fluorescence imaging (FI) [66].

18.2.3.3 Core-shell Au nanostar@ nanoMOF

To cure the triple-negative breast cancer (TNBC), one of the most dangerous subtypes among breast cancers, Zeng's group prepared core-shell gold nanostar@ MIL-101-NH_2(Fe) whose surface is covalently modified by a short peptide ZD2 able to target the TNBC. This nano-object was used for T1-weighted MRI and photothermal therapy specifically targeting TNBC (Fig. 18.5) [67]. MIL-101-NH_2(Fe) is a biocompatible and biodegradable MOF-bearing amino groups that could be further functionalized by ZD2 to achieve an active-targeted ability. MIL-101-NH_2(Fe) through its very large pores is able to upload record amounts of drugs which is of interest for further synergistic cancer therapy.

18.2.3.4 Nano-objects based on MOFs and upconversion NPs (UNCPs)

Upconversion nanoparticles (UCNPs), capable of converting near-infrared radiation to visible light, were chosen as optical probe in biological assays and medical imaging. Deng's group

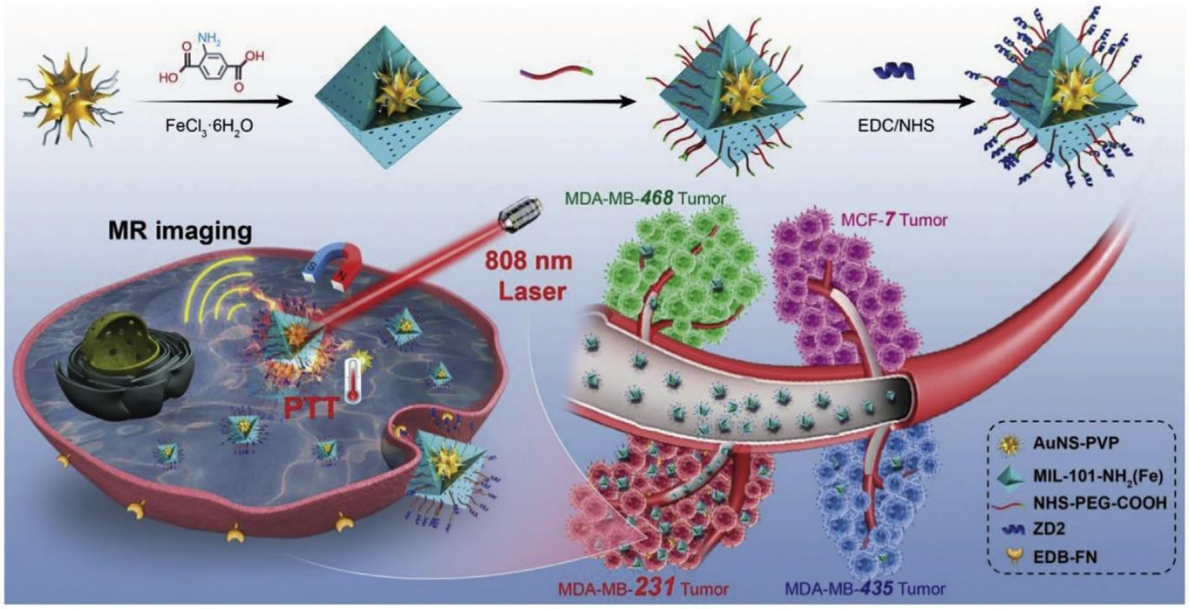

Fig. 18.5
The synthesis of AuNS@MOF-ZD2 nanoprobes and application of T1-weighted MRI and photothermal therapy specifically toward MDA-MB-231 tumor (TNBC) [67].

developed an aptamer-modified core-shell nano-objects composed of upconversion luminescent $NaYF_4:Yb^{3+}/Er^{3+}$ nanoparticles-based core and Fe-BTC MOF shell. These UCNPs@MOF nanocomposites exhibit upconverting green emission under laser excitation at 980 nm, thereby providing the possible optical imaging for in vivo bioprobes. This hybrid system showed great promises for simultaneous in vitro upconverting imaging and chemotherapy of cancer cells [68]. Apart from MIL100(Fe), ZIF-8 was also developed to encapsulate UCNPs with the modification of folic acid, which demonstrated in vitro its efficient pH-responsive drug delivery properties [69].

Cha's group used DNA-mediated assembly of core-satellite structures composed of Zr (IV)-based porphyrinic MOF (PCN-224) and UCNPs for photodynamic therapy (PDT) [70]. Herein, singlet oxygen ($^1O_2$) was generated by Zr porphyrinic MOF NPs upon photo-irradiation in NIR. By assembling UCNPs with MOFs, it was possible to take advantage of the increased penetration of NIR light. UCNP NPs were used to excite the porphyrinic ligand due to their ability to absorb in the NIR and emit visible light. A high singlet oxygen production was observed under 980 nm irradiation by using the core-satellite UCNP-PCN-224 and this amount was significantly higher than what can be produced from simply mixing UNCPs and MOF NPs.

18.2.3.5 Nano-objects based on CuS and MOF NPs

CuS NPs is one of the most common PTT agents used for the design of nanocomposites suitable for chemo-PTT. ZIF-8 was used by Luan's group to co-encapsulate the anticancer quercetin, CuS nanoparticles, in order to reach a synergy between chemotherapy and PTT [71]. Moreover, folic acid-bovine serum albumin (FA-BSA) conjugates were grafted to stabilize the CuS@ZIF-8-QT and design an active-targeting drug delivery system. As a result, in vivo and in vitro anticancer PTT/chemotherapy was demonstrated under NIR irradiation.

Yin's group developed an "all-in-one" antitumor and antirecurrence/metastasis nanocarrier by combining CuS nanoparticles, protoporphyrin IX, and Doxorubicin during the synthesis of ZIF-8 to obtain a chemo-, photothermal-, and photodynamic-nanosystem able to eliminate solid tumors under the guidance of MRI and infrared thermal imaging [72].

18.2.4 Hybrid nanoparticles by combining MOFs with organic molecules and materials

18.2.4.1 Photothermal MOFs-polymer nanocomposites

Polymers are commonly combined to MOF nanovectors not only to process and stabilize MOFs NPs, but also to enhance their blood circulation and enable specific cell targeting. In addition, polymers were also used to impart physical properties such as PTT ability. In the following, we will discuss recent examples in which polymers were used as photothermal agents.

As a type of photothermal agent, polypyrrole (PPy) has shown great potential for the photothermal treatment of cancer in vitro and in vivo. Fan's group fabricated multifunctional core-shell PPy@MIL-100(Fe) nanoparticles with PPy NPs acting as cores and the MIL-100(Fe) as the outer shell. Doxorubicin (DOX) was encapsulated in the MOF for a simultaneous photothermal therapy and chemotherapy of cancer cells. Herein, the introduction of PVP was used to facilitate the nucleation and growth of MIL-100(Fe) on the surface of PPy [73]. This resulted finally into an outstanding in vivo synergistic anticancer ability. Following a similar strategy, Wang's group further conducted Photoacoustic(PA) and MR dual-mode imaging and synergistic chemo-photothermal killing effects in vitro based on PPy@MIL-100 nanoparticles [74]. The strong NIR absorbance and T_2 relaxation signal of PPy@MIL-100(Fe) NCs were utilized for PAI and MRI and synergistic chemo-photothermal killing effects were achieved. However, these two studies were limited to in vitro theranostics.

PPy was also formed in situ in the presence of preformed MIL-53(Fe) particles which provide Fe^{3+} ions able to oxidize Py to PPy. PPy-MIL-53(Fe) nanocomposites with strong NIR absorbance can be applied for PPT to destroy cancerous cells, while anticancer drug DOX could be loaded in the composite particles. These multifunctional nanocomposites can be of interest for tumor theranostics through a combined photothermal-chemotherapy [75, 76].

Polydopamine was also combined to MOFs due to its facile synthesis, biocompatibility, and high photothermal conversion efficiency.

Zhao's group fabricated hybrid particles by coating ZIF-8 nanoparticles with polydopamine (PDA), followed by a surface modification with hyaluronic acid (HA) and Fe^{3+} for targeted drug delivery and MRI [77]. Prior to the surface modification, DOX was encapsulated in the porosity of ZIF-8. In order to realize a pH-responsive drug release system, ZIF-8 was selected considering its intrinsic pH-dependent stability. HA was used to target the prostate cancer line PC-3, while Fe^{3+} cations impart T1 MRI properties. The targeting ability of DOX@ZIF-8-HA was confirmed and the in vitro chemotherapeutic efficacy was shown, but no further in vivo study was performed.

Based on MIL-100(Fe), Zhang et al. prepared hybrid particles by coating curcumin-loaded MIL-100(Fe) NPs with PDA-modified HA and studied them for photoacoustic imaging-guided chemo-/photothermal cancer therapy (Fig. 18.6) [78]. A high photothermal conversion ability was achieved in these hybrid particles through the introduction of both curcumin and PDA-HA. The coating of HA-PDA resulted in a tumor-targeting ability as well as improved the stability of the nanoMOF in the blood, resulting in a significant antitumor effect after intravenous injection into tumor-bearing mice.

Polyaniline (PAN) exhibits strong absorption coefficients, excellent photostability, but a poor water solubility. Wang et al. synthesized nanoscale polymer-MOF UiO-66@polyaniline with

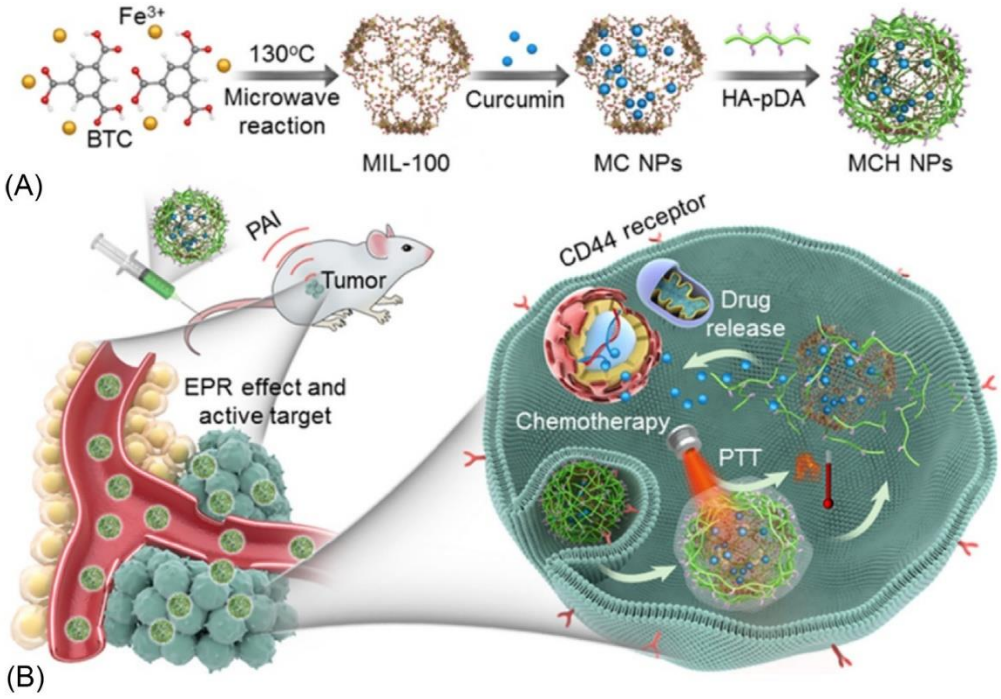

Fig. 18.6

(A) The preparation of MCH NPs through the formation of MIL-100(Fe), curcumin loading, and HA-PDA surface coating; (B) Under the guidance of PAI in vivo, efficient chemo-/photothermal combinational tumor therapy of MCH NPs was conducted via combinational-enhanced penetration and retention (EPR) and tumor-targeting effects [78].

an appropriate particle size, good water-dispersibility, strong NIR absorbance, high photostability, and photothermal conversion efficiency suitable for PTT-based cancer treatment in vitro and in vivo under guidance of photothermal imaging [79]. Due to its negatively charged surface, UiO-66 could adsorb aniline through electrostatic interaction that was further polymerized using ammonium persulfate as an oxidizing agent.

MOFs@polymer composites based on Zr dicarboxylate nanoMOFs, such as UiO-66@CyP (CyP represents cyanine polymer), were obtained for NIR fluorescence imaging-guided PTT-based cancer treatment by utilizing multicomponent passerini reaction to realize the polymerization of NIR dye cyanine (Cy) on the surface of UiO-66 nanocrystals [80]. UiO-66 nanocrystals were used as templates for the polymerization, and the resulting UiO-66@CyP exhibited high PTT performance in cancer treatment. Note that the utilization of Zr for biomedical applications is highly questionable due to the exogeneous nature of Zr as well as the very low solubility in body fluids of the biodegradation products (Zr oxides/phosphates).

18.2.4.2 C dots

Compared with toxic metal-based quantum dots (QDs), fluorescent carbon nanodots (C-dots) display strong fluorescence intensity and are harmless to the environment. This makes them appealing candidates for diagnostic analysis, bio-imaging, etc. Wang's group reported a two-step room temperature synthesis of green fluorescent C-dots incorporated into ZIF-8 as a simultaneous pH-responsive drug delivery and fluorescence imaging system [81]. These hybrid nanocomposites showed remarkable properties depending on the incorporated C-dots with versatile shapes and functions.

18.2.4.3 Graphitic carbon nitride (g-C_3N_4) nanosheets

The g-C_3N_4 nanosheets are efficient visible-light photosensitizer for PDT. Lee's group first designed an nanoscale core-shell platform based on DOX-loaded g-C_3N_4@ZIF-8 nanoparticles for photo-chemotherapy under dual-color imaging (the red fluorescence of DOX and the blue fluorescence of g-C_3N_4 nanosheets) [82]. The combination of the chemotherapeutic effects of DOX and the PDT effect of g-C_3N_4 nanosheets led to a high therapeutic efficacy.

18.2.4.4 Fluorescent dyes

Most near-infrared region (NIR) organic dyes such as Indocyanine green (ICG) are ideal imaging and photodynamic/photothermal therapy agents. However, their poor aqueous solubility, low cancer specificity, and low sensitivity in cancer theranostics have limited so far their clinic translation. To overcome these issues, Liu's group developed hyaluronic acid (HA) and ICG-engineered MIL-100(Fe) nanoparticles (MOF@HA@ICG NPs) for imaging-guided, anticancer photothermal therapy (PTT) [83].

Apart from MIL-100(Fe), NIR dyes were also combined to ZIF-8, MIL-53, or Fe(III) tetracarboxylate "socMOF" (or MIL-127), and the dye-MOF NPs inhibited tumor growth through photothermal or photodynamic therapy, while exhibited outstanding NIR or fluorescence imaging capacity both in vitro and in vivo [84–86].

Through postsynthetic surface modification process, one can also design fluorescent nanoMOFs denoted "NMOF." Damirin's group synthesized a smart multifunctional NMOF for MR/optical imaging and targeted drug delivery [87]. First, Fe-MIL-53-NH_2 was used for encapsulating the drug 5-fluorouracil (5-FU) and served as a MR contrast agent. Subsequently, the fluorescence imaging agent 5-carboxyfluorescein (5-FAM) and the targeting reagent folic acid (FA) were conjugated to the 5-FU-loaded Fe-MIL-53-NH_2. The obtained drug delivery system (DDS) showed both a good biocompatibility, tumor-enhanced cellular uptake, strong cancer cell growth inhibitory effect, excellent fluorescence imaging, and finally an outstanding MRI capability.

18.2.5 MOF NPs for nuclear medical imaging

18.2.5.1 Positron emission tomography (PET)

Compared to other imaging techniques, positron emission tomography (PET) imaging has superior detection sensitivity, deeper signal penetration, and better quantitative capacity, thus gaining more widespread use in both preclinical and clinical scenarios. Hong's group developed a biocompatible isotope zirconium-89 (^{89}Zr, $t_{1/2} = 78.4$ h)-labeled UiO-66 nanoMOF platform for PET imaging and tumor targeting DOX delivery to treat tumor-bearing mice [88]. These functionalized ^{89}Zr-UiO-66 nanoMOFs with strong radiochemical and material stability are of interest as an image-guidable, tumor-selective cargo delivery nanoplatform.

Liu's group developed a chelator-free ^{64}Cu-labeled method that can precisely tune the size of drug-loaded amorphous ZIF MOF particles at room temperature and analyze in vivo the impact between the particle size and the cancer theranostics [89] to trace MOFs through PET imaging. These 60 nm radiolabeled nanoMOFs exhibited a longer blood circulation with over than 50% higher tumor accumulation compared with larger particles of 130 nm. Although ZIF MOF is specifically promising for drug carrier, the toxicity of ZIF-8 nanoparticles cannot be ignored, which may severely limit its further clinical application. Meng's group developed biocompatible ZIF-8 nanoparticles by coating ZrO_2 onto the surface for chemo-microwave thermal tumor synergistic therapy [90]. Ionic liquid (IL) was loaded into the pore for enhanced microwave thermal therapy and ZrO_2 could also act as an excellent CT contrast agent. Meaningfully, the toxicity problem of ZIF-8 nanoparticles successfully was solved, which is helpful for further research.

Chen's group fabricated a PEGylated Zr/porphyrinic MOF-Au nanohybrid, in which AuNPs were grown in situ on the MOF NPs for O_2-Evolving Synergistic Chemoradiotherapy (Fig. 18.7) [91]. The biodistribution of the nanomedicine was investigated by PET imaging through Cu-64 radiolabeling method. Herein, AuNPs as radiosensitizers were decorated on the surface of MOF to stabilize the nanocomposite, whereas the MOF scaffold acts as a container for loading chemotherapeutic drug doxorubicin, achieving an enhanced synergistic radiochemotherapy.

18.2.5.2 Single photon emission computer tomography (SPECT)

Liu's group fabricated PEG functionalized 2D-NMOFs composed of Zn^{2+} and tetra (4-carboxyphenyl) porphyrin (TCPP) labeled with the diagnostic radioisotope ^{99m}Tc for single photon emission computer tomography (SPECT) imaging and chemo-photodynamic cancer therapy [92]. Through SPECT, efficient tumor homing of those ^{99m}Tc-labeled 2D-NMOFs was observed upon intravenous injection.

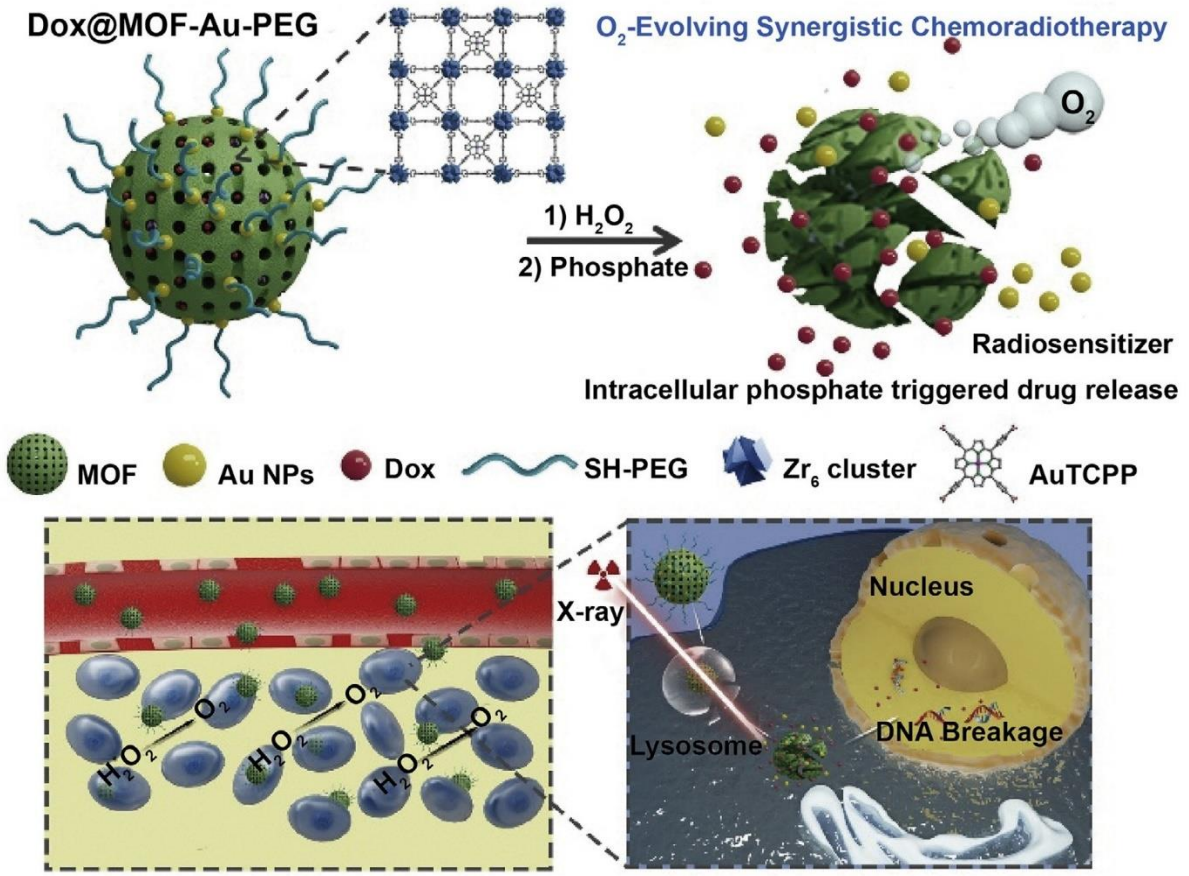

Fig. 18.7
The main components of Dox@MOF-Au-PEG and the mechanism of O_2 self-supplying synergistic chemoradiotherapy.

18.2.5.3 Computed tomography (CT)

Meanwhile, considering strong X-ray attenuating ability of the Hf element, Xie's group developed a multifunctional Hf-porphyrin NMOF platform [Hf/TCPP] with a high TPZ loading for Computed Tomography (CT) imaging that combined PDT and hypoxia-activated chemotherapy [93]. Hf/TCPP nanoparticles could efficiently produce ROS for PDT upon irradiation, while the depletion of the oxygen did further enhance the hypoxic environment of tumors to induce the activation of TPZ associated with better in vivo efficacy. Via a mixed-component strategy, photoactive chlorin was incorporated into the Hf-UiO-66 archetype structure, named TCPC-UiO, in a view of multimodal CT/thermal/photoacoustic imaging, photodynamic, and photothermal therapy (Fig. 18.8) [94]. TCPC-UiO showed an impressive anticancer activity against tumor-bearing mice in vivo, with a tumor inhibition rate above 90%.

Tumor hypoxia is a typical feature of solid tumors, which limits the applications in radiotherapy because of radiation resistance. Based on the upregulated expression of CA IX by hypoxia in

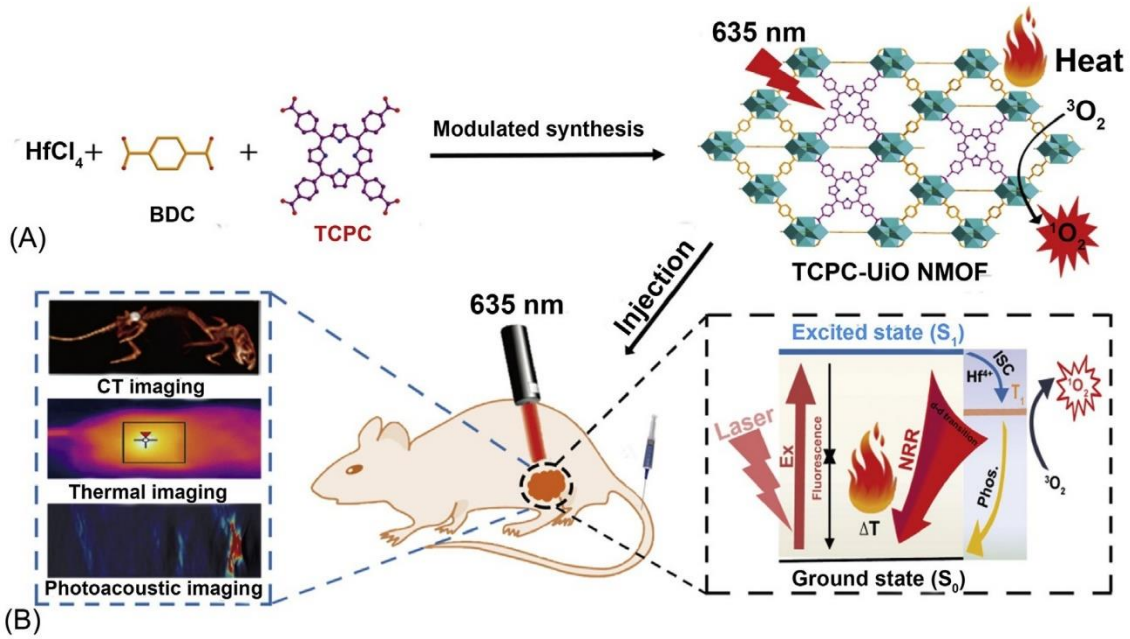

Fig. 18.8

The synthesis and mechanism for cancer therapy of TCPC-UiO by light activation. (A) Synthesis of TCPC-UiO NMOF and schematic description of heat and singlet oxygen generation under laser irradiation. (B) Photophysical mechanism for cancer therapy under light activation of a combination therapy guided by CT/thermal/photoacoustic imaging.

tumor, Meng's group developed quercetin-modified Zr MOFs for simultaneously enhancing RT therapeutic effects and CT imaging [95]. The 1,4-benzenedicarboxylic acid produced from Zr-MOF biodegradation can strongly bind to the Zn^{2+} of CA IX, which can inhibit the catalytic activity of CA IX and result in downregulating tumor hypoxia and quercetin (QU) acts as a radiosensitizer. The as-prepared Zr-MOF-QU as CA IX inhibitor exhibited improved radiation-mediated apoptosis.

Following again an "all-in-one" strategy, Dong's group developed zirconium-ferriporphyrin MOF (Zr-FeP MOF) nanoshuttles for multimodal imaging diagnosis, PDT, and low-temperature PTT synergistic treatments (Fig. 18.9) [96].

18.2.6 Other stimuli-responsive nanoMOF

New responsive MOFs nanocarriers sensitive to tumor microenvironment such as low pH and/or a high glutathione (GSH) concentration have been developed [97, 98]. Encapsulation of stimuli-responsive molecules into MOFs paves the way for constructing novel stimuli-responsive systems able to trigger drug release at tumor site. Qi's group developed an intrinsic GSH-responsive MOFs carrier, denoted as MOF-Zr(DTBA), using 4,4′-dithiobisbenzoic acid (4,4′-DTBA) able to release drugs in vivo [99]. Curcumin (CCM) was further incorporated

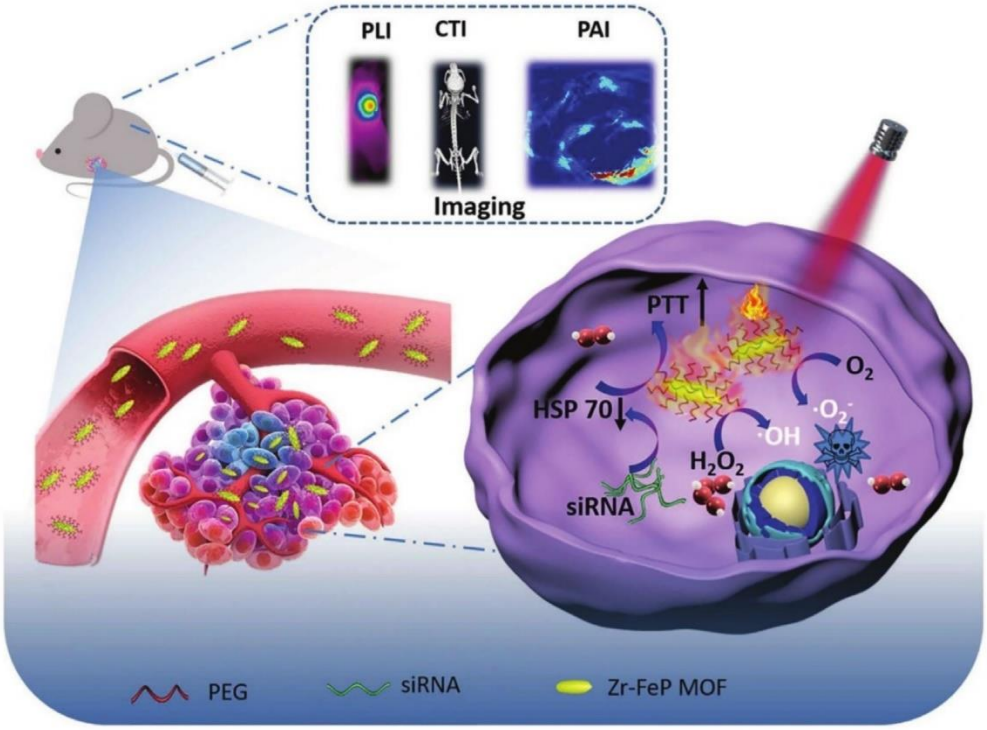

Fig. 18.9
Multimode imaging diagnosis and combination of low-temperature PTT and PDT for cancer treatment based on siRNA/Zr-FeP MOF nanoshuttles.

into MOF-Zr(DTBA) to construct CCM@MOF-Zr(DTBA). Its superior anticancer efficacy was verified through in vitro and in vivo experiments.

Fang's group-encapsulated autophagy inhibitor 3-methyladenine (3-MA) into ZIF-8 to build a pH-sensitive and tumor-targeting controlled drug delivery system denoted 3-MA@ZIF-8 NPs for antitumor application [100]. ZIF-8 framework was shown to be effective in terms of drug control release and controlling autophagy by encapsulating autophagy inhibitors. Based on ZIF-8 MOF, pH-responsive theranostic nanoMOFs have been developed for imaging, tumor suppression, and multidrug resistance (MDR), etc. [101, 102].

Oxidative stress can also affect the therapy of cancer cells, and therefore, Ning's group developed a liposomal formulation of dichloroacetic acid (DCA) and metal-organic framework (MOF)-Fe^{2+} (MD@Lip) for synergistic amplification of oxidative stress-mediated antitumor activity [103]. DCA can stimulate intracellular H_2O_2 generation and promote MOF-Fe^{2+} to convert H_2O_2 to cytotoxic •OH, inducing cancer cell apoptosis. MD@Lip showed selective accumulation in tumors and effective inhibition to tumor growth in in vivo studies.

For a better drug delivery, it is critical to pass biological barriers in vivo; biomimetic membrane camouflage of MOF strategy has been developed for the inhibition of tumor growth

considering its advantageous homotypic targeting ability, prolonged circulation, and phagocytosis prevention [104]. Li's group constructed a biomimetic cascade nanoreactor (designated as Mem@GOx@ZIF-8@BDOX) for tumor-targeted starvation therapy-amplified chemotherapy by assembling tumor cell membrane cloak and glucose oxidase (GOx) onto zeolitic imidazolate framework (ZIF-8) with the loading prodrug of hydrogen peroxide (H_2O_2)-sensitive BDOX [105]. The biomimetic cascade nanoreactor could be for fluorescent imaging, and meanwhile, remarkably improve the therapeutic efficacy through the synergistic therapy.

Considering that MOFs have emerged as promising delivery vehicles, the construction of stimuli-responsive nanoMOFs is critical for the development of cancer theranostics, and Liu's group designed a general approach for the preparation of stimuli-responsive multifunctional MOFs [106]. Different types of MOFs including ZIF-8, MIL101, and UiO-66 were synthesized first and then functionalized with polydopamine (PDA) after DOX loading, followed by the conjugation with targeting molecules for targeted drug delivery. Importantly, the stimuli-responsive multifunctional MOFs showed great potential in combined chemo-photothermal therapy.

For the purpose of precise therapy and reducing side effects, more smart targeting molecules-modified stimuli-responsive nanotheranostic probe with the ability of affording immune evasion shall be developed, and it is very meaningful to explore series of facile and general synthesis methods of stimuli-responsive nanoMOF hybrid composites based on tumor microenvironment.

18.3 Challenges

So far many new hybrid nanoMOFs systems have been constructed and have demonstrated, in most cases in vitro, a potential benefit that combines the DDS properties of the nanoMOFs and the imaging or stimuli-responsive behavior of the functional nanoparticles (organic or inorganic). However, when dealing with biomedical applications, this is necessary to consider the potential toxic effects of the system in play. In the case of such nanoMOFs hybrid systems, one should ideally demonstrate the biocompatibility, biodegradability, and lack of accumulation into the body of the nanoparticles such as done previously with the bare porous iron(III) carboxylate materials [15]. Before constructing theranostic probe, in vitro and in vivo toxicity experiments should be considered for each nanocarrier. Besides, these nanosystems shall ideally be produced following green, environmentally friendly, and energy-efficient routes using water or nontoxic organic solvents such as alcohols [107, 108]. Another very important parameter is to control the physical and chemical properties of the nanoparticles such as the particle size that should be smaller than 200 nm with an excellent control of the dispersity. This is likely that most of hybrid nanoMOFs candidates considered so far for bioapplications fail to meet these demanding criteria.

In addition, the colloidal stability of the hybrid nanoMOFs in different biological media shall strongly affect the biodistribution and pharmacokinetics in vivo [109]. If a considerable effort has been devoted to surface modification [110–113], such as conjugating targeting molecule, coating with PEG or polymer, the stability of these systems could be improved, leading to a longer blood circulation half-life, better drug delivery abilities, and therapeutic efficiencies.

18.4 Conclusion/perspectives

This paper gives a detailed description on the recent developments of hybrid nanoMOFs concerning theranostics. MOFs themselves are promising candidates for drug delivery and a large array of strategies to produce hybrid nanoMOFs combined with various active molecules or nanoparticles have been produced that bear magnetic, fluorescent, or thermal properties suitable for imaging-guided therapy. In a view of future MOFs' clinical use, one shall now focus on the development of optimal nontoxic multifunctional stimuli-responsive nanoMOFs formulations with a suitable stability in body fluids.

References

[1] S.M. Janib, A.S. Moses, J.A. MacKay, Imaging and drug delivery using theranostic nanoparticles, Adv. Drug Deliv. Rev. 62 (11) (2010) 1052–1063.
[2] J.H. Ryu, et al., Theranostic nanoparticles for future personalized medicine, J. Control. Release 190 (2014) 477–484.
[3] M.X. Wu, Y.W. Yang, Metal-organic framework (MOF)-based drug/cargo delivery and cancer therapy, Adv. Mater. 29 (23) (2017).
[4] K. Lu, et al., Nanoscale metal-organic frameworks for therapeutic, imaging, and sensing applications, Adv. Mater. 30 (37) (2018) e1707634.
[5] H.-S. Wang, Metal–organic frameworks for biosensing and bioimaging applications, Coord. Chem. Rev. 349 (2017) 139–155.
[6] P. Horcajada, et al., Metal–organic frameworks as efficient materials for drug delivery, Angew. Chem. Int. Ed. Engl. 118 (36) (2006) 6120–6124.
[7] D. Cunha, et al., Rationale of drug encapsulation and release from biocompatible porous metal–organic frameworks, Chem. Mater. 25 (14) (2013) 2767–2776.
[8] T. Simon-Yarza, et al., Nanoparticles of metal-organic frameworks: on the road to in vivo efficacy in biomedicine, Adv. Mater. 30 (37) (2018) e1707365.
[9] C. He, D. Liu, W. Lin, Nanomedicine applications of hybrid nanomaterials built from metal-ligand coordination bonds: nanoscale metal-organic frameworks and nanoscale coordination polymers, Chem. Rev. 115 (19) (2015) 11079–11108.
[10] P. Horcajada, et al., Metal-organic frameworks in biomedicine, Chem. Rev. 112 (2) (2012) 1232–1268.
[11] A.C. McKinlay, et al., BioMOFs: metal-organic frameworks for biological and medical applications, Angew. Chem. Int. Ed. Engl. 49 (36) (2010) 6260–6266.
[12] J. Della Rocca, W. Lin, Nanoscale metal-organic frameworks: magnetic resonance imaging contrast agents and beyond, Eur. J. Inorg. Chem. 2010 (24) (2010) 3725–3734.
[13] R.C. Huxford, J. Della Rocca, W. Lin, Metal-organic frameworks as potential drug carriers, Curr. Opin. Chem. Biol. 14 (2) (2010) 262–268.

[14] J. Della Rocca, D. Liu, W. Lin, Nanoscale metal-organic frameworks for biomedical imaging and drug delivery, Acc. Chem. Res. 44 (10) (2011) 957–968.
[15] W. Cai, et al., Metal-organic framework-based nanomedicine platforms for drug delivery and molecular imaging, Small 11 (37) (2015) 4806–4822.
[16] M. Giménez-Marqués, et al., Nanostructured metal–organic frameworks and their bio-related applications, Coord. Chem. Rev. 307 (2016) 342–360.
[17] S. Beg, et al., Nanoporous metal organic frameworks as hybrid polymer-metal composites for drug delivery and biomedical applications, Drug Discov. Today 22 (4) (2017) 625–637.
[18] R. Ricco, et al., Applications of magnetic metal–organic framework composites, J. Mater. Chem. A: Mater. 1 (42) (2013) 13033.
[19] P. Falcaro, et al., Application of metal and metal oxide nanoparticles@MOFs, Coord. Chem. Rev. 307 (2016) 237–254.
[20] M.D. Rowe, et al., Polymer-modified gadolinium metal-organic framework nanoparticles used as multifunctional nanomedicines for the targeted imaging and treatment of cancer, Biomacromolecules 10 (4) (2009) 983–993.
[21] H. Zhang, et al., Smart metal-organic frameworks-based nanoplatforms for imaging-guided precise chemotherapy, ACS Appl. Mater. Interfaces 11 (2019) 1886–1895.
[22] Y. Chen, et al., Folic acid-nanoscale gadolinium-porphyrin metal-organic frameworks: fluorescence and magnetic resonance dual-modality imaging and photodynamic therapy in hepatocellular carcinoma, Int. J. Nanomedicine 14 (2019) 57–74.
[23] P. Horcajada, et al., Porous metal-organic-framework nanoscale carriers as a potential platform for drug delivery and imaging, Nat. Mater. 9 (2) (2010) 172–178.
[24] K.M. Taylor-Pashow, et al., Postsynthetic modifications of iron-carboxylate nanoscale metal-organic frameworks for imaging and drug delivery, J. Am. Chem. Soc. 131 (40) (2009) 14261–14263.
[25] X.G. Wang, et al., A multifunctional metal-organic framework based tumor targeting drug delivery system for cancer therapy, Nanoscale 7 (38) (2015) 16061–16070.
[26] D. Mao, et al., Metal-organic-framework-assisted in vivo bacterial metabolic labeling and precise antibacterial therapy, Adv. Mater. 30 (18) (2018) e1706831.
[27] F. Liu, et al., Gram-scale synthesis of coordination polymer nanodots with renal clearance properties for cancer theranostic applications, Nat. Commun. 6 (2015) 8003.
[28] M. Meilikhov, et al., Metals@MOFs – loading MOFs with metal nanoparticles for hybrid functions, Eur. J. Inorg. Chem. 2010 (24) (2010) 3701–3714.
[29] J. Juan-Alcañiz, J. Gascon, F. Kapteijn, Metal–organic frameworks as scaffolds for the encapsulation of active species: state of the art and future perspectives, J. Mater. Chem. 22 (20) (2012) 10102.
[30] H.R. Moon, D.W. Lim, M.P. Suh, Fabrication of metal nanoparticles in metal-organic frameworks, Chem. Soc. Rev. 42 (4) (2013) 1807–1824.
[31] C. Rösler, R.A. Fischer, Metal–organic frameworks as hosts for nanoparticles, CrystEngComm 17 (2) (2015) 199–217.
[32] D. Wang, et al., Controllable synthesis of dual-MOFs nanostructures for pH-responsive artemisinin delivery, magnetic resonance and optical dual-model imaging-guided chemo/photothermal combinational cancer therapy, Biomaterials 100 (2016) 27–40.
[33] D. Wang, et al., Biodegradable core-shell dual-metal-organic-frameworks nanotheranostic agent for multiple imaging guided combination cancer therapy, Theranostics 7 (18) (2017) 4605–4617.
[34] A. Ray Chowdhuri, D. Bhattacharya, S.K. Sahu, Magnetic nanoscale metal organic frameworks for potential targeted anticancer drug delivery, imaging and as an MRI contrast agent, Dalton Trans. 45 (7) (2016) 2963–2973.
[35] D. Wang, et al., Magnetically guided delivery of DHA and Fe ions for enhanced cancer therapy based on pH-responsive degradation of DHA-loaded Fe_3O_4@C@MIL-100(Fe) nanoparticles, Biomaterials 107 (2016) 88–101.

[36] H.X. Zhao, et al., Theranostic metal-organic framework core-shell composites for magnetic resonance imaging and drug delivery, Chem. Sci. 7 (8) (2016) 5294–5301.
[37] V. Nejadshafiee, et al., Magnetic bio-metal-organic framework nanocomposites decorated with folic acid conjugated chitosan as a promising biocompatible targeted theranostic system for cancer treatment, Mater. Sci. Eng. C Mater. Biol. Appl. 99 (2019) 805–815.
[38] S. Sene, et al., Maghemite-nanoMIL-100(Fe) bimodal nanovector as a platform for image-guided therapy, Chem 3 (2) (2017) 303–322.
[39] D. Liu, et al., Theranostic nanoscale coordination polymers for magnetic resonance imaging and bisphosphonate delivery, J. Mater. Chem. B 2 (46) (2014) 8249–8255.
[40] H. Zhang, et al., Theranostic Mn-porphyrin metal-organic frameworks for magnetic resonance imaging-guided nitric oxide and photothermal synergistic therapy, ACS Appl. Mater. Interfaces 10 (34) (2018) 28390–28398.
[41] Q. Guan, et al., Photodynamic therapy based on nanoscale metal-organic frameworks: from material design to cancer nanotherapeutics, Chem. Asian J. 13 (21) (2018) 3122–3149.
[42] C. Fu, et al., Microwave-activated Mn-doped zirconium metal-organic framework nanocubes for highly effective combination of microwave dynamic and thermal therapies against cancer, ACS Nano 12 (3) (2018) 2201–2210.
[43] L. Zhang, et al., A porphyrin photosensitized metal-organic framework for cancer cell apoptosis and caspase responsive theranostics, Chem. Commun. (Camb) 51 (54) (2015) 10831–10834.
[44] J. Park, et al., Size-controlled synthesis of porphyrinic metal-organic framework and functionalization for targeted photodynamic therapy, J. Am. Chem. Soc. 138 (10) (2016) 3518–3525.
[45] S.Y. Li, et al., Cancer cell membrane-coated biomimetic platform for tumor targeted photodynamic therapy and hypoxia-amplified bioreductive therapy, Biomaterials 142 (2017) 149–161.
[46] L. An, et al., In situ sulfidation of Cu_2O by endogenous H2S for colon cancer theranostics, Angew. Chem. Int. Ed. Engl. (2018).
[47] K. Zhang, et al., A bacteriochlorin-based metal-organic framework nanosheet superoxide radical generator for photoacoustic imaging-guided highly efficient photodynamic therapy, Adv. Sci. (2019) 1900530.
[48] W. Poon, et al., Elimination pathways of nanoparticles, ACS Nano 13 (5) (2019) 5785–5798.
[49] Y. Li, et al., Coordination-responsive drug release inside gold nanorod@metal-organic framework core–shell nanostructures for near-infrared-induced synergistic chemo-photothermal therapy, Nano Res. 11 (6) (2018) 3294–3305.
[50] P. Jiang, Y. Hu, G. Li, Biocompatible Au@Ag nanorod@ZIF-8 core-shell nanoparticles for surface-enhanced Raman scattering imaging and drug delivery, Talanta 200 (2019) 212–217.
[51] J.-Y. Zeng, et al., Porphyrinic metal-organic frameworks coated gold nanorods as a versatile nanoplatform for combined photodynamic/photothermal/chemotherapy of tumor, Adv. Funct. Mater. 28 (8) (2018) 1705451.
[52] H. Zhang, et al., Preparation of one dimensional nanorod/metal organic framework Janus nanoplatform via side-specific growth for synergistic cancer therapy, Biomater. Sci. (2019).
[53] J. He, et al., Design of Raman tag-bridged core-shell $Au@Cu_3(BTC)_2$ nanoparticles for Raman imaging and synergistic chemo-photothermal therapy, Nanoscale 11 (13) (2019) 6089–6100.
[54] D. Li, Z. Chen, X. Mei, Fluorescence enhancement for noble metal nanoclusters, Adv. Colloid Interf. Sci. 250 (2017) 25–39.
[55] X. Jiang, et al., Ultrasmall noble metal nanoparticles: breakthroughs and biomedical implications, Nano Today 21 (2018) 106–125.
[56] N. Kaur, et al., Biomedical applications for gold nanoclusters: Recent developments and future perspectives, Nanoscale Res. Lett. 13 (1) (2018) 302.
[57] X. Bai, S. Xu, L. Wang, Full-range pH stable au-clusters in nanogel for confinement-enhanced emission and improved sulfide sensing in living cells, Anal. Chem. 90 (5) (2018) 3270–3275.
[58] Y. Li, et al., Multifunctional gold nanoclusters-based nanosurface energy transfer probe for real-time monitoring of cell apoptosis and self-evaluating of pro-apoptotic theranostics, Anal. Chem. 88 (22) (2016) 11184–11192.

[59] X. Wang, et al., Preparation of novel fluorescent nanocomposites based on au nanoclusters and their application in targeted detection of cancer cells, ACS Appl. Mater. Interfaces 9 (51) (2017) 44856–44863.
[60] C. Zhang, et al., Gold nanoclusters-based nanoprobes for simultaneous fluorescence imaging and targeted photodynamic therapy with superior penetration and retention behavior in tumors, Adv. Funct. Mater. 25 (8) (2015) 1314–1325.
[61] S.K. Katla, et al., Atomically precise $Au_{25}(SG)_{18}$ nanoclusters: rapid single-step synthesis and application in photothermal therapy, ACS Appl. Mater. Interfaces 10 (1) (2018) 75–82.
[62] S. Miyata, et al., Antimicrobial photodynamic activity and cytocompatibility of $Au_{25}(Capt)_{18}$ clusters photoexcited by blue LED light irradiation, Int. J. Nanomedicine 12 (2017) 2703–2716.
[63] X.D. Zhang, et al., Enhanced tumor accumulation of sub-2 nm gold nanoclusters for cancer radiation therapy, Adv. Healthc. Mater. 3 (1) (2014) 133–141.
[64] D. Yang, et al., Au_{25} cluster functionalized metal-organic nanostructures for magnetically targeted photodynamic/photothermal therapy triggered by single wavelength 808 nm near-infrared light, Nanoscale 7 (46) (2015) 19568–19578.
[65] R. Bian, et al., A combination of tri-modal cancer imaging and in vivo drug delivery by metal-organic framework based composite nanoparticles, Biomater. Sci. 3 (9) (2015) 1270–1278.
[66] X. Ma, et al., Multifunctional iron-based metal-organic framework as biodegradable nanozyme for microwave enhancing dynamic therapy, Biomaterials 214 (2019) 119223.
[67] L. Zhang, et al., ZD2-engineered gold nanostar@metal-organic framework nanoprobes for T1-weighted magnetic resonance imaging and photothermal therapy specifically toward triple-negative breast cancer, Adv Healthc Mater 7 (24) (2018) e1801144.
[68] K. Deng, et al., Aptamer-mediated up-conversion core/MOF shell nanocomposites for targeted drug delivery and cell imaging, Sci. Rep. 5 (2015) 7851.
[69] A.R. Chowdhuri, et al., One-pot synthesis of folic acid encapsulated upconversion nanoscale metal organic frameworks for targeting, imaging and pH responsive drug release, Dalton Trans. 45 (45) (2016) 18120–18132.
[70] L. He, et al., DNA-assembled core-satellite upconverting-metal-organic framework nanoparticle superstructures for efficient photodynamic therapy, Small 13 (24) (2017).
[71] W. Jiang, et al., CuS@MOF-based well-designed quercetin delivery system for chemo-photothermal therapy, ACS Appl. Mater. Interfaces 10 (40) (2018) 34513–34523.
[72] J.C. Yang, et al., An "all-in-one" antitumor and anti-recurrence/metastasis nanomedicine with multi-drug co-loading and burst drug release for multi-modality therapy, Chem. Sci. 9 (36) (2018) 7210–7217.
[73] Y.D. Zhu, et al., PPy@MIL-100 nanoparticles as a pH- and near-IR-irradiation-responsive drug carrier for simultaneous photothermal therapy and chemotherapy of cancer cells, ACS Appl. Mater. Interfaces 8 (50) (2016) 34209–34217.
[74] X. Chen, et al., Facile synthesis of polypyrrole@metal–organic framework core–shell nanocomposites for dual-mode imaging and synergistic chemo-photothermal therapy of cancer cells, J. Mater. Chem. B 5 (9) (2017) 1772–1778.
[75] J. Huang, et al., Metal-organic framework as a microreactor for in situ fabrication of multifunctional nanocomposites for photothermal-chemotherapy of tumors in vivo, ACS Appl. Mater. Interfaces 10 (45) (2018) 38729–38738.
[76] X. Cai, et al., Controllable synthesis of highly monodispersed nanoscale Fe-soc-MOF and the construction of Fe-soc-MOF@polypyrrole core-shell nanohybrids for cancer therapy, Chem. Eng. J. 358 (2019) 369–378.
[77] F. Shu, et al., Fabrication of a hyaluronic acid conjugated metal organic framework for targeted drug delivery and magnetic resonance imaging, RSC Adv. 8 (12) (2018) 6581–6589.
[78] Y. Zhang, et al., Engineering metal-organic frameworks for photoacoustic imaging-guided chemo-/photothermal combinational tumor therapy, ACS Appl. Mater. Interfaces (2018).
[79] W. Wang, et al., Nanoscale polymer metal-organic framework hybrids for effective photothermal therapy of Colon cancers, Adv. Mater. 28 (42) (2016) 9320–9325.

[80] L. Yan, et al., Size controllable and surface tunable zeolitic imidazolate framework-8-poly(acrylic acid sodium salt) nanocomposites for pH responsive drug release and enhanced in vivo cancer treatment, ACS Appl. Mater. Interfaces 9 (38) (2017) 32990–33000.
[81] L. He, et al., Carbon nanodots@zeolitic imidazolate framework-8 nanoparticles for simultaneous pH-responsive drug delivery and fluorescence imaging, CrystEngComm 16 (16) (2014) 3259.
[82] R. Chen, et al., Graphitic carbon nitride nanosheet@metal-organic framework core-shell nanoparticles for photo-chemo combination therapy, Nanoscale 7 (41) (2015) 17299–17305.
[83] W. Cai, et al., Engineering phototheranostic nanoscale metal-organic frameworks for multimodal imaging-guided cancer therapy, ACS Appl. Mater. Interfaces 9 (3) (2017) 2040–2051.
[84] Y. Li, et al., Facile synthesis of a metal-organic framework nanocarrier for NIR imaging-guided photothermal therapy, Biomater. Sci. 6 (11) (2018) 2918–2924.
[85] P. Yang, et al., Metal-organic framework nanoparticles with near-infrared dye for multimodal imaging and guided phototherapy, ACS Appl. Mater. Interfaces 11 (12) (2019) 11209–11219.
[86] X. Cai, et al., Interfacially synthesized Fe-soc-MOF nanoparticles combined with ICG for photothermal/photodynamic therapy, Dalton Trans. 47 (45) (2018) 16329–16336.
[87] X. Gao, et al., Controllable synthesis of a smart multifunctional nanoscale metal-organic framework for magnetic resonance/optical imaging and targeted drug delivery, ACS Appl. Mater. Interfaces 9 (4) (2017) 3455–3462.
[88] D. Chen, et al., In vivo targeting and positron emission tomography imaging of tumor with intrinsically radioactive metal-organic frameworks nanomaterials, ACS Nano 11 (4) (2017) 4315–4327.
[89] D. Duan, et al., Size-controlled synthesis of drug-loaded zeolitic imidazolate framework in aqueous solution and size effect on their cancer theranostics in vivo, ACS Appl. Mater. Interfaces (2018).
[90] L. Su, et al., High biocompatible ZIF-8 coated by ZrO_2 for chemo-microwave thermal tumor synergistic therapy, ACS Appl. Mater. Interfaces 11 (11) (2019) 10520–10531.
[91] Z. He, et al., A catalase-like metal-organic framework nanohybrid for O_2-evolving synergistic chemoradiotherapy, Angew. Chem. Int. Ed. Engl. 58 (26) (2019) 8752–8756.
[92] W. Zhu, et al., Two-dimensional metal-organic-framework as a unique theranostic nano-platform for nuclear imaging and chemo-photodynamic cancer therapy, Nano Res. (2018).
[93] M. Liu, et al., Hypoxia-triggered nanoscale metal-organic frameworks for enhanced anticancer activity, ACS Appl. Mater. Interfaces 10 (29) (2018) 24638–24647.
[94] X. Zheng, et al., Nanoscale mixed-component metal–organic frameworks with photosensitizer spatial-arrangement-dependent photochemistry for multimodal-imaging-guided photothermal therapy, Chem. Mater. 30 (19) (2018) 6867–6876.
[95] T. Ma, et al., Quercetin-modified metal-organic frameworks for dual sensitization of radiotherapy in tumor tissues by inhibiting the carbonic anhydrase IX, ACS Nano 13 (4) (2019) 4209–4219.
[96] K. Zhang, et al., Metal-organic framework nanoshuttle for synergistic photodynamic and low-temperature photothermal therapy, Adv. Funct. Mater. 28 (42) (2018) 1804634.
[97] S.Z. Ren, et al., Nanoscale metal-organic-frameworks coated by biodegradable organosilica for pH and redox dual responsive drug release and high-performance anticancer therapy, ACS Appl. Mater. Interfaces (2019).
[98] J. Zhao, et al., Redox-sensitive nanoscale coordination polymers for drug delivery and cancer theranostics, ACS Appl. Mater. Interfaces 9 (28) (2017) 23555–23563.
[99] B. Lei, et al., Constructing redox-responsive metal-organic framework nanocarriers for anticancer drug delivery, ACS Appl. Mater. Interfaces 10 (19) (2018) 16698–16706.
[100] W. Cai, et al., Gold nanorods@metal-organic framework core-shell nanostructure as contrast agent for photoacoustic imaging and its biocompatibility, J. Alloys Compd. 748 (2018) 193–198.
[101] Y. Lv, et al., Chromium-doped zinc gallogermanate@zeolitic imidazolate framework-8: a multifunctional NAnoplatform for rechargeable in vivo persistent luminescence imaging and pH-responsive drug release, ACS Appl. Mater. Interfaces (2018).

[102] H. Zhang, et al., Rational design of metal organic framework nanocarrier-based codelivery system of doxorubicin hydrochloride/verapamil hydrochloride for overcoming multidrug resistance with efficient targeted cancer therapy, ACS Appl. Mater. Interfaces 9 (23) (2017) 19687–19697.
[103] L. Sun, et al., Synergistic amplification of oxidative stress-mediated antitumor activity via liposomal dichloroacetic acid and MOF-Fe^{2+}, Small 15 (2019) e1901156.
[104] G. Cheng, et al., Self-assembly of extracellular vesicle-like metal-organic framework nanoparticles for protection and intracellular delivery of biofunctional proteins, J. Am. Chem. Soc. 140 (23) (2018) 7282–7291.
[105] H. Cheng, et al., A biomimetic cascade nanoreactor for tumor targeted starvation therapy-amplified chemotherapy, Biomaterials 195 (2019) 75–85.
[106] J. Feng, et al., Stimuli-responsive multifunctional metal–organic framework nanoparticles for enhanced chemo-photothermal therapy, J. Mater. Chem. B 7 (6) (2019) 994–1004.
[107] A. García Márquez, et al., Green microwave synthesis of MIL-100(Al, Cr, Fe) nanoparticles for thin-film elaboration, Eur. J. Inorg. Chem. 2012 (32) (2012) 5165–5174.
[108] V. Agostoni, et al., A "green" strategy to construct non-covalent, stable and bioactive coatings on porous MOF nanoparticles, Sci. Rep. 5 (2015) 7925.
[109] E. Bellido, et al., Understanding the colloidal stability of the mesoporous MIL-100(Fe) nanoparticles in physiological media, Langmuir 30 (20) (2014) 5911–5920.
[110] E. Bellido, et al., Heparin-engineered mesoporous iron metal-organic framework nanoparticles: toward stealth drug nanocarriers, Adv. Healthc. Mater. 4 (8) (2015) 1246–1257.
[111] A.G. Márquez, et al., Biocompatible polymer–metal–organic framework composite patches for cutaneous administration of cosmetic molecules, J. Mater. Chem. B 4 (43) (2016) 7031–7040.
[112] A. Zimpel, et al., Imparting functionality to MOF nanoparticles by external surface selective covalent attachment of polymers, Chem. Mater. 28 (10) (2016) 3318–3326.
[113] M. Gimenez-Marques, et al., GraftFast surface engineering to improve MOF nanoparticles furtiveness, Small 14 (40) (2018) e1801900.

Annex-2

Biomaterials Science

ROYAL SOCIETY OF CHEMISTRY

COMMUNICATION

View Article Online
View Journal | View Issue

Cite this: *Biomater. Sci.*, 2021, **9**, 5477

Received 29th April 2021,
Accepted 25th June 2021

DOI: 10.1039/d1bm00669j

rsc.li/biomaterials-science

When drug nanocarriers miss their target: extracellular diffusion and cell uptake are not enough to be effective†

Vincent Pautu, [a] Heng Zhao, [b] Angelika Mielcarek, [b] Anna Balasso, [a] Patrick Couvreur, [a] Christian Serre *[b] and Simona Mura *[a]

Biocompatible nanoscale iron carboxylate metal–organic frameworks (nanoMOFs) have already demonstrated their ability to efficiently deliver various therapeutic molecules. The versatility of the synthesis methods and functionalization strategies could further improve their drug carrier potential. However, in oncology, preclinical evaluation still suffers from the lack of relevant models able to mimic the heterogeneity and the microenvironment of human tumors. This may impact the significance of the preclinical data, hindering the clinical translation and drug development process. Motivated by this hurdle, a 3D lung tumor model is herein developed to investigate nanoMOFs, as bare nanoparticles or coated with polyethylene glycol. Loading with doxorubicin, as a model drug, enables the investigation of their penetration capacity and efficacy in the 3D tumor nodule. NanoMOFs carry a large cargo, can diffuse efficiently within the tumor and are capable of significant intracellular penetration. Nevertheless, they prove to be therapeutically ineffective because the loaded drug is sequestrated in the lysosomal compartment and does not reach the nucleus, the doxorubicin sub-cellular target. These results question the *in vivo* evaluation of these nanoMOFs and call for further optimization to achieve successful drug delivery.

Over the past 50 years, great effort has been devoted toward the development of nanoscale drug delivery systems (*i.e.*, nanomedicines) since they offer the promise of surmounting the limitations of conventional treatments.[1] Some nanomedicines have shown their ability to protect the loaded drug from rapid degradation and/or elimination as well as to avoid some non-specific distribution in the whole body. The latter forces the administration of high doses of drugs to enable at least a small amount to reach the target tissue, cell or sub-cellular compartment and this is frequently associated with the insurgence of undesired side effects.

Among the severe diseases, due to the overall poor prognosis, much work has been done in the field of cancer therapy.[2] Lipid- and polymer-based nanocarriers (*e.g.*, liposomes, nanoparticles, micelles, dendrimers) constitute the majority of the drug delivery systems designed so far.[3–5] Some of them are currently in advanced clinical trials, whereas others have already reached the marketplace, confirming the potential of nanomedicines for the efficient delivery of chemotherapeutics.[6] In addition, a variety of hybrid inorganic–organic ordered porous solids (metal–organic frameworks, MOFs) have also been proposed as nanocarriers due to their large internal pore volume and tunable environment suitable to host large quantities of challenging drugs.[7] Among them, nanoscale iron(III) carboxylate MOFs (nanoMOFs) have gained considerable interest for biomedical applications due to their proven biodegradability and safety profile.[8] One of the most interesting nanoMOF candidates is MIL-100(Fe)[9] (*i.e.*, MIL stands for Material of the Institute Lavoisier), made of trimers of iron(III) octahedra and trimesic acid linkers, which exhibit mesoporous cages of 25 and 29 Å accessible through 5.5 and 8.6 Å microporous windows. Prepared under green conditions with particle sizes of around 100 nm, these nanoMOFs can ensure very high loading and efficient delivery of a large diversity of anticancer drugs.[10,11] To prevent stability issues and improve nanoMOF stealth properties, several surface modifications have been reported to date, either through covalent or non-covalent routes.[12–15]

A relevant and predictive *in vitro* assessment of tumor exposure to the therapeutic agents requires the use of biomimetic models.[16,17] In this context, 3D culture methodologies may be used. They are able to recreate *in vitro* the cellular heterogeneity and the microenvironment of tumor tissues in humans and represent therefore a suitable alternative to

[a]*Institut Galien Paris-Saclay, UMR 8612, CNRS, Université Paris-Saclay, Faculté de Pharmacie, 5 rue Jean-Baptiste Clément, F-92296 Châtenay-Malabry cedex, France. E-mail: simona.mura@universite-paris-saclay.fr*

[b]*Institut des matériaux poreux de Paris, Ecole normale supérieure, ESPCI Paris, CNRS, PSL University, 75005 Paris, France. E-mail: christian.serre@ens.psl.eu*

†Electronic supplementary information (ESI) available: Detailed methods and supporting figures. See DOI: 10.1039/d1bm00669j

animal experiments, which are not only associated with ethical, economic and time-related issues but are also sometimes poor predictors of human disease in oncology.[18–21]

Among the various 3D models, multicellular tumor spheroids (MCTS) are largely applied for systematic drug investigations in the oncology field.[22,23] These scaffold-free spherical cell assemblies recreate in a plate well the interactions among different cell types (*e.g.*, cancer cells, fibroblasts, immune cells), the gradients of nutrients and metabolites, the accumulation of extracellular matrix components, and the influence of the microenvironment on the sensitivity of the cancer cells to the treatments and recapitulate the physical barriers (*i.e.*, tumor stroma) that must be crossed by any therapeutic treatment (*i.e.*, drugs and nanocarriers).[24] To the best of our knowledge, such an approach has not been applied yet to the *in vitro* evaluation of nanoMOFs so far routinely performed only using 2D cell cultures.

Herein, we have developed a 3D heterotype spheroid model of lung cancer to investigate MIL-100(Fe) nanoMOFs, both bare and surface-modified with hydrophilic polyethylene glycol (PEG) chains, to design nanocarriers with long circulating properties.[25,26] Loading these nanoMOFs with doxorubicin (Doxo) allowed us to assess their therapeutic efficacy and, thanks to the drug fluorescence properties, to monitor their capacity to diffuse through the tumor mass (Fig. 1).

The heterotype spheroid model of lung cancer integrating human lung cancer cells (A549) and fibroblasts (MRC5) has been constructed according to the liquid overlay technique using pHEMA-coated 96 round-bottomed well plates. Starting from a fixed number of cancer cells (5000 cells per well at day 0), a 1 : 2 seeding ratio between A549 and MRC5 cells has been applied. Optical images of these spheroids have been collected at regular time points and they revealed the formation of reproducible regular structures, whose size progressively increased, leading to a volume doubling in 7 days of culture (from 0.10 ± 0.01 mm^3 at day 3 post-seeding to 0.20 ± 0.01 mm^3 at day 10) (Fig. S1†).

Hematoxylin–eosin staining of these spheroids at day 3 revealed a compact structure rich in cancer cells (positively stained for the cytokeratin AE1/AE3 marker, specific for the identification of epithelial cells of neoplastic origin), among which cytokeratin-negative cells were distributed. The positive staining of the latter for fibronectin allowed their identification as fibroblasts, which secrete this component of the extracellular matrix (Fig. 2a–c). Further information on the cell spatial organization was provided by imaging spheroids made of A549 cancer cells and GFP-labeled fibroblasts by light sheet fluorescence microscopy (LSFM). Thanks to the high penetration depth, this microscopy technique allowed us to scan the whole spheroid and acquire high resolution images. The blue signal of the Hoechst 33342-stained nuclei revealed the distribution of the cells in this three-dimensional structure and the green fluorescence confirmed the presence of fibroblasts that are mainly localized in the central region at day 3 of culture (Fig. 2d–f). A considerable reduction of the green signal was observed in the spheroids at day 7 post-seeding and indicated a gradual loss of fibroblasts over time (Fig. S2†). Hence, the spheroid growth observed by optical imaging was mainly due to the fast proliferation of cancer cells. Based on these results, spheroids at day 3 post-seeding, showing a stable integration of cancer cells, fibroblasts and fibronectin, and thus mimicking the tumor heterogeneity, were used for the *in vitro* screening of nanoMOFs.

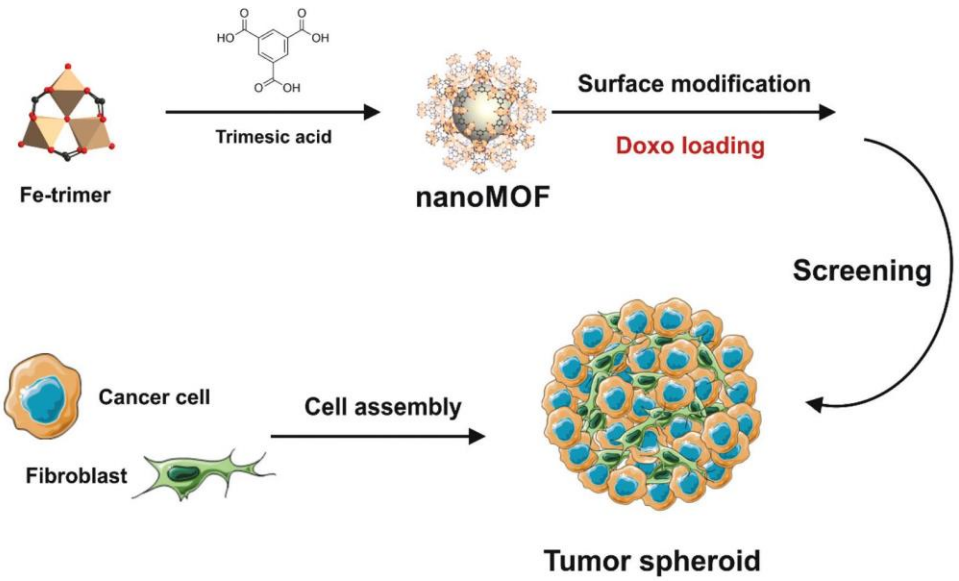

Fig. 1 Schematic representation (not in scale) of the formulation of nanoMOFs and the construction of the 3D tumor model used for their investigation.

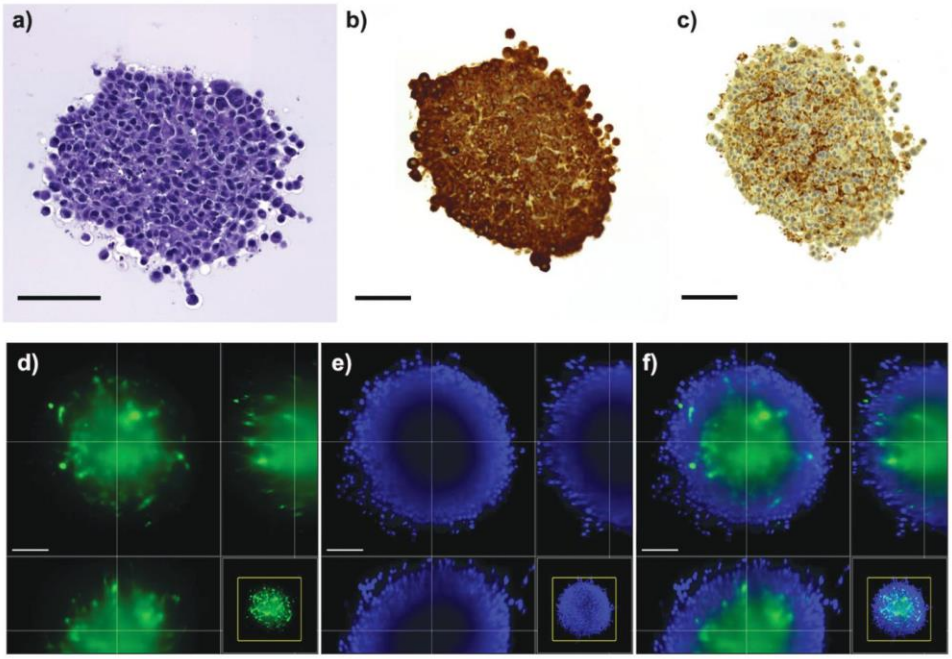

Fig. 2 Heterotype A549:MRC-5 spheroid characterization (day 3 post-seeding). Histological analysis of 5 μm sections of spheroids: (a) hematoxylin–eosin; (b) cytokeratin AE1/AE3 and (c) fibronectin staining. Scale bars: 100 μm. LSFM imaging of spheroids: (d) single green channel (GFP-labeled fibroblasts); (e) single blue channel (Hoechst 33342, nuclei) and (f) overlay of blue and green fluorescence. Scale bars: 100 μm.

Engineering the surface of nanocarriers has been largely exploited to endow them with long circulating properties as well as to promote cell targeting taking advantage of the specific receptors overexpressed on the cell surface. Herein, MIL-100(Fe) nanoMOFs with and without surface modification with hydrophilic PEG chains have been investigated. Encouraged by the previous "green" synthesis strategy, bare nanoMOFs were prepared by a recently developed low temperature synthesis method in the absence of organic solvent.[27,28] Surface decoration has been then performed according to the previously described covalent[15] (nanoMOF_Cv) or GraftFast® (nanoMOF_Gf) strategies.[13,29]

For the former, a chemical reaction between the pendent COOH groups of the external surface of the nanoMOFs and the NHS groups from the PEG allowed the PEG chains to anchor in a covalent way. On the other hand, in the GraftFast® route, radical polymerization occurred on the surface of the nanoMOFs, leading to a PEG brush that strongly interacted with the outer surface, although no precise information is available to establish the nature of the grafting (*i.e.*, covalent or dispersive interactions). Note that these modifications were performed on MIL-100(Fe) nanoparticles obtained through a microwave-assisted route with a size of around 130 nm, while we applied these grafting strategies to newly developed ambient pressure nanoparticles with a size of 60 nm. The crystallinity of the surface engineered nanoMOFs fitted well with those of the bare nanoparticles, indicating that the structural integrity of the nanoMOFs was preserved (Fig. S3†). As reported before,[30,31] partial pore blocking occurred upon Doxo loading, while new stable coordination bonds formed between Fe(III) open metal sites and the drug. Such coordination resulted in a loss of crystallinity, thus leading to a slight broadening and change in the relative intensity of the low angle Bragg peaks of the drug-loaded particles in comparison with those of the empty nanoparticles (Fig. S3†).

As shown by thermogravimetric analysis, the two surface modification strategies induced similar functionalization with a slightly higher PEG content on the nanoMOF_Gf (~39%) compared to the nanoMOF_Cv (~34%) (Fig. S4 and Scheme S1†).

It is noteworthy that the presence of PEG chains on the surface of empty nanoMOFs also did not induce any significant modification of their mean diameter compared to the naked particles (Table S1†). As reported before when using larger nanoMOFs (~130 nm), shielding of the negative surface charge was observed when the covalent strategy was applied (zeta potential shifted from −28 mV to a neutral value), while the surface charge did not change following GraftFast® PEGylation (Table S1†). In the latter case, this was due to the free pendent carboxylic groups, not involved in the coupling reaction with the PEG moieties, which were still available on the particle outer surface. The lack of cytotoxicity on both A549 lung cancer cells and MRC5 lung macrophages confirmed the biocompatibility of these nanoMOFs, independent of their surface identity (Fig. S5†).

The soaking of naked nanoMOFs in an aqueous doxorubicin solution allowed the formulation of doxorubicin-loaded particles (*i.e.*, nanoMOF_Doxo), which reached a high loading capacity of 36 ± 5%. Only a slight drug loss occurred during the

successive surface-functionalization steps and the PEG-decorated nanoMOF_Cv_Doxo and nanoMOF_Gf_Doxo exhibited loading capacities of 34 ± 2% and 31 ± 1%, respectively (Table S2†). Such a small reduction was likely due to the desorption of the drug moieties localized on the outer particle surface.

Whatever the surface functionalization strategy, we observed a crucial role of the PEG chains in the colloidal stabilization of drug-loaded nanoMOFs that, in water, maintained a narrow size distribution (*i.e.*, polydispersity index < 0.14) and a mean diameter (~170 nm) comparable with those of the empty particles (Tables S1 and S2†). Similarly, the surface charge of PEG-modified nanoMOFs was not affected by the loading of a drug, while a switch from a negative (−28 ± 3 mV) to a neutral value (4 ± 1 mV) was observed for bare nanoMOF_Doxo, compared to the empty ones. This surface charge modification, by suppressing the repulsion among particles, was likely responsible for the significant increase of the measured mean diameter due to nanoMOF aggregation (Table S2†). In spite of the different physicochemical properties, the drug release profiles from the three kinds of nanoMOFs almost overlapped. The latter did not exceed 15 wt% after 72 h in phosphate buffer (Fig. S6†) and it was not significantly influenced by the pH of the medium (*i.e.*, 5.1 or 7.4) used to mimic different intracellular compartments. Similar progressive release of the drug was observed in complete cell culture medium. Although higher, more than 70% of the loaded drug remained still encapsulated in the nanoMOF pores after 72 h (Fig. S7†). These results demonstrated a stable encapsulation, not affected by the presence of the surface coating and suitable to achieve a controlled and sustained drug liberation over prolonged periods of time.

Then, we investigated whether such successfully formulated nanoMOFs were capable of diffusing through 3D tumor spher-

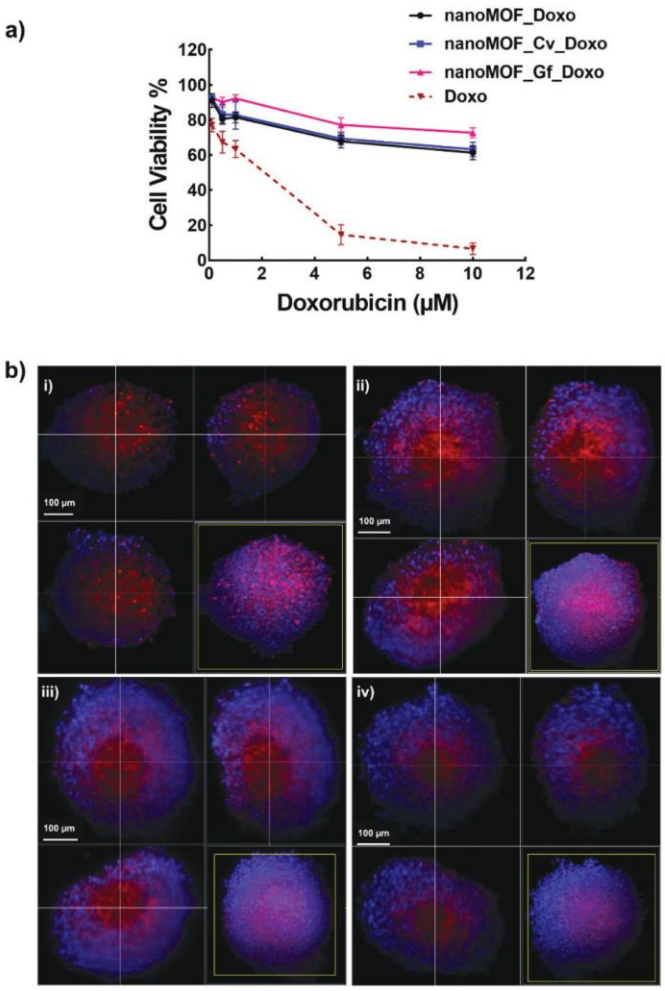

Fig. 3 (a) Spheroid viability following exposure to increasing concentrations of free doxorubicin (Doxo) or Doxo-loaded nanoMOFs for 72 h at 37 °C. Values represent mean ± standard deviation. (n = 3). (b) LSFM imaging of MCTS treated for 24 h with (i) free Doxo; (ii) nanoMOF_Doxo; (iii) nanoMOF_Cv_Doxo and (iv) nanoMOF_Gf_Doxo at a Doxo concentration of 10 μM. Merge of blue (Hoechst 33342, nuclei) and red (doxorubicin) fluorescence signals. Images represent the orthogonal section in the middle of the spheroids. For each condition, the 3D tomography of the spheroid is included in the yellow square. Scale bars: 100 μm.

oids and eventually would provide a therapeutic advantage compared to the free drug. Scanning of the whole spheroid by light sheet fluorescence microscopy (LSFM) well confirmed the diffusive capacity of the free drug through the entire lung spheroid, and the punctuate fluorescence pattern indicated the colocalization of the drug with the cell nuclei, where the doxorubicin can exert its action by intercalation within the DNA (Fig. 3b and Fig. S8†). Penetration of nanoMOFs was also observed, thus revealing the capacity of these nanoparticles to cross the biological barrier of the tumor microenvironment, which was reproduced in the 3D model. However, incubation with doxorubicin-loaded nanoMOFs led to a more diffuse signal homogeneously dispersed in the whole spheroid (Fig. 3b and Fig. S8†) Whatever their surface identity, the nanoMOFs did not display any significant difference in the spheroid distribution. As also previously reported,[31] we observed that drug encapsulation into the nanoMOFs (both bare and surface modified) induced the quenching of the Doxo fluorescence (Fig. S9†). As already described with drugs bearing phenol (φ-OH) groups able to bind open metal sites in nanoMOFs, this quenching was due to the direct coordination of the OH groups from Doxo on the iron open metal sites. Accordingly, the red signal here observed was likely due to the drug released from the particle cavities.

However, LSFM images highlighted that the doxorubicin was likely not reaching the nuclei. Such hypothesis was verified by assessing the cell viability: while exposure of tumor spheroids to the free drug induced dose-dependent cytotoxicity that increased over time, no reduction of the cell viability was observed after spheroid incubation with the Doxo-loaded nanoMOFs, independent of the treatment length (Fig. 3a, Fig. S10†). Accordingly, in spite of the release of a certain amount of doxorubicin, suggested by the recovery of the quenched fluorescence signal, the drug was not able to exert its activity.

To better elucidate the path of the free drug and the drug-loaded nanoMOFs, cleared spheroids have been imaged by confocal laser scanning microscopy (CLSM). Such a change of technique was justified by the different resolutions between the two imaging modalities. The higher magnification (40× *versus* 20×) and the larger numerical aperture (1.1 *versus* 1) of the CLSM compared to the LSFM allowed an increase in the sensitivity of the acquisition and thus to better monitor the signal at the cellular level, even when low. In agreement with the LSFM results, the collected images confirmed the capacity of the free drug to reach the cell nuclei, which was consistent with the observed reduction of the cell viability. In contrast, no nuclear localization was observed after spheroid exposure to drug-loaded nanoMOFs (Fig. 4).

Whether the different behaviors between the free drug and the drug-loaded nanoMOF particles were due to a distinct fate inside the cell was a matter of question. Hence, we performed live-cell confocal microscopy to observe A549 cells after 24 h exposure to the different treatments. Whereas the free doxorubicin accumulated in the cell nuclei, nanoMOFs amassed only in the cytosolic compartment and their distribution was not affected by their surface properties (Fig. S11†).

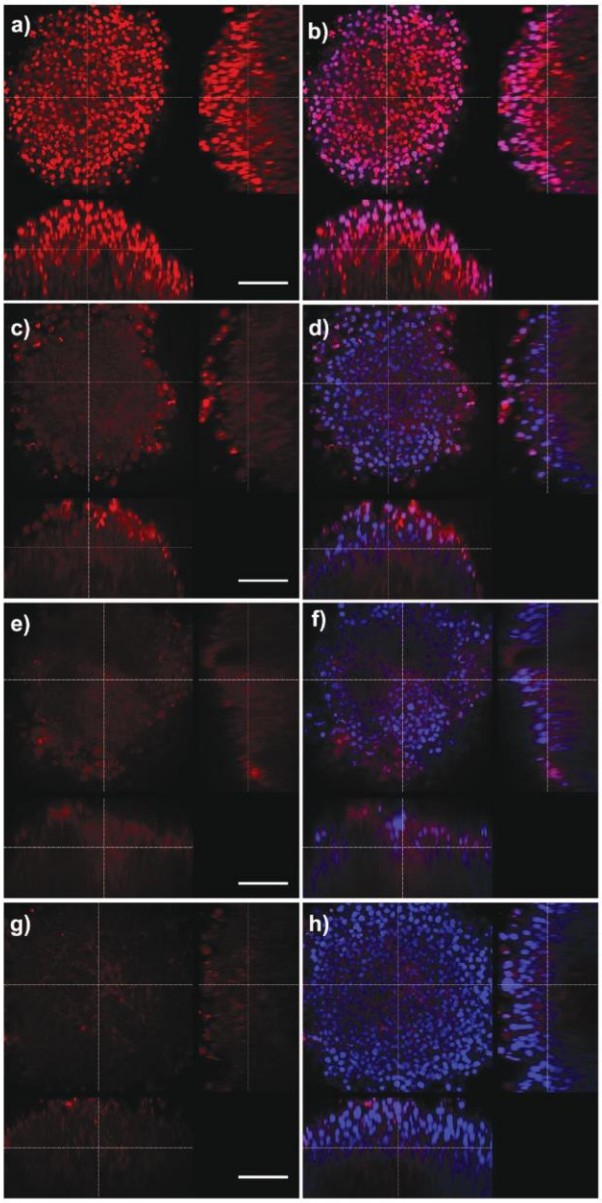

Fig. 4 Confocal imaging of MCTS treated for 24 h with (a, b) free Doxo; (c, d) nanoMOF_Doxo; (e, f) nanoMOF_Cv_Doxo and (g, h) nanoMOF_Gf_Doxo at a Doxo concentration of 10 μM. Cell nuclei were stained with Hoechst-33342 (blue signal). (a, c, e and g) single red signal (doxorubicin) and (b, d, f and h) merged fluorescence signals. Images represent the orthogonal section at 100 μm depth. Scale bars: 100 μm.

Such behavior combined with the absence of toxicity evoked the nanocarrier confinement into endo–lysosomal vesicles as already observed with other nanoMOFs in different cell lines,[32–34] which suggested an endocytosis-mediated uptake well described for nanoscale drug delivery systems.[35] Staining

of lysosomes with Lysotracker blue after cell exposure to drug-loaded nanoMOFs revealed clear colocalization of the red and the blue fluorescence signals, thus confirming lysosomal localization (Fig. 5).

The recovery of the red doxorubicin fluorescence (Fig. 5a, d and g) indicated that a fraction of the encapsulated drug was released from the nanoMOF pores; however, being ionized at lysosomal acidic pH, doxorubicin was unable to leak out of the lysosomes.[36] Accordingly the red signal allowed us to identify the subcellular site of nanoMOF accumulation. It should be noted that drug sequestration in this compartment hindered the diffusion into the cell cytoplasm and the successive translocation to the nucleus, thus abolishing its therapeutic activity.

Previous studies have demonstrated the key role of the nanoparticle physicochemical properties in their ability to penetrate and be internalized by cells in spheroids.[22,37–39] Despite the different experimental conditions (*e.g.*, building materials, range of evaluated sizes, surface chemistry, *etc.*), a general trend emerged that the smaller the nanoparticle, the better their ability to diffuse through the whole mass and to reach the core of the spheroids. However, size is not the only determinant and for instance, adjusting the surface properties of the carriers to reduce their interaction with the microenvironment (*e.g.*, by coating with PEG chains)[39] could also improve penetration.

Despite the differences in the physicochemical properties (*i.e.*, size, surface coating, charge), the doxo-loaded nanoMOFs

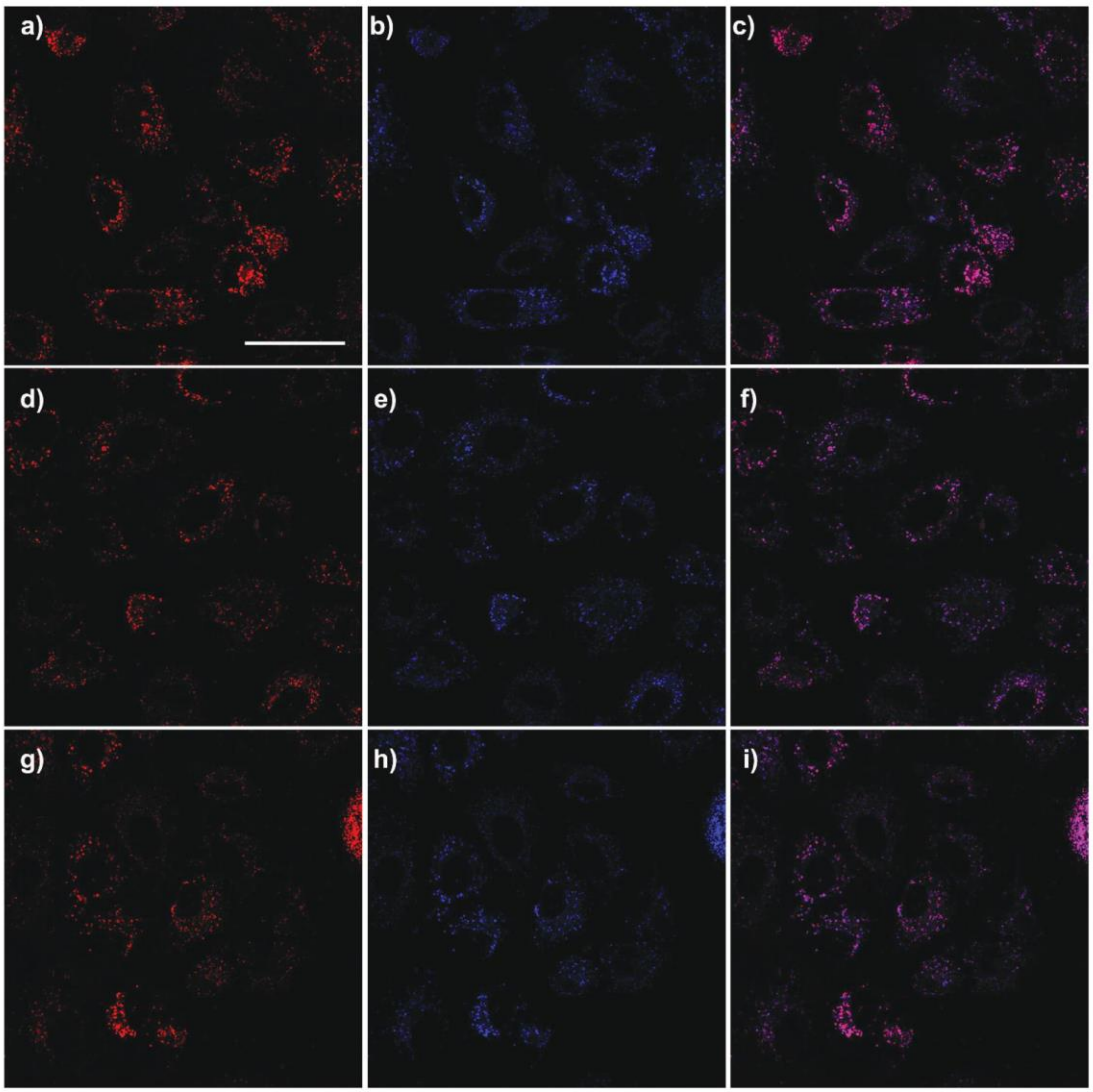

Fig. 5 Intracellular localization of doxorubicin-loaded nanoMOFs assessed by CLSM imaging. A549 cells (2D culture) were incubated for 24 h with (a–c) nanoMOF_Doxo; (d–f) nanoMOF_Cv_Doxo and (g–i) nanoMOF_Gf_Doxo at a Doxo concentration of 10 μM. (a, d and g) single red signal (doxorubicin); (b, e and h) single blue signal (lysosomal Celltracker blue); and (c, f and i) merge of red and blue fluorescence signals. Scale bars: 50 μm.

described in this study showed comparable penetration capacity through the tumor spheroids. These results suggested that once they come into contact with the proteins present in the complete cell culture medium (containing 10% FBS), in which they were diluted before incubation with spheroids, the nanoMOFs probably acquired similar biological identity and therefore similar behavior, although the initial chemical identity was not the same. Further investigation would be necessary to validate such a hypothesis, but several studies have already stressed the role of the biological identity in the fate of different nanocarriers, thus strongly supporting this assumption.[40–42]

It should be noted that discrepancies among published data may arise also from the different models used to evaluate the nanocarriers. Monotype spheroids made of different cancer cells and heterotype spheroids constructed by the assembly of cancer cells and fibroblasts, such as those described in the present study, have a different 3D structural architecture and composition that may affect the diffusion and penetration of nanoparticles.

Finally, in agreement with previous studies,[38,39] we have observed that the free drug was able to diffuse efficiently and reach the core of the spheroids. In contrast, when the drug was encapsulated in nanoMOFs, its sequestration in the acidic endo-lysosomal compartment, which abolished its pharmacological activity, was observed. An example of the efficacy of doxorubicin both in the free form or loaded in surfactant-containing vesicles has been reported.[38] However, the composition of these vesicles played a key role in the observed results. Indeed, it was assumed that the intact vesicles did not penetrate the whole spheroid, but the interaction of the surfactant molecules with the lipids of the cell membrane probably created a locally high concentration of the free drug on the spheroid surface, and the released drug was then able to diffuse freely and reach the nuclei to exert its pharmacological activity.

The above considerations suggest that a timely formulation and structural modification of nanoMOFs to provide endosomal escape capabilities are mandatory to ensure the efficient release of the loaded drug into the cell cytosol and thus achieve therapeutic efficacy.

Conclusions

Although promising results have been obtained in the last few years in nanomedicine, important obstacles still remain in the oncology field. Among them, poor drug loading and the inability to cross the multiple biological barriers that characterize the tumor tissue and its microenvironment deserve special attention. The achievement of a high drug loading and the overcoming of the stromal barrier would theoretically ensure a better exposure of the tumor to the drug, thus resulting in a significant clinical benefit.

Thus, we investigated herein doxorubicin-loaded nanoMOFs in a 3D heterotype tumor spheroid model to verify their therapeutic efficacy. The results have clearly shown that satisfying the above-mentioned conditions was not enough. Indeed, although doxorubicin was successfully encapsulated into nanoMOFs, penetrated throughout the spheroids and accumulated into the cells, it was discovered that doxorubicin failed to reach the cell nucleus.

As a result, the *in vivo* evaluation of these nanoMOFs in an animal model has not been performed.

Such a screening, combining various cell culture methodologies and imaging techniques, could allow us to identify strategies for the optimization of the nanoMOF structure and surface properties to breach the intracellular barriers, ensure endo-lysosomal escape and therefore achieve successful delivery of the drug towards the relevant intracellular target. These results would also allow us to extrapolate a correlation between the nanoMOF chemical identity and their biological fate as already shown for polymer and metal-based nanocarriers.

Overall, these results call for an accurate *in vitro* screening of any newly engineered nanomedicine in order to select the most promising ones before *in vivo* studies.

Conflicts of interest

There are no conflicts to declare.

Acknowledgements

This work has been sponsored by the Ile-de-France Region in the framework of Respore, the Île-de-France network of Excellence in Porous Solids. The CNRS and the French Ministry of Research are also warmly acknowledged for financial support. Dr Delphine Courilleau, (Plate-Forme CIBLOT, Institut Paris-Saclay d'Innovation Thérapeutique, Châtenay Malabry, France), Dr Valerie Nicolas and Dr Severine Dominichini (Plate-Forme MIPSIT, Institut Paris-Saclay d'Innovation Thérapeutique, Châtenay Malabry, France) are warmly acknowledged for the assistance with the bioluminescence measurements and the 2D/3D CLSM imaging, respectively. Miss Meriem Garfa-Traore and Mr Nicolas Goudin from the Cell Imaging Platform UMS 24 (Structure Fédérative de Recherche, Necker, Inserm US 24 CNRS UMS 3633) are gratefully acknowledged for their support with the LSFM spheroid imaging. Miss Maryline Favier and Miss Fabiola Ely-Marius from the HistIM Plate-Forme (Institut Cochin, Paris, France) are warmly acknowledged for their assistance with the histological analysis of spheroid samples.

References

1 M. W. Tibbitt, J. E. Dahlman and R. Langer, *J. Am. Chem. Soc.*, 2016, **138**, 704–717.
2 J. Wolfram and M. Ferrari, *Nano Today*, 2019, **25**, 85–98.
3 J. Nicolas, S. Mura, D. Brambilla, N. Mackiewicz and P. Couvreur, *Chem. Soc. Rev.*, 2013, **42**, 1147–1235.

4 P. P. Deshpande, S. Biswas and V. P. Torchilin, *Nanomedicine*, 2013, **8**, 1509–1528.
5 D. J. A. Crommelin, P. van Hoogevest and G. Storm, *J. Controlled Release*, 2020, **318**, 256–263.
6 A. C. Anselmo and S. Mitragotri, *Bioeng. Transl. Med.*, 2019, **4**, e10143.
7 T. Simon-Yarza, A. Mielcarek, P. Couvreur and C. Serre, *Adv. Mater.*, 2018, **30**, 1707365.
8 T. Baati, L. Njim, F. Neffati, A. Kerkeni, M. Bouttemi, R. Gref, M. F. Najjar, A. Zakhama, P. Couvreur, C. Serre and P. Horcajada, *Chem. Sci.*, 2013, **4**, 1597–1607.
9 P. Horcajada, S. Surblé, C. Serre, D.-Y. Hong, Y.-K. Seo, J.-S. Chang, J.-M. Grenèche, I. Margiolaki and G. Férey, *Chem. Comm.*, 2007, 2820–2822.
10 T. Simon-Yarza, M. Gimenez-Marques, R. Mrimi, A. Mielcarek, R. Gref, P. Horcajada, C. Serre and P. Couvreur, *Angew. Chem.*, 2017, **56**, 15565–15569.
11 P. Horcajada, T. Chalati, C. Serre, B. Gillet, C. Sebrie, T. Baati, J. F. Eubank, D. Heurtaux, P. Clayette, C. Kreuz, J.-S. Chang, Y. K. Hwang, V. Marsaud, P.-N. Bories, L. Cynober, S. Gil, G. Férey, P. Couvreur and R. Gref, *Nat. Mater.*, 2010, **9**, 172–178.
12 V. Agostoni, P. Horcajada, M. Noiray, M. Malanga, A. Aykaç, L. Jicsinszky, A. Vargas-Berenguel, N. Semiramoth, S. Daoud-Mahammed, V. Nicolas, C. Martineau, F. Taulelle, J. Vigneron, A. Etcheberry, C. Serre and R. Gref, *Sci. Rep.*, 2015, **5**, 7925.
13 M. Giménez-Marqués, E. Bellido, T. Berthelot, T. Simón-Yarza, T. Hidalgo, R. Simón-Vázquez, Á. González-Fernández, J. Avila, M. C. Asensio, R. Gref, P. Couvreur, C. Serre and P. Horcajada, *Small*, 2018, **14**, 1801900.
14 T. Hidalgo, M. Giménez-Marqués, E. Bellido, J. Avila, M. C. Asensio, F. Salles, M. V. Lozano, M. Guillevic, R. Simón-Vázquez, A. González-Fernández, C. Serre, M. J. Alonso and P. Horcajada, *Sci. Rep.*, 2017, **7**, 43099.
15 A. Zimpel, T. Preiß, R. Röder, H. Engelke, M. Ingrisch, M. Peller, J. O. Rädler, E. Wagner, T. Bein, U. Lächelt and S. Wuttke, *Chem. Mater.*, 2016, **28**, 3318–3326.
16 M. C. Cox, L. M. Reese, L. R. Bickford and S. S. Verbridge, *ACS Biomater. Sci. Eng.*, 2015, **1**, 877–894.
17 K. A. Fitzgerald, M. Malhotra, C. M. Curtin, F. J. O′ Brien and C. M. O′ Driscoll, *J. Controlled Release*, 2015, **215**, 39–54.
18 H. Ledford, *Nature*, 2016, **533**, 2.
19 J. P. Thomas, R. Z. Arzoomanian, D. Alberti, R. Marnocha, F. Lee, A. Friedl, K. Tutsch, A. Dresen, P. Geiger, J. Pluda, W. Fogler, J. H. Schiller and G. Wilding, *J. Clin. Oncol.*, 2003, **21**, 223–231.
20 G. Suntharalingam, M. R. Perry, S. Ward, S. J. Brett, A. Castello-Cortes, M. D. Brunner and N. Panoskaltsis, *N. Engl. J. Med.*, 2006, **355**, 1018–1028.
21 I. W. Mak, N. Evaniew and M. Ghert, *Am. J. Transl. Res.*, 2014, **6**, 114–118.
22 G. Lazzari, P. Couvreur and S. Mura, *Polym. Chem.*, 2017, **8**, 4947–4969.
23 G. Mehta, A. Y. Hsiao, M. Ingram, G. D. Luker and S. Takayama, *J. Controlled Release*, 2012, **164**, 192–204.
24 E. C. Costa, A. F. Moreira, D. de Melo-Diogo, V. M. Gaspar, M. P. Carvalho and I. J. Correia, *Biotechnol. Adv.*, 2016, **34**, 1427–1441.
25 D. E. Owens and N. A. Peppas, *Int. J. Pharmacol.*, 2006, **307**, 93–102.
26 J. S. Suk, Q. Xu, N. Kim, J. Hanes and L. M. Ensign, *Adv. Drug Deliv. Rev.*, 2016, **99**, 28–51.
27 M. Panchal, F. Nouar, C. Serre, M. Benzaqui, S. Sene, N. Steunou and M. G. Marquez, "Low Temperature Process for the synthesis of MOF carboxylate nanoparticles", *United States Patent Application*, 2020/0102337, 2017.
28 I. Christodoulou, T. Bourguignon, X. Li, G. Patriarche, C. Serre, C. Marlière and R. Gref, *Nanomaterials*, 2021, **11**, 722.
29 V. Mévellec, S. Roussel, L. Tessier, J. Chancolon, M. Mayne-L'Hermite, G. Deniau, P. Viel and S. Palacin, *Chem. Mater.*, 2007, **19**, 6323–6330.
30 S. Sene, M. T. Marcos-Almaraz, N. Menguy, J. Scola, J. Volatron, R. Rouland, J.-M. Grenèche, S. Miraux, C. Menet, N. Guillou, F. Gazeau, C. Serre, P. Horcajada and N. Steunou, *Chem*, 2017, **3**, 303–322.
31 R. Anand, F. Borghi, F. Manoli, I. Manet, V. Agostoni, P. Reschiglian, R. Gref and S. Monti, *J. Phys. Chem. B*, 2014, **118**, 8532–8539.
32 M. Durymanov, A. Permyakova, S. Sene, A. Guo, C. Kroll, M. Gimenez-Marques, C. Serre and J. Reineke, *Mol. Pharmacol.*, 2019, **16**, 2315–2325.
33 C. Orellana-Tavra, S. Haddad, R. J. Marshall, I. Abánades Lázaro, G. Boix, I. Imaz, D. Maspoch, R. S. Forgan and D. Fairen-Jimenez, *ACS Appl. Mater. Interfaces*, 2017, **9**, 35516–35525.
34 R. Roder, T. Preiss, P. Hirschle, B. Steinborn, A. Zimpel, M. Hohn, J. O. Radler, T. Bein, E. Wagner, S. Wuttke and U. Lachelt, *J. Am. Chem. Soc.*, 2017, **139**, 2359–2368.
35 H. Hillaireau and P. Couvreur, *Cell. Mol. Life Sci.*, 2009, **66**, 2873–2896.
36 A. R. Kirtane, S. M. Kalscheuer and J. Panyam, *Adv. Drug Delivery Rev.*, 2013, **65**, 1731–1747.
37 K. Huang, H. Ma, J. Liu, S. Huo, A. Kumar, T. Wei, X. Zhang, S. Jin, Y. Gan, P. C. Wang, S. He, X. Zhang and X.-J. Liang, *ACS Nano*, 2012, **6**, 4483–4493.
38 D. J. Kerr, A. Rogerson, G. J. Morrison, A. T. Florence and S. B. Kaye, *Br. J. Cancer*, 1988, **58**, 432–436.
39 A. Tchoryk, V. Taresco, R. H. Argent, M. Ashford, P. R. Gellert, S. Stolnik, A. Grabowska and M. C. Garnett, *Bioconjugate Chem.*, 2019, **30**, 1371–1384.
40 K. Nienhaus, H. Wang and G. U. Nienhaus, *Mater. Today Adv.*, 2020, **5**, 100036.
41 N. Bertrand, P. Grenier, M. Mahmoudi, E. M. Lima, E. A. Appel, F. Dormont, J.-M. Lim, R. Karnik, R. Langer and O. C. Farokhzad, *Nat. Commun.*, 2017, **8**, 777.
42 M. P. Monopoli, C. Åberg, A. Salvati and K. A. Dawson, *Nat. Nanotechnol.*, 2012, **7**, 779–786.

Annex-3

Journal of Materials Chemistry A

ROYAL SOCIETY OF CHEMISTRY

PAPER

View Article Online
View Journal | View Issue

Cite this: J. Mater. Chem. A, 2022, 10, 8535

A robust eco-compatible microporous iron coordination polymer for CO_2 capture†

Marvin Benzaqui,[ab] Mohammad Wahiduzzaman,[c] Heng Zhao,[b] Md Rafiul Hasan,[de] Timothy Steenhaut,[f] Ali Saad,[a] Jérôme Marrot,[a] Périne Normand,[g] Jean-Marc Grenèche,[h] Nicolas Heymans,[g] Guy De Weireld,[g] Antoine Tissot,[b] William Shepard,[i] Yaroslav Filinchuk,[f] Sophie Hermans,[f] Florent Carn,[j] Magdalena Manlankowska,[de] Carlos Téllez,[de] Joaquín Coronas,[de] Guillaume Maurin,[c] Nathalie Steunou *[ab] and Christian Serre *[ab]

Received 4th December 2021
Accepted 3rd March 2022

DOI: 10.1039/d1ta10385g

rsc.li/materials-a

Iron(III) carboxylate based metal organic frameworks (MOFs)/porous coordination polymers (PCPs) have sparked great interest owing to their high structural diversity and tunable porosity, excellent stability, tailored functionality and their scalability as well as green synthesis associated with their biocompatible and biodegradable character. Herein, we present a new robust Fe(III) based PCP (labelled MIL-178(Fe)) built up from chains of corner sharing Fe octahedra interconnected by 1,2,4-benzene tricarboxylic acid, delimiting one dimensional narrow pore channels (pore diameter < 4.5 Å) decorated with polar groups (μ_2-OH and $-CO_2H$ functions). These structural and chemical features are suitable for the selective adsorption of CO_2. MIL-178(Fe) was synthesized following a simple and green protocol in water under near ambient conditions using non-toxic reactants, allowing the production of sub-micrometer sized MIL-178(Fe) particles in a large amount (30 g). As shown by single-gas isotherms and CO_2/N_2 co-adsorption experiments as well as molecular simulations, this material exhibits a moderate CO_2 capacity at low pressure but a high CO_2/N_2 selectivity. This is fully consistent with the presence of μ_2-OH groups acting as CO_2 adsorption sites, as revealed from both molecular simulations and *in situ* PXRD experiments. Finally, the good compatibility of this MOF with the elastomer block copolymer Pebax®-3533 allowed the processing of homogeneous and defect-free mixed matrix membranes with a MIL-178(Fe) loading of up to 25 wt% that outperformed pure Pebax®-3533 membranes for CO_2/N_2 separation.

Introduction

Metal organic frameworks (MOFs) and porous coordination polymers (PCPs) are a class of porous crystalline hybrid materials constructed through the coordination of multi-metallic units called secondary building units (SBUs) with organic multitopic ligands.[1,2] They have gained widespread interest due to their high surface area, chemical diversity, unprecedented variability of pore shape/size and topology.[1] Therefore, their physico-chemical properties can be finely tuned, making them promising materials for a myriad of applications including gas storage and separation, heterogeneous catalysis, sensing, biomedicine and so on.[3–7] Remarkable advances have been made toward CO_2 capture and separation by using PCPs, MOFs and MOF based composites.[4,8–10] The main advantages of MOFs over other porous materials are their high CO_2 sorption capacity

[a]Institut Lavoisier de Versailles, UMR CNRS 8180, Université de Versailles St Quentin en Yvelines, Université Paris Saclay, 78000 Versailles, France. E-mail: nathalie.steunou@uvsq.fr

[b]Institut des Matériaux Poreux de Paris, ENS, ESPCI Paris, CNRS, PSL University, 75005 Paris, France. E-mail: christian.serre@ens.fr

[c]ICGM, Univ. Montpellier, CNRS, ENSCM, Montpellier, France

[d]Instituto de Nanociencia y Materiales de Aragón (INMA), CSIC-Universidad de Zaragoza, Zaragoza 50018, Spain

[e]Chemical and Environmental Engineering Department, Universidad de Zaragoza, Zaragoza 50018, Spain

[f]Institute of Condensed Matter and Nanosciences, Université Catholique de Louvain, 1348 Louvain-la-Neuve, Belgium

[g]Service de Thermodynamique et de Physique Mathématique, Faculté Polytechnique de Mons, Université de Mons, 7000 Mons, Belgium

[h]Institut des Molécules et des Matériaux du Mans (IMMM), UMR CNRS 6283, Université du Maine, 72085 Le Mans, Cedex 9, France

[i]Synchrotron SOLEIL-UR1, Orme des Merisiers, Saint-Aubin, BP 48, 91192, Gif-sur-Yvette, France

[j]Laboratoire Matière et Systèmes Complexes (MSC), UMR CNRS 7057, Université Paris Diderot, Bât. Condorcet, 10 rue A. Domon et L. Duquet, 75013 Paris, France

† Electronic supplementary information (ESI) available. CCDC 2112974. For ESI and crystallographic data in CIF or other electronic format see DOI: 10.1039/d1ta10385g

and high CO_2 affinity.[8–10] This largely stems from their potential high pore volume and large amount of CO_2-philic sites that can be introduced within their backbone. Typically, MOFs can integrate multiple CO_2 adsorption sites, *e.g.* open metal sites, Lewis basic sites and covalently-bound polar functional groups, that enables to achieve preferential CO_2 adsorption over other gas molecules such as N_2, CH_4 and H_2O.[8–11] In addition, post-synthetic modification has been also employed to introduce novel CO_2 adsorption sites without altering or degrading the MOF structure.[4,8–11]

While remarkable advances have been achieved for using PCPs and MOFs in CO_2 capture and separation, their large scale application in this field would require overcoming some challenges such as the limited chemical and thermal stabilities of some of them, particularly in the presence of harsh contaminants.[8,12] Indeed, numerous MOFs reported so far for CO_2 capture still lack the requisite chemical stability. Note that moisture is a major concern in industrial gas separation as it is not economically feasible to use completely dry feed-gas streams. Therefore, only hydrothermally stable MOFs can be considered for real practical applications. Various strategies have been explored to design stable MOFs by privileging the formation of strong metal-ligand coordination bonds with the use of high valent metal cations (III/IV) according to Pearson's hard/soft acid/base principle, or alternatively the incorporation of hydrophobic and/or polydentate organic linkers.[12,13]

In this context, Fe(III) carboxylates – denoted here as "Fe-MOFs"– were thus considered so far since the association of the Fe^{3+} cation with strong Lewis acid properties and carboxylate ligands can produce, although not systematically, water stable MOFs.[14,15] Moreover, iron is widely distributed in nature and environmentally friendly. The abundance of iron and its low toxicity have promoted the development of Fe-MOFs, not only for gas separation but also for (photo)catalysis, heat reallocation, (bio)sensing or biomedicine due to their good chemical stability, high porosity and biocompatibility.[14,16–19]

So far, Fe(III) MOFs of different architectures, such as the MIL-*n* (MIL-53, MIL-59, MIL-88, MIL-100, and MIL-101) series, the Fe-soc-MOF or $Fe_4(\mu_3\text{-}O)_2(BTB)_{8/3}(DMF)_2(H_2O)_2$, have been designed by assembling either di-, tri-, tetranuclear clusters or Fe-hydroxy chains as SBUs and polycarboxylate aromatic moieties as organic linkers.[18,20–23] Fe(III) sites were also introduced in the organic backbone of MOFs by using Fe(III) porphyrin ligands (PCN-223, PCN-224, and PCN-600).[24–26] The Fe(III)-phosphonate MOFs such as Fe-CAU-53 were also recently reported.[27] However, not all of these MOFs exhibit a high hydrolytic stability that is not only driven by the type of SBUs but also the connectivity as well as the size and hydrophobic character of the organic linker.[14–27] As an example, the good hydrothermal stability of MIL-53(Fe) is certainly due to its 1D micropore channel structure based on $[Fe(OH)(COO)_2]_n$ chains while the mesoporous MIL-101(Fe) and PCN-333(Fe) based on the oxo-trimer SBU present a limited water stability. Due to the presence of CO_2 adsorption sites such as Lewis acid Fe^{3+} sites or polar functions (OH and F) and a high pore volume, a few Fe-MOFs such as MIL-100(Fe), MIL-88A(Fe), soc MOF(Fe), Fe-BTB and Fe-BTC have been considered for CO_2 capture, and some of them have shown attractive CO_2 uptake at low pressure (>2 mmol g^{-1} at 1 bar, 298 K).[14,15,28,29] Recently, an Fe-MOF ($Fe_4(\mu_3\text{-}O)_2(BTB)_{8/3}(DMF)_2(H_2O)_2$), whose structure consists of two interpenetrating 3D skeletons, has shown a greater CO_2 uptake than that of several known MOFs with a larger pore volume as a result of its small pore and the presence of multiple CO_2 adsorption sites induced by the framework interpenetration.[23] Another property of MOFs and PCP that was exploited for CO_2 capture is their propensity for structural flexibility. In particular, a few Fe-MOFs or Fe-PCPs can undergo structural changes such as pore opening upon exposure to stimuli such as pressure or temperature.[30] In such cases, the CO_2 adsorption capacity of these MOFs such as MIL-53(Fe) can drastically increase at a definite gas pressure.[31] Moreover, it was demonstrated that the structural flexibility and thus CO_2 adsorption capacity of MIL-53(Fe) could be modulated through the functionalization of the organic linker of the MOF.[32] It was shown that the CO_2 adsorption capacity of MIL-53(Fe)-X could be enhanced through the introduction of groups with low polarity (X = Cl, Br, CH_3) that could modulate the μ_2-OH/CO_2 interactions instead of directly interacting with CO_2 molecules.[32]

In spite of these interesting results, the number of Fe-MOFs and Fe-PCPs that combine all the properties required for CO_2 separation (high CO_2 adsorption capacity and selectivity; high chemical and thermal stabilities) is still limited. Moreover, many challenges regarding their synthesis remain unaddressed. Numerous Fe-MOFs are often prepared in the presence of toxic organic solvents and reactants and through a solvo/hydrothermal process leading to fine powdered materials made of micron-sized particles.[14,15] This restricts their applications to a great extent. Therefore, the development of Fe(III)-MOFs using safer synthetic conditions allowing both the control of the crystal size and their large-scale production is still an open challenge for their future practical applications.[33]

Herein, we report the synthesis and characterization of a novel PCP based on iron(III) and 1,2,4-benzene tricarboxylate (Fig. 1), named MIL-178(Fe) (MIL stands for Material of Institut Lavoisier), that exhibits a 1D architecture delimiting ultra-micropores (ϕ < 4.5 Å) decorated with functional groups (–COOH, –OH). The structural behavior of this PCP under CO_2 pressure has been investigated by *in situ* powder X-ray diffraction and molecular modelling, thereby providing a detailed analysis of the preferential arrangement of the confined CO_2 molecules in the material pores and the host/guest interactions. Finally, co-adsorption CO_2/N_2 experiments and grand canonical Monte Carlo simulations were performed in tandem, revealing that this PCP presents an excellent CO_2/N_2 selectivity. Due to its high hydrothermal stability and scalability under room temperature green conditions, this PCP was used as an inorganic filler for the processing of mixed matrix membranes (MMMs). Its combination with the elastomeric block copolymer Pebax®-3533 led to defect-free composite membranes with an enhanced CO_2/N_2 post-combustion separation performance in comparison to the bare polymer. Pebax®-3533 was preferred over the most studied Pebax®-1657 due to the fact that the former is not water/ethanol soluble. Therefore, Pebax®-3533 based membranes are prone to be more stable in the separation of a realistic humid flue gas.[34]

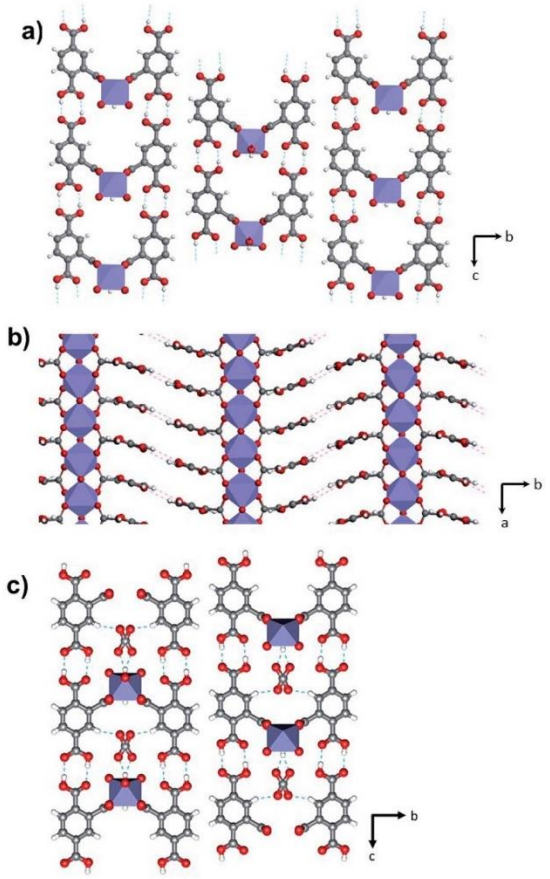

Fig. 1 Crystal structure of (a and b) MIL-178(Fe) along the (a) *a* axis and (b) *c* axis, and (c) CO_2 loaded-MIL-178(Fe) along the *a* axis. Fe octahedra, carbon, oxygen and hydrogen are in purple, gray, red and white respectively. Hydrogen bonds are represented as dotted lines.

Experimental

Chemicals

All chemicals were obtained commercially and used without further purification. The chemicals in this work were anhydrous $FeCl_3$ (Sigma Aldrich 99%) and 1,2,4-benzene tricarboxylic acid (1,2,4-BTC) (Sigma Aldrich, 95%). Pebax® MH 3533 was generously provided by Arkema, France.

Hydrothermal synthesis of MIL-178(Fe)-*hyd*. Single crystals of MIL-178(Fe)-hyd were synthesized *via* a hydrothermal route. 1,2,4-BTC (1.15 g, 5.5 mmol) was poured into a 125 mL Teflon-lined steel autoclave with anhydrous $FeCl_3$ (1.29 g, 8 mmol) and 10 mL of deionized H_2O. The mixture was stirred for 10 min and heated to 200 °C for 72 h under autogenous pressure. The resulting solution was then filtered, and a yellow powder was obtained after extensive washing with water and ethanol to remove the unreacted ligand.

Room temperature synthesis of MIL-178(Fe)-*RT*. 1,2,4-BTC (1.05 g, 5 mmol) and anhydrous $FeCl_3$ (0.81 g, 5 mmol) were poured into a 100 mL beaker with 50 mL of deionized H_2O and stirred at room temperature for 5 days. A bright yellow powder was then recovered by filtration after extensive washings (H_2O & ethanol). For the scale-up synthesis of MIL-178(Fe)-*RT*, 150 mmol of both $FeCl_3$ and 1,2,4-BTC and 1.5 L of water were used.

Fabrication of the mixed matrix membrane. The MMMs were prepared following a two-step process. First, 6 wt% Pebax® MH 3533 (of a total weight of 3 g (polymer + solvent)) was dissolved in 1-propanol: 1-butanol (75/25 (v/v)) by stirring under reflux for 1 h. Afterwards, the dissolved polymer was used to cast bare polymeric membranes for comparison. In the case of MMMs, MIL-178(Fe)-*RT* was dispersed in the dissolved polymer. The required amount of the filler (5–25 wt%), which was calculated against the amount of Pebax® MH 3533 being used, was dispersed in 1.5 mL of 1-propanol/1-butanol (75/25 (v/v)) by repeated sonication and stirring at RT for 1 h. Next, both dispersions were mixed and kept under stirring overnight at RT. In the next step, the solution was poured into a Petri dish. At the end of the process, the membranes were dried for 48 h in a top-drilled box under a solvent-saturated atmosphere under ambient conditions. MMMs are labelled MIL-178(Fe)-Pebax-*X*, where *X* represents the weight fraction of MIL-178(Fe)-*RT*. MMMs were tested in the CO_2/N_2 separation through both single gas permeability (time lag) experiments and 15/85 CO_2/N_2 mixture measurements. Further details of these experiments are provided in the ESI.†

Computational methods. MIL-178(Fe) structure models were optimized at the DFT level with the Quickstep module of the CP2K code using the PBE functional and the triple zeta basis set (TZVP-MOLOPT) for all atoms, except for the Fe centres, where double zeta functions (DZVP-MOLOPT) were employed. Semi-empirical dispersion corrections as implemented in the DFT-D3 method were considered. Force field based grand canonical Monte Carlo (GCMC) simulations were performed at 303 K to assess the single component CO_2 and N_2 and the binary mixture of CO_2/N_2 at 15 : 85 molar compositions in the DFT optimized MIL-178(Fe). The LJ parameters of the MOF atoms were taken from the universal force field (UFF), whereas CO_2 and N_2 molecules were described by the TraPPE potential models. The employed atomic partial charges were derived with the density-derived electrostatic and chemical charges (DDEC) method. Further details of these calculations are provided in the ESI.†

Adsorption measurements. Pure CO_2 and N_2 adsorption measurements have been performed at 303 K up to 10 bars by a gravimetric technique using a high-pressure magnetic suspension balance Rubotherm GmbH.[35,36] CO_2/N_2 co-adsorption measurements were performed on about 10 g of MIL-178(Fe) at 303 K and 1 and 3 bar by using an advanced homemade device that combines a volumetric apparatus and gas chromatography analysis (see the ESI† for more details).

Results and discussion

Synthesis of MIL-178(Fe), and structure resolution by single crystal X-ray diffraction

MIL-178(Fe) microcrystals were first synthesized through a hydrothermal route using the 1,2,4-BTC ligand and $FeCl_3$ as

an iron precursor. We did not consider Fe powder as a precursor due to its oxidation to Fe^{2+} that may thus lead first to the formation of the two-dimensional iron(II)-1,2,4 BTC phase (MIL-67(Fe)) as previously reported.[37] This material (*i.e.*, MIL-178(Fe)-*hyd*) was isolated as a yellow crystalline powder. The SEM images show that MIL-178(Fe) consists of uniform and anisotropic ellipsoidal microcrystals with a length and diameter of about 19 and 3 μm (Fig. 2a). The crystal structure of MIL-178(Fe) was determined by single crystal X-ray diffraction. Due to the small size of the crystals, the X-ray data acquisition was performed at SOLEIL synchrotron by using the PROXIMA 2A beamline equipped with a micro-focused beam. MIL-178(Fe) crystallizes in the orthorhombic space group *Pnma* with unit cell parameters of $a = 6.930(2)$ Å, $b = 28.420$ (6) Å and $c = 9.560(2)$ Å and a unit cell volume of 1882.8(7) Å^3. The associated chemical formula of MIL-178(Fe) is $Fe(OH)[C_9O_6H_5]_2(C_2H_5OH)_{0.5}$. MIL-178(Fe) is made of 1D infinite chains of corner sharing Fe^{3+} octahedra along the *a*-axis (Fig. 1). According to the IUPAC definitions,[38] MIL-178(Fe) can thus be described as a 1D coordination polymer due to the presence of repeating coordination entities in one dimension. Each six-coordinated Fe^{3+} is covalently linked to two oxygen atoms of bridging μ_2-OH groups and four oxygen atoms of the 1,2,4-BTC linker. The Fe–O distances range between 1.946 and 2.038 Å. Interestingly, only one carboxylate group from the ligand bridges two Fe^{3+} centers holding the 1D chain together, the two other carboxylates being free –COOH groups. The free –COOH groups from two different ligands face each other and are thus involved in strong hydrogen bonds connecting the 1,2,4-BTC linkers in the *c* direction. Finally, 1,2,4-BTC linkers coordinated to Fe^{3+} octahedra of different 1D chains also interact through hydrogen bonds in the *b*-direction. Remarkably, this structure possesses very narrow 1D channels following the *a*-axis, *i.e.* along the Fe infinite chains, that are occupied by ethanol molecules (Fig. 1). The dimensions of these channels of 3.5× 4.3 Å (see Fig. S8†) lie in the range of the CO_2 kinetic diameter (3.3 Å), thereby suggesting that this material is of potential interest for CO_2 capture. Although the structure of MIL-178(Fe) presents free carboxylic acid groups, they are not exposed to the center of pores and may not strongly interact with adsorbed CO_2 molecules. However, the μ_2-OH groups linked to Fe^{3+} octahedra decorate the internal surface of the channels and are known to be preferential adsorption sites for CO_2. MIL-178(Fe)-*hyd* was then characterized by ^{57}Fe Mössbauer spectrometry (Fig. S1†). The ^{57}Fe Mössbauer spectra of MIL-178(Fe)-*hyd* at 300 and 77 K display a doublet that consists of two quadrupolar components Γ_1 and Γ_2 with relative amounts of 83 and 17%, respectively, according to the total absorption area. The hyperfine parameters of such components are consistent with high spin Fe^{3+} species in the octahedral environment. The ^{57}Fe Mössbauer spectra at 300 and 77 K obtained after evacuating and heating the MIL-178(Fe)-*hyd* sample at 60 and 100 °C (Fig. S1†) showed only the single quadrupolar Γ_1 component (see the ESI† for more details) while the spectra of the rehydrated MIL-178(Fe)-*hyd* sample are identical to those of the as-synthesized MIL-178(Fe)-*hyd*. According to these experiments, it can be inferred that both components can be assigned to six-fold coordinated Fe^{3+} centers with an identical first coordination shell (1,2,4-BTC and μ_2-OH groups) but a different second coordination shell. In contrast to the non-hydrated Fe^{3+} site of the major Γ_1

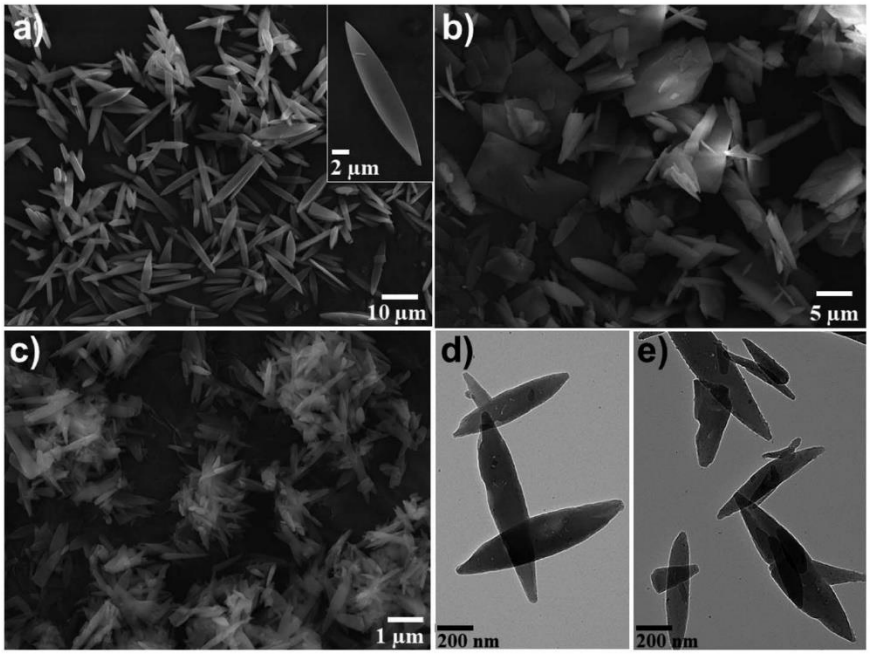

Fig. 2 SEM images of (a) MIL-178(Fe)-*hyd*. The inset shows a higher magnification image of MIL-178(Fe)-*hyd*, (b) MIL-178(Fe)-*re*, and (c) MIL-178(Fe)-*RT*; (d and e) TEM images of MIL-178(Fe)-*RT*.

component, the local environment of the Fe^{3+} site of the minor I_2 component contains water molecules that are located in the pores of this material. Similar results were previously reported for MIL-82(Fe).[39] MIL-178(Fe) was also characterized by thermogravimetric analyses (TGA) under O_2 (Fig. S2†). The first weight loss from 25 °C to 200 °C corresponds to the removal of free water and ethanol trapped in the pores. The second weight loss between 200 and 400 °C follows a two step process and corresponds to the degradation of the framework. The residual Fe_2O_3 content obtained at 400 °C (~15 wt%) is consistent with the chemical formula $Fe(OH)[C_9O_6H_5]_2(C_2H_5OH)_{0.5}$. Temperature-dependent PXRD experiments were performed, thereby confirming that MIL-178(Fe) is stable up to 200 °C (Fig. S3†). Moreover, the absence of any XRD peak shift upon increasing the temperature indicates that the framework of MIL-178(Fe) remains somehow rigid under these conditions. The FT-IR spectrum of MIL-178(Fe) shows the characteristic vibration bands of the coordinating carboxylate functions of 1,2,4-BTC (*i.e.* ν_s(C=O) = 1400 cm^{-1} and ν_{as}(C=O) = 1543 cm^{-1}) and free carboxylate functions at 1703 cm^{-1} (Fig. S4†). Temperature-dependent FT-IR spectra of MIL-178(Fe)-hyd were recorded (Fig. S4†), showing the progressive increase of two vibration bands at 1852 and 1783 cm^{-1} from 125 °C to 225 °C. These two bands at 1852 and 1783 cm^{-1} can be respectively assigned to the asymmetric and symmetric carbonyl groups of the strained anhydride. The concomitant decrease of the vibration band of the free $-CO_2H$ group at 1703 cm^{-1} upon increasing the temperature is in agreement with the condensation of the free carboxylic acid groups into the anhydride. Such a phenomenon was previously reported for other MOFs bearing a pending $-CO_2H$ group grafted in the organic linkers such as UiO-66(Zr)-(CO_2H) and UiO-66(Zr)-(CO_2H)$_2$.[40] According to temperature-dependent PXRD experiments, the formation of anhydrides does not provoke any structural phase transition. Finally, the hydrothermal stability of MIL-178(Fe) was assessed by heating the material under reflux in deionized water for 72 h. The PXRD and TGA analyses of the hydrothermally treated MIL-178(Fe) are comparable to that of the initial MIL-178(Fe) (see Fig. S5†). These results show that MIL-178(Fe) presents a high chemical stability under hydrothermal conditions and does not show any significant flexibility upon water adsorption. Such a strong stability (chemical and thermal) was, in our opinion, rather unexpected as 1D coordination polymers are often thermally unstable and/or suffer from structural collapse upon desolvation while 3D chain related compounds such as MIL-53(Fe) exhibit a higher hydrothermal stability.[12] Most likely, the strong hydrogen bonds between the free –COOH groups lead to stabilization of the framework. The excellent stability of MIL-178(Fe) is therefore of utmost importance for the further practical use of this material for post-combustion CO_2/N_2 separation.

Scale up and control over the particle size of MIL-178(Fe)

The synthetic conditions were then transferred to reflux synthesis in water to tune the crystal sizes of MIL-178(Fe) and enable a multigram scale-up of this material. MIL-178(Fe) could be obtained after heating an aqueous solution of $FeCl_3$ and 1,2,4-BTC under reflux (~100 °C) for 16 h (see the ESI† for details). The PXRD pattern of this phase (*i.e.*, MIL-178(Fe)-*re*) and TGA analysis are fully consistent with that of MIL-178(Fe)-*hyd* (Fig. 3 and S2†). The SEM images of MIL-178(Fe)-*re* show the presence of particles with a high polydispersity in diameter and shape (Fig. 2b). Ellipsoidal particles with the characteristic shape of MIL-178(Fe)-*hyd* are observed but are much smaller with a maximum length of about 5 μm and a diameter of about 3 μm. In addition, micrometer-sized platelets of about 5 × 5 μm are also obtained. Room temperature synthesis was then further explored to form particles with a lower diameter and a narrow particle size distribution. After stirring at room temperature an aqueous solution of $FeCl_3$ and 1,2,4-BTC for 5 days, a bright yellow powder (*i.e.* MIL-178(Fe)-*RT*) was obtained with a good yield (m = 1 g; yield of 81% based on Fe). The PXRD pattern of MIL-178(Fe)-*RT* displays the characteristic Bragg peaks of MIL-178(Fe), but, as expected, are broader in comparison to those of 178(Fe)-*hyd* (Fig. 3). As shown by SEM and TEM, MIL-178(Fe)-*RT* consists of sub-micrometer-sized elongated platelet crystals with a narrow size distribution (Fig. 2c–e). Their mean length, diameter and thickness of about 1 μm, 200 and 20 nm, respectively, are significantly lower than those of MIL-178(Fe) obtained at higher temperatures. Following this synthetic route, MIL-178(Fe)-*RT* could be produced at a large scale (*e.g.*, 30 g in one batch with a yield of 80% based on Fe) by increasing the amount of precursors and the solvent volume by about 30 times.

CO_2/N_2 gas sorption properties of MIL-178(Fe): single-gas adsorption, *in situ* PXRD, CO_2/N_2 coadsorption, and molecular simulations

The adsorption properties of this material were investigated. According to TGA (Fig. S2†), MIL-178(Fe)-*RT* needs to be activated by outgassing the sample to around 383 K in order to remove all the free water or residual ethanol. Single gas adsorption experiments were first performed on MIL-178(Fe)-*RT* samples. According to N_2 sorption at 77 K (Fig. S6†), MIL-178(Fe)-*RT* presents very small N_2 uptake at 77 K, which is consistent with the theoretically calculated small pore volume of 0.18 $cm^3\ g^{-1}$ and pore dimensions (<4.5 Å) of the cavities *vs.* the kinetic diameter of N_2 (3.64 Å). This PCP not only exhibits

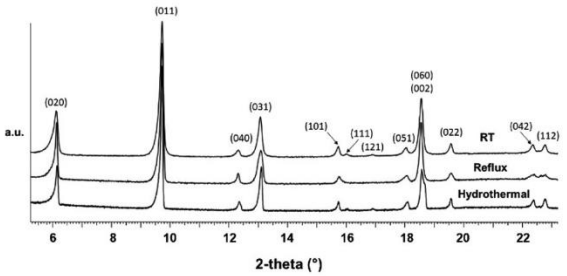

Fig. 3 Powder X-ray diffraction patterns of MIL-178(Fe) synthesized through a hydrothermal process (*i.e.* MIL-178(Fe)-hyd), under reflux (*i.e.* MIL-178(Fe)-re) or at room temperature (RT) (*i.e.* MIL-178(Fe)-RT).

very small pore apertures but also presents a good chemical stability and a framework bearing CO_2 adsorption sites (OH groups). It was thus further envisaged to address the CO_2/N_2 post-combustion separation. Fig. 4 shows the adsorption isotherms of single gas components CO_2 and N_2 obtained at 303 K. Both isotherms are of Type I with a steeper slope at low pressure for CO_2 as compared to N_2. The N_2 amount adsorbed in MIL-178(Fe) is low with a saturation capacity of 0.25 mmol g^{-1} at 10 bar. For CO_2, the adsorption uptakes are 0.6 mmol g^{-1} and 1.2 mmol g^{-1} at 1 bar and 10 bar, respectively. Grand canonical Monte Carlo (GCMC) simulations were further carried out to confirm this experimental trend (see the ESI† for details). As shown in Fig. 4a, the calculated single component CO_2 and N_2 isotherms reproduce well the experimental isotherms at low pressure (<6 bar). The consideration of a fully rigid framework in our GCMC calculations cannot however capture the experimentally observed gradual increment of the uptake amount over a higher pressure range. The GCMC derived snapshots of the spatial arrangements of the adsorbed CO_2 and N_2 molecules at low pressure (Fig. 5a and S10†) show that μ_2-OH groups act as primary adsorption sites for both CO_2 and N_2 molecules. However, the corresponding radial distribution functions (RDFs) reported in Fig. S9† clearly indicate that CO_2 molecules interact much more strongly with the μ_2-OH groups compared to N_2 molecules as evidenced by a shorter mean $O(CO_2)\cdots H(\mu_2\text{-OH})$ distance of 1.8 Å while the $N(N_2)\cdots H(\mu_2\text{-OH})$ mean distance is 2.05 Å. This preferential geometry is at the origin of a simulated adsorption enthalpy at low coverage for CO_2 (35 kJ mol^{-1}) much higher than the value obtained for N_2 (20 kJ mol^{-1}), in line with the experimental adsorption isotherm profiles observed at low pressure. Note that such a moderate adsorption enthalpy is prone to induce an easy reversibility of adsorption–desorption cycles. This is highly desirable for the adsorbent regeneration process as a balance between separation performance and energy cost is required in real adsorption processes. *In situ* PXRD experiments were then performed for various CO_2 pressures up to 10 bar in order to shed light on the possible structural changes of MIL-178(Fe) upon CO_2 adsorption. The whole patterns do not exhibit any drastic modification upon increasing the partial pressure of CO_2 with Bragg peaks showing only an intensity change. This indicates that the overall framework of the material is maintained upon loading with CO_2. A model of MIL-178(Fe) with empty pores was therefore created using the Fox simulated annealing software[41] by starting from the structure solved from single crystal X-ray diffraction in which the solvent molecules were removed. CO_2 molecules were added, and their positions were optimized by using the pattern obtained under the highest CO_2 pressure. Once the position of CO_2 and occupancy at this loading were determined, Rietveld refinement was conducted using the Fullprof/Winplotr software (see the ESI† for details).[42] Sequential Rietveld refinement was then performed at all the experimental CO_2 pressures. On the basis of these *in situ* PXRD data, adsorption/desorption CO_2 isotherms were calculated and compared to the gravimetric sorption data (see Fig. 4b). The good fit at each pressure point suggests that the CO_2 molecules progressively fill the pores without a major change of the host structure or a reorientation of the ligand. Diffraction data

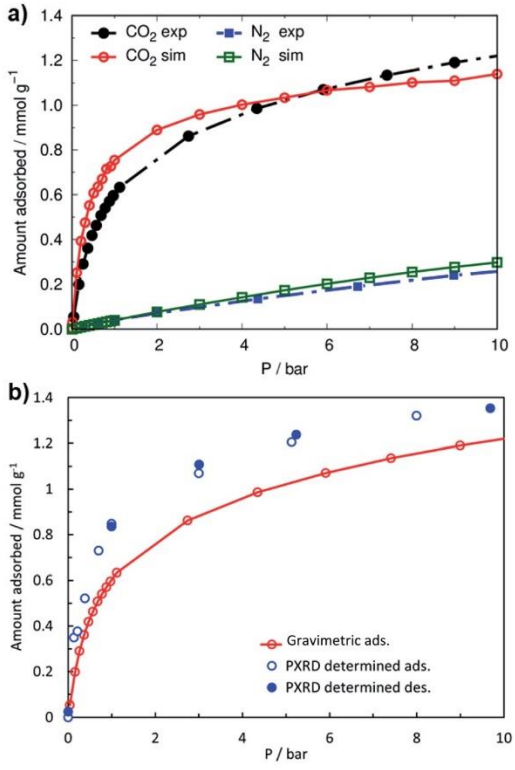

Fig. 4 (a) GCMC calculated and experimental adsorption isotherms for the single components CO_2 and N_2 in MIL-178(Fe)-*RT* at 303 K. (b) PXRD determined adsorption–desorption CO_2 isotherms of MIL-178(Fe)-*RT* in comparison to the experimental adsorption CO_2 isotherm.

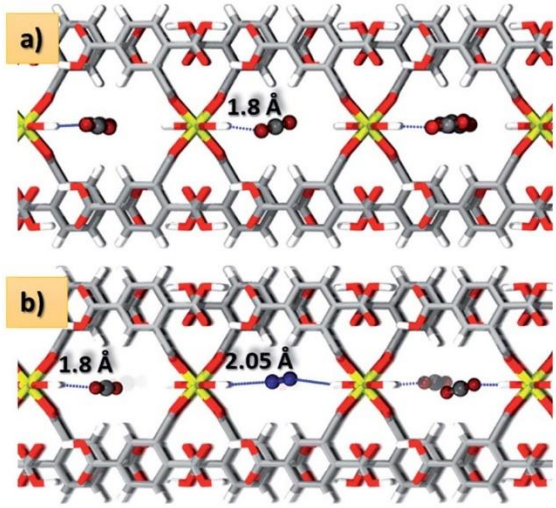

Fig. 5 Microscopic view of the GCMC derived preferential sittings at low pressure for (a) CO_2 molecules as single components and (b) both CO_2 and N_2 molecules in the binary mixture in the 1-D channel of MIL-178(Fe).

suggest that the saturation with CO_2 is reached slightly above the half-filling of the site, and this CO_2 adsorption capacity is slightly higher than that found by gravimetric adsorption isotherm (see Fig. 4). As shown in Fig. 1c, CO_2 molecules could be located in the structure of MIL-178(Fe). The center of the guest CO_2 molecule is located on the mirror plane but the molecules are orientationally disordered outside the plane of symmetry. The closest contacts of CO_2 molecules with the host framework are defined by hydrogen bonds of the hydroxyl group, O(μ_2O)–H$\cdots$O(C), having a H$\cdots$O distance of about 1.82 Å and an O–H$\cdots$O angle of 149 degree, which is fully consistent with the GCMC derived preferential sitting reported in Fig. 5.

Since MIL-178(Fe) shows a simulated adsorption enthalpy difference between CO_2 and N_2 of more than 15 kJ mol^{-1}, it is expected to be attractive for the selective adsorption of CO_2 over N_2. GCMC simulations were thus conducted on the binary mixture with a 15/85 CO_2/N_2 molar composition. The relatively high simulated CO_2/N_2 selectivity value $\sim$80 at 1 bar (see Fig. S11†) confirms the promise of this material for CO_2 capture. Fig. 5b shows that the preferential adsorption site of CO_2 in MIL-178(Fe) remains the same for the CO_2/N_2 mixture as with the CO_2 single component. This prediction motivated us to perform binary mixture adsorption experiments by considering post-combustion CO_2 capture, *i.e.*, for a gas mixture CO_2/N_2 = 10/90 and 15/85 at 1.0 bar and 3.0 bar, *i.e.*, the typical industrial concentration and pressure conditions for the separation of flue gas emitted from power plants. Such real co-adsorption data were rarely reported in the literature.[43] Each mixture point was repeated 3 times giving an average selectivity. A high selectivity value of 116 $\pm$ 16 was obtained at 1 bar and 303 K for CO_2/N_2 = 10/90 and increases further to a value of 145 $\pm$ 15 upon increasing the CO_2 concentration (CO_2/N_2 = 15/85). This selectivity value is comparable with or greater than that of numerous well-known MOFs with low CO_2 heat of adsorption studied under the same conditions while it remains lower than that of a few MOFs recently reported (see Table S2†). By increasing the pressure to 3 bar, the selectivity values decrease but interestingly remain rather high (*i.e.* $S_{EXP} = 66 \pm 5$ for CO_2/N_2 = 10/90).

Processing of the mixed matrix membrane (MMM) for CO_2/N_2 separation

Since MIL-178(Fe) particles present a good colloidal stability in 1-propanol and 1-butanol solvents (see Fig S14†), MMMs were prepared by dispersing MIL-178(Fe)-*RT* in a solution of Pebax®-3533 in a 1-propanol/1-butanol solvent mixture (see the Experimental part for details). Pebax®-3533 is a poly(amide-6-*b*-tetramethylene oxide) block copolymer composed of 70% of a rubbery poly(tetramethylene oxide) (PTMO) block with high affinity towards CO_2 molecules and 30% of a glassy polyamide (PA) block providing mechanical strength.[44–46] This polymer has the advantage to be commercially available and soluble in non toxic alcohol solvents. In the past few years, the series of Pebax polymers was used as a continuous phase in MMMs owing to their promising separation performances resulting from their structural flexibility and solubility-selective gas separation.[47–55] Moreover, a few rubbery Pebax-MOF MMMs have shown better MOF-polymer interfacial properties in comparison to numerous MMMs based on rigid glassy polymers.[47–55] MIL-178(Fe)-Pebax-*X* MMMs with different MIL-178(Fe) contents (X = 5–25 wt%) were fabricated following a two-step protocol (polymer dissolution and filler dispersion followed by casting), as explained in the Experimental section. PXRD patterns of the different MIL-178(Fe)-Pebax-*X* MMMs display the characteristic Bragg peaks of MIL-178(Fe), the intensity of which increases with the amount of MIL-178(Fe) (Fig. 6). This indicates that the crystalline structure of MIL-178(Fe) is preserved upon their association with the polymer. The PXRD pattern of MMMs displays also a broad peak at $2\theta = 20°$ corresponding to the crystalline region of PTMO. The FT-IR spectra of MIL-178(Fe)-Pebax-*X* MMMs (Fig. S15†) present the characteristic vibration bands of both MIL-178(Fe) and Pebax®-3533, in agreement with the incorporation of the PCP in the polymer matrix and with the prevalence of the PCP crystallinity upon the MMM preparation. The morphology of the membranes was investigated by SEM. In contrast to the pure Pebax®-3533 membrane that presents a smooth and homogeneous surface, the surface of MIL-178-Pebax-10 is rougher due to the embedding of well-dispersed MIL-178(Fe) platelets with a random orientation in the polymer matrix as shown in Fig. S16.† However, when the MOF content reached a loading of 15 wt%, the morphology of the MMMs changes drastically. As shown in Fig. 6, the top surface of MIL-178-Pebax-15 is smooth and exhibits a lamellar microstructure. Such layered structuration of the MIL-178-Pebax-15 MMM is also observed in cross-sectional SEM images and is certainly imparted by the stacking of MIL-178(Fe) platelets parallel to the substrate. A similar morphology was observed for the MMM with 25 wt% of MIL-178(Fe)-*RT* (Fig. S16†). The thickness of the MMMs lies between 40 and 45 μm. The thermal stability of MIL-178(Fe)-Pebax-*X* MMMs was evaluated by TGA in comparison to the pure MIL-178(Fe) and bare polymer (see Fig. S17†). First, negligible weight loss below 250 °C shows the removal of any residual solvent in the MMM. The onset decomposition temperatures of MIL-178(Fe)-Pebax-10 and MIL-178(Fe)-Pebax-15 MMMs are slightly higher than that of pure Pebax®-3533 ($\sim$220 °C for the MMM *vs.* 180 °C for neat Pebax®-3533) as a result of the good thermal stability of MIL-178(Fe). In contrast, the thermal stability of MIL-178(Fe)-Pebax-25 is significantly lower than that of MMMs with a lower PCP content and pure polymer. This suggests that the interfacial interactions between the PCP and Pebax®-3533 in MIL-178(Fe)-Pebax-25 are presumably lower than that of MIL-178(Fe)-Pebax-*X* with $X = 10$ and 15. Nevertheless, the overall thermal stability of all MMMs is enough to meet the requirement for CO_2/N_2 separation. The residual amount above 500 °C of the MMMs is consistent with their respective MIL-178(Fe) contents. DSC experiments were performed to evaluate the impact of the MIL-178(Fe) filler on the degree of crystallinity of Pebax®-3533.[47] More precisely, as the DSC curves are characterized by a single endothermic peak corresponding to the melting of the PTMO phase ($T_m^{PTMO} \sim 10$ °C), we have quantified the degree of crystallinity of this phase. This was done for each MMM by calculating the ratio between the enthalpy of fusion (ΔH_f) obtained by integration of the peak

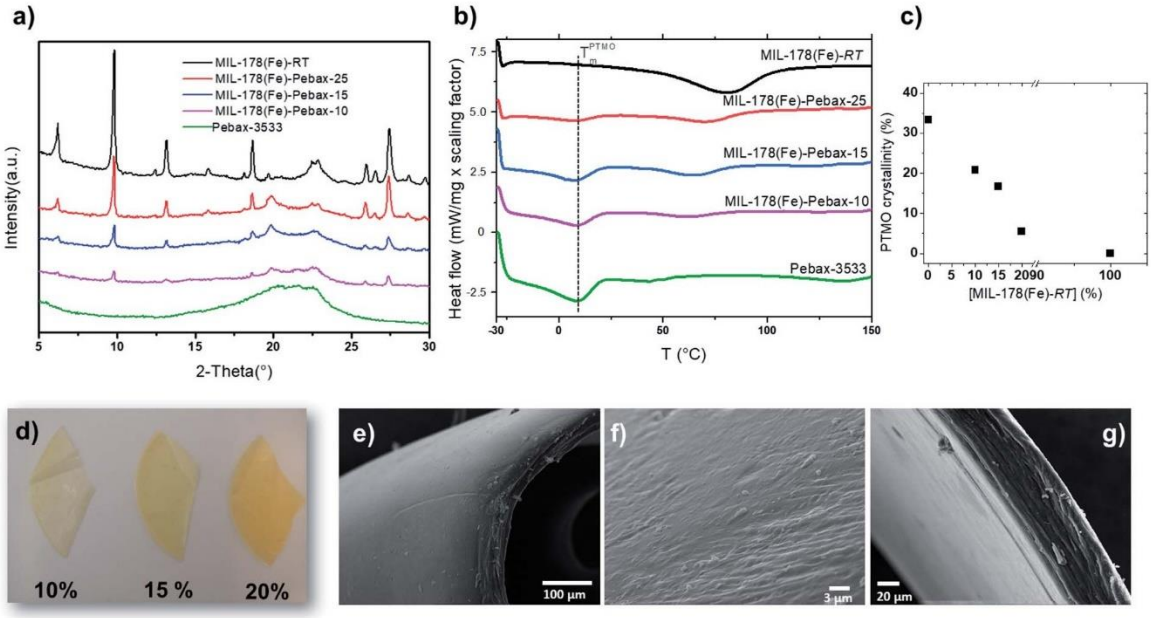

Fig. 6 (a) PXRD of MIL-178(Fe)-Pebax 3533 MMMs in comparison with the pure polymer and MIL-178(Fe)-RT, and (b) DSC curves of neat Pebax®-3533 and typical MIL-178(Fe)-Pebax-*X* MMMs. The curves are shifted vertically for clarity; (c) crystallinity degree of PTMO as a function of the content of MIL-178(Fe)-RT, and (d) photographs of MMMs with different MIL-178(Fe) contents. (e and f) SEM images of the top surface and (g) cross-sectional SEM image of the MIL-178-Pebax-15 MMM.

and the enthalpy of fusion corresponding to a purely crystalline PTMO phase as obtained from the literature ($\Delta H_f^* \approx 200$ J g^{-1})[56] (see the ESI† for details). The plot of the crystallinity degree as a function of the MIL-178(Fe)-*RT* concentration shows a continuous decrease from 33% to 5% when the MIL-178(Fe)-*RT* concentration varies from 0 to 20%. Thus, it appears that MIL-178(Fe)-*RT* inhibits the crystallization of the PTMO phase which should favor a significant softening of Pebax®-3533 considering that this polymer contains 70% of PTMO. Therefore, the addition of MIL-178(Fe) fillers to Pebax-3533 induces the presence of a larger amount of flexible PTMO chains. This is consistent with the mechanical properties of the membranes that were characterized at large deformation by performing tensile tests until failure. Fig. S19† shows the stress-strain curves for the MIL-178(Fe)-Pebax-*X* MMMs with $X = 10$ and 15 in comparison to the pure Pebax®-3533 matrix. Table S3† provides the values of Young's modulus (E), the stress at break (σ_{break}) and elongation at break (e_{break}). Compared to the pure Pebax®-3533 matrix, the mechanical properties of MIL-178(Fe)-Pebax-*X* MMMs are significantly enhanced. These materials are much more extensible, which is consistent with the presence of a larger amount of the rubbery PTMO phase as shown by DSC. Note that the deformability of MIL-178(Fe)-Pebax-15 is slightly lower than that of MIL-178(Fe)-Pebax-10. This can be imparted by the increasing amount of MIL-178(Fe) particles that can act as reinforcing fillers of the polymer as also shown by the higher value of Young's modulus of MIL-178(Fe)-Pebax-15 in comparison to those of the other MMMs. Finally, the long-term chemical stability of the MIL-178(Fe)-Pebax-*X* MMMs with $X = 10$, 15 and 25 was confirmed by PXRD and FT-IR experiments after ageing the composite membranes, under humid ambient air for about 8 months, with no evidence of structural evolution (see Fig. S20†).

Gas separation measurements were carried out by feeding the post-combustion gaseous mixture of CO_2/N_2 (15/85 cm^3(STP) min^{-1}) at an operating pressure of 3 bars to the feed side at 35 °C. A schematic representation of the GC module is given in Fig. S21.† Fig. 7 and Table S4† show the CO_2 permeability and CO_2/N_2 selectivity of MIL-178(Fe)-Pebax-*X* MMMs and pure Pebax®-3533. Remarkably, the addition of MIL-178(Fe) to Pebax®-3533 up to 10 wt% of MIL-178(Fe) led to

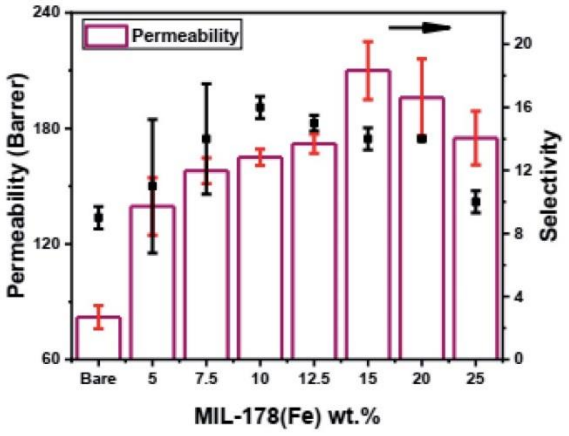

Fig. 7 Permeation analysis of MMMs, and their comparison with the bare polymer membrane.

a significant increase of both the CO_2 permeability and CO_2/N_2 selectivity. The CO_2 permeability of MIL-178(Fe)-Pebax-10 (165 $\pm$ 4 Barrer) increased by a factor of 2 compared to that of the pure Pebax®-3533 (83 $\pm$ 6 Barrer) while the CO_2/N_2 selectivity of MIL-178(Fe)-Pebax-10 (16.0 $\pm$ 0.7) was improved by about 80% in comparison to that of the pure polymer (9.0 $\pm$ 0.7). Further increase of MIL-178(Fe) content to 15 wt% led to membranes with the highest CO_2 permeability (210 $\pm$ 15 Barrer) at the expense of a slight decrease of the CO_2/N_2 selectivity (14.0 $\pm$ 0.7). These results indicate that the inclusion of MIL-178(Fe) fillers in the Pebax-3533 matrix can induce a high increase of both permeability and CO_2/N_2 selectivity values up to about 160% and 80%, respectively, in comparison to the bare membranes. The promising performance of these MMMs can be explained by the high CO_2/N_2 selectivity of the bare MIL-178(Fe) and the good compatibility of the MOF filler with the polymer matrix. Moreover, the ultra-micropores of MIL-178(Fe) are presumably fully accessible to CO_2 molecules since the penetration of polymer chains is not likely to occur in the MOF channels (ϕ < 4.5 Å). To shed light on the solubility and diffusivity contributions of the gas permeation results, time lag experiments were carried out to obtain CO_2 and N_2 single gas permeabilities, and subsequently CO_2 and N_2 diffusivities and solubilities. It is worth mentioning that CO_2 permeability and CO_2/N_2 selectivity values of the bare membrane and MMM obtained by time lag and mixture separation analyses are in good concordance, as shown in Table S5.† Time lag experiments have demonstrated that the inclusion of the PCP in the polymer increases the CO_2 solubility (Table S5†). CO_2 solubility values are 7.3×10^{-2} and 3.3×10^{-1} (cm^3(STP)/(cm^3 cmHg)) for the pure polymer membrane and the MIL-178(Fe)-Pebax-10 MMM, respectively. In contrast, the CO_2 diffusivity decreases (and so does the N_2 diffusivity) from the pure polymer to the MIL-178(Fe)-Pebax-10 MMM from 1.3×10^{-7} to 3.8×10^{-8} cm^2 s^{-1}, in agreement with the narrow microporosity of MIL-178(Fe) and the tortuosity created in the MMM by the addition of the filler particles. Therefore, the enhanced permeability of the MMM in comparison to the pure Pebax®-3533 can be partly explained by the increased content of the more permeable amorphous PTMO (lower crystallinity degree) as was previously reported for a few MOF-Pebax MMMs.[47]

Conclusions

A new water stable 1D microporous coordination polymer, MIL-178(Fe), was discovered, presenting interesting features for CO_2 capture such as hydrothermal and thermal stabilities as well as ultra-micropores decorated with polar OH groups acting as CO_2 adsorption sites. This material was synthesized through an easily-scalable and environmentally friendly protocol with non-toxic reactants, allowing the achievement of the production of a large amount of this material with high yield. Monodisperse MIL-178(Fe) sub-micrometer sized particles were synthesized at room temperature and were used for the preparation of MMMs. The complete characterization of the CO_2/N_2 gas sorption properties of MIL-178(Fe) by combining CO_2/N_2 adsorption/coadsorption experiments, *in situ* CO_2 PXRD and molecular simulations revealed that MIL-178(Fe) presents a moderate CO_2 adsorption capacity at low pressure but retains a high CO_2/N_2 selectivity in the 1–3 bar pressure range due to the high affinity of CO_2 molecules toward μ_2-OH groups located on corner-sharing Fe octahedral chains. MMMs based on MIL-178(Fe) and the Pebax®-3533 elastomer with a PCP loading up to 25 wt% were cast, showing significantly enhanced CO_2/N_2 separation performance in comparison to the pure Pebax®-3533. Such results are likely due to the excellent dispersion of MIL-178(Fe) particles in the polymer matrix with the absence of any interfacial microvoid defects, the enhancement of the MMM CO_2 solubility and the lower crystallinity degree of the Pebax matrix in comparison to the pure polymer. Finally, its excellent stability and cheap composition make this PCP interesting for other separation applications as well as sensing or catalysis.[57]

Author contributions

MB performed the synthesis and characterization of MIL-178(Fe) by PXRD, TGA, FT-IR and N_2 sorption under the supervision of CS and NS. MW and GM performed the molecular simulations. HZ characterized MIL-178(Fe)-RT by TEM and the MMMs by PXRD, FT-IR and TGA under the supervision of NS and CS. MRH prepared the MMMs and studied their gas separation properties under the supervision of MM, CT and JC. AS characterized the MMMs by SEM under the supervision of NS. TS, YF and SH performed the CO_2 pressure-dependent PXRD experiments and related data analysis. JM, AT and WS characterized MIL-178(Fe) by single-crystal X-ray diffraction. JM determined its crystalline structure. JMG characterized MIL-178(Fe) by ^{57}Fe Mössbauer spectrometry. PN, NH and GDW performed the CO_2 and N_2 single gas and co-adsorption experiments. FC characterized the MMMs by DSC and performed the tensile tests on the MMMs. NS wrote the article with the contribution and help of all authors.

Conflicts of interest

There are no conflicts of interest to declare.

Acknowledgements

We acknowledge the European Community Seventh Framework Program (FP7/2007-2013) for funding the research presented in this article under Grant Agreement No. 608490 (Project M4CO2). The computational work was performed using HPC resources from GENCI-CINES (Grant A0100907613).

Notes and references

1 Z. Ji, H. Wang, S. Canossa, S. Wuttke and O. M. Yaghi, *Adv. Funct. Mater.*, 2020, **30**, 2000238.
2 S. Krause, N. Hosono and S. Kitagawa, *Angew. Chem., Int. Ed.*, 2020, **59**, 15325–15341.
3 D. Zhao, P. K. Thallapally, C. Petit and J. Gascon, *ACS Sustainable Chem. Eng.*, 2019, **7**, 7997–7998.

4 J. Li, P. M. Bhatt, J. Li, M. Eddaoudi and Y. Liu, *Adv. Mater.*, 2020, **32**, 2002563.
5 P. Kanti Bharadwaj, P. Feng, S. Kaskel and Q. Xu, *Chem.–Asian J.*, 2019, **14**, 3450–3451.
6 J. W. M. Osterrieth and D. Fairen-Jimenez, *Biotechnol. J.*, 2021, **16**, 2000005.
7 F. Demir Duman and R. S. Forgan, *J. Mater. Chem. B*, 2021, **9**, 3423–3449.
8 M. Ding, R. W. Flaig, H.-L. Jiang and O. M. Yaghi, *Chem. Soc. Rev.*, 2019, **48**, 2783–2828.
9 Z. Hu, Y. Wang, B. B. Shah and D. Zhao, *Adv. Sustainable Syst.*, 2019, **3**, 1800080.
10 R. L. Siegelman, E. J. Kim and J. R. Long, *Nat. Mater.*, 2021, **20**, 1060–1072.
11 R. Luo, M. Chen, X. Liu, W. Xu, J. Li, B. Liu and Y. Fang, *J. Mater. Chem. A*, 2020, **8**, 18408–18424.
12 J. Duan, W. Jin and S. Kitagawa, *Coord. Chem. Rev.*, 2017, **332**, 48–74.
13 H. Assi, G. Mouchaham, N. Steunou, T. Devic and C. Serre, *Chem. Soc. Rev.*, 2017, **46**, 3431–3452.
14 Q. Xia, H. Wang, B. Huang, X. Yuan, J. Zhang, J. Zhang, L. Jiang, T. Xiong and G. Zeng, *Small*, 2019, **15**, 1803088.
15 S. Zhang, Y. Zhang, F. Baig and T.-F. Liu, *Cryst. Growth Des.*, 2021, **21**, 3100–3122.
16 A. Permyakova, S. Wang, E. Courbon, F. Nouar, N. Heymans, P. D'Ans, N. Barrier, P. Billemont, G. De Weireld, N. Steunou, M. Frère and C. Serre, *J. Mater. Chem. A*, 2017, **5**, 12889–12898.
17 S. Cui, M. Qin, A. Marandi, V. Steggles, S. Wang, X. Feng, F. Nouar and C. Serre, *Sci. Rep.*, 2018, **8**, 15284.
18 S. Patra, S. Sene, C. Mousty, C. Serre, A. Chaussé, L. Legrand and N. Steunou, *ACS Appl. Mater. Interfaces*, 2016, **8**, 20012–20022.
19 S. Sene, M. T. Marcos-Almaraz, N. Menguy, J. Scola, J. Volatron, R. Rouland, J.-M. Grenèche, S. Miraux, C. Menet, N. Guillou, F. Gazeau, C. Serre, P. Horcajada and N. Steunou, *Chem*, 2017, **3**, 303–322.
20 C. Serre, C. Mellot-Draznieks, S. Surblé, N. Audebrand, Y. Filinchuk and G. Férey, *Science*, 2007, **315**, 1828–1831.
21 D. Lenzen, J. G. Eggebrecht, P. G. M. Mileo, D. Fröhlich, S. Henninger, C. Atzori, F. Bonino, A. Lieb, G. Maurin and N. Stock, *Chem. Commun.*, 2020, **56**, 9628–9631.
22 M. Pang, A. J. Cairns, Y. Liu, Y. Belmabkhout, H. Chun Zeng and M. Eddaoudi, *J. Am. Chem. Soc.*, 2013, **135**, 10234–10237.
23 S. B. Choi, M. J. Seo, M. Cho, Y. Kim, M. K. Jin, D.-Y. Jung, J.-S. Choi, W.-S. Ahn, J. L. C. Rowsell and J. Kim, *Cryst. Growth Des.*, 2007, **7**, 2290–2293.
24 D. Feng, Z.-Y. Gu, Y.-P. Chen, J. Park, Z. Wei, Y. Sun, M. Bosch, S. Yuan and H.-C. Zhou, *J. Am. Chem. Soc.*, 2014, **136**, 17714–17717.
25 D. Feng, W.-C. Chung, Z. Wei, Z.-Y. Gu, H.-L. Jiang, Y.-P. Chen, D. J. Darensbourg and H.-C. Zhou, *J. Am. Chem. Soc.*, 2013, **135**, 17105–17110.
26 K. Wang, D. Feng, T.-F. Liu, J. Su, S. Yuan, Y.-P. Chen, M. Bosch, X. Zou and H.-C. Zhou, *J. Am. Chem. Soc.*, 2014, **136**, 13983–13986.
27 F. Steinke, A. Javed, S. Wöhlbrandt, M. Tiemann and N. Stock, *Dalton Trans.*, 2021, **50**, 13572–13579.
28 S. Wongsakulphasatch, W. Kiatkittipong, J. Saupsor, J. Chaiwiseshphol, P. Piroonlerkgul, V. Parasuk and S. Assabumrungrat, *Greenhouse Gases: Sci. Technol.*, 2017, **7**, 383–394.
29 E. Soubeyrand-Lenoir, C. Vagner, J. W. Yoon, P. Bazin, F. Ragon, Y. K. Hwang, C. Serre, J.-S. Chang and P. L. Llewellyn, *J. Am. Chem. Soc.*, 2012, **134**, 10174–10181.
30 J.-J. Zheng, S. Kusaka, R. Matsuda, S. Kitagawa and S. Sakaki, *J. Am. Chem. Soc.*, 2018, **140**, 13958–13969.
31 F. Nouar, T. Devic, H. Chevreau, N. Guillou, E. Gibson, G. Clet, M. Daturi, A. Vimont, J. M. Grenèche, M. I. Breeze, R. I. Walton, P. L. Llewellyn and C. Serre, *Chem. Commun.*, 2012, **48**, 10237–10239.
32 T. Devic, F. Salles, S. Bourrelly, B. Moulin, G. Maurin, P. Horcajada, C. Serre, A. Vimont, J.-C. Lavalley, H. Leclerc, G. Clet, M. Daturi, P. L. Llewellyn, Y. Filinchuk and G. Férey, *J. Mater. Chem.*, 2012, **22**, 10266.
33 S. Wang and C. Serre, *ACS Sustainable Chem. Eng.*, 2019, **71**(4), 11911–11927.
34 A. S. Embaye, L. Martínez-Izquierdo, M. Malankowska, C. Téllez and J. Coronas, *Energy Fuels*, 2021, **35**, 17085–17102.
35 G. De Weireld, M. Frère and R. Jadot, *Meas. Sci. Technol.*, 1999, **10**, 117.
36 N. Heymans, S. Vaesen and G. De Weireld, *Microporous Mesoporous Mater.*, 2012, **154**, 93–99.
37 M. Riou-Cavellec, C. Lesaint, M. Noguès, J.-M. Grenèche and G. Férey, *Inorg. Chem.*, 2003, **42**, 5669–5674.
38 S. R. Batten, N. R. Champness, X.-M. Chen, J. Garcia-Martinez, S. Kitagawa, L. Öhrström, M. O'Keeffe, M. Paik Suh and J. Reedijk, *Pure Appl. Chem.*, 2013, **85**, 1715–1724.
39 M. Sanselme, J. M. Grenèche, M. Riou-Cavellec and G. Férey, *Solid State Sci.*, 2004, **6**, 853–858.
40 F. Ragon, B. Campo, Q. Yang, C. Martineau, A. D. Wiersum, A. Lago, V. Guillerm, C. Hemsley, J. F. Eubank, M. Vishnuvarthan, F. Taulelle, P. Horcajada, A. Vimont, P. L. Llewellyn, M. Daturi, S. Devautour-Vinot, G. Maurin, C. Serre, T. Devic and G. Clet, *J. Mater. Chem. A*, 2015, **3**, 3294–3309.
41 V. Favre-Nicolin and R. Cerny, *J. Appl. Crystallogr.*, 2002, **35**, 734–743.
42 J. Rodriguez-Carvajal, *Phys. B*, 1993, **192**, 55–69.
43 M. Benzaqui, R. S. Pillai, A. Sabetghadam, V. Benoit, P. Normand, J. Marrot, N. Menguy, D. Montero, W. Shepard, A. Tissot, C. Martineau-Corcos, C. Sicard, M. Mihaylov, F. Carn, I. Beurroies, P. L. Llewellyn, G. De Weireld, K. Hadjiivanov, J. Gascon, F. Kapteijn, G. Maurin, N. Steunou and C. Serre, *Chem. Mater.*, 2017, **29**, 10326–10338.
44 L. Martínez-Izquierdo, M. Malankowska, J. Sánchez-Laínez, C. Téllez and J. Coronas, *R. Soc. Open Sci.*, 2019, **6**, 190866.
45 L. Wang, Y. Li, S. Li, P. Ji and C. Jiang, *J. Energy Chem.*, 2014, **23**, 717–725.
46 J. H. Kim, S. Y. Ha and Y. M. Lee, *J. Membr. Sci.*, 2001, **190**, 179–193.

47 S. Meshkat, S. Kaliaguine and D. Rodrigue, *Sep. Purif. Technol.*, 2018, **200**, 177–190.
48 A. Sabetghadam, X. Liu, M. Benzaqui, E. Gkaniatsou, A. Orsi, M. M. Lozinska, C. Sicard, T. Johnson, N. Steunou, P. A. Wright, C. Serre, J. Gascon and F. Kapteijn, *Chem.–Eur. J.*, 2018, **24**, 7949–7956.
49 M. Mozafari, R. Abedini and A. Rahimpour, *J. Mater. Chem. A*, 2018, **6**, 12380–12392.
50 S. Meshkat, S. Kaliaguine and D. Rodrigue, *Sep. Purif. Technol.*, 2020, **235**, 116150.
51 N. Liu, J. Cheng, W. Hou, X. Yang and J. Zhou, *J. Appl. Polym. Sci.*, 2021, **138**, e50553.
52 J. Shen, G. Liu, K. Huang, Q. Li, K. Guan, Y. Li and W. Jin, *J. Membr. Sci.*, 2016, **513**, 155–165.
53 J. Deng, Z. Dai, J. Hou and L. Deng, *Chem. Mater.*, 2020, **32**, 4174–4184.
54 N. Habib, Z. Shamair, N. Tara, A.-S. Nizami, F. Hassan Akhtar, N. M. Ahmad, N. Amjad Gilani, M. Roil Bilad and A. Laeeq Khan, *Sep. Purif. Technol.*, 2020, **234**, 116101.
55 C. Song, R. Li, Z. Fan, Q. Liu, B. Zhang and Y. Kitamura, *Sep. Purif. Technol.*, 2020, **238**, 116500.
56 I. J. W. Bowman, D. S. Brown and R. E. Wetton, *Polymer*, 1969, **10**, 715–718.
57 M. Benzaqui, R. Semino, F. Carn, S. Rodrigues Tavares, N. Menguy, M. Giménez-Marqués, E. Bellido, P. Horcajada, T. Berthelot, A. I. Kuzminova, M. E. Dmitrenko, A. V. Penkova, D. Roizard, C. Serre, G. Maurin and N. Steunou, *ACS Sustainable Chem. Eng.*, 2019, **7**, 6629–6639.

Annex-4

International Journal of
Molecular Sciences

MDPI

Article

MIL-100(Fe) Sub-Micrometric Capsules as a Dual Drug Delivery System

Marina Paiva Abuçafy [1], Regina Celia Galvao Frem [2], Giulia Polinario [3], Fernando Rogerio Pavan [3], Heng Zhao [4], Angelika Mielcarek [4,5], Cedric Boissiere [6], Christian Serre [4,*] and Leila Aparecida Chiavacci [1,*]

1 Department of Drugs and Medicines, School of Pharmaceutical Sciences, São Paulo State University (UNESP), Araraquara 14801-902, Brazil; marina.abucafy@gmail.com
2 Institute of Chemistry, Inorganic Chemistry, São Paulo State University (UNESP), Araraquara 14800-060, Brazil; regina.frem@unesp.br
3 Department of Biological Sciences, School of Pharmaceutical Science, São Paulo State University (UNESP), Araraquara 14801-902, Brazil; gpolinario@gmail.com (G.P.); fernando.pavan@unesp.br (F.R.P.)
4 Institut des Materiériaux Poreux de Paris, ESPCI Paris, École Normale Supérieure, CNRS, PSL University, 75005 Paris, France; zhao.heng@ens.psl.eu (H.Z.); angelika.mielcarek@gmail.com (A.M.)
5 NanoBioMedical Centre, Adam Mickiewicz University, 61-614 Poznan, Poland
6 Laboratoire de Chimie de la Matière Condensée de Paris (LCMCP), Collège de France, PSL, UMR 7574, Sorbonne Université, CNRS, 4 Place Jussieu, 75005 Paris, France; cedric.boissiere@upmc.fr
* Correspondence: christian.serre@espci.fr (C.S.); leila.chiavacci@unesp.br (L.A.C.)

Abstract: Nanoparticles of metal–organic frameworks (MOF NPs) are crystalline hybrid micro- or mesoporous nanomaterials that show great promise in biomedicine due to their significant drug loading ability and controlled release. Herein, we develop porous capsules from aggregate of nanoparticles of the iron carboxylate MIL-100(Fe) through a low-temperature spray-drying route. This enables the concomitant one-pot encapsulation of high loading of an antitumor drug, methotrexate, within the pores of the MOF NPs, and the collagenase enzyme (COL), inside the inter-particular mesoporous cavities, upon the formation of the capsule, enhancing tumor treatment. This association provides better control of the release of the active moieties, MTX and collagenase, in simulated body fluid conditions in comparison with the bare MOF NPs. In addition, the loaded MIL-100 capsules present, against the A-375 cancer cell line, selective toxicity nine times higher than for the normal HaCaT cells, suggesting that MTX@COL@MIL-100 capsules may have potential application in the selective treatment of cancer cells. We highlight that an appropriate level of collagenase activity remained after encapsulation using the spray dryer equipment. Therefore, this work describes a novel application of MOF-based capsules as a dual drug delivery system for cancer treatment.

Keywords: MOF capsules; dual release systems; enzyme encapsulation

Citation: Abuçafy, M.P.; Frem, R.C.G.; Polinario, G.; Pavan, F.R.; Zhao, H.; Mielcarek, A.; Boissiere, C.; Serre, C.; Chiavacci, L.A. MIL-100(Fe) Sub-Micrometric Capsules as a Dual Drug Delivery System. *Int. J. Mol. Sci.* **2022**, *23*, 7670. https://doi.org/10.3390/ijms23147670

Academic Editor: Mario Ledda

Received: 25 May 2022
Accepted: 27 June 2022
Published: 12 July 2022

1. Introduction

Metal–organic frameworks (MOFs) are crystalline hybrid porous materials comprised of metal ion nodes and organic linkers with exceptional structural and chemical diversity. These have gained significant attention for various applications (e.g., separation, catalysis, sensing, etc.) due to their attractive properties, which include high porosity, large surface area and structural stability [1–3]. In biomedicine, biocompatible MOFs are attractive candidates, particularly for drug delivery and imaging, due to their record drug loading and, in some cases, controlled delivery under body fluid conditions [4].

Biocompatible MOFs possess pore sizes typically within the micro- or mesoporous domain, e.g., within the 0.3–4 nm range, which restrict their ability to encapsulate large bioactive molecules, such as proteins. Capping of the external surface of MOF NPs is still a possibility, but such a strategy is associated both with challenges in surface modification to avoid any burst release as well as loading limitations. Therefore, to overcome this, developing new drug delivery systems (DDS) comprising MOF capsules has been proposed very

recently due to their desirable properties, including large cavities, selective permeability and high stability [5,6]. This hierarchical system allows the incorporation of a large amount of a drug while enabling the loading, within the capsule, of a significant amount of macromolecules, such as proteins, carbohydrates, lipids, nucleic acids and enzymes. This enables the drug to be administered in combination with a bioactive molecule that acts in synergy, such as a drug and a protein, thereby increasing the efficiency of the treatment.

MOF capsules with a controlled chemical composition can be synthesized using several methods, including solid mold [7], liquid mold [5] and Pickering emulsion [8]. Such techniques are indeed not suitable for preparing a large amount of sub-micrometric capsules. For instance, the use of emulsion to synthesize capsules is far from being straightforward to directly prepare reproducible capsules based on MOF NPs due to the complexity of preparation using polar/nonpolar solvents and surfactants as well as stability issues. Besides these limitations, the synthesis of MOF capsules still suffers from many additional challenges, such as achieving good chemical and mechanical stability, without any coalescence as well as a robust simple and scalable production method of capsules associated with a controlled superstructure.

The spray-drying method offers many advantages to sort out these issues. This method allows the production of chemically homogeneous droplets containing pre-formed MOF NPs with no need for any additional immiscible toxic solvents, surfactants, polymers or the use of sonication [9]. Herein, we have selected spray-drying as a rapid, low-cost and scalable green route for the synthesis of MOF capsules of a sub-micrometric size with controlled hierarchical porosity. The technique has previously been used to produce dry suspensions, encapsulate biomolecules for pharmaceutical applications [10] and synthesize MOF NPs [11,12], and it is also suitable to develop a spherical hierarchical pore system from a suspension of dispersed MOF NPs to produce small-size MOF NPs capsules. Furthermore, spray-drying is a common technique used for the encapsulation of drugs and bioactive molecules in materials capable of protecting them and increasing their stability, releasing them in a controlled manner in the body, with the possibility of association with other drugs [13].

Among all the MOFs nanocarriers reported to date, the mesoporous iron trimesate MIL-100(Fe) (MIL stands for Materials from Institute Lavoisier) is one of the most promising MOFs in biomedicine due to its very high porosity, open metal sites as well as its lack of toxicity due to its bio-friendly composition and biodegradable character [14,15]. Previous studies indicated that MIL-100(Fe) NPs are stable in aqueous and ethanolic solution but degrade progressively in simulated biological media, particularly at pH 7.4 [16,17]. However, we hypothesize here that aggregating MOF NPs to form a porous capsule by spray-drying can interfere with the rate of degradation of the nanoparticles, and, thus, the release of the drugs, while enabling the enzyme to be incorporated within the additional mesopores from the capsule (interparticular and internal cavities). Moreover, the MIL-100(Fe) micronic capsules should be ideal candidates for oral or intraperitoneal administration routes but are not suitable for intravenous administration [18]. The closer system reported in the literature is a simple composite material made of ~125 nm MIL-100(Fe) submicronic particles, aggregated with carbohydrates by spray-drying [19].

Herein, we propose the synthesis and processing of MIL-100(Fe) hierarchical submicronic capsules as a dual drug delivery system coupling an efficient anticancer drug with an enzyme, potentializing the drug efficiency in vivo. The material reported and tested here is structurally more sophisticated than previously described spray-dried MOFs. The encapsulated drug and enzyme are localized in different porous cavities of the capsule in order not to interfere in terms of loading while slowing down their release. Methotrexate (MTX) is an antimetabolite chemotherapeutic agent specific for growing cell populations, such as tumor cells; collagenase (COL) is an enzyme that also acts as a protector against tumor progression and metastasis due to its ability to enhance degradation of the dense extracellular matrix (ECM) surrounding tumor cells. MTX was encapsulated in the mesopores of MIL-100(Fe) NPs from an aqueous solution prior to the uptake of collagenase directly

into the interparticular cavities of MOFs colloids during the formation of the MIL-100 capsules by spray-drying. This resulted in the formation of MTX@COL@MIL-100 capsules that may have a potential application in the selective treatment of cancer cells.

2. Results

In order to prepare the MIL-100(Fe) capsules, preformed MIL-100(Fe) NPs were synthesized separately at ambient temperature, as previously reported by our group [20]. All characteristics were, on the whole, in agreement with previous results, including a BET surface area of 1300 $m^2\ g^{-1}$. The nanoparticles exhibited a mean diameter of 80 ± 30 nm, as determined by dynamic light scattering (DLS) (Figure S1), 66 ± 12 nm, as determined by transmission electron microscopy (TEM) (Figure 1D) associated with a ζ potential (deionized water) of −24 ± 0.6 mV, consistent with the literature [16,17]. Furthermore, the nitrogen physisorption of MIL-100(Fe) NPs exhibited BET surface area and BJH pore size distribution according to what was previously reported in the literature, as shown in Figure S2.

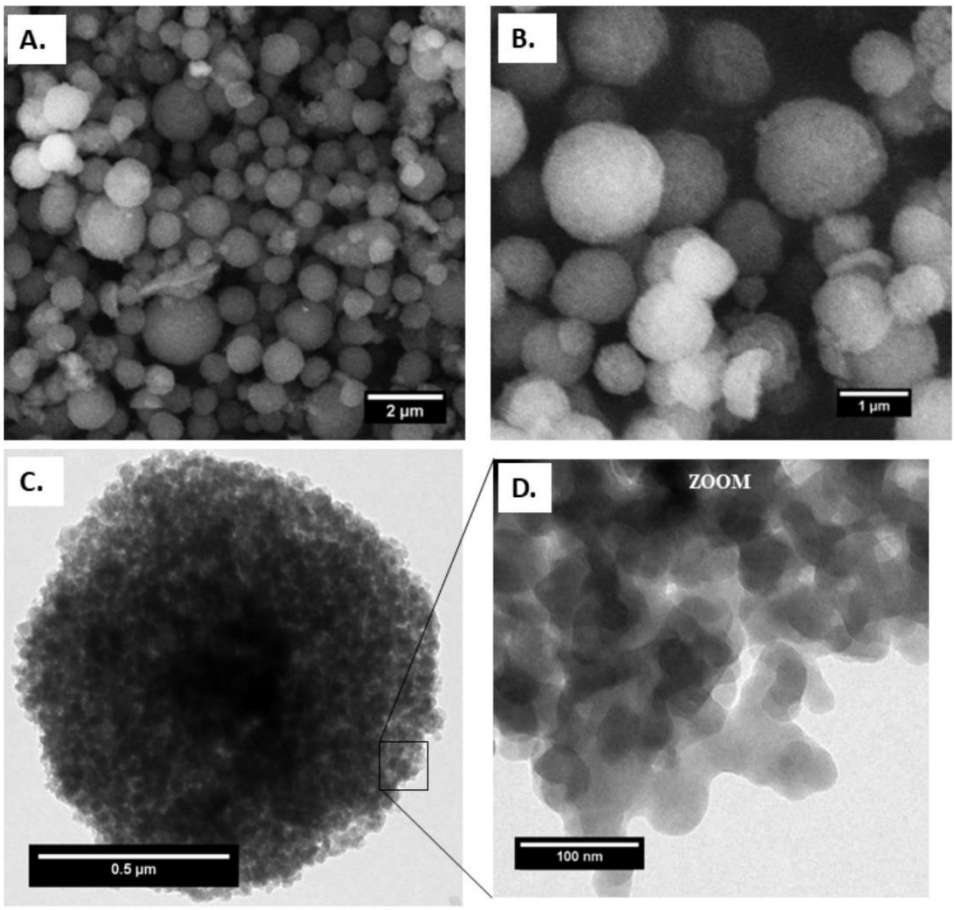

Figure 1. (**A**) and (**B**) field emission gun scanning electron microscopy (FEGSEM), (**C**) transmission electron microscopy (TEM) images of capsules and (**D**) MIL-100(Fe) NPs on the capsule surface.

The resulting MIL-100(Fe) capsules preserved the crystallinity of MIL-100, as confirmed by PXRD and FTIR studies, in comparison with the pre-formed MIL-100(Fe) NPs (Figures S3 and S4). Nitrogen physisorption measurements on the capsules indicated a porosity similar to that of the bare nanoparticles, with a measured surface area of 1613 $m^2\ g^{-1}$, with micropore and mesopore volumes of 0.64 (calculated via t-plot) and 0.85 $cm^3\ g^{-1}$ (calculated via BET).

A complete study of the morphology and structure evolution of the MIL-100(Fe) capsule was performed by electron microscopy. The SEM and TEM images of MIL-100 capsules, shown in Figure 1, confirm the homogeneous non-hollow materials and reveal the absence of any significant cracks or defects.

Figure 1A,B show the external structure of the spray-dried capsules. SEM shows that the latter exhibit a spherical shape with an average diameter of 800 nm, as shown in Figure S5. In addition, the constitutive MIL-100(Fe) NPs exhibit the same size and morphology as the bare nanoparticles, being ca. 70 nm in diameter, as shown in Figure 1D.

In order to further investigate the microstructure of the capsule, focused Ga^+ ion beam (FIB) SEM analysis was carried out. Hence, FIB/SEM is an ideal combination of high-resolution nanoparticle imaging slices. A slice of the capsule was first produced, leading to a plane cutting through it, and imaging evidenced the presence of large cavities, as shown in Figure 2.

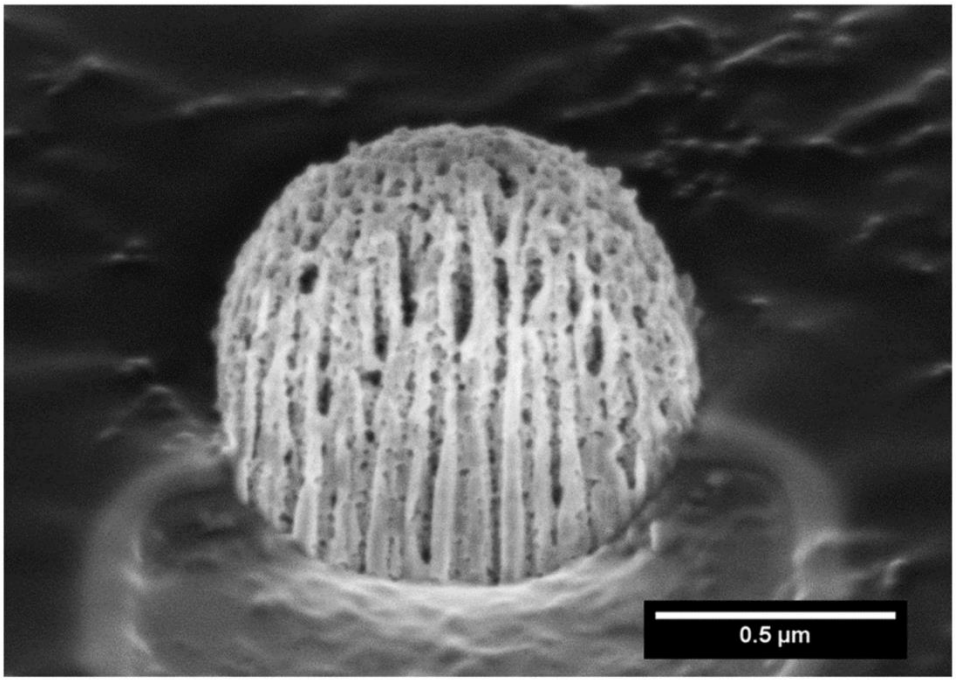

Figure 2. Focused ion beam scanning electron microscopy (FIB-SEM) of a MIL-100 capsule slice.

After complete characterization of the material, the drug MTX and the collagenase enzyme were incorporated into the MIL-100 capsule. The crystalline structure of the MOF remained intact after the loading experiments with little changes in the PXRD patterns in comparison with the starting nanoparticles (Figure S6A) [14].

The presence of MTX and collagenase in the structure of the capsule was further confirmed by FTIR spectroscopy (Figure S6B). The spectrum of the MTX@COL@MIL-100 capsule (blue line in Figure S6B) shows bands of the drug, such as the one at 1616 cm^{-1} attributed to the C=O stretching mode of MTX molecules. In addition, a band at 1504 cm^{-1}, attributed to N-H bending of the amidic group, as well as the one of the –C–O stretching of the carboxylic group of MTX, was displaced from 1268 cm^{-1} for the encapsulated material. The IR spectrum of the MIL-100 capsules (red line in Figure S6B) was also similar to that of the MIL-100 capsule with collagenase (blue line in Figure S6B), except for the latter additional band characteristics of the enzyme, i.e., amide I at 1651 cm^{-1} (mainly from C=O stretching), amide II at 1547 cm^{-1} and amide III at 1238 cm^{-1}. This confirmed the presence of collagenase in the MOF capsule, even after the washing steps.

The porosity of the capsule was also analyzed by N_2 porosimetry and compared with bare MIL-100(Fe) nanoparticle and also before and after the encapsulation, as shown in

Figure 3. Figure 3B compares the pore size distribution (PSD) of the MIL-100(Fe) capsules and the different loaded samples prepared. The two peaks correspond to the pore diameter of MIL-100(Fe) meso- and micro-sized internal cavities (≈2.4 and 1.58 nm).

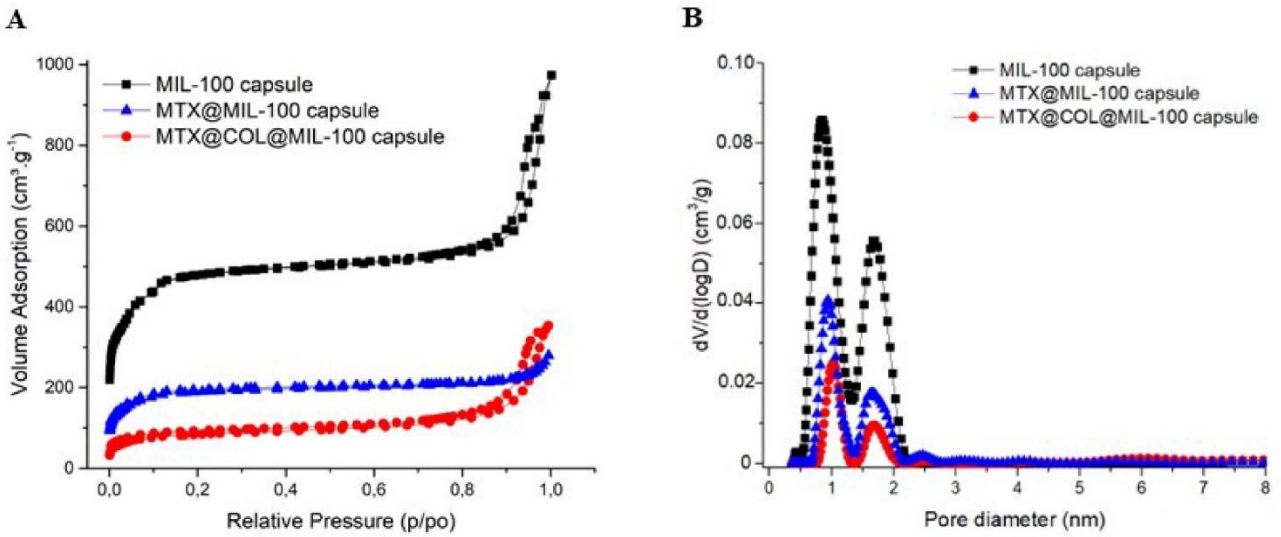

Figure 3. Nitrogen sorption isotherms (**A**) and pore size distribution curves (**B**) at 77K (Po = 1 bar) of MIL-100 capsules (black), MTX@MIL-100 capsules (blue) and MTX@COL@MIL-100 capsules (red).

The SEM and TEM micrographs of the MTX@COL@MIL-100 capsule are shown in Figure 4. The MIL-100 capsules showed well-defined particles with a homogenous density, while moderately electron-dense spots could be seen through the MTX@COL@MIL-100 capsule (Figure 4B), possibly associated with the presence of collagenase (or MTX agglomerates) inside the MOF capsules.

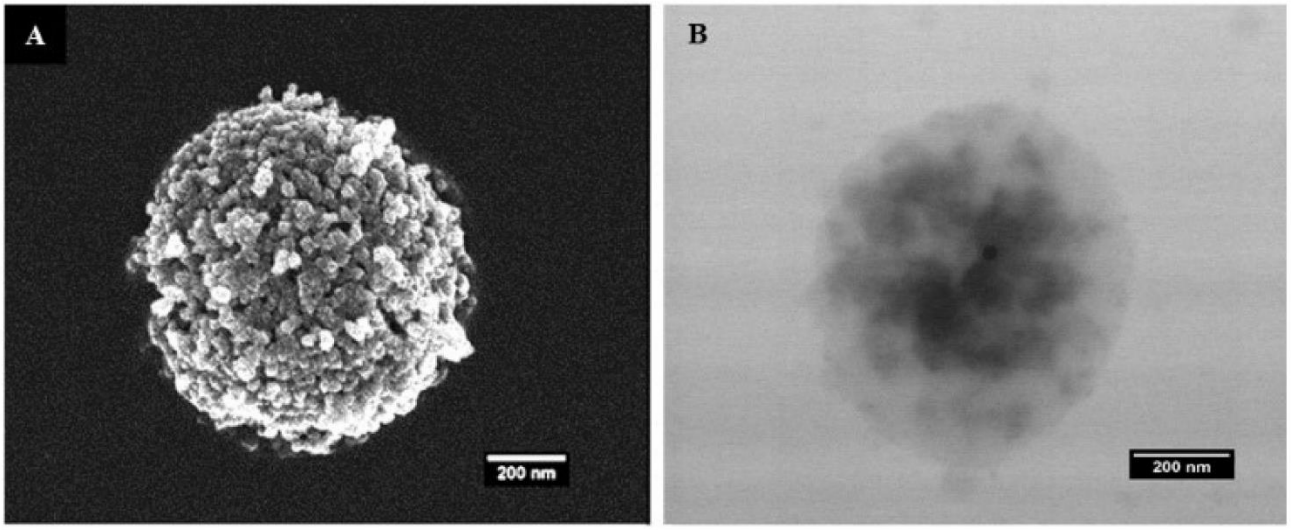

Figure 4. (**A**) field emission gun scanning electron microscopy (FEGSEM) and (**B**) transmission electron microscopy (TEM) images of MTX@COL@MIL-100 capsule.

The MTX entrapment efficiency (EE%) in MIL-100 NPs was 50.3%. The structural integrity of the MOF was kept after encapsulation of MTX, while the residual porosity was low due to the drug loading (see characterizations in the Supplementary section).

In a second iteration, MTX@MIL-100(Fe) NPs were added to a collagenase ethanolic suspension and the mixture was pumped into a spray dryer. The liquid fed into the spray dryer produced fine atomized droplets. These droplets were injected into a drying gas chamber, where vaporization occurred with outlet air temperature of 45 °C. Considering that the residence time in the drying chamber is between two and three seconds (estimated from the dry air flow rate and the volume of the drying chamber), the drying process has a small impact and should not significantly denature the collagenase [21], which was confirmed by the enzymatic activity experiment. After drying, MTX@COL@MIL-100 capsules were formed. The EE% of collagenase in the MIL-100 capsules was 91.74%, which demonstrates the high encapsulation yield of this process. We, therefore, demonstrated the ability of these MOFs capsules to be a high loading dual delivery system for active drugs and enzymes, collagenase and MTX in this case. During this step of the experiment, we carefully prepared capsules by spray-drying in a maximum period of 30 min, considering that MTX would almost not be released during this process, as shown in the MTX release curve in Figure 5.

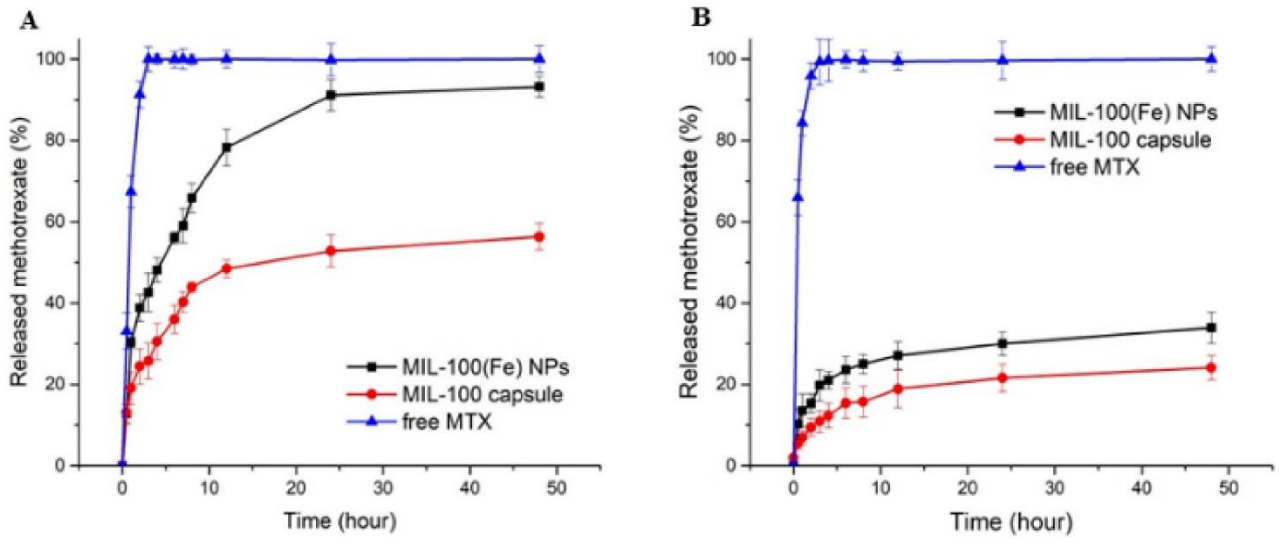

Figure 5. Release profiles of MTX at 37 °C from MIL-100(Fe) NPs and MIL-100 capsules in PBS at pH 7.4 (**A**) and pH 5 (**B**).

At pH 7.4 (Figure 5A), the drug release from MTX-loaded capsules exhibits a lower degree of initial burst release when compared to the bare nanoparticles and, furthermore, the drug continues to be released from the capsule after this period. In addition, the cumulative drug release within 48 h reaches approximately 93% for the MIL-100 NPs, against ca 50% for MIL-100 capsules. Nanoparticles have very large surface area to volume ratios compared to the capsules, and, therefore, the hierarchical packing of MIL-100(Fe) colloids into capsules can slow down the MIL-100(Fe) degradation from the phosphate anions present in the medium associated with the drug release, ultimately resulting in slower MTX release. At pH 5.0 in the first 4 h, only 12% and 21% of the drug were released from the MIL-100 capsules and the bare nanoparticles, respectively, while the maximum amounts of MTX released from the MIL-100 capsules and bare nanoparticles after 48 h were only about 24% and 34%, respectively.

The collagenase release profiles from collagenase-loaded MIL-100 capsules (pre-loaded with MTX) at pH 7.4 and pH 5 are shown in Figure 6.

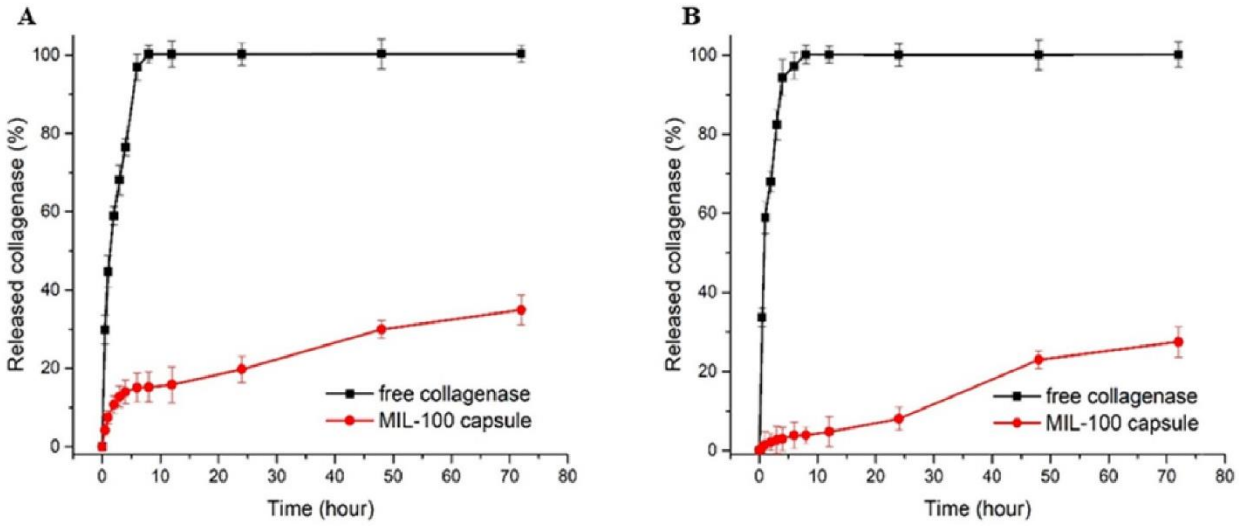

Figure 6. Collagenase release profiles from free enzyme and collagenase-loaded MIL-100 capsules at pH 7.4 (**A**) and pH 5 (**B**).

In detail, one can observe a tiny burst release at the early stage of the delivery, with about 15.4% of the collagenase released from the MIL-100 capsules within the first 8 h. Between 8 and 12 h, the release profile was stabilized, and, after 12 h until the end of the assay (72 h), an 18% increase in the enzyme release was observed. At pH 5.0, the initial burst release was decreased to only 3.8%, while, after 24 h, the maximum amount released was only 26.9%, which is 8% less than the value obtained at pH 7.4. The tumor tissue environment is moderately acidic compared to healthy cells; therefore, a pH-responsive drug delivery system may reduce the undesirable effects related to drug transport in blood circulation and improve anticancer drug delivery to the tumor tissue.

The kinetic MTX and COL release profiles were further fitted using the following mathematical models, using the Sigma Plot10.0 software (Systat Software, San Jose, CA, USA): Korsmeyer–Peppas, Higuchi, Hixson–Crowell, first order and Weibull. The kinetic release values are shown in Tables S3–S5. The MTX and COL release from the MIL-100 NPs and MIL-100 capsules at both pH values showed a strong correlation with the Korsmeyer–Peppas model. Values of η between 0.45 and 0.89 represent cases of anomalous or non-Fickian transport.

In vitro activity experiments were carried out to verify the properties of the dual MOF capsule carrier system. The enzymatic activity of collagenase released from the MTX@COL@MIL-100 capsule on gelatin degradation was first measured, as shown in Figure 7. It was found that pure gelatin solidifies back to a hydrogel at 4 °C (group 1). In addition, gelatin could still form a steady hydrogel at low temperature even after co-incubation with empty MIL-100 capsules (group 2), free MTX (group 5) and MTX@MIL-100 capsules (group 6) for 24 h, indicating that these samples could not degrade gelatin. However, gelatin co-incubated with free collagenase (group 4) remained in a liquid state after 3 h, while the one co-incubated with COL@MIL-100 capsule (group 3) or MTX@COL@MIL-100 capsule (group 7) maintained a liquid state for between 12 and 24 h from the beginning of the assay.

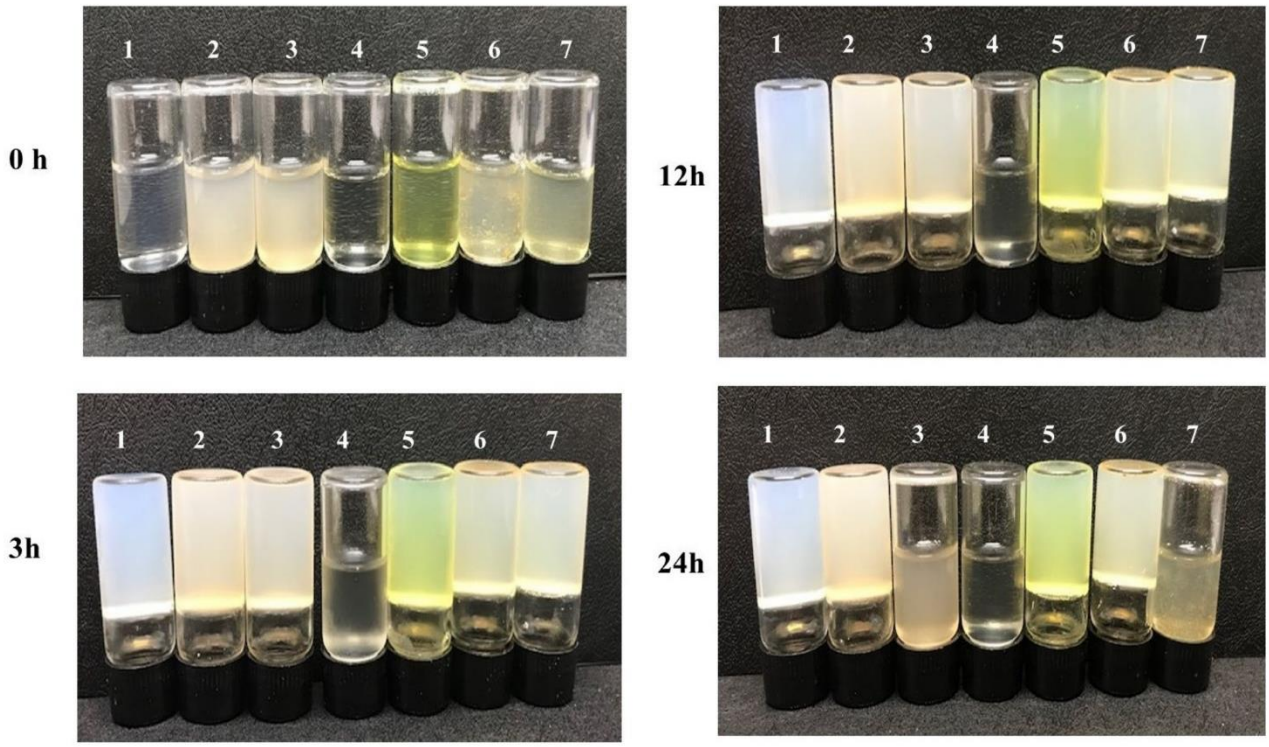

Figure 7. Gelatin solution cocultured with each sample at 37 °C and then stored at 4 °C for 3, 12 or 24 h; (**1**) pure gelatin; (**2**) MIL-100 capsule; (**3**) COL@MIL-100 capsule; (**4**) collagenase; (**5**) MTX; (**6**) MTX@MIL-100 capsule and (**7**) MTX@COL@MIL-100 capsule.

To confirm the possibility of using this system for drug delivery, cytotoxicity tests were performed using the resazurin assay, which estimates the metabolic activity of living cells by the quantitative conversion of the reagent into a fluorescent indicator. These tests were carried out between concentrations of 0.586 μg/mL and 150 μg/mL, and the IC_{50} and selectivity index (SI) values obtained in this study are shown in Table 1.

Table 1. Results of the IC_{50} (μg/mL) and selectivity index (SI).

Sample	IC50		SI
	A-375	HaCaT	HaCaT/A-375
MTX	10.37 ± 5.1	>150.00 ± 0.0	>14.46
MIL-100 capsule	69.33 ± 5.5	>150.00 ± 0.0	>2.16
MTX@MIL-100 capsule	16.29 ± 2.0	>150.00 ± 0.0	>9.21
MTX@COL@MIL-100 capsule	13.06 ± 7.9	>150.00 ± 0.0	>11.48
COL@MIL-100 capsule	18.99 ± 14.7	>150.00 ± 0.0	>7.90
Collagenase	>150.00 ± 0.0	>150.00 ± 0.0	1
DMSO	>150.00 ± 0.0	>150.00 ± 0.0	1

All the samples revealed toxicity (IC_{50} values) in the A-375 cell line; however, for the normal cell line, HaCaT, no toxicity was observed, even at the highest concentration tested, confirming its safety. The hollow MIL-100 capsule showed an IC_{50} value of approximately 70 μg/mL for the A-375 cell line, and, after encapsulation of MTX or collagenase, the IC_{50} decreased, as expected, to 16 and 19 μg/mL, respectively. Furthermore, the IC_{50} value for the capsule with the dual encapsulation of collagenase and MTX was 13 μg/mL for the tumor cell line, in agreement with a synergetic effect of both MTX and collagenase.

3. Discussion

The synthesis of the MOF capsule was possible due to some intrinsic properties of MIL-100(Fe) NPs. Therefore, the negative surface charge, attributed to the free carboxylate groups from the trimesic acid linkers exposed on the outer surface of the MOF NPs, suggests that electrostatic repulsion forces helped to avoid rapid aggregation on the capsule formation process during the spray-drying.

The spray-drying method enabled the formation of hot water droplets containing the MIL-100(Fe) NPs and the drugs loaded. The process starts with the atomization of the precursor solution to form micron- and submicron-size droplets using a two-fluid nozzle (mixing fluid and air). Precursor droplets came into contact with a turbulent hot gas stream with outlet air in 45 °C, promoting a rapid solvent evaporation. In each droplet, all the constituents move both by diffusion and convection, while the droplet diameter decreases with evaporation, resulting in the rapid formation of capsules made of MIL-100(Fe) NPs stacked concentrically with each other. To benchmark our spray-drying technique with results previously reported by some of us [11], we initially focused on the most important input parameters, such as the solid concentration (1 $mg{\cdot}mL^{-1}$), the drying gas inlet temperature (80 °C), the solvent type (ethanol) and the drying gas flow rate (0.05 $mL{\cdot}min^{-1}$), aiming to form nano-micrometric and spherical capsules. The adjustment in the gas inlet temperature influences the evaporation rate, thus transfer of suspended constituents from the surface to the deepest area inside the drop, and this can create hollow spaces in the particle. In this study, the temperature used, outlet temperature of 45 °C, was judiciously low, high enough to evaporate the aqueous suspension and low enough for limiting the degradation of the enzyme [22].

The TEM and SEM images, as shown Figures 1 and 4, confirm that the selected low-temperature spray-drying conditions enabled the gentle aggregation of pre-formed MIL-100(Fe) NPs without using emulsion, most commonly used in the literature [12,23].

We highlight here that this processing procedure produces non-hollow particles, which allows adjusting the final particle size simply by adjusting the concentration of the MIL-100 nanoparticle suspension. This point is of crucial importance for it allows easily tuning the aerodynamic diameter of the particles if optimized lung delivery is targeted, which is not the case in the article previously reported, in which dextran and alpha cyclodextrine/MIL-100 spray-dried particles, as reported previously, are hollow and, thus, for which the density is not a priori predictable and changes with the particle diameter [19]. In addition, nitrogen physisorption measurements, shown in Figure 3 and S2, confirmed that the spray-drying process does not affect the textural quality of the previously synthesized MOFs. The N_2 sorption isotherm of the MIL-100 capsules is associated with a combination of the intrinsic micro/mesoporosity of the bare nanoparticles and the additional interparticular porosity of the voids between the nanoparticles aggregates delimiting the capsules. The FIB/SEM of the capsule slice also showed large cavities (Figure 2), which are of a strong interest for carrying large active biomolecules, such as collagenase.

These cavities, combined with the intrinsic micro/mesopores from the MIL-100 constitutive particles, comprise a promising hierarchical pores carrier for the controlled delivery of a large variety of drugs and biomolecules to treat cancer. As a proof of concept, we first selected MTX, a folate antimetabolite and potent anticancer molecule that interacts with the reduced folate carrier and the folate receptor, which is overexpressed on the surface of several types of cancer cells [24,25]. Furthermore, to take advantage of the large voids from the capsule, we also selected the COL, which is part of a group of enzymes called proteases that have the ability to hydrolyze peptide bonds. These enzymes are used in cancer therapies to degrade extracellular proteins and tumor cell growth factors, thereby preventing tumor progression and metastasis [26]. Therefore, this MOF-based capsule system with a multi-modal porosity represents a promising strategy to associate two bioactive molecules into a single material, known as a dual delivery system [27,28].

The MTX encapsulation was higher than what has been previously reported in the literature by other nanocarriers. For example, Trotta et al. reported an EE% in liposomes

of 39.6%, while another group showed an EE% of only 10.2% for silver nanoparticles coated with PEG [29]. These results confirm the excellent capacity of MIL-100 NPs to incorporate a large amount of this drug. The structural integrity of the MOF was maintained after encapsulation of MTX, while the residual porosity was low due to the drug loading (Figure S6 and Table S2). Besides that, the high encapsulation of collagenase in the MIL-100 capsules demonstrates the ability of these MOFs capsules to be a high loading dual delivery system for active drugs and enzymes, collagenase and MTX in this case.

The porosity of the capsule analyzed by N_2 porosimetry properties (please see Table S2) showed a decrease in the specific surface area of the capsule, which can be justified by the incorporation of a large amount of MTX and collagenase. Besides that, the incorporation of the drug and collagenase led to an even stronger decrease in pore volume, as expected.

The SEM and TEM micrographs of the MTX@COL@MIL-100 capsule, presented in Figure 4, show that the spherical morphologies of the capsules were maintained after drug and enzyme encapsulation.

In drug release experiments, whose results are shown in Figures 5 and 6, the higher release in MIL-100 NPs is justified by large surface area to volume ratios compared to the capsules, and, therefore, the hierarchical packing of MIL-100(Fe) colloids into capsules can slow down the MIL-100(Fe) degradation from the phosphate anions present in the medium associated with the drug release, ultimately resulting in slower MTX release. At pH 5.0, an even slower and lower MTX release rate is observed in comparison with the profile at pH 7.4, as expected from these iron MOFs that are more stable under acidic conditions. Briefly, the amount of drug released in a more acidic environment was approximately half the amount of drug released at pH 7.4. This is mainly due to the greater stability of MIL-100 in an acidic medium, which is in line with previous studies that showed that MOF NPs progressively release their ligand in neutral PBS, whereas, in acidic conditions, the degradation kinetics was much lower [16,17]. Therefore, these results highlight that MTX is released slowly from the MIL-100 capsules in a simulated physiological medium, in favor of their use as advanced controlled release systems.

Noteworthily, in both cases, at pH 7.4 and 5, the release profiles are, on the whole, in agreement with a very slow release of collagenase. Further, the collagenase is in the interparticle space MIL-100(NPs), suggesting that it may be located more superficially or deeper in the capsule. The initial release can tentatively be attributed to the presence of the enzyme in cavities close to the outer surface of the capsule. The release profile stabilizing between 8 and 12 h of the experiment is due to the enzyme located within the internal cavities of the capsules. After 12 h, the increase in the enzyme release is in agreement with the slow diffusion of the enzyme through the cavities of the capsule. At pH 5.0, the kinetics of release was overall slower than the one observed at pH 7.4. Such a difference in release profiles could be due to the greater stability of the constitutive MOF (and, thus, MOF capsule) in the acidic medium, releasing only a small amount of collagenase present inside the MIL-100 capsule and more pronounced degradation in a neutral PBS, which, consequently, led to a higher collagenase release [17]. This longer sustained release of the enzyme, which fits well with the one of MTX under the same conditions, can be explained by its localization within the core of the capsule. It is known that collagenase, as a large biomolecule 11.5 nm in diameter [30], cannot diffuse through the MIL-100(Fe) microporous windows; therefore, to be released, it must diffuse through the routes of inter-particular spaces.

The quantitative interpretation of the in vitro release values obtained is facilitated by using equations that mathematically translate the release profile according to some parameters, as shown in Tables S3–S5. Mathematical modelling has been an important tool regarding the physical–chemical processes involved during the drug release process in the studied matrix. The MTX and COL release from the MIL-100 NPs and MIL-100 capsules showed a correlation with the Korsmeyer–Peppas model and with anomalous or non-Fickian transport. The non-Fickian diffusion includes more than one physical–chemical process in release mechanisms simultaneously, such as swelling, diffusion and

system dissolution [31]. Thus, the release of MTX must occur by diffusion and erosion as the MIL-100 NPs degrade in the medium, likely to be associated with a change in their surface chemistry with the attack of the phosphate present in the medium [17].

Finally, in vitro collagenase activity experiments, whose photos are presented in Figure 7, showed that the MOF capsule carrier system with COL, as it was co-incubated with gelatin, maintained a liquid state, indicating that the gelatin was degraded, which demonstrated that the collagenase maintained an appropriate level of enzymatic activity after encapsulation to be used in association with the MTX to be used in antitumor application.

The cytotoxicity test results, shown in Table 1, highlight the strong selectivity of our system for the tumor cell line used in the experiment. The hollow MIL-100 capsule already showed tumor selectivity; however, it increased by nine times after MTX encapsulation and seven times after collagenase encapsulation. In addition, the SI assay showed that the multidrug incorporation of MTX and collagenase led to an even higher selectivity (×11), suggesting that the MTX@COL@MIL-100 capsule may have a potential role in the selective treatment of cancer cells. Therefore, such dual drug delivery systems developed based on MIL-100 capsules are promising candidates for multimodal antitumor treatment.

4. Materials and Methods

4.1. Production of MIL-100(Fe) Capsules by Spray-Drying

The spray-drying procedure was conducted on a laboratory scale (Mini Spray Dryer B290) with two concentric fluid nozzles (fluid and air). The key parameters controlling the final particle size are the spray mesh size, concentration of solids, pump flow and aspirator and inlet temperature [13]. The pre-formed MIL-100(Fe) NP suspension was injected simultaneously with hot air in the spray-drying apparatus with a nozzle orifice diameter of 0.5 mm. After a comprehensive investigation and studies previously carried out by some of us, the parameter settings were established, specifically a suspension concentration of 1 mg·mL^{-1}, inlet air temperature of 80 °C, outlet air temperature 45 °C, dry air pressure of 50 bar and pump flow rate 0.05 mL·min^{-1}.

4.2. Characterization

Powder X-ray diffraction patterns (PXRD) were obtained by a Bruker D8 Advance diffractometer (0–2θ) using Cu K_α radiation (λ = 1.5418 Å). Transmission IR spectra were recorded in the range of 400–4000 cm^{-1} on a Nicolet iS5 iD7 ATR spectrometer. N_2 sorption isotherms were obtained at 77 K using an ASAP porosimeter (accelerated surface area and porosimetry system, model 2013; Micromeritic) connected to a computer. Prior to the analysis, samples were evacuated at 120 °C under primary vacuum. Brunauer–Emmett–Teller (BET) surface area and pore volume were estimated at a relative pressure ranging from 0.05 and 0.25. Field emission gun scanning electron microscopy (FEGSEM) observations were obtained by using a TopconSM-300 microscope with a secondary electron detector and an electron acceleration voltage of 10 kV. Dual beam focused ion beam scanning electron microscope (FIB/SEM) images were obtained by using an FEI microscope (HELIOS NANOLAB 600i) with a gallium ion column. HRTEM images were recorded on a FEI Tecnai G^2 F20 transmission electron microscope (TEM) operating at 200 kV, equipped with an electron scattering transmission emission. Samples were prepared by the deposition of one droplet of colloidal suspension onto a carbon-coated copper grid, which was left to air dry.

4.3. Methotrexate Encapsulation and Release

Methotrexate was loaded by soaking 60 mg of MIL-100 NPs in 40 mL of an aqueous solution of MTX (1 mg·mL^{-1}) under constant stirring at 37 °C overnight. The suspension was then centrifuged (14,000 rpm, 10 min) and the supernatant was removed. The solid was washed two times with water, recovered by centrifugation (14,000 rpm, 10 min) and dried under vacuum overnight. The drug in the supernatant was measured in triplicate

by UV–Vis spectroscopy (Cary 60 Spectrophotometer; Agilent, Australia) at 306 nm. The entrapment efficiency (EE%) was calculated according to Equation (1).

$$\text{Entrapment efficiency (EE\%)} = \frac{\text{weight of drug in MIL} - 100 \text{ nanoparticles}}{\text{weight of drug fed initially}} \times 100 \quad (1)$$

The MTX release profiles were obtained by using simulated physiological media (phosphate buffered saline (PBS) solution 0.1 M) at pH 5.0 and pH 7.4, representing the cancer environment and the physiological pH, respectively. MTX@MIL-100(Fe) NPs and MTX@MIL-100 capsules (10 mg) were suspended in PBS solution (10 mL) and incubated at 37 °C under constant stirring, prepared in triplicate. Samples were removed after 0.5, 1, 2, 3, 4, 6, 7, 8, 12, 24 and 48 h, and an identical volume of fresh PBS was immediately replaced, keeping up the MTX concentration far from saturation.

The release of MTX was quantified in triplicate by UV–Vis spectroscopy (Cary 60 Spectrophotometer; Agilent, Sidney, Australia) at 306 nm.

4.4. Collagenase Encapsulation and Release

Collagenase was loaded into the capsule through a spray-drying technique. Collagenase (10 mg) was added into 50 mL of an MTX@MIL-100 capsule ethanolic suspension (1 mg·mL^{-1}). The mixture was quickly subjected to spray-drying using the parameters described in Section 4.1. Low-temperature dry air was used for limiting enzyme denaturation. After obtaining the MTX@col@MIL-100 capsules by spray-drying, the material was washed three times with water to remove any free collagenase present at the outer surface of the capsules. The presence of collagenase in the supernatant was determined in triplicate through UV–Vis spectroscopy (Cary 60 Spectrophotometer; Agilent, Australia) at 258 nm.

The release of collagenase was studied by suspending 10 mg of the drug-loaded MOF capsule powder in 30 mL of PBS (pH 7.4 and pH 5). This suspension (in triplicate) was kept under constant stirring for 48 h at 37 °C. At each time point, a 0.5-mL aliquot of supernatant was recovered following centrifugation (14,000 rpm, 10 min) and replaced with the same volume of fresh PBS, keeping up the total volume of solution. The release of collagenase was quantified in triplicate by UV–Vis spectroscopy (Cary 60 Spectrophotometer; Agilent, Australia) at 258 nm.

The in vitro release data were analyzed according to various kinetic models, including zero order, first order, Korsmeywer–Peppas and Huguchi models, to determine the most appropriate release models that described the release patterns of the drug and enzyme. Model selection was based on the highest correlation coefficient (r) of the assessed parameters, as suggested by Burnham and Anderson (Table S1) [32].

4.5. Enzymatic Activity

The enzymatic activity of collagenase after encapsulation within the MOF capsules was investigated according to the procedure previously described by Wang et al. (2018) [33]. First, 30 mg/mL of an aqueous solution of gelatin type B (from bovine Sigma-Aldrich G9391) was prepared at 37 °C. The gelatin solution was divided into seven groups: pure gelatin, MIL-100 capsules, free collagenase, free MTX, MTX@MIL-100 capsules, col@MIL-100 capsules and MTX@col@MIL-100 capsules. The collagenase concentration was equal in all samples, based on the amount encapsulated in the MOF capsules. For each time interval (3, 12 and 24 h), the sample was stored at 4 °C for 30 min before an image was obtained using a digital camera.

4.6. In Vitro Toxicity Assay

The cell viability of HaCaT (human keratinocytes) and A-375 (human melanoma) cell lines was determined by resazurin redox assay according to the procedure described by Pagé and coauthors [22] and adapted by Pavan and collaborators [34]. Cells were cultured in DMEM-HG supplemented with 10% FBS (Gibco) and 1% antibiotic gentamicin sulfate (50 mg/L) and antimycotic solution, amphotericin B (2 mg/L), at 37 °C, with 5% CO_2 and

95% humidity. Cells were seeded into 96-well microplates (TPP) to achieve a concentration of 1×10^6 cells/well, then incubated under standard culture conditions for 24 h to allow cell adhesion. The free MTX, MIL-100 capsule, MTX@MIL-100 capsule, collagenase, collagenase@MIL-100 capsule and MTX@collagenase@MIL-100 capsule treatments were prepared and incubated in serial dilutions starting at a concentration of 150 μg/mL. The positive control consisted of wells containing cells and the negative control consisted of only culture medium. The microplates were again incubated for 24 h. After this period, the culture medium was removed and 50 μL of 0.01% resazurin was added. The plates were again incubated for 2 h, then the fluorescence was read in a Synergy H1 microplate reader (excitation at 530 nm and emission at 590 nm). The resulting fluorescence signals were normalized to the fluorescence signal of the negative control. The IC_{50} was defined as the highest concentration that allowed 50% cell viability. All experimental points were assessed in duplicate, and bars represented the standard error of the mean.

5. Conclusions

Spherical metal–organic capsules, based on MOF MIL-100(Fe) capsules, were successfully synthesized through a gentle green and scalable low-temperature spray-drying process, starting from pre-formed small-size nanoparticles (<100 nm). The sub-micron-size (800 nm) capsules revealed good stability and large internal voids (30 nm), which combined to the intrinsic porous character of the MOF NPs, making them promising as a dual drug carrier system. The capsules could successfully concomitantly encapsulate a high loading of the anticancer drug MTX and collagenase associated with a controlled release in PBS over a few days, slower than what was achieved for the bare nanoparticles. The loaded MIL-100 capsule was found to be safe when applied to normal cells, while the drug loaded capsules showed a synergetic effect between MTX and collagenase, known to enhance the degradation of the dense extracellular matrix (ECM) around tumor cells through in vitro activity tests. This confirms the high potential of such porous MOF capsules as multimodal antitumor therapies.

Supplementary Materials: The following supporting information can be downloaded at: https://www.mdpi.com/article/10.3390/ijms23147670/s1.

Author Contributions: Data curation, M.P.A., G.P., H.Z. and A.M.; funding acquisition, M.P.A. and L.A.C.; investigation, M.P.A., R.C.G.F., C.B., C.S. and L.A.C.; writing—original draft, M.P.A. and G.P.; writing—review and editing, R.C.G.F., F.R.P., C.B., C.S. and L.A.C. All authors have read and agreed to the published version of the manuscript.

Funding: This work was supported by National Council for Scientific and Technological Development (CNPq)—Brazil, Coordination for the Improvement of Higher Education Personnel—Brazil (CAPES) Finance Code 001 and São Paulo Research Foundation (FAPESP) (16/11563-4 and 18/00442-7) Brazilian agencies.

Institutional Review Board Statement: Not applicable.

Informed Consent Statement: Not applicable.

Data Availability Statement: Not applicable.

Acknowledgments: We would like to acknowledge all researchers in our laboratory for their help. Some of the authors thank Anselmo Gomes de Oliveira from the School of Pharmaceutical Sciences of São Paulo State University, UNESP and Celso Valentim Santilli from the Chemistry Institute of São Paulo State University, UNESP.

Conflicts of Interest: The authors declare no conflict of interest.

References

1. Hoskins, B.F.; Robson, R. Infinite Polymeric Frameworks Consisting of Three Dimensionally Linked Rod-like Segments. *J. Am. Chem. Soc.* **1989**, *111*, 5962–5964. [CrossRef]

2. Bowen, R.J.; Fernandes, M.A.; Hitchcock, P.B.; Lappert, M.F.; Layh, M. Synthesis and Crystal Structures of Novel 1-Aza-2-Silacyclobut-3-Enes. *J. Chem. Soc. Dalton Trans.* **2002**, *16*, 3253–3259. [CrossRef]
3. Yaghi, O.M.; Li, G.; Li, H. Selective Binding and Removal of Guests in a Microporous Metal–Organic Framework. *Nature* **1995**, *378*, 703–706. [CrossRef]
4. Horcajada, P.; Gref, R.; Baati, T.; Allan, P.K.; Maurin, G.; Couvreur, P.; Ferey, G.; Morris, R.E.; Serre, C. Metal–Organic Frameworks in Biomedicine. *Chem. Rev.* **2011**, *112*, 1232–1268. [CrossRef]
5. Ameloot, R.; Vermoortele, F.; Vanhove, W.; Roeffaers, M.B.J.; Sels, B.F.; De Vos, D.E. Interfacial Synthesis of Hollow Metal–Organic Framework Capsules Demonstrating Selective Permeability. *Nat. Chem.* **2011**, *3*, 382–387. [CrossRef]
6. Shi, J.; Zhang, L.; Jiang, Z. Facile Construction of Multicompartment Multienzyme System through Layer-by-Layer Self-Assembly and Biomimetic Mineralization. *ACS Appl. Mater. Interfaces* **2011**, *3*, 881–889. [CrossRef]
7. Guo, J.; Ping, Y.; Ejima, H.; Alt, K.; Meissner, M.; Richardson, J.J.; Yan, Y.; Peter, K.; von Elverfeldt, D.; Hagemeyer, C.E. Engineering Multifunctional Capsules through the Assembly of Metal–Phenolic Networks. *Angew. Chem. Int. Ed.* **2014**, *53*, 5546–5551. [CrossRef]
8. Bian, Z.; Xu, J.; Zhang, S.; Zhu, X.; Liu, H.; Hu, J. Interfacial Growth of Metal Organic Framework/Graphite Oxide Composites through Pickering Emulsion and Their CO_2 Capture Performance in the Presence of Humidity. *Langmuir* **2015**, *31*, 7410–7417. [CrossRef]
9. Sosnik, A.; Seremeta, K.P. Advantages and Challenges of the Spray-Drying Technology for the Production of Pure Drug Particles and Drug-Loaded Polymeric Carriers. *Adv. Colloid Interface Sci.* **2015**, *223*, 40–54. [CrossRef]
10. Ré, M. Formulating Drug Delivery Systems by Spray Drying. *Dry. Technol.* **2006**, *24*, 433–446. [CrossRef]
11. Garcia Marquez, A.; Horcajada, P.; Grosso, D.; Ferey, G.; Serre, C.; Sanchez, C.; Boissiere, C. Green Scalable Aerosol Synthesis of Porous Metal-Organic Frameworks. *Chem. Commun.* **2013**, *49*, 3848–3850. [CrossRef]
12. Carné-Sánchez, A.; Imaz, I.; Cano-Sarabia, M.; Maspoch, D. A Spray-Drying Strategy for Synthesis of Nanoscale Metal–Organic Frameworks and Their Assembly into Hollow Superstructures. *Nat. Chem.* **2013**, *5*, 203–211. [CrossRef]
13. Arpagaus, C.; Collenberg, A.; Rütti, D.; Assadpour, E.; Jafari, S.M. Nano Spray Drying for Encapsulation of Pharmaceuticals. *Int. J. Pharm.* **2018**, *546*, 194–214. [CrossRef]
14. Horcajada, P.; Surblé, S.; Serre, C.; Hong, D.Y.; Seo, Y.K.; Chang, J.S.; Grenèche, J.M.; Margiolaki, I.; Férey, G. Synthesis and Catalytic Properties of MIL-100(Fe), an Iron(III) Carboxylate with Large Pores. *Chem. Commun.* **2007**, *100*, 2820–2822. [CrossRef]
15. Horcajada, P.; Chalati, T.; Serre, C.; Gillet, B.; Sebrie, C.; Baati, T.; Eubank, J.F.; Heurtaux, D.; Clayette, P.; Kreuz, C.; et al. Porous Metal–Organic-Framework Nanoscale Carriers as a Potential Platform for Drug Delivery and Imaging. *Nat. Mater.* **2010**, *9*, 172–178. [CrossRef]
16. Bellido, E.; Guillevic, M.; Hidalgo, T.; Santander-Ortega, M.J.; Serre, C.; Horcajada, P. Understanding the Colloidal Stability of the Mesoporous MIL-100(Fe) Nanoparticles in Physiological Media. *Langmuir* **2014**, *30*, 5911–5920. [CrossRef]
17. Christodoulou, I.; Bourguignon, T.; Li, X.; Patriarche, G.; Serre, C.; Marli, C.; Gref, R. Degradation Mechanism of Porous Metal-Organic Frameworks by In Situ Atomic Force Microscopy. *Nanomaterials* **2021**, *11*, 722. [CrossRef]
18. Dhand, C.; Prabhakaran, M.P.; Beuerman, R.W.; Lakshminarayanan, R.; Dwivedi, N.; Ramakrishna, S. Role of Size of Drug Delivery Carriers for Pulmonary and Intravenous Administration with Emphasis on Cancer Therapeutics and Lung-Targeted Drug Delivery. *RSC Adv.* **2014**, *4*, 32673–32689. [CrossRef]
19. Fernández-Paz, C.; Rojas, S.; Salcedo-Abraira, P.; Remuñán-López, C.; Horcajada, P. Biological and Medical Applications of Materials and Interfaces Metal-Organic Framework Microspheres Formulation for Pulmonary Administration Metal-Organic Framework Microspheres Formulation for Pulmonary. *ACS Appl. Mater. Interfaces* **2020**, *12*, 25676–25682. [CrossRef]
20. Panchal, M.; Nouar, F.; Serre, C.; Benzaqui, M.; Sene, S.; Steunou, N.; Giménez Marqués, M. Low Temperature Process for the Synthesis of Mof Carboxylate Nanoparticles. U.S. Patent US11034711B2, 29 January 2018.
21. Collagenase-Creative Enzymes. Available online: https://www.creative-enzymes.com/similar/collagenase_148.html (accessed on 28 January 2022).
22. Page, B.; Page, M.; Noel, C. A New Fluorometric Assay for Cytotoxicity Measurements In Vitro. *Int. J. Oncol.* **1993**, *3*, 473–476. [CrossRef]
23. de Souza Lima, R.; Ré, M.I.; Arlabosse, P. Drying Droplet as a Template for Solid Formation: A Review. *Powder Technol.* **2020**, *359*, 161–171. [CrossRef]
24. Li, Y.; Lin, J.; Wu, H.; Jia, M.; Yuan, C.; Chang, Y. Novel Methotrexate Prodrug-Targeted Drug Delivery System Based on PEG—Lipid—PLA Hybrid Nanoparticles for Enhanced Anticancer e Ffi Cacy and Reduced Toxicity of Mitomycin C. *J. Chem. B* **2014**, *2*, 6534–6548. [CrossRef]
25. Chatterjee, M.; Maity, R.; Das, S.; Mahata, N.; Basu, B.; Chanda, N. Electrospray Based Fluorescent Nanoparticle Synthesis from Pyrene Butyric Acid-Functionalized Poly (D, L-Lactide-Co-Glycolide) Polymer for the Efficient Delivery of Anticancer Drug and Self-Monitoring Its Effect in the Drug-Resistant Breast Cancer Cells. *Mater. Adv.* **2020**, *1*, 3033–3048. [CrossRef]
26. Soria-Valles, C.; Gutiérrez-Fernández, A.; Guiu, M.; Mari, B.; Fueyo, A.; Gomis, R.R.; López-Otín, C. Correction: The Anti-Metastatic Activity of Collagenase-2 in Breast Cancer Cells Is Mediated by a Signaling Pathway Involving Decorin and MiR-21. *Oncogene* **2019**, *38*, 5739. [CrossRef]
27. Jang, B.; Kwon, H.; Katila, P.; Lee, S.J.; Lee, H. Dual Delivery of Biological Therapeutics for Multimodal and Synergistic Cancer Therapies. *Adv. Drug Deliv. Rev.* **2016**, *98*, 113–133. [CrossRef]

28. Abánades Lázaro, I.; Wells, C.J.R.; Forgan, R.S. Multivariate Modulation of the Zr MOF UiO-66 for Defect-Controlled Combination Anticancer Drug Delivery. *Angew. Chem. Int. Ed.* **2020**, *59*, 5211–5217. [CrossRef]
29. Trotta, M.; Peira, E.; Carlotti, M.E.; Gallarate, M. Deformable Liposomes for Dermal Administration of Methotrexate. *Int. J. Pharm.* **2004**, *270*, 119–125. [CrossRef]
30. Eckhard, U.; Schönauer, E.; Nüss, D.; Brandstetter, H. Europe PMC Funders Group. Structure of Collagenase G Reveals a Chew and Digest Mechanism of Bacterial Collagenolysis. *Nat. Struct. Mol. Biol.* **2012**, *18*, 1109–1114. [CrossRef]
31. Korsmeyer, R.W.; Peppas, N.A. Macromolecular and Modeling Aspects of Swelling Controlled System. *Control. Drug Deliv. Syst.* **1992**, *196*, 83.
32. Burnham, K.P.; Anderson, D.R. A Practical Information-Theoretic Approach. In *Model Selection Multimodel Inference*, 2nd ed.; Springer: New York, NY, USA, 2002; Volume 2.
33. Wang, X.; Luo, J.; He, L.; Cheng, X.; Yan, G.; Wang, J.; Tang, R. Hybrid PH-Sensitive Nanogels Surface-Functionalized with Collagenase for Enhanced Tumor Penetration. *J. Colloid Interface Sci.* **2018**, *525*, 269–281. [CrossRef] [PubMed]
34. Pavan, F.R.; da S. Maia, P.I.; Leite, S.R.A.; Deflon, V.M.; Batista, A.A.; Sato, D.N.; Franzblau, S.G.; Leite, C.Q.F. Thiosemicarbazones, Semicarbazones, Dithiocarbazates and Hydrazide/Hydrazones: Anti-Mycobacterium Tuberculosis Activity and Cytotoxicity. *Eur. J. Med. Chem.* **2010**, *45*, 1898–1905. [CrossRef]

Résumé - Francais

Résumé - Francais

L'objectif de cette thèse est de développer de nouveaux matériaux hiérarchisés associant des nanoparticules/nanoclusters inorganiques et des MOFs (metal-organic frameworks), pour des applications en théranostique dans le traitement de certaines maladies inflammatoires et de cancers. Les solides poreux tels que les MOFs ont récemment fait l'objet d'une attention considérable pour la libération contrôlée de médicaments et sont actuellement développés en théranostique à des fins de médecine personnalisée. En terme de construction de MOFs théranostiques, l'une des principales stratégies consiste à encapsuler directement des nanoparticules inorganiques dans des MOFs. Cependant, la majorité des travaux reposent sur des synthèses complexes dans des conditions "dures", en présence de réactifs parfois toxiques, ce qui représente un frein évident pour des applications pratiques notamment en biomédecine. Pour surmonter ce défi, nous avons synthétisé une série de NPs@MOF via une stratégie de synthèse *in situ* à température ambiante. En choisissant le MOF MIL-100(Fe), carboxylate de fer mésoporeux peu toxique, comme exemple représentatif, nous avons obtenu pour la première fois des nanocomposites maghemite@MIL-100(Fe) et nanoclusters d'or@MIL-100(Fe). Ces nanocomposites ont montré une capacité d'encapsulation de principes actifs élevée, une libération contrôlée de ces principes actifs, sensible aux stimuli, et d'excellents effets anti-inflammatoires. En outre, ces nanocomposites sont prometteurs pour des applications en imagerie telles que l'imagerie par résonance magnétique (IRM) et l'imagerie de fluorescence dans la seconde fenêtre proche infrarouge (NIR II). De plus, outre le MIL-100(Fe), les nanoclusters d'or (Au NCs) stabilisés/fonctionnalisés par la cystéine, et présentant des propriétés optiques potentiellement améliorées, pourraient également être encapsulés dans des MOF à base de zinc (ZIF-8) et des MOF à base de zirconium (UiO-66) ; les propriétés des nanocoomposites ainsi obtenus n'ont pas été entièrement étudiées en raison de contraintes de temps.

Dans le détail, cette thèse est divisée en cinq chapitres, résumés ci-dessous :

1. Introduction : Nanoparticules pour des traitements anti-inflammatoires et MOFs fonctionnels pour des applications en théranostique
2. Nanovecteurs MOFs superparamagnétiques hiérarchisés pour des applications en nanomédecine anti-inflammatoire théranostique
3. Nanoclusters d'or - MIL-100(Fe) pour l'administration de dexaméthasone et la thérapie synergique des maladies inflammatoires
4. Nouveaux hybrides nanoclusters d'or@MOFs
5. Discussion générale et perspectives

Le chapitre 1 est divisé en deux parties, à savoir «les nanoparticules pour l'anti-inflammation» et «les MOF fonctionnels pour des applications en théranostique». La première partie est consacrée à l'état de l'art sur les nanoparticules utilisées pour des traitements anti-inflammatoires. Ces nanoparticules sont utilisées soit comme vecteurs pour la libération de médicaments anti-inflammatoires soit directement en tant qu'agents anti-inflammatoires. Concernant leur utilisation comme vecteur de principe actif, les nanoparticules à base de polymères et les nanoparticules à base de lipides ont été largement utilisées pour l'administration de médicaments anti-inflammatoires et elles sont prometteuses pour le transfert clinique. Dans le même temps, il a également été démontré que les nanoparticules de silice mésoporeuses, en tant que matériaux poreux, permettent une libération contrôlée des médicaments anti-inflammatoires. D'autres nanoparticules inorganiques telles que les nanoparticules d'or, d'argent, de zinc ou d'oxyde de cérium possèdent des propriétés anti-inflammatoires intrinsèques en diminuant l'expression des cytokines pro-inflammatoires, en inhibant l'activation de la voie inflammatoire ou en diminuant la production de dérivés réactifs de l'oxygène (ROS) par des activités enzyme-mimétique. Au delà des nanoparticules précédentes, les nanoparticules biomimétiques, en camouflant les nanoparticules avec la membrane cellulaire, ont permis de réduire la capture et l'élimination par le système immunitaire, facilitant une libération ciblée du principe actif. Ces 15 dernières années, les MOF se sont avérés être très prometteurs comme vecteurs pour la libération contrôlée de médicaments en raison de leur porosité élevée et de leur grande diversité chimique et structurale. Plus récemment, ils ont été utilisés comme vecteurs de principes actifs pour le traitement de maladies inflammatoires. La théranostique est un concept combinant thérapie et diagnostic, et dans la seconde partie de ce chapitre, un chapitre de livre publié en 2020 (Metal-Organic Frameworks for biomedical applications, Elsevier, 2020, 397-423) résume l'état de l'art sur les MOFs fonctionnels pour des applications en théranostique. Compte tenu du développement rapide et récent dans le domaine au cours des deux à trois dernières années, le chapitre de livre a été mis à jour avec les articles récemment publiés. En résumé, sont principalement présentés les MOFs à l'échelle nanométrique utilisés en théranostique pour le traitement de cancers et autres maladies théranostiques, au cours des dix dernières années, ainsi que des séries de MOF pour des applications en théranostique tels que des nanoMOF magnétiques, des nanoMOF incorporant des nanoparticules de métaux nobles, des nanoMOF enrobés de polymères, des nanoMOF fluorescents, des nanoMOFs pour laphotothérapie, des nanoMOFs pour l'imagerie médicale ainsi que des nanoMOFs sensibles à des stimuli. Notablement, les MOF hiérarchisés ouvrent une nouvelle voie pour concevoir des systèmes avancés d'imagerie multimodale et de thérapie synergique.

Dans le chapitre 2, un nanoobjet hiérarchisé poreux (noté USPIO@MIL) a été obtenu par une stratégie de synthèse *in situ* à température ambiante, combinant un nanoMOF de référence (nanoparticules de

MIL-100(Fe)) et des particules d'oxyde de fer superparamagnétique (USPIO, ultrasmall superparamagnetic iron oxide, ou maghémite). Brièvement, pour obtenir des hétérostructures USPIO@MIL, des USPIO préformées ont été mélangées avec des précurseurs de MIL-100(Fe) dans l'eau à température ambiante. La méthode de synthèse est facile, peu onéreuse, respectueuse de l'environnement et peut aisément être mise à l'échelle. Le couplage synergique des propriétés physico-chimiques et fonctionnelles des nanoparticules USPIO et MIL-100(Fe) confère à ces nano-objets des caractéristiques intéressantes telles qu'une stabilité colloïdale élevée, une biodégradabilité, une faible toxicité, une capacité élevée d'encapsulation et une libération contrôlée de médicaments ainsi que des propriétés superparamagnétiques. Notablement, en plus des techniques courantes de marquage par fluorescence, à notre connaissance, l'ensemble du processus d'internalisation et de dégradation cellulaire de nanoparticules hiérarchisées USPIO@MIL a été visualisé pour la première fois par Bio-TEM. Après plus d'une semaine de suivi, leur biodégradabilité a été largement confirmée. Ce nanoporteur bimodal USPIO@MIL possédait une grande capacité d'encapsulation de médicaments anti-tumoraux ou anti-inflammatoires (doxorubicine ou méthotrexate), et étonnamment, l'encapsulation de doxorubicine s'est avérée quatre fois plus élevée par rapport au MIL-100(Fe) reporté précédemment, sans doute en raison de défauts dans la structure du MOF. La libération contrôlée par des stimuli de doxorubicine encapsulé dans les USPIO@MIL a permis de mettre en évidence des activités anti-inflammatoires et anti-tumorales élevées. De plus, les nanoobjets USPIO@MIL ont présenté d'excellentes propriétés relaxométriques et leur utilisation en tant qu'agent de contraste efficace pour l'imagerie par résonance magnétique a été démontrée. Ce chapitre met en évidence le fort potentiel des maghemite@MOF, intégrant des fonctions d'imagerie et de thérapie, pour des applications en théranostique anti-inflammatoire. Ce travail a été soumis sous forme de publication.

Dans le chapitre 3, suivant la stratégie décrite dans le chapitre 2, des nanoparticules de nanoclusters d'or@MIL (Au NCs@MIL) ont été synthétisés en encapsulant des nanoclusters d'or stabilisés/fonctionnalisés par le glutathion ($Au_{25}SG_{18}$ NCs) dans le MOF MIL-100(Fe). Le phosphate de dexaméthasone (DexP) est un anti-inflammatoire glucocorticoïde, dont les dimensions permettent d'envisager son encapsulation dans les mésopores du MIL-100(Fe). Par ailleurs,la coordination des groupements phosphate du DexP sur les sites acides de Lewis du MIL-100(Fe) peut aussi être envisagée. Comme attendu, les nanoparticules Au NCs@MIL hiérarchisées ont montré une capacité d'encapsulation du DexP (Au NCs@MIL/DexP) élevée et une libération contrôlée du DexP, sensible aux stimuli. Les résultats sont comparables à ceux décrits dans le chapitre 2 pour les USPIO@MIL encapsulant du méthotrexate. De plus, le copolymère acide hyaluronique-polydopamine (HA-PDA) a pu être utilisé pour recouvrir le nanoMOF et ralentir la libération de DexP par les nanoparticules Au

NCs@MIL/DexP dans un environnement physiologique neutre. Outre le DexP, les nanoclusters d'or pourraient également agir comme agents thérapeutiques anti-inflammatoires tout en présentant un potentiel en imagerie médicale. En termes d'anti-inflammation in vitro, les nanoparticules Au NCs@MIL/DexP ont spécifiquement inhibé la croissance des cellules inflammatoires, piégé les dérivés réactifs de l'oxygène intracellulaire (ROS) et abaissé la sécrétion de cytokines pro-inflammatoires. Ils pourraient par ailleurs bloquer efficacement certaines voies inflammatoires telles que la voie du facteur nucléaire kappa B (NF-κB) et la voie du facteur régulateur de l'interféron (IRF). Au total, la co-libération de principes actifs et de nanoclusters métalliques par les MOF permet de proposer une nouvelle approche pour le traitement et le diagnostic des maladies inflammatoires. La rédaction d'un article sur ce travail est en cours.

Le chapitre 4 est consacré au développement de nouveaux hybrides Au NCs@MOFs aux propriétés optiques améliorées. Les propriétés de fluorescence dans la seconde fenêtre de l'infrarouge (NIR-II) des nanoclusters $Au_{25}SG_{18}$ sont quenchées en présence de MIL-100(Fe). Dans ce chapitre 4, des nanoclusters d'or Au_{25} ont été stabilisés par la cystéine ($Au_{25}Cys_{18}$ NCs) et différents MOF ont été utilisés afin de limiter/supprimer ce quenching de fluorescence. En utilisant l'approche décrite au chapitre 3, synthèse *in* situ à température ambiante, une variété de nanoobjets Au NCs@MOF ont été synthétisés et caractérisés : $Au_{25}Cys_{18}$ NCs ont été utilisés ainsi que différents MOF (MIL-100(Fe), ZIF-8 (Zn) et UiO-66 (Zr)). Il n'a pas été possible de finaliser l'ensemble des caractérisations de ces nanocomposites pour des raisons de temps. Leurs applications possibles en bio-imagerie, pour l'administration de médicaments, le traitement antimicrobien ou même en catalyse sont finalement discutées en perspectives.

Dans le dernier chapitre, une conclusion générale est proposée ainsi que des perspectives telles que des applications antiinflammatoires et antibactériennes in vivo, par thérapie combinée chimio- et photodynamique, l'imagerie de fluorescence dans la seconde fenêtre infrarouge et en catalyse. Par ailleurs, des travaux et articles dans lesquels je suis co-auteur sont présentés en annexe.

RÉSUMÉ

Les MOFs (Metal-Organic Frameworks) présentent un intérêt particulier pour la libération contrôlée de principes actifs en raison de leur porosité importante et de leur grande versatilité. Ces dernières années, en lien avec le principe de la théranostique, un nombre croissant de MOFs nanométriques (nanoMOFs) ont été développés pour le traitement de tumeurs. Concernant le traitement de maladies inflammatoires, l'utilisation de nanoMOFs reste peu développée. Dans cette thèse, des nanoparticules de maghémite et des nanoparticules d'or ont été associées à des nanoparticules de MIL-100(Fe) en utilisant une stratégie de synthèse *in situ*, "verte" et à température ambiante. Les hétérostructures ainsi obtenues ont été étudiées pour des applications de libération de médicaments. Ces MOFs hiérarchisés biodégradables montrent de remarquables capacités d'encapsulation de médicaments, une libération contrôlée de ces principes actifs, d'excellents effets anti-inflammatoires et sont prometteurs pour des applications en imagerie de résonance magnétique (MRI). Par ailleurs, des nanoclusters Au_{25} ont été associés à différents nanoMOFs biocompatibles à base de zinc ou de zirconium, ouvrant des perspectives prometteuses pour le suivi de traitements par imagerie de fluorescence dans la seconde fenêtre du proche infrarouge.

MOTS CLÉS

Metal-organic frameworks (MOFs), nanoparticules, maghémite, clusters d'or, synthèse *in situ*, anti-inflammatoire, théranostique

ABSTRACT

Metal-Organic Frameworks (MOFs) are of strong interest in drug delivery due to their porosity and versatility. Encouraged by the concept of “theranostics”, an increasing number of theranostic nanoscale MOFs (nanoMOFs) have been widely developed for tumor treatment in recent years. However, concerning inflammatory disease therapy, nanoMOFs are still in their infancy. *Via* an *in situ* room temperature green synthesis strategy, maghemite nanoparticles and gold nanoclusters (Au_{25} NCs) have been successfully integrated into MIL-100(Fe) nanoparticles in this thesis. The obtained heterostructures were further investigated for drug delivery applications. These biodegradable hierarchical MOFs showed extremely high drug loading capacity, stimuli-responsive release and ideal anti-inflammatory effects including promises for magnetic resonance imaging (MRI). As a perspective study, fluorescent cysteine capped Au_{25} NCs could also be assembled into different biocompatible zinc or zirconium based nanoMOFs, which paves the way for near infrared II window fluorescence imaging guided therapy.

KEYWORDS

Metal-organic frameworks (MOFs), nanoparticles, maghemite, gold clusters, *in situ* synthesis, anti-inflammatory, theranostics